JOINT INSTITUTE FOR NUCLEAR RESEARCH

December 9, 2022

Technical Design Report of the Spin Physics Detector

The SPD collaboration

Draft version 2022.057

This draft is the internal document of the SPD collaboration and must not be shown in public!

Contents

Preface

According to astrophysical and cosmological data, the relative contribution of visible baryonic matter, properties of which are determined by strong and electromagnetic interactions, is about 5% of the Universe mass. With respect to two other components, dark matter and dark energy, baryonic matter seems to be a well-studied subject. In fact, despite the great advances in quantum chromodynamics made in describing the interaction of quarks and gluons within the framework of the perturbative approach, the question of why nucleons are exactly like we see them, remains open. Understanding the structure and fundamental properties of the nucleon directly from the dynamics of its quarks and gluons based on first principles is one of the main unsolved problems of QCD.

The nucleon behaves like a spinning top with a spin of $\hbar/2$. This spin is responsible for such fundamental properties of Nature as the nucleon magnetic moment, different phases of matter at low temperatures, the properties of neutron stars, and the stability of the known Universe. That is why the study of the spin structure of the nucleon is of particular importance. The naive quark model has successfully predicted most of the gross properties of hadrons, such as charge, parity, isospin and symmetry properties and their relations. Some of the dynamics of particle interactions can be qualitatively understood in terms of this model as well. However, the model falls short of explaining the spin properties of hadrons in terms of their constituents. Since the famous "spin crisis" that began in 1987, the problem of the nucleon spin structure remains one of the most intriguing puzzles in contemporary high-energy physics. The central problem, for many years attracting both enormous theoretical and experimental efforts, is the problem of how the spin of the nucleon is built up from spins and orbital momenta of its constituents – the valence and sea quarks as well as gluons. A full description can be given in terms of the so-called transverse-momentum dependent parton distribution functions.

Over the last 25 years, both polarized deep inelastic scattering experiments (CERN, DESY, JLab, SLAC) and high-energy polarized proton-proton collisions (RHIC at BNL) have been the major providers of information about spin-dependent structure functions of the nucleon. Nevertheless, our knowledge of the internal structure of the nucleon is still limited. This is especially true of the gluon contribution. New facilities for spin physics, such as the Electron-Ion Collider at BNL and the fixed-target experiments at CERN LHC are planned to be built in the near future to obtain the missing information.

The Spin Physics Detector, a universal facility for studying the nucleon spin structure and other spin-related phenomena with polarized proton and deuteron beams, is proposed to be placed in one of the two interaction points of the NICA collider that is under construction at the Joint Institute for Nuclear Research (Dubna, Russia). At the heart of the project is extensive experience with polarized beams at JINR. The main objective of the proposed experiment is the comprehensive study of the unpolarized and polarized gluon content of the nucleon. Spin measurements at the Spin Physics Detector at the NICA collider have bright prospects to make a unique contribution and challenge our understanding of the spin structure of the nucleon.

The Conceptual Design Report of the Spin Physics Detector was presented at the 54th meeting of the

JINR Program Advisory Committee for Particle Physics in Jan. 2021 and approved at the 56th meeting in Jan. 2022 based on the report of the international SPD Detector Advisory Committee.

In this document the Technical Design of the Spin Physics Detector is presented.

Chapter 1

Executive summary

The Spin Physics Detector collaboration proposes to install a universal detector in the second interaction point of the NICA collider under construction (JINR, Dubna) to study the spin structure of the proton and deuteron and other spin-related phenomena using a unique possibility to operate with polarized proton and deuteron beams at a collision energy up to 27 GeV and a luminosity up to 10^{32} cm^{-2} s^{-1}. As the main goal, the experiment aims to provide access to the gluon TMD PDFs in the proton and deuteron, as well as the gluon transversity distribution and tensor PDFs in the deuteron, via the measurement of specific single and double spin asymmetries using different complementary probes such as charmonia, open charm, and prompt photon production processes. Other polarized and unpolarized physics is possible, especially at the first stage of NICA operation with reduced luminosity and collision energy of the proton and ion beams. The SPD physics program is described in detail in [1–3]. This document is dedicated exclusively to technical issues of the SPD setup construction.

The SPD experimental setup is designed as a universal 4π detector with advanced tracking and particle identification capabilities based on modern technologies that will be installed in the SPD experimental hall of the NICA collider. The silicon vertex detector (VD) will provide resolution for the vertex position on the level of below 100 μm needed for reconstruction of secondary vertices of D-meson decays. The straw tube-based tracking system (ST) placed within a solenoidal magnetic field of up to 1 T at the detector axis should provide the transverse momentum resolution $\sigma_{p_T}/p_T \approx 2\%$ for a particle momentum of 1 GeV/c. The time-of-flight system (PID) with a time resolution of about 60 ps will provide 3σ π/K and K/p separation of up to about 1.2 GeV/c and 2.2 GeV/c, respectively. Possible use of the aerogel-based Cherenkov detector in the end-caps will extend this range. Detection of photons will be provided by the sampling electromagnetic calorimeter (ECal) with the energy resolution $\sim 5\%/\sqrt{E}$. To minimize multiple scattering and photon conversion effects for photons, the detector material will be kept to a minimum throughout the internal part of the detector. The muon (range) system (RS) is planned for muon identification. It can also act as a rough hadron calorimeter. The pair of beam-beam counters (BBC) and zero-degree calorimeters will be responsible for the local polarimetry and luminosity control. To minimize possible systematic effects, SPD will be equipped with a free-running (triggerless) DAQ system. A high collision rate (up to 4 MHz) and a few hundred thousand detector channels pose a significant challenge to the DAQ, online monitoring, offline computing system, and data processing software.

The SPD operation should start already in 2028 using the possibilities of polarized p-p and d-d collisions at $\sqrt{s} < 9.4$ GeV and $\sqrt{s} < 4.5$ GeV/nucleon, respectively, as well as A-A collisions. The starting configuration should consist of the range system, solenoidal magnet, straw tube-based tracking system, and a pair of zero-degree calorimeters. A simple micromegas-based central tracker will be installed in

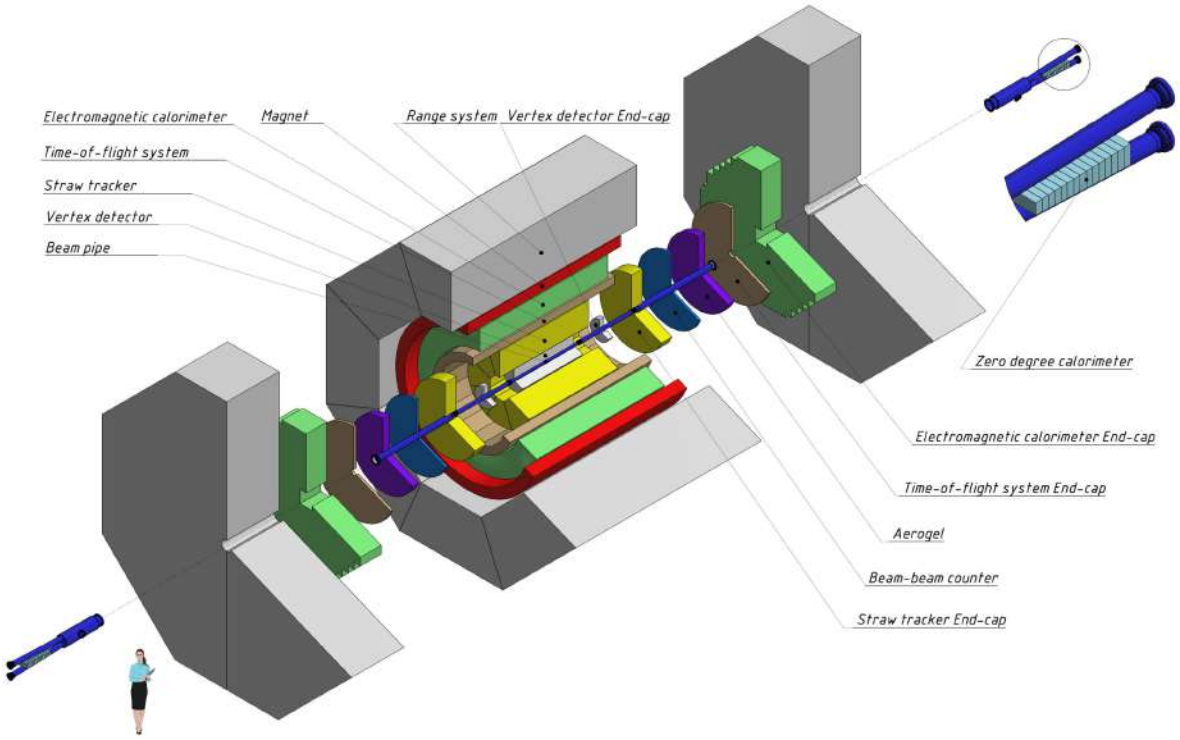

Figure 1.1: General layout of the SPD setup.

the central region instead of the sophisticated silicone vertex detector to keep a reasonable momentum resolution.

The estimated cost of the Spin Physics Detector in its full configuration is about 80 M$ at current prices (**Feb, 2022, 1 Euro = 1.15$**). 40 M$ of this amount is the cost of the first stage. Any expenses related to the development and construction of the infrastructure for polarized beams at NICA are out of this estimation.

Chapter 2

General concept of the SPD experiment

NICA, a new research facility aimed at the study of the properties of the strong interaction, is under construction at JINR and should be put to operation at the end of 2023. At the first stage of operation, the study of hot and dense baryonic matter will be performed in heavy-ion collisions with the MultiPurpose Detector (MPD) placed at the first interaction point of the collider. This study should shed light on the in-medium properties of hadrons and the nuclear matter equation of state, the onset of deconfinement, chiral symmetry restoration, phase transition, existence of mixed phase and the critical end-point, etc. The collider also provides the ability to operate with polarized proton and deuteron beams of high intensity that will be used for the study of the polarized structure of proton and deuteron with the Spin Physics Detector (SPD) installed in the second interaction point.

The main goal of the SPD experiment is to get information about the gluon Transverse Momentum-Dependent Parton Distribution Functions (TMD PDFs) in the proton and deuteron, as well as the gluon transversity distribution and tensor PDFs in the deuteron, via the measurement of specific single and double spin asymmetries using such complementary probes as charmonia, open charm, and prompt photon production processes [2]. This physics task imposes general requirements on the concept of the experimental setup.

Unlike the case of high-energy collisions where the collision energy $\sqrt{s}$ is a few orders of magnitude higher than a typical hard scale Q of the studied reactions, at the SPD energies for all the probes planned to be used to access the gluon content of the colliding particles $Q \sim M_{J\psi} \sim 2M_D \sim p_{T\gamma\,min}$ is just a few times less than $\sqrt{s}/2$. Therefore, one should expect quite a uniform distribution of all signal particles (muons from the J/ψ decay, prompt photons, products of D-mesons decay, etc.) over the kinematic range. In other words, there is no preferable range in rapidity, which could be specified for each probe for the optimal overall performance. Together with the relatively small cross-sections of the discussed probes, this fact leads to a requirement of $\sim 4\pi$ coverage of the SPD setup.

The Spin Physics Detector must have sufficient tracking capabilities and a magnetic system for spectrometric purposes for the majority of the addressed physics tasks. It has to be equipped with a muon system thick enough for effective separation of muons and hadrons to make it possible to deal with the decay $J/\psi \to \mu^+\mu^-$. A precision vertex detector is needed for the recovering of the secondary vertices from the decays of $D^{\pm/0}$ mesons and other short-lived particles. An electromagnetic calorimeter ensures the capability to detect signal and background photons. A low material budget and general transparency of the setup should also provide favorable conditions for photon physics. Hadron identification capability is needed for any physics task with protons and/or kaons in the final state, in particular, to enforce a signal-to-background ratio for D-mesons selection, and also to improve tracking at low momenta. Since tiny effects are intended to be investigated, a triggerless DAQ system is planned in order to minimize

possible systematic uncertainties of the measurements. Table 2.1 brings together elements of the SPD physics program and the requirements to the experimental setup.

Table 2.1: Required setup configuration for each point of the SPD physics program. (++) – needed, (+) – useful.

Physics goal	VD	Tracker	PID	ECAL	RS	BBC	ZDC
Study of polarized gluon content in proton and deuteron with:							
– charmonia		++		++	++		
– open charm	++	++	++	+	+		
– prompt photons		+		++			
Elastic pp and dd scattering		++	+			++	+
Single-spin physics		++	++			++	+
Vector light and charmed meson production		++	++		++		
Scaling behavior of exclusive reactions with lightest nuclei and spin observables		++	+			++	+
Multiquark correlations and exotic hadron state production		++	++				
Exclusive hard processes with deuteron		++	+			++	++
Search for deconfinement in pp and dd central collisions		++	++				
Search for dibaryons		++	+			+	+
Search for lightest neutral hypernuclei with strangeness -1 and -2		++	++				
Problems of soft pp interactions		++	++				
Measuring antiproton production cross-section for dark matter search		++	++				+?
Hadron formation effects in heavy ion collisions		++	++				
Polarization of hyperons		++	+				

Strict limitations to the SPD detector layout arise from the external conditions, such as the maximal possible load to the floor of the SPD experimental hall (1500 tons together with the lodgement and the detector moving system). Together with the requirement to have the overall thickness of the muon system not less than 4 nuclear interaction lengths (Λ_I), this limits the outer size of the SPD detector and the size of the inner part of the detector. The location of the collider infrastructure, in particular, of the focusing elements, also defines the size of the SPD setup along the beam axis.

Although p-p and d-d collisions can be studied at MPD as a reference, and SPD setup has limited capabilities to operate with ion collisions, each of the detectors is optimized for its tasks. MPD with the TPC-based tracking system can disentangle hundreds of charged tracks, but can not operate at luminosity above 10^{29} cm^{-2} s^{-1}. The design of the MPD detector does not provide for the construction of a full-fledged muon system. Conversely, the SPD is optimizdd for operation at high luminosity (up to 10^{32} cm^{-2} s^{-1}) but low track multiplicity. Optimum physics analysis in these two neighbouring experiments requires different luminosities. Therefore they have to take turns in recording data at NICA. Based on the plans for putting into operation and commissioning of the accelerator complex, development of the NICA polarized infrastructure, the plans of the MPD collaboration for technical and physics runs, as well as on realistic assumptions of the SPD funding, we propose the following stages of the SPD project implementation. The **first stage** of the SPD experiment will be devoted to the study of polarized

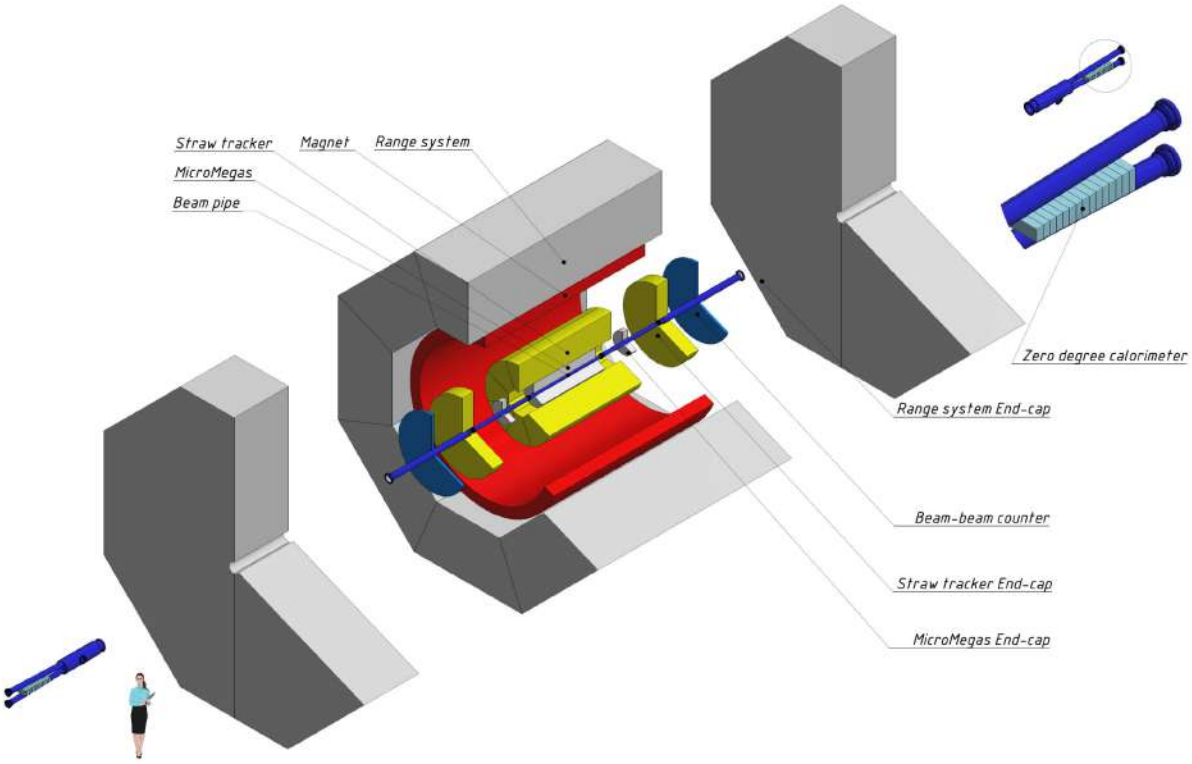

Figure 2.1: General layout of the SPD setup at the first stage.

and non-polarized phenomena at low energies and reduced luminosity using heavy ion (up to Ca) and polarized proton and deuteron beams such as: polarized phenomena in elastic p-p and d-d scattering and other exclusive reactions, spin effects in hyperon production, production of dibaryon resonances and hypernuclei, near-threshold charmonia production, etc. The duration of the first stage can be up to two years. It implies construction of a minimum setup configuration that should include (see Fig. 2.1):

- a Range System (supporting structure of the entire installation and a magnet yoke, muon identification);
- a superconducting magnet (charged particle momentum reconstruction);
- a Straw-based Tracking system (charged particle momentum reconstruction);
- a simple Micromegas-based Central Tracker to improve event vertex and charged particle momentum reconstruction;
- a Beam-Beam Counter (local polarimetry, luminosity control, and timing);
- a Zero Degree Calorimeter (local polarimetry and luminosity control).

It could also include some elements of an Electromagnetic Calorimeter for physics with photons and a local π^0-based polarimetry.

We expect that for the first stage the collider will be able to operate with polarized protons and deuterons in the spin transparency mode. The absolute value of the beam polarization should be not less than 0.5 for protons and 0.6 for deuterons. Collisions of longitudinally and transversely polarized particles, p-p and d-d (in all combinations: LL, TT, TL, and LT), will be available at any energy up to $\sqrt{s} = 9.4$ GeV for protons and $\sqrt{s} = 4.5$ GeV/nucleon for deuterons. The corresponding luminosity is up to about 10^{31} cm^{-2} s^{-1} and 10^{30} cm^{-2} s^{-1}, respectively. Both vertical and radial directions will be possible for the transverse polarization. Tensor polarization for deuteron will also be available. Absolute polarimetry is expected to be provided with accuracy not worse than 5% for both vertical and radial directions. We also expect that it will be possible to operate in the mode of heavy-ion collision.

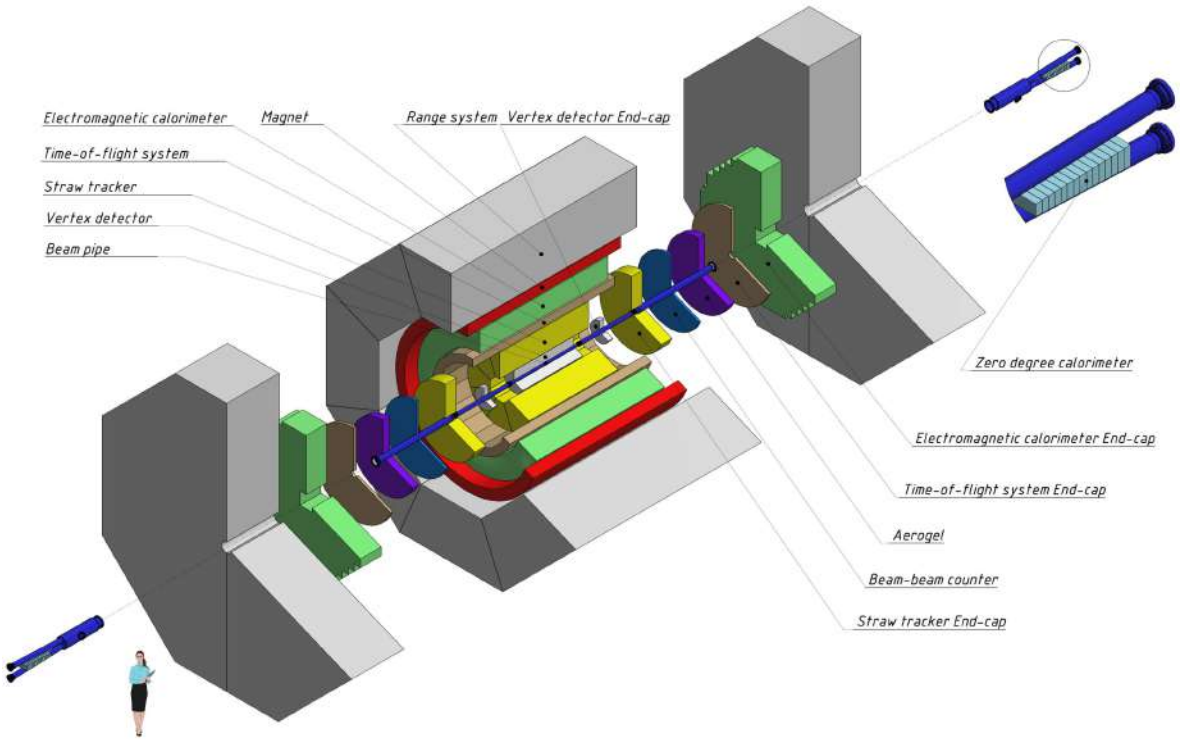

Figure 2.2: Final layout of the SPD setup.

The main part of the SPD physics program of the experiment, the study of the polarized gluon content in proton and deuteron, is planned to be implemented during the **second stage** with the full setup (see Fig. 2.2). This stage should last not less than 4 years. By then we expect the accelerator to be able to deal with polarised protons and deuterons up to energies of 27 and 13.5 GeV/nucleon in the centre of mass system and luminosities of 10^{32} cm^{-2} s^{-1} and 10^{31} cm^{-2} s^{-1}, respectively. The transverse polarisation for protons will be available for all energies, while the longitudinal polarisation will be available at spin resonance points with a beam energy step 0.51 GeV. The tentative operating plan of the SPD project is presented in Fig. 2.3.

Taking into account the high degree of integration of the detector subsystems, we decided to present the SPD Technical Design Report as a single document. The general subsystems as well as the subsystems

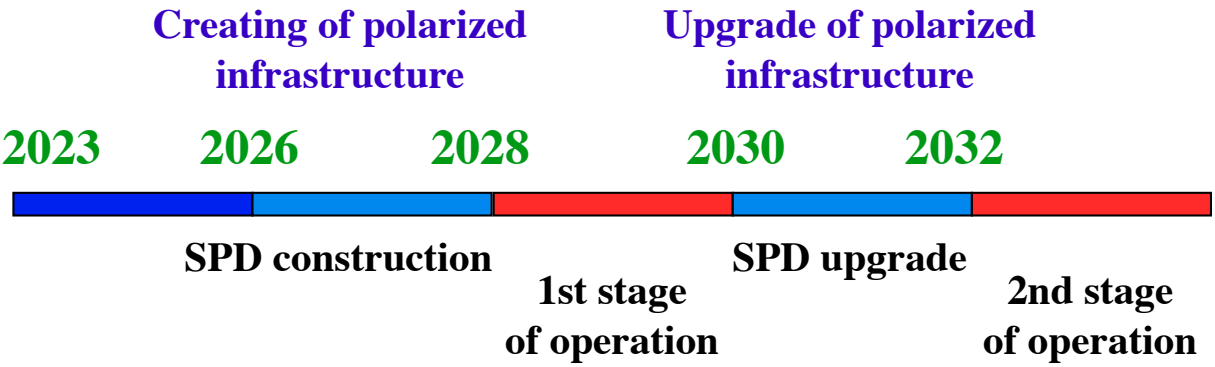

Figure 2.3: Tentative operating plan of the SPD project.

that are assumed to be part of the first phase are highly elaborated. The subsystems of the second phase are described in a more schematic way.

Chapter 3

Detector summary

To describe the SPD setup, we use a global coordinate system, where the z-axis is oriented along the nominal beam direction, the y-axis is vertical, and the x-axis is perpendicular to them and is directed toward the center of the collider ring. The origin of the coordinate system is the nominal center of the setup. We often refer to it as the Interaction Point (IP), although the real beam-crossing region has a gaussian shape along z-axis with σ_z of about 30 cm (zero beam-crossing angle) [4]. As for timing, we suppose that in the p-p mode we will have a bunch crossing every 76 ns.

The detector consists of a barrel part and two end-caps. A pair of Zero-Degree Calorimeters should be installed far enough from the interaction point to be surrounded by a beam-line equipment. A scheme of the detector in the full configuration with basic dimensions is shown in Figs. 3.1 and 3.2. Longitudinal and radial geometric dimensions of subsystems and technological gaps between them, required for the assembling and installation, are given in the Tab. 3.1 and Tables 3.2, respectively.

Table 3.1: Longitudinal dimensions of the SPD subsystems.

#	Layer	Δz, mm	z_{min}/z_{max}, mm
1	Beam pipe	8980	-4490/4490
2	Vertex detector	2360	-1180/1180
3	Z-gap 1	30	–
4	Straw tracker	286	1210/1496
5	Z-gap 2	30	–
6	Aerogel	160	1526/1686
7	Z-gap 3	30	–
8	Beam-beam counter	50	1716/1766
9	Z-gap 4	30	–
10	Time-of-flight system	60	1796/1856
11	Z-gap 5	30	–
12	Electomagnetic calorimeter	550	1886/2436
13	Z-gap 6	30	–
14	Solenoidal magnet	4080	-1988/1988
15	Z-gap 7	30	–
16	Range system	1390	2466/3856

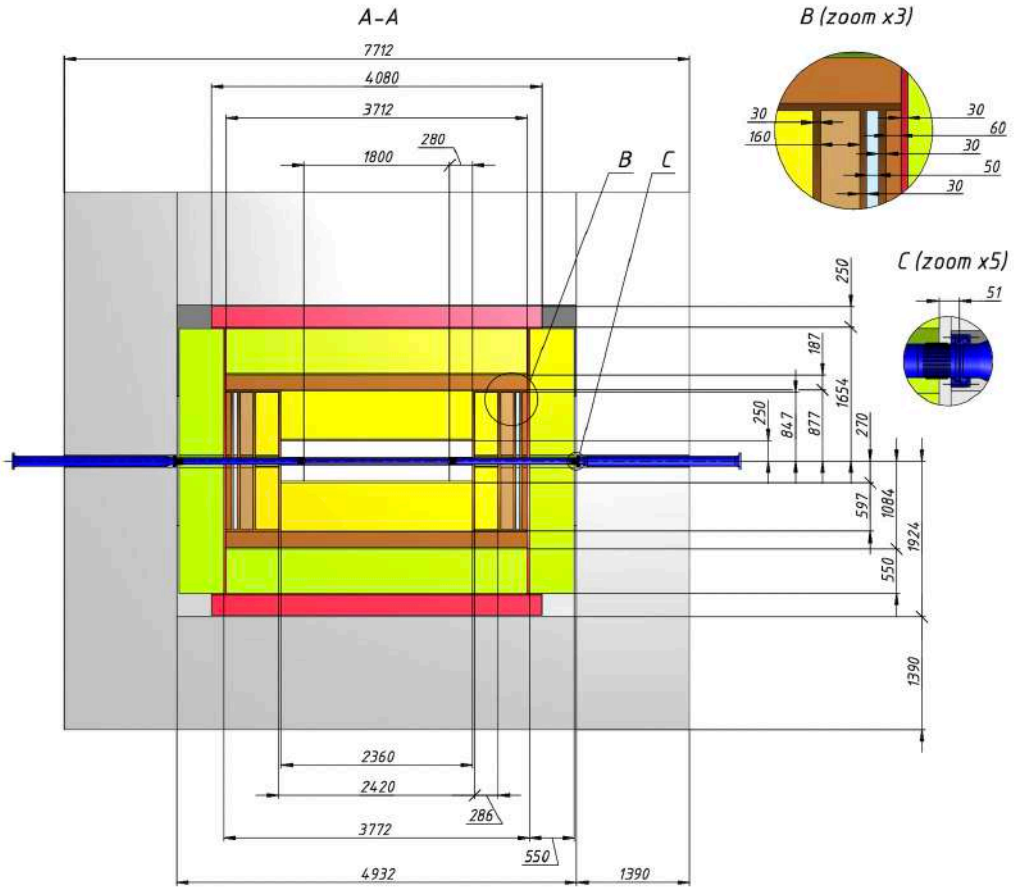

Figure 3.1: Cross section of the barrel part of SPD.

The main parameters of the SPD setup as a whole, its subsystems, and their resolutions are listed in Tables.3.3, 3.4 and 3.5, respectively.

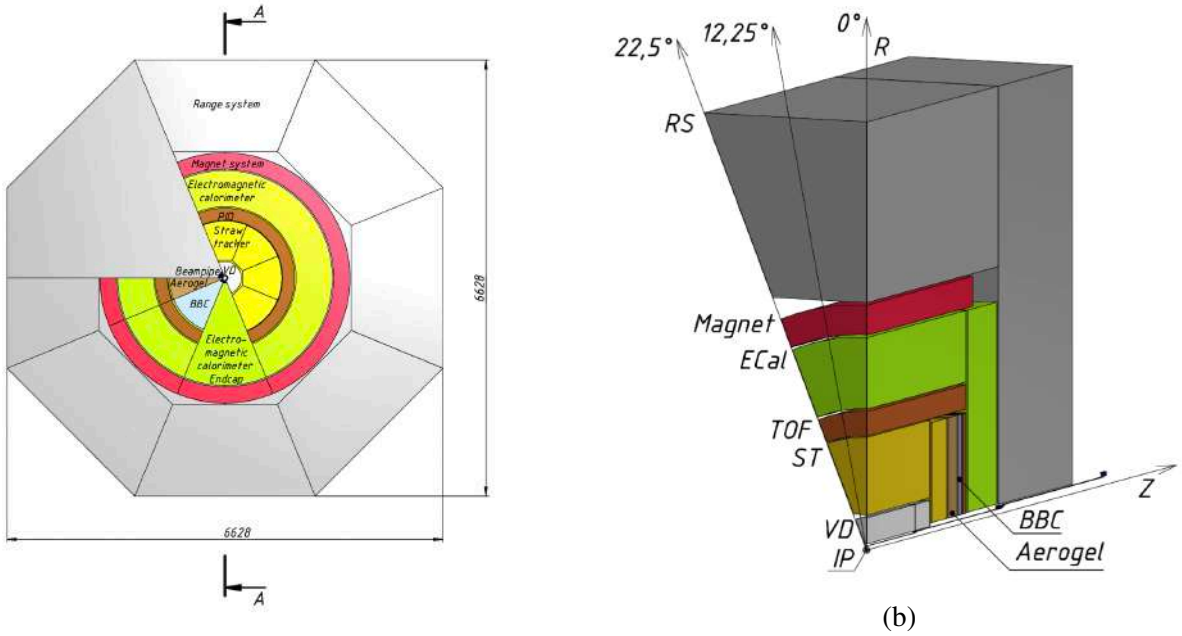

(a) (b)

Figure 3.2: (a) End view of the detector. (b) Junction of barrel and end-cap parts of the detector.

Table 3.2: Radial dimensions of the SPD subsystems.

#	Layer	ΔR, mm	R_{min}/R_{max}, mm
1	Beam pipe	32	0/32
2	Vertex detector	218	32/250
3	Z-gap 1	20/42	–
4	Straw tracker	597	270/867
5	Z-gap 2	10	–
6	Time-of-flight system	187	877/1064
7	Z-gap 3	20	–
8	Electomagnetic calorimeter	550	1084/1634
9	Z-gap 4	20	–
10	Solenoidal magnet	230	1654/1884
15	Z-gap 5	20/176	–
16	Range system	1390	1924/3314

Table 3.3: Main parameters of the SPD setup.

	Stage I	Stage II
Maximum luminosity, 10^{32} cm^{-2} s^{-2}	up to 0.1	1
Interaction rate, MHz	up to 0.4	4
Magnetic field at IP, T	up to 1.2	1.2
Track momentum resolution $\frac{\delta p}{p}$ at 1 GeV/c, %	$\sim$2	$\sim$2 for DSSD $\sim$1 for MAPS
Photon energy resolution, %		$5/\sqrt{E} \oplus 1$
$D^0 \to K\pi$ vertex spatial resolution, μm	200$\div$300	60 for DSSD 35-40 for MAPS
PID capabilities	dE/dx, RS	dE/dx, Ecal, RS, TOF, Aerogel
Number of channels, 10^3	180	558 (for DSSD)
Raw data flow, Gb/s	up to 1	20
Total weight, t	1232	1236
Power consumption, kW	107	144

Table 3.4: Main parameters of the SPD setup subsystems.

Subsystem	Stage	Main task	Active element	Weight, t	Power, kW	N channels, 10^3
RS	I+II	μ-ID	mini drift tubes Ar + CO_2, 70/30	927	47	130.2
ECAL	II	γ detection	Pb/scint.-shashlyk	57	8	26.1
TOF	II	PID	RPC chambers ($C_3H_2F_4$)	4	4	8.8
Aerogel	II	PID	aerogel	0.1	0.5	0.3
Straw	I+II	tracking, PID	straw tubes Ar + CO_2, 70/30	0.2	4	30.5
SVD MAPS	II	vertex, tracking	Si pixels	< 0.1	2	*
SVD DSSD	II	vertex, tracking	Si strips	< 0.1	2	327
MCT	I	tracking	gas chambers Ar + CO_2+iC_4H_{10}, 70/20/10	< 0.1	1	25.6
BBC inner	I+II	polarimetry	MCP	$\ll 0.1$	$\ll 1$	0.3
BBS outer	I+II	polarimetry, timing	scint.	0.1	0.5	0.5
ZDC	I+II	n,γ det.	W/scint.	0.3	2	2
Magnetic system	I+II			24	23	
Supporting structure	I+II			220.3		

Table 3.5: Spatial, time and energy resolution, as well as, signal length for each of the subsystem.

Detector	Spatial resolution	Time resolution	Energy resolution	Signal length
RS	3 mm (wires), 1 cm (strips)	150 ns	$90\%/\sqrt{E}$ (p, n)	250÷500 ns
ECAL	5 mm (γ, 1 GeV)	1 ns	$5\%/\sqrt{E}\oplus 1\%$	
TOF	10 cm	50 ps	–	
Aerogel	$\sim$10 cm	1 ns	–	
Straw	150 μm	1 ns	$8.5\%(dE/dx)$	120 ns
SVD MAPS	25 μm	–	–	
SVD DSSD	27.4 μm (ϕ)	–	–	
	81.3 μm (z)			
MCT	150 μm	10 ns	–	$\sim$ 300 ns
BBC inner	?	50 ps	–	
BBC outer	$\sim$ 10 cm	400 ps	–	
ZDC	$\sim$ 1 cm	150 ps at 0.4 GeV	$50\%/\sqrt{E}\oplus 30\%$ (n)	
			$20\%/\sqrt{E}\oplus 9\%$ (γ)	

Chapter 4

Range (muon) System

1 General description

The Range System (RS) of the SPD detector serves the following purposes: (i) identification of muons in the presence of a significant hadronic background and (ii) estimation of hadronic energy (coarse hadron calorimetry). It is important to stress that the Range System is the only subdetector of the main part of the SPD setup, which can identify neutrons (by combining their signals with the electromagnetic calorimeter and the inner trackers). Muon identification (PID) is performed via muonic pattern recognition and further matching of the track segments to the tracks inside the magnets. The precise muon momentum definition is performed by the inner trackers in the magnetic field. The Mini Drift Tubes (MDT) [5, 6] are used in the Range System as tracking detectors, providing two-coordinate readout (wires and strips running perpendicularly). Such readout is mostly needed for the events with high track multiplicity and also for the reconstruction of the neutron spatial angle.

One of the main physics goals of the Range System is the identification of muons from $J/\psi \to \mu^+\mu^-$ decays contaminated by misidentified pions and their decays.

As for the design and construction of the present system, we hope to capitalize on the experience gained by the JINR group in the development of the PANDA (FAIR, Darmstadt) Muon System [7]. These two systems (PANDA and SPD), dealing with muons of comparable momentum ranges and solving the same PID tasks, should look very similar in their design and instrumentation.

2 System layout

The Range System serves as an absorber for hadrons and a ”filter” for muons. It also forms the magnet yoke. It consists of a Barrel and two End-Caps (ECs). The schematic 3D view of the system and its main sizes are shown in Fig .4.1 (a). The absorber structure is shown in Fig. 4.1 (b). The two outer 60-mm steel layers are used for bolting the modules together, for attachment of internal detectors (inside) and external service devices (outside). The 30-mm thickness of the main absorber plates (nineteen in total) is selected as comparable with muon straggling in steel, thus giving the best possible muon-to-pion separation, and also providing a rather good sampling for hadron calorimetry. The interlayer gaps of 35 mm are taken for the reliable mounting of the detecting layers (twenty in total) comprising of the MDTs, the stripboards and the front-end electronic boards on top of them, and corresponding cables.

The barrel consists of eight modules, and each end-cap consists of two halves (sashes) divided vertically, each sash in its turn is also divided in two equal parts in vertical plane running perpendicular to the beam direction. Such subdivision of the system (16 parts in total) is chosen to optimize its further assembly

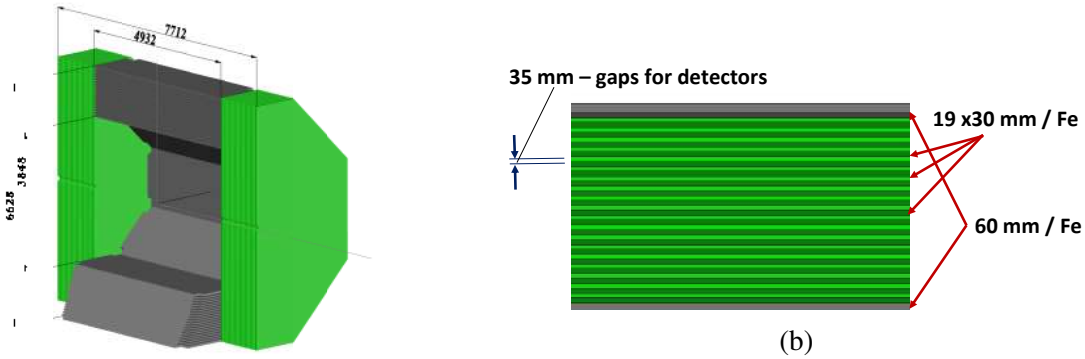

(a) (b)

Figure 4.1: 3D view (half cut) and sizes (in mm) of the Range System: (a) barrel is shown in grey, end-cap disks – in green; (b) absorber structure.

and to satisfy the constructional requirements of the SPD experimental hall (80 ton crane capacity). The total weight of the system is about 927 tons, including 37 tons of detectors. The total number of MDT detectors is about 10000 units. The MDTs are deployed in the following way: along the beam direction in the barrel, and perpendicular to the beam (horizontally) in the end-caps.

The absorption thicknesses of the barrel and end-caps are selected to be equal to 4 nuclear interaction lengths (λ_I) each. It provides a rather uniform muon filtering in all directions. Together with the thickness of the electromagnetic calorimeter ($\sim 0.5\ \lambda_I$), the total thickness of the SPD setup is about 4.5 λ_I.

3 Mechanical design simulation

The calculations were made to evaluate the stress and displacement of the SPD detector (the barrel and two end-caps with all internal detectors/systems), together with Support and Transportation Systems (STS), as well as to choose a rational design for STS, wherein the Range System is fully included in the model (force diagram/scheme) of the entire design of the SPD detector. Ultimately, the total weight of the installation and its distribution over 3 pairs of support carts and additional supports in the case of open end-caps were determined.

The following cases were considered: the full SPD installation in the operating position - the end-caps are closed, and the case with the EC sashes as far apart as possible. For control purposes, the cases with intermediate positions of the EC sashes were also considered. To reduce the order of the calculation task, a double symmetry of the entire setup was used, that is, a quarter of the installation was considered. The pictures demonstrating the results, which are presented below, were obtained using this double symmetry of the task (a quarter of the setup).

It was assumed that:

- in the working position and while moving along the rails, the installation is based on three pairs of support carts, the weight of one cart was assumed to be ~400 kg;
- the weight of all internal detectors and systems is about 100 tons in total, which is applied as a distributed load over the entire internal surface of the barrel;
- the weight of the upper platform with the equipment (cryogenics and electronics racks) located on it was taken as 40 tons, which are applied as a distributed load over the surface of the upper load-bearing elements of the SPD setup model;

– in the case of the EC open sashes, the consoles of the STS power beams were additionally loaded (supported) on 2 pairs of supports (except for the carts).

This simulation of the mechanical design takes into account only the forces of gravity. When the magnetic field of the SPD setup is turned on, the elements of the Range System will experience additional magnetic forces, since the Range System is the yoke of the superconducting solenoid of the assembly. These forces will have the greatest impact on the central (axial) part of the end-caps - the field will push it inward. According to preliminary estimates, it will be possible to keep displacements within acceptable limits by simple design solutions. However, the corresponding calculations for the final selection of the end-caps design will be carried out in the near future.

The maximum displacements (see Fig. 4.2) are observed in the elements of the upper barrel module in the region of the largest plates of the barrel module, and do not exceed $2 \div 2.25$ mm, which at this stage is considered as an acceptable result. In the elements of end-caps, displacements are insignificant, due to the vertical arrangement of the metal plates of the structure.

It should be mentioned that the stresses in all considered cases (see Fig. 4.3) correspond to low or medium values for the main material of the structure (usual construction steel), and do not exceed $600 \div 800$ kg/cm^2.

A rational arrangement of the support cart pairs has been selected, which provides an approximately uniform distribution of the total weight of the SPD on these cart pairs. In the case of the assembly in the working position, the weight distribution is 36% for the central pair and 32% for each of the outer pairs.

In other cases, the maximum load on any pair of carts or additional support does not exceed 33.5%.

The RS and STS weights (excluding (100 + 40) tons mentioned above) are shown in Table 4.1.

Table 4.1: The RS and STS weight.

SPD elements:	Barrel module	Barrel total	1/2 EC	EC	2 × EC	6 carts	STS
Weight, tons	60.1	480.8	111.45	222.9	445.8	2.5	77.8

Total weight of the RS is about 927 tons. Total weight of the fully constructed SPD detector - RS with all internal systems (electromagnetic calorimeter, solenoid, PID systems, inner tracker etc.) together with top platform (including the corresponding equipment) and support and transportation systems equals to about 1147 tons.

4 Assembly of Range System

The RS should be assembled in the following sequence. Pre-assembled detector layers (each consisting of MDT detectors attached to stripboard and equipped with FEE electronic cards) are placed in the assembly hall in a horizontal position (Fig. 4.4 (a)). Each barrel module, also placed in a horizontal position in the assembly hall, is equipped with these detector layers (Fig. 4.4 (b)). The module is lifted by a crane using a special traverse and moved on to the support and transportation system for assembling (Fig. 4.5). The modules are mounted in pairs, maintaining symmetry (left-right) about the longitudinal axis of the installation. The assembly of the barrel is completed by the last upper closing module (Fig. 4.6). After that, the STS upper load-bearing elements are mounted.

Installation of the end-caps is carried out in a similar way, first equipping them with the detector layers of MDTs in a horizontal position. Since the weight of one EC sash exceeds 80 tons (maximum crane

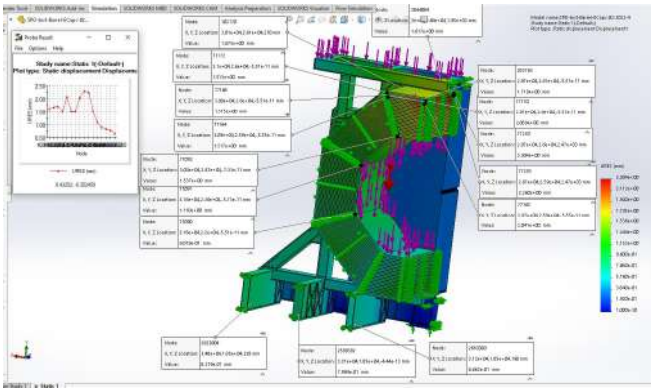

(a)

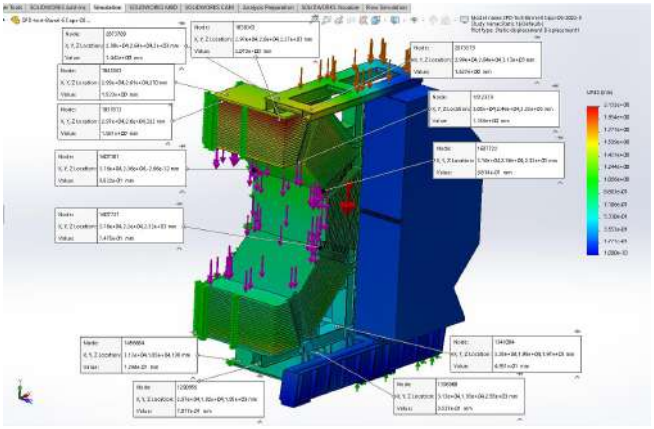

(b)

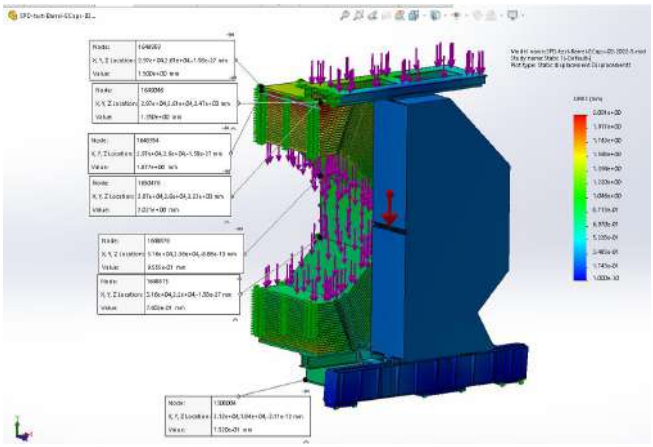

(c)

Figure 4.2: Displacements of system elements for the case of fully assembled SPD detector (including Range System, all inner detectors, solenoid magnet and the weight of the top platform with corresponding equipment) loaded on support and transportation system (six carts) (a), fully opened end-caps (b) and partially opened end-caps (c).

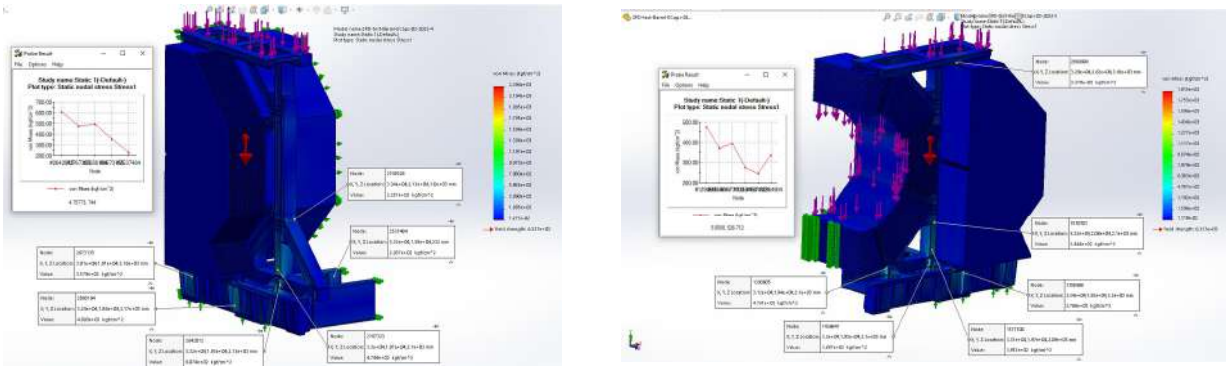

(a) (b)

Figure 4.3: Stress map of fully assembled SPD detector (a) and SPD detector with fully opened end-caps (b) Blue color demonstrates acceptable level of stress.

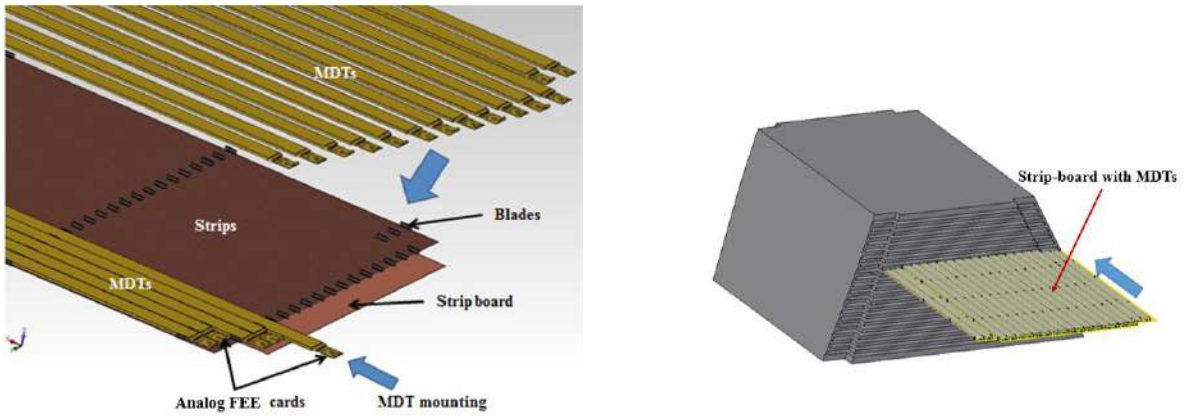

(a) (b)

Figure 4.4: (a) Mounting of MDT detectors on the strip board, forming the detecting plane. (b) Assembly of barrel module with detecting layers (MDTs with strip board and corresponding electronics).

capability), the design of the sash involves structurally dividing it into two parts along the beam. The final view of the RS before mounting of the internal SPD detectors and the upper platform is shown in Fig. 4.7.

5 Mini drift tubes detector

The Mini Drift Tubes detector was initially developed and produced at JINR for the Muon System of the D0 experiment at FNAL [8]. Later on, an MDT-based muon system was also produced for the COMPASS experiment at CERN [9]. The two-coordinate readout modification of the MDT with open cathode geometry and external pickup electrodes was developed, proposed to and accepted by the PANDA collaboration at FAIR for the muon system of their experimental setup. This new version of the MDT is proposed for the SPD project, as it has all the necessary features – radiation hardness, coordinate resolution and accuracy, time resolution, robustness, as well as the advanced level of already conducted R&D within the PANDA project.

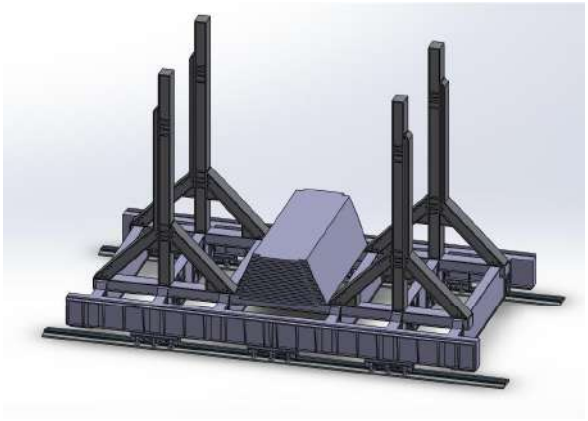

Figure 4.5: Support structure of SPD detector with first barrel module positioned on the transportation system.

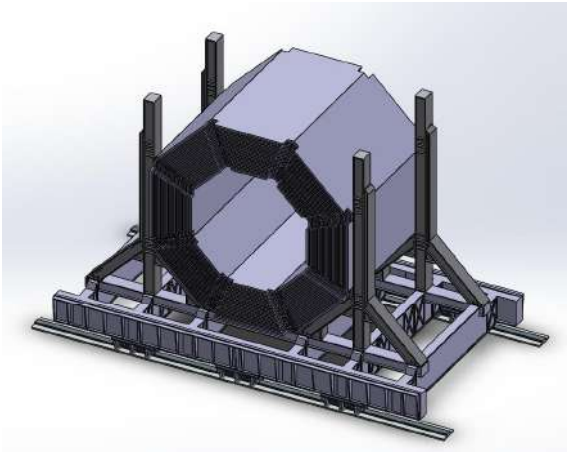

Figure 4.6: Fully assembled RS barrel.

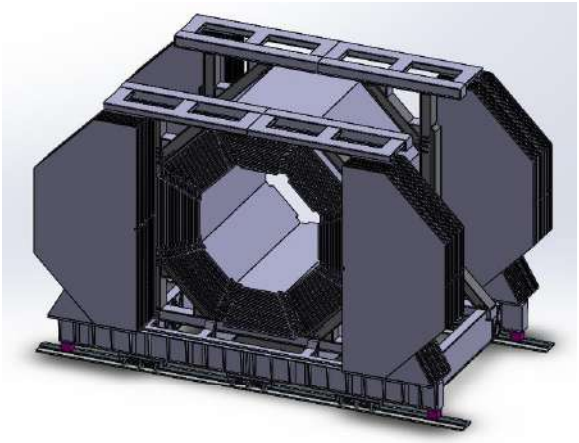

Figure 4.7: Fully assembled Range System with opened end-caps.

The cross-section and layout of the MDT with open cathode geometry are shown in Fig. 4.8. The detector consists of a metallic cathode (aluminum extruded comb-like 8-cell profile), anode wires with plastic supports, and a Noryl envelope for gas tightness.

The comb-like profile of the cathode provides each wire with an opening left uncovered to induce wire signals on the external electrodes (strips) perpendicular to the wires. The strips are applied to obtain the second coordinate readout. The shape of the induced signal repeats the initial one, having the opposite polarity, but the amplitude is about 15% of the wire signal (see Fig. 4.9). Thus, the strip signal readout requires higher signal amplification and proper electromagnetic shielding.

Application of an open cathode leads to the loss of the electric field symmetry in each of the 8 detector cells, resulting in lower gas gain for the applied voltage compared to the standard MDT (cathode openings closed with stainless steel lid). The conducted R&D proved that the MDT with open cathode geometry easily achieves the parameters of the one with a closed cathode at higher voltages. The comparative plots for counting rate, efficiency, and gas gain for both detector types (see Fig. 4.10) show that the MDT with open cathode geometry repeats the standard MDT performance at a high voltage shift of +100 V. The drift time and the amplitude spectra of both detector variants also match, if we set this voltage shift between their operating points.

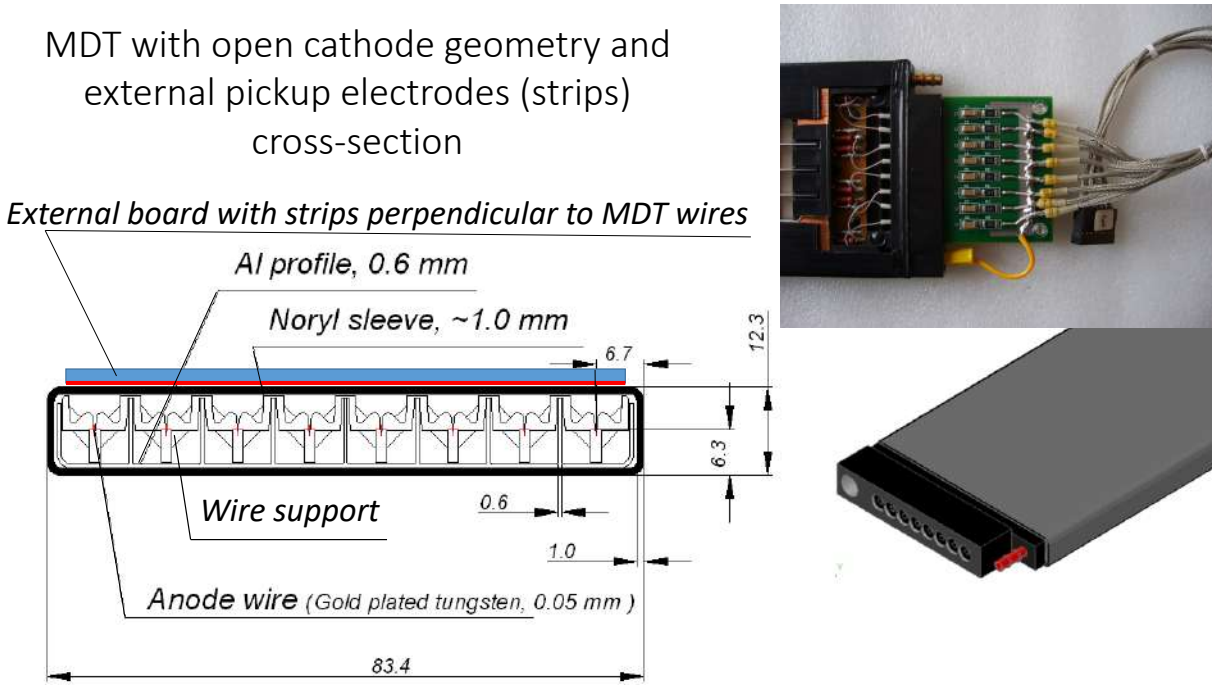

Figure 4.8: Mini Drift Tube with open cathode geometry cross-section (left) and layout (right).

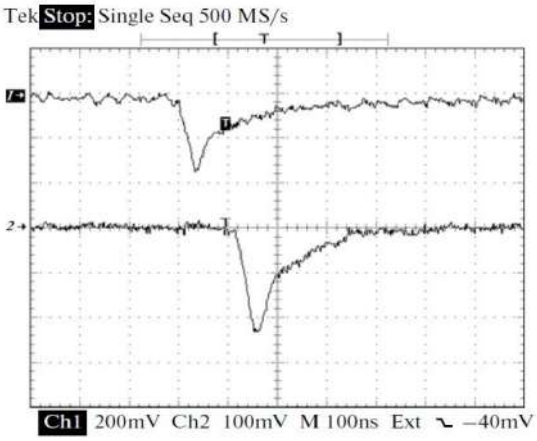

Figure 4.9: Oscillograms of single signals: from the anode wire (1) and the strip (2, inverted); the conversion factors are 60 and 480 mV/μA, respectively.

According to the results of the MDT (open cathode geometry) ageing tests, accumulation of a 1 C/cm total charge does not produce any significant effect on the detector performance. To monitor the ageing effects, measurements of the counting rate curves (Co-60 source) together with oscilloscopic observations of the MDT average signals (256 events) for Co-60 and X-rays were made twice a week over the whole period of intense irradiation (see Fig. 4.11). Later on, these measurements (with X-rays) were repeated for up to 3.5 C/cm of irradiation without any visible degradation of the MDT performance. This should ensure a stable MDT performance for the lifetime of the SPD project.

All R&D studies were made with a gas mixture of 70% Ar + 30% CO_2 at atmospheric pressure, the one to be used in the proposed SPD Muon System. It is non-flammable, radiation hard and fast enough (150$\div$200 ns drift time, depending on incoming angle). The wire pitch in the present design equals 1 cm, and a 3-cm strip width is selected for the second coordinate. These spatial parameters provide the

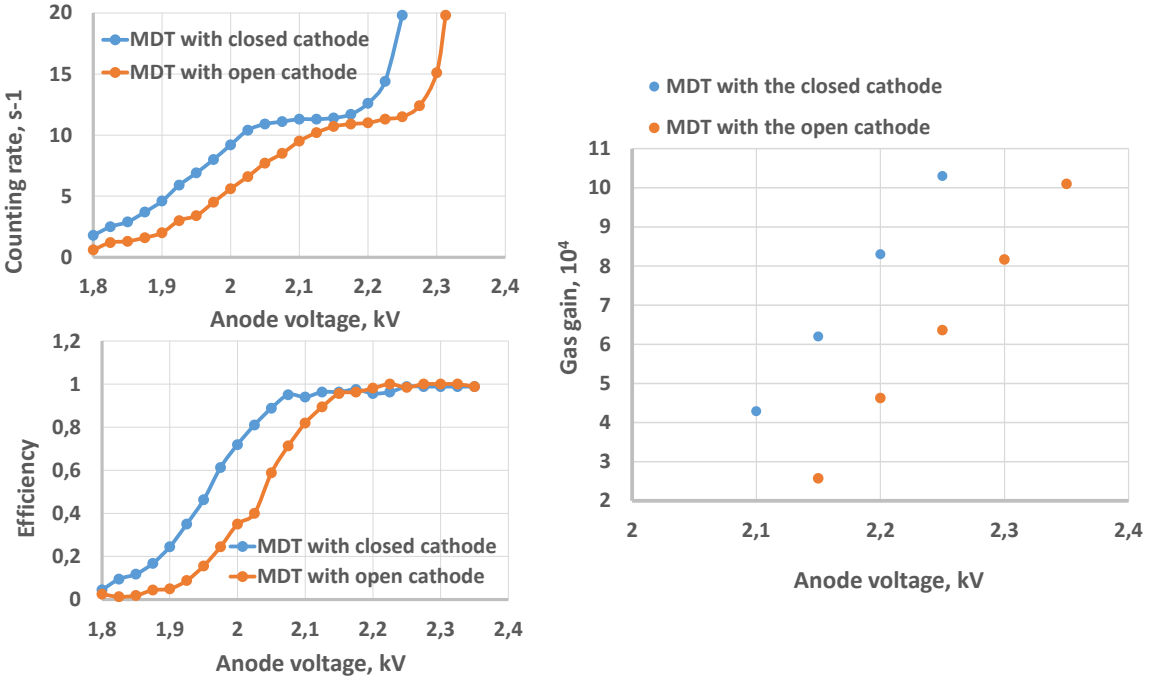

Figure 4.10: Comparative plots for counting rate, efficiency, and gas gain versus the supply voltage for the MDT with closed and open cathode geometry.

615 Range System with coordinate accuracy well enough for identification of muons and give the system the
616 features of a digital hadron calorimeter.

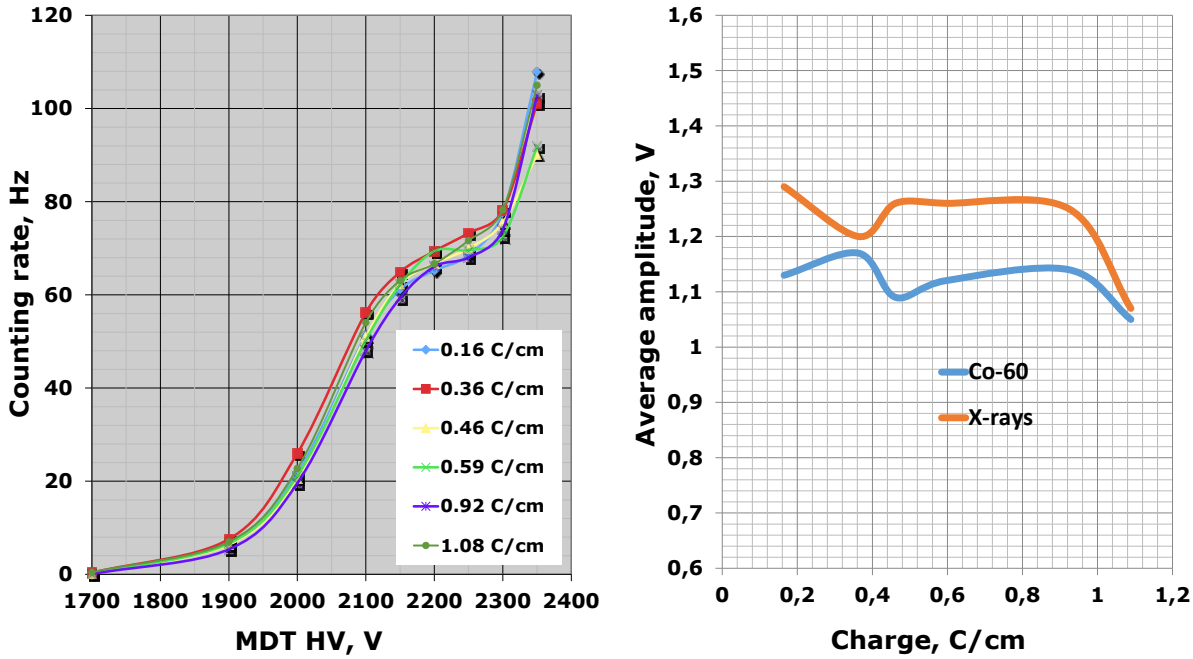

Figure 4.11: Counting rate curves for different accumulated charges (0.16÷1.08 C/cm) (left); average wire signal amplitudes vs accumulated charge for Co-60 and X-ray sources (right), the peculiar view of the curves (generally demonstrating stability of the amplitude within few percent) is due to the long duration of the monitoring (several months)

and absence of amplitude correction for the atmospheric conditions (pressure and temperature).

6 Gas system

The Range System will use quite a simple gas system (see Fig. 4.12). It should prepare and distribute over the whole detector volume the non-flammable, non-explosive and cheap gas mixture of argon and carbon dioxide: Ar:CO_2 = 70:30. Such a mixture, being cheap, does not require a closed circuit for recuperation of the outgoing gas flow. This mixture had been successfully used for years in the operation of the Muon Wall 1 and Rich Wall subsystems of the COMPASS experiment at CERN, which have practically the same MDT detectors. It is supposed now that the mixture composition will be prepared by the mass flowmeters. The required accuracy is about 1% (relative value with respect to the smaller component, so CO_2), and purity is of the standard technical value. The main components - Ar and CO_2 - should be centrally supplied by a standard gas distribution system of the SPD setup to the inputs of mass flowmeters. The two outputs of mass flowmeters feed a mixer volume. From this volume the mixture is distributed over the Range System channels. The distribution is done in a simple way by using the mechanical flowmeters (rotameters).

Presently, we assume to have 16 main channels for the control of the incoming gas flow (rotameters) and their outlets (simple bubblers). These 16 channels are comprised of the following parts: 8 octant modules of the barrel and 8 half-sashes of the end-caps. The gas volumes of these channels are the following: about 4 cubic meters for each barrel module and 2 cubic meters for each half-sash of ECs. In each channel/module the detecting planes are connected in parallel, and the MDT detectors of each plane are connected in series.

Technical details which reflect the features of the gas system are the following:

- The total volume of the Range System is about 50 cubic meters.
- The gas exchange rate, which defines the flow, is about $(1/2 \div 1) \times V_0$/day, where V_0 is the nominal system volume ($\sim$50 m^3). This corresponds to the total fluxes in the range of 1000$\div$2000 liters per hour. For the normal system operation (long term stable running) the flux of 1000 l/h is assumed.
- For fast gas exchange, the flushing mode should provide for $2 \times V_0$/day, which corresponds to 4000 l/h. This large value occurs in very rare occasions and should not be taken into consideration in the overall total gas balance of the SPD setup.

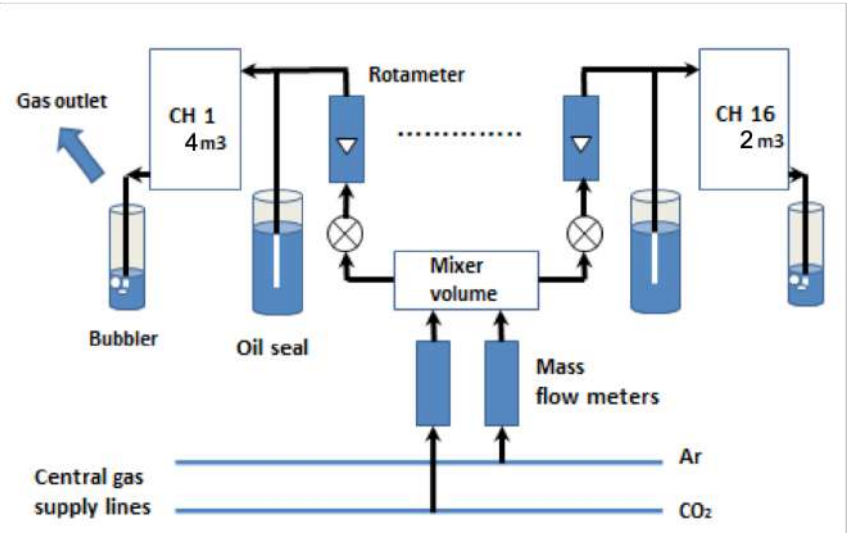

Figure 4.12: Schematic diagram of the gas system.

7 Analog front-end electronics

As the SPD Muon System inherits all technical solutions developed for the PANDA Muon System, for the analog front-end electronics (FEE) we also will use general ideas of wire and strip signals readout, already developed and well tested using the PANDA Range System prototype. Thus, we are planning to use the analog front-end electronics solutions (with minor modifications) developed for the D0/FNAL and the COMPASS/CERN experiments and also accepted by the PANDA/FAIR.

The signal readout is based on two ASIC chips: 8-channel amplifier Ampl-8.3 [10] and 8-channel comparator/discriminator Disc-8.3 [11]. To arrange wire readout, we need a high voltage distributor and a signal connector circuit followed by an amplifier – discriminator circuit with LVDS outputs. Combination of HV/S-8 and ADB-32 cards [12] is the most common among the existing variants (see Fig. 4.13 (a), (b)). For the strip signal readout we use a circuit with two stages of Ampl-8.3 followed by the discriminator with LVDS output. Combination of preamplifier cards A-32 (Fig. 4.13 (c)) and ADB-32 (Fig. 4.13 (b)) fulfills this task. Mentioned electronic cards without any modifications can be applied for the wire and strip signals readout of the end-caps. The view of the basic FEE cards is shown in Fig. 4.13.

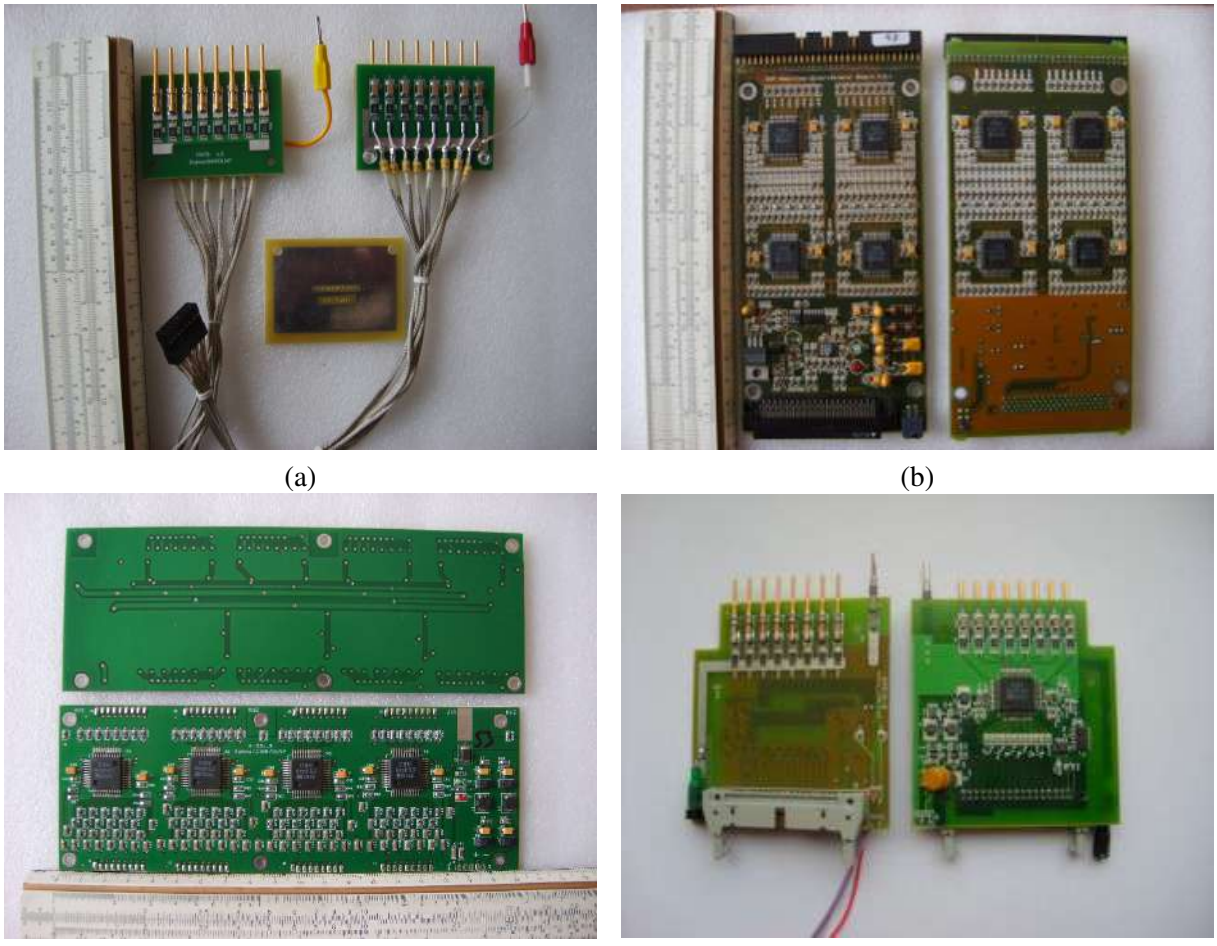

(a) (b)

(c) (d)

Figure 4.13: Front-end analog electronics cards: HV/S-8 (a), ADB-32 (b), A-32 (c), and HVS/A-8 (d).

For the barrel part we use the same general idea of the readout circuitry, but its implementation will differ from electronics mentioned above. This is connected to the fact that the barrel analog FEE is a constructive part of the detector layer and will be buried inaccessible.

By now, we assume to use 8-channel electronic cards for both wire and strip readout in the barrel with

all needed circuitries implemented in a single card. For the wire readout it will be a modification of HVS/A – 8 (Fig. 4.13 (d)) designed for the PANDA barrel – the new board will contain high voltage distribution circuit, amplifier and discriminator with all related circuitry. Strip analog FEE will also be an 8-channel board containing preamplifier, amplifier and discriminator with all related circuitry. To match 8-channel electronics with 32-channel inputs of the digital FEE part, we are planning to use special "patch panel" cards that will be placed on the edge of the detector layer and stay accessible. These cards will also act as LVDS drivers and LV and threshold distributors with a manual LV adjustment.

Analog FEE cards are located mostly inside the slots of the RS iron absorber – fully (for the wires and strips) in the barrel and partially (for the strips only) in the end-caps. Corresponding power dissipation (see Table 4.2), despite looking quite large, does not impose any practical limitations, as it is "immersed" into the massive iron "radiator" of the RS absorber. So, we do not plan to use additional ventilation apart from the natural convective cooling.

Table 4.2: Analog FEE power dissipation.

	Barrel, kW	End-Caps, kW	Total, kW
Wires	6.5	9.75	16.25
Strips	7.2	6.93	14.13
Total	13.7	16.68	30.38

We still continue our R&D work intended to improve strip board performance, results of this work will influence the detector layer design. In collaboration with the Institute of Physics of the National Academy of Science of Belarus we also continue R&D devoted to Ampl-8.3 modification that will improve its applicability for the strip signal readout and reliability of long-term operation. Results of these R&D works can significantly influence the PCB design of the barrel analog FEE, that is why the development of these particular cards is postponed.

Totally, the Range System has 130200 readout channels (80000 of which are wires and 50200 strips), see Table 4.3.

Table 4.3: FEE channels.

	Barrel	End-Caps	Total
Wires	32000	48000	80000
Strips	25600	24600	50200
Total	57600	72600	130200

7.1 Ampl-8.51 – low input impedance amplifier for the Muon System wire and strip readout

As mentioned above, all present analog FEE designed for the Muon System use Ampl-8.3 to read both wire and strip signals. The amplifier ASIC was specially designed for MDT, but also managed to cope with strip signals when used in the two-stage circuit. Generally, Ampl-8.3 meets the strip readout requirements well, but not perfectly. In terms of the set stripboard parameters, value of the strip wave impedance varies in range of $R_z \sim 10 \div 30$ Ω, but Ampl-8.3 has a 50 Ω input impedance. The present impedance mismatch does not seem significant, but anyway matching is preferred, especially for the long strip signal readout. Moreover, it would be much better to have an input impedance less than 10 Ω, so that after matching the wave impedance of the strip (or wire) with the input impedance of the

amplifier, carried out using a series-connected resistor R_d, the maximum value of the high-voltage surge is reduced by the resulting voltage divider in $(R_d + R_{in})/R_{in}$ times, increasing the amplifier's resistance to high-voltage breakdown, increasing its lifetime and reliability. In addition, the low input impedance of the amplifier reduces external pickup at its input, which increases its immunity to self-excitation and external interference. Low or absent accessibility of strip and wire readout electronics of the RS barrel makes a real demand for increased reliability of the amplifiers. Following the given considerations, it was decided to develop a low input impedance modification of Ampl-8.3 that would keep all proven virtues of its predecessor.

The new amplifier chip design was carried out under the following guidance:

1. the amplifier general parameters should correspond the ones of Ampl-8.3 (or close);
2. an input stage should be made on a common base npn transistor to provide low input resistance;
3. amplifier inputs should be protected by the diodes against HV pulses (both negative and positive);
4. input Rush amplifier circuit should be followed by differential amplifying stages to minimize cross-talks;
5. the amplifier should belong to a trans-resistance type; it should not have a common feedback to exclude possibility of parasitic generation by excluding stray capacitances and resistors of the feedback integrated capacitors and resistors between the input and output of the amplifier;
6. maximum layout symmetry to minimize DC voltage shift at the amplifier's differential outputs at a quiescent mode.

As a result, an Ampl-8.51 circuit has been developed to meet all requested parameters. Amplifier circuit design together with spice simulations have been done using Cadence 6 CAD software. General parameters of the Ampl-8.51 spice model are presented in Table 4.4. All parameters are given taking into account the technological spread of the circuit elements values. For resistors, it is $\pm$ 20% of the nominal values. The Rush cascade cannot be implemented in an integral design with a small scatter of parameters, since they are determined not only by the ratio of the resistors, but also by their nominal values. The spread of the main parameters of the ASIC Ampl-8.51 will repeat the technological spread of the resistor values.

The oscillograms of the Ampl-8.51 output signals within the boundaries of the technological spread of the circuit elements parameters are shown in Fig. 4.14 – the simulation is performed for the so-called fast, typical and slow models of the circuit elements. In these figures, fast models are represented by brown lines, typical models - by green lines, and slow models - by red lines.

Figure 4.15 presents the plots of the Ampl-8.51 input impedance frequency response. At a frequency of 30 MHz, the value of the input resistance will vary within 3.32 $\div$8.7 Ω due to technological spread in the values of the circuit elements. At a frequency of 10 MHz, the value of the input impedance remains within 0.9$\div$2.2 Ω, and at low frequencies it does not exceed 0.25 Ω.

The presented simulation results of the Ampl-8.51 with the Rush cascade show that the main parameters of the developed integrated circuits correspond to the requirements of the technical specifications for typical values of the parameters of the circuit elements and retain the operating values within the technological spreads of the circuit elements parameters.

The topology of the Ampl-8.51 and the AISIC have been made using BJT-JFET technology by the research and production corporation "Integral" (Minsk, Belarus).

Table 4.4: Ampl-8.51 general parameters (spice simulation).

Parameter	Value
Input impedance for signal bandwidth: 1 MHz, Ohm 10 MHz, Ohm 30 MHz, Ohm	 0.25 0.9÷2.2 3.32÷8.7
Input signal polarity	$\pm$
Input $\pm$ overvoltage protection:	Yes
Differential output	Yes
Gain, mV/μA	100÷150
DC output offset voltage, V	< 1.0
Output load, W	1000
Output signal leading/trailing edge (0.1, 0.9), ns	8÷12
I_{noise} for detector capacitance: CD = 0, r.m.s., nA CD = 40 pF, r.m.s., nA CD = 1800 pF, r.m.s., nA CD = 5000 pF, r.m.s., nA	 63÷110 96 315 572
Dynamic range for signals of both polarities, dB	48
Channel-to-channel cross-talk, dB	<-40
Voltage supply, V	$\pm$ (2.8÷3.2)
Dissipated power at $\pm$3 V supply, mW/channel	64
Channels per chip	8

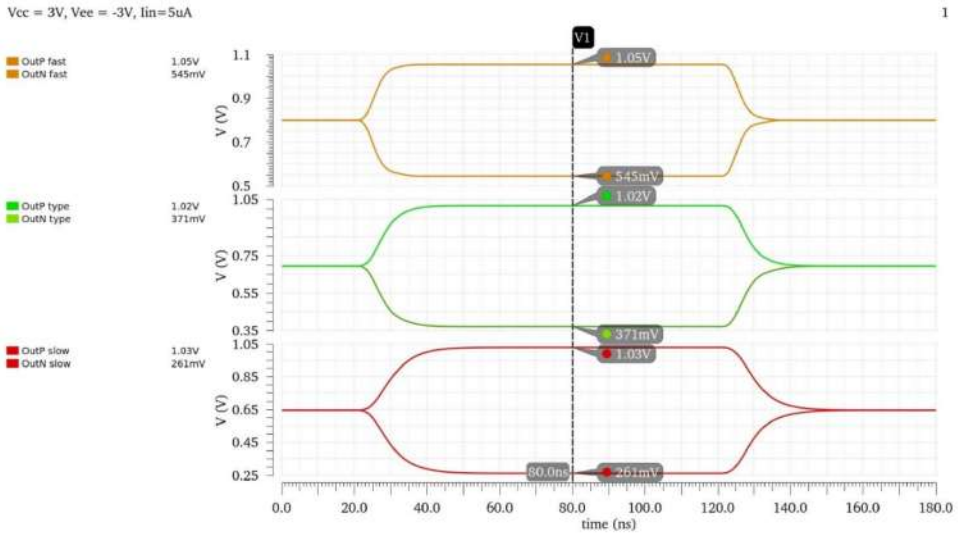

Figure 4.14: Ampl-8.51 output signals, Iin = 5 μA.

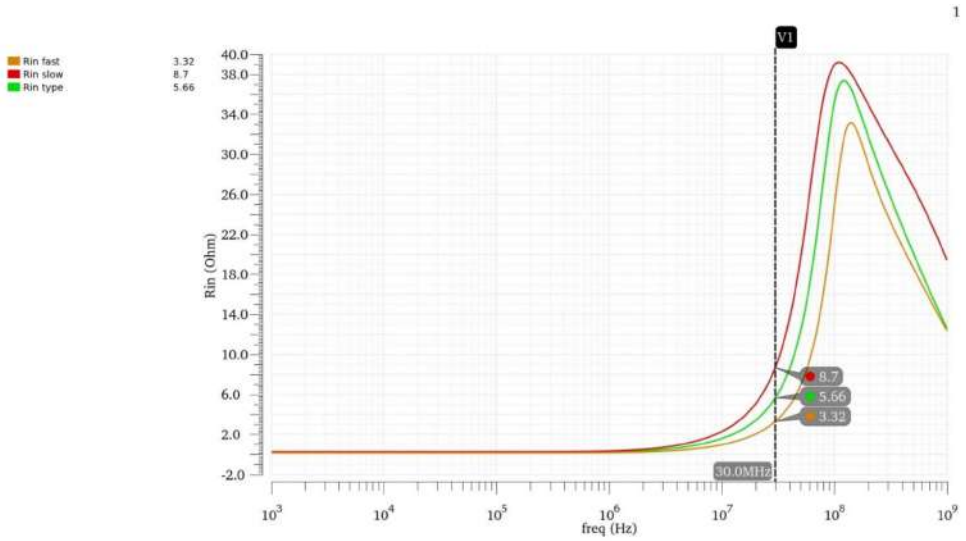

Figure 4.15: Ampl-8.51 input impedance frequency response.

First tests of the manufactured chip showed that this iteration has two general problems – low operating stability (self-excitations) and imbalance of the differential output offset. According to preliminary examination, these problems are due to the following mistakes in microchip topology (circuit peculiarities were not taken into account):

- inadequate power bus and traces width (R≠0, V drop);
- series power connections (not star type) in the circuit parts most sensitive to power;
- complimentary parts of differential circuit powered from different power bus points (operation point floats);
- the same power bus for input current amplifier and following differential amplifier, power traces are mixed (input senses current jerks of the output circuit, resulting in self-excitations);
- common input ground (input amplifier circuits sense neighbors, resulting in self-excitations).

To minimize described negative effects 1-st and 8-th amplifier channels were disconnected from common ground and power bus (applied to 4 chips). Separated channels restore the output baseline and operate without self-excitations, giving a chance to check general amplifier parameters. General parameters of Ampl-8.51 individual channels were measured, and its ability to provide a strip signal readout was checked, test stand is shown in Fig. 4.16.

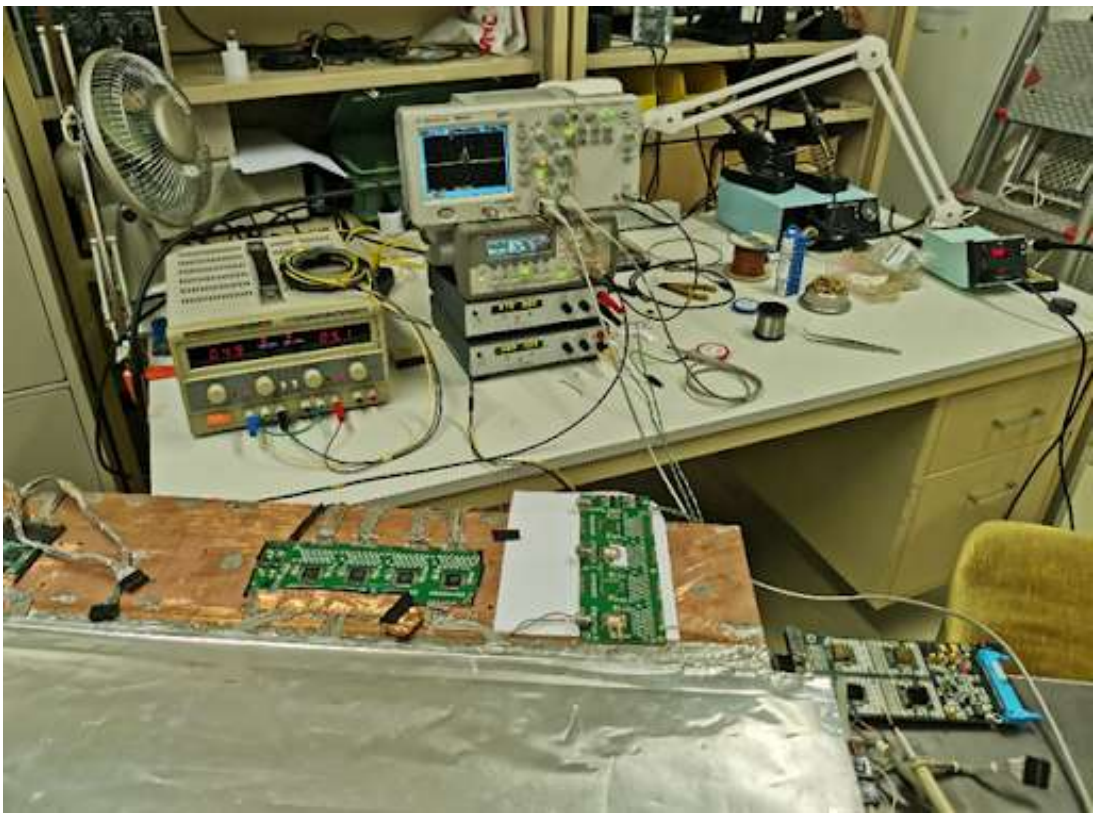

Figure 4.16: Ampl-8.51 single-channel tests.

Measured single-channel parameters (see Table 4.5) perfectly matched the technical requirements.

Table 4.5: Ampl-8.51 single-channel parameters.

Parameter	Value
Input impedance (30 MHz), Ohm	5.4
Gain, mV/μA	131
Rise time/fall time, ns	9.2
I_{noise} (CD = 1.8 nF), nA	550
Dynamic range (CD = 0 nF), dB	48
Dissipated power, mW/channel	63

As it stands, we still need to achieve a combined 8 channel stable operation of the amplifier. We will try to apply all possible and necessary corrections to the metal layers of existing chips (with unfinished metallization) to fulfill this task.

8 Digital front-end electronics

The digital electronics being created for the Muon System is based on the use of FPGA chips. The prototype of the digital 192-channel MFDM module (see Fig. 4.17) (Muon FPGA Digital Module) that we have developed includes a XC7A200T chip of the Xilinx Artix 7 family. Functionally, mechanically, in data format, and DAQ interface this unit is compatible with the previously developed MWDB (Muon Wall Digital Board) unit [13] made on the basis of TDC F1 (ASIC) and successfully used for data readout from the Muon System of the COMPASS experiment (CERN). This approach allows both types of units to be used in the same readout system, thus making it possible for the new MFDB cards to be tested under actual operating conditions.

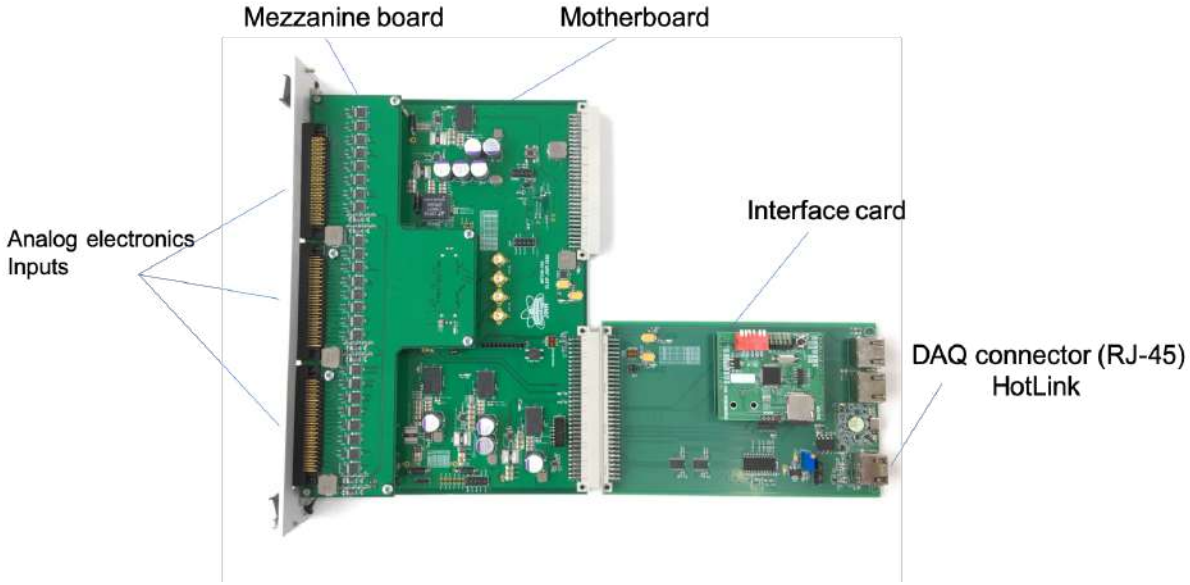

Figure 4.17: MFDM readout unit.

The MFDM unit is made in the VME standard (6U, 2M) with the following technical parameters:

- the number of registered channels - 192;
- input signals levels - LVDS;
- discrimination of input signals from the detector is carried out in the range of (0 ÷ +3V);
- the unit operates in the latch mode;
- the maximum time interval for digitizing input signals $\sim 9\ \mu$s;
- discreteness of the time interval digitizing (bin size) – (4÷5) ns;
- power consumption per unit is about 24 W.

The unit includes three electronic boards (Fig. 4.18): motherboard, mezzanine card, and interface card.

The motherboard accepts 96 LVDS signals from the analog electronics through 3 high-density connectors, converts them to LVTTL levels and writes to the FPGA, and also communicates with two other boards. The mezzanine card accepts the remaining 96 LVDS signals through 3 connectors, converts them to LVTTL levels and transmits through the 120-pin board-to-board connector to the motherboard. The interface card is designed to connect the MFDM module with the DAQ via the HotLink interface

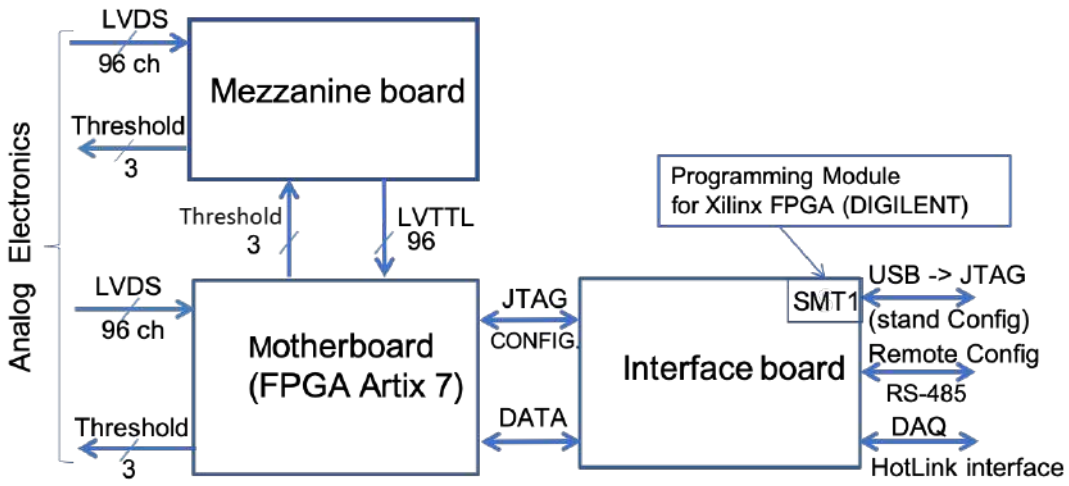

Figure 4.18: Block-diagram of the MFDM module.

(RJ45 connector), to download the firmware to the FPGA from a local computer, as well as to download the firmware via the RS-485 interface (RJ45 connector) from a remote computer. Interface card is installed on the backside of the VME crate in the P2 connector.

To treat the total information from 130200 channels (wires and strips) we need 679 digital modules (housed in 76 VME 6U crates) with total power consumption about 16.3 kW.

Tests of the MFDM unit performed at CERN with the Muon System prototype (250 MDT detectors, 4000 readout channels) on cosmic rays gave encouraging results. Figure 4.19 shows the structure of a stand-alone data acquisition system, based on GeSIca and a multiplexer (MUX) units from COMPASS DAQ, in which two MWDBs (F1 TDC / ASIC) were replaced by two MFDM modules (FPGA) in order to verify their performance.

Figure 4.20 displays the tracks and the time spectra obtained from the tests, using only MWDB (F1 TDC) units (a) in one case, and two MFDMs (FPGA) (b) instead of two MWDBs (planes No. 17, 18) in the other. In both cases, the obtained results were the same – in planes No. 17, 18 the triggered wires are in correct position on the track, the time spectra also coincide with small deviations due to the peculiarities of TDC F1 operation in the latch mode. The maximal drift time of MDT ($\sim$150 ns) defines the time resolution of the Muon System providing the time interval / window for assembly of the event (association of the hits from different detectors in one event) by event builder.

The final tests of the MFDM unit will be carried out with a prototype of SPD range system (1300 channels of wire and strip readout) in the SPD test zone. Described stand-alone readout system will be used at the first stage of the prototype operation. Further on, MFDM HotLink interface is meant to be replaced with an optical interface. This will significantly simplify and improve reliability of the stand-alone readout system by direct connection of the MFDM units to the FPGA-based block HDmx (data handling multiplexer) (VME 6U, 2M) (Fig. 4.21), which is used as a first level concentrator in the COMPASS/AMBER DAQ. This block contains 15 optical input ports (UCF protocol) to connect with FEE electronics; one output port (Slink), and also several service interfaces: JTAG for downloading firmware program into HDmx FPGA; IPbus for connection via Ethernet, and a TCS channel for connection with the Trigger Control System. The output data from the concentrator is transmitted via the PCIe card to the computer.

In the SPD DAQ, the connection between FEE of the muon system and the first level concentrator DAQ is supposed to be carried out through serial, local electrical links (e-links), including the following communication lines:

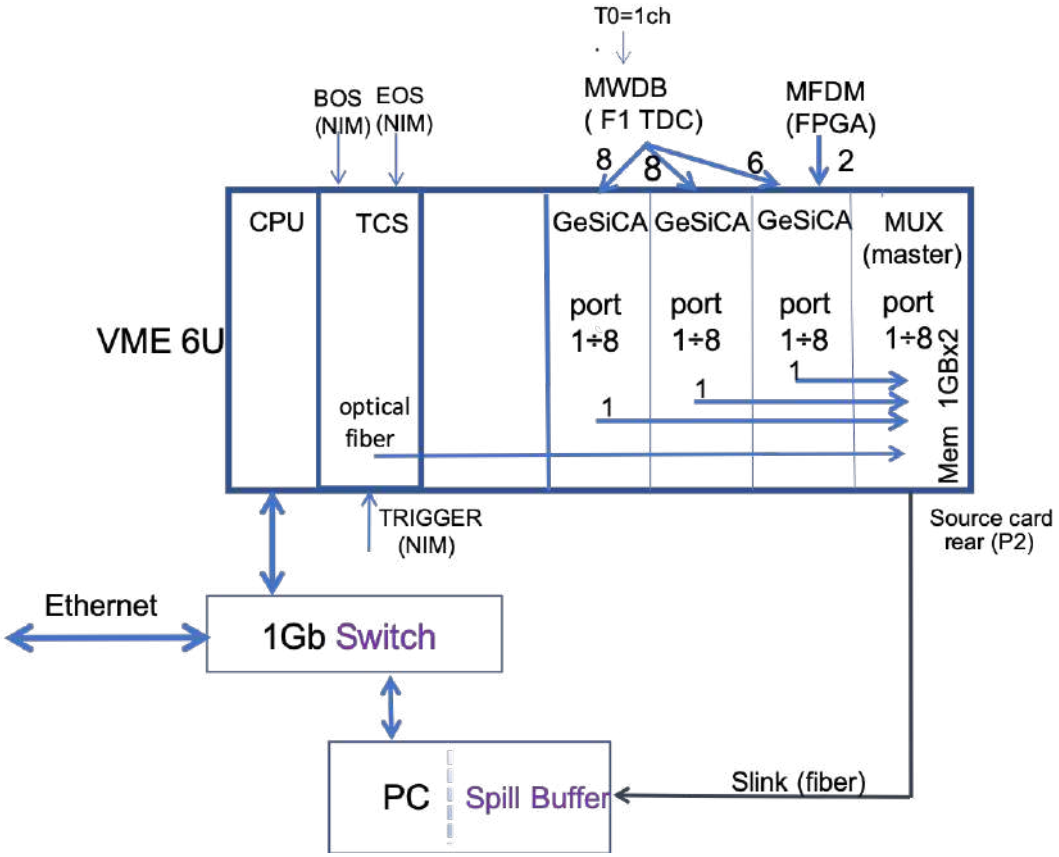

Figure 4.19: Stand-alone DAQ block-diagram.

- reset (LVTTL) from DAQ;
- reference Clock (LVDS/SLVS) from DAQ;
- synchronization signals Start of Slice, Start of Frame, and Set next Frame (LVDS/SLVS) from DAQ;
- data/clock for FEE initialization (I2C interface, bidirectional, LVTTL);
- data link FEE (LVDS/SLVS).

Communication between the first and second level concentrators uses optical link designed for the total bandwidth of e-link lines. As part of R&D in digital electronics for the Muon System, interface cards with an option of connecting MFDM unit to DAQ through either an optical channel or e-link lines will be created.

A general view of the data flow structure for the Muon System is shown in Fig. 4.22.

9 Prototyping

The evaluation of the main parameters of the proposed Range System is being performed with a big prototype installed at CERN within the PANDA program. The prototype (see Fig. 4.23) has a total weight of about 10 tons (steel absorber and detectors with electronics) and comprises 250 MDT detectors with 4000 readout channels (2000 for the wires and 2000 for the strips, 1 cm wide; finally, the 3 cm wide strips were adopted for the SPD Range System). It has both samplings (3 cm and 6 cm) present in the

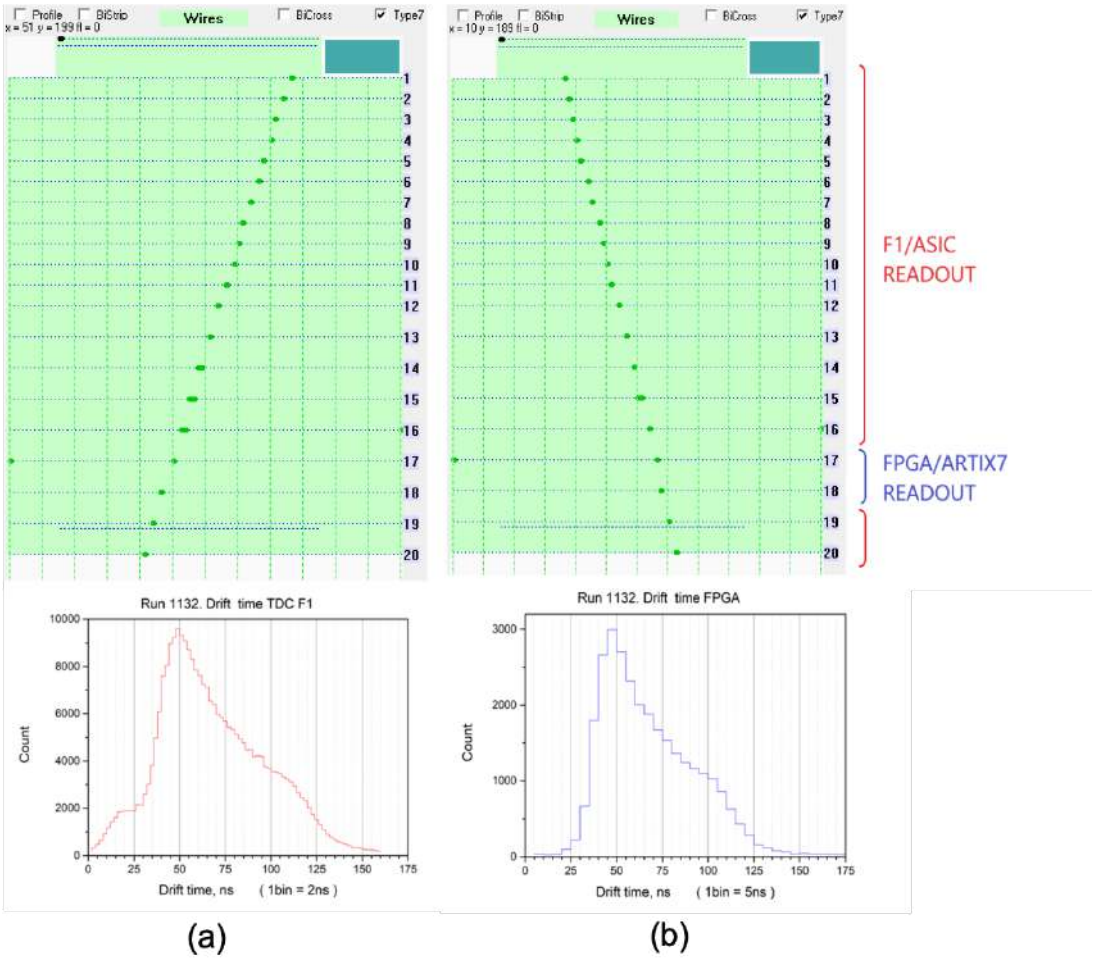

Figure 4.20: FPGA digital readout test.

system (PANDA barrel and end-caps) and provides an opportunity for direct calibration of the response to muons, pions, protons, and neutrons.

Figure 4.24 gives examples of the prototype response to different particles. The patterns demonstrate excellent PID abilities of the Range System. The data were taken during the May and August runs in 2018 at the T9/PS/CERN test beam. The beam particles hit the prototype from the top of the picture. The beam momentum for all the particles is 5.0 GeV/c. Neutrons were generated by a proton beam on a carbon target placed in the very vicinity of the first detecting layer. The points on the pictures represent hit wires, thus giving the impression of a typical device response with an accuracy of $\sim$ 1 cm.

In addition to good PID quality, the Range System also has rather good features as a measuring device – in calorimetry and tracking. Figure 4.25 demonstrates the linearity of the RS response to the kinetic energy of the hadrons and modest resolution (due to the sampling). Such calorimetric signal may potentially help in data analysis in combination with the signals from the electromagnetic calorimeter and tracking system (used for precise momentum definition). Most importantly, this calorimetric signal is the only one to register the neutrons and roughly estimate their energy.

The Range System may also provide additional space information – space angle for track segment or shower, and entry point to the system. Figure 4.26 shows an example of track and angle resolution obtained for the muons in (R, φ) plane. (It depends on accuracy about 1 cm provided by the wire readout and smeared by the multiple scattering in the massive absorber.) Accuracy of the reconstruction for the

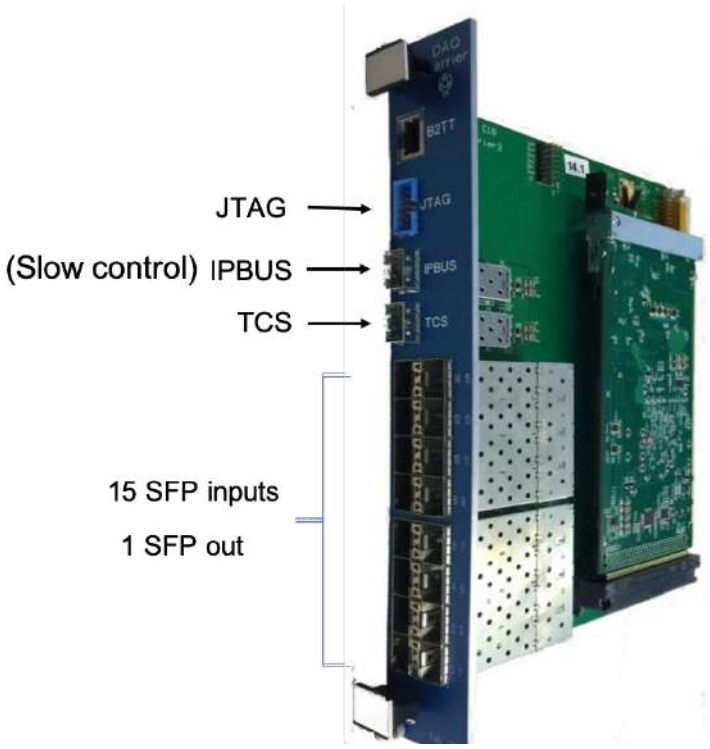

Figure 4.21: Compass/Amber FPGA-based concentrator.

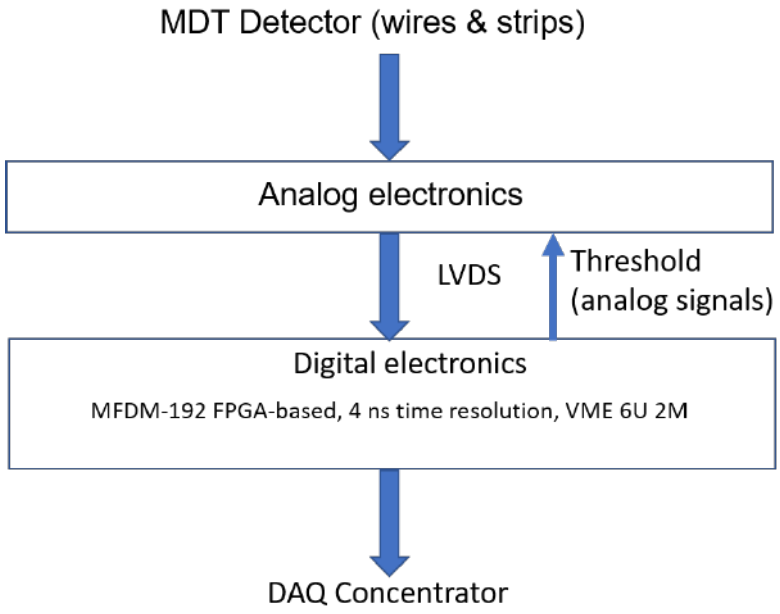

Figure 4.22: Data flow diagram – from the RS to the DAQ.

entry space point may be estimated as ~ 3 cm, and is limited by the strip width.

10 Simulations and performance

The performance of the Range (Muon) System was evaluated using Monte Carlo simulations of the detector within the SpdRoot framework as well as R&D program conducted with the RS prototype on

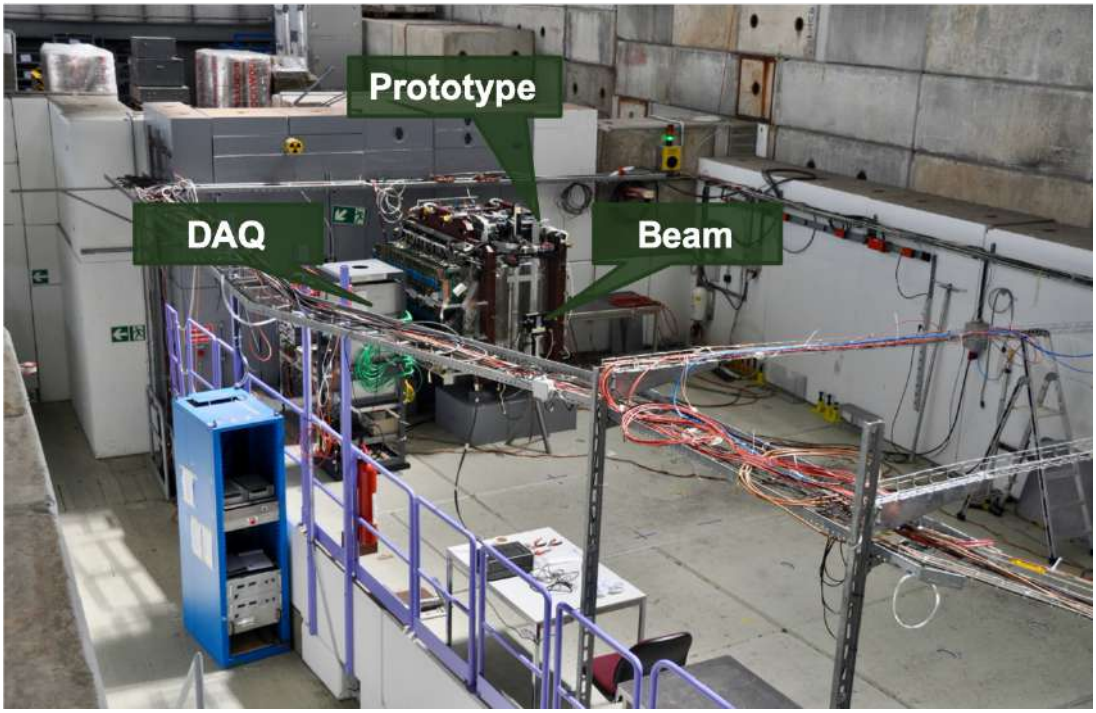

Figure 4.23: Range System prototype (10 tons, 4000 readout channels) at CERN.

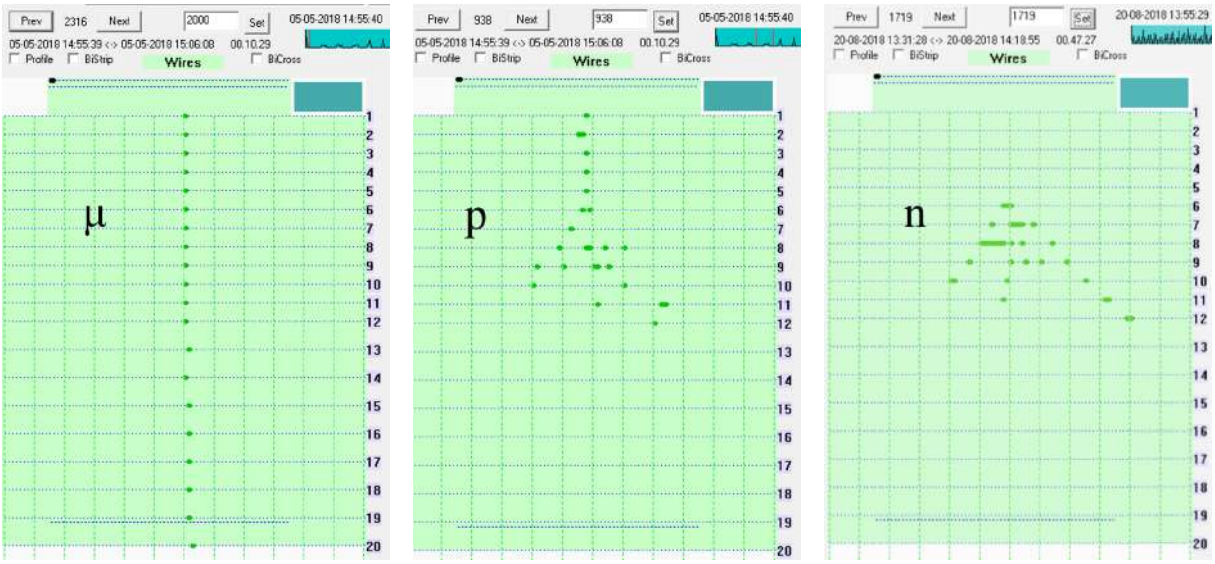

(a) (b) (c)

Figure 4.24: Demonstration of PID abilities: patterns for (a) muon, (b) proton, and (c) neutron.

test beams (see Section 4.9). The studies included system response to the passage of particles with different momenta, the efficiency of muon/hadron separation, testing pattern recognition algorithms, and tuning the parameters of Monte Carlo simulation using experimental data.

The full simulation of the RS detector is based on the geometrical model of the SPD Range System, incorporated within the SpdRoot framework from engineering drawings. The model of the RS prototype was also implemented within the SpdRoot package, which made possible a direct comparison of the detector response to traversing particles.

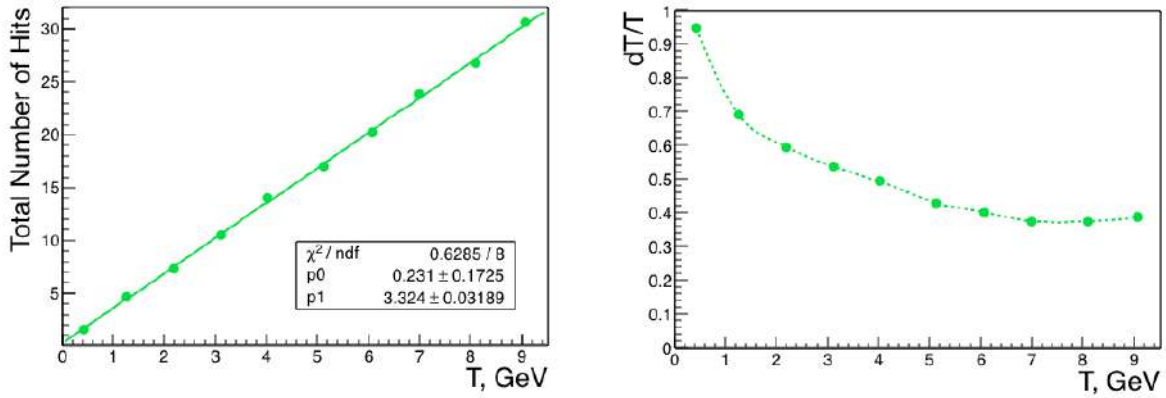

(a) (b)

Figure 4.25: Calorimetric signal (a) and energy resolution (b) vs kinetic energy (T) of hadrons.

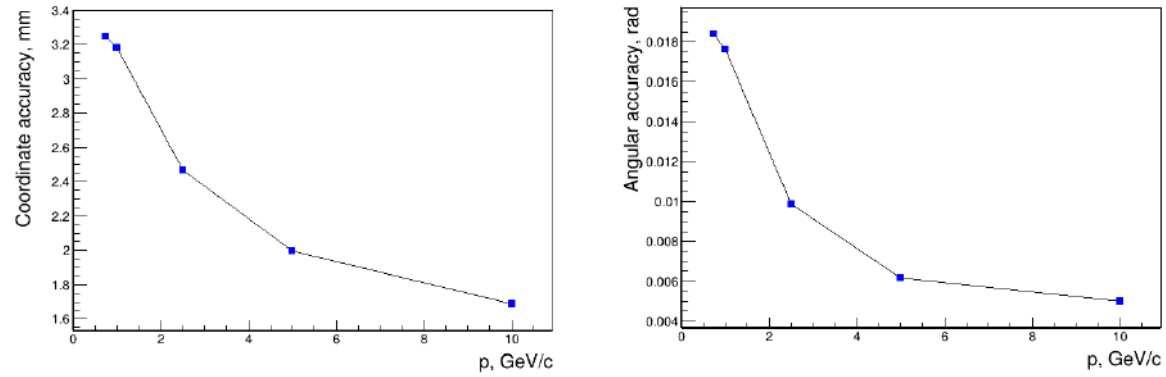

(a) (b)

Figure 4.26: Coordinate (a) and angular (b) accuracy of the Range System vs muon momentum.

10.1 Detector model

Preliminary Range System model was created and simulated using Geant4 and encapsulated within the SpdRoot framework. It consists of a barrel and two end-caps with equal thickness $4\lambda_I$. MC-point is created by Geant4 in a sensitive detector volume when a particle traverses through it.

Digitization is used while converting MC-points into hits (detector signal). The procedure is based on at least one of two requirements:

- Cut 1: minimum passage in active volume $\geq$ 1 cm;
- Cut 2: minimum energy deposited in active volume $\geq$ 1 keV.

Figure 4.27 shows main reference signal/response distributions: average hits per wire (all layers), average hits per layer, and normalized hit multiplicity in an event. It shows good agreement between data and MC with the digitization procedure applied.

10.2 PID algorithms

One of the primary purposes of the Range System is reconstruction of charged particles traversing the RS and identification of muons and hadrons. Charged particles produce hits in the MDT detectors forming

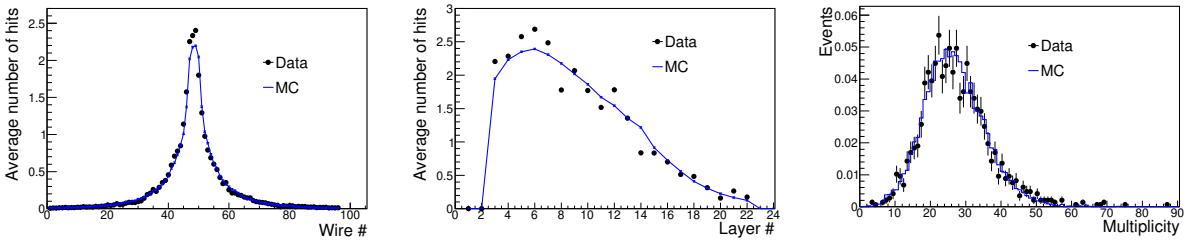

(a) (b) (c)

Figure 4.27: Calorimetric signal/response to the protons with momentum 6 GeV/c: (a) average hits per wire (all layers), (b) average hits per layer, and (c) normalized hit multiplicity in an event.

a hit profile in a layered structure of the Range System. Two approaches may be applied: a Kalman propagation algorithm for fitting tracks and algorithms based on machine learning (ML) techniques. The second approach can be represented as a pipeline of algorithms that process the resulting hit profile in two steps: (a) forming groups of hits by clustering algorithms and (b) assigning the obtained clusters to muons or hadrons by classification algorithms. The main advantage of the described procedure is a relatively high processing speed, compared to traditional track-reconstruction algorithms, since it exploits only the signals from the Range System alone with no need of assigning tracks to those reconstructed in the Straw Tracker.

10.3 Clustering

Clustering is one of the unsupervised machine learning tasks and only hard clustering algorithms (each hit belongs to a cluster or not) are considered. The most basic class of clustering algorithms is the centroid-based K-Means algorithm. Each data point is classified by computing the distance between that point and each group centre, and then classifying the point to be in the group whose centre is closest to it. Then the group centre is recomputed by taking the mean of all the vectors in the group. These steps are repeated for a chosen number of iterations or until the group centres do not change much between iterations. Despite the speed and linear complexity, the application of the algorithm is found to be nearly impossible for our aims, since the number of clusters should be known in advance. As a result, it splits hadron showers and muon tracks into segments.

A possible solution could be the application of density-based algorithms that do not require a pre-set number of clusters at all. The DBSCAN algorithm (Density-based Spatial Clustering Application with Noise) considers clusters as areas of high density separated by areas of low density. The algorithm identifies outliers as noise, associates hits to clusters of arbitrary shapes, naturally exploits 3D coordinates of hits (wire/strips), and has only two hyper-parameters. The main downside is that it doesn't perform as well as others, when the clusters are of varying density.

Figure 4.28 illustrates the results of the DBSCAN clustering algorithm performed in barrel and end-caps of the RS for all hits within polar angle $\pi/16 < \theta < 15\pi/16$ for a single $J/\psi \to \mu^+\mu^-$ MC event.

In order to estimate the quality of the algorithm, we use two evaluation metrics: clustering purity and V-measure. Clustering purity (P) is defined as a ratio of the sum of correctly defined hits over the total number of hits $P = \sum_i N_{i,hits}^{correct} / N_{hits}^{total}$. It is found to be a very straightforward and transparent metrics, but it increases as the number of clusters increases. Another metrics is defined by the values of *homogeneity*, where each cluster contains only members of a single class, and *completeness*, where all members of a given class are assigned to the same cluster. The V-measure is defined as a harmonic mean between the homogeneity and completeness. The advantages of this metrics is that it is normalized between 0 and 1, and it can be used to compare different clustering models that have different number of clusters. The downside is that the random labelling will not yield zero scores, especially when the number of clusters

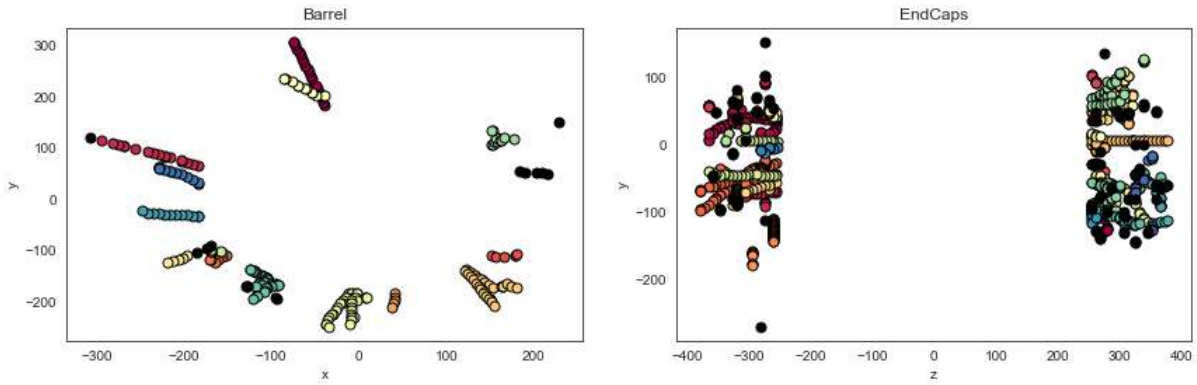

(a) (b)

Figure 4.28: Result of the DBSCAN clustering algorithm performed in (a) barrel and (b) end-caps of the RS for all hits within polar angle $\pi/16 < \theta < 15\pi/16$ for a single $J/\psi \to \mu^+\mu^-$ MC event.

is large. Figure 4.29 shows the DBSCAN evaluation metrics as a function of polar angle threshold $\theta_{thrd} < |\theta| < (\pi - \theta_{thrd})$. The performance of the clustering procedure looks reasonable, starting from the $\pi/16 < \theta < 15\pi/16$ that approximately corresponds to pseudorapidity requirement $|\eta| < 2.4$, quite regularly used by J/ψ physics analyses.

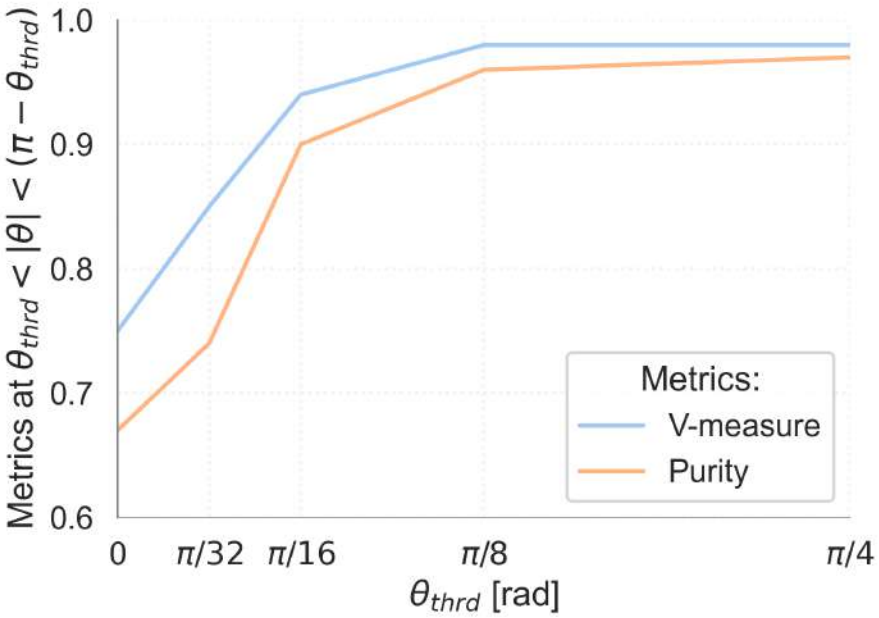

Figure 4.29: The DBSCAN evaluation metrics as a function of polar angle threshold.

10.4 Muon/hadron separation

The second stage of the reconstruction is used to separate between muon and hadron clusters found in the clustering stage by using ML classification algorithms. A hit profile in the Range System corresponding to a particular kind of particle with a certain momentum has a specific pattern. Low-momentum hadrons (p $<$ 1 GeV/c) are almost indistinguishable from muons with the same momentum (see Fig. 4.30). The increasing energy of hadrons significantly changes the profile of hits, forming a cascade of secondary particles for hadrons with momentum up to 10 GeV/c (see Fig. 4.31).

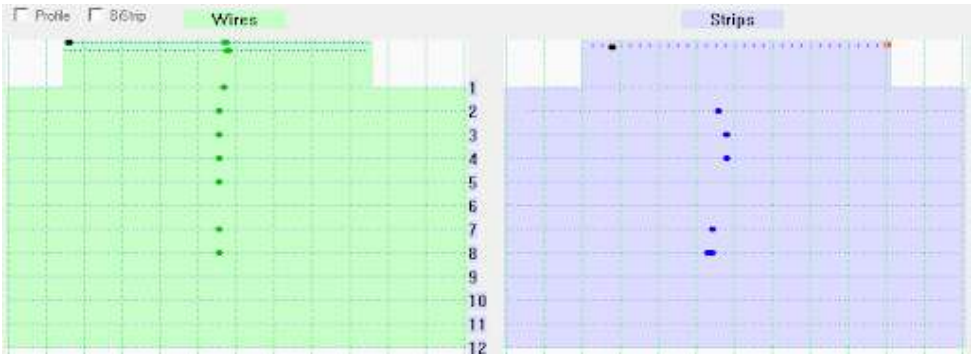

(a)

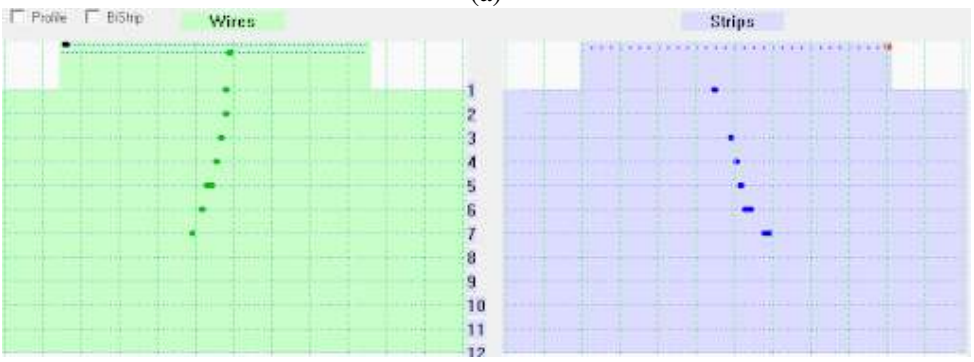

(b)

Figure 4.30: Comparison of wire (green) and strip (purple) patterns in the RS Prototype for (a) muons and (b) pions with the same momentum 0.5 GeV/c.

Finding variables sensitive to differences in such patterns is directly related to the possibility of separation between muons and hadrons. It can be used as an input to various Machine Learning techniques.

As a starting point, a Decision Tree classification algorithm is used to separate between signal (muon) and background (protons and pions) samples in Data and MC. The chosen technique is a well-known solution for binary classification (DecisionTreeClassifier from scikit-learn library). The main advantages of the algorithm are its robustness, transparency, and limited number of hyper-parameters for optimization. Events in both samples were labeled using time-of-flight detectors only. Later, the Cherenkov counter tags will be used to fix the muons. The following variables are chosen as an input to the Decision Tree: hit multiplicity in an event, first and last fired layers, splitting layer number (the lowest number of a layer having $\geq$ 2 hits), and number of hits in the last layer. The normalized distributions of hit multiplicity per event and last fired layer number for muons compared to protons with momentum p = 1 GeV/c and p = 6 GeV/c obtained with SPD Range System (MC) are shown on Fig. 4.32 and Fig. 4.33.

The hit multiplicity is found to be the most powerful discriminative variable while the last fired layer number also showed high importance for muon/hadron separation. The applied technique allows to differentiate between the classes with 95$\div$97% accuracy for muons/pions (see Fig. 4.34 (a)) and 96$\div$99% for muons/protons (see Fig. 4.34 (b)). The analogous method was applied on RSP dataset and showed less accuracy for muons/protons separation (93%), mainly due to the impurity of the signal in the muon sample, since the events in data were labeled using TOF detectors only. Later, the Cherenkov counter tags will be used to fix the muon data sample.

The combined algorithms based on ML-technics and Kalman propagation can be expected to be more effective. The preliminary MC-simulations show that the pion suppression rate below 1% can be achieved, but it has not been confirmed yet in the analysis of data from the RS prototype.

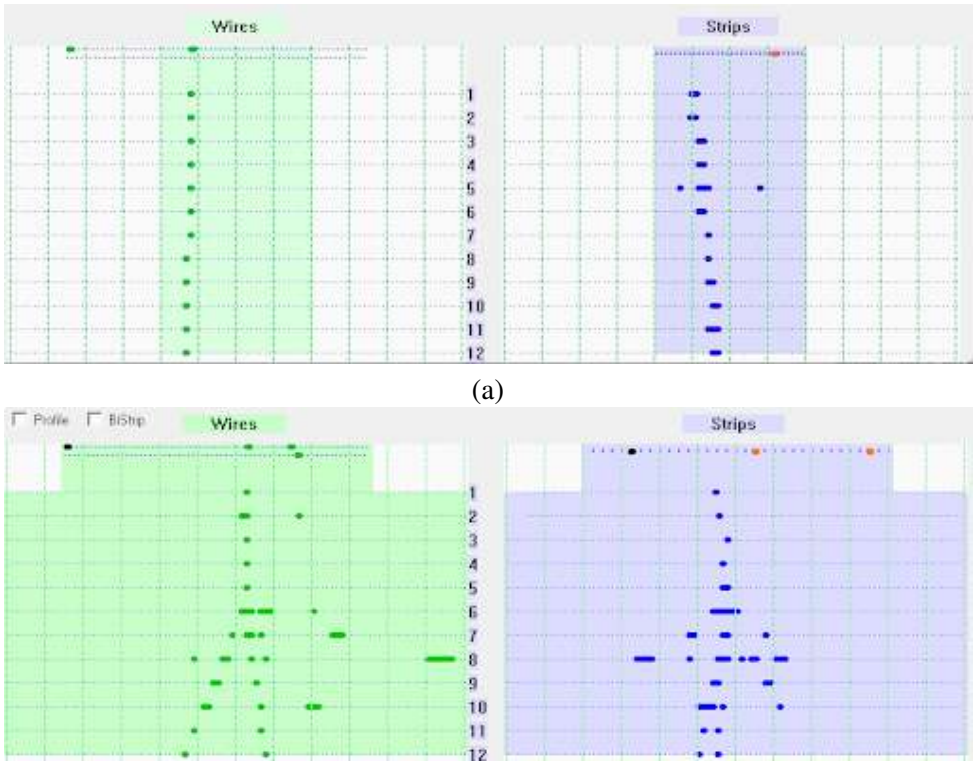

(a)

(b)

Figure 4.31: Comparison of wire (green) and strip (purple) patterns in the RS Prototype for (a) muons and (b) pions with the same momentum 10 GeV/c.

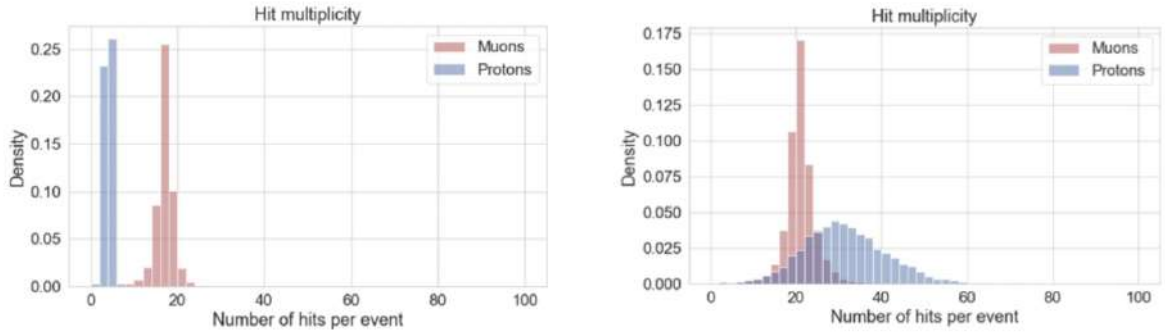

(a) (b)

Figure 4.32: Normalized distribution of hit multiplicity per event for muons compared to protons with momentum (a) p = 1 GeV/c and (b) p = 6 GeV/c in SPD Range System (MC).

11 Cost estimate

The preliminary cost estimate for the Range System is presented in Table 4.6.

12 MDT workshop: production and test areas

MDT (see Fig. 4.8) are gaseous detectors manufactured from thin-walled (0.6 mm thickness) 8-section aluminum profiles (see Fig. 4.35 (a)), with tungsten wires of a 50 μm-diameter stretched inside each section. The profile is placed in a plastic case (see Fig. 4.35 (b)) sealed with plastic end-plugs from both ends (see Figs. 4.36 and 4.37). The end-plugs have special openings designed for the input and output

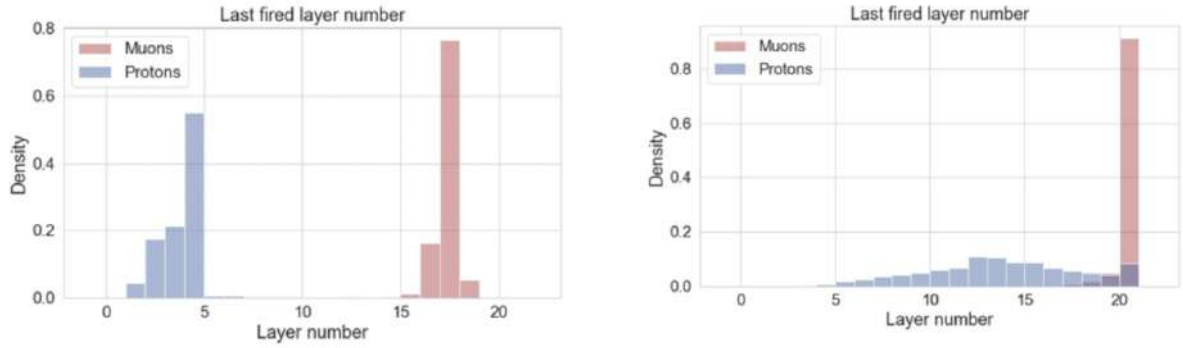

(a) (b)

Figure 4.33: Normalized distribution of last fired layer number for muons compared to protons with momentum (a) p = 1 GeV/c and (b) p = 6 GeV/c in SPD Range System (MC).

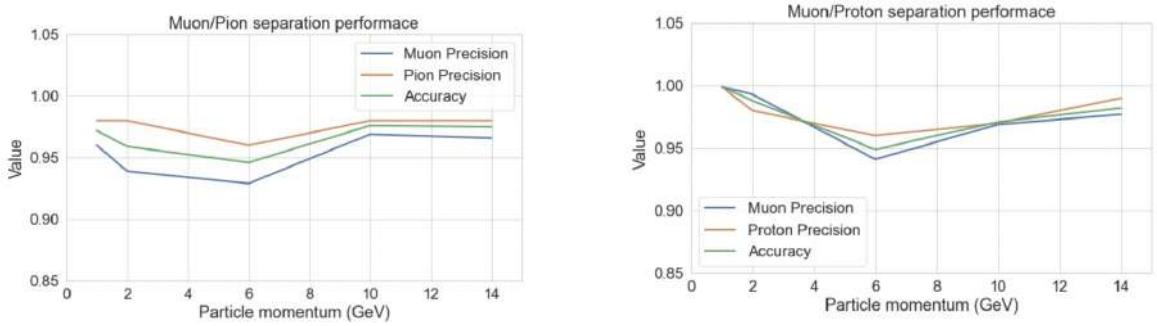

(a) (b)

Figure 4.34: Muon/pion (a) and muon/proton (b) separation performance as a function of particle momentum.

Table 4.6: Cost estimate for the RS.

	Cost, M$
MDT detectors with stripboards	2.94
Analog front-end electronics (including cabling)	3.41
Digital front-end electronics (including VME crates and racks)	3.75
Yoke/absorber (without support and transportation system)	6.00
Total	16.1

of the working gas, as well as for high voltage supply and detector signals readout.

It is planned to organize a full cycle for the serial production of a large number of MDT detectors with length dimensions reaching up to 4.5 m in building 73. The production cycle implies the presence of the following premises: two procurement halls, a washing room, assembly and test areas.

12.1 Technological process of MDT production

The preparation of the MDT plastic cases and aluminium profiles with the desired lengths, as well as perforation (penetration of holes for laying the bases) of profiles , are made in the procurement area. Then cases are blown with compressed air to remove the dust, and moved to a separate rack in the assembly

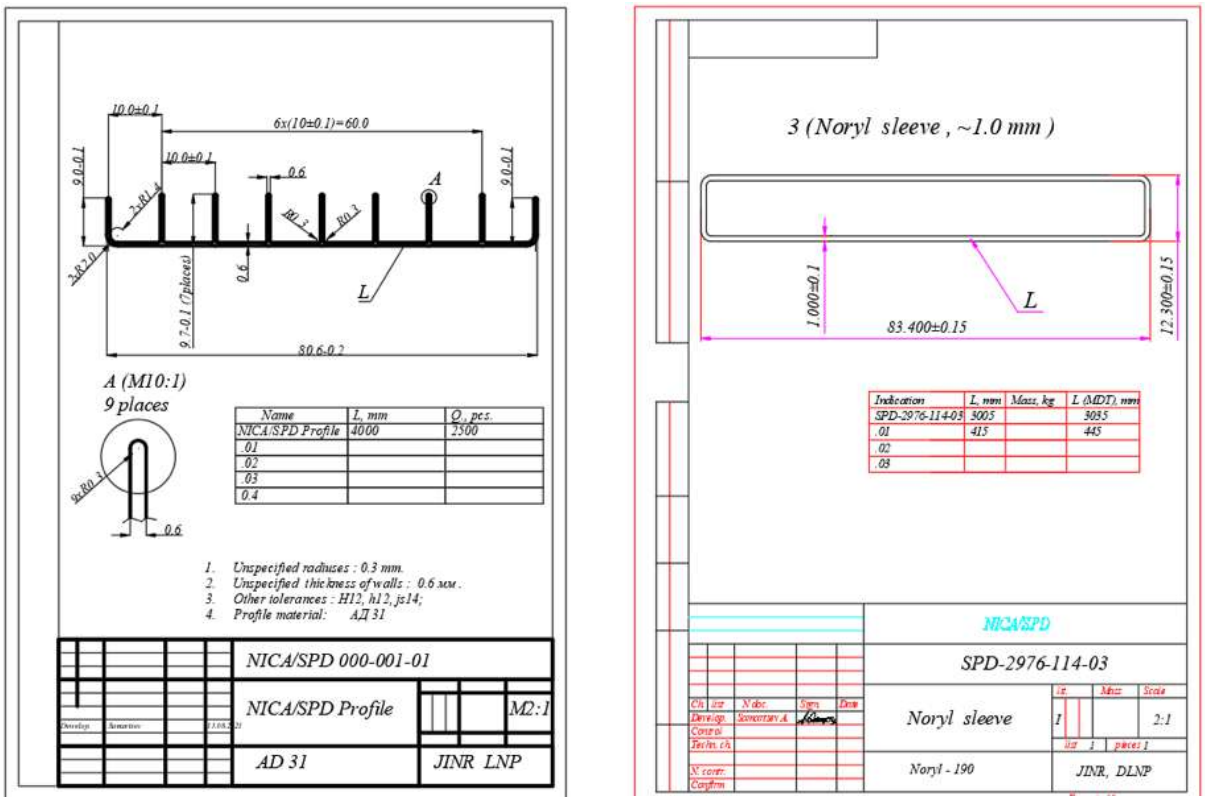

(a) (b)

Figure 4.35: (a) Drawing of aluminum extruded profile manufactured by AGRISOVGAZ. (b) Drawing of plastic envelope for MDT detector.

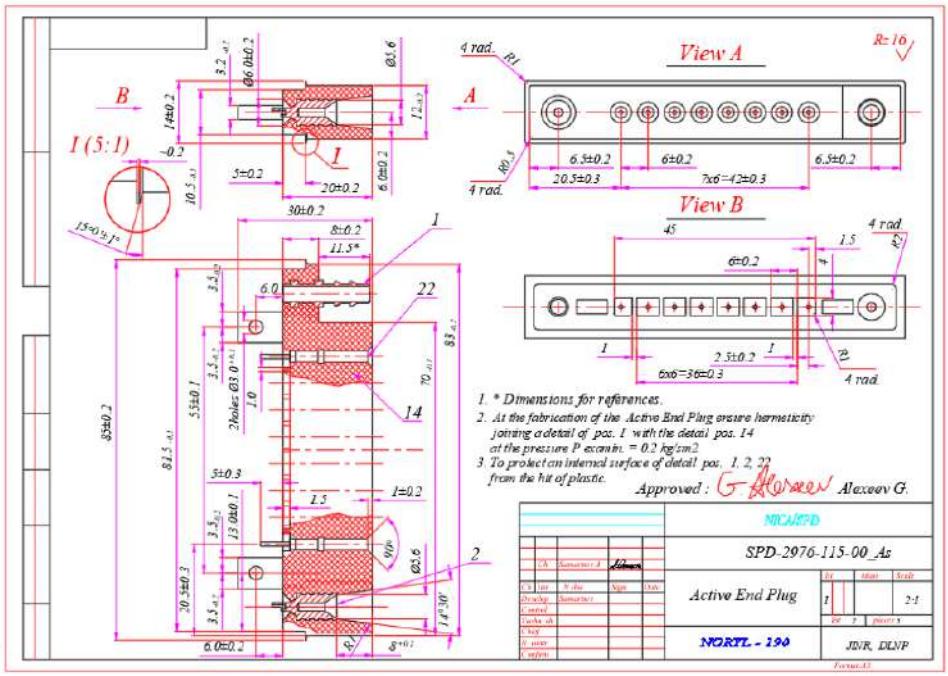

Figure 4.36: Drawing of active end-plug which contains 8 signal connectors, high voltage and gas connectors.

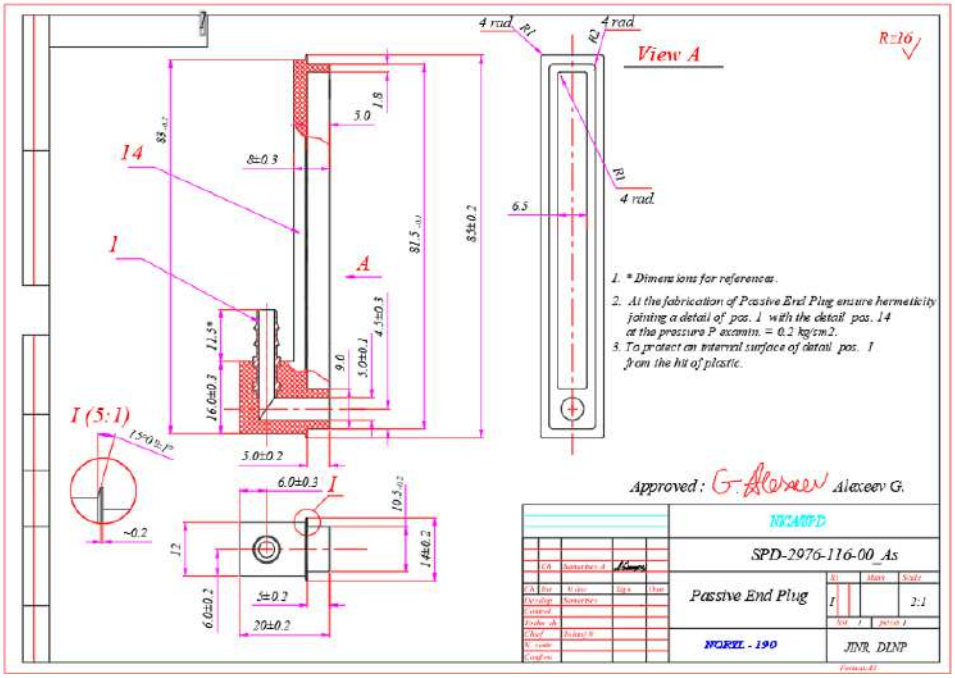

Figure 4.37: Drawing of passive end-plug which contains only gas connector.

area. Ready profiles are moved to the washing room, where they go through a washing procedure in 3 stages. At the first stage, the profiles are cleaned in hot water containing detergent powder at a temperature of about 60 °C to remove possible grease stains and other contaminants. In the second and third stages, the profiles are rinsed in hot and distilled water, respectively.

The washed and dried profiles are stored on the racks in the second procurement hall. In a separate room, the selection, purging and washing of the plastic parts (end-plugs, covers, bases, boards, support spacers) are carried out in a solution of ethyl alcohol with water; wires are soldered to the active end-plugs and matching resistors to the boards; installation and welding of bases into profiles is done; spacers are marked and laid into the profiles. Then the profiles are transferred to the assembly area.

Soldering of the 8 anode wires, laid along the profile sections on the spacers, is made using a semi-automatic winding machine. Then the spacers are welded on the brewing machine to fix them in certain places inside the profile. After that, the wires of the active end-plug are soldered to the boards installed in the profile. Then a plastic case muffled from one end by a passive end-plug is put on the profile.

After that, the testing cycle begins on special stands for the anode wire tension test and preliminary high voltage test. In the case of a positive test result, the second end of the case is muffled by the active end-plug and welded using a brewing machine. Then the ready tube is filled with the working gas and passes high-voltage training. The last stage of testing is a gas tightness check.

Verified MDTs are stored on special racks.

12.2 The terms of reference

The terms of reference provides for:

1. Partial reconstruction of building 73.

2. Allocation of manufacturing facility (previously used at the JINR Experimental Workshop) for the MDT mass-production and testing in the announced building.

3. Fulfillment of all requirements for production and auxiliary premises, workplaces, equipment and personnel, needed:
   - to provide safe working conditions in the manufacture of products at all stages of the technological process of assembly and installation;
   - to manufacture the products that meet the requirements.

The building plan is given in Fig. 4.38, and includes the following premises distinguished by the type of work:

1. Service and utility rooms:
   (a) Room 1, 1A - physicists rooms;
   (b) Room 2 - warehouse;
   (c) Room 3 - service room;
   (d) Room 11 - computer room;
   (e) Room 11A - service room;
   (f) WC room - bathroom and shower;
   (g) Meeting and relaxation room, 3^{rd} floor.
2. Industrial premises:
   (a) Room 4 – assembly room:
      i. C - table for washing and preparation of plastic parts (end-plugs, bases, spacers, covers);
      ii. MC - assembly table for soldering wires to active end-plugs and putting on shrink tubes.
   (b) Room 5 - procurement area No. 1:
      i. Racks $5_{1,2}$ - racks for profiles and plastic cases before processing;
      ii. Racks 5_3 - rack for finished products;
      iii. Electric hoist for 0.5 ton.
   (c) Room 6 - washing area:
      i. B1, B2 and B3 – three baths for sequential washing of profiles. Baths B1 and B2 are filled with hot water (about 0.6m^3) from the plumbing system and maintained at a temperature of about 60 $^\circ$C using electric heaters. Dimensions of B1 and B2: $600\times600\times6000$ mm^3, B3: $400\times400\times6000$ mm^3. Bath B3 is filled with distilled water (about 0.4m^3) at a room temperature.
      ii. D – distiller. Overall dimensions: $700\times700\times2000$ mm^3.
      iii. B4 – tank for checking the gas tightness of the manufactured MDT. Dimensions B4: $300\times360\times7000$ mm. Bath B4 is filled with distilled water (about 0.4m^3).
      iv. B – a cylinder with N2 gas.
      v. Czh6 – rack for preliminary drying of washed profiles.
   (d) Room 7 – procurement area No. 2:
      i. installation of boards, bases, spacers;
      ii. Szh7 – rack for prepared profiles;
      iii. St1 and St2 – machines for profiles trimming and perforating;
      iv. St3 – machine for cutting of plastic cases.

(e) Room 8 – Assembly area:
   i. C1 – machine 1 for wire winding;
   ii. C2 – machine 2 for spacers welding;
   iii. C3 – workstation for soldering wires of active end-plugs to boards;
   iv. C4 – machine 4 for welding of the end-plugs to the plastic cases;
   v. Collection table – mobile table for MDT assembly;
   vi. B – tank with cooling water for machine tool 4;
   vii. Szh8 – rack for MDTs prepared for testing.

(f) Room 9 – area for testing of manufactured MDT:
   i. Stand 1 – wire tension test bench;
   ii. PC - personal computers (3 pcs.);
   iii. Stand 2 – stand for testing MDT for dark current;
   iv. Stand 3 – stand for high-voltage training of MDT with a working gas mixture of 30% CO_2 + 70% Ar;
   v. Szh9 – rack for finished product.

(g) Room 10:
   i. GP – gas control panel;
   ii. Cylinders with CO_2 (1–2 pieces) and Ar (3–4 pieces);
   iii. Szh10 – rack.

(h) Room 12 – Scintillator site:
   i. Stand 4 – stand for scintillator assembly, gluing and taking of scintillator samples optical characteristics;
   ii. Szh12 – rack 12.

(a) (b)

Figure 4.38: Plan of the building to be used for the MDT detectors mass production workshop and deployment of the equipment for production of auxiliary parts for the MDT detectors: (a) first (b) second and third floors.

Chapter 5

Magnetic system

A superconducting magnet is one of the most important parts of the AMBER setup. Together with the tracking system, it provides the measurement of charged particle momenta with accuracy of about 2%. The steel elements of the Range System serve as a yoke of this magnet. Two fundamentally different magnet designs are currently under consideration. The first, proposed by the Institute of Nuclear Physics (Novosibirsk), is based on the experience of creating a magnet for the PANDA setup. The second is proposed by JINR and is based on the experience of creating superconducting magnets for accelerators. The final decision should be taken by the SPD Technical Board till the end of 2022.

1 Novosibirsk option

1.1 General performance requirements

1.1.1 Magnetic field

The magnetic field along the solenoid axis should be at least 1.0 T.

1.1.2 Main dimensions and parameters of the magnet

The cryostat of the magnet with the coils, cold mass, and thermal shields is located inside the yoke. A distribution box called control dewar is located on the upper octant of the yoke. The overall dimensions are driven by the area allocated for the SPD subdetectors and by the magnet field parameters. Outside diameter of the cryostat is 3808 mm, and the gap between the yoke and the cryostat is about 20 mm. In the transverse direction, a free space with a diameter of 3308 mm is left for the inner SPD detectors. The length of the magnet is 4080 mm. The magnet should be installed symmetrically inside the yoke (see Fig. 5.1).

1.2 Technical specification of components

1.2.1 Magnetic analysis

The SPD solenoid is designed to provide a magnetic field of 1 T over a length of about 4 m in a bore of 3.2 m. In general, the uniformity of the field is not a critical factor. The field variation up to 20% in the area of the tracking detectors ($|z| < 1.4$ m, $r < 0.9$ m) is acceptable. To meet the above requirements, the cold mass design detailed in foresaw splitting of the solenoid in three inter-connected windings, featuring 300, 150 and 300 turns in the upstream, center and downstream coils, respectively. Two options of the operating current of 4.4 kA and 5.2 kA are considered, which correspond to the value of the field in the center of the magnet 1 T and 1.2 T, respectively.

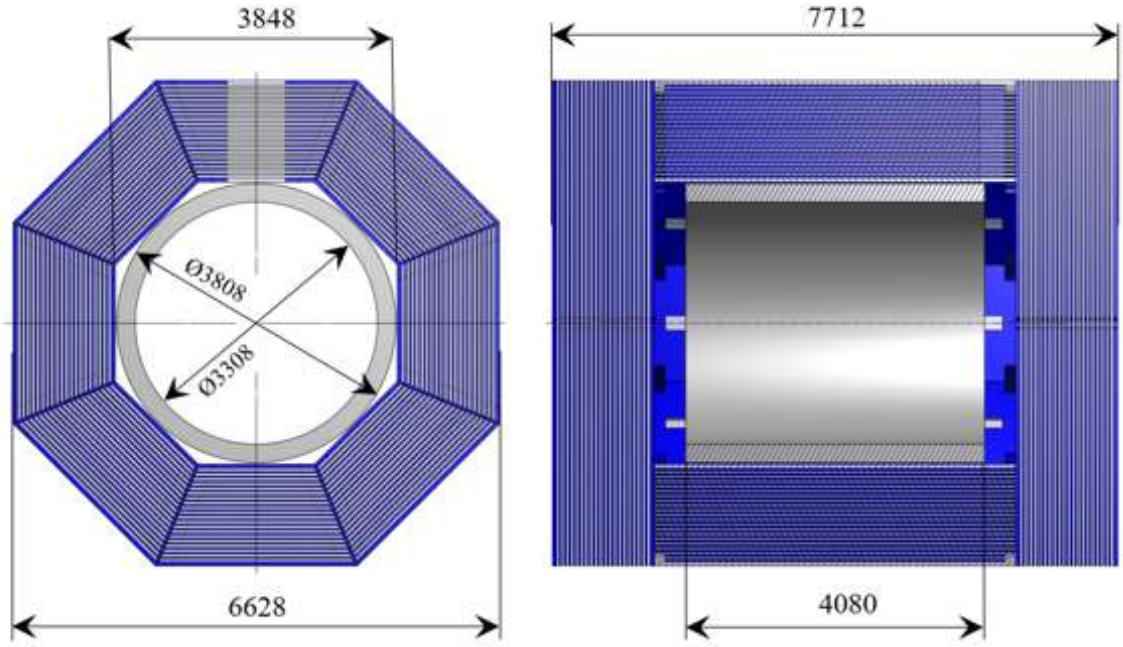

Figure 5.1: The main dimensions of the cryostat and the yoke.

1.2.1.1 3D simulation The following conditions were applied for the 3D simulation: the configuration of the superconducting coil and magnetic design according to the latest STEP model with three coils. The coil arrangement is shown in Fig. 5.2. The current of the coil is 5200 A. Conductor cross-section is 8 mm × 12 mm. Length of the side coils is 2×1260 mm, while length of the central coil is 630 mm. The calculations were carried out using the MASTAC software package. Three options were considered:

1. the basic version with three coils;
2. the correction coils added to the basic version (see Table 5.1);
3. the central coil is absent to increase the field uniformity.

Figure 5.3 shows the identification of the supercondiucting coils. The "A" configuration is a basic three coils arrangement, "B" and "C" are the types of correction coils added. Table 5.2 shows the correction coil designs in terms of the number of layers and ampere-turns.

Table 5.1: Design of the correction coils.

Configuration	Coil "B"	Coil "C"
1	2 layers of 60 turns	2 layers of 60 turns
2	2 layers of 20 turns	2 layers of 50 turns
3	2 layers of 50 turns	2 layers of 50 turns
4	2 layers of 40 turns	2 layers of 40 turns

Table 5.2 presents the uniformity for simulation of cases described in Table 5.1. From the data in Table 5.2, it can be seen that for coils 40×2 + 40×2 the results are optimal. This field map can be considered as a reference for estimating the rate of reconstruction in a homogeneous field.

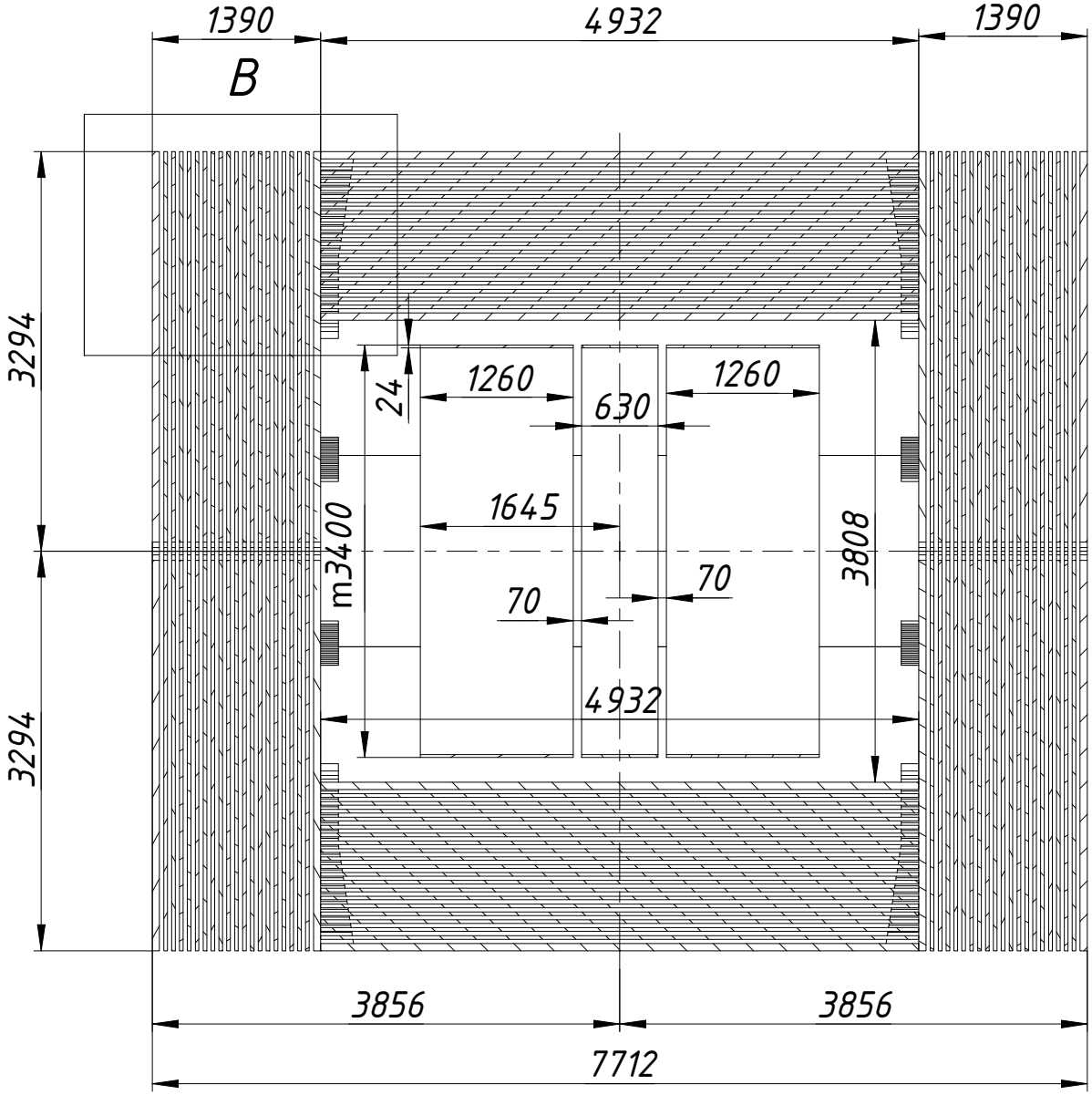

Figure 5.2: Cross-sectional view of the magnet demonstrating the arrangement of superconducting coils for the basic option with three main coils and without correction coils.

Table 5.2: Maximum values of deviations of $B_z(z)$values from $B_z(0)$ in % at different vertical Y positions.

	Y=0 m	Y= 0.5 m	Y=1.0 m
65×2	12.2	10.8	3.7
60×2 + 60×2	5.7	2.9	13.7
20×2 + 50×2	9.7	8.0	3.9
50×2 + 50×2	6.6	4.2	10.1
40×2 + 40×2	8.3	6.3	5.8
80×2 + 30×2 + 30×2	3.9	3.4	15.8

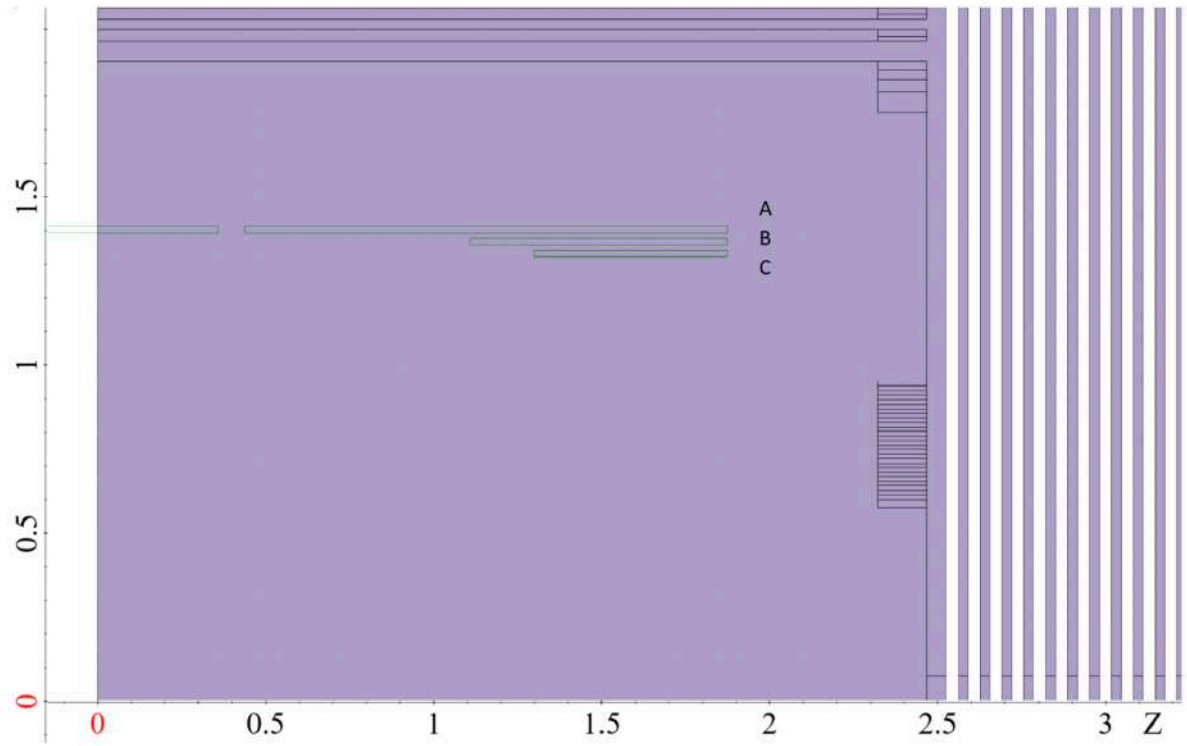

Figure 5.3: Schematic cross-section view of the yoke and coils for the configuration of the solenoid with correction coils.

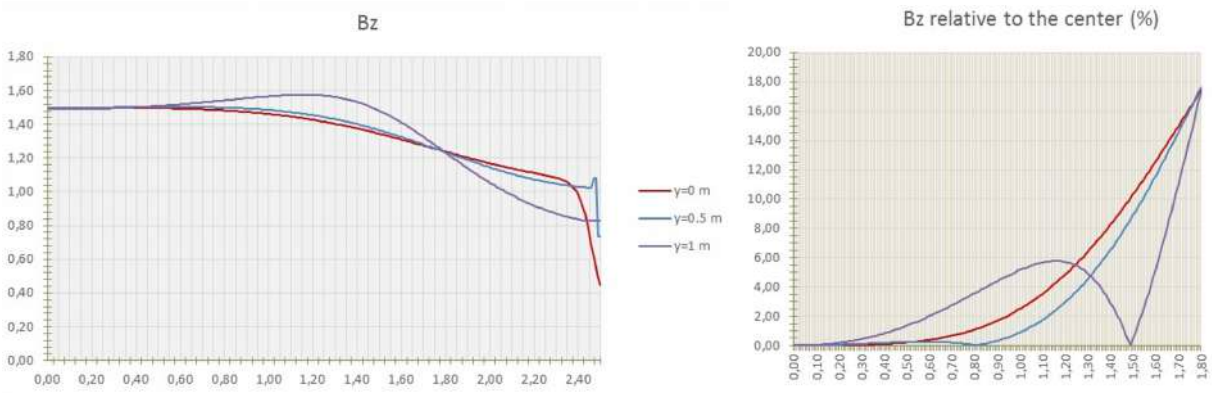

(a) (b)

Figure 5.4: Distribution of the axial component of the magnetic field B_z along the z axis for the magnet configuration with correction coils $40\times2+40\times2$ and the current of 5200 A. (a) shows the absolute value of B_z and (b) shows B_z normalized to its value at $z=0$. Three curves correspond to the displacements $y=0$ m, $y=0.5$ m, $y=1$ m at $x=0$ m.

The distribution and uniformity of B_z field component in the section YZ at X = 0 for coils 40×2 + 40×2 are shown in Fig. 5.4 (a) and (b), respectively. The color plot for B_z component is presented in Fig. 5.5.

Switching off the central coil in order to reduce its contribution to the central region of the solenoid is considered a potential option for improving the field uniformity without the use of the additional correction SC coils. In this case, the uniformity improves up to 10% (see Figs. 5.6 and 5.7). The disadvantage of this method of improving uniformity is the decrease in the solenoid field and, as a consequence, the need to increase the current from 5200 A to 6500 A to achieve 1.1 T at the center of

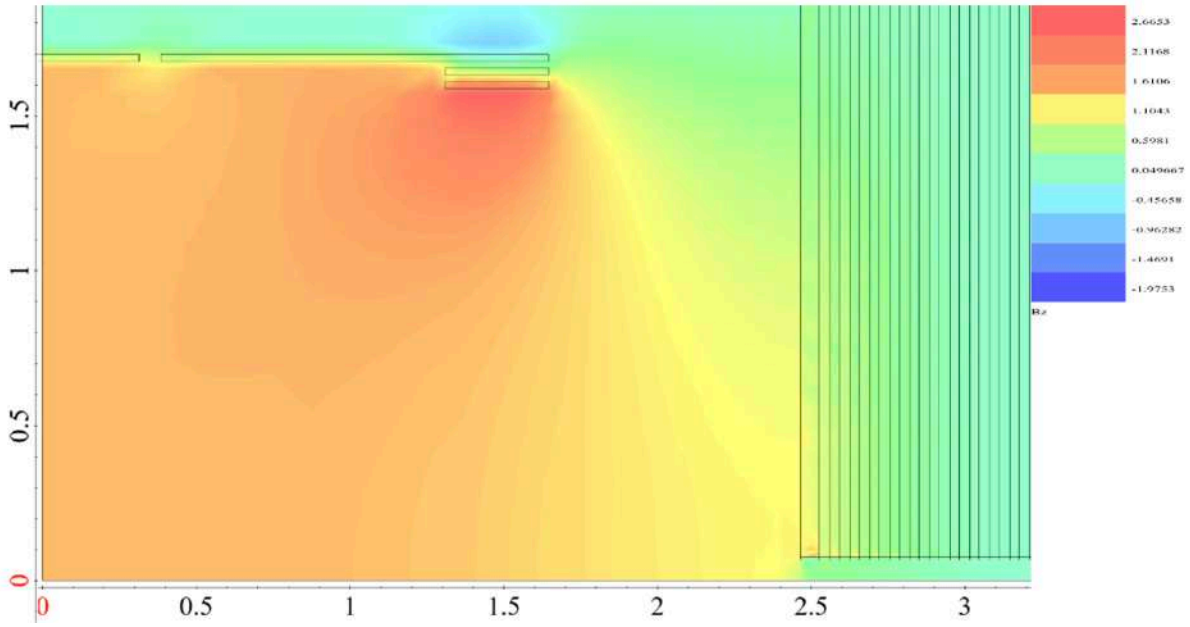

Figure 5.5: Distribution of the B_z component of the magnetic field in the YZ section at X = 0 for correcting coils configuration $40 \times 2 + 40 \times 2$.

the solenoid. The distribution and uniformity of B_z in the section YZ at x = 0 for central coil switch off are shown in Fig. 5.8 (a) and (b). The color plot for B_z component for this case is presented in Fig. 5.8.

Therefore, the three coils version of Fig. 5.2 is the basic variant. The distribution and uniformity of B_z in the section YZ at x = 0 for basic version are shown in Fig. 5.8 (a) and (b).

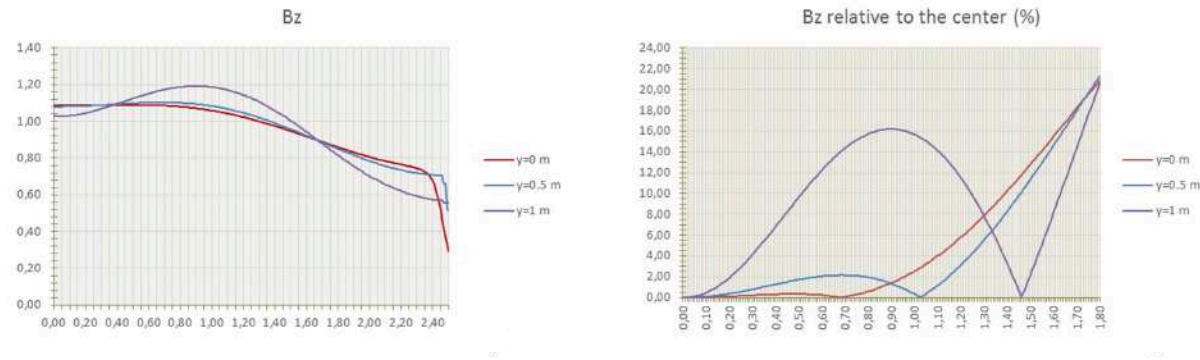

(a) (b)

Figure 5.6: Distribution of the axial component of the magnetic field B_z along the z axis for the magnet configuration without the main central coil and the current of 6500 A. (a) shows the absolute value of B_z and (b) shows B_z normalized to its value at $z = 0$. Three curves correspond to the displacements $y = 0$ m, $y = 0.5$ m, $y = 1$ m at $x = 0$ m.

1.2.1.2 Magnetic forces Simulation of the magnetic forces was performed with the Maxwell tensor method from 3D magnetic field data. The results of simulation are shown in Table 5.3. The elements on which the force acts are shown in Figure 5.9.

Figure 5.10 shows a map of the distribution of magnetic forces acting on one of the door wings. The force values are calculated for the centers of the corresponding grid elements 0.1×0.1 m and displayed in color ranges of 200 Newtons. The results of calculation for magnetic forces acting on the coils during

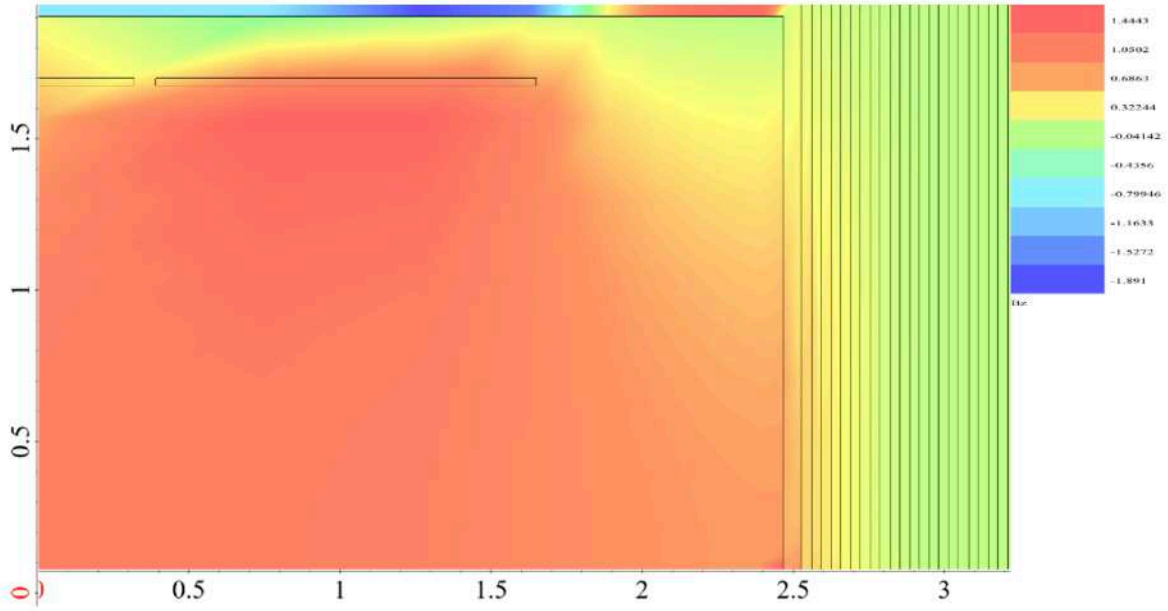

Figure 5.7: B_z component of the magnetic field in the YZ section at X = 0 for the central coil switched off and current 6500 A.

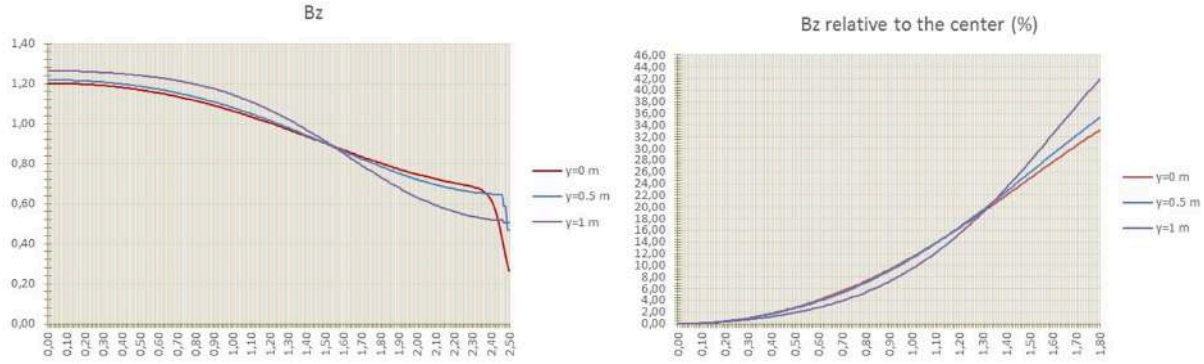

(a) (b)

Figure 5.8: Distribution of the axial component of the magnetic field B_z along the z axis for the basic magnet configuration with three main coils and a current of 5200 A. (a) shows the absolute value of B_z and (b) shows B_z normalized to its value at $z = 0$. Three curves correspond to the displacements $y = 0$ m, $y = 0.5$ m, $y = 1$ m at $x = 0$ m.

1094 their displacement are shown in Table 5.4.

Table 5.3: Magnetic forces in kN acting on the elements of the solenoid (1 mm air gap before end-caps). Calculations were performed for the basic configuration of the magnet with three coils.

Force component	Barrel top sector (half along Z)	Barrel top sector	End-caps (half)	End-caps	Central coil (1/8 of top sector)	Side coil (1.8 of top sector)
X	0	0	-12.4	0	0	0
Y	-143.8	-287.6	0	0	658.9	1185.9
Z	67.5	0	-694.1	-1388.2	0	-594.1

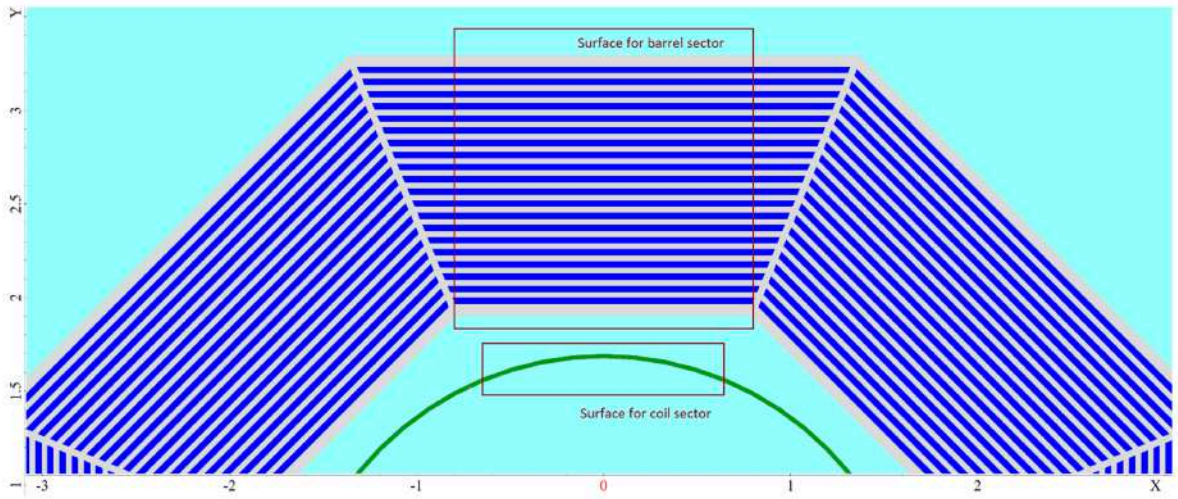

Figure 5.9: Schematic view of contour surfaces for force calculation.

Table 5.4: Magnetic forces in kN acting on the displaced coils.

Displacement, mm	Force comp.	Left coil	Central coil	Right coil
0	X	0	0	0
0	Y	0	0	0
0	Z	4748.0	0	-4748.0
5 in Z	X	0	0	0
5 in Z	Y	0	0	0
5 in Z	Z	4521.4	-69.6	-4743.4
5 in Y	X	-2152.8	-1065.1	2152.8
5 in Y	Y	0	0	0
5 in Y	Z	4752.8	-0.3	-4753.3

1.2.2 Cold mass with conductor and coil

The SPD solenoid is designed to operate at a current of 4.4 kA, that is 24% of the critical current at 4.5 K, and 2.05 T peak magnetic field in the coil and 1.0 T magnetic field in the axis of the solenoid.

The conductor is a superconducting NbTi/Cu wire-based Rutherford cable, co-extruded with a high purity aluminum-stabilizing matrix. The insulated conductor dimensions at 4.5 K are 10.90 mm in width and 7.90 mm in height. The Rutherford cable is composed of 8 strands with a diameter of 1.40 mm and a Cu/SC ratio of 1.0. The critical current density of the superconductor at 4.2 K and 5 T shall be larger than 2800 A/mm^2 to ensure a temperature margin for a quench well above 2.0 K. The same type of the conductor is produced in Russia and used for the PANDA solenoid, FAIR, Darmstadt.

The SPD solenoid consists of three 2-layer coil modules to be wound on a collapsible mandrel. After curing, aluminum alloy support cylinders are placed over each module and the assemblies are epoxy bonded. The pre-assembled modules are then removed from the mandrel to be electrically connected and bolted together to form a single cold mass assembly before installation in the cryostat.

The magnet is indirectly cooled by a network of aluminum alloy cooling tubes, securely bonded to the outer surface of the aluminum alloy support cylinder, ensuring proper heat conduction. During normal operation, two-phase helium is circulated through the cooling tubes by natural convection.

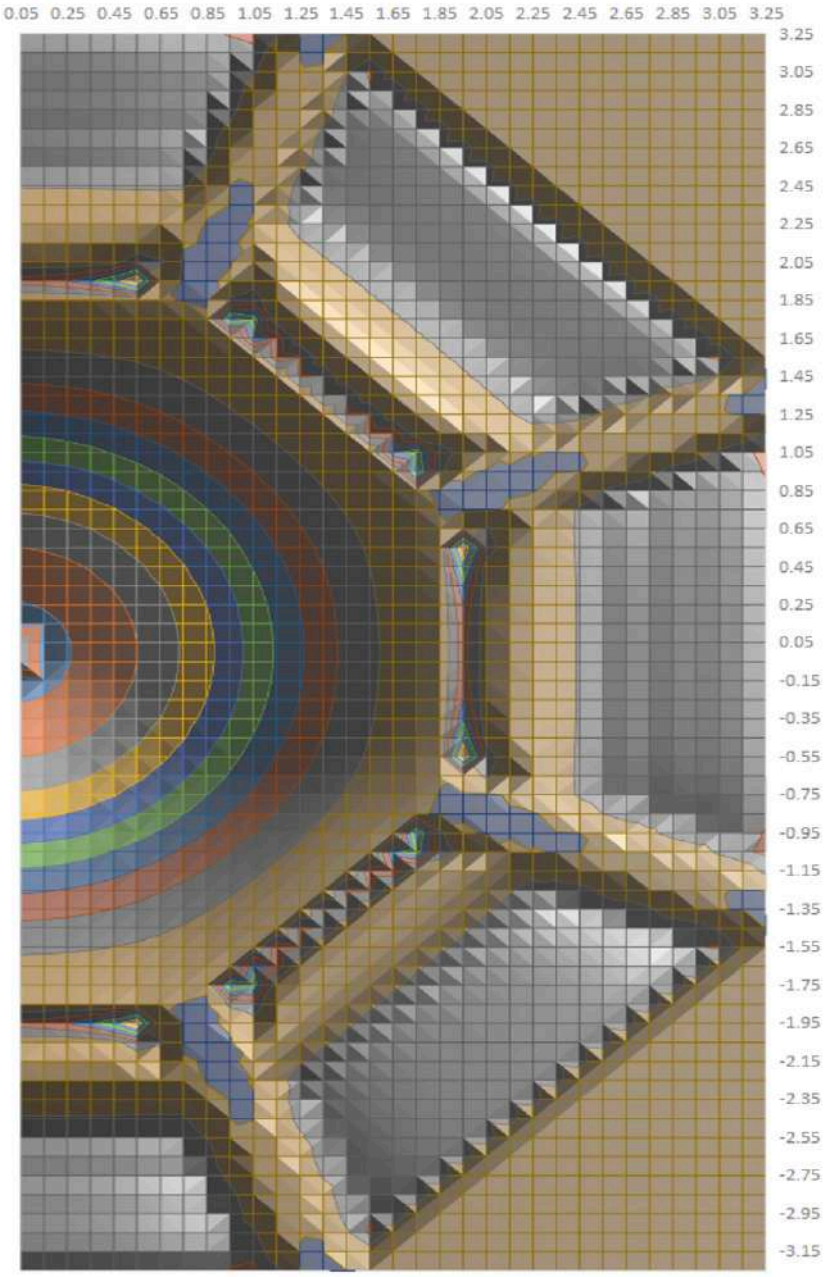

Figure 5.10: Magnetic forces map for one of the door wings.

The magnet quench protection system relies on the continuous monitoring of the coil's voltages and the extraction of the energy to an external dump resistor, once a quench is detected. The maximum coil winding temperature and electrical voltage across the coil terminals during a quench has to be limited to 100 K and 500 V, ensuring a robust and extremely low-risk operation, as appropriate for the unique particle detector magnets. Quench propagation across the coil winding is accelerated by using the quench-back effect of the support cylinder, as well as the aluminum heat drains.

The cold mass of the SPD solenoid consists of three epoxy resin impregnated coils, reinforced by shells made of structural aluminum.

The upstream and downstream winding packs are identical and feature 2 layers of 150 turns. The center coil, instead, is smaller, featuring 2 layers of 75 turns. The conductor is wound around the aperture with

a tension. The tension of the conductor is set with tensioning rollers weighing about 50 kg. The coils should be prepared and impregnated in vacuum according to the standard BINP technological scheme TTS4 STO 103-2011.

Figure 5.11 shows the dimensions of the coil envelopes at room temperature, as computed taking into account thermal shrinkage, shrink fit, and the magnetic field. Note that the dimensions include both cable insulation and ground insulation.

The cold mass components are shown in Fig. 5.12 (a).

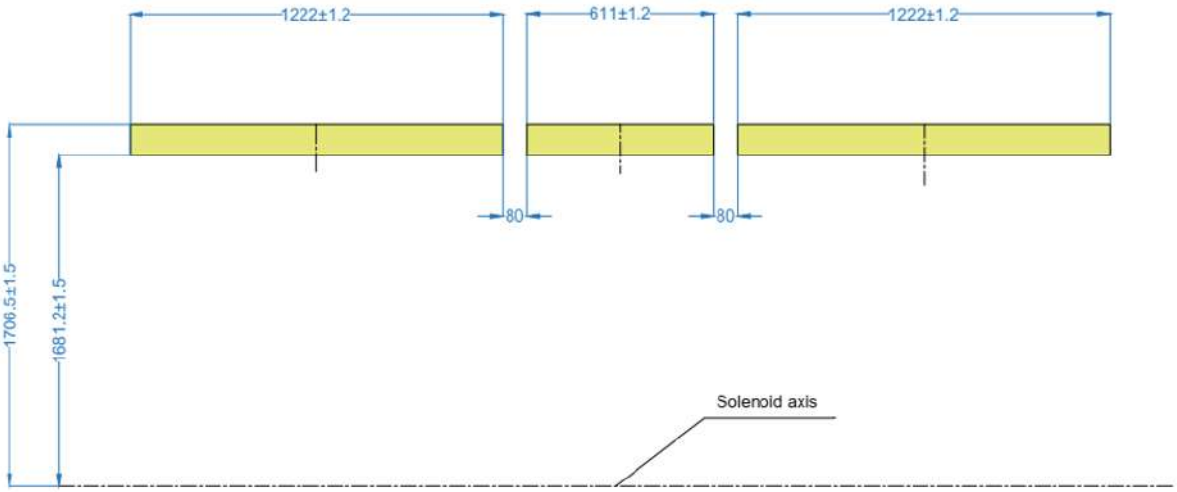

Figure 5.11: Room temperature dimensions in mm of the coil envelopes, including cable and ground insulation.

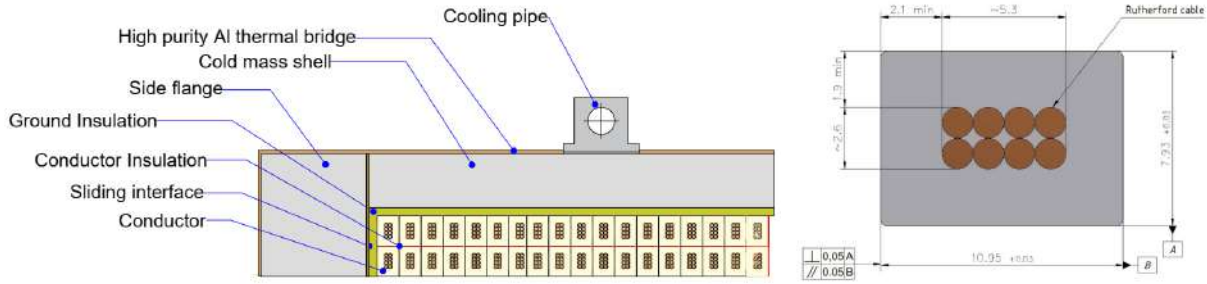

(a) (b)

Figure 5.12: (a) Part of the cold mass cross-section, showing the layout at the end flange. (b) Cross-section of the solenoid conductor, showing the 8 strands Rutherford cable enclosed by the Al matrix, including sizes and their tolerances.

1.2.3 Conductor

Al stabilized conductors for detector magnets are selected for the following reasons:

- simplicity of conduction cooling; affordable, since no dynamic operation is needed; quasistationary;
- simplicity and reliability of electrical connection;

Table 5.5: NbTi/Cu strand mechanical and electrical specifications.

Parameter	Unit	Value	Tolerance
Diameter filament	μm	< 20	–
Diameter strand	mm	1.400	$\pm$ 0.005
Cu/SC ratio	–	1.00	$\pm$ 0.05
Surface coating	–	none	–
NbTi Jc (at 4.2 K, 4.05 T)	A/mm^2	> 2800	–
Critical current (at 4.2 K, 4.05 T)	A	> 2600	–
n-value (at 4.2 K, 4.05 T)	–	> 30	–
Conductor RRR	–	> 100	–
Twist direction	–	left	–
Twist pitch	mm	25	$\pm$ 5

Table 5.6: Rutherford cable mechanical and electrical specifications.

Parameter	Unit	Value	Tolerance
Number of strands	–	8	–
Cable width	mm	5.3	$\pm$ 0.1
Cable thickness	mm	2.60	$\pm$ 0.05
Transposition angle	degree	20.0	$\pm$ 0.5
Twist direction	–	right	–
Critical current (at 4.2 K, 4.05T)	A	> 20800	–
Critical current degradation of extracted strand (at 4.2 K, 4.05 T)	%	< 5	–
RRR of extracted strands	–	> 100	–
Residual twist on 1 m of cable	degree/m	< 45	–

- high-purity Al stabilized, the residual-resistance ratio (RRR) $\geq$ 1000, maximum MPZ (m), much larger λ/ρ than copper;
- particle transparency for minimum particle scattering.

This type of conductors was used in production of larger detectors, such as CELLO, CDF, TOPAZ, VENUS, ALEPH, DELPHI, CLEO, SDC, BELLE, ATLAS CS, ATLAS ECTs, ATLAS BT, CMS, PANDA and Mu2e solenoids. Exactly the same conductor, as was used for the PANDA solenoid is supposed to use in SPD. The solenoid conductor consists of three components:

- superconducting NbTi/Cu multi-filamentary strand with 1.4 mm diameter;
- Rutherford-type flat cable with 8 strands;
- high purity aluminum stabilizer of 10.95 mm $\times$ 7.93 mm cross-section, clad by a co-extrusion or plating process (or another qualified process).

Pure aluminum features a very high electrical and thermal conductivity at low temperatures, providing the best possible stability in terms of maximum MPZ (Minimum Propagation Zone), making the coil least sensitive to mechanical disturbances that can cause coil training during commissioning and quenching during normal detector operation. Furthermore, aluminum stabilized superconductors can be made by co-extrusion of several kilometers long. Precise rectangular conductor shapes can be obtained, allowing for high accuracy in the coil winding. The cross-section of the conductor is shown in Fig. 5.13 (b).

Table 5.7: Solenoid conductor mechanical and electrical specifications.

Parameter	Unit	Value	Tolerance
Width (after cold work) at 300 K	mm	10.95	$\pm$ 0.03
Thickness (after cold work) at 300 K	mm	7.93	$\pm$ 0.03
Width (after cold work) at 4.5 K	mm	10.90	$\pm$ 0.03
Thickness (after cold work) at 4.5 K	mm	7.90	$\pm$ 0.03
Minimum Al layer thickness in height	mm	$>$ 1.9	–
Minimum Al layer thickness in width	mm	$>$ 2.1	–
Surface roughness	–	Ra $<$ 3.2	–
Critical current (at 4.2 K, 4.05 T)	A	¿ 20800	–
Critical current (at 4.5 K, 3.6 T)	A	¿ 23400	–
Critical current degradation of extracted strand w.r.t. virgin wire	%	$<$ 15	–
Overall Al/Cu/superconductor ratio	–	10.5/1.0/1.0	–
Extracted strand RRR	–	$>$ 100	–
Aluminum RRR (at 4.2 K, 0 T)	–	$>$ 600	–
Al 0.2% yield strength at 300 K	MPa	$>$ 30	–
Al 0.2% yield strength at 4.2 K	MPa	$>$ 40	–
Shear strength Al to strands	MPa	$>$ 20	–
Unit length for upstream & downstream coils	m	2 $\times$ 3203	–
Unit length for center coil	m	1604	–
Total length of conductor	m	8010	–
Minimum bending radius during production and on spools	mm	$>$1000	–

Tables 5.5, 5.6, and 5.7 present a summary of the main mechanical and electrical properties of the strands, Rutherford cable, and Al-stabilized conductor. The full technical specifications for manufacture, inspection, and test can be found in reference [?????].

The conductor has a temperature margin of about 2,4 K. The shape of the conductor allows to easily wind the coil from both the wide and the narrow sides.

1.2.4 Insulation

The main requirement for coil insulation is to provide the required electrical strength in terms of breakdown voltage, while maximizing heat conduction, in order to reduce the peak temperature in the conductor in the 2-layer windings. The conductor insulation used in PANDA is proposed for the SPD solenoid. The insulation scheme relies on the use of fiberglass 3$\div$5 mm thick in the first and the last layers, and a nominal conductor insulation between layers. The nominal cable insulation thickness is 0.200 mm per side. It is made of two half-overlapped layers of 100 μm thick fiberglass tape. The tape is wrapped around the surface of the conductor. BINP technology of a vacuum impregnation provides a reliable electrical strength and a good resistance to coil winding imperfections, especially when using two layers of the conductor, in the SPD case.

Ground insulation is added at the outer surface and sides of the coil modules. No ground insulation is applied at the inner diameter, where detector vacuum already provides the necessary dielectric strength. At the outer diameter (3$\div$5 mm thick), the first layer is wound, which is then machined, after curing of the coil module to obtain precise fitting to the supporting cylinder-to-coil interface. The precise thickness of ground insulation after machining depends on the control of the radial dimensions of the coil during winding. A minimum thickness of 2.0 mm is recommended.

The envisaged thickness of ground insulation at the coil sides is 2.80 mm for the upstream and downstream coils and 1.50 mm for the central coil. The thickness of the axial ground insulation can be adjusted

to correct winding tolerances, since dielectric strength is always ensured by the mylar layer, located at the sliding interface. At the side flange, used as the base for coil winding, the axial ground insulation is provided in the form of epoxy shims, precisely machined, in order to accommodate winding tolerances. At the opposite side, axial ground insulation is provided by filling the empty spaces between the winding pack and the flange with epoxy resin after the flange assembly.

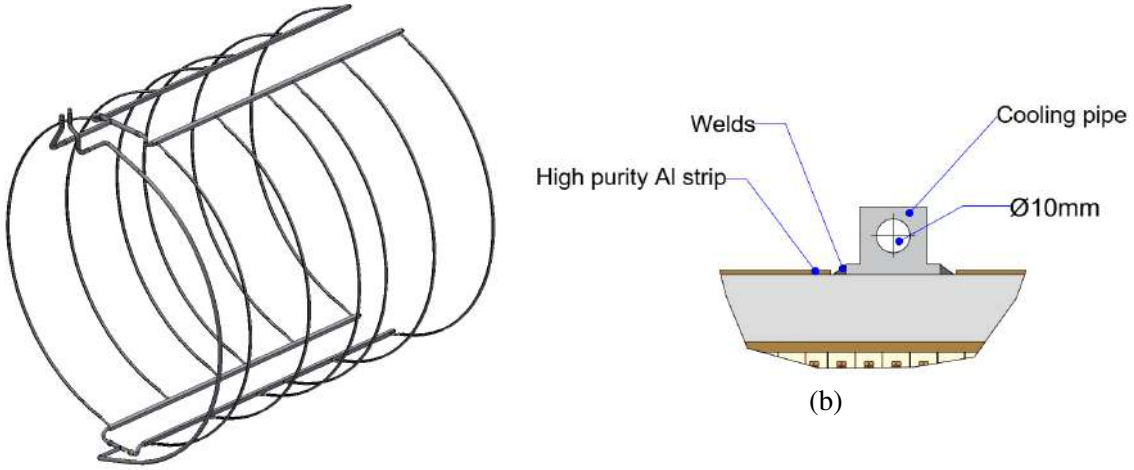

(a) (b)

Figure 5.13: (a) Thermo-syphon circuit. (b) Connection of the cooling tubes and aluminum strip on the outer surface of the aluminum alloy support cylinder.

1.2.5 Thermo-syphon cooling circuit

The cold mass of the SPD solenoid is indirectly cooled by circulating two-phase helium by natural convection. Homogenous model, used for the preliminary study for CMS [14] and then BINP, is also used for cooling of the PANDA detector solenoid and the CBM detector dipole magnet.

The main advantages of a thermo-syphon system are its simplicity and reliability, as it does not require any moving parts, such as cold pumps and high pressure for piping of the coils. On top of this, thermo-syphon cooling ensures constant and uniform temperature, since the helium flow automatically adjusts to the heat load distribution.

The thermo-syphon circuit consists of two manifolds, at the top and bottom of the cold mass, connected by two sets of six syphon tubes, as illustrated in Fig. 5.13 (a).

The SPD coils feature six cooling tubes with two tubes for each.

The material selected for the thermo-syphon circuit is Al-1100 due to its high thermal conductivity. The extruded tubes have a diameter of 10 mm and are welded to the support cylinder – a technically proven solution to ensure reliable thermal contact, as shown in Fig. 5.13 (b).

The thermo-syphon circuit is assembled as two halves consisting of six cooling tubes, welded to the top and bottom manifolds. The division in two halves is on purpose, as then each half-circuit can be fully tested for leaks, prior to installation on the cold mass, including the bimetallic (steel-aluminum) joints at the connectors, interfacing the manifolds and the cryogenic lines to the cold box.

1.2.6 Sliding Interface

Due to the presence of NbTi/Cu strands in the Al-stabilized conductor, the thermal contraction of the coil is less than that of the aluminum alloy, used for the support cylinder and flanges. On top of this, small gaps tend to develop at the coil winding-to-flange interfaces under the bending action of the Lorentz force.

In order to prevent the risk of stress accumulation at the coil winding-to-flange interfaces that could result in cracks in the insulation, triggering magnet quenches, the coil is allowed to slide with low friction and, if needed, separate from the flange. Therefore, sliding interfaces are created between coil windings and flanges by placing a 0.1 mm Mylar foil and 0.4 mm of Kapton®.

1.2.7 Support cylinder

In order to limit coil deformation and stress, due to the Lorentz force, support cylinders are placed around the coil windings. The cylinders are made of graded aluminum alloy Al-5083-O, exhibiting good mechanical strength at cryogenic temperature. Being the main structural elements of the cold mass, the shells must be produced as single pieces with uniform material properties.

The assembly formed by coil winding and support cylinder is referred to as a coil module. The assembly operation is performed via shrink fit with interference in order to ensure radial pre-stress. The required radial interference between coil windings and shells is 0.70 mm at room temperature. For this purpose, the support cylinders are produced with oversized dimensions to allow for machining of the inner surface. The thickness of the cylinders after machining shall not be less than 20 mm.

The coils are permanently bonded to the support cylinders by means of epoxy resin or grease (for example Apiezon N), suitable for cryogenic applications. The shells are connected together using bolts passing through the flanges, as described in the next section.

1.2.8 Flanges, bolts, spacers and venting holes

The flanges are disks made of aluminum alloy Al-5083-O that cover the coil winding ends (outer flanges) or separate the coil modules (inner flanges). Similar to the requirements for the support cylinders, the flanges have to be produced as single pieces. Joining several flange pieces by welding is not allowed.

The bolt calculations assume a safety factor of 1.5 and are based on the Eurocode 3, which is the standard adopted at CERN/DESY/FAIR. All bolted interfaces should be designed to hold the weight of the cold mass in tension during assembly and for all operating conditions. All bolted interfaces should be designed to be slip-critical under any condition. As such, the friction force under each bolt shall be higher than the shear force. Therefore, the bolts need to be sufficiently pre-loaded during the assembly. The recommended pre-load at room temperature amounts to 60% of the tensile strength of the bolt. Since the thermal contraction of the material SS A4 is lower than that of Al-5083-O, the pre-load will reduce to 35% of the bolt tensile strength after a cool-down. Compressive forces during the magnet operation will also reduce the bolt pre-tension to some extent.

Bolt tightening shall be performed in steps with a torque wrench, and each bolt pre-load should be measured using an ultrasonic stress meter. Bolts shall be tightened uniformly, with an acceptable pre-load variation of $\pm 10\%$. It is recommended to re-measure the bolt pre-load, and adjust if necessary, prior to the installation of the cold mass in the cryostat to correct possible relaxation, due to a local yielding and creep in the material.

Gaps of 8 mm are envisaged between the inner flanges that are to be shimmed with aluminum spacers. The gap allows for adjusting the axial position of the coil modules, in order to compensate winding and assembly tolerances and obtain the correct magnetic field profile (Fig. 5.14). The axial dimensions of

the spacers are to be determined after the dimensions of the coil modules have been precisely measured.

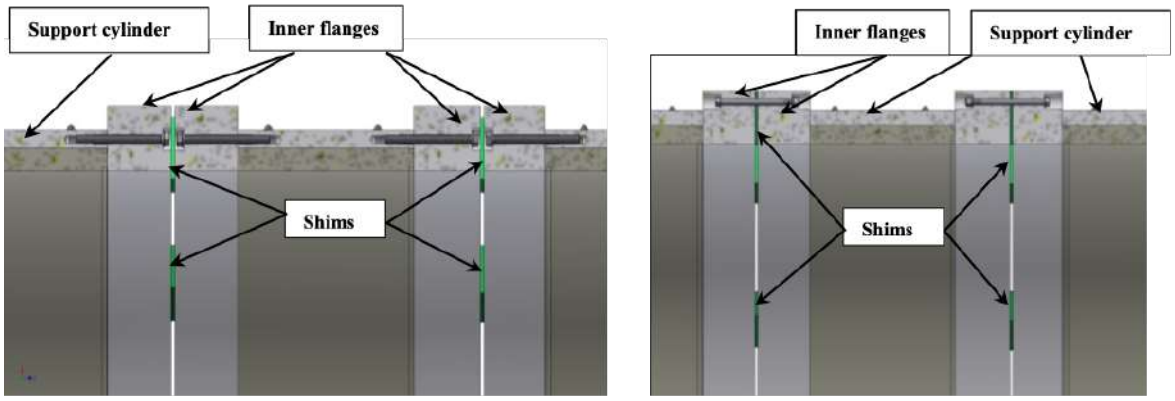

Figure 5.14: Connections ”inner flanges – support cylinder” (left) and ”inner flange – inner flange” (right).

In order to reduce the work associated with shimming and not interfere with the thermal bridges, spacers will be placed only at the locations of the bolts. Shimming of the entire surface of the flange is not required: based on the maximum axial force on the coil modules, the Al 5083-O yield strength (145 MPa) and, assuming a sufficient safety factor, the minimum shim area is 0.04 m^2. The value is much smaller than the surface of the inner flanges ($\sim$1 m^2).

When the thermal bridges are placed in correspondence with the position of the bolts, and hence of the spacers, attention shall be paid to limit the stress on the soft aluminum, so that the thermal conduction of the strip is not degraded.

To reduce the air evacuation time of the cryostat during pumping, it is recommended that all closed volumes should have a hole to vent to the cryostat vacuum (minimum diameter of 1 mm).

Venting holes are recommended at the location of the bolt connections, although at present they are not included in the technical drawings of the cold mass. When the threaded hole is filled with epoxy, venting holes allow for an exit of excess resin, which can be regarded as an indicator of good bond quality.

1.2.9 Cold mass thermalization

The cryogenic scheme of the SPD solenoid relies on indirect cooling of the cold mass by circulating saturated helium at 4.5 K by natural convection. A thermosyphon circuit consists of a bottom and top manifold connected by 12 parallel syphon tubes, attached to the outer surface of the support cylinder, as in Fig. 5.15.

The cooling method chosen for the SPD magnet’s superconducting coil is based on the natural convection of liquid helium flow. It is a self-regulating thermosyphon circulation flow system. Natural circulation loop works on the principle that a heat load on the channels of the heat exchanger produces a two-phase flow that is, on average, less dense than the liquid phase.

The liquid from the helium vessel of the control dewar will be fed through the front pipeline and manifolds at the bottom of the support cylinder. Then, the liquid will be heated in the tubes of the heat exchanger (a rib cage configuration) on the surface of the support cylinder. The two-phase helium from the top manifold will return back through the reverse pipeline to the upper part of the helium vessel.

The design of the thermosyphon cooling circuit includes the definition of the optimal size for the syphon

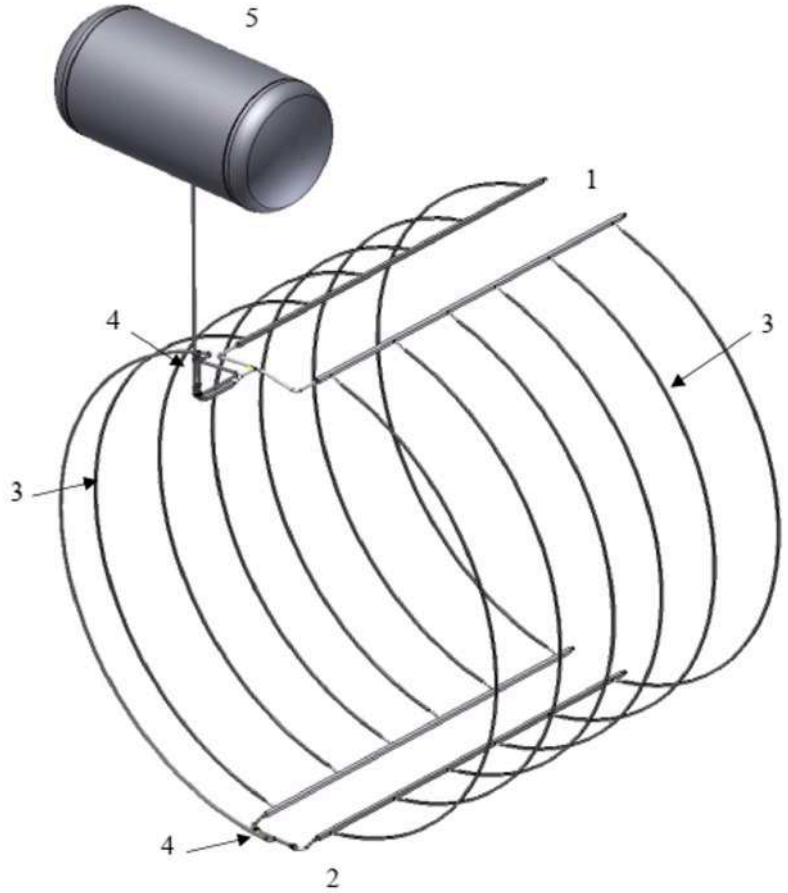

Figure 5.15: Design of the cooling cold mass circuit: 1 – upper manifold; 2 – lower manifold; 3 – syphon tubes; 4 – Al-SS bi-metal adapters; 5 – vessel with liquid helium.

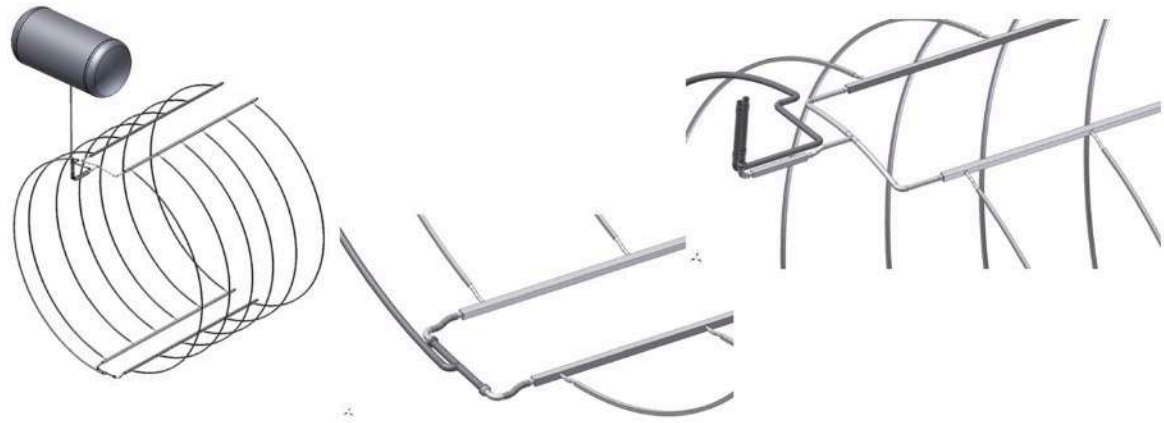

Figure 5.16: Thermosyphon circuit of the SPD solenoid showing the two-halves assembly of the cold mass, as well as the height of the chimney and position of the control dewar.

tubes and their position on the cold mass support cylinder. PED and AD2000 pressure vessel rules have to be applied for the construction of the cryogenic system.

In order to verify the feasibility of thermosyphon cooling, the expected mass flow rate and vapor fraction have been assessed with the homogenous model, described in Ref. [15]. In the model, the required quantities are determined by balancing the driving hydrostatic pressure difference, which results in the

thermally induced density gradient between the hot and cold sides of the loop, with the fluid acceleration and friction pressure drops in the supply and return tubes. The reported diameters correspond to the inner diameters of the pipes. It must be noted that the current technical drawings may contain out-of-date values for the dimensions of the pipes of the thermosyphon circuit.

The model thus confirms that the height of the control dewar installed on the upper platform of the SPD yoke with respect to the bottom of the magnet is sufficient to guarantee the driving hydrostatic pressure. The thermosyphon tubes and supply/return lines are also properly dimensioned to guarantee minimal pressure drop along the cooling circuit (Fig. 5.16). The main advantages of a thermosyphon system are its reliability, since it does not include any moving part, and its ability to maintain a uniform temperature, as the helium flow automatically adjusts to the heat load distribution and variations.

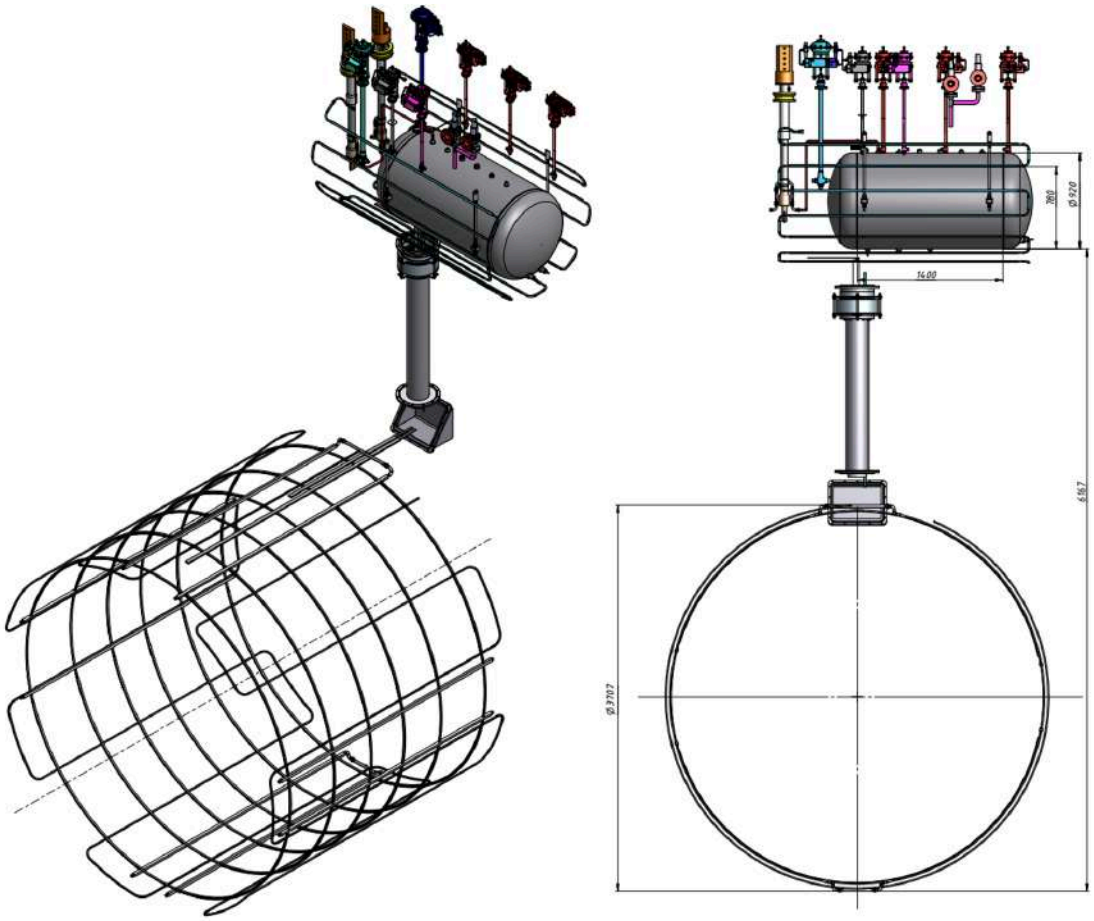

Figure 5.17: General view of the SPD cryostat with the control dewar.

1.2.10 Cryostat and control dewar

All materials and components used in the construction of the cryostat and control dewar must be suitable for the use for which they are intended, in particular for the use at low temperatures. The choice of materials has to be in line with the directive 2014/68/EU PED and must be made according to the regulation prescribed by the AD/AD2000 Technical Rules for Pressure Vessels. The general view of the SPD cryostat with the control dewar is presented in Fig. 5.19. The cryostat comprises of the cold mass with the superconducting coil, surrounded by a thermal screen and suspended on low heat conduction triangle supports. The cryostat should be mounted on the supports connected to the magnet yoke. The design of the cryostat supports will be defined later.

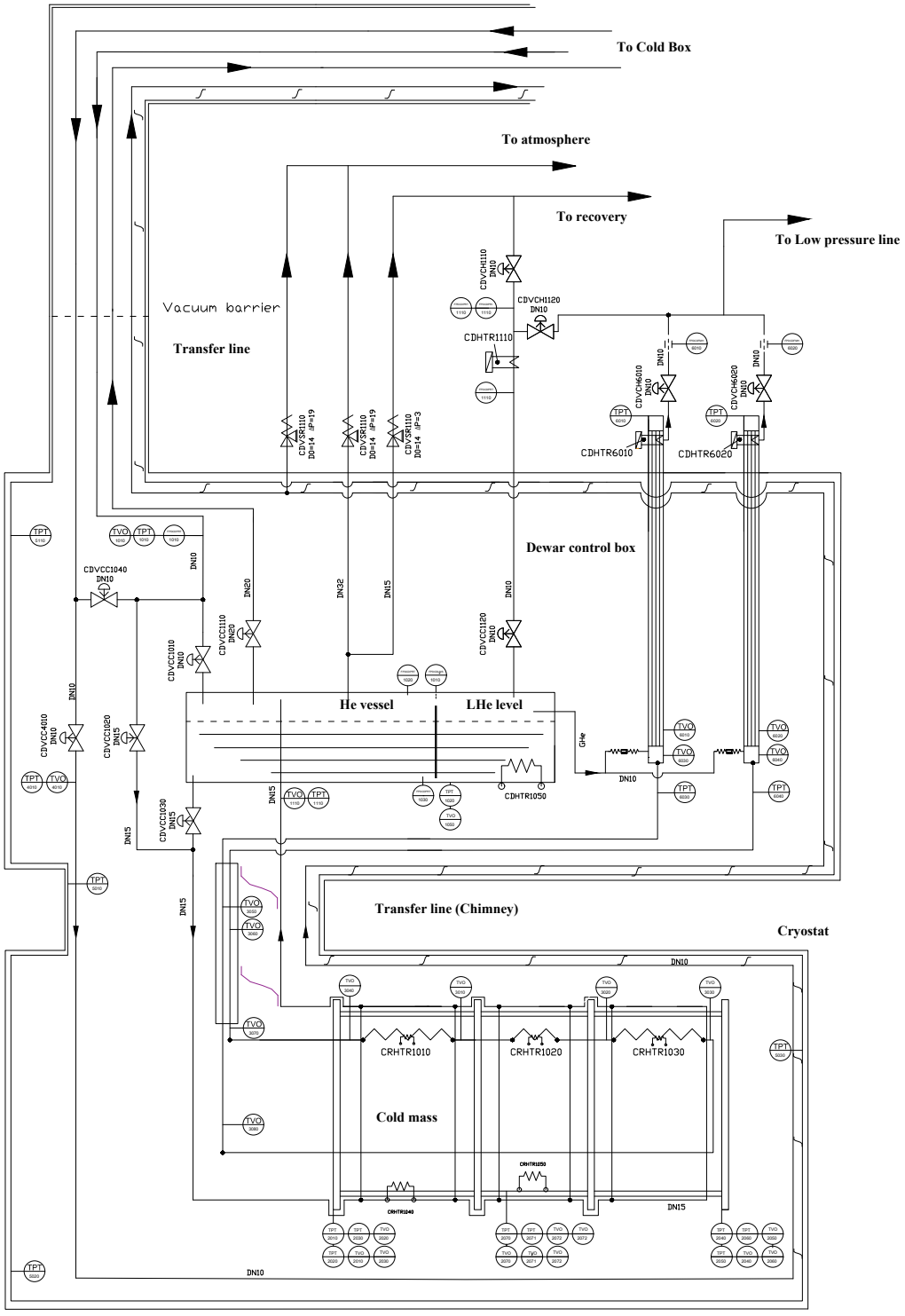

Figure 5.18: Process flow diagram of the SPD cryogenic system.

The control dewar is a functional unit of the cryogenic system and is intended to maintain the required parameters of liquid and gaseous helium (flow rate, pressure, temperature) and to provide cooling of the current leads. In the process flow diagram of the SPD cryogenic system, it is located between the cryostat and the helium liquefier.

Physically, the control dewar is located on the top of the yoke. The vessel for liquid helium, current leads, piping, control and relief valves, and temperature sensors are placed in the horizontal vacuum tank of the control dewar.

Cryogenic and current supplies will be connected from the control dewar to the cryostat through the service chimney in a special slit at the backward end of the yoke barrel. In the bottom part of the chimney an interface box is located, which is intended to accommodate connections of the cryogenic pipelines and current bus bars from the cryostat and the control dewar.

Based on the experience of creating a similar superconducting magnet, when assessing the cyclic strength of the cryostat, it was estimated that the solenoid parts should allow for 1000 cooldown cycles from room temperature to the operating temperature and back to room temperature, and 2500 energization cycles to the nominal current or any fraction of it.

The cryogenic system of the cryostat and the control dewar will be designed to handle the loads resulting from all operation scenarios. Design pressure for all pipelines and helium vessel is 19 bar absolute (bar-a).

Liquid helium that is used for cooling the cold mass is fed from the liquefier at 4.5 K. Thermal shields of the solenoid surround the cold internal parts and are cooled by gaseous helium, which passes through the pipes of the heat exchanger of serpentine type. The helium flow leaves the liquefier at a temperature level of 40 or 50 K and returns to the liquefier after passing the thermal shields at a temperature level of about 80 K. The process flow diagram of the SPD cryogenic system has the same principle as for CMS solenoid (CERN) and PANDA (FAIR), and is shown in Fig 5.18.

The main components of the cryogenic system are:

1. the cryostat, which includes:
   - the superconducting coil cooled indirectly via the thermal contact with the aluminum support cylinder,
   - thermal shields cooled by gaseous helium,
   - a vacuum vessel;
2. the control dewar, which includes:
   - a vessel for liquid helium,
   - current leads,
   - thermal shields cooled by gaseous helium,
   - valves, gauges and other instrumentation,
   - a horizontal vacuum tank with pumping system;
3. a transfer line (chimney) connecting the vacuum shell of cryostat and the control dewar;
4. the helium liquefier;
5. the transfer lines for helium supply connecting refrigerator and the control dewar.

1.2.11 Thermal loads of cryostat and control dewar

Estimated thermal loads of the control dewar, cold mass, and thermal shields of the SPD solenoid are summarized in Table 5.8.

Table 5.8: Heat loads of the control dewar, transfer line, and cryostat.

T=4.5K	Heat loads, W		
	Normal condition	Without magnetic field	Current ramping
Cryostat			
radiation	7.8	7.8	7.8
supports	5*	5*	5*
eddy current loss in cold mass	-	-	11.50**
eddy current loss in conductor	-	-	0.09**
current leads, 6.5kA B=1.25T	15	9	9
Control dewar			
radiation	0.45	0.45	0.45
supports	0.26	0.26	0.26
cold valves	1.05	1.05	1.05
safety relief valves	3,22	3,22	3,22
vacuum barrier	0.35	0.35	0.35
Transfer line			
radiation	0.06	0.06	0.06
supports	0.20	0.20	0.20
Total	33,39	27,39	44,98
T=60K	Heat loads, W		
	Normal condition	Without magnetic field	Current ramping
Cryostat			
radiation	160	160	160
supports thermal shields	12.00	12.00	12.00
eddy current loss in thermal shields	-	-	47.00**
Control dewar			
radiation	10.66	10.66	10.66
supports thermal shields	6.30	6.30	6.30
supports helium vessel	16.50	16.50	16.50
cold valves	22.50	22.50	22.50
safety relief valves	1.07	1.07	1.07
vacuum barrier	1.18	1.18	1.18
Transfer line			
radiation	0.99	0.99	0.99
supports	2.00	2.00	2.00
Total	233,2	233,2	280.2

*ATLAS data; ** PANDA data

Table 5.9: Vacuum vessel dimensions and operating conditions.

Envelope	Dimension
Inner radius	1604 mm
Outer radius	1834 mm
Length	3800 mm
Inner cylinder thickness	8 mm
Outer cylinder thickness	12 mm
End plates thickness	45 mm
Operating conditions	
Operating pressure inside/outside	0/1 bar-a
Designed inside overpressure against 1 bar-a	1.45 bar-a

1.2.12 Cryostat vacuum vessel

The cryostat vacuum vessel is designed as two concentric shells with thick annular end plates, all made of stainless steel, according to AD2000 W10; its basic parameters are given in Table 5.8. A cross-section of the cryostat is shown in Fig. 5.19.

The nominal wall thickness is 12 mm for the outer cryostat shell and 16 mm for the inner shell. The thickness of the flanges is 45 mm. The thickness of the shells allows to minimize the displacement of the cold mass under the action of the magnetic forces, relative to its nominal position. The flanges are attached to the vacuum vessel shells by 96+96 stainless steel bolts, according to the State Standard 11738-84 (DIN912) M10$\times$1.5 (L = 60 mm).

The installation of the ECal, weighing 44 tons, requires the cryostat to be optimized, taking into account additional loads. It may be possible to increase the thickness of the inner shell. The calorimeter is proposed to be installed on two horizontal rails, welded to the inner shell.

The cryostat supports (to be designed later) will provide a high rigidity of the construction for all structural loads, including the action of the magnetic forces, and will take into account the minimal dimensions between the outer shell of the cryostat and the yoke (see Fig. 5.20). The 18 supports will be installed, 9 pieces for each side. The maximal load (about 64 tons) should be on the bottom octant of the yoke. To distribute this load, four supports are installed on the top plate of the octant next to the edges, whereas the biggest part of the load goes on the side plate of the octant. The mechanical stress analysis shows that the maximum dimensional deformation is 1.6 mm for the top octant plate and the maximum stress is about 140 MPa (Fig. 5.21). Also, these supports make it possible to align the solenoid axis with the beam axis.

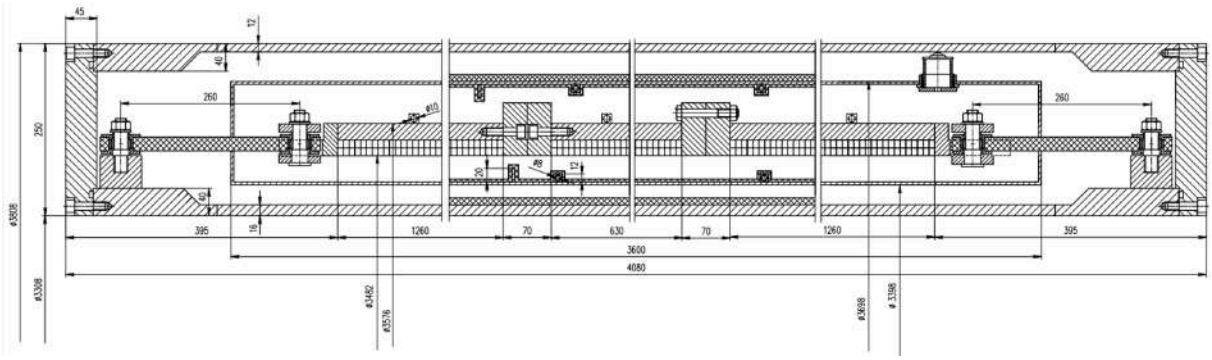

Figure 5.19: Cross-section of the cryostat.

The axial and radial gaps between the cryostat vacuum shell and the thermal shield, as well as between

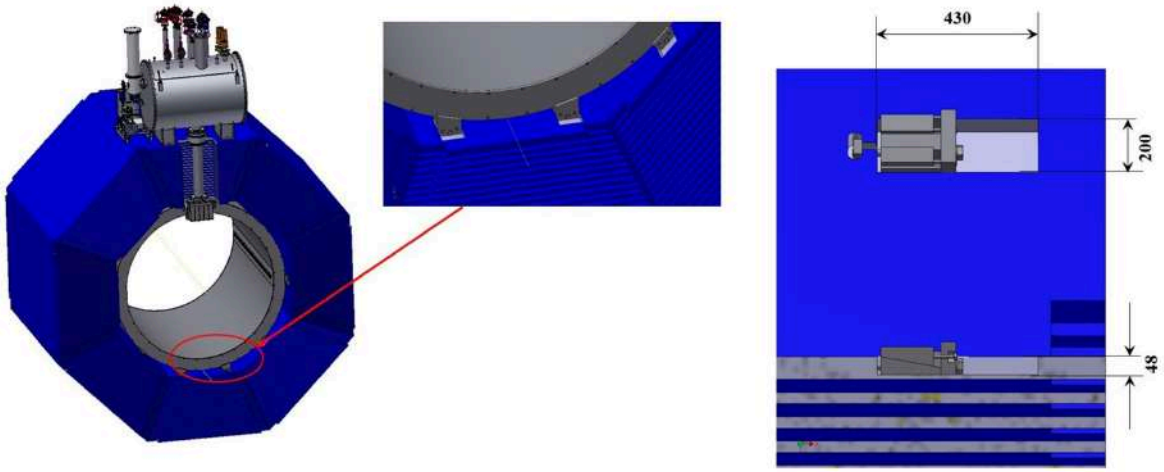

Figure 5.20: Location of the cryostat in the yoke and arrangement of the cryostat supports.

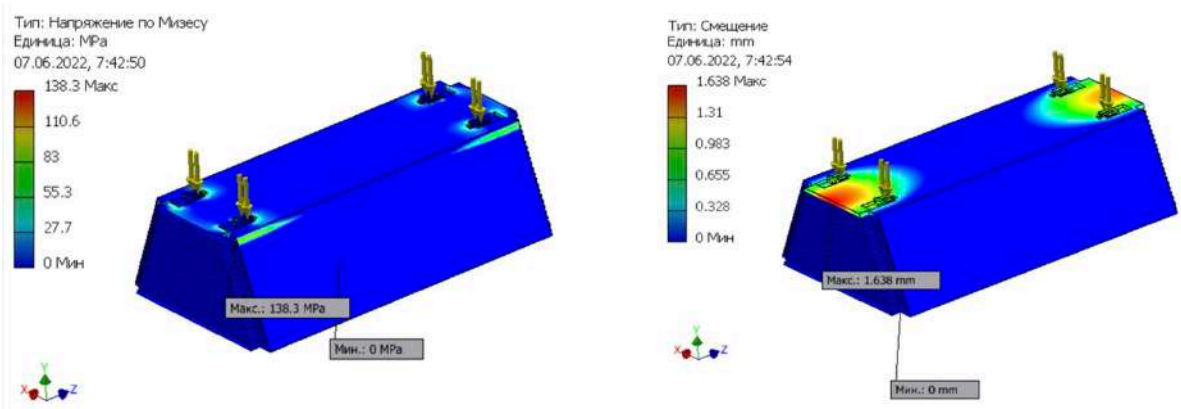

Figure 5.21: Calculation of mechanical and magnetic loads on the bottom octant.

the shield and the cold mass in warm and cold state, are indicated in Fig. 5.19. They are not sufficient for the cryostat assembly and for avoiding of thermal contacts between the shells after cooling. A certain amount of space is needed for adjusting the optimal mutual positions of the holes for the triangle supports in the support flanges on the inner cryostat shell and in the brackets or holes for connecting the triangle supports to the cold mass. There are 12 triangle supports on each side. The wide side of a triangle support is attached to a part of the vacuum shell by a special flange with two M16 bolts. The apex of the triangle is attached to the cold mass. The shape of the support takes into account the mechanical and thermal loads, as a compromise. To compensate for the radial changes in lengths of the cold mass and the vacuum shell (more than 12 mm), spherical washers are installed in all attachment points. To minimize the change in the position of the cold mass, we assume the pre-setting of the cold mass to be at + 5÷6 mm from the plane of the support flange, and after cooling down to 4.5 K – at -5÷6 mm from the plane of the support flange. To compensate for the longitudinal changes in length (more than 12 mm), a slot is proposed in the cold mass, at the point of attachment of the triangle apex. The design of a triangle support is shown in Fig. 5.22 and the mechanical analysis in Fig. 5.23. The estimated loads on the triangular supports are given in Table 5.10.

As a material for the supports, it is proposed to use STEF1 or some type of carbon fiber. Mechanical calculations were made for a support with a thickness of 20 mm and a load of 10 kN (Fig. 5.23). Calculations indicate an acceptable stress level of 96 MPa, with Limit stress of STEF1 – 132 MPa and with a maximal deformation of 0.9 mm. Testing of the triangle supports at room and cryogenic

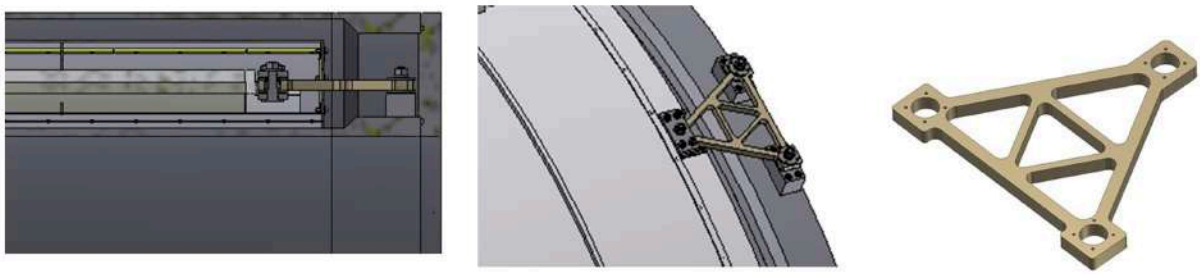

Figure 5.22: Design of the triangle support of the SPD cold mass.

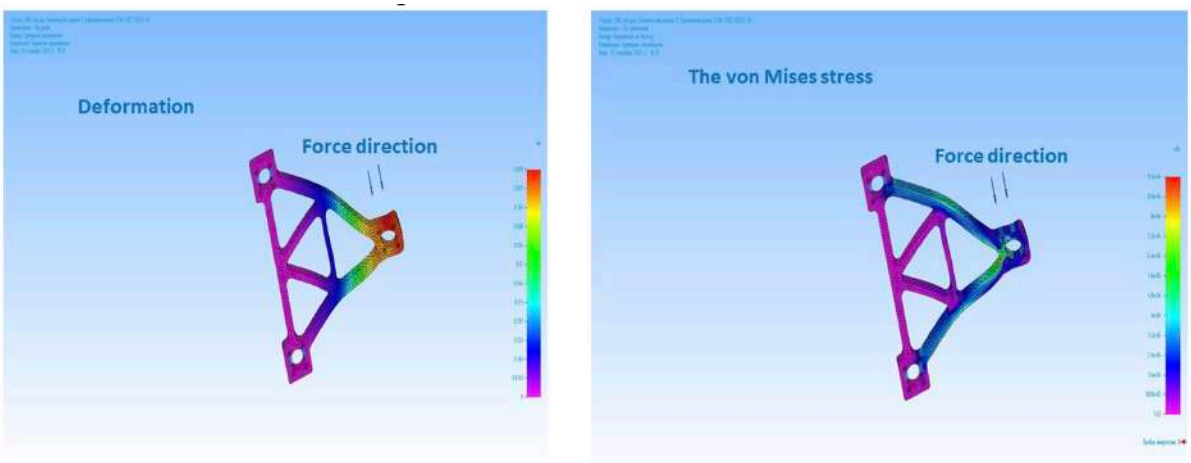

Figure 5.23: Calculated mechanical loads on the triangle support.

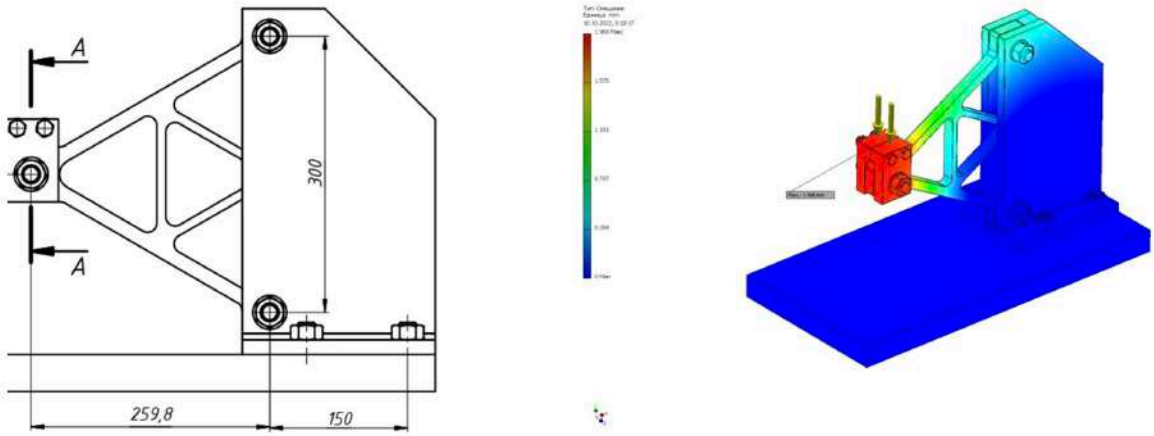

Figure 5.24: Triangle support test device.

temperatures is planned. The proposed scheme of the tests is shown in Fig. 5.24.

The exact location of the cold mass inside the cryostat after its assembly should be defined with maximum precision. This is necessary to determine an optimal position of the superconducting coil inside the yoke aperture. After the cryostat assembly, any correction of the cold mass position inside the cryostat is impossible. A correction of the coil position, relative to the yoke aperture, can only be provided by means of fitting spacers in the cryostat support legs. This correction can be implemented in accordance with the results of field measurements in the tracker area and measurements of forces in the suspension

Table 5.10: Loads on the triangilar support.

Load conditions	Load, kN	Maximum load to support, kN
Cold mass weight	42	4.0
Decenytering force (5 mm)	47.5	4.47
Total load	89.5	8.47

rods.

In the normal operative condition mode, the inner cryostat volume is evacuated, which leads to general membrane compressive stresses in the outer cryostat shell, due to the action of the outer atmospheric pressure. In the process of magnet operation, an emergency situation may happen, when an overpressure up to 0.05 MPa appears in the inner volume. This leads to general membrane compressive stresses in the inner cryostat shell.

The buckling analysis of the cryostat shells is based on an FE model. The considered load cases are the following:

- cryostat weight;
- weight load of the cold mass and thermal screen octants, applied to the outer cryostat shell;
- weight loads of the thermal screen octants and of the inner detectors, applied to the inner cryostat shell;
- outer overpressure of 0.1 MPa (first variant);
- inner overpressure of 0.05 MPa (second variant).

According to computations, the stability of the cryostat shell under the action of an outer overpressure of 0.1 MPa is ensured with a safety margin of 8.5. The stability of the cryostat shell from the action of an inner overpressure of 0.05 MPa is ensured with a safety margin of 17 (Fig. 5.25).

1.2.13 Control dewar

1.2.13.1 Vacuum vessel The outer vacuum housing of the control dewar encloses the stainless steel vessel for liquid helium, control valves, current leads, and process piping, surrounded by a thermal shield, located between the outer housing and the interior of the control dewar (Fig. 5.26). The vacuum vessel of the control dewar has a horizontal barrel shape and is made of stainless steel.

The thickness of the outer walls of the vessel is 8 mm and the weight of the assembled control dewar is about 1600 kg. The main dimensions of the control dewar are shown in Fig. 5.26. The diameter of the vacuum shell is 1500 mm, the height with valves is about 2500 mm, the width of the control dewar is 2780 mm and with the vacuum pump system – 3425 mm. The flanges of the control dewar lids are tightened by 2×48 studs M12.

The vapor-cooled current leads of the solenoid and the cryogenic relief valves are mounted on the top plate of the control dewar housing.

Vacuum vessels, shells of transfer lines and the cryostat must handle the loads from all possible operating scenarios. Design pressure of all vacuum vessels is 0.45 bar(g).

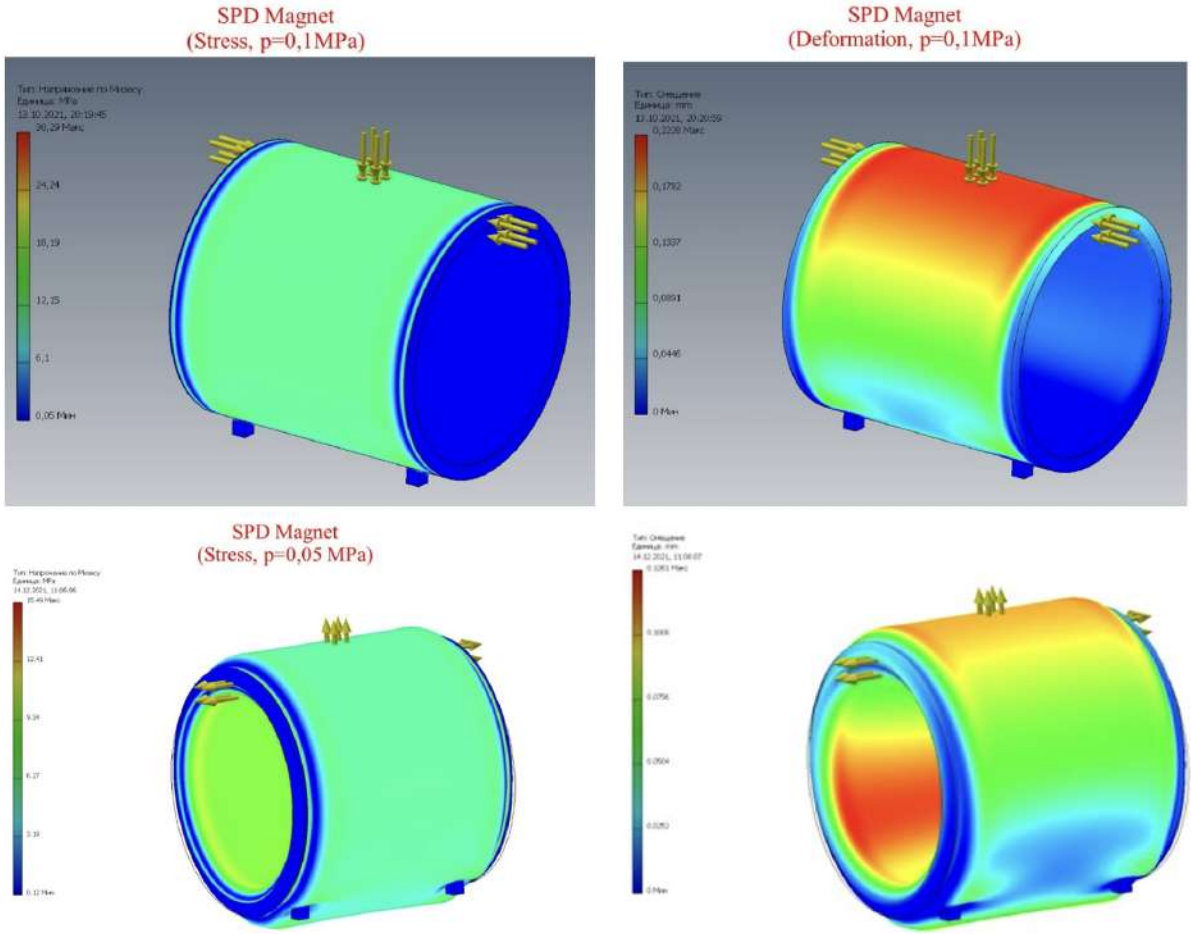

Figure 5.25: Calculations of the cryostat stresses and deviations. The load of the calorimeter is not included.

1.2.13.2 Valves of the control dewar Chosen types of the control dewar valves are listed in Table 5.11. The regimes of the flow through the heat exchangers of the cold mass and the thermal shield will be defined in detail later. The positions of valves of the control dewar for various magnet operation regimes are established in accordance with Table 5.12, where the positions of controlled valves are indicated for each regime.

1.2.13.3 Vessel for liquid helium A stainless steel vessel for liquid helium, required to maintain the operating conditions of the solenoid, is placed inside the control dewar. The hydraulic volume of the helium bath of the vessel is chosen to provide stable operation of the magnet with heat inflows to the control dewar and the superconducting coil during the period necessary for safe de-energizing the superconducting coil, when the liquefier is stopped. The heat flow into the vessel and to the superconducting coil, including heat losses in current leads, amounts to 50 W, which corresponds to a liquid helium flow rate of 71 l/h. Since it takes more than 60 minutes for safe de-energization of the coil, the volume of the helium vessel is chosen to be 300 liters, to have a sufficient safety margin. The outer surface of the vessel is covered by a multilayer screen-vacuum insulation to reduce heat inflows.

The volume and the outer surface area of the vessel for liquid helium is 300 l and 2.5 m^2, respectively. It is possible to increase the volume of the helium vessel, because the space on the upper yoke platform allows a placement of the control dewar with bigger dimensions. The helium vessel suspensions are made by combining a pipe and a rod (Fig. 5.27). The heat load on the suspension (0.09 W) is calculated

Table 5.11: Control dewar valves.

Part	Nominal diameter, mm	Rated pressure, bar	Rated temperature, K	Valve type
CV1	10	25	4.5÷300	pneumatically-actuated control valve with digital positioner (0...100%)
CV2	10	25	4.5÷300	pneumatically-actuated control valve with digital positioner (0...100%)
CV3	25	25	4.5÷300	pneumatically-actuated control valve with digital positioner (0...100%)
CV4	10	25	4.5÷300	pneumatically-actuated control valve with digital positioner (0...100%)
CV5	10	25	4.5÷300	pneumatically-actuated control valve with digital positioner (0...100%)
CV6	8	25	80÷300	pneumatically-actuated control valve with digital positioner (0...100%)
CV7	8	25	80÷300	pneumatically-actuated control valve with digital positioner (0...100%)
CV8	8	25	40÷300	pneumatically-actuated control valve with digital positioner (0...100%)
CV9	8	25	40÷300	pneumatically-actuated control valve with digital positioner (0...100%)
SV1	15	25	80÷300	pneumatically-actuated shut-off valve (open/closed)
SV2	20	25	80÷300	pneumatically-actuated shut-off valve (open/closed)
RV1	20	20	4.5÷300	safety relief valve
RV2	20	20	4.5÷300	safety relief valve

Table 5.12: Positions of the control dewar valves for various SPD magnet operation regimes. C: valve closed, O: valve open, R: valve regulated.

Valve	Initial setting	Cool down from 300 to 4.5 K	Steady-state	Warm-up	Cooling of the thermal shields	Emergency (coil quenching)	Cooling after coil quenching	Emergency (refrigerator failure)	Emergency (power failure)	Emergency (current lead voltage rise above allowable level)	Emergency (loss of vacuum)
CV1	C	R	C	R	C	C	R	C	C	R	C
CV2	C	R	R	C	C	C	R	C	C	C	C
CV3	C	C	O	C	C	C	C	O	O	C	C
CV4	C	O	O	R	C	C	O	C	C	R	C
CV5	C	C	C	R	C	O	R	R	R	R	O
CV6	C	R	R	R	C	C	R	R	R	R	C
CV7	C	R	R	R	C	C	R	R	R	R	C
CV8	C	R	R	R	R	R	R	C	C	R	C
CV9	C	O	O	O	O	O	O	C	C	O	C
SV1	C	C	C	O	C	C	C	C	C	O	C
SV2	C	O	O	C	C	O	O	O	O	C	O

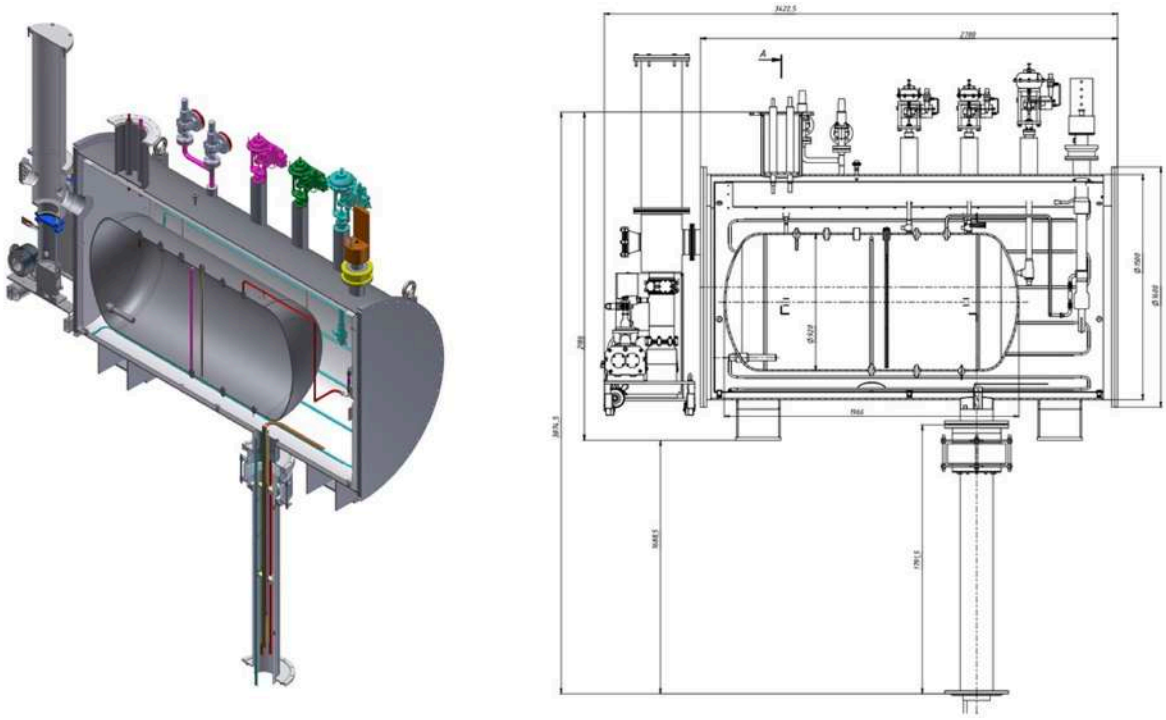

Figure 5.26: Layout of the control dewar.

with the following parameters: the temperature of the shell – 300 K, of the helium vessel – 4.5 K, and of the thermal shields – 60 K. The components of the suspension are:

- a stainless steel rod 217 mm long with a diameter of 40 mm;
- a stainless steel pipes with a diameter of 21.3×2, length 588 mm;
- a rod 200 mm long, stainless steel M12.

Stability of the helium vessel, when it is exposed to external pressure of −1 bar(g) (vacuum inside the vessel), is provided with a sufficient safety margin. The conditions of static and cyclic strength and the stability condition will be fulfilled in this case as well.

An electrical heater is installed in the helium bath to maintain the required level of liquid helium and to control the rate of the return helium flow to the helium liquefier (maintenance of thermal balance). The heater power of about 400 W corresponds to the maximum cooling capacity of the liquefier. This heater is also used for rapid evaporation of liquid helium from the bath. The power capacity of the heater may vary from zero to the maximum value, determined by the cooling power of the liquefier at a temperature level of 4.5 K. Two identical liquid helium level-meters (one active, one spare) will be installed in the helium vessel.

It is also suggested to install a differential pressure sensor. The first point of pressure measurement is the upper part of the helium vessel with gas medium; the second capillary should be installed at the bottom of the helium vessel. The value of the ΔP equals to the level liquid helium in the vessel. The control of the liquid helium level in the vessel will be included in the control system of the magnet.

1.2.14 Chimney and interface

The vacuum pipe (chimney) connects the vacuum volumes of the cryostat and the control dewar. The outer diameter of the chimney is 219.1 mm, the wall thickness is 2 mm. It encloses the superconducting

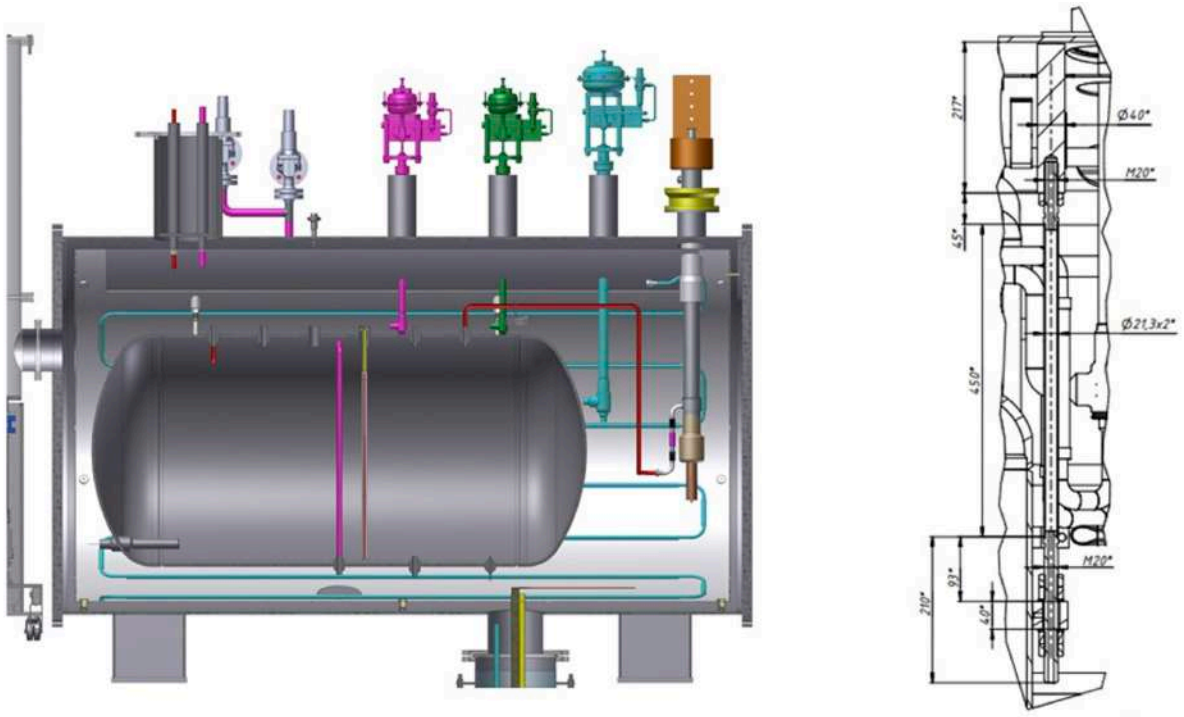

Figure 5.27: Arrangement of the helium vessel into the control dewar and a scetch of the suspension of the helium vessel.

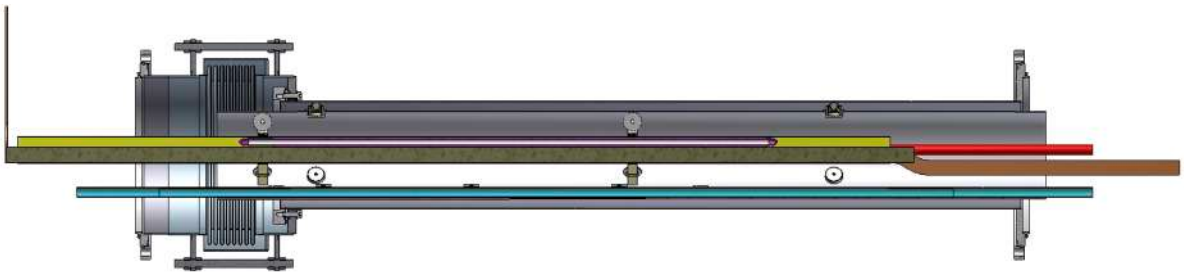

Figure 5.28: Section of the chimney with the control dewar.

bus-bars, direct and return pipes for gaseous and liquid helium flows, measurement wiring, all of which are surrounded by a thermal shield (Fig. 5.28). Its bottom part is supplied by a weld ring flange DN 250 ISO-K with rotatable bolt ring DN 250 ISO-K (both made of stainless steel 304/1.4301). This flange is tightened to the flange on top of the interface box by 12 bolts M10. The rotatable bolt ring facilitates the connection procedure of the flanges at the stage of the cryostat and control dewar assembly.

A decoupling spring bellow (made of stainless steel 1.4541), supplied with two flanges DN 250 ISO-K (made of stainless steel 304/ 1.4301), is placed at the top of the chimney, in order to compensate for mutual shifts of the control dewar and the cryostat during assembly, reloading of the magnet from stationary supports to roller skates and back, and during magnet movement along the rail track. The upper flange of the decoupling spring bellow is connected to the flange at the bottom of the control dewar. The main parts of the chimney are shown in Figure 5.29.

The current leads and process piping surrounded by a thermal shield are located between the outer shell and cold part with temperature 4.5 ÷ 50 K. The 80-K return pipe should be fixed to the chimney thermal shield and have the copper thermal bridges installed every 350÷400 mm. To fix the location of the thermal shield in the vacuum shell, a few ball supports are installed (see Fig. 5.30). Also, these supports

allow the movement of the thermal shield, relateive to the vacuum shell, after cooling and shrinkage of the thermal shield. The material of the thermal shield is stainless steel 304/ 1.4301. One edge of the copper thermal bridges is brazed to the stainless steel 80-K return pipe, and another edge is connected to the thermal shield by screw rivets. Apiezon N grease provides a reliable heat contact of the connection.

The positions of the 4.5-K forward and return pipes, the 50-K forward pipe, and bus-bars into the chimney are fixed by two G10 spacers. The spacers will be equipped with two or three G10 wheels, to compensate for the changing dimensions of this assembly, relative to the thermal shield during all operating conditions. The 50-K return pipe has a rigid fixation to the spacers, while other pipes and bus-bars have a slippery fixation. To avoid any risk of heating the bus-bars and high risk of quenching or even overheating of the superconductor, the bus-bars are connected to an assembly with a 4.5-K return pipe (Fig. 5.31).

1.2.14.1 Interface box The interface box is located in the bottom part of the chimney and is fixed on the flange of the cryostat. The box accommodates connections of the pipelines, as well as joints of the superconducting bus-bars of the cryostat and the control dewar. The flanges with connectors for sensors are located on the side cover of the interface box. Testing of the solenoid welds of superconducting cables in the interface box will be performed using extensions of the bus-bars (Fig. 5.32). The joints will be made by edge welding of Al to Al stabilizer, up to three times. These extensions can be cut to allow dismounting of the solenoid a few times.

1.2.14.2 Thermal shields Thermal shields of the solenoid surround the cold internal parts and are cooled by gaseous helium, which flows through the pipes of the heat exchangers. The design of the cooling circuit of the screen provides its cooling independently from the cold mass cooling. The helium flow leaves the liquefier at temperature of 50 K and passes the heat exchangers of the thermal shields of the cryostat, chimney and control dewar successively. After that it returns to the liquefier at temperature of 80 K. Heat gains to the thermal shields of the cryostat, chimney and control dewar, as well as the temperature of the cooling gas at inlet and outlet of the heat exchangers of each circuit element in the steady-state regime, are indicated in the flow scheme. The total length of the cooling tube of the heat exchangers is about 76.3 m (cryostat, control dewar, and chimney).

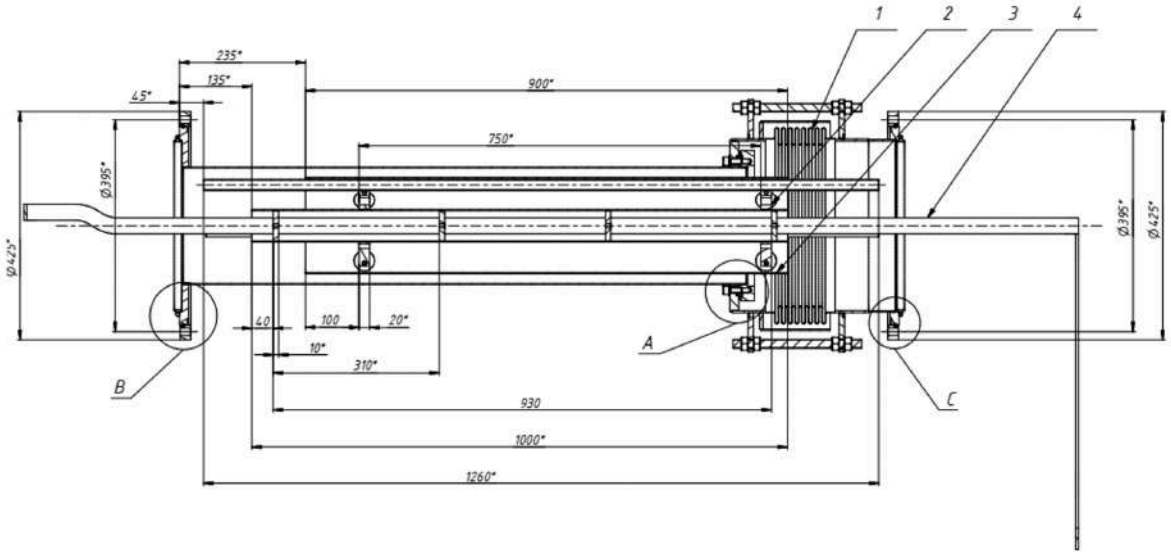

Figure 5.29: The main dimension of the chimney. 1 – bellows; 2 – G10 spacer; 3 – thermal shield; 4 – bus-bar.

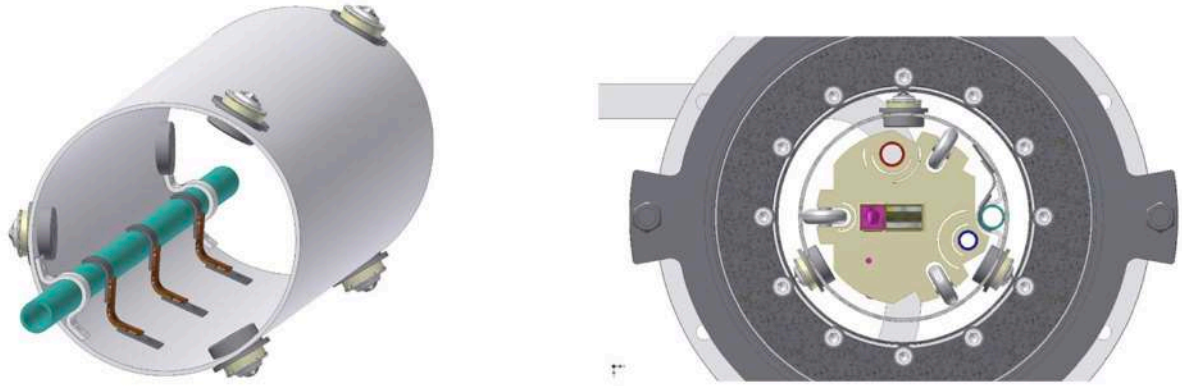

Figure 5.30: Views of the chimney's thermal shield with thermal bridges and a cross-section of the chimney.

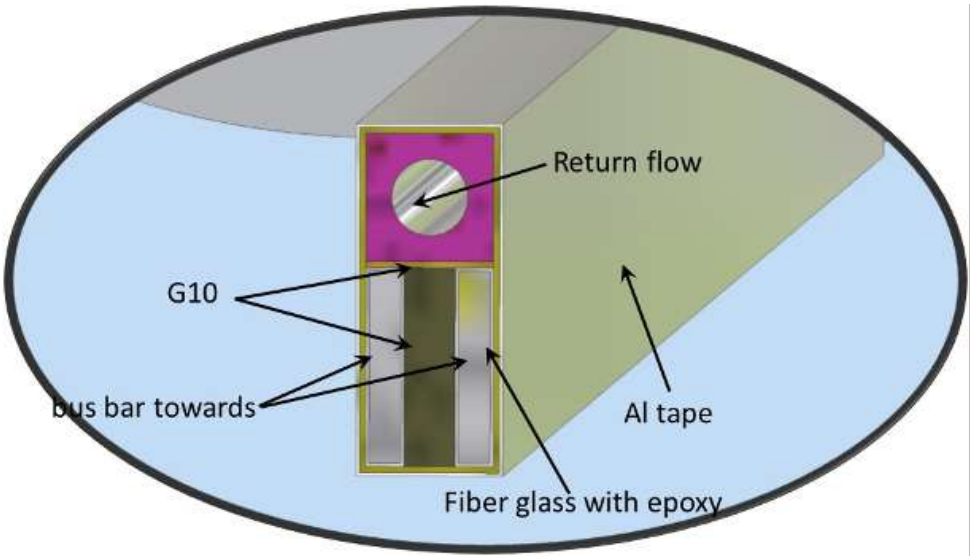

Figure 5.31: Cross-section of a bus-bar assembly.

Figure 5.32: Connecting bus-bars and process pipes into the Interface box.

1.2.15 Thermal shield of the cryostat

The cryostat thermal shield surrounds the cold mass with the coil. It consists of two cylindrical sectors and two flanges. The heat exchanger of the cryostat thermal screen consists of Al alloy pipes with a diameter of 12×2 mm fixed on the outer and inner shells of the quadrants and connected by intermittent welding. The cooling pipes were optimized for 50 K helium gas, but it is possible also to use liquid nitrogen.

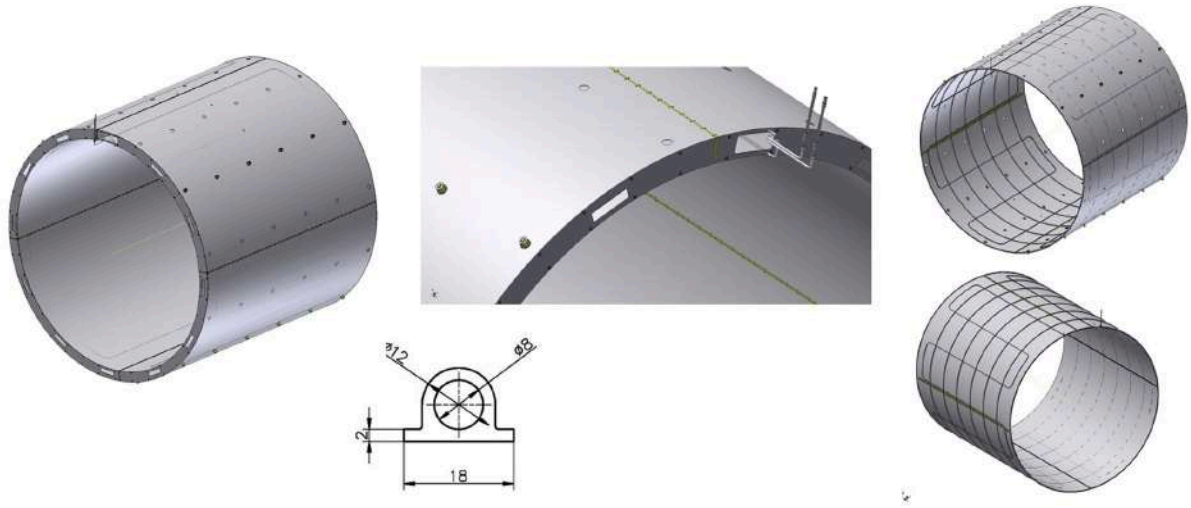

Figure 5.33: Cryostat thermal shield.

The shield envelope is split up into electrically separated parts (quadrants) (Fig. 5.33), to avoid damage and deformations of the screen, when the coil undergoes an emergency discharge. The quadrant shells are separated by gaps of about 14 mm, covered by sheets of insulating material G10. In addition, there are radial flange cuts of 10 mm. As can be seen from these pictures, there are four different types of quadrant configuration (depending on the shape of the heat exchanger tube and on the positions of the attachments for the temperature interceptions of the cold mass suspension).

The inner and outer shells of the octants are supported by the stiffening ribs (angled profile 30×20 mm) and interconnected by the flanges at the ends. Shells, flanges and stiffening ribs of the octants are made of aluminum alloy AL 5083 (AMg5). The thickness of the sheets of the shells and flanges is 4 mm. The mass of the outer shell of a quadrant is about 60 kg, the mass of the inner shell is about 52 kg. These masses are convenient for assembling. The total area of the screen surface of the cryostat is 78 m^2. The total mass of the cryostat screen is 880 kg.

The shield is positioned into the cryostat with the help of the ball support units with a G10 ring. On the outer and inner surface of the shield 30 layers of superinsulation will be placed. The total heat inflow through the shield supports is about 15 W. Appropriately oriented slots, made in the octant shells, are intended to reduce the lateral loads applied to the studs, caused by thermal shrinkage of the shield material.

1.3 Electrical systems

1.3.1 Electrical connections of the coils

The SPD solenoid relies on the following electrical joints:

- two layer-to-layer joints in the upstream and downstream coil modules;
- two coil-to-coil joints connecting the center coil module to the upstream and downstream coil modules;
- two terminal joints connecting the solenoid to the bus-bars.

The routing of the coil-to-coil joints and terminal joints on the cold mass is displayed in Fig. 5.34. The joints are aligned with the magnetic field lines to avoid forces. The joints are clamped and glued

to the cold mass, resulting in good thermal contact with the cold surface of the support cylinder. No thermalization of the joints to the cooling circuit is envisaged in this reference design, due to the expected low heat generation. A support bracket, shown in Fig. 5.35 (a), holds the weight of the bus-bars at the upstream end of the cold mass. The bracket is designed to sustain a total weight of 800 N, while the expected weight of the bus-bars is about 300 N.

Although the current routing of the bus-bars and joints is such as not to interfere with the other components installed on the cold mass, it is advisable to further optimize the layout of the upstream end of the cold mass. The present design of the area is crowded, due to the necessity to route both the electrical and cooling lines through the cryogenic chimney.

In Fig. 5.35 (a) it is possible to distinguish the grooves in the inner flanges, allowing routing of the conductor from the coil to the outer surface of the cold mass. The cross-section of the coil conductors is 8×11 mm^2.

The area is crowded due to the presence of the radial rod supports and cooling line manifold, connecting the thermo-syphon circuit to the cold box.

The design of the joints between the SPD solenoid conductors is essentially the same as applied in the ATLAS magnets. The configuration of the layer-to-layer and coil-to-coil joints is shown in Fig. 5.35 (b) left. Terminal joints are instead illustrated in Fig. 5.35 (b) right. The use of the left-over conductor, developed for the ATLAS end-cap toroids, is intended in this reference design for the bus-bars of the SPD solenoid.

All conductor joints inside the cryostat are made without removing the aluminum stabilizer. The joints are made by TIG welding of the adjoining cables. Al-1050 is recommended as the filler material, as used for the conductor in the ATLAS toroids. The use of different aluminum alloys is also possible, depending on the expertise of the firm, building the SPD solenoid. After welding and cleaning, the conductor insulation is applied around the layer-to-layer joints. Ground insulation, instead, has to be wrapped around the coil-to-coil and terminal joints.

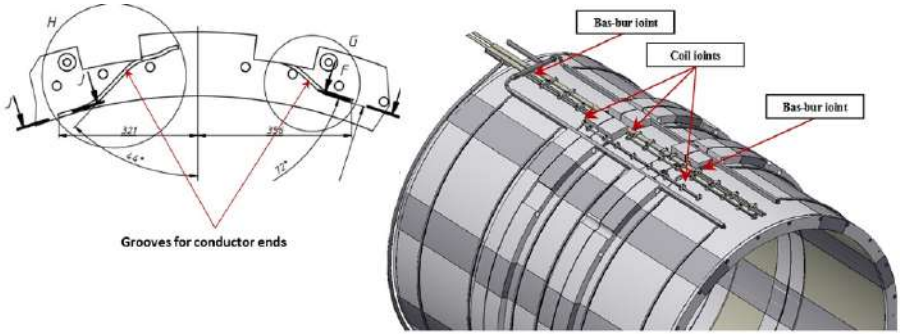

Figure 5.34: Position of coil-to-coil and terminal joints on the PANDA solenoid cold mass as an example.

The electrical resistance of the joint shall not exceed 1.0 nΩ at 4.2 K and 3 T. The joint length resulting in the envisaged resistance is determined experimentally by welding and testing the conductor samples. In this reference design a minimum joint length of 700 mm is assumed for all joints (note that some joints in the drawings of this document may have erroneously a shorter length). Cooling and interruption of welding must be applied to the joints during welding, in order to limit the duration of the superconducting cables inside the conductors at temperatures above 600 K, to avoid critical current degradation. The critical current degradation in the superconducting cables due to the joint welding shall not exceed 5%.

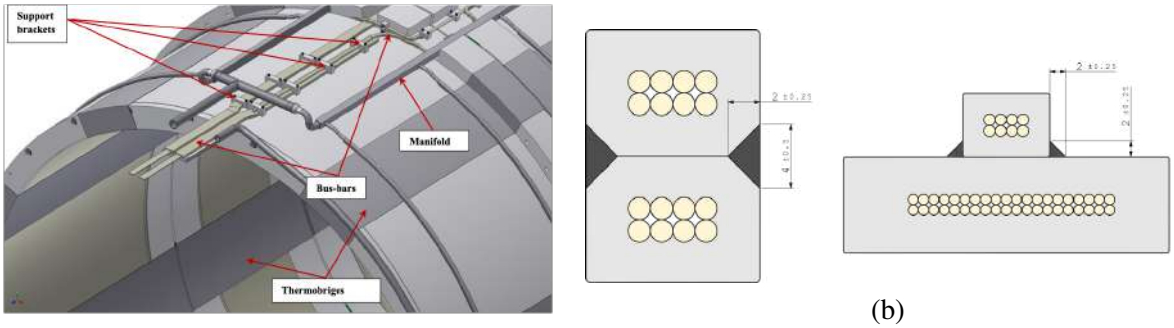

(a) (b)

Figure 5.35: (a) Upstream end of the cold mass showing the bus-bars and their support bracket. (b) Layer-to-layer and coil-to-coil (left) and terminal (right) joint layouts.

1.3.2 Power converter

The magnet is powered by a DC power supply, providing an operational current 5.7 kA, 6.5 kA. It is possible to increase the value of the current to 8 kA by installing additional power converters, when the planned field at the solenoid axis is 1.5 T. The bus-bars connecting to the power supply are equipped with the circuit breakers. The bus-bars resistance is negligible, compared to the circuit resistance during slow and fast dumps. The slow discharge of the magnet is achieved by opening the circuit breakers, to disconnect the magnet from the power supply. The current is discharged via the slow dump unit, composed of several diodes in series. A series of four diodes is assumed, featuring a total resistance of 3 mΩ, which results in a discharge time of 2000 s. Block scheme of the electrical racks is shown in Figure 5.36 (a).

The power convertor assembly design is shown In Fig. 5.36 (b). It is proposed to use the TDK-Lambda type current source. One current source has a value of the current up to 1000 A. Seven or eight current sources are connected in parallel.

1.3.3 Quench protection

The quench protection system is designed to limit the peak temperature on the coil windings to 80 K and the peak voltage to ground to 500 V during any normally protected quench. The system relies on the monitoring of the resistive voltages, associated with the normal zone spread, and the quench development via the voltage taps, installed on the coil modules, as well as on the joints and bus-bars. A schematic view of the magnet electrical circuit is shown in Fig. 5.37 (a).

The quench protection system (QPS) continuously monitors the magnet voltage during operation. In case a resistive voltage exceeding the threshold of 0.5 V is detected, the QPS waits for 1 s to eliminate false signals and gives the magnet a chance to recover, if the perturbation energy was below the minimum quench energy. If a quench recovery does not occur, the QPS activates the circuit breakers (Fig. 5.37 (b)) to disconnect the power supply from the magnet, and the current is discharged in the fast dump resistor. The value of the resistor is set to 62.5 mΩ, to limit the voltage to ground. The grounding circuit is designed to symmetrically divide the voltage across the magnet terminals. Quench protection, in the case of a fast dump, is helped by the quench-back effect of the support cylinder, which improves quench propagation, thereby reducing the temperature increase of the coils.

To assess the quench performance of the SPD solenoid, quenches have been initiated at different locations in each of the three sub-coils (i.e. across the two layers, as well as at the edges and the center of the winding packs). The quench is initiated by rising the temperature of the selected turn above the critical value.

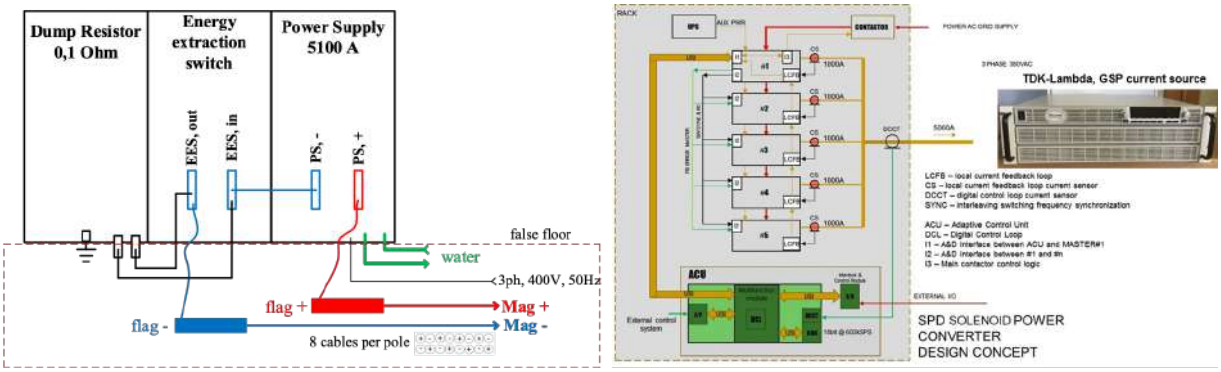

(a) (b)

Figure 5.36: (a) Cabling diagram of the power supply scheme. (b) General design of five paralleled current sources controlled by ACU.

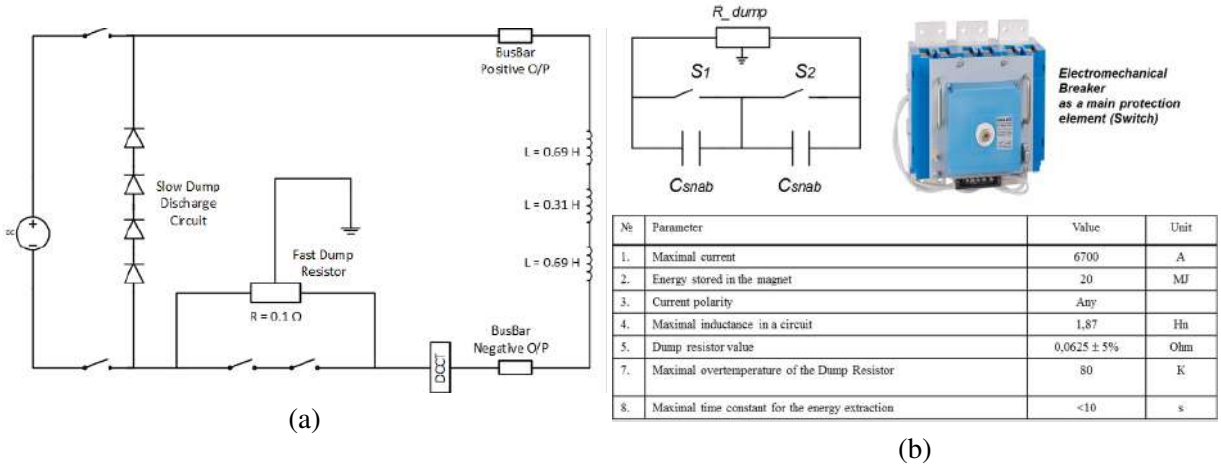

(a)

№	Parameter	Value	Unit
1.	Maximal current	6700	A
2.	Energy stored in the magnet	20	MJ
3.	Current polarity	Any	
4.	Maximal inductance in a circuit	1,87	Hn
5.	Dump resistor value	0,0625 ± 5%	Ohm
7.	Maximal overtemperature of the Dump Resistor	80	K
8.	Maximal time constant for the energy extraction	<10	s

(b)

Figure 5.37: (a) Electrical quench protection scheme of the PANDA solenoid. (b) Main parameters of the electromechanical breaker.

During a fast dump, independently from the location of origin of the quench, the current in the coils decays with a time constant of 9.5 s. The maximum voltage drop is 360 V, well below the maximum design limit of 500 V (Fig. 5.38). The hot spot temperature is limited to a very safe value of 60 K.

The total stored energy E is:

$$E = \frac{1}{2\mu_0} B_0^2 \times V = 19.3MJ. \tag{5.1}$$

With the present layout of the quench protection system, 58% of the initial magnetic field energy is dissipated in the dump resistor, 26% as eddy current loss in the coils and casing, and the remaining 16% in the diode unit.

The results of the quench analysis show that proper operation of the QPS limits the peak coil temperature and voltage well below the threshold values. The maximum temperature reached by the coils is here re-assessed in the case of failure of the QPS, which results in the entire stored energy being dissipated in the winding. Under the assumption that the quench-back effect of the support cylinder causes a rapid propagation of the normal zone to the entire coil without extracting energy from the system, the magnet would heat up to 80 K. Even in the unrealistic case that the energy is entirely dumped in only one of the sub-coils, the temperature would reach 112 K and 161 K for the upstream/downstream and center coils, respectively. Although unwanted from the cooling point of view, these temperature values do not pose

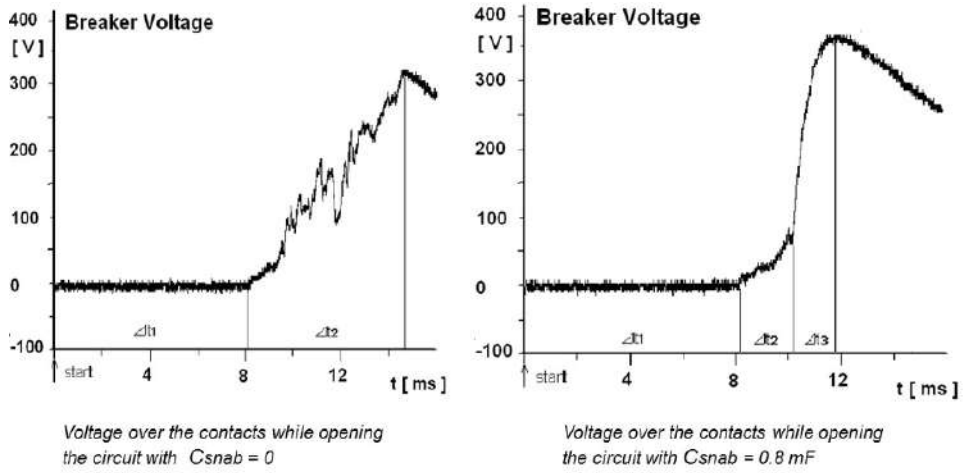

Figure 5.38: Electromechanical breaker and help of snubber against the arc.

risks for the integrity of the solenoid.

1.4 Vacuum system of the SPD magnet

The control dewar, chimney, and cryostat with superconducting coil have a common vacuum volume. A pumping station with rotary and turbo-molecular pumps performs the vacuum pumping. The pressure to be obtained by vacuum pumping before cooling and cryostatic temperature regulation is 10^{-5} mbar. Further pumping will be performed in the process of cooling by cryogenic panels, mounted on the outer surface of the support cylinder. The vacuum system is shown in Fig. 5.39 (a). The pumping station is placed on the upper platform of the magnet. Two pressure sensors are fitted on the vacuum casing of the control dewar to check the pressure. For pumping of the vacuum volumes of the control dewar, chimney,

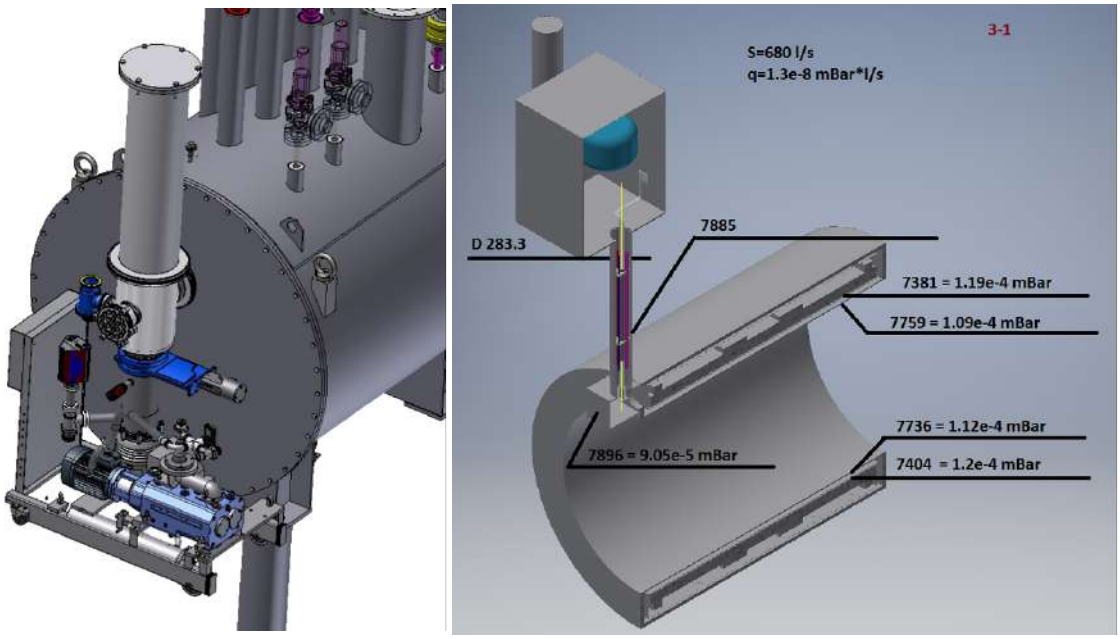

(a) (b)

Figure 5.39: (a) Vacuum equipment. (b) Distribution of the pressure inside of the vacuum system.

and superconducting coil cryostat up to 10^{-1} mbar with a safety factor of 2, a rotary pump could be employed with a pumping speed of 15÷18 l/s. For pumping down to 10^{-5} mbar, a turbo pump with a

Table 5.13: Instrumentation summary for the cold mass of the SPD solenoid.

Function	Location	Quantity	Sensor type	Notes
Quench detection	Coil modules	6	Voltage taps	3 Primary/Redundant pairs
	Coil-to-coil joints	4		2 Primary/Redundant pairs
	Terminal joints	4		2 Primary/Redundant pairs
	Bus-bar joints	4		2 Primary/Redundant pairs
	Vertical bus-bars	4		2 Primary/Redundant pairs
	Current leads	4		2 Primary/Redundant pairs
Cryogenic monitoring	Coil modules	6	Cryogenic temperature sensor	1 Top/Bottom
	Bus-bars	4		2 Primary/Redundant sensors
	Cryogenic lines	2		1 Supply/Return line

pumping speed of 500÷680 l/s can be chosen. Distribution of the pressure inside the vacuum system is presented in Figure 5.39 (b). Calculation was done by software "MOLFLOW+ 2.6.62".

The cryostat and control dewar of the SPD solenoid will be built according to AD2000. The worst-case scenario concerning the safety of the cryostat would arise, if a leak evolved in the part of the liquid helium (LHe) cooling circuit that runs through the vacuum vessel. Only in this case the pressures balance could actually be reversed, and the pressure inside the cryostat could exceed the atmospheric pressure.

The cryostat vacuum vessel, control dewar, and all connections have to be verified to resist up to a pressure of 1.50 bar (absolute pressure) from the inside. This provides a good safety margin, as the coolant circuit will be working at an absolute pressure of 1.30 bar, and we foresee safety flange DN250. For the outer cryostat shell, the stability against a pressure reverse is easily guaranteed, since it is designed to work with 1.0 bar from the outside. This is naturally different for the inner wall of the cryostat, which is designed to keep, under normal operation, the atmospheric pressure from inside. However, the inner wall of the cryostat is designed to keep safely the full load of the detector, mainly the weight of the ECal with minimum deformation. The extra thickness needed to fulfill this requirement is more than enough to guarantee against buckling of the inner wall of the cryostat in case of a pressure reversal, due to a leak in the helium circuit.

A system of safety valves has been foreseen to prevent an excessive pressure rise in the vacuum vessel of the cryostat, control dewar, and chimney. A relief flange opening at 0.3 bar is foreseen. In case of LHe vaporization, the relief valve would open, venting the helium gas to the atmosphere and preventing damages to the cryostat vessel.

1.5 Proximity cryogenics safety

The different parts composing the cryostat should be designed, fabricated, and inspected according to the intent of the AD2000 norm, including corresponding documentation, certificates, and used standards.

The choice of indirect cooling of the solenoid will greatly reduce the amount of liquid helium in the cryogenic system. The pipes, guaranteeing the coil refrigeration, will contain ∼10 l of refrigerant. This includes the two manifolds placed on the top and on the bottom of the cold mass for the thermo-syphon circulation. Another ∼300 l of liquid helium will be stored in the helium vessel, housed in the control dewar.

The operating pressure of the SPD coil cryogenic system will be 130 kPa (absolute pressure), corresponding to a coolant temperature of 4.5 K during cooldown and warmup. The two phases of liquid helium, used by the cooling system, will be fed to the helium vessel of the control dewar through a transfer line from the helium liquefier during normal operation. Liquid helium from this vessel will give the coil cryogenic system the capability to operate for up to 60 min. for safe de-energization of the coil.

Table 5.14: List of purchasing equipment for control dewar cryogenic system.

No.	Type device/ instrument	Producer
1	Cold Valves	Velan Weka Stoehr Flowserve
2	Relief valves	Leser
3	Warm valves	Velan Weka Stoehr Flowserve
4	Pressure transmitters	Emerson/ Siemens/ WIKA
5	Pressure indicators	Swegelok
6	T platinum sensors	Heraeus
7	Low-temperature thermometers	Business Logistix Ltd OXFORD/ JINR/ BINP
8	Warm flow meters	BROOKS Smart series/ BRONKHORST
9	Heaters	many companies
10	Level meters	AMI
11	Connectors, 2 bars	Fischer
12	Connectors, 2 bars for heaters	Fischer
13	Connectors, 40 bars	Serie_Hermetique_Jager
14	Pumps, preliminary and TMP	Edwards/ Laybold or equal
15	Gate valve DN150	VAT
16	Vacuum angle valves	many companies
17	Fittings	Swegelok
18	MLI	Groupe HUTCHINSON ex- JEHIER/ RUAG
19	Ball supports	Bosch Rexroth

The transfer line will decouple the refrigerator from the solenoid cryogenics, in case of refrigerator failure. In the worst case, the gas would be transferred into the helium vessel at the full pressure of the running compressor of the liquefier (∼16 bar). In this case, it would be vented to the air through the relief valve and safety flange DN250. Furthermore, it will help that the liquefier and the control dewar will be connected through a long transfer line. This line will hydraulically decouple them in the scenario of a liquefier failure with the 16 bar helium gas, at the temperature of the last heat exchanger, transferred into the system.

As an additional safety measure, all the cooling loops and distribution lines inside the cryostat (including the intermediate radiation shields) are designed for a nominal operating pressure of 16 bar. The helium vessel of the control dewar, operating at 1.3 bar, is designed for an overpressure of 19 bar and will be equipped with a relief valve, venting the vessel into the atmosphere for the pressure p = 1.8 bar in case of helium boiling off, due to a quench or vacuum failure.

1.6 Cold mass instrumentation

The instrumentation of the cold mass of the SPD solenoid, taken as an example, falls under two groups: quench protection and cryogenic monitoring. Table 5.13 provides a summary of the sensors to be installed.

The quench protection system monitors the coil modules and superconducting bus-bars for resistance growth, and provides a trigger for the current breaker to isolate the power converter from the solenoid, in order to limit the rise of conductor temperature, due to Joule heating. The quench detection system relies on voltage taps. Voltage taps are critical sensors and, therefore, must have redundancy. The voltage taps, installed on the joints, also provide the capability to monitor the joint resistance. Similarly, voltage taps are installed on the current leads to monitor the lead resistance.

Cryogenic monitoring is based on temperature sensors to control cooldown, warmup, steady state operation, and changes in response to a heat load, such as a quench. Temperature sensors are installed on the cold mass and bus-bars, as well as on the supply and return cryogenic lines.

Appropriate instruments and tools are required to control cryogenic processes. There are cryogenic cold and warm control valves with transmitters and actuators, flowmeters, pressure transmitters and manometers, thermosensors, level meters and related accessories. The minimal list of needed instruments and tools is presented in Table 5.14.

2 JINR option

Main distinctions between the SPD magnet and the existing or projected magnets for detectors of particles are the design features of the solenoid. The technology using a hollow composite superconducting cable, proposed in the Veksler and Baldin Laboratory of High Energy Physics (VBLHEP) and well-proven in magnets of the synchrotron Nuclotron [16], was chosen as the basis for its production. In this case, the winding is cooled by the circulation of a supercritical helium flow in the cooling channels of a hollow cable. The SPD magnet is designed to create a uniform magnetic field with a nominal induction of 1 T in its aperture. The superconducting solenoid will be surrounded by an iron yoke, designed to close the magnetic flux and form a magnetic field with the required uniformity.

The requirements to the SPD magnet are:

- maximum field on the solenoid axis – $B_z \leq 1$ T;
- uniformity of the magnetic field on the axis – $dB_z/B_z \leq 0.05$;

– diameter of the ”warm” aperture – 3.2 m;

– solenoid length – 3.8 m.

2.1 Solenoid design

The technology using a hollow composite superconducting (SC) cable (Fig. 5.40), proposed at VBLHEP and well-proven in magnets of the Nuclotron, was chosen as the basis for the production of the solenoid. VBLHEP has a base for the production of such a cable, which only requires an upgrade of the existing equipment.

Since the solenoid operates at a constant current value, the SC wires can be soldered to the cooling tube, and the tube can be made of copper. Unlike the Nuclotron cable operating in a pulsed magnetic field, the SPD solenoid cable does not have a fixing wire. A solenoid with an average winding radius of 1.742 m and a length of 3.8 m should have a high uniformity of the magnetic field in the aperture. The two-layer winding is planned to be made of 10 coils (see Fig. 5.41 (a)) of 2 sections each. The 0.38 m coil, as it is shown in Fig.5.41 (b), contains 30 turns of a hollow superconducting cable.

2.2 Solenoid from the Nuclotron-type superconducting cable

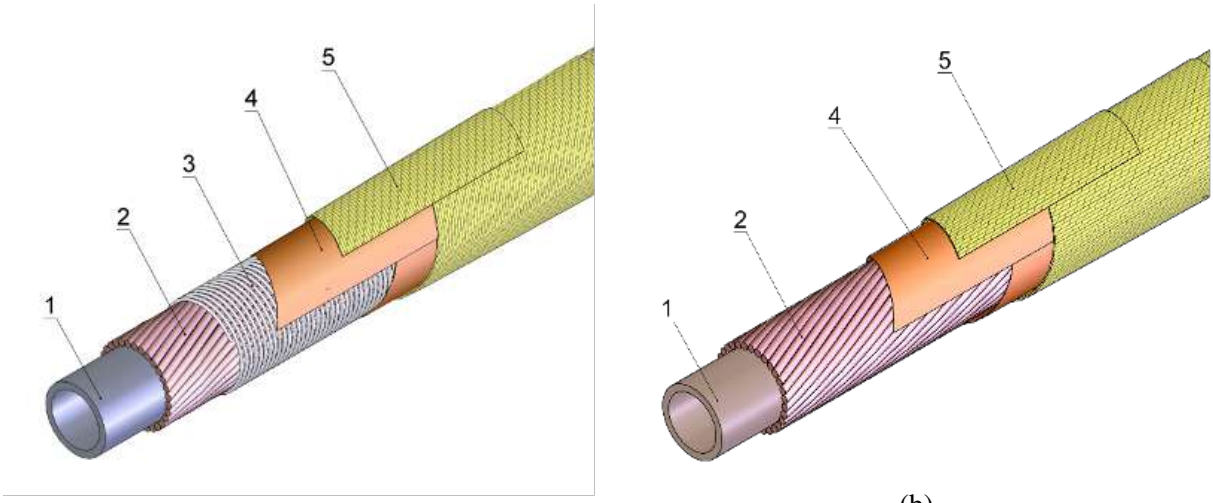

(a) (b)

Figure 5.40: (a) Hollow SC cable of the Nuclotron and (b) the SPD solenoid: 1 – a tube with a channel for cooling; 2 – SC wire; 3 – fixing wire; 4 – polyimide tape; 5 – glass fiber tape impregnated with epoxy compound for hot hardening.

The SPD winding of 10 coils is carried out on a mandrel, made of stainless steel. Profiled copper inserts are laid below and above each layer of the coil (see Fig. 5.42), filling the voids between the turns. At the bottom of each layer of the coil, shunts are laid-winding heaters, which are necessary to protect against overheating at quench. A bandage of stainless steel wire is wound over the coil. After the winding of both sections of the coil, the coil is heat-treated to polymerize the epoxy compound. The coils are assembled together on a special device. In this case, the mandrels of the individual coils are mechanically interconnected. Then, the helium cooling lines of the solenoid are connected, and the electrical connections between the coils are made.

The magnetic and stress calculations have been performed using the OPERA simulation software. The value of B_z component equal 1 T at the axis of the magnetic system is achieved by the current in the coils of 5067 A. The variation of B_z at the axis is less than 5%, which satisfies the requirement of the SPD

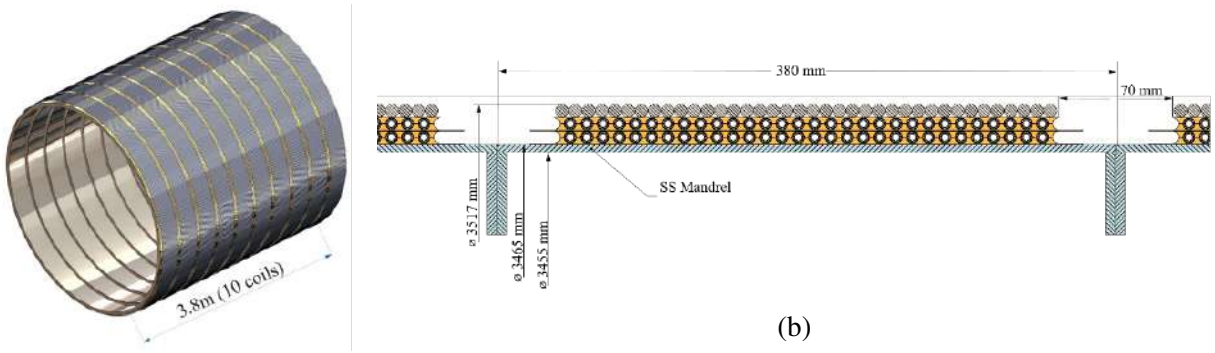

(a) (b)

Figure 5.41: (a) SPD solenoid of 10 coils. (b) Coil winding with two sections.

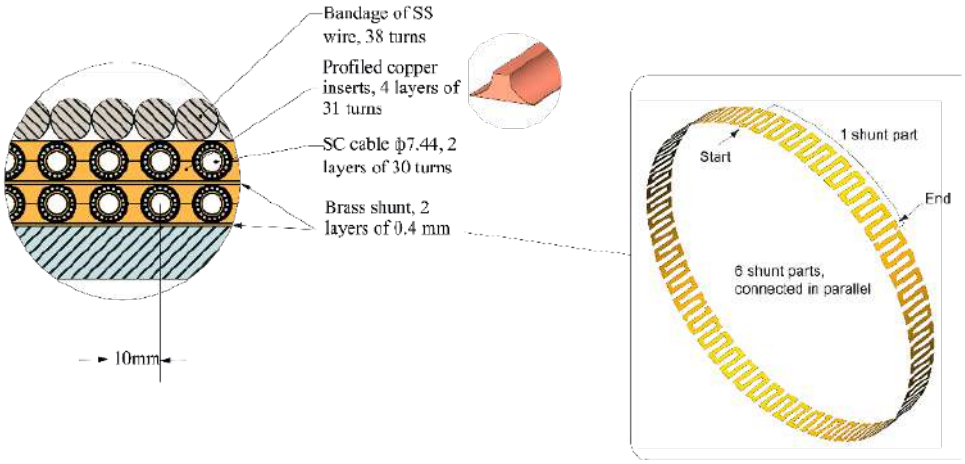

Figure 5.42: Elements of the SPD solenoid coil.

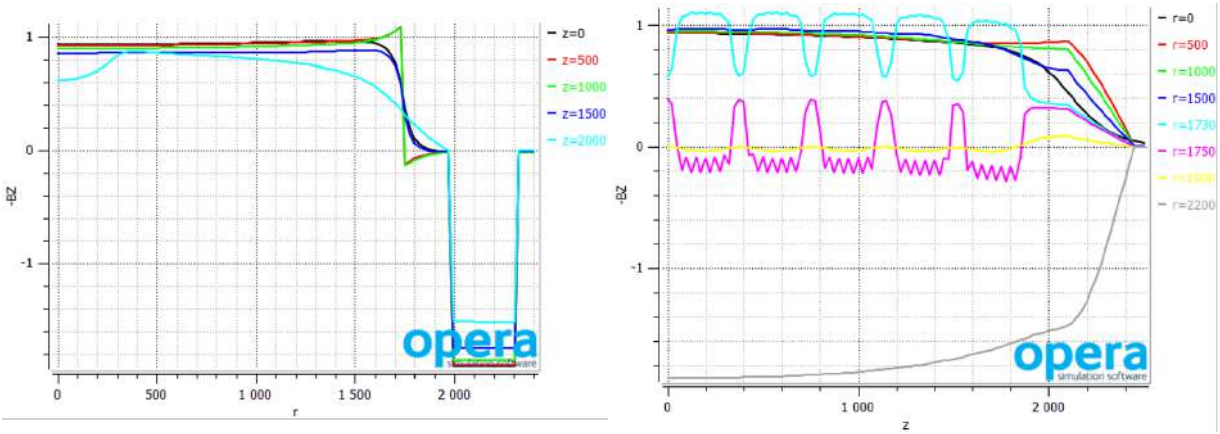

(a) (b)

Figure 5.43: B_z as a function of radius (a) for various distances from the center of the solenoid and distances (b) from the center of the solenoid for various radii. Detector working area is $Z \leq 1900$ mm, $r \leq 1570$ mm.

magnetic system. The maximal value of the forces acting between the neighboring coils is 1.36 MN. The pressure of the magnetic field on the solenoid is 0.398 MPa. Dependence of B_z on radius r and z coordinate is shown in Fig. 5.43. The magnetic field lines of force are shown in Fig. 5.44.

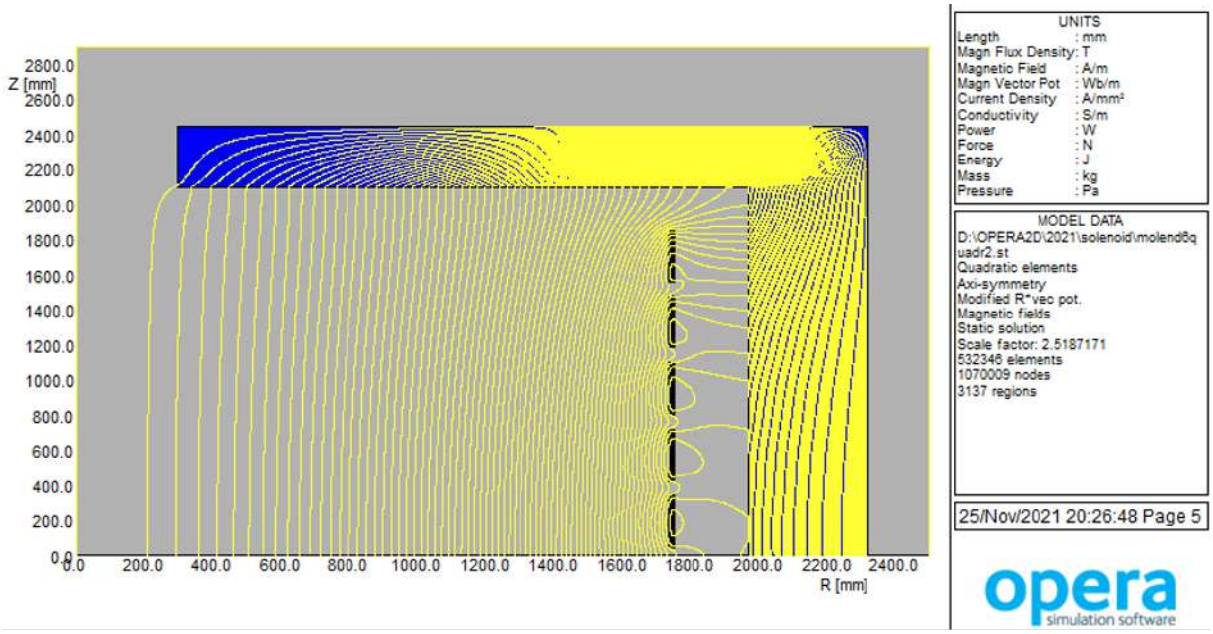

Figure 5.44: Magnetic field lines.

The characteristics of the SPD cable and winding are presented in Table 5.15.

2.3 Cooling system

The solenoid winding is cooled by a supercritical pressure helium flow, which is pumped inside the cooling channel of the cable. In total, there are 20 parallel cooling channels (10 coils of 2 sections each). Each section of the solenoid is connected in parallel to the supply and return helium collectors. The operating temperature of the winding is 4.8 K, the nominal flow rate of liquid helium through the solenoid is about 16 g/s. The cold mass of the solenoid is about 7.9 tons. Cooling of the solenoid is planned by a helium refrigerator with a nominal cooling capacity of 100 W, which will be installed close to SPD. Some characteristics of the cold mass and cooling system are presented in Table 5.16.

The calculated values of the heat load on the cooling system are shown in Table 5.17.

2.4 Quench protection system

Protection of the magnet against overheating at its transition from the superconducting state to the normal state is achieved by solenoid sectioning [17] and uniform dissipation of energy over the whole winding. For this purpose, the winding is divided into 20 electrical sections. The energy stored in the magnet is dissipated both on the external resistance and on 20 shunts – heaters, located on the inner radius of each layer of the winding. The external resistance R_e = 0.04 Ω limits the maximum voltage, with respect to ground to ±100 V. The shunts divide the winding into 20 sections, in each of which a shunt made of brass tape is connected in parallel to the winding section (see Fig. 5.45). The shunt is electrically connected in parallel to the SC cable of its section and has good thermal contact with the SC cable along its entire length, which provides a very high velocity of the normal zone propagation in the winding.

Part of the energy released in the winding will be about 54% of the energy stored in the solenoid or 7.9 kJ, and the time constant of the energy dissipation process will be about 13 s, calculated by the following equation:

$$\tau_1 = L/(R_e + \sum R_{sec.aver.}), \tag{5.2}$$

where τ_1 is a time constant of energy dissipation, L is the inductance, R_e and $R_{sec.aver.}$ are the external

Table 5.15: Characteristics of the SPD solenoid.

Cable	
Parameter	Value
Helium cooling channel diameter, mm	4
Cooling tube outer diameter, mm	5
Cooling tube material	Cu
Number of strands	19
Lay pitch of strands, m	0.1
Diameter with insulation, mm	7.44
Copper sectional area, mm^2	15.77
Superconductor sectional area mm^2	3.38
Cu/SC ratio	4.66/1
Length in section, m	328.3
Total length in the winding, m	6566
Strand	
Diameter, mm	0.9
Superconductor	Nb–Ti/Cu
(Nb–Ti)/Cu – volumetric ratio	1/2.57
Nb–Ti filament diameter, *mu*m	7
Operational current I_{max}, A	270
Critical current at 2 T and 4.2 K, A	≥ 670
Supporting cylinder	
Inner diameter, m	3.455
Outer diameter, m	3.465
Material	Steel 12X18H10T
Winding	
Nominal (maximal) magnetic field B_0, T	1.0
Inner diameter, m	3.465
Outer diameter, m	3.498
Length, m	3.8
Number of layers	2
Number of winding sections	2×10
Number of turns	$30 \times 2 \times 10$
Operational current I_{max}, A	5067
Inductance L, H	1.144
Stored energy E at I_{max}, MJ	14.7

Table 5.16: Some characteristics of the SPD solenoid cold mass and cooling system.

Cold mass at 4.8 K, kg	
Parameter	Value
Cu in conductor, M_1	560
Cooling tube, M_2	413
Cu inserts in winding voids, M_3	2402
Brass electrical shunts	162
SS bandage	1670
SS mandrel	2500
Nb–Ti alloy in strands	158
Total	7865
Cooling	
Operating temperature, K	4.8
Operating pressure, MPa	0.3
Heat load at operational condition, W	≤ 40
Heat load at energy input, W	≤ 74
Nominal He mass flow rate, g/s	16
Number of parallel cooling channels	20
Nominal pressure drops in channel, kPa	≤ 50
Pressure in cooling channel, MPa	≤ 3
Cool down time from 300 K to 4.8 K, hours	≥ 50

Table 5.17: Calculated values of the heat load on the SPD magnet cooling system.

Heat inflow	Value, W
Residual gases	7.6
Thermal radiation	6.2
By suspensions	14.4
By current leads	11.0
Total W	39.2

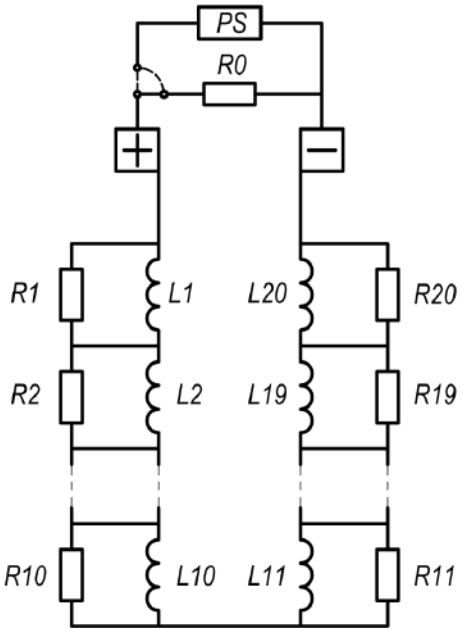

Figure 5.45: Electrical circuit diagram of the one section.

resistance and average resistance per section, respectively.

An estimated maximum heating temperature of the winding (at initial winding temperature $T_0 = 4.2$ K), as a result of its transition to the normal state (quenching) is calculated under the following assumptions:

- energy, released in the solenoid, dissipates in the superconducting wires, a copper tube, and copper inserts;
- normal zone propagation velocity $v = \infty$.

So,

$$\Delta T \approx 0.54E/(M \times C), \tag{5.3}$$

where ΔT, K is the temperature rise after the quench at the point of origin of the normal zone; E is the stored energy at maximum current I_{max}. $M = M_1 + M_2 + M_3$, where $M_1 = 560$ kg is the mass of copper in the SC wire, $M_2 = 413.2$ kg is the mass of the copper tube, and $M_3 = 2402$ kg is the mass of the copper inserts. $C = 39.31$ J/ (kg$\times$K) is the heat capacity of copper at an average temperature of 34.1 K. $\Delta T = 59.8$ K, thus the maximum temperature of the winding after the quench is $T_{max} = T_0 + \Delta T \leq 65$ K.

2.5 Cryostat

The cryostat for the SPD solenoid is being developed. The design of the solenoid suspension system in the cryostat is underway. The basic characteristics of the cryostat are presented in Table 5.18.

The design of a superconducting solenoid made of a Nuclotron cable is proposed based on the technology developed at VBLHEP in the production of magnets for the Nuclotron and NICA accelerators [18]. The use of this technology makes it possible to produce a solenoid at JINR involving enterprises of the Moscow Region. Calculations show that the solenoid will have the required field quality, the reliable cooling and quench protection system, and maintainability. Less time and money are expected to be spent for producing a solenoid using the Nuclotron technology, compared to a commercially available solenoid produced using traditional technology.

Table 5.18: Basic characteristics of the cryostat.

Parameter	Value
Length, m	4.0
Diameter of the heat shield at 80 K	
Inner shield, m	3.305
Outer shield, m	3.617
SS vacuum shell diameter	
Inner shell , m	3.175
Outer shell, m	3.767
Number of solenoid supports	24
Mass of vacuum shells, kg	15330
Mass of thermal shields, kg	1340
Total mass of the cryostat, kg	16700

3 Cost estimate

An estimate of the cost of each of the two magnetic system options is presented in the Table 5.19. To the indicated values, we must add the cost of the system of detailed measurement and control of the magnetic field of 500 k$. Development of the magnet control and monitoring system is additionally estimated at 1 M$.

4 Cryogenic system

The magnetic field is formed by a superconducting (SC) coil. The NbTi superconductor, which has an operating temperature of 4.5 to 9.0 K, has been selected for the SC coil of the detector SPD. Keeping the SC coil in the SC state implies the use of a non-standard cryogenic system operating at 4.5 K. The working substance being gas/liquid helium. For the SPD magnetic system project, two fundamentally different variants of structures and technical solutions of SC coils are being developed. One concept is based on the application of a tubular SC cable of the Nuclotron type; this variant is proposed by the JINR LHEP working group (the first variant). To cool the proposed SC coil, supercritical helium is required, which requires the use of a refrigerator-type cryogenic plant. The second concept implies the use of a Rutherford SC cable and for this SC coil a thermosiphon cooling method is used, which means the use of a liquefier type of cryogenic plant, this variant was proposed by the INP working group (second variant). The cryogenic helium plant with the input cryostat will be placed on a technical platform, which is moved together with the SPD detector. The cryogenic system consists of three main subsystems: helium and nitrogen systems, as well as auxiliary systems. The helium system includes the cryogenic plant, high- and low-pressure helium flow pipelines, and cryogenic flexible pipeline for liquid and vapor helium. Nitrogen system: two cryogenic tanks for liquid nitrogen storage, cryogenic pipeline, pipeline for nitrogen vapor. Auxiliary systems: vacuum, measuring, cryogenic monitoring and control system, order gas system and water-cooling system. The cryogenic systems for both variants of SC coils will differ in the type of cryogenic plant and the design of the input cryostat.

4.1 Helium cryogenic system

4.1.1 Cryogenic plant for the JINR variant of the SPD magnet

The concept of the first version of the SC coil requires the use of a cryogenic helium plant of refrigeration type. It has the ability to work with supercritical helium flow and allows slow cooling of the SC coil by

Table 5.19: Cost estimate (kEuro).

Milestone	Description	Novosibirsk option	JINR option
1	Project management and testing	**1870**	**1220**
	Technical project	800	500
	Plan review	170	120
	Preliminary design review	250	200
	SAT full solenoid	650	400
2	Conductor	**1650**	**850**
	Contract conductor with ext. firm	360	
	Production conductor material and Cu inserts at ext. firm		400
	Production conductor at LHEP		200
	FDR conductor	160	100
	Start of conductor production at ext. firm	870	
	FAT conductor	260	150
3	Cryostat and cold mass	**1060**	**640**
	Cryostat design	140	100
	FDR cryostat	140	70
	Procurement components	250	150
	FAT cryostat	420	250
	SAT cryostat	110	70
4	Cryogenics	**740**	**1840**
	Control dewar design	100	
	Control dewar vacuum equipment	150	
	Feed box design		100
	Helium refrigerator		1100
	Vacuum equipment		150
	FDR	170	170
	FAT	220	220
	SAT	100	100
5	Electrical components	**760**	**760**
	Contract el. components	120	120
	FDR el. components	180	180
	Procurement of el. components	340	340
	FAT el. components	120	120
6	Magnet alarm safety system	**120**	**120**
	FDR safety system	40	40
	Tender of components for safety system	60	60
	FAT safety system	20	20
7	Coil winding	**580**	**490**
	Design coil winding	40	40
	Tooling design	30	30
	FDR coil	60	60
	Procurement of coil components	180	150
	FAT coil winding	220	160
	Cold mass integration	50	50
	Total (with installation and commissioning)	**6780**	**5920**

Table 5.20: Main operating parameters of the cryogenic plant for the JINR option of the magnet.

p.	Operating parameters	Unit
1	Cooling capacity	100 W 4.5K
2	Temperature of outlet flow from the SPD	4.8 K (2.5 bar)
3	Temperature of inlet flow from the SPD	4.8 K (3.0 bar)
4	Hydraulic resistance of the SC coil	0.5 bar
5	Cold weight	7865 kg
6	Maximum pressure in coil	5 MPa
7	Mass flow rate	$\leq$16 g/s
8	Equipment Requirement	Maximum reliability, energy efficiency, compactness, automatic mode
9	Interval of repair/regulatory work of the plant	Not more than once a year

Table 5.21: Main operating parameters of the cryogenic plant for the Novosibirsk option of the magnet.

p.	Operating parameters	Unit
1	Cooling capacity	140 l/h
2	Temperature of outlet flow from the SPD	4.3 K (1.05 bar)
3	Temperature of inlet flow from the SPD	4.5 K (1.15 bar)
4	Hydraulic resistance of the SC coil	0.1 bar
5	Cold weight	3800 kg
6	Maximum pressure in coil	5 MPa
7	Maximum heat load	45 W
8	Equipment Requirement	Maximum reliability, energy efficiency, compactness, automatic mode
9	Interval of repair/regulatory work of the plant	Not more than once a year

helium vapor, at a rate of about 4 K/h, as well as step-by-step cooling of the heat shields. The main operating parameters of the cryogenic plant are given in Table 5.20.

The plant must have an additional outlet of liquid nitrogen from the nitrogen vessel to provide cooling of the SC coil heat shields, as well as meet all modern solutions in the cryogenic technology.

The plant includes flexible lines to connect to the input cryostat for transportation of liquid and gaseous helium and nitrogen flows. Maximum heat load for flexible lines: for helium communications is 3 W/m; for nitrogen communications is 5 W/m. All cryogenic flexible lines and pipelines are vacuum insulated, condensate formation on external surfaces of communications is not allowed.

The power consumption of the cryogenic plant is 2 kW.

4.1.2 Cryogenic plant for the Novosibirsk option of the SPD magnet

The concept of the second variant of the SC coil requires the use of a cryogenic helium liquefaction plant, which allows to cool the SC coil and heat shields with helium vapor, the maximum cooling rate is 1 K/h. This variant uses the thermosiphon method of SC coil cooling. A similar cooling principle and SC coil design is used in such projects of MPD, PANDA, etc. detectors.

The plant must have an additional outlet of 50 K helium flow with a smooth adjustable temperature from 297 K to 50 K, to cool the heat shield of the detector SC coil. The plant includes flexible lines to connect to the input cryostat for transportation of liquid and gaseous helium flows. The maximum heat

load for flexible lines of helium communications is 3 W/m. All cryogenic flexible lines and pipelines are vacuum insulated, condensate formation on external surfaces of communications is not allowed. The power consumption of the cryogenic plant is 2 kW.

4.1.3 Helium pipelines

The cryogenic system requires pipeline installation along the route from the central cryogenic station to the location of the SPD detector. Figure 5.46 shows the routing of the high- and low-pressure helium flows. The total length of the traces is about 220 meters. Pipelines of high-pressure helium flow have a 60 mm diameter and low-pressure helium flow has a 100 mm diameter. The material of the pipelines is stainless steel 12X18H10T or analog. Tracing has the following route. From the room 177 the route goes piping with other communications in one route to room 109/1 (about 120 meters of traces). From the room 109/1 the route goes to the courtyard of building 17 and on the ramp comes to the room 140/2.

The pipelines section from the entrance to room 140/2 to the cryogenic plant is made of flexible lines. Figure 5.46 shows the location of the cryogenic equipment on the technical platform and the flexible line. The pipelines have a system of safety devices, to provide safe operation.

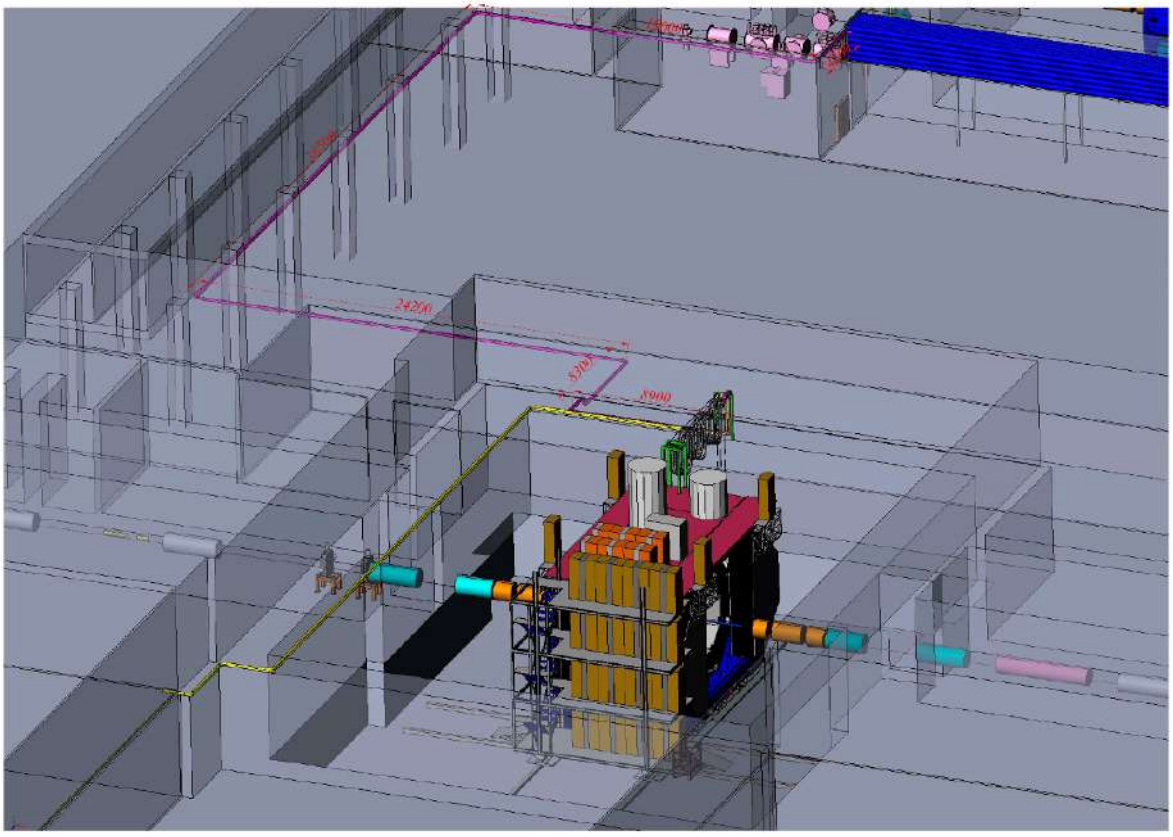

Figure 5.46: Tracing pipelines of high- and low-pressure helium flows.

4.2 Nitrogen system

To provide operation of the cryogenic helium plant it is necessary to create a nitrogen system. The nitrogen system includes the following main elements: two cryogenic storage tanks for liquid nitrogen, cryogenic pipeline and flexible line. The system uses two cryogenic tanks each with a capacity of 20 m^3, the main technical parameters are presented in Table 5.22.

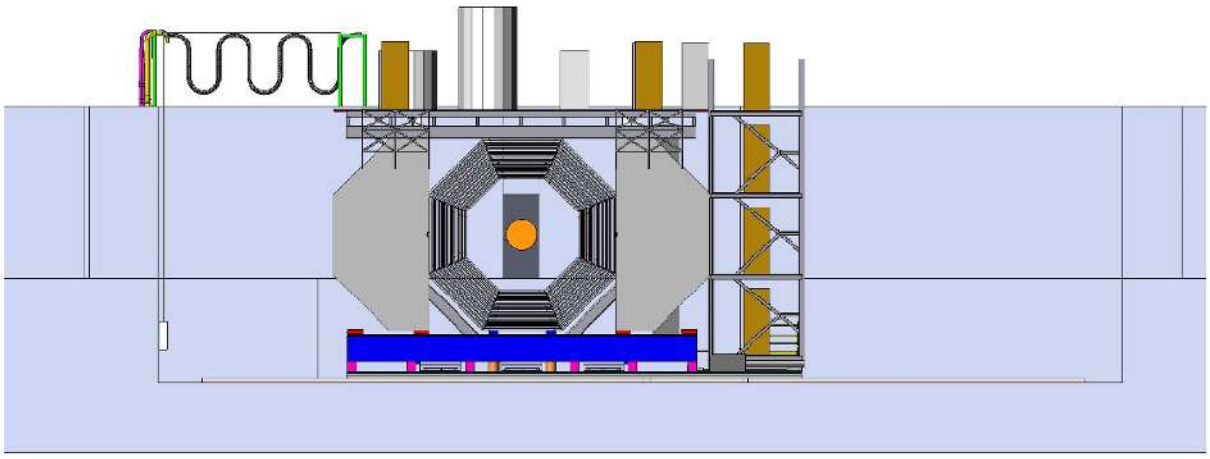

(a)

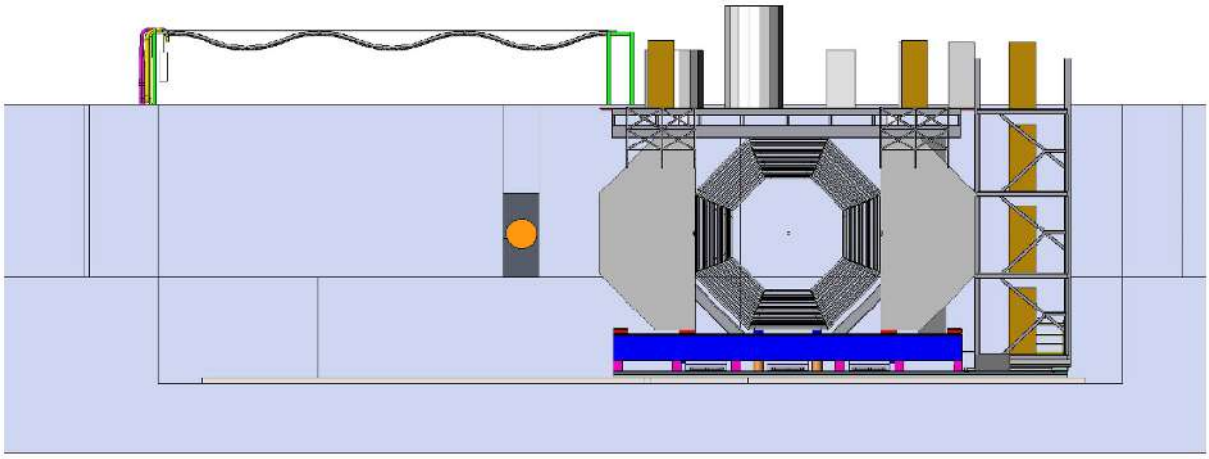

(b)

Figure 5.47: Flexible lines in the room 140/2 when SPD is in the ”beam” (a) and ”servise” (b) position.

The cryogenic storage tanks are located on a special foundation to the Building 17 on the side of the room 140/1. Liquid nitrogen is supplied through a cryogenic pipeline by raising the pressure to 4.0 bar in the cryogenic storage tank. When the minimum liquid nitrogen level in the first cryogenic storage tank is reached, the control system automatically switches the liquid nitrogen supply from the first cryogenic storage tank to the second cryogenic storage tank. The cryogenic pipeline is vacuum insulated and condensate formation on external surfaces of communications is not allowed. Total length of the route is about 120 meters. The pipeline is made on a tube-in-tube type, the inner pipeline is 30 mm in diameter, the outer pipeline is 70 mm in diameter. The material of the pipeline is stainless steel 12X18H10T or analog. The route has the following (Figure 5.48 shows a preliminary route): from the tanks the pipeline rises to a height of 6 meters for the passage over the road, then along the wall of the building 17, room 140/1, enter the room and bring it to the cryogenic plant. The route has a system of safety devices, to ensure safe operation.

The discharge of gaseous nitrogen is carried out according to the principle of the shortest route with exit to the atmosphere. The discharge pipelines?s diameter is 70 mm. Energy consumption of the system is 2 kW.

Table 5.22: Main technical parameters of the cryogenic storage tank.

p.	Operating parameters	Value
1	Overall volume	20 000 l
2	Maximum daily evaporation rate depending on pressure 100 kPa and ambient temperature15 $^{\circ}$ C	0.17 %
3	Maximum outlet flow rate (nitrogen)	600 Nm^3 / h
4	Maximum operating pressure	1.8 MPa
5	Operating pressure range	From 1.2 bar to 4.0 bar
6	Minimum permissible wall temperature (inner vessel)	77 K
7	Maximum pressure in vacuum space at T=293 K	10 Pa
8	Interval of repair / regulatory work of the plant	Not more than once a 7 years.

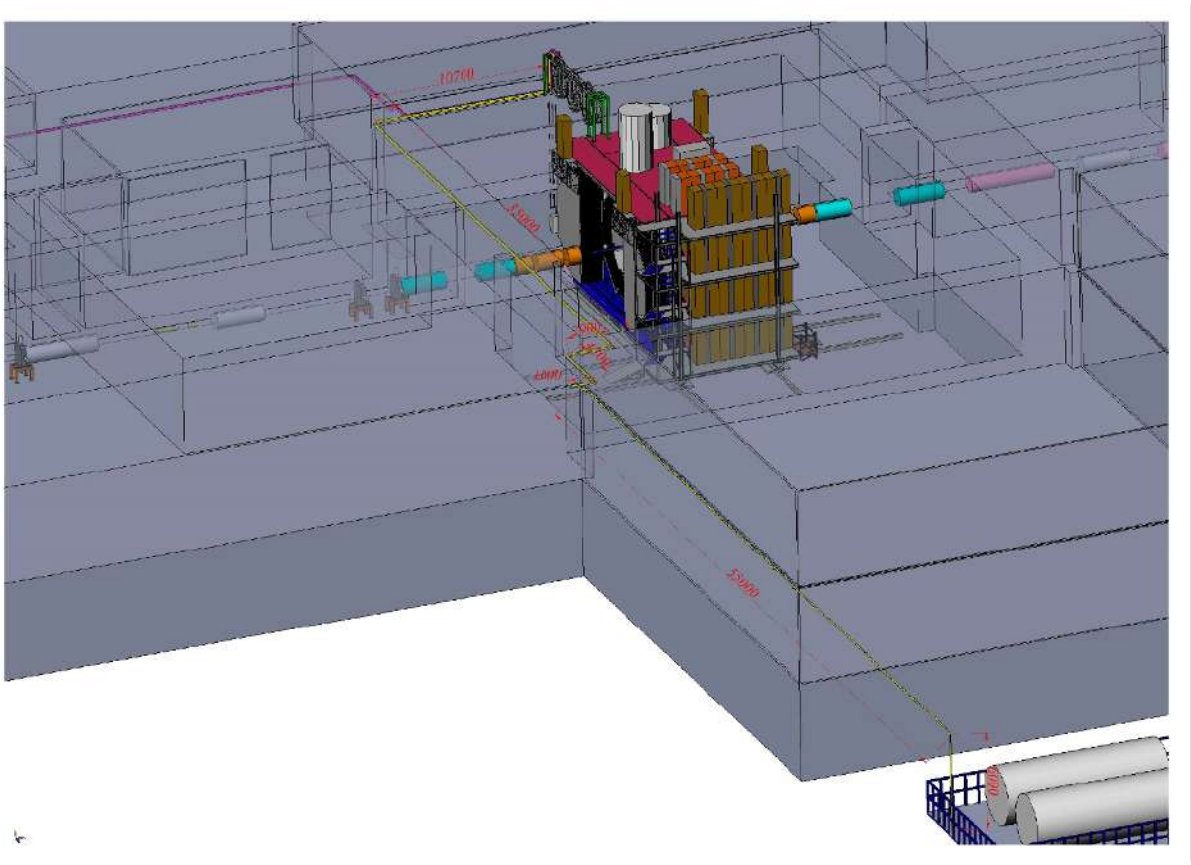

Figure 5.48: Tracing cryogenic pipelines of nitrogen flow.

4.3 Auxiliary systems

Vacuum subsystem provides maintenance of discharged medium in isolation volumes of the cryogenic plant, input cryostat and SC coil cryostat. Maximum pressure value in the isolation volumes at 293 K (before start of cooling) is 1×10^0 Pa, maximum pressure value at 4.5 K (after cooling) for the cryogenic plant is 1×10^{-3} Pa, for inlet cryostat and SC coil cryostat is 1×10^{-5} Pa.

The subsystem includes several types of vacuum pumps: rotary vane pumps, Roots pumps, diffusion vapor pumps and turbomolecular pumps. The subsystem equipment is located on the technological platform of the detector SPD. The total power consumption of the subsystem is 14 kW.

Pneumatic valves and valves are used to control technological processes of the cryogenic system, their

Table 5.23: Costs and required equipment capacity

p.	Name of system	Cost, k$	Power consumption, kW
1.1	Cryogenic plant (JINR option)	3 000	2
1.2	Cryogenic plant (Novosibirsk option)	3 330	2
2	Helium pipeline	500	-
3	Nitrogen system	1 500	2
4	Vacuum subsystem	500	14
5	Pneumatic subsystem	50	3
6	Cryogenic system control	500	2
	Total (JINR option)	6 050	23
	Total (Novosibirsk option)	6 380	23

stable operation is ensured by the ordering of gas. The ordered gas subsystem has the following characteristics: working pressure 6 bar, working gas – dry air. The system includes: air screw compressor, receiver, moisture separator and various fittings (valves and reducers). Power consumption of the subsystem is 3 kW.

The cryogenic system is controlled by means of data acquisition from all related subsystems (cryogenic unit, helium pipelines, nitrogen system, pneumatic system, vacuum system and data from SC coil control system). Figure 5.49 presents a block diagram of cryogenic control system. The control system has automatic circuits with which the following steps are carried out: preparation, cooling of the SC coil, cryostatting at workloads, and heating.

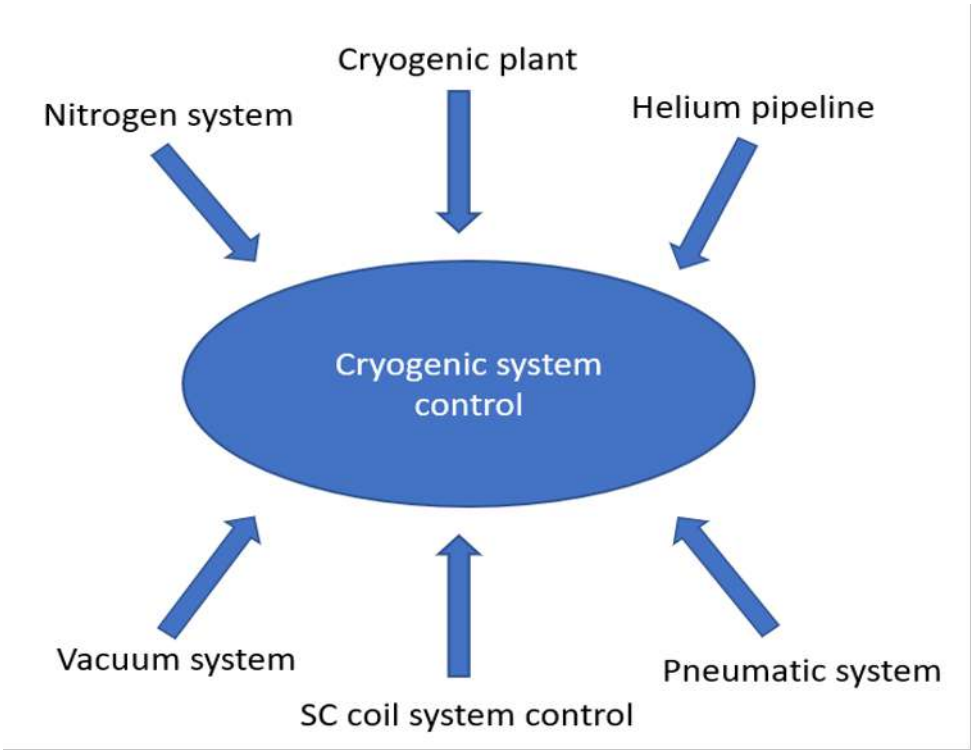

Figure 5.49: Tracing cryogenic pipelines of nitrogen flow.

4.4 Cost estimate

The cost of the equipment described above and the required capacity are presented in Tab. 5.23.

Chapter 6

Electromagnetic calorimeter

1 Electromagnetic calorimeter concept

The electromagnetic calorimeter (further calorimeter) should meet the criteria imposed by the physical goals of the SPD [19] experiment of various nature and importance. The most important criteria arises from the physical requirements for the measurement accuracy of energies, impact positions, and timing of photons and electrons. the technological possibilities of modern experimental physics should be taken into account when choosing the calorimeter setup. Cost factors should be considered also to ensure the feasibility of the project. High multiplicity of secondary particles leads to the requirements of high segmentation and high dense of absorber's medium with a small Moliere radius. It is required in order to have a sufficient spacial resolution and a capability to resolve overlapping showers. The transverse size of the calorimeter cell should be of the order of the Moliere radius. A reliable reconstruction of photons and neutral pions is possible only for small a overlap of showers. Occupancy should not exceed 5%, in order to make possible an efficient photons reconstruction with high precision. The SPD experiment imposes the following requirements on the calorimeter characteristics:

- reconstruction of photons and electrons in the energy range from 50 MeV to 10 GeV;
- energy resolution for the above-mentioned particles: $\sim 5\%/\sqrt{E}[\text{GeV}]$;
- good separation of two-particle showers;
- operation in the magnetic field;
- long-term stability: $2\div3\%$ in a six-month period of data taking.

The energy range requirement follows from the kinematic range of secondary particles, which are produced in a collision of protons with energy up to 27 GeV and emitted into 4π solid angle. Good energy resolution is required for the identification and quantitative measurement of single photon and neutral pion energies. Good two-particle separation is needed to separate photon showers from the π^0 decay in order to suppress background events in measurements with prompt photons. Long-term stability is necessary for polarization measurements featuring π^0 reconstruction in the calorimeter, especially in the end-caps. Calorimeter instability may result in false asymmetry values. While it is essential to meet the physics requirements imposed on the calorimeter design, one should also take into account the cost estimate and the technical feasibility when choosing its granularity, because a larger number of cells leads to higher costs of manufacturing and readout electronics.

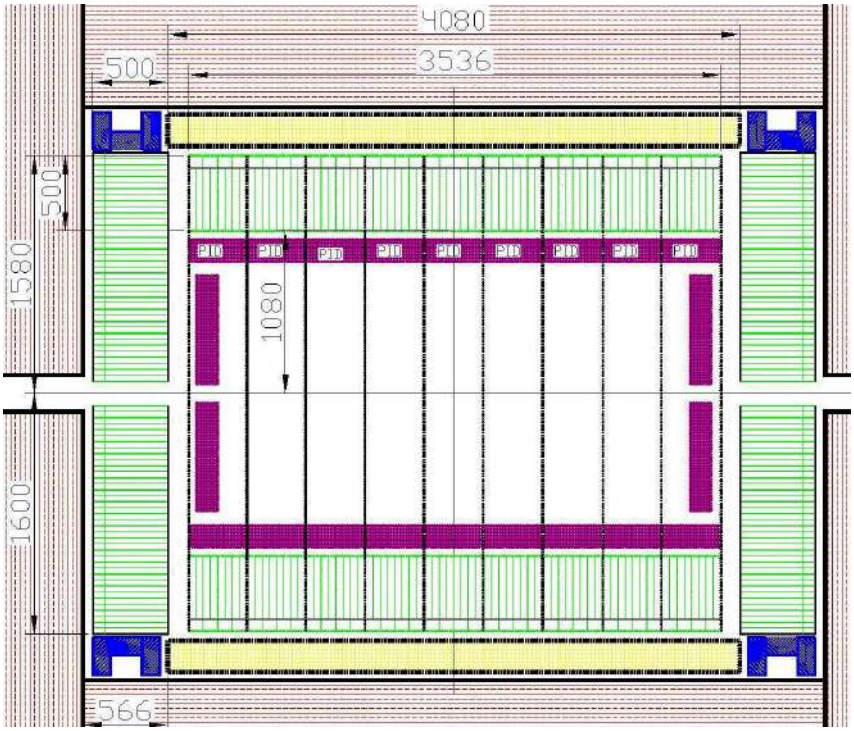

Figure 6.1: Barrel and end-cap parts of the calorimeter (green), side view. Purple – PID, yellow – cryostat, red – muon RS, blue – the frame for the end-caps.

2 Overview of the SPD calorimeter

The SPD electromagnetic calorimeter is placed between the cryostat with magnet coils and the Particles Identification Detector (PID), as shown in Fig. 6.1. The calorimeter consists of a barrel and two end-caps, covering a 4π solid angle. The outer dimensions of the calorimeter are determined by the inner size of the cryostat. The thickness of the calorimeter is determined by the required thickness of the active part and the size of the readout block consisting of a photodiode and the amplifier boards, as well as by the size of the flexible part of the fibers. For an efficient absorption of electrons and photons with energies up to 10 GeV, the calorimeter thickness, which is defined by the number of sampling layers, should be at least $17 \div 20$ X_0 in terms of radiation lengths X_0.

For the sampling structure of 190 layers of 1.5-mm polystyrene scintillator and 0.5-mm lead, the length of the active part is 380 mm, which corresponds to 17.6 X_0. The flexible parts of the fibers take up to 8 cm. The transverse size of the calorimeter cell should be on the order of the effective Moliere radius of the calorimeter medium, which is, in its turn, defined by the scintillator-to-lead sampling ratio. The selected structure has a Moliere radius of 5.8 cm. The separation efficiency of two photons with energies from 200 MeV to 500 MeV depends on the cell size and reaches a plateau at a cell size of 40 mm, as it was determined in the MC simulation. Therefore, we have selected $\sim$40 mm cell granularity for both the barrel and the end-caps. The cells in the barrel part of the calorimeter have a trapezoidal shape in the azimuthal direction to minimize the gaps between the modules. The vertex angle of the trapezoid equals 1.87°.

2.1 Barrel

A schematic drawing of the calorimeter barrel part is shown in Fig. 6.1. Its transverse size is limited by the cryostat and PID. The barrel part is composed of the cells of trapezoidal shape in the azimuthal direction with a vertex angle of 1.87°. The front size of one cell is equal to 34 mm. In the direction

along the beam axis the cell size is equal to 48 mm. A schematic drawing of the calorimeter barrel part is shown in Fig. 6.2 (a), an isomeric calorimeter view is shown in Fig. 6.2 (b). The barrel consists of 44 annular layers, located one after another along the beam axis. Each layer of the calorimeter's barrel is composed along the ϕ angle of 96 modules (4 cells per module). The design of the modules is described in more detail in Section 6.3. Every four layers of the calorimeter barrel are grouped, forming a ring containing 384 modules weighting 4 tons. The ring is made up of two half-rings to facilitate moving and handling at installation. Four layers are combined into a single block using 2 mm thick stainless steel sheets, which finally determine the gap between the layers. Subsequently, the half-rings are combined into a single ring and mounted on two rails fixed to the cryostat inner side, as shown in Fig. 6.3. The calorimeter ring is divided into 24 sectors by the angle ϕ, thus forming a cluster of 64 cells which are read by one ADC, as shown in Fig. 6.2 (b). The calorimeter barrel is composed of 9 rings, as shown in Fig. 6.3. In total, there are 13824 cells with the weight of 36.41 tons.

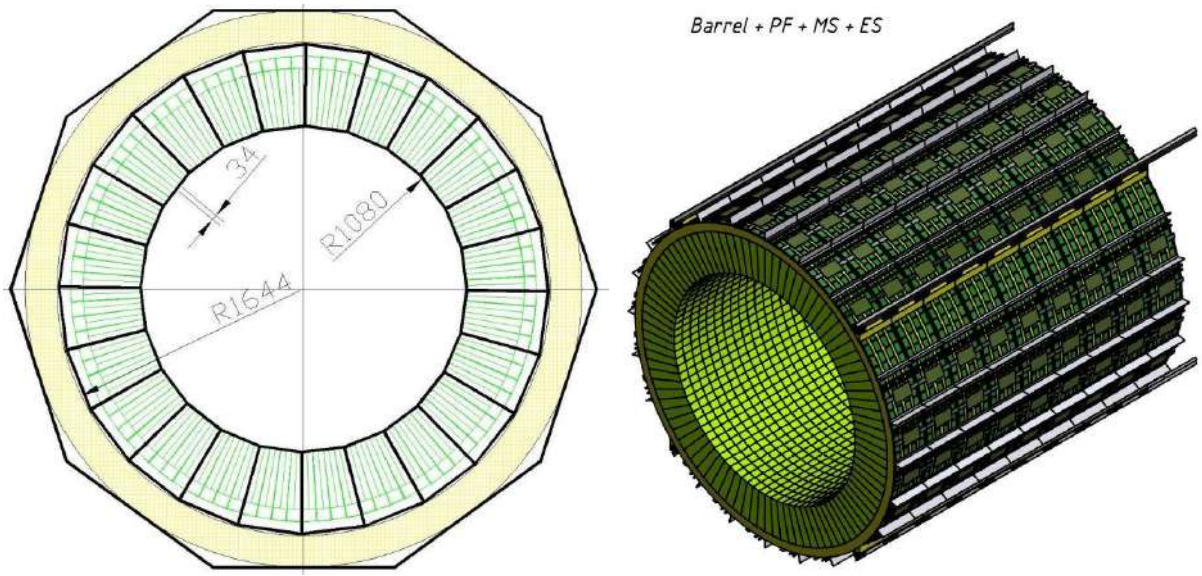

(a) (b)

Figure 6.2: Schematic drawing (a) of a cross-section of the barrel part of the calorimeter. It is sectioned into 192 cells azimuthally, with a vertex angle of 1.87°. All dimensions are in millimeters. The isometric view (b) shows an assembled barrel part.

Bias voltage for all 1536 cells of one ring is provided by 96 front end-cards (FE-boards), and data acquisition from all these cells is provided by 24 pcs. of 64-channel ADC boards. All of 96 pcs. of FE-boards, intended for one ring bias voltage, are controlled and powered by one HV module. See more details about related electronics below in Sections 6.5, 6.6. The HV control box is located outside of the barrel. It can be remotely placed at a distance up to 100 meters from the calorimeter. All 96 pcs. of FE-boards of one ring are connected to one HV control box by one flat cable of 5-pair twisted wires. FE-cards are mounted directly on the calorimeter module together with scintillator light sensors MPPCs. The power supply concept of ADCs and FE-boards is shown in Table 6.3.

ADC and cable traces are located along the surface of the ring, as shown in Fig. 6.4. A free space of 60÷80 mm between the cryostat and the top of the calorimeter should be provided for the placement of ADC and cable traces. This space is also required for the air flow that cools the ADCs. Air flow must be forced from outside of the calorimeter to avoid overheating. The rails for fastening of the ECAL's barrel inside of the cryostat are mounted in this gap also.

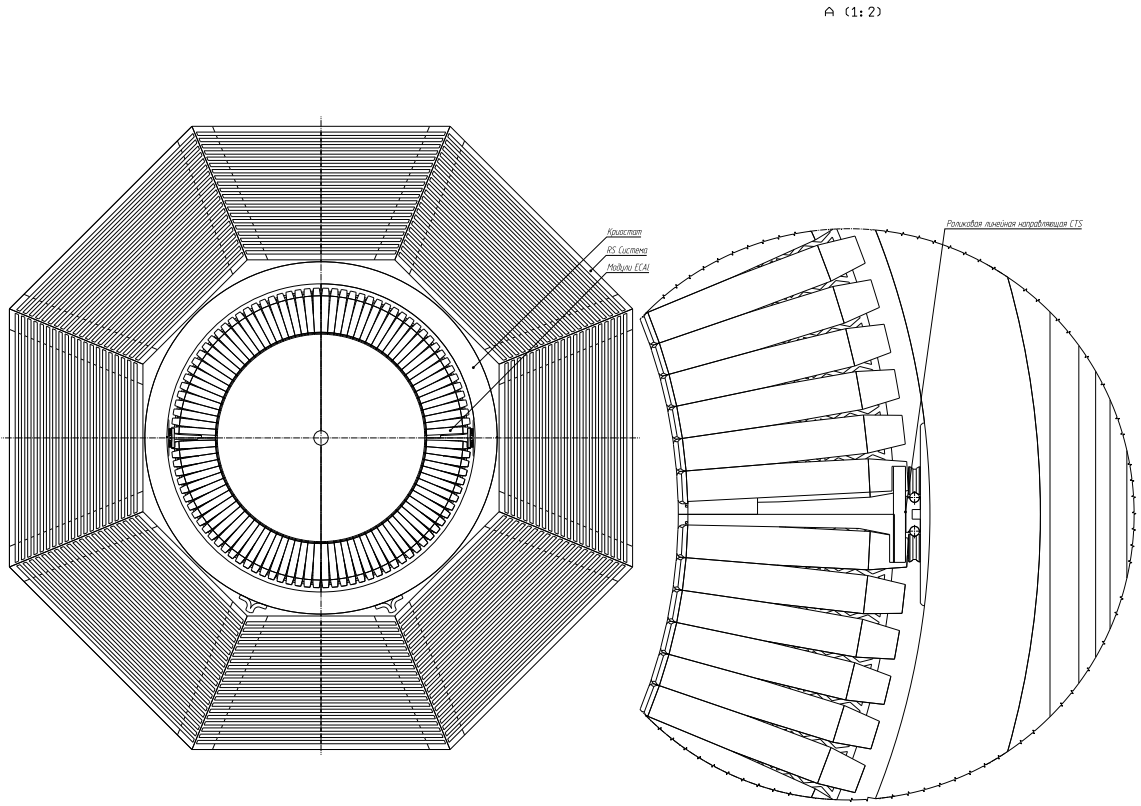

Figure 6.3: The rails to ECAL support and fastening to the cryostat inner side. Two roller trays support each calorimeter ring. There are 9 such rings installed inside of cryostat. One ring weights about 4 tons.

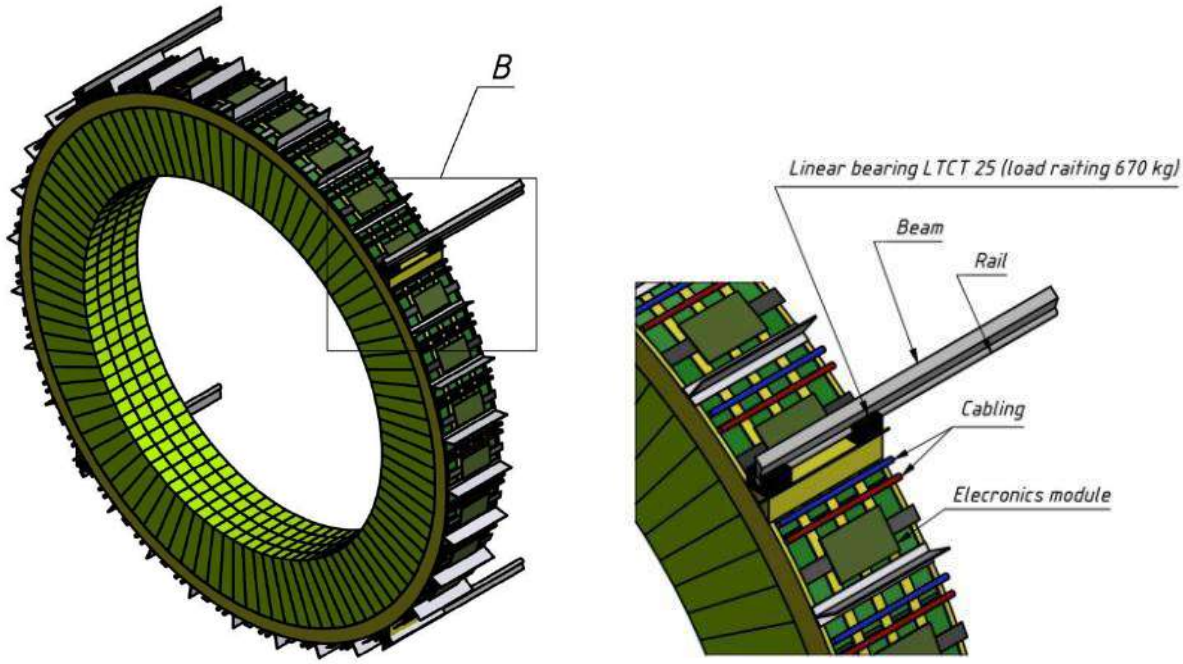

(a) (b)

Figure 6.4: The isometric view of one ECAL barrel ring (a) and supporting rails are shown (b). Electronics (ADC) are located according to calorimeter clusters.

2.2 End-caps

Each end-cap (one is shown in Fig. 6.5) consists of 4576 cells, grouped by 64, forming 72 clusters. All 64 cells of each cluster are connected to 4 pcs. of 16-channel FE-boards for MPPC's bias voltage control and their readout is provided by one ADC. A complete list of ECAL's main components – ADC, FE, HV, MPPC, etc. is presented in Table 6.2. The cell cross-section is 40×40 mm^2 and the length is 500 mm along the beam. The end-cap has the absorber length equal to 17.6 X_0. The weight of one end-cap is 10.1 tons and for two parts 20.2 tons, respectively, as it is shown in Table 6.1. In total, there are 9152 cells in both end-caps. There is a hole for the beam pipe in the center of each end-cap. The hole has a size of 320×320 mm^2, which is equivalent to 64 cells.

The end-cap is mounted in the frame that supports it and shapes its geometry. The frame is installed directly on the barrel RS, as shown in Fig. 6.5. There is a gap about 6 cm between the end-cap of the RS and calorimeter's end-cap for the ADC's placement and cable routes (Fig. 6.1). This gap is also necessary for air circulation of the ADC cooling.

3 Design of the calorimeter module prototype

The first version of the module, which was described in CDR of SPD in 2020 and published in [20], had a sampling structure of 220 layers of 1.5 mm and 0.3 mm scintillator and lead respectively. This version had the absorber length of $12.6X_0$ and a Moliere radius equal to 7.6 cm. The second (new) version of the module, which was made for testing purposes, consisted of 190 alternating layers of polystyrene scintillator and lead with a thickness of 1.5 mm and 0.5 mm, respectively. The new version of the modules with 190 layers of scintillator and lead has a shorter length along the absorbed particles path (48.8 cm instead of 58 cm), but has a greater absorption quality of $17.6X_0$ and a smaller Moliere radius of 5.8 cm. The lead plates are intended to absorb the particle energy and develop an electromagnetic shower,

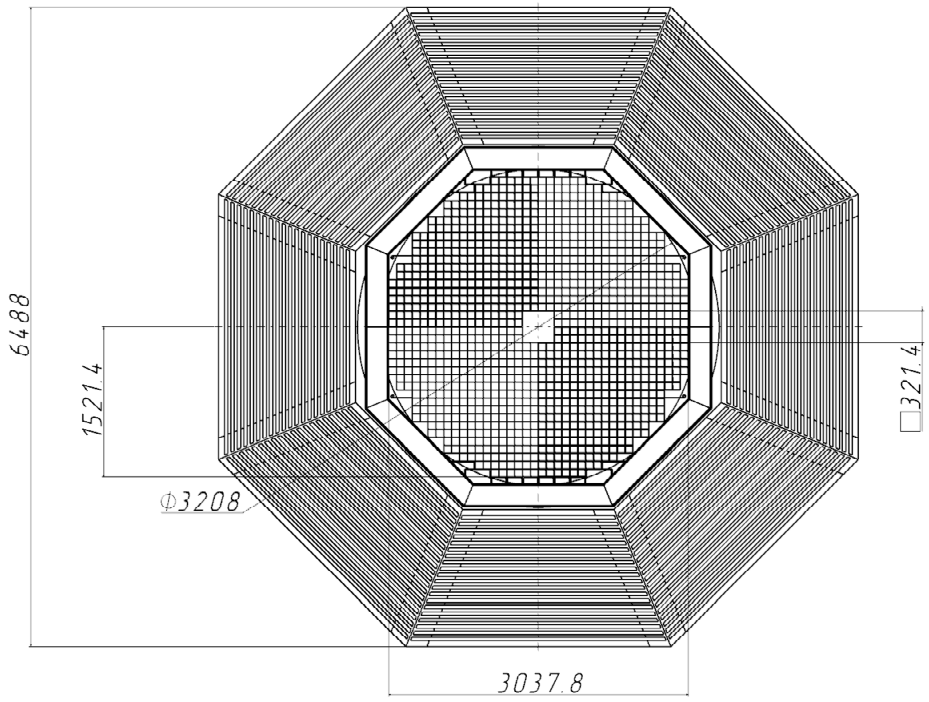

Figure 6.5: The end cap-part of the calorimeter in the frame, installed in RS. One end-cap consists of 4608 cells with a total weight of 11.1 tons. The holes of size 320×320 mm^2 for the beam pipe can be seen in the centers of the end-caps. All dimensions are in millimeters.

whereas the scintillator plates produce an amount of light proportional to the energy of the particles. The properties of the absorber and the scintillator define the Moliere radius, which is equal to 5.8 cm for the selected structure [21]. The energy resolution for 1 GeV photons is assumed to depend on the calorimeter sampling fraction and is expected to be ∼5% [22]. The scintillator plates are made of polystyrene beads with an added luminophore admixture of 1.5% p-Terphenyl and 0.05% POPOP ($C_{24}H_{16}N_2O_2$) [23, 24]. It has scintillation time of about 2.5 ns and light output of 60% of anthracene, which are good results. The radiation hardness of the scintillator is sufficient for radiation doses up to about 10 Mrad (10^5 Gy), which is important for operating the calorimeter in the radiation field of secondary particles in the vicinity of the interaction point. The luminophore admixtures re-emit the energy of excitations in polystyrene in the form of visible light. The first admixture (p-Terphenyl) emits light with a wavelength of maximum emission at 340 nm. This light is absorbed by the second admixture (POPOP) and is re-emitted into a spectrum with a wavelength of maximum emission of 420 nm, which is seen as a light of blue glow. The light from the scintillator plates is gathered using wavelength shifting fibers (WLS) [25]. Fibers of type Y-11 manufactured by KURARAY are used.

The fibers absorb the light from the POPOP and re-emit it into a spectrum with a wavelength of maximum emission of 490 nm. Thirty six WLS fibers go along each cell, gather in one bundle and transmit light to one multi-pixel 6×6 mm^2 photodiode (multi-pixel photon counter, or MPPC). The schematic module drawing is shown at Fig. 6.6 (a). The active part of the module is 380 mm and the total module length is ∼490 mm without MPPC board. A single module consists of 4 cells with 190 layers of the scintillator and the absorber with a thickness of 1.5 mm and 0.5 mm, respectively. The period of the structure is set to 2 mm in order to avoid optical contact between the lead and the scintillator, and because of the connection technique involves special ”Lego” spikes. Four bundles of fibers for guiding the light to the MPPC can be seen on the photo in Fig. 6.6 (b). Two modules with different sampling structure are shown at Fig. 6.7. These modules have different lengths due to differing number of layers – the first version

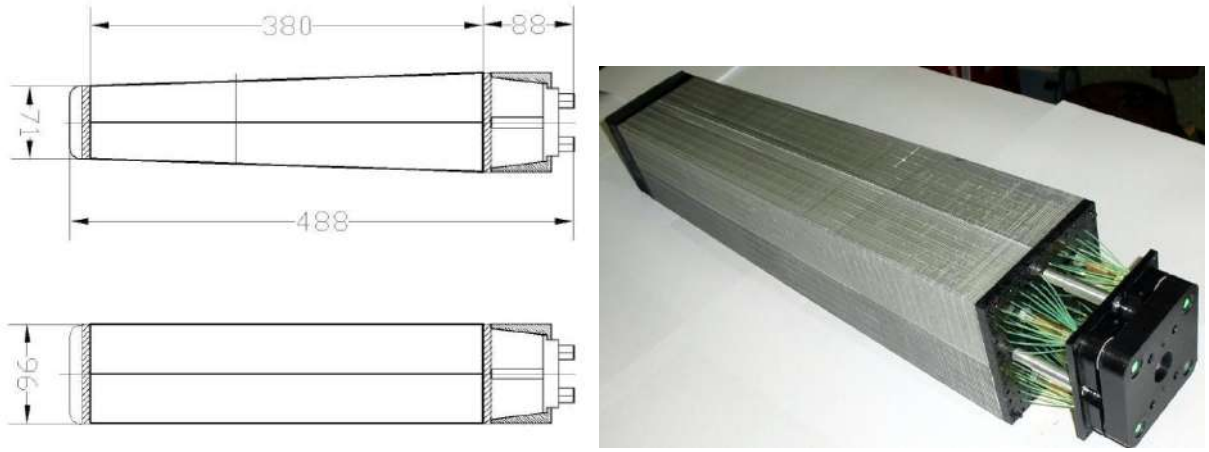

(a) (b)

Figure 6.6: ECAL module drawing (a) and photo (b) without light shielding cover.

Figure 6.7: Two calorimeter modules covered in light isolation paper are shown in this photo. The modules have different lengths due to a different number of layers (190 and 220) and a different absorber thickness of 0.5 and 0.3 mm, respectively.

with 220 layers and the second version with 190 layers, and a different absorber thickness of 0.3 mm and 0.5 mm, respectively. The length of the shortest one (second version) does not exceed 500 mm.

4 Scintillator production

4.1 Injection molding technology

As it was mentioned in detail in Section 6.3, calorimeter employs polystyrene scintillator plates from Polystyrene with an added luminophore admixture of 1.5% p-Terphenyl and 0.05% POPOP (C24H16N2O2) [23, 24]. Scintillation plates for calorimeter prototypes were manufactured by injection molding technology at the pilot plant of IHEP [26]. Scintillation material of this type has been successfully used in calorimeters for the last 20 years. It has a high radiation hardness (about 10^7 rad = 10^5 Gy), a good

Figure 6.8: Thermo plastic injection molding machine, general view.

light output (60% of anthracene), a fast decay time (1.2 ns), a high transparency for blue light (420 nm) with attenuation length ∼60 cm. The injection molding technology requires a special machine (Fig. 6.8) and a matrix form (Fig. 6.9) for scintillation plates production with given dimensions. Thermo plastic injection molding machines are a standard series of injection molding machines designed to perform most typical tasks that do not require the use of special materials or particularly high requirements for molded products. These injection molding machines have incorporated the most reliable, time-tested and effective solutions. The production procedure is automatic and allows a production rate of about one cycle per one minute (4 tiles). Granulated Polystyrene PSM-115 [27] with dopants (1.5% Pt-Terphenyle [23] and 0.05% POPOP [24]) is used for scintillator production. All used components are pre-dried and then mixed in special mixers. Then the prepared mixture is fed into the receiver of the injection molding machine.

4.2 Matrix form

One of the important points is the molding press-form for the scintillator production. It should be built of high-precision components, made of high-quality materials (see Fig. 6.9 (a)). The number of molding cycles should be in the order of one million to produce 4 million plates required for the SPD calorimeter. Figure 6.9 shows 4 pcs. of scintillator plates coming out of the injection machine. Each injection cycle for 4 plates takes one minute. The total number of SPD calorimeter scintillator plates is about 4,000,000 pieces with a total weight of about 15 tons.

4.3 Time estimate for calorimeter modules production

Taking into account that one injection molding machine cycle is one minute and with two molds running 24 hours a day, a total of 583 days are needed to produce the required amount of the scintillator and absorber tiles. Considering 273 working days per year, production process of the tiles will take about 2 years. Assembly of the calorimeter modules at the rate of 10 modules per day allows to complete this process within 2.4 years, as it is shown in Table 6.5. In order to produce the SPD calorimeter by 2030, it is necessary to manufacture components and assemble modules in parallel.

(a) (b)

Figure 6.9: a) 4-set matrix for scintillator production; b) The scintillation plates released from the molding machine, details of the molding system are visible.

5 Multi-pixel photodiodes

All of the MPPCs that are used in this prototype have the same size of 6×6 mm^2. The S13360-6025 [28] series has the best response speed, low capacitance and a large number of pixels, but the largest temperature coefficient of K_t ∼0.054 V/$^\circ$C. The temperature coefficient represents a linear dependence of breakdown voltage on temperature. Temperature dependence of MPPC's breakdown voltage leads to MPPC's gain variation, if this temperature dependence is not compensated. To achieve calorimeter's stability of about 2%, one needs to ensure temperature stability of the surrounding environment, or use the breakdown voltage compensation scheme:

$$U_{OP}(T) = U_{BR} + \Delta U + (K_t \times \Delta T), \tag{6.1}$$

where: U_{OP} and U_{BR} are MPPC bias voltage at temperature T and MPPC's breakdown voltage at device characterization temperature, respectively. ΔU is a given over-voltage and $\Delta T = T - 20^\circ C$ is a deviation of the current temperature (T) from temperature selected by the compensation program, typically 20 $^\circ$C. MPPCs of the S14160-6050 series have a higher photodetector efficiency but fewer pixels, which is worse in terms of the dynamic range. This series has a small temperature coefficient. An optimal solution would be usage of MPPCs with properties similar to the S13360-6025 or S14160-6050 series but with a smaller pixel size of 15 ÷ 20 μm, i.e. larger amount of pixels, which would make them more suitable for the calorimeter. Four MPPCs are surface-mounted on a circuit board, as it is shown at Fig. 6.10. A thermistor is also installed on the board to measure the photodiode's temperature. The circuit board is attached to a module in such a way that the photodiodes are located exactly opposite the ends of fiber bundles. There is no optical contact between the photodiode and the WLS, there is an air gap of about 0.1 mm instead. Optical grease is not used in order to avoid instability in the conditions of light guiding. A light insulating basket made of black plastic is installed above of the circuit board.

The MPPC boards are connected to the amplifier / bias control board (FE-board) (Fig. 6.11 (a)) with up to

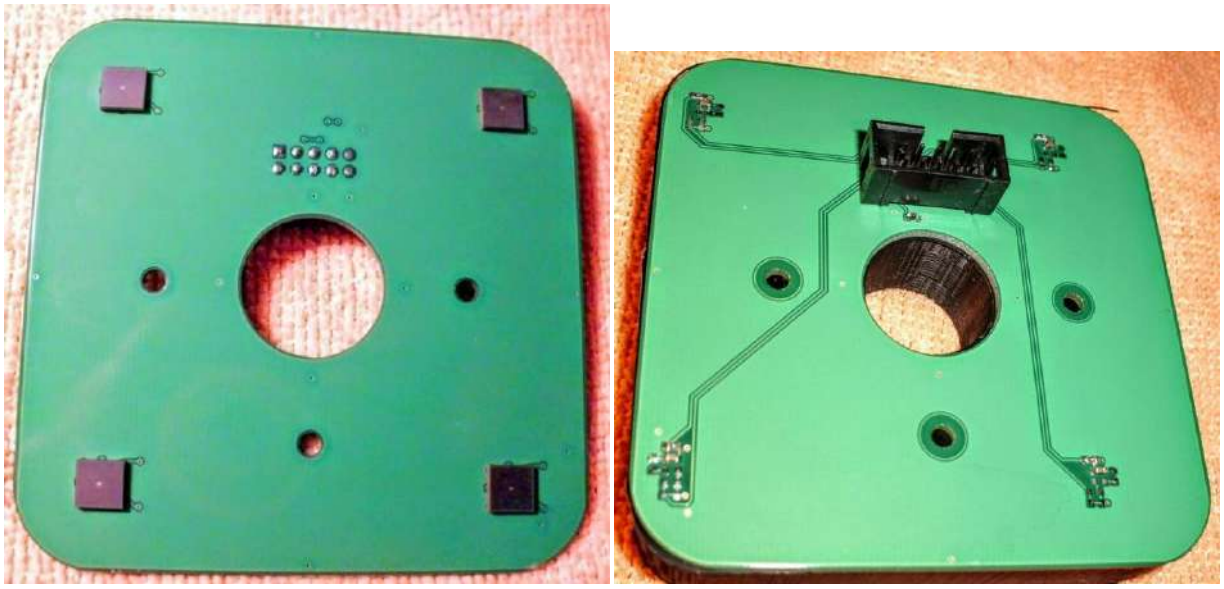

(a) (b)

Figure 6.10: Printed circuit board with 4 MPPC diodes: front (a) and back (b) sides.

1-meter of flat 5-pair twisted-pair cable. Four wires transmit signals from four MPPCs to the amplifiers of FE-board. One wire is used to provide regulated common bias voltage to all MPPCs on the board (up to ∼55 V) and another one to connect the thermistor for local temperature measurement of MPPCs. Output signals of each MPPC are transmitted via twisted pairs of wires (signal/GND). Small regulated individual reverse bias voltage can be applied by FE-board on signal wires of each MPPC in the range from 0.0 to ∼3.0 V for individual adjusting of bias voltage. This way, the bias voltage of each MPPC can be individually and precisely trimmed in a small range with a 10-bit precision (i.e. ∼3 mV step) in order to take into account and compensate for the possible variations of individual parameters of each MPPC. FE-board provides hardware control of regulated MPPC's bias voltage and also amplifies MPPC's signals and converts them to a differential type, which is required by the ADC board. Calculations required for the bias voltage compensation with temperature are performed at a software level by the control PC, taking into account the local temperature measured by the thermistor installed on the MPPC's circuit board. This approach allows calorimeter operation without special measures for MPPC's temperature stabilization. Signal stability on the order of 1% was achieved during measurement over an extended period of time with the usage of such technique.

6 MPPC readout and high voltage control

6.1 Analog-to-digital converter (ADC)

The readout electronics consists of a 64-channel ADC board – an analog-to-digital converter ADC-64 (Fig. 6.11 (b)). The ADC continuously performs simultaneous samples on all 64 input channels with a fixed frequency and provides a full digital representation of an input signal time-shape. Samples are done at a 64-MHz frequency, which corresponds to the sampling period of 15.625 ns. Each sample is digitized with a 12-bit conversion. At present, there is an ADC-64ECal modification, which improves digitization up to 14-bit and significantly extends the dynamic range of the measured amplitudes. The new ADC-64ECal [29] modification also allows operation in strong magnetic fields, which is necessary for experiments at the NICA accelerator complex.

The ADC-64ECal power consumption is about 13 W per one 64-channel board, i.e. ∼200 mW/ch.

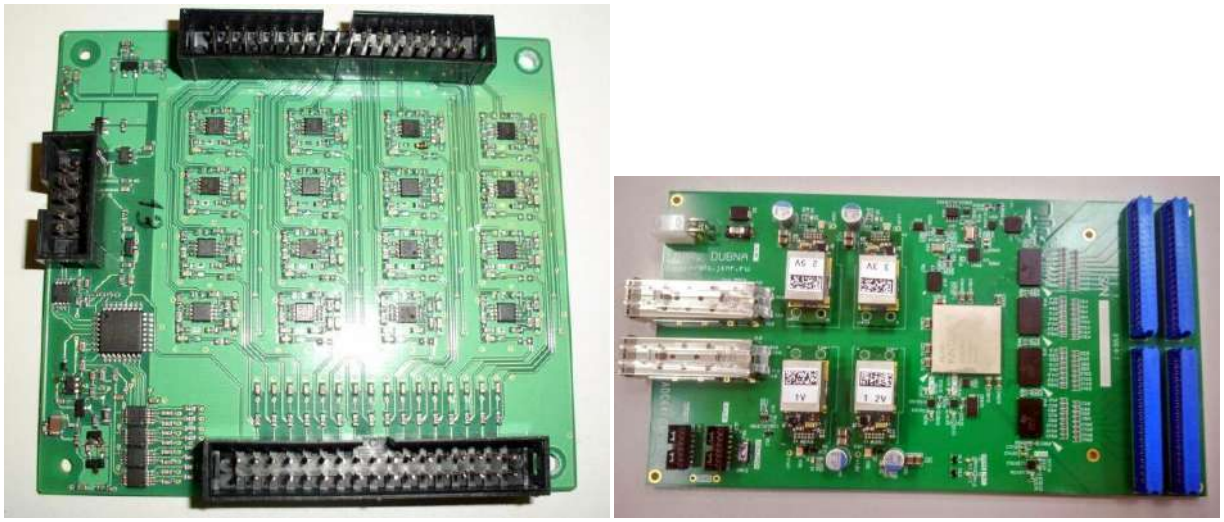

(a) (b)

Figure 6.11: (a) 16-channel amplifier / bias control board (FE-board). (b) ADC-64ECAL digitizer. The ADC-64ECal power consumption is about 13 W per one 64-channel board.

ADC's total power consumption is shown in Table 6.3. It is equal to 2.8 kW for the barrel and 0.9 kW for the calorimeter end-cap. the ADC card will be located directly on the calorimeter to reduce signal noise and reduce the cabling bundles between ADC and data collectors. ADC provides two Ethernet interfaces (shown in Fig. 6.11 (b)): one for data transfer to a higher level of data acquisition system, and another one for time synchronization (White Rabbit technology is employed), which provides sub-nanosecond accuracy. 50 Ω coaxial input can be used as external trigger for readout synchronization. The ADC can also operate in the streamer mode due to a dedicated firmware.

6.2 Front-end amplifier

the Front-end (FE) electronics will be located directly on the calorimeter. Small path of the analog signal to FE means less signal distortion and pickup noise. FE electronics card with an 16-channels amplifier / bias control is shown in Fig. 6.11 (a). It is used to:

- control the MPPC's bias,
- amplify MPPC's output signals,
- convert them to a differential type and transmit them to the analog inputs of ADCs (Fig. 6.11 (b)).

Each FE-board can service up to 4 pcs. of MPPC boards (Fig. 6.10). The FE-board and the MPPCs must be located close to each other, therefore they will be placed on the same printed circuit board. The FE-board has a power consumption of about 33 mW, i.e. ∼2 mW/ch., and their total power consumption is ∼1.4 kW for the whole calorimeter.

6.3 High voltage system

All required power supply voltages for FE-boards (High voltage, required for MPPC's bias, and Low voltage, required for internal circuits of FE-boards) are supplied from the specially designed HV control power box [30], which is shown in Fig. 6.12. The HV control box can provide the required power supply for up to 127 pcs. of FE-boards, which are connected in parallel on a 10-wire flat cable. The HV control

Figure 6.12: Control power box (HV) for MPPC's bias voltage.

box has Ethernet control from outside. The HV control box communicates with FE-boards by the RS-485 interface for MPPC's bias voltage control and temperature feedback. The flat cable length can be over 100 meters. Therefore, this box can be installed outside of the calorimeter at a distance of up to 100 meters. The consumed power of this unit is up to 100 watts. Taking into account that 20 such units are needed for the calorimeter, their total consumption is up to 2 kW (Table 6.3).

6.4 LED generator

To make a precise calibration of each ECAL channel and for the continuous monitoring of channel amplification a LED generator has been designed [31] and built. The main requirement for this device is its stability. Light intensity variation should be below 1%. To reach such stability and to reduce residual variations of LED light intensity, the feedback loop has been implemented on the device. A pin diode has been located on the LED back side. Light from the LED back side is detected by the pin diode and analyzed by control circuits to organize a feedback control and improve LED's stability. Light from the LED front side has a high luminosity and can be distributed by the optical fiber light guides to a large number of calorimeter cells. One such generator can supply light for up to 100 channels with the intensity of about 1000 photoelectrons, which is enough to provide MPPC's gain control and sensitivity monitoring. This LED control system was used in the test setup, shown in Fig. 6.13, for monitoring long-term stability during data-taking on cosmic rays.

6.5 Slow-control system

The main objectives of the slow-control system (SC) are:

- operating equipment parameters control;
- monitoring of low and high-voltage power supplies;
- recording of slow-control commands and data;
- notification about problems (alarms);
- recording of LED signals for the long-term stability check.

High voltage (HV) has been designed especially for the MAPD-based devices and is part of the slow-control system. Specific points of HV are:

- multichannel (∼30 000 channels);
- very precise voltage setting for each channel;
- need for voltage correction depending of temperature of MAPD;
- temperature control for the ADC boards.

7 Cosmic ray test results

7.1 Energy resolution

A test setup was made from four calorimeter modules consisting of 16 cells with a cross-section of 55×55 mm^2 and then tested on cosmic rays. In this prototype, light detectors were based on MPPC types S13360-6025 with 25 micron pixel pitch. For testing on cosmic rays, a small setup of 4 modules (each 11×11 cm^2) with the total cross-section of 22×22 cm^2 was used (Fig. 6.13). The cells, 55×55 mm^2 each, are assembled in a 4×4 setup. The modules are placed vertically, while the direction of the registered cosmic rays is determined by trigger counters. Trigger counters are scintillator detectors based on multi-pixel photodiodes of FC6035 type and size 6×6 mm^2. All photodiodes of the counters were connected to a coincidence circuit to make a trigger for the ADC for cosmic rays events selection. Auxiliary trigger signals from the generator which controls the LEDs were also logically added (by the "or" function) to the cosmic rays trigger signals. LEDs were used for control and calibration of the calorimeter cells, estimations of the light yield, and for the long-term stability check. Data acquisition was conducted by the 64-channel ADC board, similar to the one described in Section 6.1 with intended software usage from the ADC developer [29]. During a data-taking period of $5\div6$ days, statistics on the order of million events was obtained. The setup allows one to measure energy depositions and trajectories of cosmic ray particles. Relativistic muons with energy above 250 MeV pierce through the calorimeter and form a peak in the deposited energy spectrum. In order to select straight tracks of the particles, which pass vertically through one module, only those events that have the number of hits equal to 1 are selected to avoid side tracks.

Signals obtained on cosmic muons were used for amplitude alignment and calorimeter energy calibration. Only events with exactly one cell hit were selected. The bordering cells have more events with smaller amplitudes due to angled tracks. We perform calorimeter calibration using only vertical tracks. Each maximum position in terms of ADC units is mapped to the corresponding energy deposition. The energy scale is determined from the Monte-Carlo simulation as the scale factor between the energy deposition in scintillator plates for the given structure of an electron with 1-GeV energy and a relativistic muon with energy above 1 GeV. From this proportion we estimate the MIP signal in this calorimeter to be 240 MeV. This value divided by the position of the muon's peak maximum is used as a calibration coefficient for each cell. This calibration procedure involving the MIP energy deposition is not absolute or conclusive. Primarily, it aligns the gain coefficients in each cell to ensure an equal response of each cell. The measured electron or photon energy can be further revised by reconstructing neutral pions or calibrating the calorimeter using electron or photon beams of known energy. The electromagnetic calorimeter measures electron or photon energy by summing up signals from all 16 cells. Each cell can only contain a fraction of energy deposited by the particle in the calorimeter (if the particle is not a relativistic muon or a MIP). The energy resolution of the calorimeter for vertical cosmic ray particles is 9.0% (Fig. 6.14 (a)). This value corresponds to energy deposition of 240 MeV. Assuming the resolution depends on the energy as $\sqrt{E}$, the energy resolution at 1 GeV is estimated to be 5%. The energy resolution dependence on the ADC's threshold is shown in Fig. 6.14 (b).

Figure 6.13: Photo of the calorimeter test setup consisting of 4 modules of the size 11×11 cm^2 , with the total cross-section of 22×22 cm^2. The environment temperature was measured by thermistors, provided for each of the 4 MPPC boards, and by a digital thermometer as well. One of the boards in light protection cover and the digital thermometer were placed on top of the setup. The optical fibers (visible on this photo) distributed the light from the LED generator.

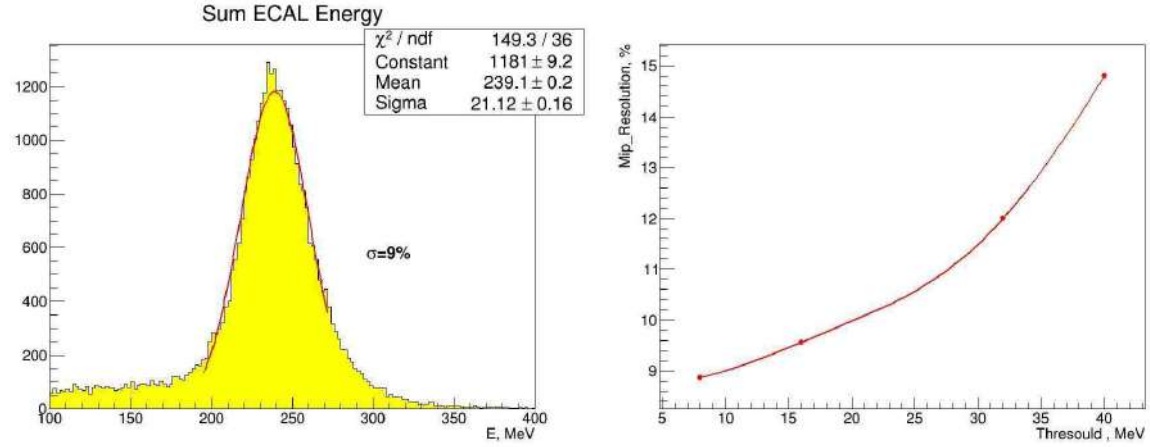

(a) (b)

Figure 6.14: (a) Energy spectrum from the calorimeter for vertical cosmic ray particles with energy resolution of 9%. This point corresponds to ADC threshold ∼8 MeV. (b) Energy resolution dependence on the ADC threshold in MeV.

7.2 Long-term stability

Temperature dependence of calorimeter stability was estimated with usage of daily temperature variations in the range of 18-26 °C. Signals from cosmic rays particles as well as signals from LEDs of a 1-Hz frequency were captured during the measurement over 10 days. Photodiode's temperature was continuously monitored by FE-board through MPPC's board thermistor. The bias voltage on photodiodes was corrected during data capture in accordance with a measured temperature using a linear dependence:

$$U_{bias}(T) = U_{base} + K_t \times (T - 20), \tag{6.2}$$

where T is the MPPC board temperature, (°C),
$U_{bias}(T$ is the total bias voltage applied to MPPC at temperature T, (V),
U_{base} is the MPPC base voltage from power supply [30] at 20 °C (V).

The temperature coefficient K_t = 0.054 V/°C that was used for temperature compensation of bias voltage is shown in Fig. 6.15 (a, b), and depends on MPPC type.

The lower temperature dependence typical for diodes with a low breakdown voltage as S14160-6050. But this type of MPPC has few pixel numbers (∼14000) and therefore recently new type S14160-6015 was developed with 160000 pixels of 15 μm pixel pitch and it will be tested soon.

Dependences of the calorimeter signals on the measurement time are shown in Fig. 6.16 (a, b). These data are presented in % with respect to the first 5 minutes of the measurement period for normalization. The temperature variations during the measurement were about ±4°C. After compensation was employed, daily variations in the MPPC signal amplitude were constrained within ±0.5%. The calorimeter can operate with a stability of ∼1% during time over 10 days, if the temperature compensation of the operating voltage is maintained, as it can be seen from these results and is shown in Fig. 6.16 (a, b).

8 Cost estimate and the time scale

The cost of the calorimeter is proportional to the number of channels. Mechanical assembly of a calorimeter cell from the scintillator and the lead plates costs 60$ per channel. Another expensive ele-

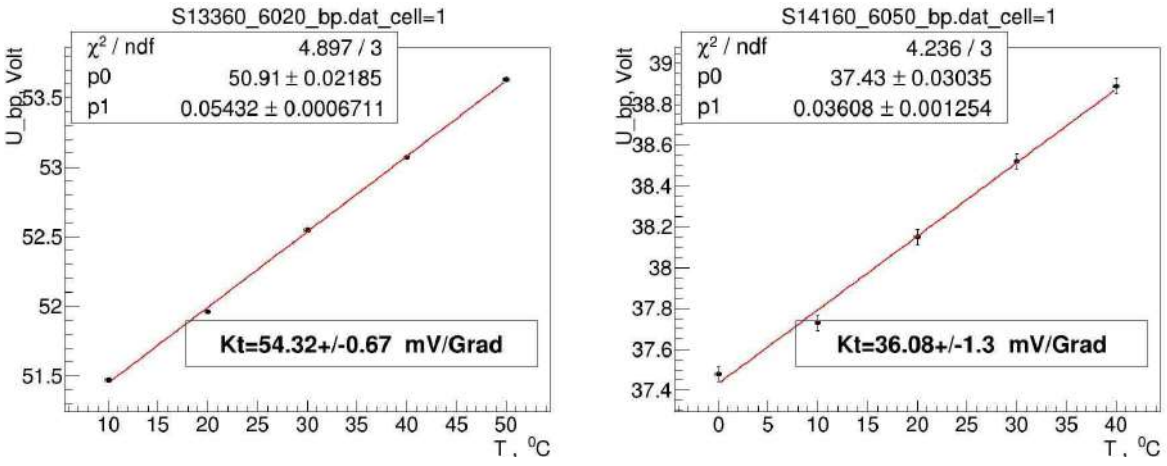

(a) (b)

Figure 6.15: Dependencies of MPPC breakdown voltage on temperature for different MPPC types: (a) for S13360-6025, (b) for S14160-6050.

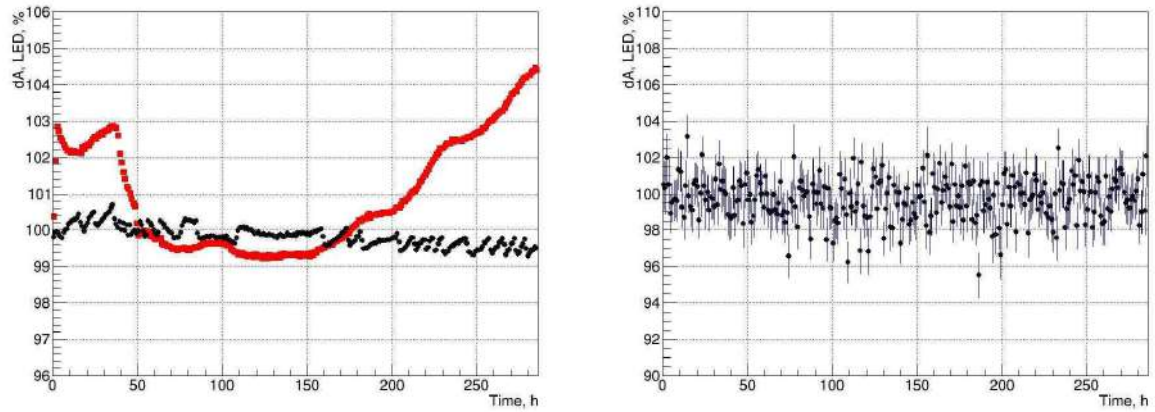

(a) (b)

Figure 6.16: Dependences of the sum (average value) of MPPC signals on the time of measurement (in hours). (a) LED signals with temperature-dependent bias voltage compensation (black) and ones without compensation (red). (b) MIP signals with temperature-dependent bias voltage.

ment is the wavelength shifting fibers. For a 40×40 mm^2 cell, 16 fibers of the total length of 8 m are used. Assuming an average price of 5$/m, the price per channel amounts to 40$. The cost of photodiodes depends on the quantity. For purchases of tens of thousands of units, their price is about 50$ per unit. The electronics also contributes significantly to the total cost, especially the ADC with a price of 52$ per channel. The cost of the supply and voltage control systems is 28$ per channel. The total cost of a calorimeter cell is about 342$. Thus, the total cost of a 22976-cell calorimeter is 7.866 M$, as it is shown in Table 6.4. Starting in 2022 with the Technical Design Report, at first, we need to prepare first the technical documentation with drawings of the calorimeter components. Then we can start production operations. The readout front-end electronics should correspond to the data acquisition system. It should have low power consumption and high rate of data acquisition. For these, a new electronic base should be used to achieve these goals.

Table 6.1: The weight distribution for the ECAL parts. Columns 2, 3 are related to the absorber (lead) and scintillator in a single cell; 4 – single cell weight in kg; 5, 6 – lead and scintillator contribution in tons. 7 – the total weight of the calorimeter main parts, the supporting mechanical frame is also taken into account.

1	2	3	4	5	6	7
Material	Lead	Scint	Cell	Lead	Scint	Total
Units	kg	kg	kg	ton	ton	ton
Barrel	2.07	0.56	2.63	28.62	7.79	36.41
EC-1	1.73	0.47	2.19	7.89	2.15	10.04
EC-2	1.73	0.47	2.19	7.89	2.15	10.04
Total	5.52	1.50	7.02	44.41	12.09	56.50

Table 6.2: Number of the main ECAL components: 2 – number of calorimeter cells, 3 – number of 64-channel ADC boards, 4 – number of 16-channel front-end boards (FE-boards), 5 – number of HV power control units, 6 – number of MPPC , 7 – length of WLS fiber in meters.

1	2	3	4	5	6	7
Item	N cells	ADC64E	FE	HV	MPPC	Fiber, m
Barrel	13824	216	864	12	13824	110592
EC-1	4576	72	286	4	4576	36608
EC-2	4576	72	286	4	4576	36608
Total	22986	359	1436	20	23110	183808

Table 6.3: Power consumption of the ECAL in kW for: 2 – ADC [32], 3 – FE-boards [31], 4 – HV power units, 5 – total in kW.

1	2	3	4	5
Item	ADC	FE	HV	Total
mW/ch	200	63	1.2	264
Barrel	2.8	0.9	1.2	4.8
End cap-1	0.9	0.3	0.4	1.6
End cap-2	0.9	0.3	0.4	1.6
Total	4.6	1.4	2.0	8.0

Table 6.4: The calorimeter cost estimate. EC-1 and EC-2 – the cost of the end-caps. The cost per channel of various calorimeter components in $ is shown on the bottom line. In the lines above, the cost in k$ is shown for barrel, end-caps, and the entire calorimeter. The cost of assembling the calorimeter modules and manufacturing of the supporting mechanical frame is estimated in columns 6 and 7.

1	2	3	4	5	6	7	8	9	10	11	12
Item	N cells	ADC	FE	HV	Assembl.	Frame	MPPC	Fiber	Lead	Scint	Total
Barrel	13824	720	369	10	1382	85	691	553	725	130	4666
EC-1	4576	238	122	2	458	85	229	183	240	43	1600
EC-2	4576	238	122	2	458	85	229	183	240	43	1600
Total	22976	1197	613	14	2298	256	1149	919	1206	216	7866
USD/ch	342	52	27	1	60	11	50	40	52	9	342

Table 6.5: ECAL components manufacturing time estimate. 2 – number of cells; 3*, 4* – time for scintillator and lead plates production, in days; 5 – time for calorimeter modules assembling, in days, at estimated production rate of 10 modules / day; 6 – total time required for calorimeter's main parts production, in years. *) – tasks in columns 3 and 4 must be carried out in parallel.

1	2	3*	4*	5	6
Item	N cells	Scintillator	Lead	Assembling	Years
Barrel	13824	228	228	346	1.5
EC-1	4576	151	151	114	0.5
EC-2	4576	151	151	114	0.5
Total	23110	530	533	574	2.4

Chapter 7

Time-of-Flight system

The purpose of the time-of-flight (TOF) system is to distinguish between charged particles of different masses in the momentum range up to a few GeV/c. Current cofiguration of the TOF detector at about 87.7 cm from the collision point implies that to separate pions from kaons up to a momentum of 2 GeV/c, the time resolution of the TOF system would have to be 70 ps or better. The beam length RMS of about 30 cm means that the true collision event time t_0 can not be set to the nominal bunch crossing clock time form the accelerator as the uncertainty would be of the order of 1 ns (larger than the required time resolution). Therefore, TOF system will be used in events with multiple charged tracks to determine both the collision event time t_0 and the individual track identification. For details of this analysis, see Section 1.4 of Chapter 9 of the SPD CDR [1]. In addition to particle identification, the detector will also provide a start time to the straw drift tubes.

The TOF system will consist of a barrel and two end-cap parts with an overall active area of 27.1 m^2. The charged particle rate that detector will have to withstand is 0.1 kHz/cm^2 for the barrel. The rate increases rapidly when moving closer to the beam axis. Thus, for the TOF elements located in the end-caps 20 cm off the beam axis, the rate of about 1 kHz/cm^2 is expected (see Fig. 16.1 for details). The MRPC technology is being considered for the TOF detector.

1 General layout

Layout of the SPD TOF detector is shown in Fig. 7.1.

Table 7.1: Parameters of the SPD TOF system.

	Element	Number of elements	Number of readout strips	Sensitive area m^2	Number of FEE cards	Number of FEE channels
Barrel	MRPS	1	24	0.14	3	48
	Module	10	240	1.4	30	480
	Total	120	2880	16.8	360	5760
End-cap	MRPS	1	16	0.06	2	32
	Module	3	48	0.18	6	96
	Total	96	1536	5.8	192	3072
TOTAL		216	4416	22.6	552	8832

The Multigap Resistive Plate Chamber (MRPC) is a stack of resistive glass plates with high voltage

applied to external surfaces. The pickup electrodes are located inside the chamber. A fast signal, induced on the pickup electrodes by an electron avalanche, is further transported to FEE located nearby. In order to increase the speed of gas exchange and reduce gas consumption, we designed a new self-sealed MRPC. The schematic cross-section of the MRPC is shown in Fig. 7.2 [33]. In order to achieve a good time resolution around 50 ps, two MRPC stacks with 10×0.22 mm gaps can be used in SPD. The number of MRPCs for barrel and end-caps TOF, and the number of the corresponding readout channels are shown in Table 7.1. In total, the TOF system consists of 216 MRPCs and 8832 readout channels.

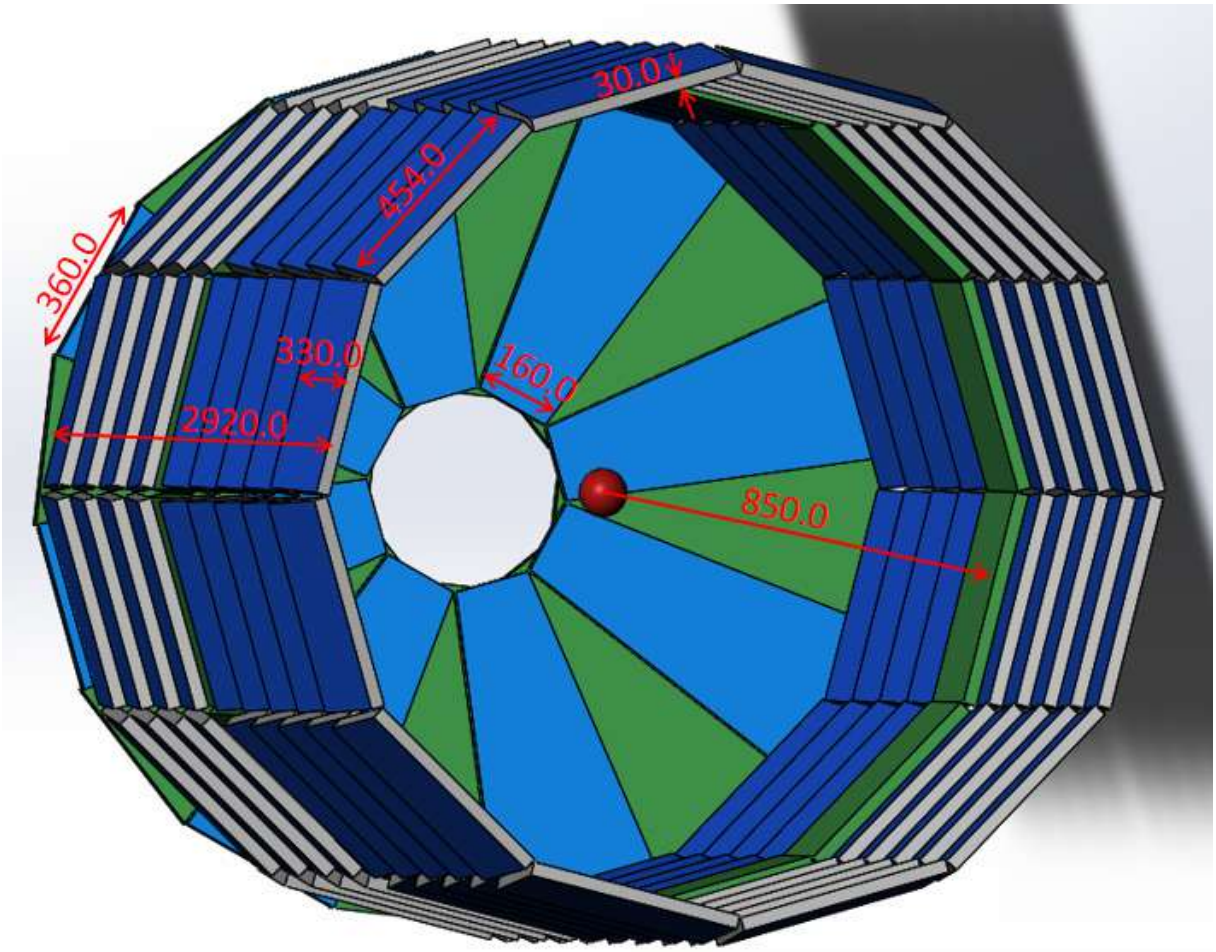

Figure 7.1: Multigap Resistive Plate Chambers, MRPCs, are considered for the PID system. Barrel and one of two end-cap parts are shown.

2 MRPC-based TOF system

The required time resolution for SPD is better than 60 ps, while the efficiency of particle registration at high rate (few kHz/cm^2) should be above 98%. Based on the experience of building similar systems in such experiments as ALICE [34], HARP [35], STAR [36], PHENIX [37], and BM@N [38], a glass Multigap Resistive Plate Chamber could be used as a base time detector. For example, the TOF-700 wall in the BM@N experiment, placed at a distance of 8 m from the target, provides the p/K separation up to 3 GeV/c and p/K separation up to 5 GeV/c, under the assumption that the time resolution of the start timing detector is below 40 ps. As we know, the time jitter of MRPC should be correlated with the width of the gas gap. In order to study the intrinsic time resolution of MRPC, a 32-gap MRPC with 0.128 mm of gas gap was developed. The structure is shown in Figure 7.3 (a) [39]. Six readout strips

with 1 cm pitch are configured on the PCB sheets. Five PCBs are required in this design. The cathode and anode signals are transmitted through differential cables. During the preliminary cosmic ray test, the high-performance Analog Front-end Electronics (AFE) and the Lecroy oscilloscope (10 GHz pulse sampling) were used. The crossing time of a signal is determined when setting a fixed threshold, and it is related to the amplitude of the signal. The time spectrum of the difference of the two MRPCs is shown in Figure 7.3 (b). It can be seen that the time resolution of each MRPC is 23.24 ps / $\sqrt{2}$ =16.4 ps.

Beside the implementation of the MRPC type described above, it is possible to realize cameras in the variant with the application of the resistive layer on each of the camera glasses. This option was created and tested in IHEP (Protvino) [40], it showed time resolution better than 40 ps. An additional advantage in terms of reduced power supply voltage, in comparison with the camera described above.

3 Advantage of self-sealed MRPC

The choice of the working gas mixture for MRPCs has always been an important topic. It should allow the MRPC detector to perform successfully and stably for different purposes, and be eco-friendly at the same time. This indicates that the gas mixture should have a low ozone depletion power (ODP) and global warming potential (GWP). The tetrafluoroethane currently used in MRPCs is ozone-friendly, but with a GWP of about 1430 (the reference GWP of CO_2 is 1). Therefore, a lot of research has gone into looking for possible replacements. Among the possibilities, HFO-1234ze (1,3,3,3-tetrafluoropropene, $C_3H_2F_4$) with a GWP of 6 is one of the most popular candidates, and tests of gas mixtures based on it are ongoing. Another reasonable approach is to reduce gas consumption or recycle gas. The CSR external target experiment (CEE) in Lanzhou, China, will adopt a sealed technology of MRPC to construct the TOF system. The MRPC detector, shown in Figure 7.2, is sealed by gluing an integral 3D-printed frame and the outermost electrodes together. It can operate stably with a gas flux of 4 ml/min, which is extremely low, compared to when MRPCs are placed in a sealed box.

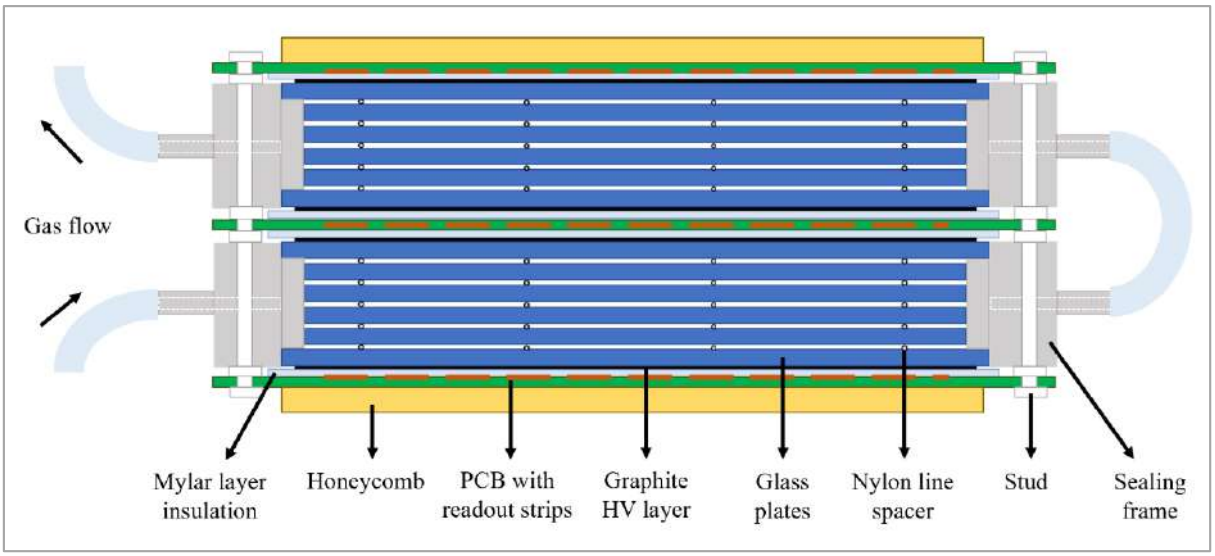

Figure 7.2: Schematic view of self-sealed MRPC [33].

3.1 Prototype test results

Two sealed MRPC prototypes have been assembled for the testing performance. They were different in number of strips (32 and 16), while the same in geometry parameters: 10 gas gaps of 0.25 mm thickness, 48 $\times$ 1.5 cm^2 strip size, and 0.2 cm gap between strips. Working (sensitive) area 5 cm width was splited to a 4-strip interval and signals are readout from a connector located at both end of strips. Under cosmic

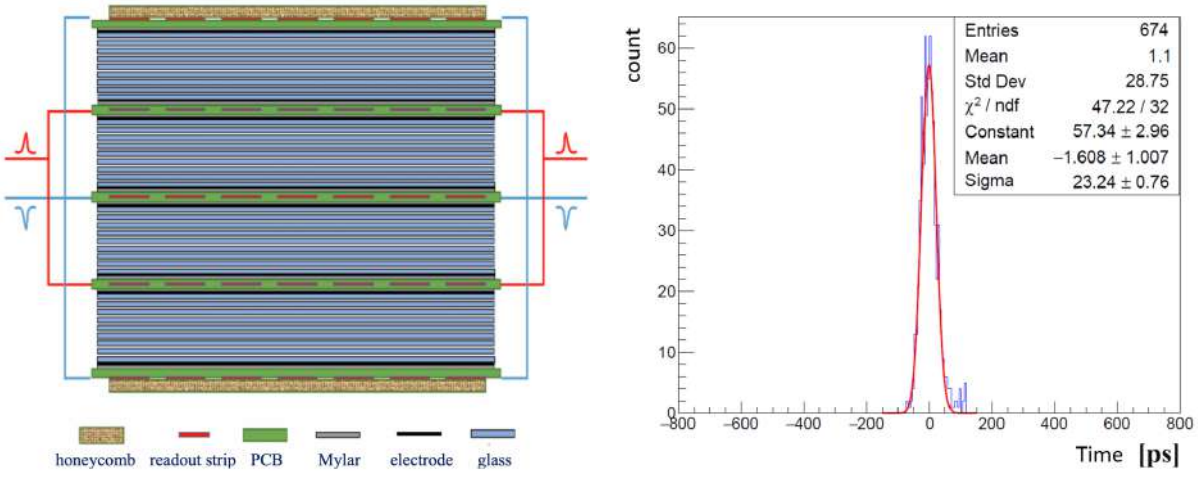

(a) (b)

Figure 7.3: (a) Schematic picture of the 32-gap MRPC chamber [39]. (b) Time resolution results of the cosmic test.

rays, the signal characteristics and time resolution were examined with different readout methods. Figure 7.4 (a) shows the cosmic test layout, in which both prototypes operate under $\pm$6900 V high voltage. The readout strips are read out at both ends for each counter. We use a fast amplifier (described in Section 4.1) and a Tektronix MSO58 oscilloscope to process the waveform. In this way, the dynamic range of the MRPC signal is obtained, as shown in Fig. 7.4 (b). It can be translated to a 40-200 fC dynamic range.

The distribution is filled by the amplitudes of the largest signal for each event, so the loss of these signals will lead to the loss of detection. Based on the idea above, the MRPC efficiency in variant electronic thresholds is plotted in Fig. 7.4 (c). Based on the result, the suggested threshold is 40 fC, and the prototype can reach an efficiency over 97%.

The dynamic range is very helpful when testing the prototypes with NINO-TDC chain, since the proper level of threshold for NINO has been determined in advance. Figure 7.4 (d) shows the flight time distribution between two counters after a series of corrections, e.g., gain correction, time delay correction, and slewing correction in Figure 7.5. For a single time start/stop of counter-electronic combination, the time resolution is $75/\sqrt{2} = 53$ ps. Meanwhile, from the number of reconstructed events and that of triggers, we can estimate that the efficiency of both counters is greater than 97.3%, It compares well with earlier tests.

At last, it is important to note that the two prototypes worked stably during the test period of about 25 days, with a gas flow of less than 5 ml/min. The working gas consumption is decreased by a factor of 10, compared to operations of traditional MRPCs.

3.2 Test results on the sealed MRPC constructed TOF super module

The proposed prototype of the TOF system is based on end-cap Time of Flight (eTOF) wall, developed for the External target Experiment (CEE)[41]. It has a sensitive area of 320×160 cm^2 divided into 7 super modules. Each module includes 3 or 4 sealed MRPCs according to the position of the module. The assembled module for the test is shown in Fig. 7.6 (a). For the gas flow, we follow a strategy of connecting each gas chamber in sequence. All the counters worked stably at nominal high voltage under a 10 mL/min gas flow. During that time, noise level and dark current have been recorded to study the detector training procedure. As it is shown in Figure 7.6 (b), a brand new counter shows an initial noise level around 0.7 Hz/cm^2, and after the 3-week training in high voltage the noise dropped to 0.35

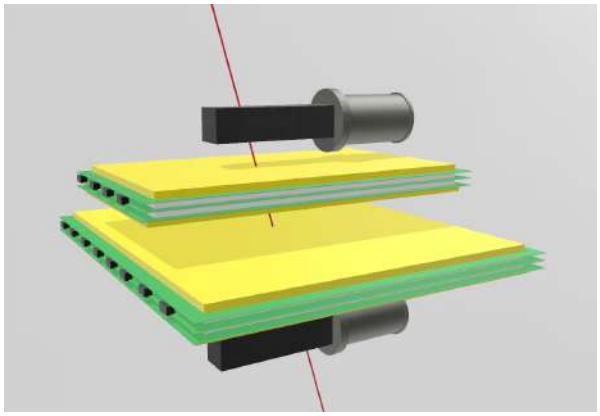

(a)

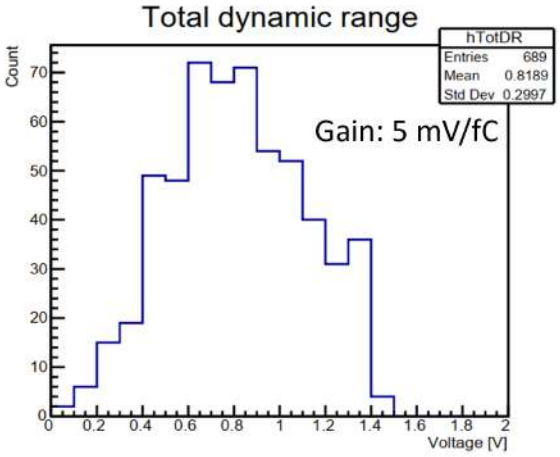

(b)

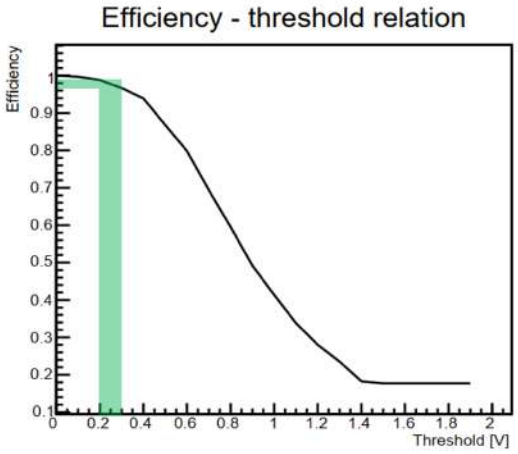

(c)

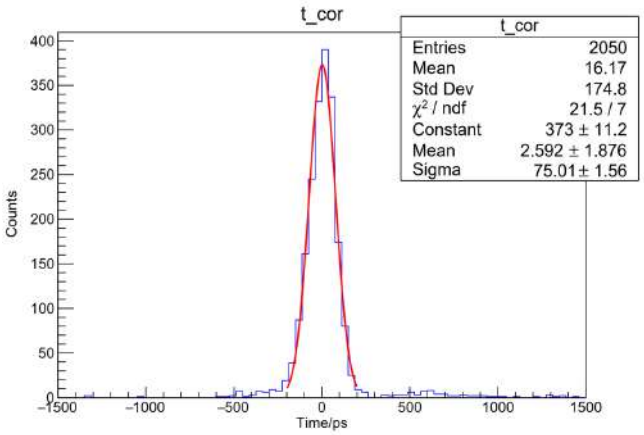

(d)

Figure 7.4: (a) Cosmic test layout. (b) Dynamic range of signal amplitudes of the sealed MRPC. (c) Efficiency vs. threshold dependence for the sealed MRPC. (d) Flight time distribution of two prototypes.

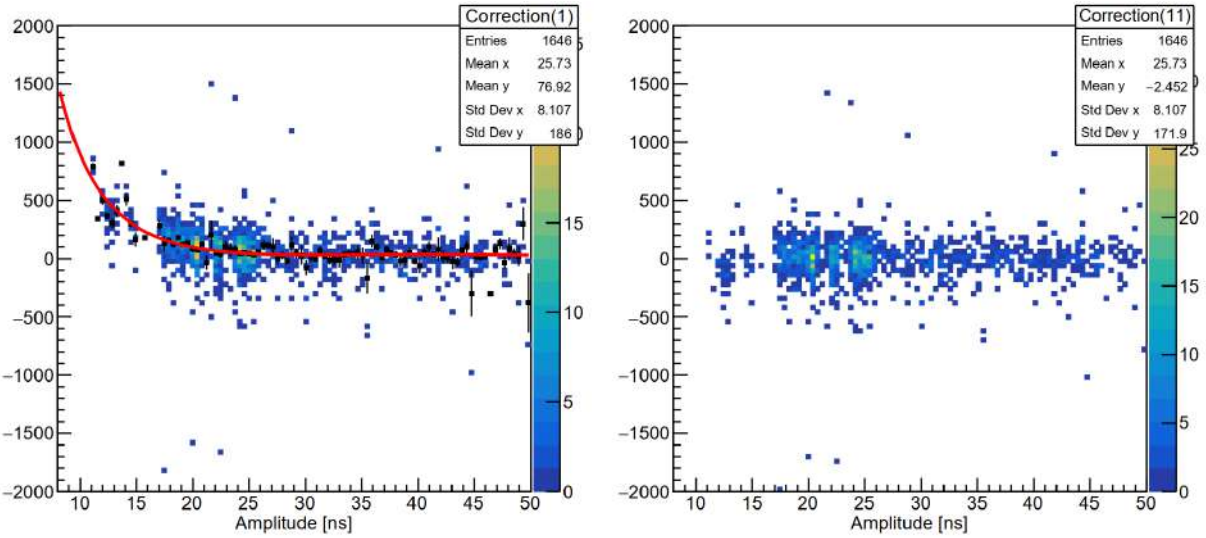

Figure 7.5: Slewing correction and the result.

(a)

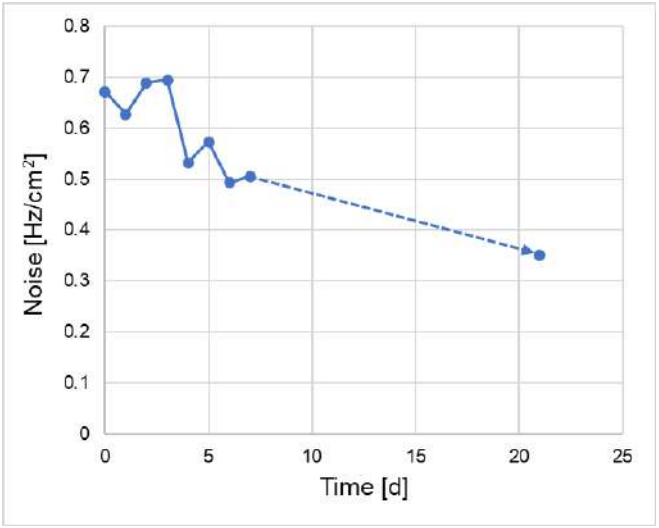

(b)

Figure 7.6: (a) The CEE-eTOF super module. (b) Noise decay of a brand new sealed MRPC.

Hz/cm^2. This will benefit the signal-to-noise ratio in experiment operations. Besides, after the training the summed dark current of the super module settled to around 70 nA.

4 TOF-related electronics

A very important part of the high performance time-of-flight system is the readout electronics. For the full exploitation of the excellent timing properties of the Multigap Resistive Plate Chamber, front-end electronics with special characteristics is needed. The signals from MRPCs must be amplified as fast as possible without losses. Leading times of the signal must be digitized and measured with accuracy much better than the time resolution of the detector. The readout electronics for the SPD TOF will consist of the front-end electronics (FEE) and the data acquisition system (DAQ).

In order to maximize the time performance of MRPC, the FEE should have a high bandwidth and low time jitter, the time digitization should also have a low jitter. The readout of MRPC can be done with the technologies described in [42, 43].

4.1 Option 1: fast amplifier + pulse shape analyzer

As we know, the time jitter of high sampling rate pulse shape analyzer is very low. For example, the time jitter of DRS4 is usually less than 5 ps. The time jitter of a high bandwidth fast amplifier is also low. The schematic diagram of USTC fast amplifier is shown in Fig. 7.7. It consists of eight channels and its time jitter is around 4 ps. The schematic diagram of the DRS4-based pulse shape digitizer is shown in Fig. 7.8.

4.2 Option 2: CFD-based solution

The analog signals from any detector have a spread in their own amplitude and width. Therefore, to determine the time of occurrence of the signal very accurately, it is necessary to take into account the

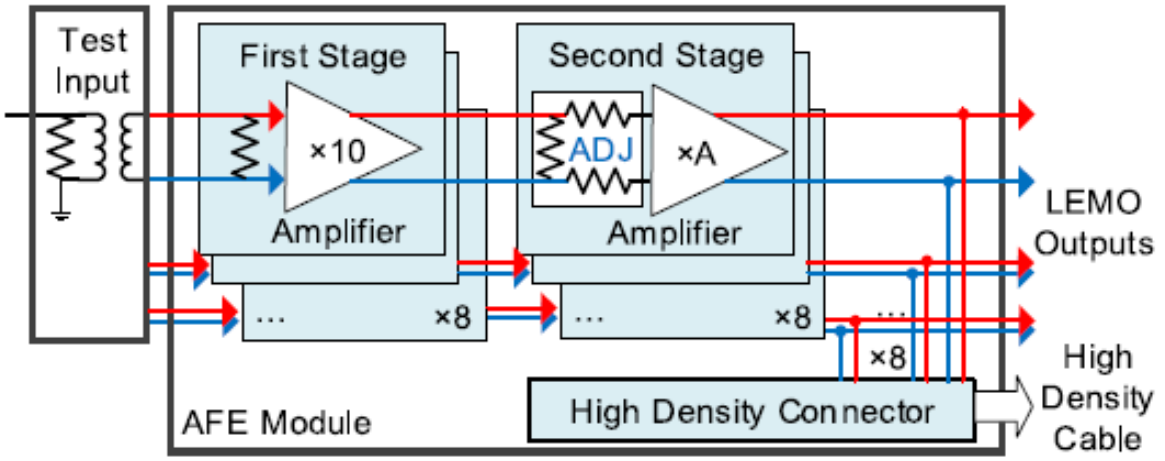

Figure 7.7: Schematic diagram of the USTC fast amplifier.

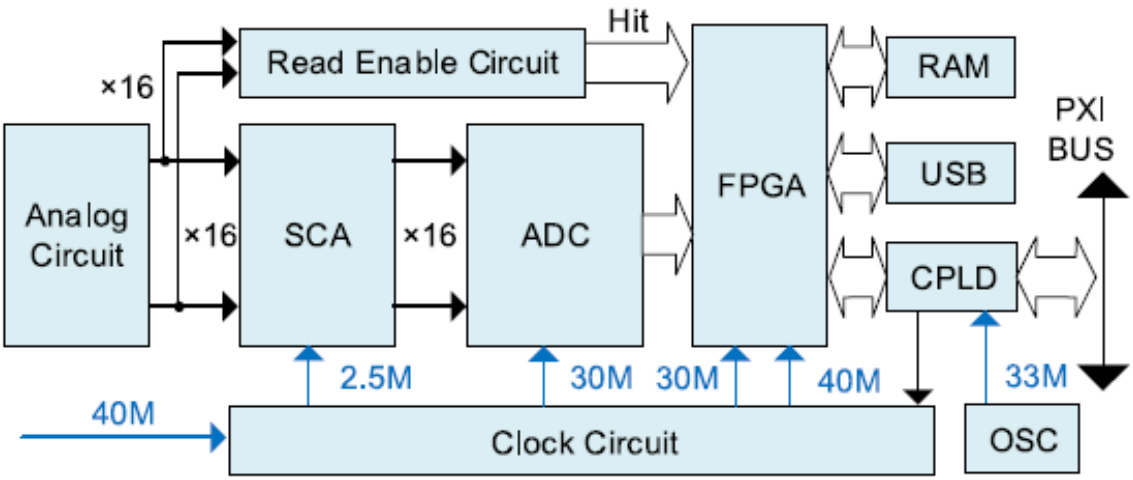

Figure 7.8: Schematic diagram of pulse shape digitizer.

shape parameters of that signal. Traditionally, correction is carried out using three possible solutions:

- hardware Constant Fraction Discriminator (CFD);
- multichannel Analog to Digital Converter (ADC);
- Time Over Threshold method (TOT).

The first is a hardware solution, implemented in various applications of the CFD method. The commonly used in the past CFD method is currently not utilized for the following reasons:

- the cost: cheap and fast ADCs have appeared on the market for some time;
- the complex structure and specific components of the CFD dramatically increased in cost;
- the CFD-based systems, known from past experiments, turned out to be ineffective and required constant complex configuration.

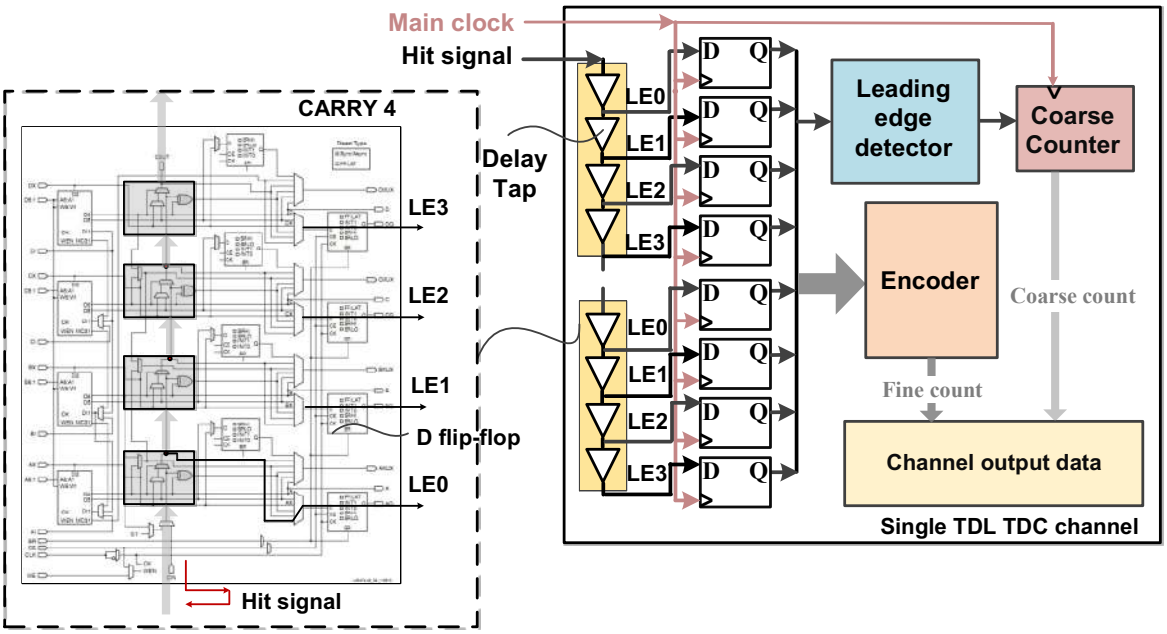

Figure 7.9: Schematic diagram of the FPGA TDC.

The ADC is used in the second method. The method is characterized by the high power consumption and price. The price also includes the cost of communication cables, which further reduce the reliability of the system.

The TOT method has lowered the price for different applications. We are considering two versions of this method. The first and simplest one is implemented in the NINO chip. The second one is implemented in the electronics of the TOF detector of the BM@N experiment. The second one meets our requirements to a greater extent, but has higher costs. Two methods of constructing the readout electronics with MRPC are being considered today. The first is the long-standing time-over-threshold method. The second one is the constant fraction (CF) method. Both methods have their own advantages and disadvantages. The FE electronics for the TOT method are quite simple to manufacture and use. The TOT method shows the time resolution of about 45 ps, instead of the desired 30 ps. The CF method requires more complex FE electronics. However, according to our measurements, this method allows to receive a better time resolution. To implement the capabilities of the CF method, a TDC with a time resolution of at least 10 ps is required. An attempt is now being made to combine both methods to achieve the utmost time resolution. It should be noted that such amplifiers (TOT and CF), integrated into the microcircuit are not available now. Therefore, it was decided, at the first stage, to use commercial microcircuits of the amplifiers and comparators. The developed amplifiers with the CF method have already shown encouraging results. A time resolution of about 40 ps was obtained. The main priority of the readout system is its cost. The main contribution to the cost is made by multi-channel readout systems, including analog ASIC and TDC digitization channels. Schematic diagram of the FPGA based TDC setup proposal presented in Fig. 7.9. The main problem is that there are no commercially available parts, unlike for the DAQ system, which is entirely based on commercial components.

4.2.1 Special analogue ASIC for MRPC readout

Systems with a large number of readout channels require the use of special integrated circuits, such as NINO and PADI. We can not yet get the right number of chips, but we could fix the parameters of these chips as required to be completely sufficient. The Table 7.2 summarizes the main parameters of NINO and PADI ASICs.

Both chips are specially designed for time-of-flight applications, but they have significant differences. The main difference of PADI is the absence of the TOT function of measuring amplitudes. The absence of the TOT function will require the use of an additional ADC channel to measure the charge. The second problem of PADI is a large Preamplifier Voltage Gain 250, against Gain 30 of the NINO chip. For this reason, PADI is unstable, especially when building large systems. PADI applications are limited, due to the absence of a pulse stretcher in its structure (pulse duration range is $1 \div 6$ ns), the used TDC have restrictions on the minimum duration of the input pulse, usually $5 \div 10$ ns. This is an important parameter that must be considered when choosing both an amplifier-discriminator and TDC types. Summing up, we can say that the PADI chip, although developed considering making of a NINO chip and produced using faster technology, does not exceed the parameters of the NINO chip due to errors in the task formulation, and in some applications is inferior. For these reasons, when determining the required parameters of the analog part of the electronics in the project, we will use as a prototype the basic parameters of the NINO chip indicated in Table 7.2.

Table 7.2: NINO and PADI ASICs specifications.

Main parameters comparison	NINO ASIC (ALICE)	PADI ASIC (GSI)
Channels per chip	8	8
Conversion Gain, mV/fC	1080	1900
PA Bandwidth, MHz	500	410
PA Voltage Gain, V/V	30	250
TOT function available	Yes	No
Stretch timer	Yes	No
Baseline DC offset, mV	2	1
Equivalent Noise Charge, e RMS	1750	1150
Input Impedance Range, Ω	$35 \div 75$	$30 \div 160$
Power consumption, mW/channel	27	17
Threshold type	external	SPI protocol
Timing jitter, ps	< 5	< 5

5 TOF performance

The performance of particle identification with TOF is estimated with MC-simulation in the SpdRoot framework. For the simulation it assumed that t_0 is determined (see CDR [1] for details) and the flight-time resolution $t_{TOF} - t_0$, where t_{TOF} is the TOF measurement) is 60 ps. Given the flight time and reconstructed track, the particle mass squared is reconstructed. In this procedure the average velocity of track from the Kalman fit is used. The performance estimated for minimum bias events in the pp collisions at 27 GeV is shown in Fig. 7.10.

6 Cost estimate

As it was mentioned above, the whole TOF consists of 216 MRPCs and 8832 readout channels. At around 3000$ per MRPC, the cost of 216 MRPCs is about 650 k$. Assuming that the price of FFE and DAQ is about 60 and 80 $ per channel, the total cost adds up to 1.24 M$. The cost of ASIC development ($\sim$ 150 k$) has to be accounted for additionally.

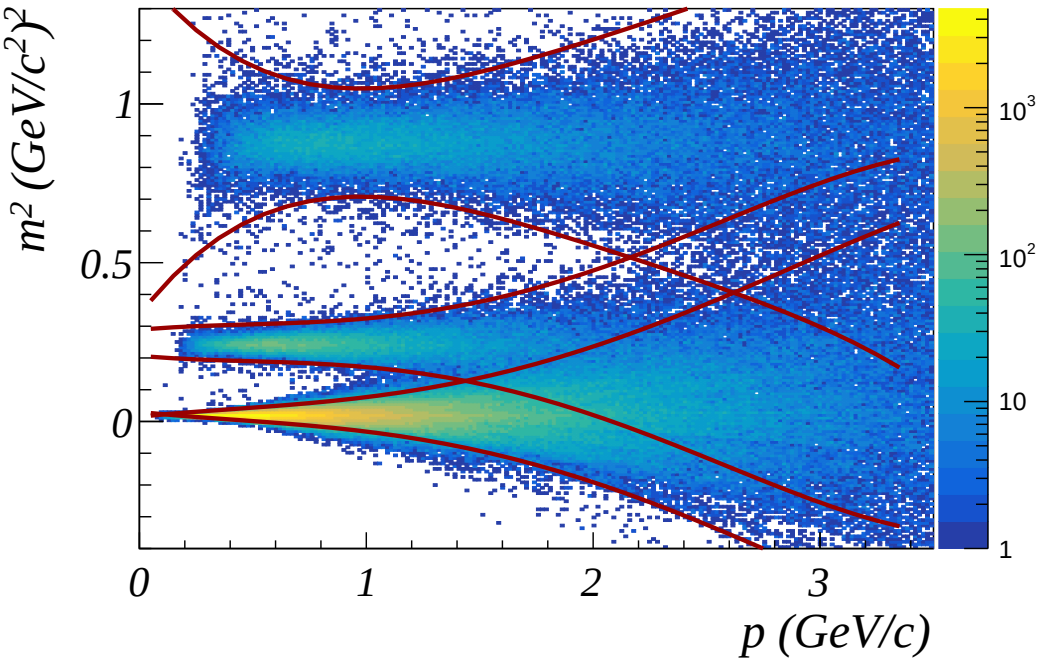

Figure 7.10: Reconstructed particle m^2 as a function of the initial track momentum for pions, kaons, and protons. For each particle type 3σ intervals are also shown. The figure is obtained for the minimum bias sample of pp collisions at 27 GeV.

Chapter 8

Aerogel counters

For particle identification in the end-cap regions, it is proposed to install threshold Cherenkov aerogel counters (in addition to another PID detector, MRPC). This will extend the momentum range of π/K/p separation compared with the TOF detectors of SPD.

1 Aerogel properties and production

Aerogel, first synthesized by S.S.Kistler in 1931, is a highly porous material of silica clusters with a micro-structure smaller than the wavelength of visible light. The first successful attempt to use silica aerogel in Cherenkov counter was made in 1974 [44]. This material is ultra-light and contains more than 90% air inside a volume. The complicated and prolonged process of the aerogel production includes two main stages: forming of gel in the medium of a corresponding solvent, and drying at the super-critical conditions of high pressure and density.

The technology of the aerogel production is well mastered at present in two centers: one in Japan (KEK/Chiba/Panasonic groups), another one in Russia (Budker INP and Boreskov Institute of Catalysis, Novosibirsk).

Aerogel has found an application, in particular, as a radiator in Cherenkov counters. Actually, aerogel fills the gap in the refractive index values between gases and liquids. This feature of aerogel allows one to use it in Cherenkov counters for particle identification in conditions when other Cherenkov radiators are not applicable, for instance, for π/K separation at the momenta from a few hundred MeV/c to about 3 GeV/c. Aerogel may have a refractive index in the range between 1.0006 and $\sim$1.25, the refractive index for various density aerogel materials is roughly given by $n = 1 + 0.21\rho$. The exact value of n is specified at the production stage. Selection of the refractive index value defines the region of momenta where separation is effective. The momentum threshold P of a particle with mass m is given by $P = m/\sqrt{n^2-1}$. Table 8.1 shows the threshold momenta of particles for different n values.

Table 8.1: Threshold of Cherenkov radiation in GeV/c for different particles and refractive indices n of aerogel.

n	1.05	1.04	1.03	1.02	1.015	1.01
π	0.44	0.49	0.57	0.70	0.80	0.99
K	1.54	1.73	2.00	2.46	2.84	3.48
p	2.93	3.29	3.80	4.67	5.40	6.62

Aerogel has a short scattering length of light, 12÷40 mm depending on wavelength. Therefore, the directivity of Cherenkov light cannot be used because directivity disappears soon after emission. For this reason, diffusive reflectors are used at the walls. No scintillation has been observed in aerogel. No detectable degradation of the optical properties of the aerogel (transmittance, refractive index) was observed up to radiation doses of ∼10 Mrad [45]. Aerogel samples suffered from hygroscopicity for a long time, but in the 1990s the technology of hydrophobic aerogel has been developed.

Aerogel is manufactured in the form of tiles with dimensions up to $20\times 20\times (1\div 5)\,\mathrm{cm}^3$. If a thicker radiator is needed, it is arranged as a stack of a few tiles. In order to put tiles into a needed shape, mechanical treatment is done with a diamond saw or with a water-jet cutter.

There exists a positive experience of using threshold aerogel Cherenkov counters, in particular, in experiments KEDR (BINP, Novosibirsk) [46], [47], BELLE (KEKB, Tsukuba) [48, 49], DIRAC [50]. In the BELLE experiment a threshold aerogel Cherenkov counter with refractive index from 1.010 to 1.030 provided π/K separation in the momentum region up to 3.5 GeV/c. In the KEDR detector, the aerogel counters with refractive index 1.05 provided π/K separation in the range from 0.6 to 1.5 GeV/c. In DIRAC aerogel radiators with refractive indices 1.015 and 1.008 were used, the resulting amplitudes for kaons were on average 6.9 photoelectrons in the momentum range 4.0÷5.2 GeV/c (for n=1.015) and 3.9 p.e. for momenta 6÷8 GeV/c (for n=1.008).

In SPD, to extend to higher momentum values the region of π/K identification, compared with provided by the TOF system, we have to use a rather low refractive index, below the most commonly used $n = 1.05$. On the other hand, the lower the value of the refractive index, the lower the Cherenkov photon output, which is proportional to *n-1*.

As is well known, the maximum of the Cherenkov light emission spectrum lies in a short-wave region, below the visible light. Light absorption length in aerogel decreases with decreasing of the wavelength, and below λ=300 nm it drops very sharply. Therefore, it is needed to shift the original Cherenkov light to larger wavelengths, to a region of maximum sensitivity of light detectors (PMT, APD, MPPC).

In Fig. 8.1(a) the principle of the KEDR aerogel counter (ASHIPH) operation is shown. Cherenkov light from aerogel is captured by a wavelength shifter (WLS) and leads it to a light sensor. Fig. 8.1(b) shows the drawings of the KEDR counter. A PMMA light guide doped with BBQ dye is used as a wavelength shifter. BBQ has 250–430 nm absorption band, and λ=500 nm emission peak, Fig. 8.2(a), which matches a sensitivity region of many light sensors. Cross-section of WLS is $3\times 17\,\mathrm{mm}^2$. The microchannel plate photomultipliers served as light sensors in KEDR, but for later developments the APDs were used (BELLE-II), also, SiPMs were proposed for aerogel detectors in PANDA (GSI) and FARICH ($c\tau$-factory in Novosibirsk).

If a particle crosses WLS, it produces a signal much higher than a particle traversing aerogel. To avoid misidentification, a two-layer structure is used with shifted layers with respect to the WLS position, so that a particle cannot cross WLS in both layers. The thickness of one layer in KEDR is 74 mm, the total amount of material in both layers is 0.24 X_0.

For relativistic cosmic muons that cross both counter layers of KEDR, the average number of photoelectrons was 9.3 ± 0.4, and the detection efficiency $99.3\pm 0.1\%$ at the threshold equal to 2 p.e. For under-Cherenkov-threshold muons ($200 < p_\mu < 300$ MeV/c) the efficiency was $3\pm 1\%$.

2 Aerogel detector in SPD

In the SPD a threshold aerogel counter in SPD, similar to the one used in the KEDR experiment, can be inserted between the ST end-caps and the Beam-Beam Counter. The available gap is 200 mm.

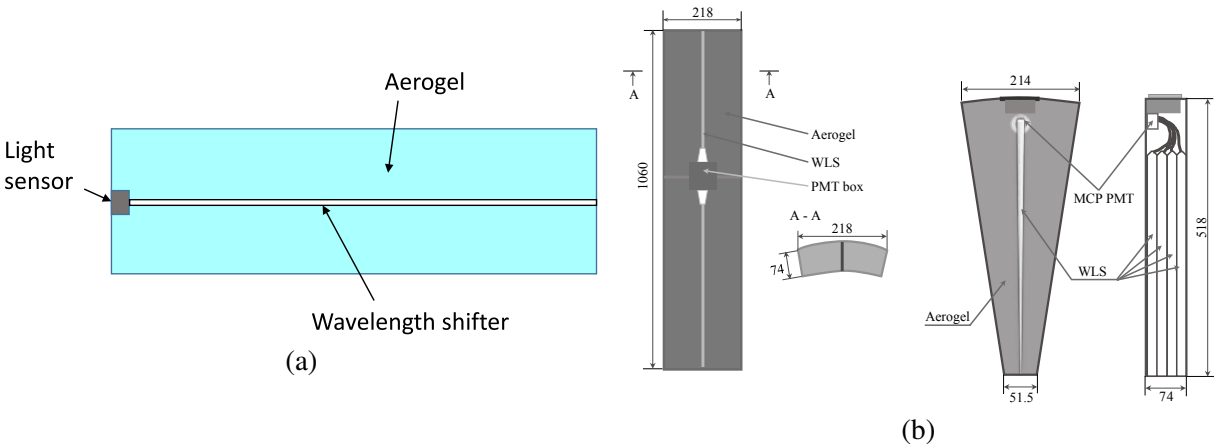

(a) (b)

Figure 8.1: (a) Principle of ASHIPH operation. (b) KEDR aerogel counters: two barrel counters in a single housing (left), end-cap counter (right) [46].

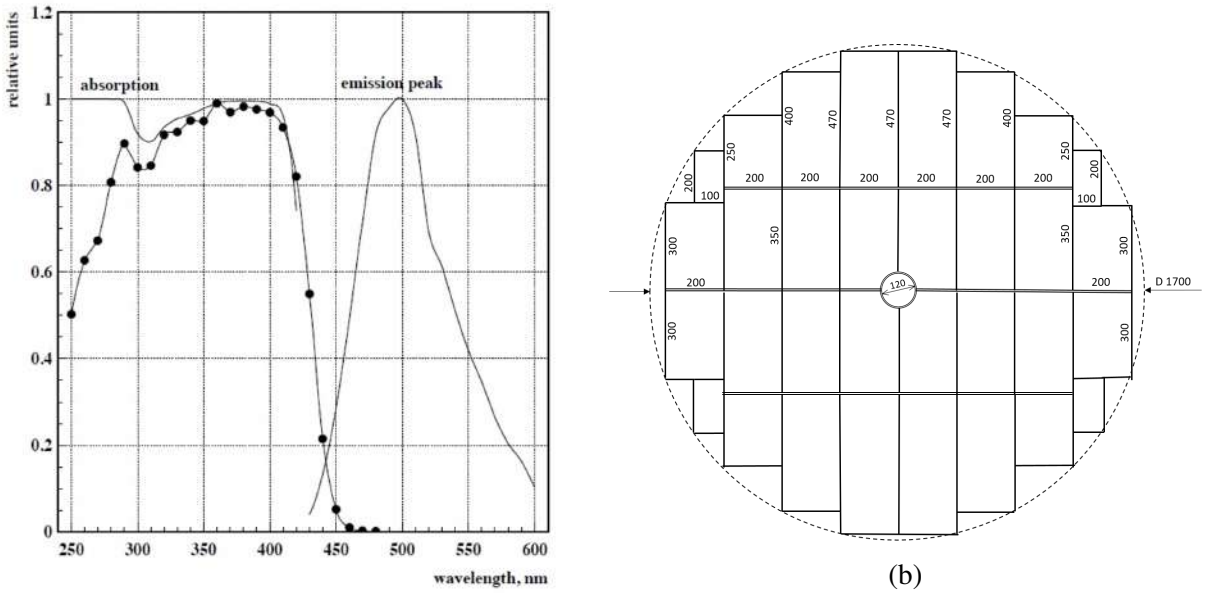

(a) (b)

Figure 8.2: (a) Absorption and emission spectra of the BBQ wavelength shifter. (b) Aerogel layer composed of tiles.

The value of the refractive index has to be selected for the momentum region where π/K separation with the TOF system becomes less reliable, that is above 1.5 GeV/c. This requires rather low n values. At the same time, the Cherenkov light output drops with decreasing refractive index, therefore, some compromise is needed.

As was illustrated in SPD CDR (Fig. 4.38 (d) in SPD CDR [1]), refractive index $n = 1.02$ allows for π/K separation in the region of momenta from 1 to 2.5 GeV/c. From a numerical estimation, it follows that in aerogel with $n = 1.02$ a relativistic particle produces 30 Cherenkov photons per cm in the wavelength range 250$\div$430 nm (this is just an absorption band of the wavelength shifter BBQ).

The plan is to build the end-cap aerogel detector consisting of two layers with a shifted position of the wavelength shifters in each layer with respect to each other. Each layer has 80 mm thickness, the surface of a layer is composed of 32 rectangular aerogel tiles of different dimensions up to 200×470 mm^2 as

shown in Fig. 8.2 (b). The innermost tiles are machined so that their form fits a circular beam pipe.

WLS is made of polymethylmethacrylate with a BBQ dye. It extends along the full length of a tile and has a $3\times14\,\mathrm{mm}^2$ cross-section, with a long side (14 mm) along the Z direction. With a 3 mm thickness of a WLS bar, the Cherenkov photons are re-emitted with about 100% probability. An output surface of the shifter ($3\times14\,\mathrm{mm}^2$) is attached to two MPPCs Hamamatsu S13360-6075, each having a $6\times6\,\mathrm{mm}^2$ photosensitive area, 50% photon detection efficiency and a high gain (4×10^6), Fig. 8.3 (a). Another option is to use four MPPCs S13360-3060 with a $3\times3\,\mathrm{mm}^2$ sensitive area, and a 40% photon detection efficiency. We are planning to collect light from both ends of a shifter bar. Low noise of the photosensors is an important condition for a clear detection of weak Cherenkov signals.

In KEDR the probability of a Cherenkov photon conversion into a photoelectron was 2%-4%, depending on the distance between the point of a photon absorption and a light sensor, ranging between 5 and 40 cm. This was achieved with MCP of 23% quantum efficiency and one-end light collection. In SPD, light collection from both ends and higher quantum efficiency of MPPC (40% or 50%), though with a shorter long side of WLS (14 mm instead of 17 in KEDR), would allow to reach not less than about 4% conversion efficiency. Then, with 30 Cherenkov photons per cm and 8 cm aerogel thickness, a total of 240 Cherenkov photons would produce about 10 photoelectrons.

The position of the shifters is seen from Fig. 8.3 (b). WLS bars in adjacent tiles are slightly shifted in order to avoid collision of MPPCs. The probability for a particle to hit the shifter in one layer is about 3 mm/200 mm ≈2%, a high signal, in this case, may lead to misidentification. The second layer of the aerogel detector has the same structure, but the WLS are shifted so that a particle cannot hit WLS in both layers, thus excluding misidentification. Horizontal gaps of a few millimeters between the tiles serve for placing MPPCs and the connecting cables. Similarly, horizontal gaps in the two layers are shifted so that a particle cannot pass through the gaps in both layers and escape detection. The aerogel volume of each tile is covered with the diffusive reflective material like Millipore paper or Gore®DRP®Diffuse reflector which have reflectivity above 97%.

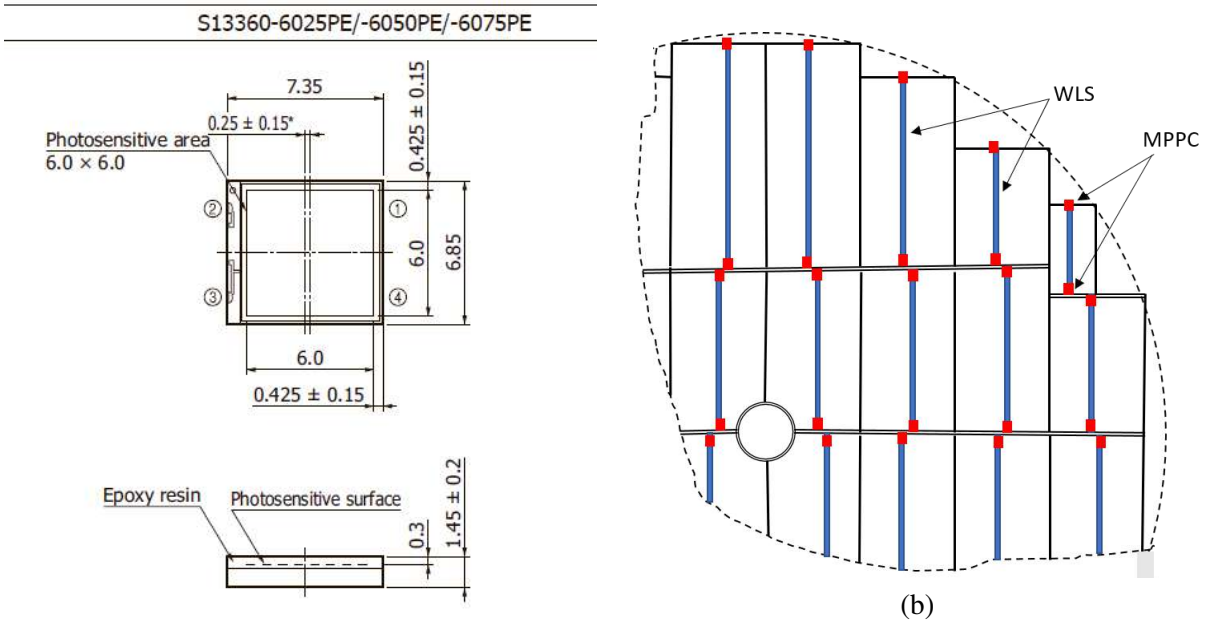

(a) (b)

Figure 8.3: (a) Drawings of the MPPC Hamamatsu S13360-6075. (b) Wavelength shifters (blue) and light sensors MPPC (red) in the aerogel layer.

Table 8.2: Aerogel detector components and cost estimate.

Component	Units	Quantity	Price per unit, $	Total price, k$
Aerogel	l	800	2500	2000
Reflective material	m^2	40	1000	40
WLS	pc	128	150	20
MPPC	pc	1024	40	40
Electronics	channels	256	150	40
Mechanics and assembling				260
Total				2400

The electronic channel of the aerogel counter consists of an amplifier and a digital part. The amplifier should include the summing of the analog signals of all (2 or 4) MPPCs at the end of a shifter. The digital part may be arranged similar to that of the electromagnetic calorimeter of SPD. Only MPPCs are positioned at the front view of the aerogel layer, the amplifiers and digital electronics can be placed outside of the aerogel aperture.

Rectangular tiles leave empty areas at the outer region of a circular aperture of the end-cap, this results in 10% geometrical inefficiency, which is quite affordable, especially since it happens at the periphery of the end-cap. In principle, we could fill these empty areas with aerogel, too, but at the moment we do not consider this obligatory.

One end-cap includes two aerogel layers with 32 tiles in each layer. When WLS is viewed from both ends, the number of the electronic channels in one end-cap will be 2 (layers) $\times$ 32 (tiles) $\times$ 2 (ends) = 128, or 256 channels for both end-caps. The number of MPPCs is 256 $\times$ 2 (4) = 512 (1024) depending on the selected MPPC type. Table 8.2 summarizes information about the SPD aerogel detector and the cost estimate. Thus, the cost of two aerogel end-caps is estimated at 2.4 M$.

Chapter 9

Straw tracker

The purpose of the Straw Tracker (ST) is to reconstruct tracks of primary and secondary particles with high efficiency, to measure their momenta with high precision, based on a track curvature in a magnetic field, and to contribute to a particle identification via energy deposition (dE/dx) measurements. A spatial resolution of ST is required to be about 150 µm. It has to be achieved when operating in a magnetic field of about 1 T.

The detector is planned to be built of low-mass straw tubes, similar to those used in many modern experiments, such as NA62 [51], COMET [52], SHiP [53], Mu2e [54], COMPASS [55, 56], NA64 [57], and others.

The tracker will consist of the barrel part and two end-caps. Two different kinds of straw tubes are considered to be used for them.

1 Barrel part

1.1 Welded straw tubes

1.1.1 Material

The detector is assembled from about 26 000 straw tubes. A single straw tube is manufactured from a thin polyethylene terephthalate (PET) foil, which is welded longitudinally by ultrasonic welding to form a tube. The straw has an active length from 10 cm to 2.7 m and a nominal inner diameter of 9.8 mm. Its inner surface has a metal coating (Cu/Au) to provide electrical conductance on the cathode, while the electrons, produced in ionization processes, will drift towards the central wire anode.

The choice of the straw material is a compromise between many different requirements, i.e. radiation length, permeation of gases, mechanical properties, adhesion to metal coating, bonding with epoxy and the ability to be ultrasonically welded into a tube. A summary of the specifications is given in Table 9.1.

The straw tubes for the tracking detector in the SPD experiment are manufactured from a biaxially oriented coextruded film made of polyethylene terephthalate (PET). One side of the film is chemically pre-treated to improve adhesion. This side was chosen for the epoxy bonding between the straw tube and the polyetherimide (PEI) straw fixation plug. The nontreated side is coated by a conductive layer of 50 nm of Copper (Cu) followed by a protective layer of 20 nm of gold (Au). Once the production of the tube is completed, the conductive layer is on the inside of the tube, while the outside remains uncoated and pre-treated chemically for bonding. The thickness of the film is 36 μm.

Table 9.1: Summary of coated material specifications.

Description	Specifications
PET film	polyethylene terephthalate type Hostaphan RNK 2600 of (36 ± 2) μm thickness
Density	1.4 g/cm^3
Copper layer thickness	50 nm
Gold layer thickness	20 nm
Resistivity of straw tube (2.1 m)	$\sim$70Ω
Permeation of naked film, (10^{-12} Torr*l*cm/s*cm^2*Torr)	6 for He, 0.06 for Ar, 1 for CO_2

1.1.2 Long-term tests

Long-term tests were carried out with the straws mounted under tension with a load of 15 N applied before the extremities of the tubes are bonded to the PEI supporting parts. The sag and the tension of the tubes were measured during a long-term test lasting 18 months. The values are recorded with the straws under pressure and compared to a reference straw at the atmospheric pressure. The results are shown in Fig. 9.1.

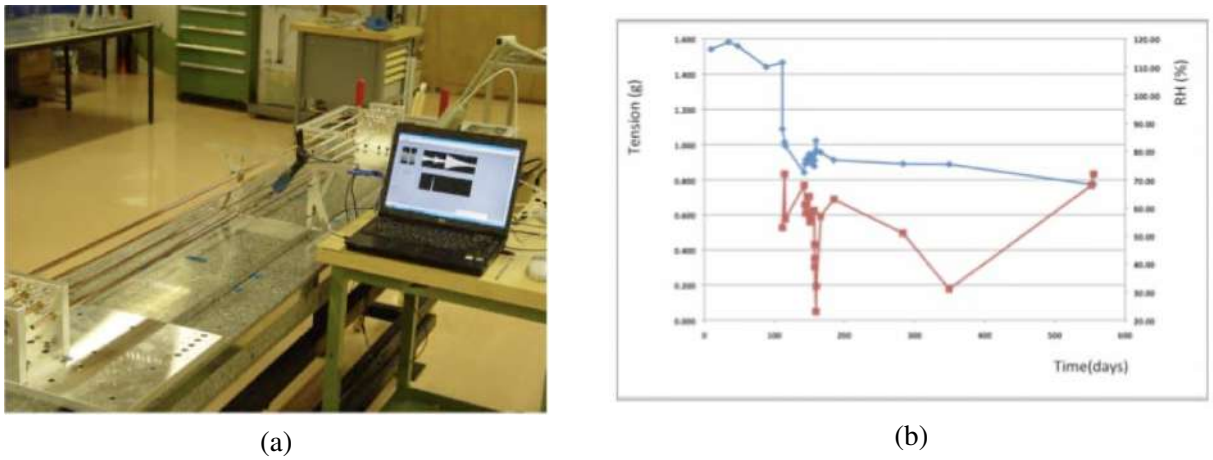

(a) (b)

Figure 9.1: (a) View of the long-term test setup. (b) Straw tension as a function of time (blue curve) plotted together with humidity (red curve).

1.1.3 Tensile test of PET samples

The base material for the straw tubes was tested in CERN using the Instron tensile test apparatus. A close-up view of the apparatus with a tested film sample is shown in Fig. 9.2 (a). The values observed for welded samples are typically 25% lower than those of the coated unwelded PET. Unwelded PET has a tensile strength close to 130 MPa, whereas welded and coated samples fail at $\sim$100 MPa. The stress in the straws due to the pressure difference of 1 bar is 13 MPa, which gives sufficient safety margin.

1.1.4 Coating and permeation

The metal coating is accomplished by a sputtering process. The metallisation provides electrical conductivity, as well as an improvement in the permeation properties of the PET substrate. Measured values of the permeation through a 50 nm Cu coated membrane show a barrier improvement factor of 8.5 for He

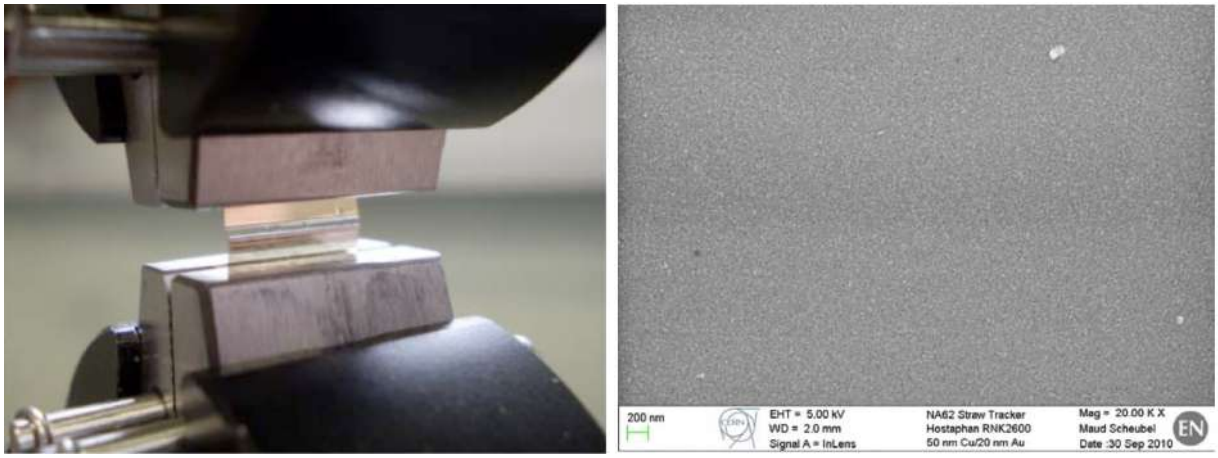

(a) (b)

Figure 9.2: (a) Close-up view of the tensile test apparatus with a tested film sample (the weld is in the center). (b) Typical view of a coated PET with a magnification of 20 000 (RNK 2600).

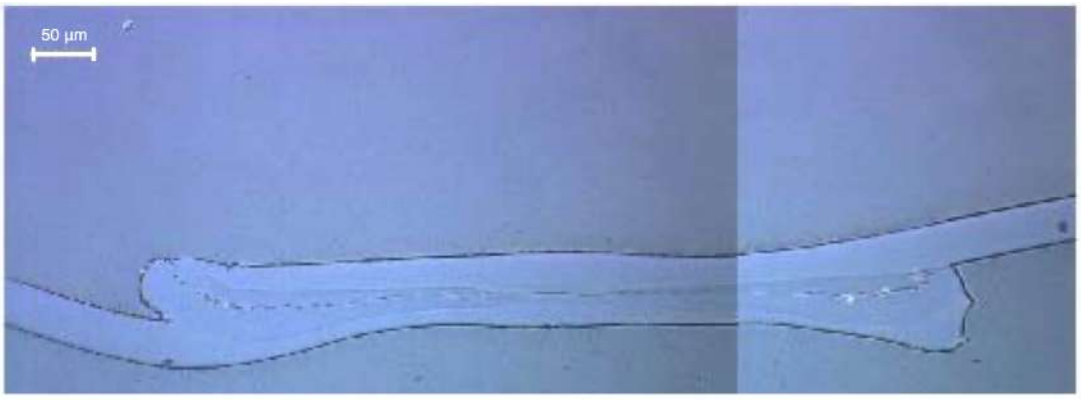

Figure 9.3: Cross-section of a welded seam where the two sides of the strip are fused.

(helium), 9 for CO_2 and 5 for Ar (argon). The quality of the sputtered coating is measured by a peel test using adhesive tape.

1.1.5 Studies using a scanning electron microscope

The coated PET was examined using the Scanning Electron Microscope (SEM) in order to determine the quality of the coating and sputtering on the substrate. The SEM was also used to verify the metal coating thickness, not as a direct measurement, but by using the energy-dispersive X-ray spectroscopy facility and a third party software. The metal coating and weld quality of the seam were checked using both the SEM and the traditional optical microscopy, as shown in Fig. 9.2 (b) and Fig. 9.3.

1.1.6 Glue bonding test

The adhesion between the outer side of the straw tube and the PEI straw support is critical. The chosen epoxy resin for this operation was TRA-BOND 2115, fabricated by Tra-Con Inc., whose outgassing properties and radiation hardness were studied at CERN. This epoxy has a good resistance to stress and temperature cycles. Its pot life is close to two hours and curing in 24 hours. Samples of PET were peel tested after being bonded to an aluminium plate. The bond of the selected candidate was better than the natural resistance of the material. The selected material was also analysed by the X-ray photoelectron spectroscopy. This allowed us to better understand the chemical treatment made by the PET suppliers

and its effects on bonding.

1.1.7 Straw manufacturing and welding

A dedicated machine for the straw production has been designed and constructed to manufacture 8000 straws for the NA62 experiment (diameter 10 mm, thickness 36 μm), 2000 straws for the COMET experiment (diameter 10 mm, thickness 20 μm), and 100 straws for the SHiP experiment (diameter 20 mm, thickness 36 μm). Straw sets are currently being produced for prototypes intended for the NA62 upgrade and the straw tracker for DUNE (diameter 5 mm, thickness 20 μm). An ultrasound head with a movable fixation at the frame and an anvil for the straw welding are shown in Fig. 9.6. They were designed and constructed to obtain a good quality of the welding seam (see Fig. 9.5) and to minimize differences in the straw diameter down to $\sim$10 μm. The distribution of the straw seam widths and tube diameters, obtained during the production of a large set of straws, are shown in Fig. 9.7. After manufacturing, each straw is equipped with the glued end-plugs and tested for leaks. All measurements are individually recorded in a logbook where all straw characteristics are stored, i.e. material, manufacturing date, inner diameter, etc. A unique serial number is allocated to every straw tube. Using this number one can access the straw information at any moment of the detector assembly.

A few straws with a diameter of 10 mm were used for the dedicated mechanical tests. They were cut in 20 segments of about 25 cm long and tested under overpressure until the breaking point. The other straws were cut to 5.3 m and the cut ends were preserved for further analysis. The breaking pressure was found to be 9 bar on average; and not one sample broke under 8.5 bar. The quality control procedure was the same as for NA62 straws. During the ultrasonic welding process, the seam quality was verified by a digital microscope and recorded to file for each straw. Furthermore, the seam quality was checked by an operator in real time.

Several measurements and tests are performed post-fabrication. The seam width and straw inner diameter are measured by an optical method. The cathode electrical DC resistance is measured. The elongation and breaking force are measured on the test samples (cut straw ends). The straws undergo a long-term overpressure test with temporary end-plugs glued into both ends of each straw. An overpressure test to $\Delta P \approx 2$ bar is performed for a period of about 1 hour. Subsequently, the straw is subjected to a long-term overpressure test at $\Delta P \approx 2$ for a period of at least 30 days. A gas leak estimation is obtained by measuring the loss of pressure over time. The local straw deformation is measured under an applied weight of 300 g, and the pressure is derived from the calibrated relation between loss of pressure and deformation. The design of an individual straw tube is shown in Fig. 9.4.

1.1.8 Straw conditioning

Once the ultrasonic welding apparatus produces the straws, they need to be carefully stored, prior to installation into the detector. The straws need to be stored during a period of time that varies from several weeks to several months. The tube storage has several constraints that need to be addressed. Namely, the inner diameter of the tube must remain free of dust and of foreign particles. The tube must also have the ability to be manipulated by technicians without buckling. With the above constraints in mind, it was decided that the optimal way to store the tubes would be under pressure. This would also have the added value of being able to observe changes in pressure in the pipe over time. Straws that show gas leakage and have poor weld quality can be removed. Taking into account further quality control tests that are performed on the tubes before installation, and the manipulation of the tube itself during its installation into the detector, a dedicated system was developed, in the form of valves. For storage, the straws are gas-filled with an approximate overpressure of 1 bar. The pressure loss over time is measured indirectly by measuring the local deformation of a straw under a 300 g weight and comparing it to the day it was first subjected to pressure. The first valve must have the ability to let gas into the straw, then

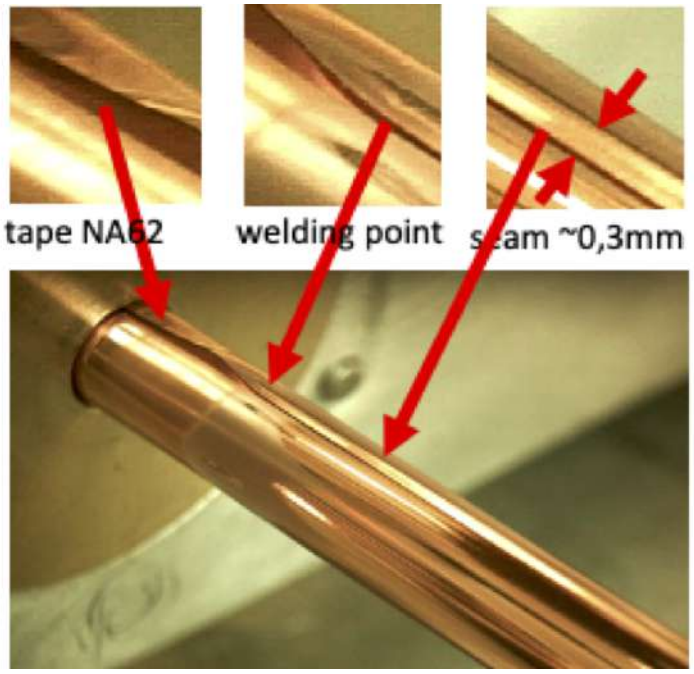

Figure 9.4: A single straw tube for the SPD barrel.

Figure 9.5: Quality of the welding seams of 0.4 mm (left) and 0.85 mm (right) at $\times 60$ magnification.

act as a non-return valve, thus keeping the straw under pressure. The valve design is loosely based on the ”Dunlop” / ”Woods” valve design, with an additional feature. To prevent leakage through the non-return system, an O ring and a threaded screw have been added. This is also used to fit the gas connector.

The second valve used at the other end of the straw tube is a simplified version without a non-return mechanism. To run a leak test, we simply connect the test system to an M4 thread inside the valve and pressurize the straw. To simplify measurements of the sagitta of a freely supported tube, both valves have the same weight. In addition, the ends have the ability to be connected to the standard M4 threads. Furthermore, both valves have an outer diameter smaller than the straw tube outer diameter, which allow the installation of a straw tube under pressure. This facilitates handling of the straws and reduces the risk of buckling the straw wall and the welding seam.

1.1.9 Mechanical properties and pre-tension of the straw

In order to determine the necessary straw pretension, a dedicated setup was developed to measure the straw sag and the vibration frequency of the straws as a function of pressure, as shown in Fig. 9.8. The

Figure 9.6: The straw production setup with an ultrasound head with movable fixation at the frame.

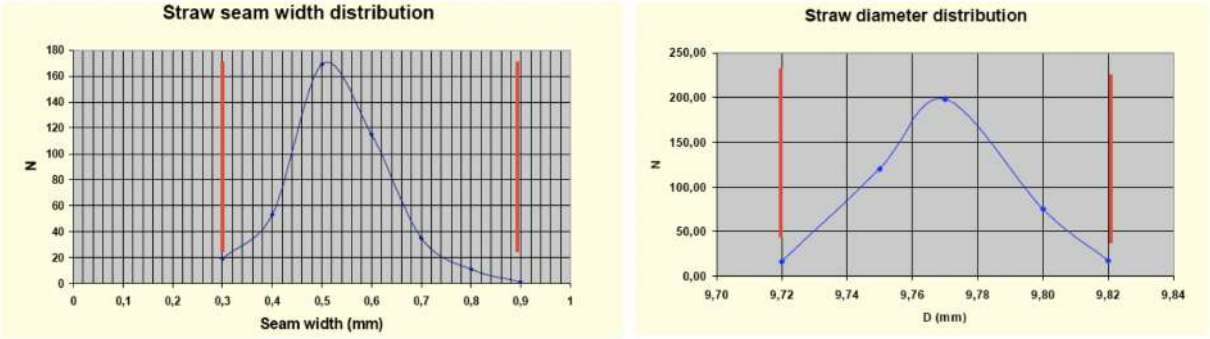

(a) (b)

Figure 9.7: Welding seam width (a) and straw diameter (b) distributions.

straw was connected to a gas bottle, and the absolute pressure inside the straws was set to 2 bar. Four straws were glued horizontally into two plates. One straw was equipped with a sliding fixation on one end to allow for a variable straw pre-tension. The sliding end of the straw was blocked (clamed ends) before measuring the deformation (sag) and frequency. The results of the measurements are shown in Fig. 9.9 (a). The increase in sag is clearly visible as the pressure inside the straw decreases.

1.1.10 Pressure influence

A study of the straw sag as a function of overpressure at different pre-tension was carried out to determine the required straw tension. The results are shown in Fig. 9.9 (b). A minimum tension of 10 N is necessary to obtain an acceptable straw straightness. We have decided to apply a force of 15 N during installation, in order to allow for some loss of tension over time.

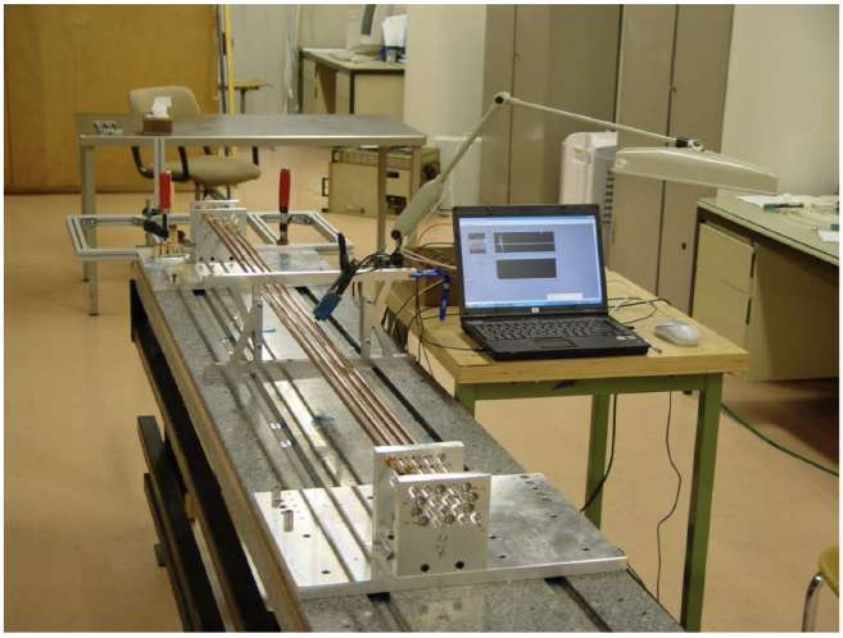

Figure 9.8: Setup for the measurement of the straw sag and frequency as a function of different pre-tension and pressure. The computer is connected to an IR emitter and receiver (OPB732) to measure the frequency of the vibrating straw.

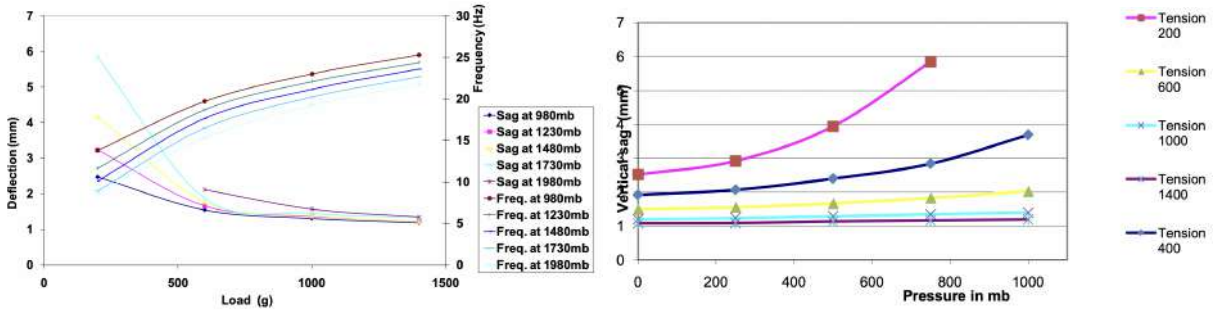

(a) (b)

Figure 9.9: (a) Measured sag and frequency of the straw as a function of pre-tension at different over-pressures. (b) Straightness as a function of pressure for a 1.85 m long horizontal straw for different values on the pre-tension.

1.1.11 Wire centering and wire offset

In order to evaluate the effect of electrostatic forces on the wire, the dependence of the wire displacement on the straw length and high voltage was calculated. The following formula was applied:

$$y = \frac{C}{k^2}\left(\frac{1}{\cos(kL/2)} - 1\right), \tag{9.1}$$

where $C = \rho g \sigma$ and k is calculated using the expression

$$k^2 = 2\pi\varepsilon_0 E_0^2(b)/T. \tag{9.2}$$

Here ρ is the density of the wire material, σ is the cross-section of the wire, T is the straw tension, E_0 is the field strength at the straw wall, L is the length of the straw tube, and ε_0 is the vacuum permittivity constant.

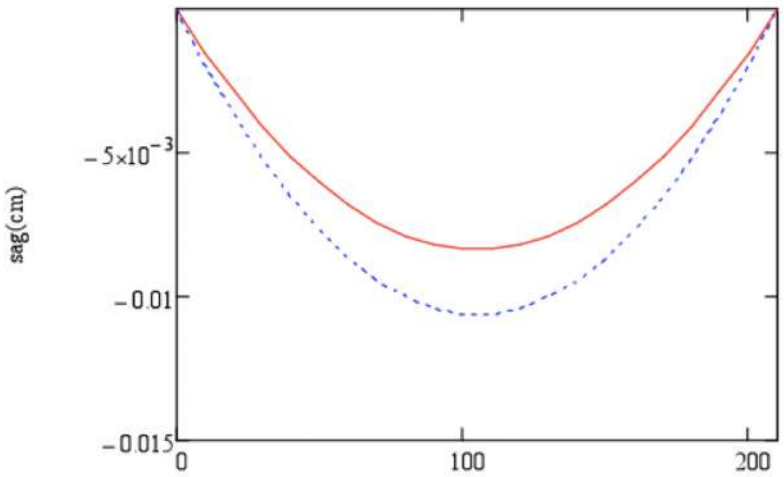

Figure 9.10: The wire deflection for a 2.1 m long straw with (blue dashed line) and without (red solid line) electrostatic deflection at 2.5 kV.

The results are presented in Fig. 9.10. In the case when the voltage was set to 2.5 kV (slow gas) and the tension in the wire was set to 90 g, the increase in wire sag due to electrostatic forces is about 27% with respect to the case without electric field. For the fast gas with a high voltage of 1.8 kV, the corresponding increase in the wire sag is 9%.

1.2 Detector response simulation

1.2.1 Choice of the gas mixture and high voltage operating point

The initial choice of the gas mixture and high voltage settings was based on experience of the NA62 experiment [58], where the straw tracker consists of the straw tubes of identical design. Its performance requirements are similar to those of the SPD straw tracker. The $Ar(70\%) + CO_2(30\%)$ gas mixture was demonstrated to provide the stable straw operation, sufficient spatial resolution and high detection efficiency. Moreover, it does not contain any flammable or non-ecological components. The optimal operation voltage was chosen to be 1750 V, which corresponds to a gas gain of about 4.5×10^4. In the case of the NA62 experiment readout electronics, based on the CARIOCA chip [59], such voltage allows for efficient operation with a spatial resolution better than 120 μm.

The straw spatial resolution and detection efficiency has been studied with the GARFIELD simulation software [60, 61] for the NA62 readout electronics models. The results as functions of the high voltage and signal discriminator thresholds are presented in Ref. [62] and are also shown in Fig. 9.11 . The considered discriminator thresholds correspond to 4, 10 and 15 fC of the charge induced on an anode wire. The results are shown for charged tracks crossing the straw at the distance of 3 mm from the anode wire.

1.2.2 GARFIELD simulation of the straw tube response

Detailed studies of a straw tube response are ongoing for the SPD straw tracker operation environment. To evaluate influence of the SPD magnetic field on the tracker performance, GARFIELD simulation of the intrinsic straw response to a 1 GeV muon has been performed for two extreme cases of 0 T and 1.5 T field, aligned with the straw longitudinal axis. Muon tracks are generated to be normal to the anode wire at the distance of 3 mm. Drift trajectories of xthe electrons produced in clusters of primary ionization for 0 T and 1.5 T magnetic fields are compared in Fig. 9.12 (a) and (b), respectively.

The relative coordinate of the primary ionizing particle is reconstructed from the measured electron drift

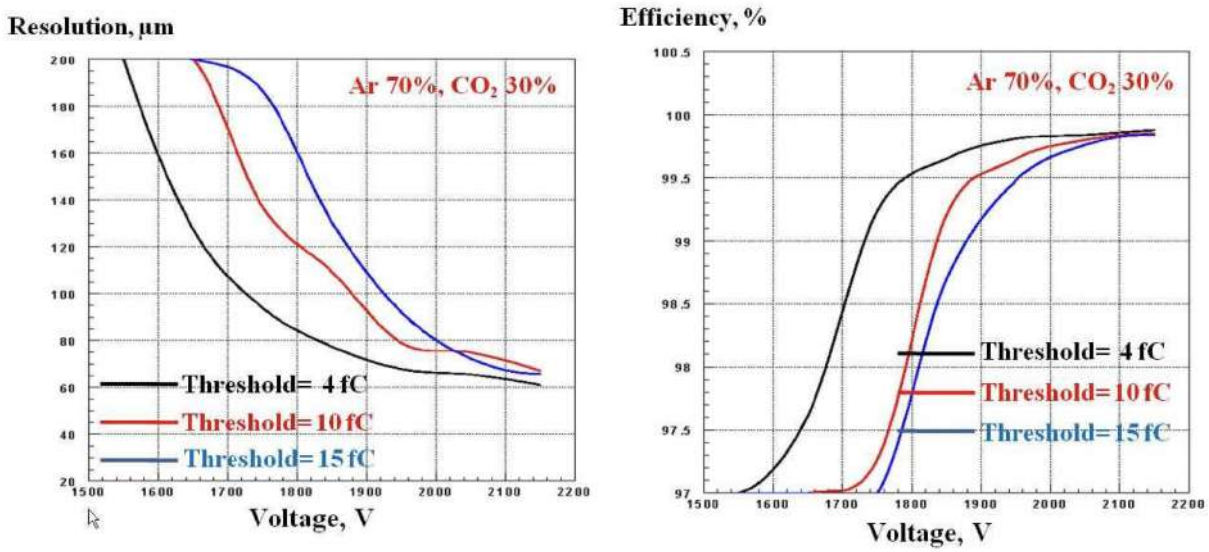

(a) (b)

Figure 9.11: GARFIELD simulation results for the straw spatial resolution (a) and detection efficiency (b) as functions of the high voltage and discriminator thresholds for a charged track crossing a straw at the distance of 3 mm from the anode wire [62].

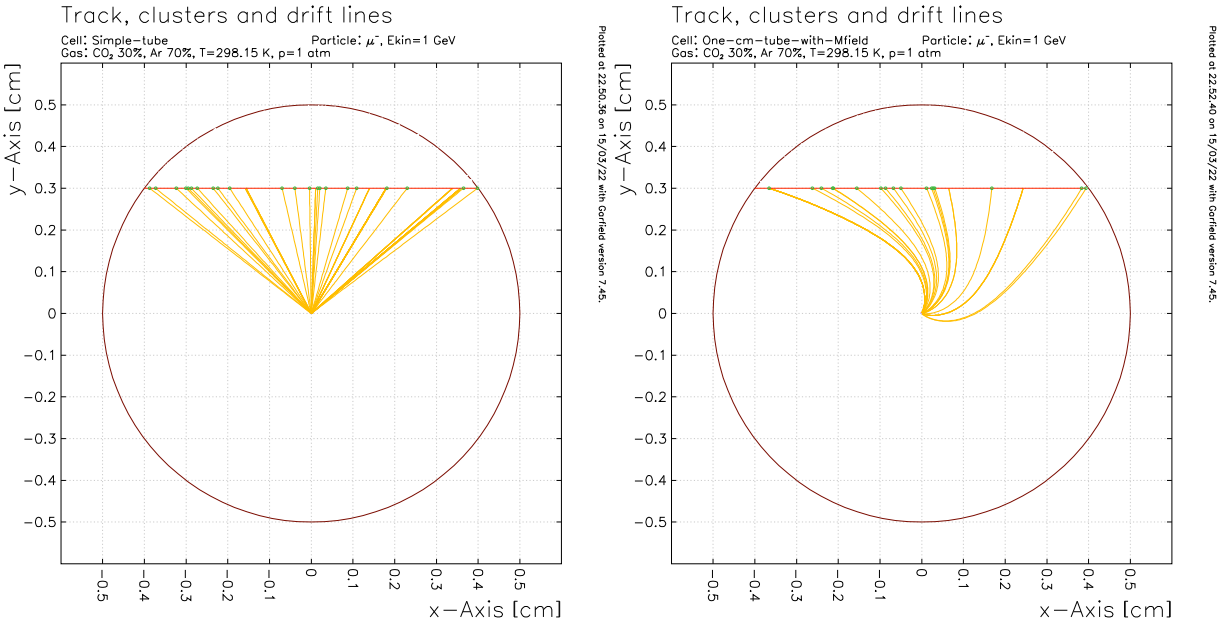

(a) (b)

Figure 9.12: Muon track (red), primary ionization clusters (green), and electron drift trajectories (yellow), simulated with GARFIELD for 0 T (a) and 1.5 T (b) magnetic field, aligned with the straw longitudinal axis.

time and is affected by its fluctuations, which, in turn, depend on fluctuations in the primary ionization cluster distribution, together with longitudinal diffusion as well as on characteristics of the readout electronics. To evaluate intrinsic performance of the straw tubes, the drift time of the first and second ionization clusters arriving at the anode is studied as a function of the distance between the muon track and anode wire. No transformation of the straw signal by the readout electronics is implemented at that

stage. Examples of the obtained time distributions for the first and second arriving clusters, produced by a muon passing at a distance of 4 mm from the anode wire, are shown in Fig. 9.13 for a magnetic field of 0 T and 1.5 T.

The small width of the obtained time distributions (much smaller than 0.1 ns) points to a negligible contribution of the cluster distribution fluctuations and electron diffusion to the straw time resolution. The influence of the magnetic field on the most probable arrival time is clearly noticeable, while the time distribution widths are not affected (first arriving cluster) or affected slightly (second cluster). The dominating influence of the read-out electronics on the straw tube time resolution will be demonstrated later in Section 1.2.3.

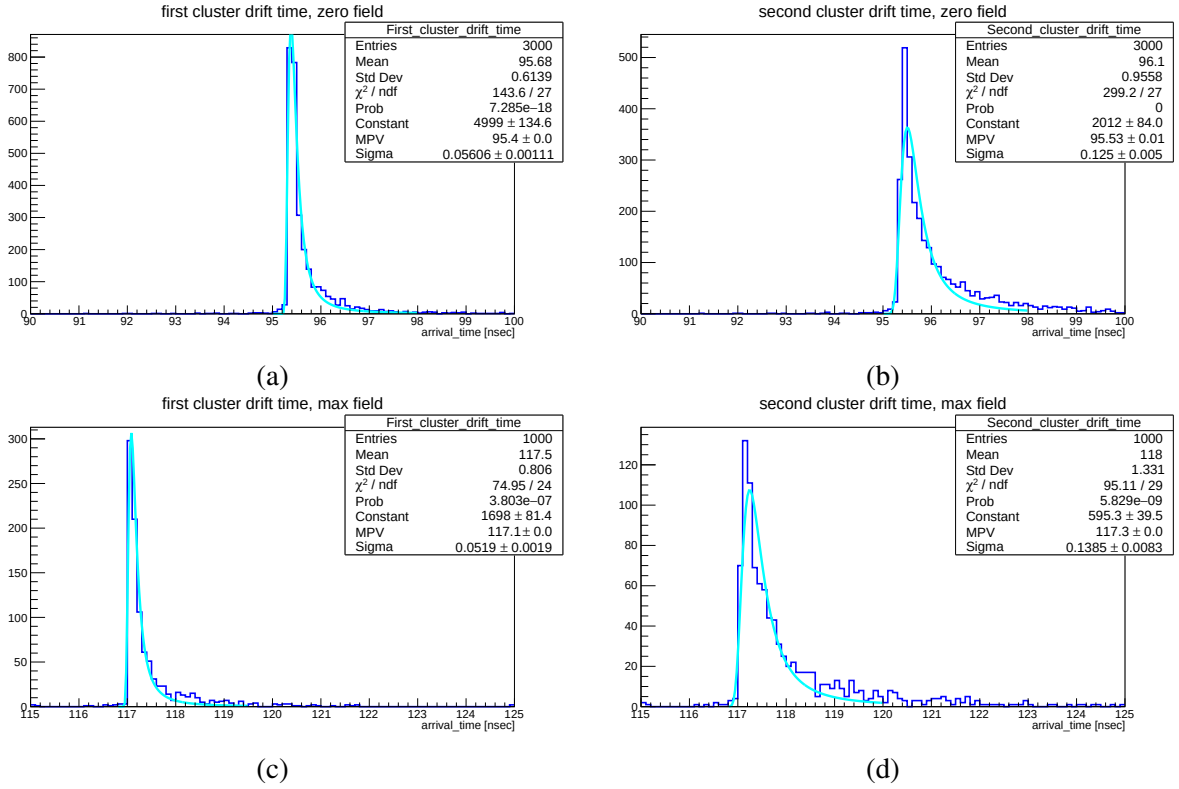

Figure 9.13: Examples of the obtained drift time distributions for the first (left) and second (right) arriving ionization clusters for a track passing at 4 mm from the anode wire for 0 T (top) and 1.5 T (bottom) magnetic field. To compare the most probable value (MPV) and the distribution width (RMS), the spectra (dark blue) are fitted to a Landau distribution (cyan).

The most probable values (MPV) of the arrival time distributions, obtained for field-free simulations using GARFIELD and GARFIELD++ [63] packages as functions of a distance between the muon track and anode wire, are shown in Fig. 9.14 (a). The measurements performed at the NA62 experiment with the nominal tracker read-out electronics are shown for comparison as a two-dimensional histogram. The simulation results are shifted by a constant delay to compensate for the time delays introduced by the read-out chain in real measurements. Comparison of the MPV obtained in the simulation for a magnetic field of 0 T and 1.5 T is presented in Fig. 9.14 (b).

1.2.3 Influence of realistic electronics readout on the straw time resolution

Influence of the readout electronics on the straw spatial resolution is studied using a combination of GARFIELD and LTSpice [64] electronics simulation package. Individual straw signals simulated with GARFIELD are processed with LTSpice for a given electronics chain model. One of the possible SPD

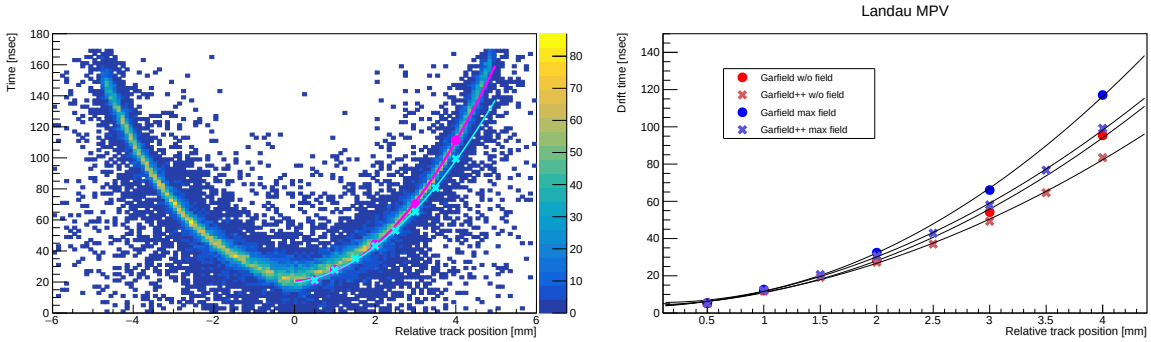

(a) (b)

Figure 9.14: The most probable drift time of the first arriving cluster simulated with GARFIELD and GARFIELD++. (a) Values obtained with GARFIELD (magenta points) and GARFIELD++ (cyan points) delayed with a constant value compared to the experimental results, obtained for an NA62 tracker straw (2D histogram). (b) Most probable values of the first cluster arrival time for 0 T and 1.5 T magnetic field. The simulation results are fitted to a quadratic function.

ST front-end electronics options, based on a VMM3a ASIC[REF], is considered in the study, and the corresponding model provided by the RD51 Collaboration (CERN) is used. Details of the read-out electronics are described in Section 9.3. At this stage, electronic noise and the influence of the magnetic field are not taken into account.

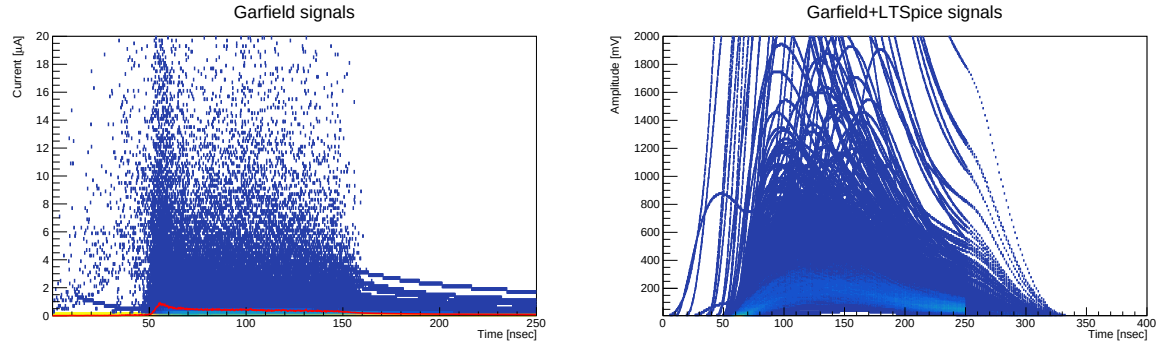

(a) (b)

Figure 9.15: (a) Signals induced at the straw anode due to an avalanche development as generated by GARFIELD for 1500 muons crossing a straw at the distance of 3 mm from the anode wire. (b) Corresponding electronics responses emulated with LTSpice.

A current induced at the straw anode due to an avalanche development upon a muon crossing the tube at the distance of 3 mm from the anode wire as generated with GARFIELD is shown in Fig. 9.15 (a). 1500 individual signals are shown together with the average trend. The corresponding readout electronics signals, emulated with LTSpice, are shown in Fig. 9.15 (b). The electronics chain model is set to describe the VMM3a operation mode with the shortest signal peaking time of 25 ns. A 10 mV signal discrimination threshold is chosen to correspond to 3 fC of the input charge. The time distributions of the first arriving cluster and the discriminator threshold crossing are shown in Fig. 9.16 (a) and (b), respectively. In the case of realistic electronics, the time distribution is significantly wider. For the chosen electronics parameters, the time resolution was found to be 3.6 ns. The corresponding distribution, obtained with an NA62 straw readout with the original electronics, is shown Fig. 9.16 (c). The time of the discriminator threshold crossing, measured for the relative muon track distances of 3.05 ± 0.05 mm, was obtained from the NA62 results shown in Fig. 9.14 (a).

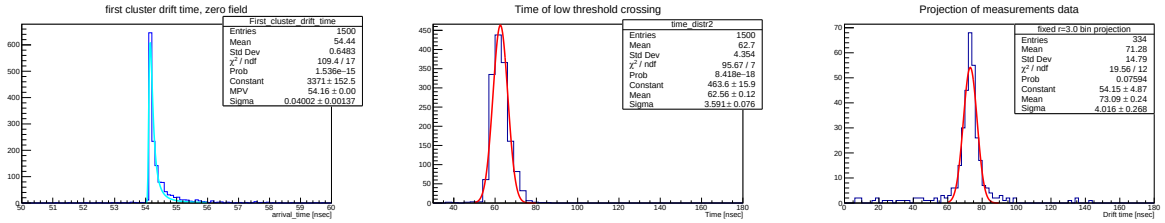

(a) (b) (c)

Figure 9.16: Drift time distribution, obtained for first arriving clusters as simulated with GARFIELD together with a Landau fit (a), and the time distribution of the VMM3a-based readout electronics response, modeled for the corresponding signal sample with LTSpice for 25 ns peaking time and 10 mV discriminator threshold together with a Gaussian fit (b). (c) Corresponding distribution obtained with an NA62 straw readout with the original electronics. The time of the discriminator threshold crossing is measured for the relative muon track distances of 3.05 ± 0.05 mm.

1.3 Chamber design, construction and installation

1.3.1 Detector geometry and layout

The mechanical construction proposed for the SPD ST is based on engineering solutions, which were already efficiently applied in the ATLAS and PANDA experiments. The straw tracker consists of three parts: a barrel part and two end-caps. The barrel has inner and outer radii of 270 and 867 mm, respectively. It is subdivided azimuthally into 8 modules, with 31 double layers of straw tubes each, as shown in Fig. 9.17. The layout of a single module with the supporting frame are shown in Fig. 9.18 and Fig. 9.19.

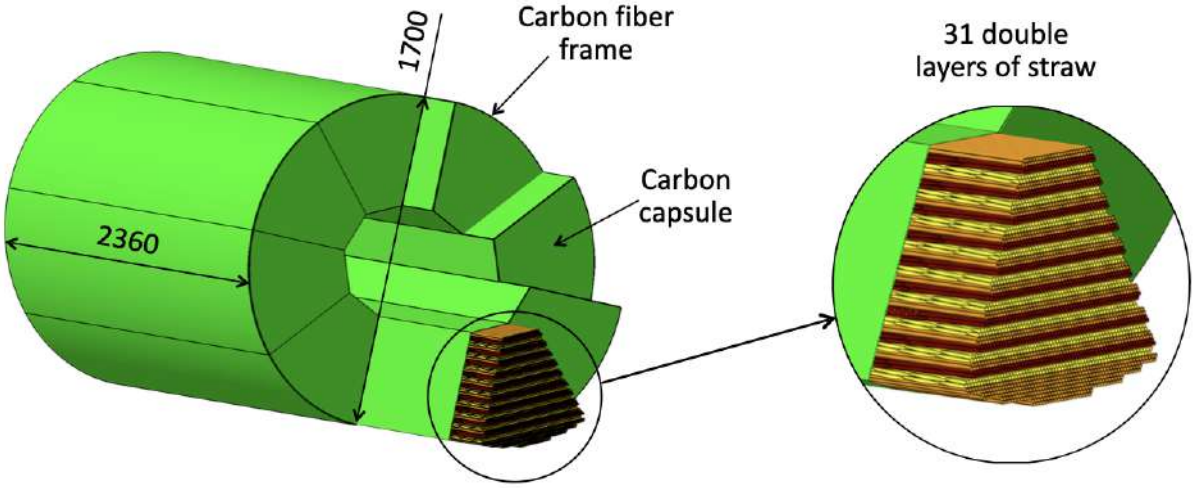

Figure 9.17: General layout of the barrel part of ST, which shows 8 modules (octants). Each module contains 31 double layers of straw tubes encased in a composite-polymer capsule.

The main axes of the straw direction are Z, U, V. The Z axis is along the beam axis. The angle between the U, V and Z axes is ± 5 degree. The value of the angles by layers is shown in Table 9.2. Each tube has a diameter of 9.8 mm. Each module is enclosed in a 400 μm thick carbon fiber mesh capsule. The capsule provides the positioning of the individual straw tubes with a 50 μm accuracy. One side and two ends of the capsule have 5 mm holes, where straw end-plugs will be fixed. The FE electronic boards, which will be connected to these plugs, will additionally serve as the capsule covers, thereby isolating the inner volume from the external environment.

The straw tubes will only be read out from one side. Each octant contains about 1100 tubes with parallel and about 2200 tubes with oblique angles to the beam direction. The total number of electronic channels

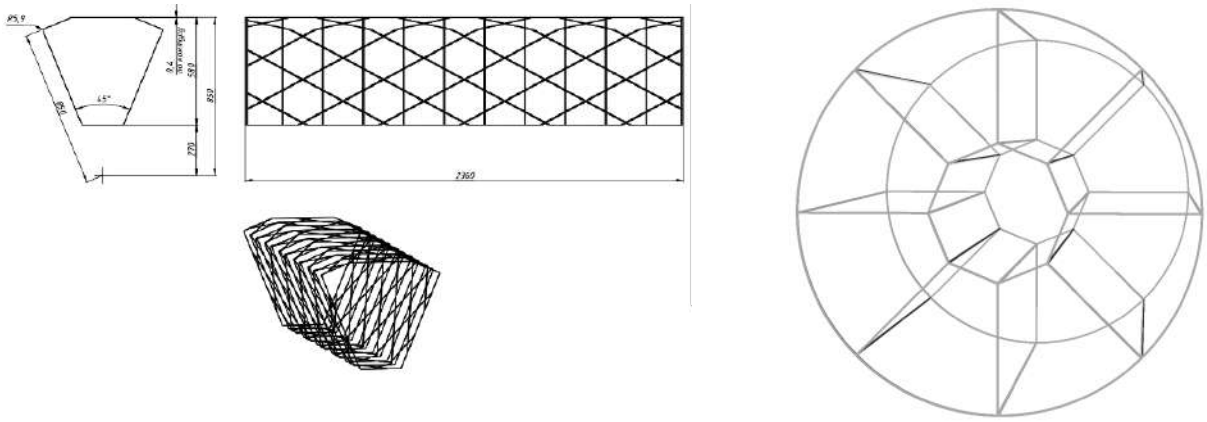

(a) (b)

Figure 9.18: (a) Power frame of a single octant. (b) The barrel supporting frame for eight ST octants.

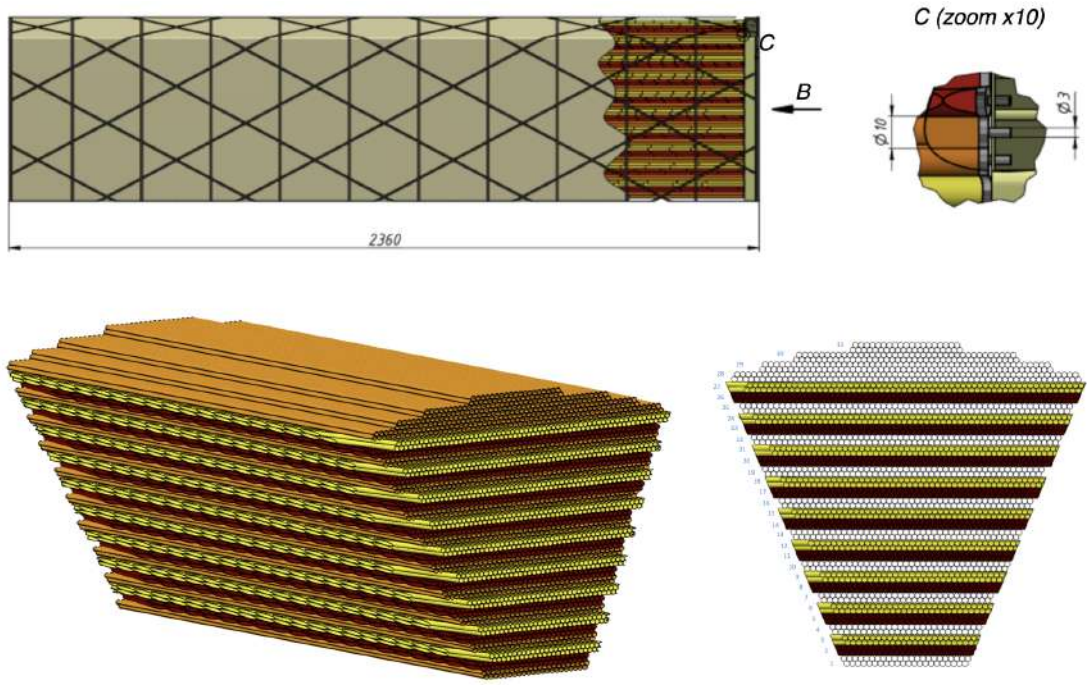

Figure 9.19: Sketch of one module (octant) of the barrel part of the straw tracker.

per octant is 3238. Thus, the total number of channels in the barrel part of ST is $3238 \times 8 = 25904$. The rigidity of the structure is assured by the low overpressure of gas inside the tubes and their fixation inside the capsule volume. The anode wire positioning accuracy is achieved by the wire fixation in the carbon fiber covers. The capsule also serves to thermally stabilize the gas, circulating inside the detector volume, and to protect the straw surface from humidity. The sketch of one octant is shown in Fig. 9.19. One meter of straw tube has a weight of 1.15 g. Thus, the weight of all the tubes in one octant with the glued end-caps is about 17 kg.

1.3.2 Assembling the straw tracker

Prior to the octant assembly, the straws of a proper length have to be prepared with the end-plugs glued to both ends of the straw. Layers Z, U, and V will be installed one by one, forming the octant. Each straw of the stereo-layers U or V will have one end positioned at one of the octant ends, while the opposite end

Table 9.2: Straw tubes in different layers of one octant of the ST barrel part.

Layer	1	2	3	4	5	6	7	8	9	10	11	12
Angle, deg	0	+5	-5	0	+5	-5	0	+5	-5	0	+5	-5
Straws, pcs.	45	83	85	53	91	95	61	99	103	73	111	111

Layer	13	14	15	16	17	18	19	20	21	22	23	24
Angle, deg	0	+5	-5	0	+5	-5	0	+5	-5	0	+5	-5
Straws, pcs.	81	119	123	89	127	131	99	139	139	109	147	151

Layer	25	26	27	28	29	30	31
Angle, deg	0	+5	-5	0	0	0	0
Straws, pcs.	117	155	158	123	103	79	39

Total			
0	+5	-5	0,±5
1071	1071	1096	3238

of the straw will be located at the octant side and will be connected to the gas pipes during the assembly.

A frame with precise holes for the straw end-plugs will be glued into the octant ends, maintaining the straw alignment. Then the anode wires are inserted into the straws, and their crimp tubes are connected to the flexible webs, as was implemented in the NA62 Straw Tracker and is shown in Fig. 9.20.

At each end of the octant, four front-end covers (one per an octant quarter) will be installed, sealing the gas volume. A 50 μm thick mylar foil, plated with 50 nm of aluminum, will be glued over the octant sides. Finally, carbon fibers will be glued onto the foil.

The ST installation procedure is demonstrated in Fig. 9.21. Two separate halves of the carbon fiber frame are inserted into the inner volume of the SPD detector prior to mounting the octants. After that, the octants are installed into the frames one by one.

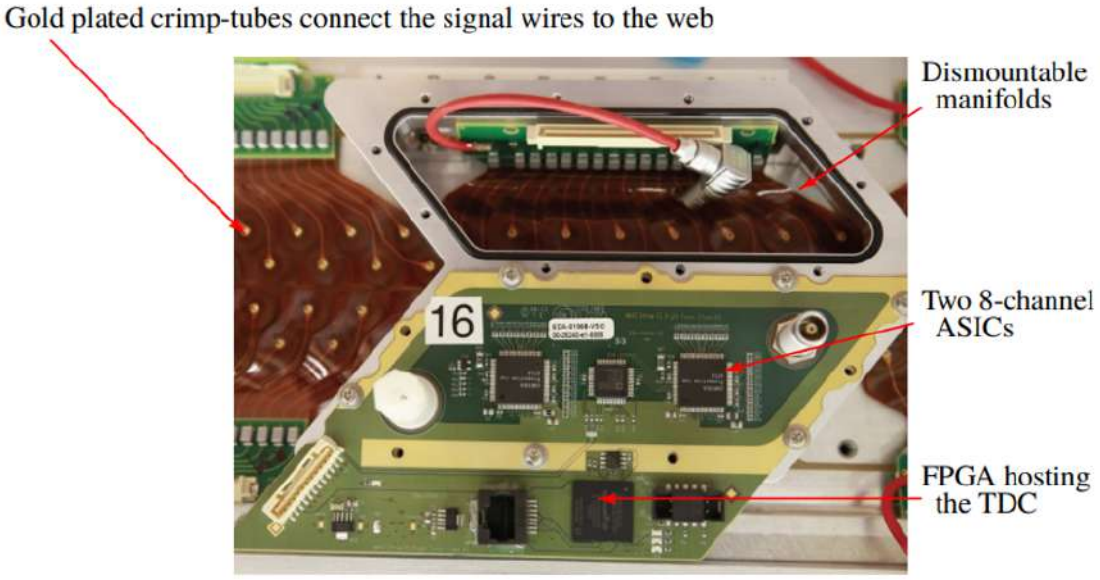

Figure 9.20: Picture of the straw end connectivity and gas manifold. A rigid-flex circuit board (web) connects high voltage to the signal wires and transmits the signal to the front-end cover. The cover also houses the high-voltage connector and feedthrough for the gas.

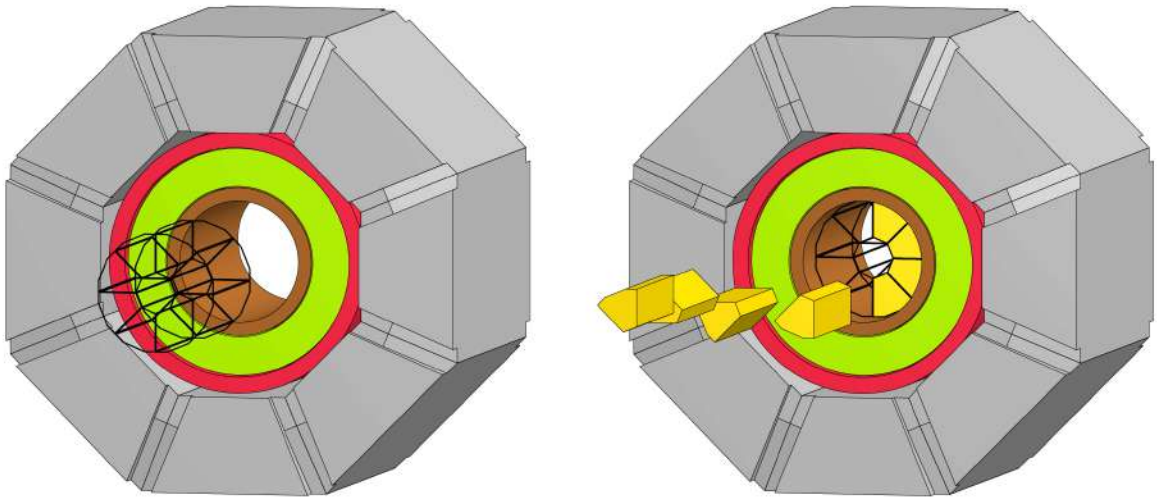

Figure 9.21: Straw tracker installation procedure. Left: installation of the carbon frame. Right: installation of the pre-assembled ST octants.

1.4 Detector components and assembly principles

1.4.1 Active web and wire connection

A cross-section of the octant end mechanical structure holding the straws is shown in Fig. 9.22 (a). A carbon frame has holes for precise positioning of the straws and wires. The modularity in terms of HV, gas supply, and a readout system is represented by four sections containing about an equal number of straws. Removable partitions for the gas manifold and a dedicated polyurethane joint for gas tightness were developed. The partitions also serve as supports for the so-called cover, which contains the front-end electronics, high-voltage and gas connections. Polyetherimide (PET) insulating sockets are glued between the straws and the frame.

High voltage is transfered to the wire by an active web, which also transmits the signal back to the front-end electronics. The web is a multi-layer rigid-flex printed circuit board having two connectors per straw, namely one for HV and one for the signals. The web has a connector to be plugged to the backside of the cover, as shown in Fig. 9.22 (b). The cover does not only provide the leak tightness of the manifold, it also comprises the front-end electronics, high-voltage and gas connections.

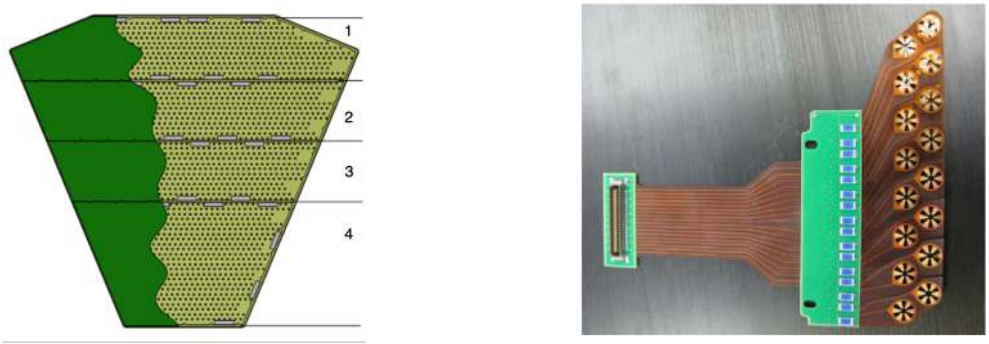

(a) (b)

Figure 9.22: (a) Four gas volumes of an octant. (b) Detail of the rigid-flex circuits board (web) that connects to the straws (ground) and the wire (high voltage and signal).

The wire is tensioned and positioned using a copper tube inserted in the so-called connection, shown in Fig. 9.23. The copper tube connects to the second layer of the web, which brings high voltage to the wire and the signal back to the front-end electronics.

1.4.2 Measurement of the straw straightness

Once the straws are fixed at both ends in the detector frame, their straightness is measured layer by layer with two light sources and a CCD camera/microscope. The two laser diodes illuminate the straw and the camera/microscope takes a photograph of the straw section. The system is calibrated using a wire stretched from top to bottom, parallel to the straws. A stepper motor moves the camera, and a picture is taken at 10 equidistant positions along the straw. A dedicated LabVIEW® program transforms the pictures into a black and white image and finds the two straw edges automatically. The program then calculates the position of the straw center (straightness) in the XY-plane and the diameter of the straw.

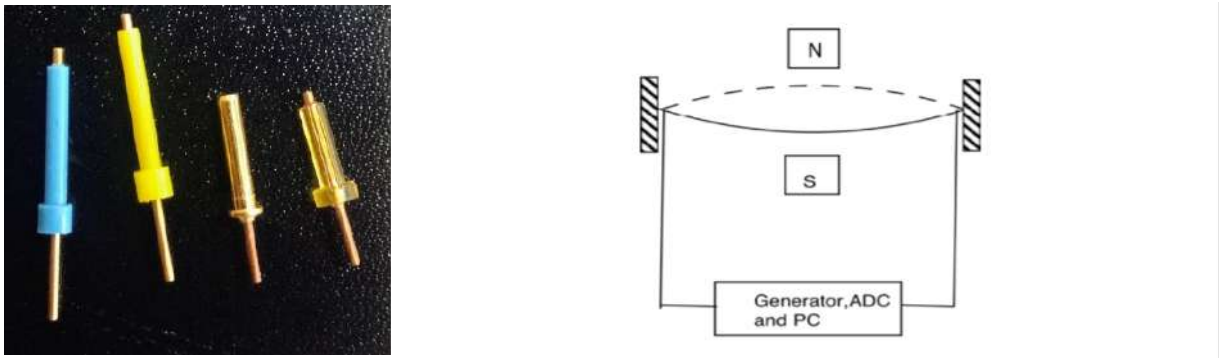

(a) (b)

Figure 9.23: (a) Connection plugs. (b) Schematic view of the wire tension measurement device.

1.4.3 Wiring

A gold-plated tungsten wire from Toshiba with a diameter of 30 μm is chosen for anode. The limit of elastic deformation has been measured up to 150 g and the rupture occurs around 220 g. The nominal wire tension is set to 90 g. The detector is placed in a horizontal position and the straw resistivity is measured. All straw diameters are measured and recorded in the logbook. The webs are then installed and the ground circuit is fixed to the inside of the straw with the help of the connection plug, which is shown in Fig. 9.23 (a). A tight fit is necessary to ensure a good electrical contact. The ground petals are formed with a special tool to facilitate the insertion of the PET plugs. A wire with a diameter of 0.1 mm (”needle” wire) is blown through the straw. The 30 μm wire is fastened to the needle wire and kept under a small tension at all times during installation to avoid kinks. The wire is gently pulled through the straw. From both sides, the 30 μm wire is inserted in the copper tubes and the copper tubes are then inserted through the electronic circuit into the contact plugs. Once the wire is fixed to the web side, a 90 g weight is suspended to the wire on the opposite side and fixed. The electrical continuity between the two pins is checked, as well as insulation between wire and straw (broken wire). After wiring one layer, the wire tension is measured and a HV test is performed to measure the leak current, which should not exceed 1 or 2 nA per high voltage group at 1600 V.

1.4.4 Measurement of wire tension

The full straw tracker contains a total of about 26000 anode wires, and the wire tension need to be verified during and after installation. The wire resonance frequency is close to 50 Hz for a tension of 80 g and a wire length of 2200 mm. Since 50 Hz is close to the frequency of the 220 V voltage supply, in order to avoid this frequency, the nominal wire tension was set to 90 g. The acceptable values of wire

tension during the module production are between 85 and 95 g. The upper limit of 95 g is considered to be comfortably below the elastic limit of 150 g, while the lower limit is high enough to allow good operation of the straw. Electrical instability of the wire was found for tensions below 35 g. Therefore, to minimize electrostatic deflections on the wire, the lower limit is set to 85 g.

The principle of measuring wire tension is presented in Fig. 9.23 (b). Namely, the wire oscillations are stimulated in an external magnetic field with the help of a current generator, and the resonant frequency of the wire is measured. The current induced on the wires will be amplified with a high-input impedance amplifiers and an input signal threshold (typically of about 1.5 mV). Signals will be digitized by a PC based A/D board and the measured frequency will be translated into applied wire tension T (in grams), following the formula:

$$T = \frac{4\mu L^2 \nu^2}{a}, \tag{9.3}$$

where L is the free wire length in cm, ν is frequency in Hz, μ is the mass per unit length in g/cm and a is the gravitational acceleration. Uncertainties in the measured tension arise from variations in the wire diameter and the length of the vibrating wire. The minimum uncertainty can be estimated to be of about 1%. The readout electronics, connected to a cell of 16 straws, measures the main resonance vibration frequency of each wire. The magnetic field near the tested wire must be at least 100 G. The operator can modify the parameters of the pulse generator and Fourier analysis on the Labview-based computer panel. The tension of the wires will be measured during the stringing process itself, and a final global wire-tension measurement of all wires in the module will be carried out before the next assembly step. The results of the measurement will be written to the production database. Loss of wire tension can happen between module assembly at the assembly hall and arrival at the SPD hall, so the wire tension will be measured again after delivery to the nominal position. Major attention will be paid to wires, which show a tension loss of more than 10 g. These wires will be investigated carefully and replaced if necessary.

1.4.5 Gas tightness tests

The next stage will be to verify the joints glued between the straws and the frame. It is important to perform this test at this stage because the straws and their joints are still easily accessible and repairable in case of a problem. A dedicated gas-tightness setup is to be used to verify the quality of about 8000 joints (per octant), glued between the straws and their end-plugs, and between the end-plugs and the straw support frame. The system contains a temperature sensor, pressure gauges, vacuum stand and a system of valves and pipes. Straws and gas manifolds will be filled with Ar from a bottle with a pressure of 100 mbar above atmospheric pressure. The volume of the octant to be tested is about 1 m^3. The leak rate (mbar$\times$ l/sec) will be evaluated by measuring the pressure drop inside the straws as a function of time, once the pump has been stopped. A module will be approved for subsequent assembly, whenever the measured leak rate does not exceed 10^{-2} mbar$\times$l/sec. Nevertheless, every effort will be made to get the leak value as low as possible.

1.5 Gas system

The gas system consists of two parts. First, the mixer system which delivers quantity, mixing ratio and pressure conditioning to downstream elements. Second, the distribution system, which delivers the gas in well defined quantities to the individual detector components.

1.5.1 Gas system requirements

The total gas flow chosen corresponds to a normal gas flow rate of $2 \div 4$ cm^3/min per straw. The gas modularity is optimized in order to minimize the number of lines between the detector and the distribution

racks, and, on the other hand, to minimize the loss of performance in the case of an accidental leak in any module.

1.5.2 Mixer

The detector shall be supplied with a constant gas mixture of Ar:CO_2=70:30 with a precision better than 1%. The total flow of the mixer will be 1500 l/h. Each primary gas line is equipped with a Digital Mass Flow controller to measure the component flow with appropriate accuracy. An output pressure regulator adjusts the downstream pressure from 0.2 to 2 bar. The control system provides a flow an independent mixing ratio and adequate error handling. The mixer has to automatically follow the demands of the distribution system.

1.5.3 Gas distribution

The gas from the mixer is distributed to the eight gas distribution racks, one for each octant. The major design criteria of the distribution system is the uniform gas supply to each cell with adequate separation capabilities, in case of pressure loss, due to a leaking straw. Each octant is divided into four gas volumes, as it is shown in Fig. 9.22.

1.6 Aging studies

In order to validate the different components and materials in the detector, a dedicated prototype was built. The prototype contains two straws: one with aluminium coating and another with copper/gold. The straw end-pieces were made from ULTEM, and the connection to the straws was made with a section of the web. The wire is the 30 μm gold-plated Tungsten from Toshiba, foreseen for the chamber production. Final crimp tubes were used for electrical and mechanical connections of the wire to the web. The prototype was mounted in the CERN aging test facility. A gas mixture of 70% argon and 30% CO_2 was used. The parameters during the aging test are summarized in Table 9.3.

Table 9.3: Parameters of setup for aging testing.

Gas mixture	Gas flow	Current	Total charge	Irradiation area	High voltage	Fe-55 scan slit size
Ar (70%)+ CO_2 (30%)	0.5 cm^3/min	280 nA	0.27 C/cm (500 hours)	10 mm	1700 V	1 mm

A scan with a Fe-55 source is made at intermediate irradiation levels along the straw length from 10 mm to 75 mm. The results are shown in Fig. 9.25. No change in amplitude can be seen up to a total charge of 0.27 C/cm. The estimated accumulated charge for the hottest straws in the experiment is 0.04 C/cm. After the initial run with Ar/CO_2, it was decided to dismount the prototype and investigate the wire and the inner surface of the straw around the irradiated region.

2 End-cap part of ST

The design of the ST end-cap has to satisfy the following criteria. The detector must have the shape of a disk, have a relatively small central hole, which is defined by a vacuum beam pipe, and have a small amount of matter in the sensitive region of the detector. The detection layers should be thin, and the number of layers should be sufficient to identify particles via dE/dx measurement.

For efficient registration of interactions with a large multiplicity, a detector with drift tubes, arranged so that they form an X, Y, U, V coordinate system, is proposed. Each coordinate plane consists of two

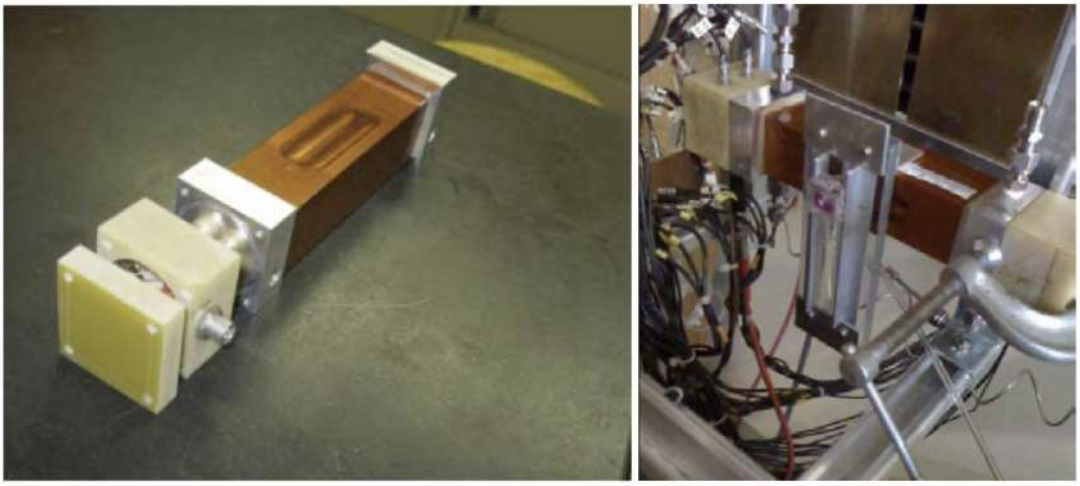

Figure 9.24: Straw prototype for material validation (left), mounted in the setup (right).

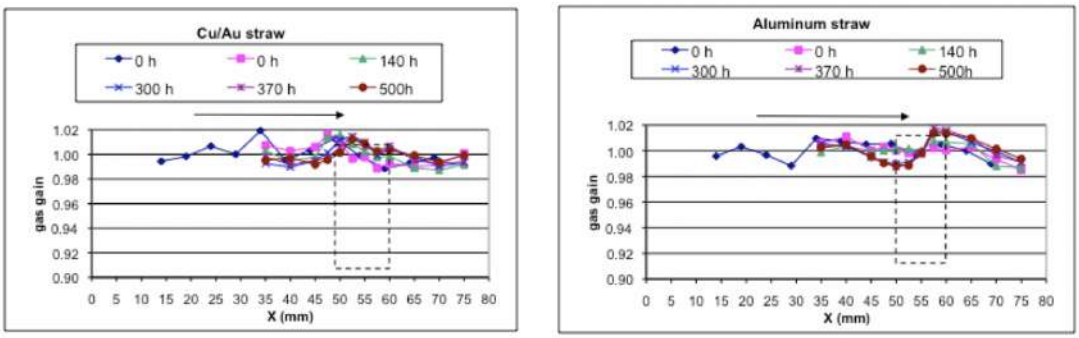

Figure 9.25: Scan of signal amplitude along the straw length for straws with two types of coatings Cu/Au (left) and Aluminium (right). Different graphs correspond to different accumulated charge.

halves separated by a distance for installation on a vacuum tube, as shown in Fig. 9.26. All coordinate planes are mounted sequentially on a solid base that can be attached to other power element of the SPD detector.

It is possible to implement such a detector on the basis of thin-walled drift tubes, made by winding two ”kapton” tapes, as shown in Fig. 9.27 (a). The technology of manufacturing such detectors is being successfully developed in LHEP JINR. Over two decades, the straw chambers have been created for several large experiments, such as SVD-2 and Thermalisation at Protvino, ATLAS, COMPASS, and NA64 at CERN, CBM in Darmstadt, etc.

It is supposed to use straw tubes with a diameter of 9.56 mm, made of two layers of polyimide film. The outer layer of the straw tube consists of a polyimide tape with a thickness of 25 microns. A copper coating with a thickness of 100 nm is applied on one side. The surface resistance is 1 ± 0.1 Ω/square. Polyurethane hot-glue coating with a thickness of 4 ± 1 μm is applied on the other side. The inner layer of the straw tube consists of a similar polyimide tape. The layer of hot glue is applied to one side, and on the other side - a layer of aluminum 0.2 μm thick. Graphite with a thickness of 6 ± 2 μm is applied on aluminum. The resistivity of this surface is about 10 Ω/square. The outer and inner tapes are glued together on a calibrated rod, as shown in Fig. 9.27 (a), heated to 170 $^{\circ}$C.

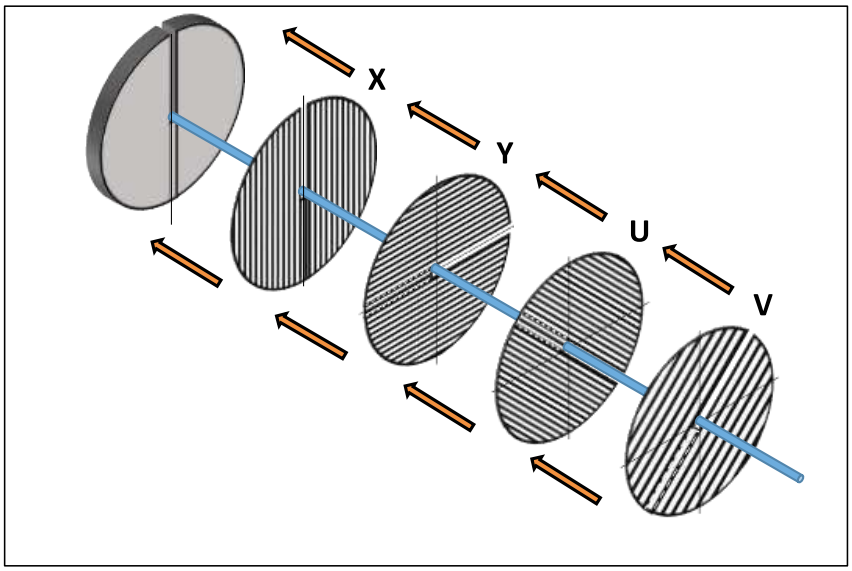

Figure 9.26: General layout of the ST end-cap detector with drift tubes.

(a) (b) (c)

Figure 9.27: (a) Twisted structure of the straw tube. The picture illustrates a winding on a precision rod. The end-plug (b) and the crimping pin (c) are used to fix the anode signal wire.

2.1 Elements of technology for assembling twisted straw tubes

Before assembling the detector or its parts, each straw tube is filled with precision steel balls with a diameter of 6.010 ± 0.003 mm or 9.525 ± 0.003 mm for the straw tubes of the corresponding diameter. Filling with balls occurs automatically. It takes about 1 minute to fill a 1.8 m long straw tube. Tubes with balls are assembled into the size of a detector on a precision table and glued together to form a single straw array. Araldite 2011, VK-9, and ALK-5.8 are used for gluing planes and other structural elements. The amount of glue used does not exceed 60% of the weight of the straw tubes. After removing the straw balls, the tubes are installed in a common plane on a large precision table.

The end-plug and crimp pins, located at both ends of the straw, are used for the installation and positioning of the anode signal wire. The end-plug and the crimping pin are shown in Fig. 9.27 (b) and (c), respectively. The positioning accuracy of the signal wire is not worse than 100 μm. The end-plug has a bronze spring contact that connects the inner conductive layer to the ground. It also has two longitudinal grooved channels for supplying a gas mixture.

Internal supports of the signal wire (spacers) are installed inside the tubes and serve to prevent sagging of the signal wires. Spacers are pre-glued to the signal wire in the tubes with a length of more than 800 mm. The drawing and appearance of the spacer are shown in Fig. 9.28.

External supports serve to reduce the sagging of the straw tubes. The support elements are made of thin

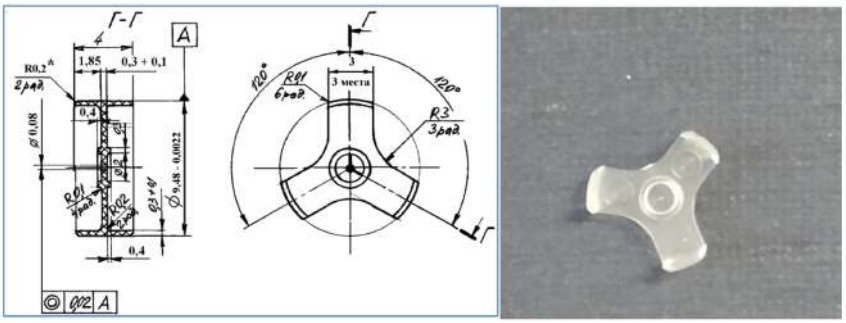

Figure 9.28: Technical drawing (left) and photo (right) of the internal backing of the signal spacer wire.

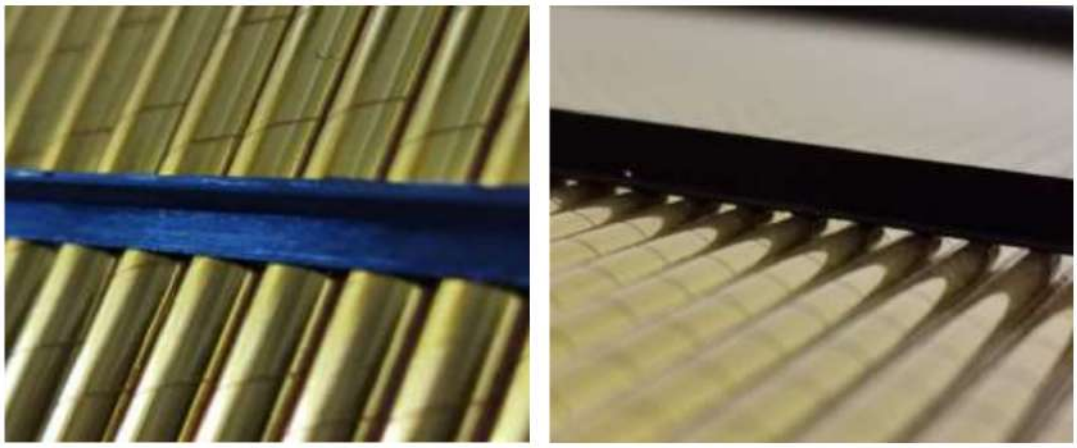

Figure 9.29: Example of carbon fiber strips used as external support for the straw tubes.

carbon fiber plates, glued to the tubes. An example of such elements is shown in Fig. 9.29. Transverse T-shaped strips of 0.5×9 mm^2 are used to increase the geometric stability of the transverse dimensions of the straw array, which are glued in the direction perpendicular to the straw axis of the tubes.

The positioning accuracy of each signal wire in the straw tubes is determined by the accuracy of the straw manufacturing and the accuracy of the plastic end-bushings and pins. The general positioning of the tubes in the detector plane is carried out on a precision table using precise rulers, as a result of which the accuracy does not exceed 0.1 mm.

2.2 The main characteristics of twisted straw tubes

The main characteristics of the drift detectors are given in Table 9.4.

2.3 Radiation properties of twisted straw tubes

Properties of the materials that are usually used for the straw production are given in Table 9.5.

Figures 9.31 - 9.32 illustrate the results of calculating the radiation thickness of a straw detector consisting of two layers shifted by half the diameter of the tubes. The tubes in each layer are glued together without gaps into a single coordinate plane.

2.4 Coulomb scattering in the straw material

A charged particle passing through the medium is deflected repeatedly on the nuclei of the medium. Most of this deviation is due to Coulomb scattering on the nuclei. For many applications, it is sufficient to use the Gaussian approximation for the projection of the angular distribution with a width of θ_0, for

Table 9.4: Main characteristics of the drift straw tubes.

Drift tube diameter	6 ÷10 mm
Gas amplification at 1800 V	2.5×10^4
Operating voltage range	200 V
Electron collection time for $B = 0$ T	0 ÷100 ns
Electron collection time for $B = 2$ T	+20%
Registration threshold	2÷3 fC
Resolution when measuring drift time	100÷200 μm
Registration efficiency for a two-layer detector at 1 MHz	99.7%
Gas mixture	Ar:CO_2 = 70:30

Table 9.5: Characteristics of the materials used in the construction of the straw tubes.

Material	Density, g/cm^3	Rad. length, g/cm^2	Rad. length, cm
Tungsten, W	19.3	6.76	0.35
Graphite, C	2.2	42.70	19.4
Polycarbon Lex	1.2	41.50	34.6
Kapton	1.4	39.95	28.5
Acrylic (PMMA)	1.19	40.55	34.1
Polystyrene	1.06	43.79	41.3

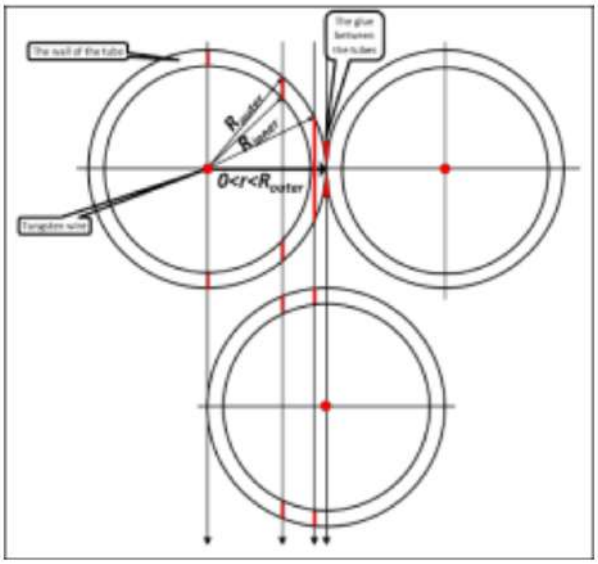

Figure 9.30: A typical arrangement of tubes in a two-layer detector, where the layers are shifted relative to each other by half the diameter.

2903 the scattering medium in units of radiation length $10^{-3} < x/X_0 < 100$:

$$\theta_0 = \frac{13.6\ MeV}{p\beta c} z\sqrt{x/X_0} \times (1 + 0.038 ln(x/X_0). \tag{9.4}$$

2904 For 8 double-layer single-coordinate chambers with a diameter of straw 10 mm and a radiation thickness

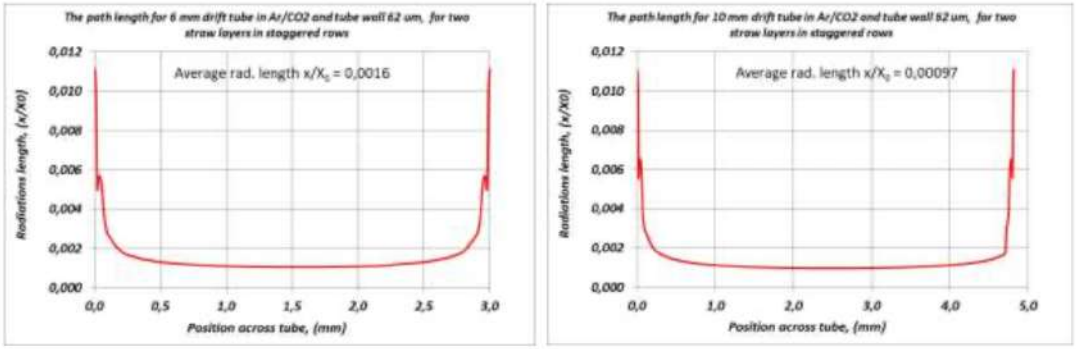

Figure 9.31: Dependence of the thickness of the two-layer straw detectors in radiation units x/X_0 on the place of passage of the particle through the two layers of tubes for two diameters of a straw.

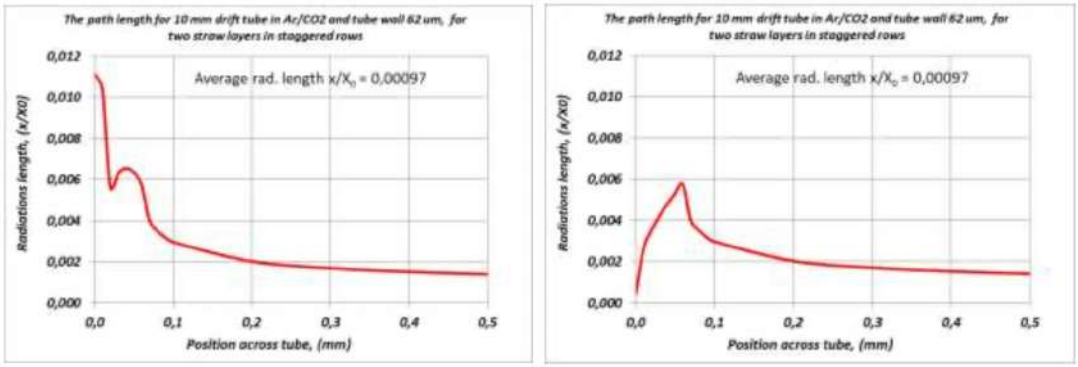

Figure 9.32: A more detailed picture for particles passing between tubes of the same layer. The figure on the left takes into account the adhesive layer between the tubes of the first layer and the substance of the signal wire 30 μm in the second layer. On the right, only the substance of the tube walls in two layers without signal wire and glue is taken into account.

$x/X_0 = 9 \times 10^{-4}$ and for a single-charged particle with a momentum p = 1 GeV/c the multiple scattering angle θ_0 is 9.4×10^{-5} that corresponds to a deviation at a 1 m baseline of 0.094 mm. For the straw tubes of 6 mm ($x/X_0 = 1.64 \times 10^{-3}$) the corresponding numbers are 1.3×10^{-4} and 0.13 mm. For the detector frame material made of aluminum 0.8 cm, radiation thickness ($x/X_0 = 0.1$) the values θ_0 and spatial deviation are 3.7×10^{-4} and 0.37 mm, respectively.

2.5 Humidity and ambient temperature. Influence on the parameters of the tubes

The straw tubes are made by winding of kapton tapes on a rod, followed by sintering. It is known that the walls of the tubes change their size depending on the temperature and humidity of the environment. During the development of straw detectors for the COMPASS experiment in 2002, estimates of the elongation value depending on humidity were carried out. The elongation of the straw tubes depending on humidity is shown in Figures 9.33 and 9.34. The test showed that the length of the straw tubes is preserved after they are dried with dry air, i.e. the tubes have a range of elastic deformation.

The same study was carried out when creating straw detectors with copper-coated tubes for the NA64 experiment in 2019. As a result, the elongation value of the straw tubes was found to be 1.4 ± 0.2 mm/m for copper-coated tubes with diameters of 6 mm and 10 mm for a change in relative humidity from 50% to 80%.

The temperature coefficient of expansion of the straw tubes 25.2×10^{-6} K^{-1} is mainly determined by the material of the tube walls and does not depend much on the diameter and type of coating. Changing

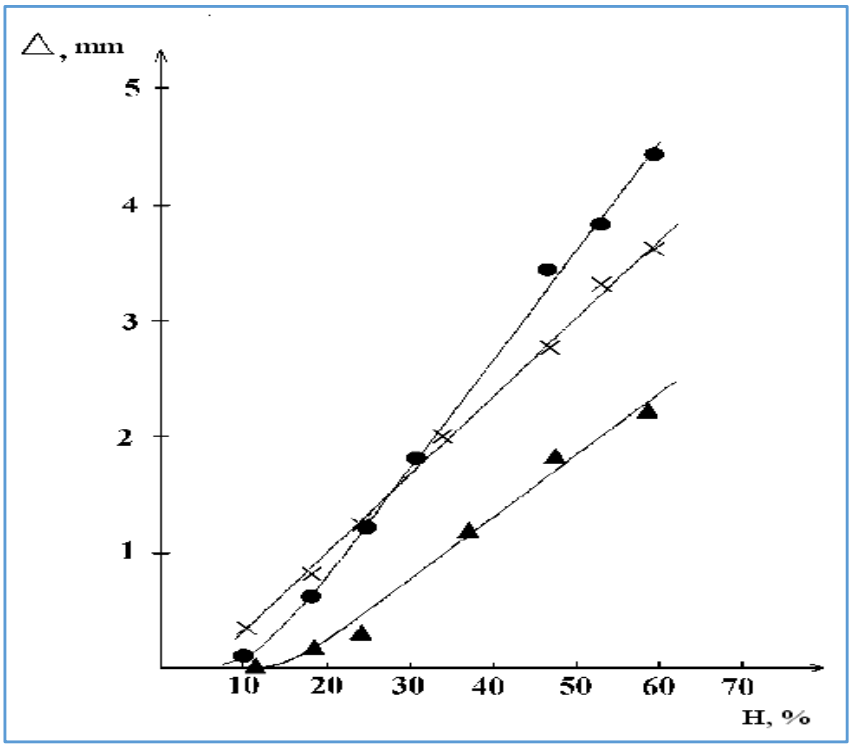

Figure 9.33: Dependence of the elongation of single tubes ∅6 mm and ∅10 mm with a length of 3.2 m employed in the COMPASS experiment. A large spread of data is observed for different tube materials.

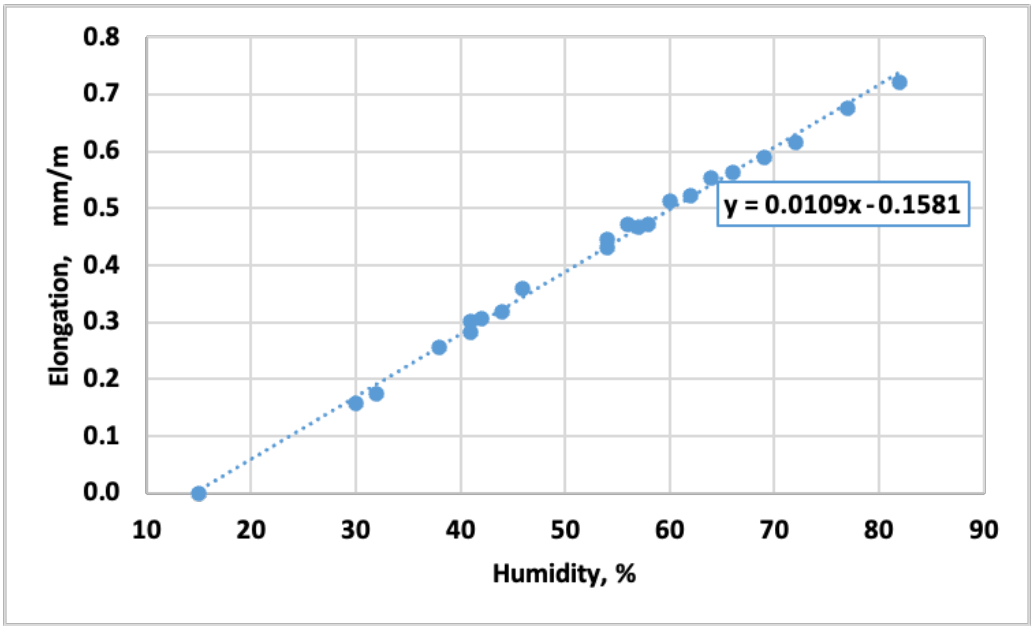

Figure 9.34: Effect of humidity on the elongation of tubes with a diameter of 10 mm and carbon/kapton coating.

the temperature by 28 degrees elongates the straw tube by 0.7 mm. Elongating the tubes from humidity by 0.7 mm/m is equivalent to changing the temperature of the straw detector from 20 to 48 degrees. In our case, the detectors are in normal conditions at a temperature that will vary within 5÷10 °C. This may cause a change in the length of the tubes by 0.1 ÷ 0.2 mm/m. This temperature dependence must be taken into account when developing detectors. For comparison, the coefficients of thermal expansion

of some materials that can be used for construction are (in units of 10^{-6} K^{-1}): 23 for kapton, 18 for aluminium, and 27 for mylar.

The presented results show that it is advisable to install straw planes in the frame of the chamber at a temperature not higher than the operating temperature of the chamber and humidity not lowers than the corresponding elongation will be in the future. The effect of different operating and assembling temperature/humidity can be compensated by applying additional compressive forces to the frame elements during the assembling procedure, or by stretching the frame after installing the straw tubes, compensating for the influence of climatic factors.

2.6 Mechanical properties of the straw tubes

Mechanical tests were carried out for the straw tubes with a diameter of 6 mm and 10 mm. The tubes were subjected to stretching. The test results are shown in Fig. 9.35 (a), from which it can be seen that in order to compensate for the influence of humidity, it is enough to stretch the frame of the detector by 0.7 mm per meter of straw length. At the same time, it was shown that the tensile force applied to the tube of about 5.5 N does not cause plastic deformations of the tube for a long period. Measurements were carried out for about 2 years. When the twisted tube is stretched, twisting may occur. The study of this effect was done at high gas pressure inside the tubes. The practical absence of twisting was shown, see Fig. 9.35 (b). The pressure of 2 atm stretches the tube with a force of 5.5 N (570 g of force).

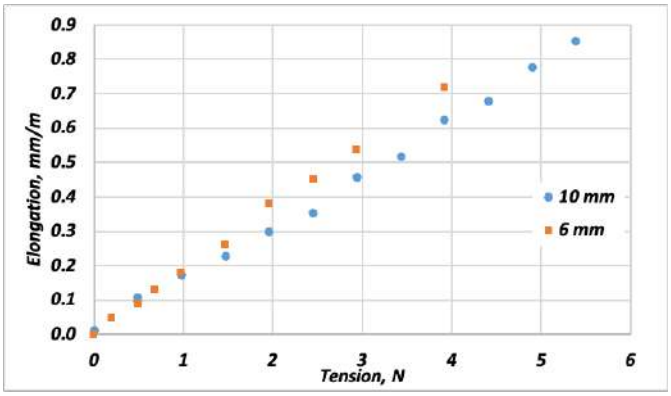

(a)

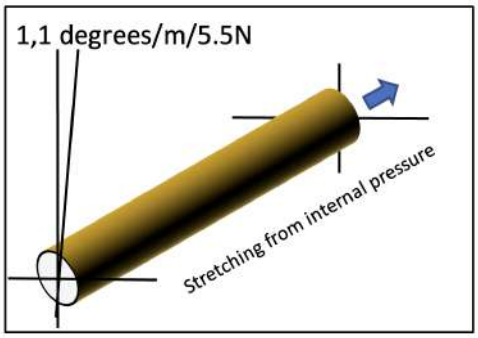

(b)

Figure 9.35: (a) Elongation of straw tubes depending on the applied force. Round dots are for tubes with a diameter of 10 mm, while square dots for 6 mm tubes. (b) The twisting angle of a straw tube with a diameter of 6 mm when stretched under pressure. Angle is 1.1 degrees for 1 m long tube and tensile force of 5.5 N directed along the tube.

The tensile force can be created by excessive pressure inside the tubes when gluing the tubes into the frame. This pressure changes not only the tube length, but also its diameter. Thus, at an excessive pressure of 0.5 atmospheres, there is an increase in the diameter of the tube by 0.5 μm, which leads to a change in the positions of tubes and an increase in the width of the array of 288 tubes by 0.14 mm.

2.7 End-cap design based on a two-layer array of twisted tubes

End-cap is proposed with an octagonal arrangement of the drift coordinate planes at an angle of 45 degrees, which form an X, Y, U, V coordinate system, see Fig. 9.36 (a). In total, 8 coordinate planes are supposed to be used in one end-cap. Each coordinate plane consists of two halves of a disk with an interval for installing a vacuum tube. The thickness of one coordinate plane is 30 mm. Eight coordinate planes are mounted together, forming a rigid block, 240 mm thick. A free octagonal zone 150 mm wide is formed in the center of the block, in which a vacuum pipe of accelerator with a diameter of up to

100 mm is located. The assembled end-cap must be put on the vacuum tube and, together with the rest of the internal detectors, attached to the external part of the SPD installation. The common view of the end-cap is presented in Fig. 9.36 (b).

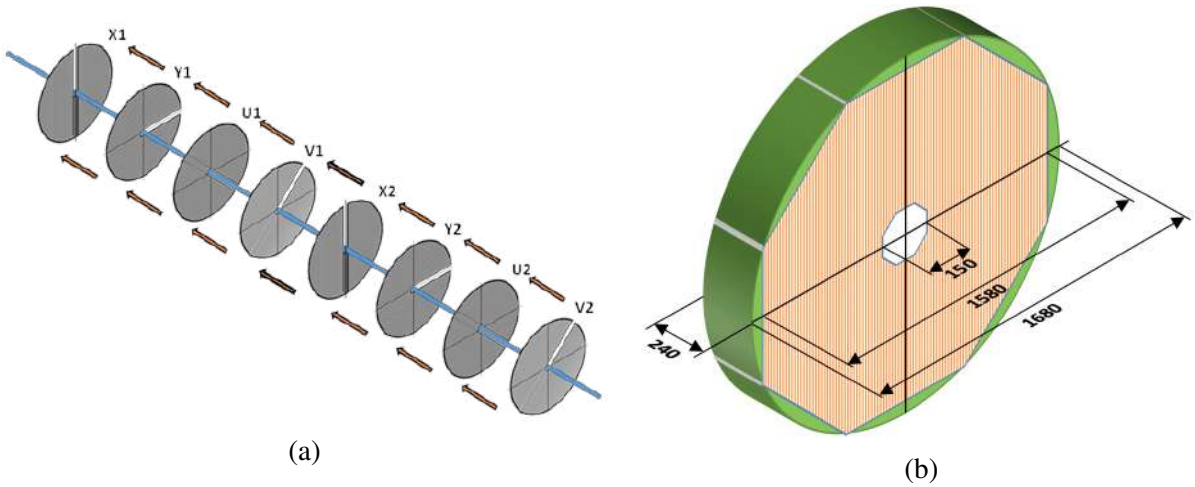

(a) (b)

Figure 9.36: (a) ST end-cap consisting of 8 coordinate planes assembled together. (b) Common view and main dimensions.

Figure 9.37: Four double-layer planes with a central gap for a vacuum tube are depicted.

As mentioned above, the tubes in the detector layers must be pre-stretched before gluing into the detector frame. For this purpose, a special technological frame is made, into which all the tubes of the array are glued before installation of the signal wires. Frame size is 2×2 m^2, see Fig. 9.38. Then the frame is stretched by mechanical screws together with an array of tubes to the required compensating size. The compensating elongation of the array of tubes should be $0.7 \times 2 = 1.4$ mm for the tubes 2 meters long. An array of tubes is glued in a stretched state on a precision table into the detectors frame, and each tube is cut along the contour of the frame. The second array is also glued to the technological frame with a half-shift in the diameter of the tubes, stretched and glued to the chamber frame from the reverse side. Frame thickness is 2 mm of carbon fiber, width is 50 mm.

Each half of the array consists of $72 \times 2 = 144$ straw tubes with a diameter of 9.56 mm. The width of the array is 688.3 mm. There is a total of 288 tubes in the two layers of one chamber, which must be pre-stretched with a force of $5\text{N} \times 288 = 1440$ N (14.6 kg load). Calculations carried out in the Inventor program show that the deformation of the chamber's frame does not exceed 50 μm. Further installation

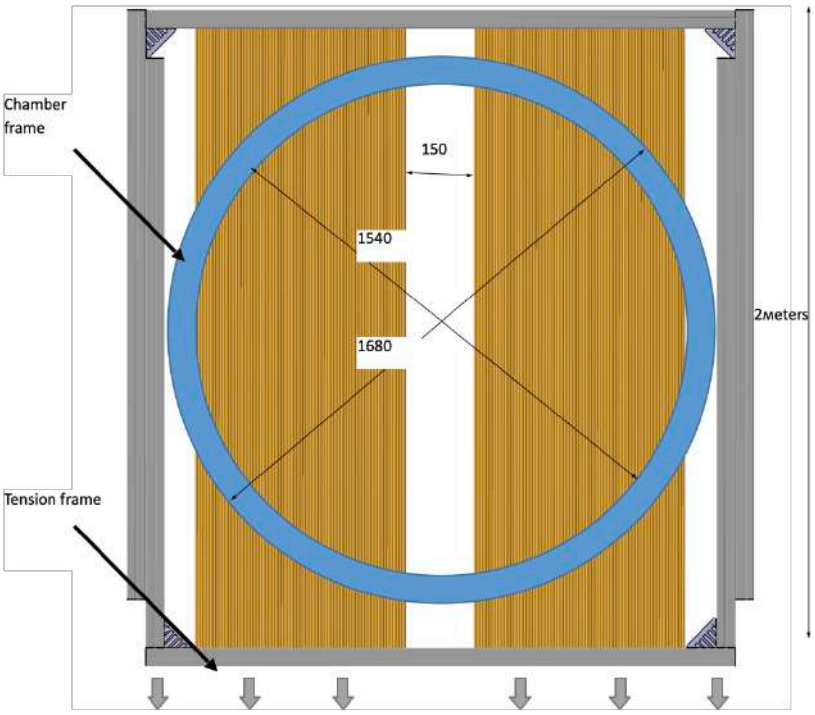

Figure 9.38: Pre-tensioning device for straw arrays.

(a) (b)

Figure 9.39: (a) Technological equipment for assembly. (b) Octagonal rotary platform and a portable honeycomb board for assembling are shown. The diameter of the portable board is 2300 mm, the thickness is 50 mm.

of the signal wires, gas supplies, and matching electronic circuits (motherboards) is carried out according to the proven standard technology. The straw planes are assembled on a rigid portable honeycomb board on a rotatable octagonal frame shown in Fig. 9.39.

2.8 Front-end electronics

The electronics, which are located directly on the chambers, perform the function of matching, amplifying and integrating straw charge signals, as well as providing high voltage to the signal wires of the detector. One straw layer consists of 288 registration channels. 9 ”motherboards” and 9 amplifiers for 32 channels will be required to read information from one layer. The diagram of the 32-channel moth-

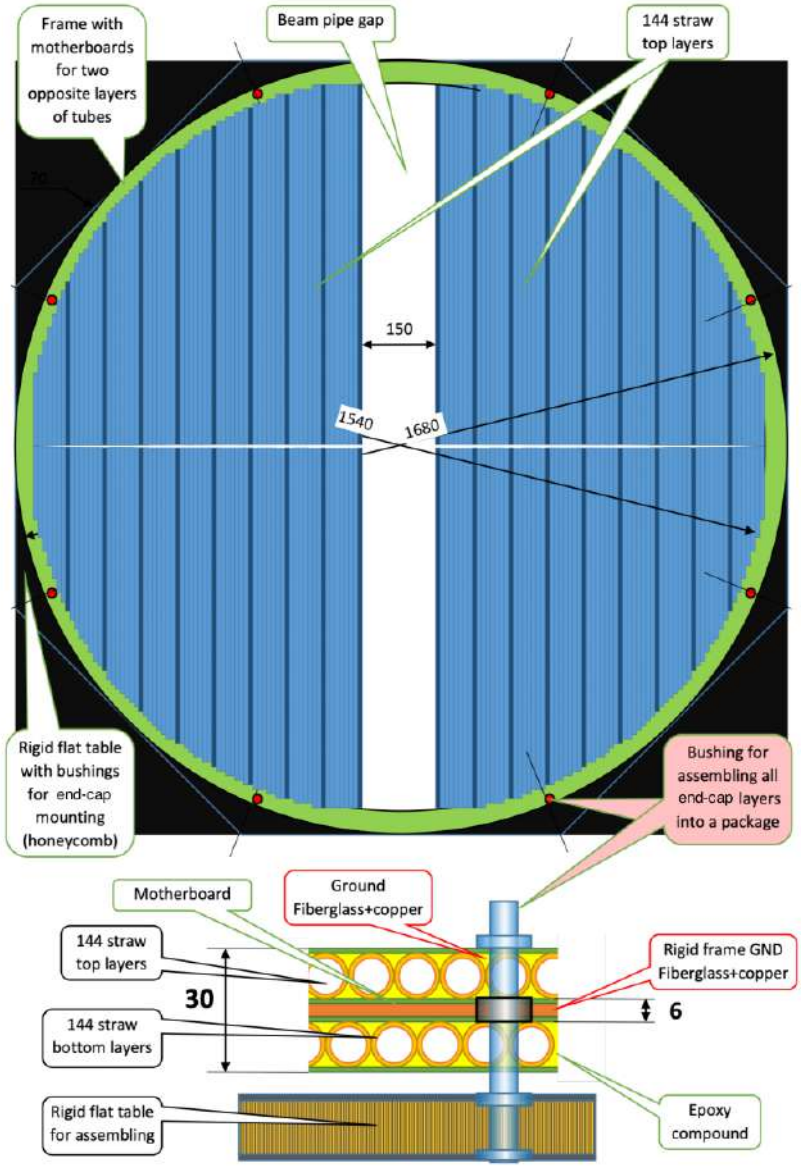

Figure 9.40: One of eight coordinate planes with a central gap for the installation of a vacuum tube. A technological honeycomb portable board is also shown.

erboard is shown in Fig. 9.41. In total, for two end-caps with 16 coordinate layers of 4608 registration channels, 144 motherboards and 144 amplifiers will be required. Subsequent recording electronics are being developed and will be described in Section 9.3.

2.9 End-cap design option with annular cylindrical frame

An end-cap will consist of eight ring straw chambers, deployed relative to each other. Each chamber consists of two layers of straw mounted in an annular carbon fiber frame with an outer diameter of 1510 mm and a thickness of 5 mm. Total thickness of one end-cap is 400 mm. The straw layers are shifted relative to each other by the value of the straw radius, see Fig. 9.42. The rows are arranged along the chords of the frame. The working length of the rows in the chamber varies from 360 mm to 1500 mm, depending on the location of the rows. A section of the frame with holes, in which straw tubes are installed, is shown in Fig. 9.43.

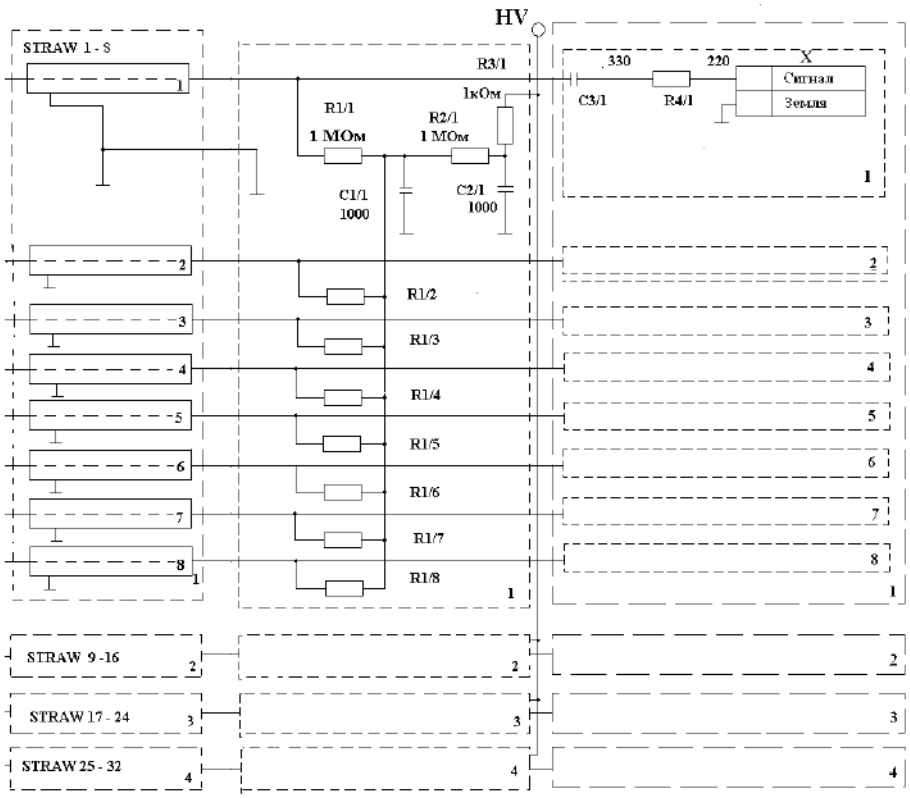

Figure 9.41: The scheme of reading signals from one group of 32 straw channels – ”motherboard”.

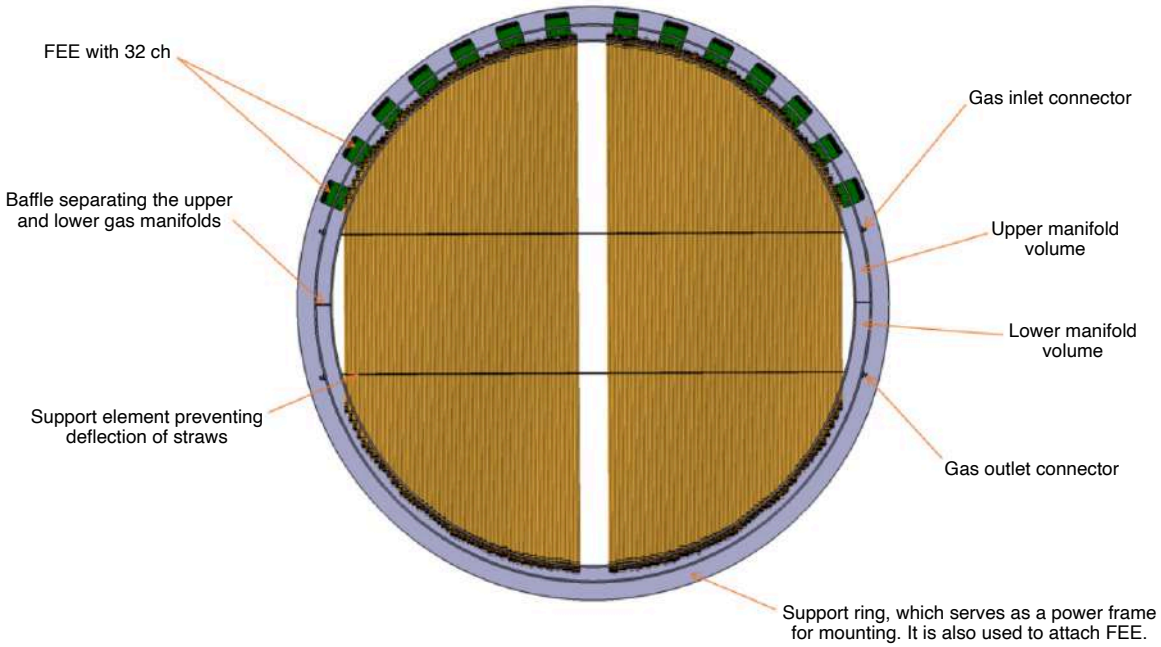

Figure 9.42: Cross-section view of one chamber indicating possible layout of the readout electronics and gas manifolds.

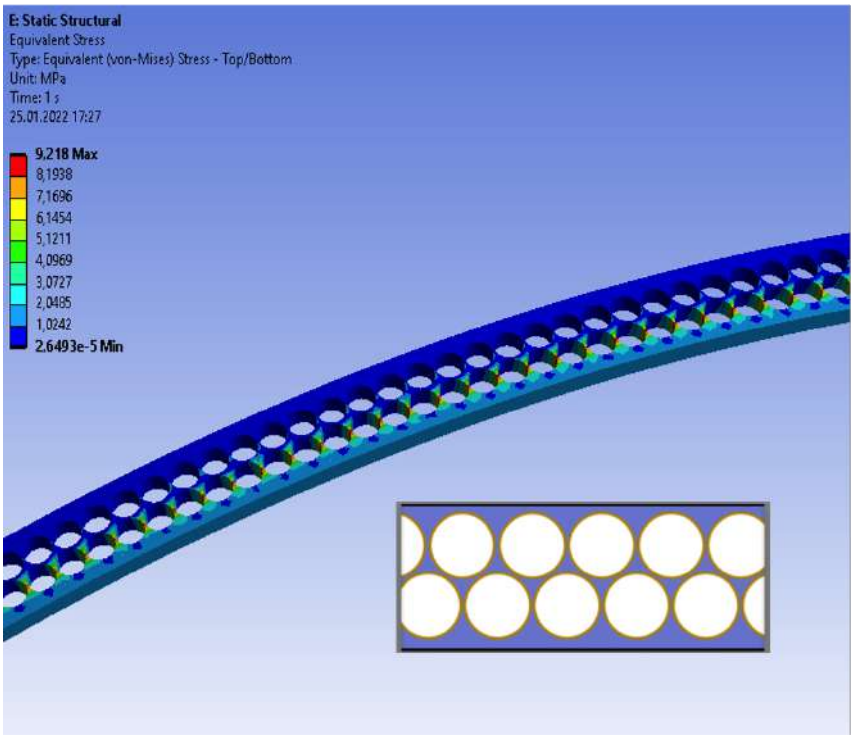

Figure 9.43: Section of the frame with holes in which straw tubes are installed.

The straw tubes are glued individually into the frames under a tension of 500 g each, to avoid sagging of the straw tubes, possible due to high humidity. Also, to avoid sagging of the straw tubes in the chamber, 4 carbon fiber supports are used, shown in Fig. 9.42, two on each side of the chamber. Each row layer contains 256 rows, 128 on each side relative to the center of the chamber. After sealing the tubes, anode wires are installed in them under a load of 90 g each. As calculations have shown, the deflection of the frame after that will not exceed 30 μm. Motherboards are glued from the end of the frame after installing the anode wires. Motherboards are designed to supply high voltage to the straws and connect the signal from them to the amplifiers. The boards are made in such a way that there are no gaps between the boards after being glued to the frame. The ground contacts of all lines, as well as the signal pins are soldered using short insulated wires to the corresponding contacts on the board. Then, a second carbon fiber ring with a thickness of 5 mm is glued to the boards with an outer diameter of 1570 mm. Gas connectors are installed in the ring to supply the working gas mixture to the straw tubes.

The resulting Π-shaped box is divided into 4 separate sections to ensure the decoupling of gas flows. The box is hermetically sealed from above with fiberglass plates.

3 Front-end electronics

3.1 Signal parameters, processing and straw properties

When registering electrons produced in the ionization process, the straw tube itself serves as a cathode, and the wire located in the center of the tube serves as an anode. The cathode is formed by a very thin layer of copper and gold, few hundred atomic layers thick, so the electrical properties are determined by the surface effects (one does not need to consider the skin effect). Indeed, the measured DC resistivity of the cathode is $\sim$70 Ω, entirely determined by the surface effects. The anode is a gold-plated tungsten wire with a diameter of 30 μm. The straw can be considered as a very lossy transmission line, and the termination effects on both ends should be evaluated. With the gas mixture Ar:CO_2=70:30, the electron's

total drift time is about 150 ns. As a response to each cluster of primary and secondary electrons, created by the passage of particle, the straw outputs a current signal with an approximately hyperbolical shape and few microamperes amplitude. The shape differs from a hyperbolical curve for the first few ns, due to the variable ion mobility. Also, when the selected gas would contain electronegative components, like CO_2, the signal becomes distorted and of smaller amplitude, due to an electron attachment. The leading edge of the signal is quite short, of the order of 1 ns, the trailing edge time depends on a number of factors like geometry, gas and voltage applied. The ion tail lasts up to several 100 μs. The electrical properties of the straws are the following:

- characteristic impedance of 350 Ω (calculated) at 20 MHz and 1000 Ω at 1 MHz;
- capacitance of 23 pF;
- attenuation of 2.3 at 20 MHz;

In order to achieve excellent resolution in terms of coordinates, time and energy deposit, the following requirements are imposed on the ST for the readout electronics of the straw tubes:

- possibility to measure both time and deposited charge;
- time resolution not worse than 1 ns;
- low threshold to identify charge from a single cluster;
- dynamic range better than 1000 for charge measurement;
- low power consumption to reduce heating.

To address these requirements we propose a front-end electronics readout based on the VMM3a custom Application Specific Integrated Circuit (ASIC). This ASIC will be connected to the straw anodes, providing precise charge and time measurements. Each chip can read out 64 individual channels, making it appropriate for compact electronic boards, where high-channel density is useful. The low power consumption ($<$15 mW/ch) and cost per channel ($\sim$0.9 \$/ch) are equally useful for a compact detector readout. A fast programable gain preamplifier, semi-gaussian shaper, a tail cancellation circuitry, baseline restorer, and a single threshold discriminator are integrated into each channel of the VMM3a chip. Input impedance of the preamplifier is a compromise between good straw impedance matching and a small crosstalk. The lower value is advantageous, as it guarantees lower crosstalk and signal enhancement due to current increase during signal reflection on low termination impedance. The reflected signal, which returns after traveling to the far end of the straw and being reflected backwards, is already strongly attenuated and does not contribute significantly to the output. The shaping time should be short enough, in order to get a response from the first primary cluster and, thus, better time resolution, but should be long enough to integrate all the clusters, so that there is only a single charge measurement per particle crossing the straw (150$\div$200 ns).

3.2 Employment of VMM3a ASIC for straw tubes readout

For a conventional gaseous tube readout design, each channel generally has a double threshold discriminator (low/high) and a start/stop time digitizer. The rising edge of the signal (start) above the lower threshold is used for precise drift time measurement, and the track to wire distance is obtained from it with a known $r-t$ calibration. The trailing edge of the signal (end) is simultaneous for all straws

crossed by the same charged particle, see Fig. 9.44. It is generally used for time measurement validation or even as a crude time measurement. It is also ideal for building a fast hardware trigger or veto for multiple charged tracks. The second higher threshold is used for the stray gamma detection and/or rejection. VMM3a measures Time of Threshold with a built-in Time to Amplitude Converters, as shown

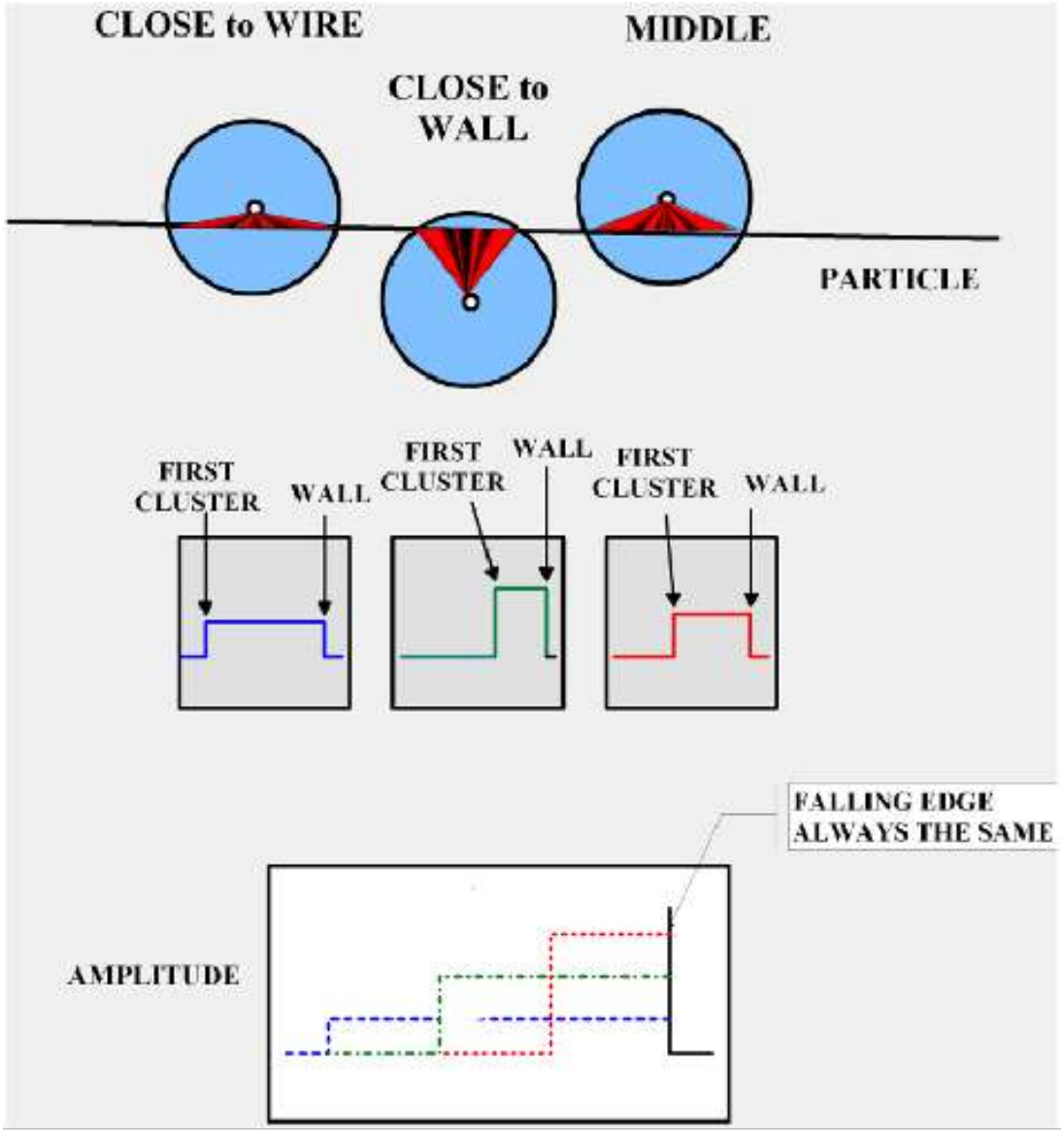

Figure 9.44: The trailing edge of signals is almost the same for all straws crossed by a single charged particle.

in Fig. 9.45. It has different TAC slopes which can be set to 60/150/350/650 ns. The preamplifier shaping circuit can be configured to use one of four different peaking times (25, 50, 100, and 200 ns) and eight gain settings (0.5, 1, 3, 4.5, 6, 9, 12, 16 mV/fC). A channel-specific discriminator is triggered on input signals above a configurable threshold to initiate digitization of the amplified pulse with a 10-bit Analogue to Digital Converter (ADC) and timing information with an 8-bit ADC. To sum up, VMM3a channel can measure time interval from threshold crossing to the falling edge of the reference clock pulse next after the peak of the integrated charge is found. For the collider application, VMM3a reference clock is set to a bunch-crossing clock. Thus, a time interval between the collision and the first cluster's arrival at the tube wire can be measured with a VMM3a chip.

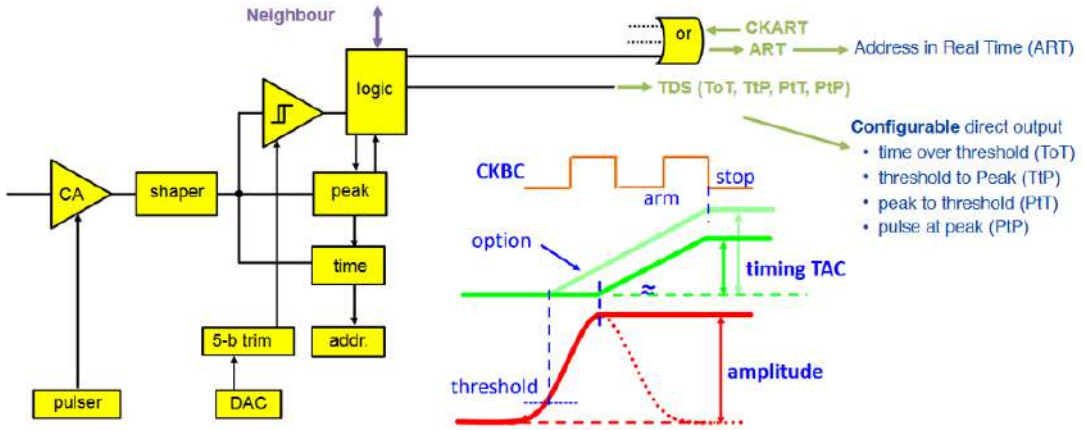

Figure 9.45: Block diagram of one of the VMM3a channels with a timing diagram demonstrating the conversion of time to amplitude.

VMM3a has no inner circuitry for trailing edge digitization, but it has 64 direct-time outputs that can be programmed to generate pulses for external use as time reference, veto signal, trigger, etc. Such a design requires an extra multichannel TDC, which would increase cost per channel. Also, VMM3a provides an integrated charge measurement, which can be used for the gamma rejection in place of the second higher threshold.

3.3 Noise and internal crosstalk, straw termination

The threshold setting is a compromise between time resolution and the rate of noise hits. The lower the threshold, the better the time resolution and efficiency should be, notwithstanding the higher rate of noise hits. The chip discriminator thresholds are adjusted in VMM3a by a global 10-bit Digital to Analogue Converter (DAC) with additional channel-specific 5-bit trimming DACs. These features enable VMM3a to meet the ST requirements of the lowest threshold level for time measurements, while keeping noise at low level.

Scans of equivalent noise charge (ENC) of VMM3a as a function of the input capacitance for various shaping time settings are shown in Fig. 9.46 (a). As can be seen, ENC of better than 1000 e- can generally be achieved with input capacitance less than 100 pF. Based on this information, we can assume that VMM3a can likely meet the ST low charge threshold requirement, if the straw tube gain is greater than 10^4 with input capacitance lower than 100 pF. Crosstalk can also cause fake hits, so multiple measures have been taken to reduce it as low as possible. For conductive crosstalk, the return paths of the straw signals are separated already at the level of the web connection and kept until the front-end board input connector. The capacitive coupling effect can be mitigated by lowering input impedance of the readout electronics and eventually by individual shielding of the straw cathodes. Input impedance is the sum of preamplifier input impedance and input discharge protection resistor. The input impedance of the VMM is about 50 Ω at the working frequencies; the value of the protection resistor is of the order of 50 Ω, too. Thus, the total load impedance for straw is ∼100 Ω, to be compared with the 350 Ω straw's characteristic impedance. The lower load impedance will cause signal reflections, but in a useful manner: it will increase the input current, thus enhancing the input signal. As the straw is a transmission line with very high loss, the signal which returns after reflecting from the far end of the straw is already negligible. The other possibility, considered for lowering capacitive crosstalk, is covering the straws from the outside by a very thin metallic layer, connected separately to the ground of the front-end board. The straw's far end is left open. This should enable collecting as much charge as possible, as the straw has a very high attenuation (2.3) at working frequency.

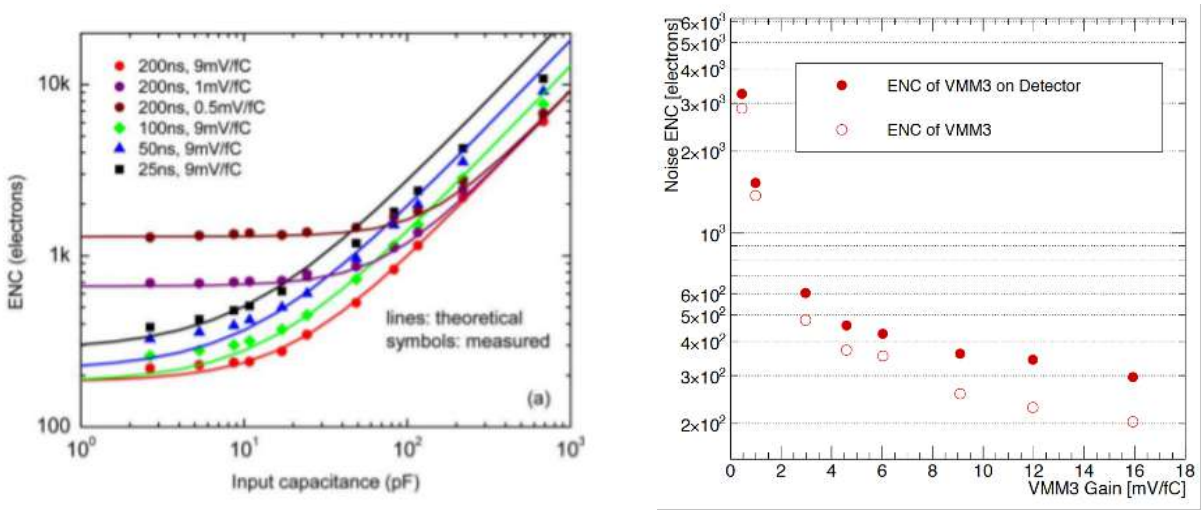

(a) (b)

Figure 9.46: (a) Equivalent noise charge (ENC) of VMM3a as a function of the input capacitance for various shaping time settings. (b) ENC as a function of gain.

3.4 External crosstalk, grounding and shielding

Electrically active objects surrounding the detector, such as a crane, a magnet, power supplies of other detectors, wireless connections, etc., can create interference, hereinafter referred to as external crosstalk. Another possible source of problems for the detector electronics is the mismatch in the voltage levels used in front- and back-end electronics. Therefore, it is necessary to ensure that all conductive parts are connected to a safety ground. The proposed grounding and shielding scheme for the ST detector is shown in Fig. 9.47. This scheme ensures that signals received from the cathode of the straws are separated and connected close to preamplifier inputs at the front-end board. This scheme was implemented in the 64-straw prototype.

The ground of the front-end board is connected along its perimeter to a metal case that surrounds the whole detector, thus forming a tight electromagnetic shield. The conductive layer of the straw tubes is grounded only on one end to prevent external currents flowing through the cathodes. All cable shields are connected on both ends: one side directly to the front-end board, back-end side through damping impedance. All metallic pipes for gas supply or cooling of the ST detector will also be electrically connected to the metal frame. The metal case of the station should be connected to safety ground at one point. The back-end electronics (VME crates) must be connected to the same ground, thus providing both required safety connection and eliminating potential difference between front-end and back-end electronics.

High channel density of VMM3a leads to small front-end PCB outlines, allowing digitizers to be set up directly inside the shielded metal case, resulting in even lower ambient noise levels.

3.5 Studies with a prototype straw read-out based on VMM3a and SRS system

To investigate the performance of VMM3a ASIC as a possible front-end electronics for the straw tubes, a dedicated setup is being developed using a VMM3a-based readout, implemented by the RD51 collaboration (CERN) within the Scalable Readout System (SRS) [65]. The setup allows to study the readout performance with generator test pulses, cosmic ray muons, and radioactive sources. First measurements with the SPS muon beam at CERN have already been performed as well.

The developed setup consists of a straw tube chamber, reference tracker, and a scintillator, which provides

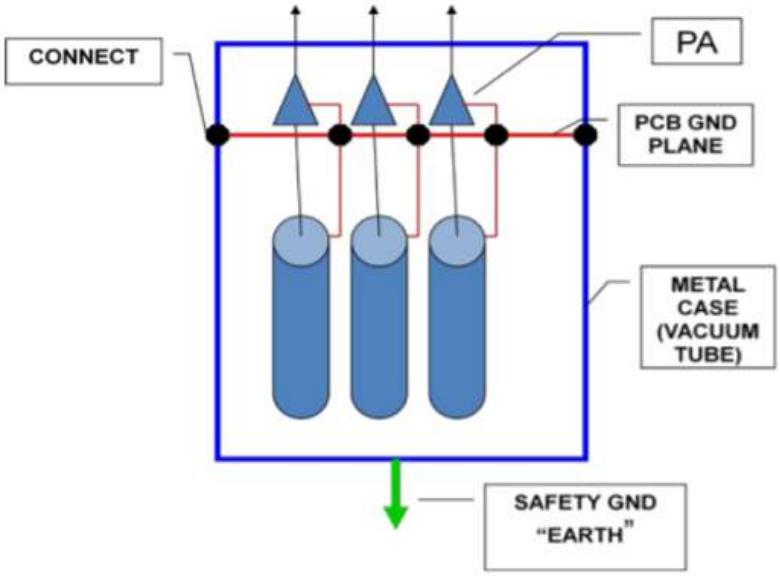

Figure 9.47: Grounding and shielding scheme of ST.

a precise reference time measurement. The straw chamber used for the first measurements has two layers of tubes with a 6 mm diameter, shifted by a tube radius with respect to each other. As a tracker, a plane of a triple GEM or a set of several planes are used. Both the straw chamber and the GEM tracker are read out with the individual custom VMM3a hybrid front-end boards developed by the RD51 collaboration, and the SRS is used for the data acquisition and power distribution. Each hybrid contains two VMM3a ASICs. A scintillator counter, equipped with a silicon photomultiplier and a constant fraction discriminator, has the internal time resolution of a sub-nanosecond level and is read out with a single hybrid channel. The GEM planes have a strip size of 400 μm and, in the case of three aligned planes and cluster-based hit position reconstruction, allow to reach a muon track spatial resolution of about 50 μm.

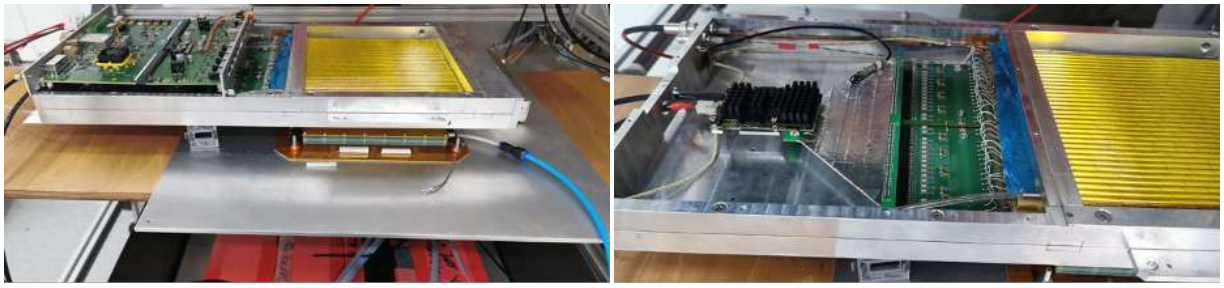

(a) (b)

Figure 9.48: Assembled laboratory setup with the straw chamber, GEM plane and a scintillator (a). VMM hybrid mounted to the straw chamber via a cross-board (b).

A photo of the assembled laboratory setup with the straw chamber placed on top of a single GEM plane is shown in Fig. 9.48. The aluminum supporting plate has a hole aligned with the scintillator beneath. The photo on the left shows the assembled setup with the VMM hybrid below the Front-End Card (FEC) of the SRS system. The photo on the right shows the hybrid itself, mounted to the straw chamber via a cross-board.

The first laboratory tests during the setup development are performed with a Ru-106 β source and cosmic muons. The current VMM3a hybrid readout of the straw chamber is being tested in both the time-at-peak

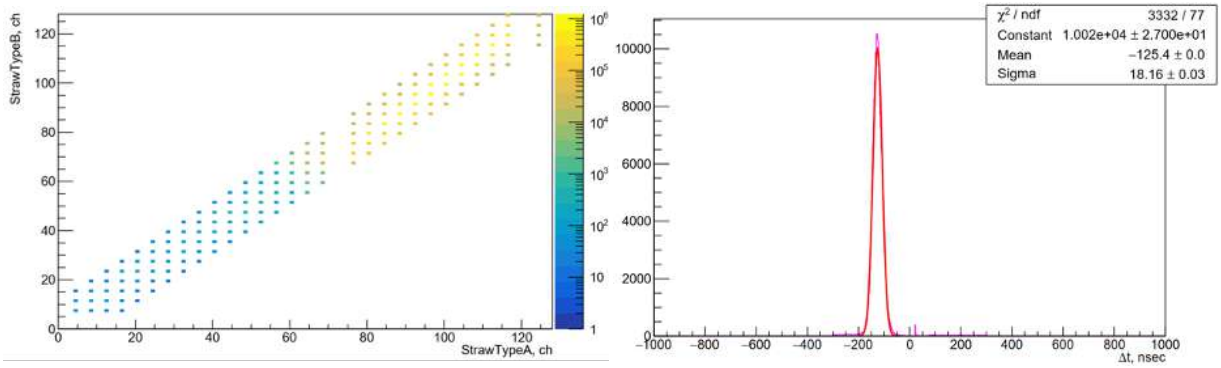

(a) (b)

Figure 9.49: (a) Straw chamber hit pairs found in both the top and bottom layers within a time window of 50 ns and 5 cm distance between each other. (b) Time difference between the scintillator and the straw signal peaks (right). Both for the Ru-106 source and time-at-peak VMM3a readout mode.

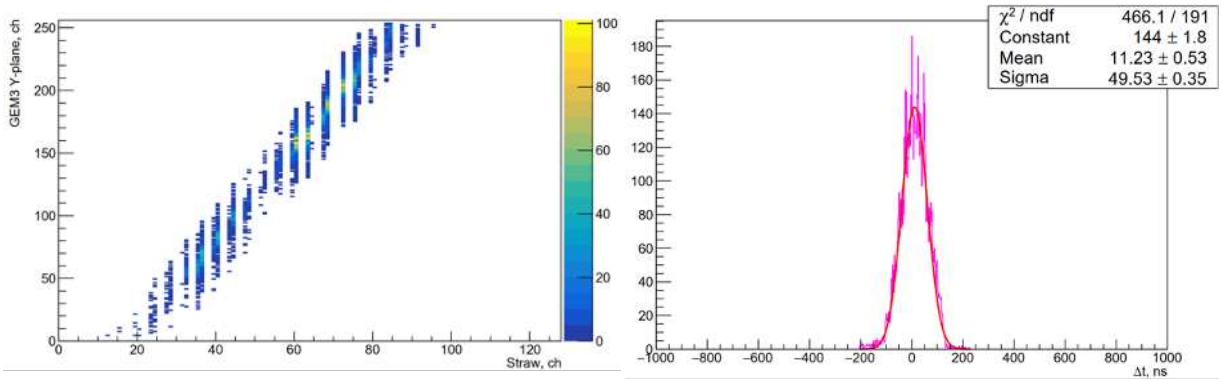

(a) (b)

Figure 9.50: (a) Hit pairs found in straw tubes and GEM strips within 200 ns time window. (b) Time difference between the scintillator signal peak and the straw time-at-threshold. Both for the muon beam at SPS (CERN), November 2021.

and time-at-threshold modes. The GEM readout hybrid is operated at the nominal time-at-peak mode. A spatial correlation of the straw hit pairs found in the top and bottom layers within a time window of 50 ns is shown in Fig. 9.49 (a). The correlation between the straws and the GEM channels is shown in Fig. 9.49 (b).

A similar setup was used during the SPS test beam data taking. The corresponding plots were obtained with a muon beam in the time-at-peak mode. Though the general compatibility of the VMM3a hybrid-based readout was demonstrated, the operation of the straw readout in the time-at-threshold mode needs to be studied in detail. First systematic studies of the VMM3a straw readout, operated in the time-at-threshold mode with different parameters, were started with the muon beam at SPS. Figure 9.50 shows the observed spatial correlation between the straw tubes and the strips of the GEM tracker for the hit pairs found within a time window of 200 ns. At the first stage of time-at-threshold studies, a long signal peaking time of 200 ns was used, and neither ADC nor TDC calibration was applied. Both the laboratory studies and the test beam measurements are to be intensively continued.

4 DCS

4.1 DCS architecture

The Detector Control System (DCS) provides control and monitoring of the detector hardware. In addition, it will perform archiving of the hardware parameters to the database to provide access to this information during the offline data analysis. It has been decided to use the common DCS system, now under development at CERN, which is based on the PVSS II SCADA toolkit and the JCOP framework. The Straw Tracker controlled and monitored equipment includes the following items:

- low voltage power supplies;
- high voltage power supplies;
- gas mixing and distributing systems;
- low voltage and temperature monitoring system.

4.2 Low voltage system

The LV system provides power to the front-end (FE) boards placed on the four straw tracker chambers. Each chamber contains four views and each view contains 30 FE boards. In the present design, one FE board consumes 1 A at 5 volts and, therefore, one module requires the LV power supply to provide a current of about 30A at 5 V. These requirements could be fulfilled by eight Wiener power supplies MPV8008, which have eight channels of 10 A output current each. One view requires four channels and, therefore, two power supplies will provide the required power for one chamber. The MPV8008 could be controlled in a similar solution used in the LHC experiments. It includes a CAN-bus interface card and the OPC-server providing the interface to PVSS. A second possibility to control the MPV8008 is to use the TCP/IP protocol together with the corresponding TCP/IP PVSS driver, which is part of the PVSS driver package.

4.3 High voltage system

The Straw Tracker requires a high-voltage (HV) source with voltage below 2 kV and low current. The present design assumes two HV channels per view, with 32 channels in total. The CAEN HV power supply board A1535, containing 24 channels with 3.5KV/3mA output, should be sufficient. To have 32 HV channels, two boards of this type, housed in CAEN SY2527LC mainframe, are needed. The mainframe should be controlled via Ethernet line with TCP/IP protocol and corresponding CAEN OPC server. The JCOP framework is suitable for the board A1535 and is already available, having been developed for the CMS ME1/1 muon chambers.

4.4 Gas system controls

The gas system for the straw tracker should provide and distribute Ar/CO_2. Due to the fact that the straws are placed in the inner layers of the detector, the gas system should rapidly close the gas line to a cell, in case of a leak in a straw. Pressure sensors will detect a sudden drop in pressure on the supply lines. In this case, the gas system should also send a signal to the Straw Tracker DCS to switch off the corresponding HV channels or the whole HV system. The plan is to use the CERN standard gas mixing/distribution system based on PVSS, with the possibility to control and monitor the gas mixing and gas flow values from the DCS PC. For this purpose, PVSS distribution manager will be used. Both software and hardware interlock signals to prevent HV turning on, if the gas flow is missing or an incorrect gas mixture is distributed.

4.5 Thermometry and FE monitoring

In order to get information about the cover (front-end) temperature at the straw group inlet, one thermo-sensor per FE cover will be mounted. Two voltages (one for the FE boards and one for the current consumed by a board) will be measured using Embedded Local Monitoring Boards (ELMBs). A chamber view has 30 boards, and four thermo-sensors will be mounted directly on the mechanics structure. In total, one view needs to measure 34 temperature values and 90 voltages. Therefore, to read out all monitoring information from one chamber, 10 ELMBs are needed. The readout should be performed via CAN-bus and OPC server, which is similar to monitoring the LV power supply. It seems reasonable to have one CAN-bus branch per chamber, which gives four CAN-bus branches in total. In case the LV power supplies control protocol is compatible with the ELMB control protocol, the LV power supplies will be connected to the chamber CAN-bus branches. The final decision depends on the final choice of the FE electronics.

4.6 Logical trees in DCS and FSM

To get a convenient way of navigation through the detector elements, the DCS logical tree will have a structure including both tracker nodes and gas system nodes. Due to the fact that the detector has only a few LV and HV channels, the bottom node of the tree will be linked to the corresponding channel of the LV or HV power supply in the hardware tree. The FSM tree should correspond to the Straw Tracker logical tree. The states of FSM should correspond to the states of the whole detector.

4.7 DCS development and maintenance

The plan is to use our own DCS PC running tracker PVSS system and DCS OPC servers for all detectors on one Windows-based computer. This PC should have CAN-bus adapter cards installed. After the development is finished and to simplify the maintenance of the detector DCS, the plan is to create a JCOP FW component containing all tracker PVSS panels and scripts, and to port it to the SPD central DCS computer. A copy of this component should be stored in the SPD DCS repository. The ST DCS PC should be used to run the DCS servers and to house the CAN-bus adapters. To simplify the control of the detector during further hardware development, debugging and maintenance, the PC to access PVSS panes located at the central DCS PC, will be used. For this purpose, the DCS PC will be equipped with a PVSS User Interface software installed.

5 Cost estimate

5.1 ST barrel

The configuration for the proposed ST is based upon 8 octant in the barrel part. Each octant contains about 3200 straws. Assuming one-end reading for each straw, the total number of electronic channels is about 26 000. The core cost is estimated for the construction of the complete ST, using a mixture of updated quotes from vendors, costs of the similar detector components used in different experiments. The risk associated with the project is relatively small. The ST design is based upon well established technology, using low mass straws, successfully developed for various modern projects. This does not require serious research and development in the field of detectors.

The corresponding costs for the various items of the ST barrel are summarized in Table 9.6.

5.2 ST end-caps

The configuration for the proposed ST is based upon 16 double-layer modules in two end-cap parts (8 modules on each side). Each module contains 288 straws. Assuming one-end reading for each straw,

Table 9.6: Cost estimate for the barrel part of ST.

Item	Cost, k$
Straw tubes	220
Glue	20
End-plugs	100
Crimping pins	90
Anode wire	60
Other components	90
Mechanics & C-fiber frames	150
ST tools	150
Safety equipment & consumables	60
Gas system	240
Cooling system	120
Front-end electronics (VMM3 & boards)	400
Back-end electronics	150
HV components	110
LV components	110
Cables & connectors	120
Prototyping	320
Total	2510

the total number of electronic channels is 4608.

The corresponding costs for the various items of the ST end-cap are summarized in Table 9.7.

6 Identification of particles using energy loss dE/dx in straw tubes

The ST will be the only detector able to separate $\pi/K/p$ during the first stage of the SPD experiment, and its performance is crucial for many physics tasks suggested in Ref. [3]. Particle identification in the detector is based on measurements of ionization energy losses. The energy losses follow the Landau distribution and are subjected to strong fluctuations due to rare acts of ionization with large energy loss. A truncated mean method is used to achieve a good resolution. For this method a certain fraction (10 – 50%) of signals with the highest amplitudes are discarded. The obtained mean value can be compared to different particle hypotheses and the corresponding probability can be assigned for each particle type.

The full simulation of PID performance must include description of the straw tracker, simulation of the ionization losses and gas gain in tubes, and response of the electronics. The simplified simulation accounting for the first two points within the SpdRoot framework has been performed, the impact of the electronics will be discussed later. The resolution dependence on the fraction of discarded signals is shown in Fig. 9.51 for the barrel part of the detector. One can see that it weakly depends on truncation parameter in the range 0.3 – 0.6. For the following estimations this parameter is set to 35%. The truncated mean value of dE/dx calculated per track as a function of momentum follows the Bethe-Bloch distribution and is shown in Fig. 9.52 for tracks crossing the ST barrel and the ST end-caps. The particle separation capability for pions, kaons, and protons can be estimated from curves indicating 1σ and 3σ displacement intervals.

In general case, the signal amplitude is defined by a convolution of raw signal and the electronic response function. For the long shaping time, the amplitude will depend on the collected charge only. In our case,

Table 9.7: Cost estimate for the end-cap part of ST.

Unit	Quantity	Unit cost, $	Total cost, k$
Straw tubes (3m/straw), m	15000	2.5	37.5
Anode wire (4m/straw), m	20000	2	40
Pins	10000	3	30
End plug	10000	2	20
Spring contact	10000	2	20
Spacers	5000	1	5
Glue, chemical materials, consumables			1
Straw frame	16	3000	48
Rigid flat mounting frame	2	6000	12
Covers for frames	80	100	8
Frame for tension	2	2000	4
Precision rulers for 16 straw, combos	3000	10	30
Measuring table for alignment	1	3000	3
Prototype	2	25000	50
Gas equipment			20
Tension control equipment	1	5000	5
Tooling for cutting	2	500	1
Motherboard plate and frontend	150	1000	150
Total			484.5

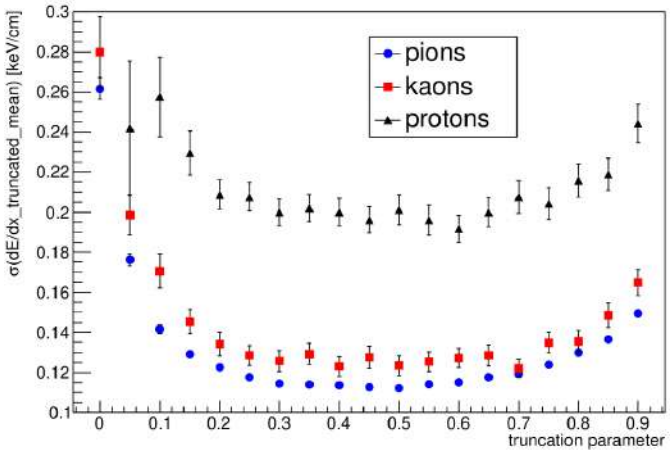

Figure 9.51: Dependence of the truncated mean resolution on the fraction of discarded signals for tracks, reconstructed in the barrel part of the ST detector.

the shaping time setting for VMM3 is 100 or 200 ns, and the total drift time is about 100 ns for a 10 mm straw tube. The charge collection efficiency in this case will depend on the signal shape, which depends slightly on the track-to-wire distance. The signal duration for tracks coming close to the wire is much larger as compared to tracks passing at large distances. This requires to introduce amplitude, which can be done in a routine way.

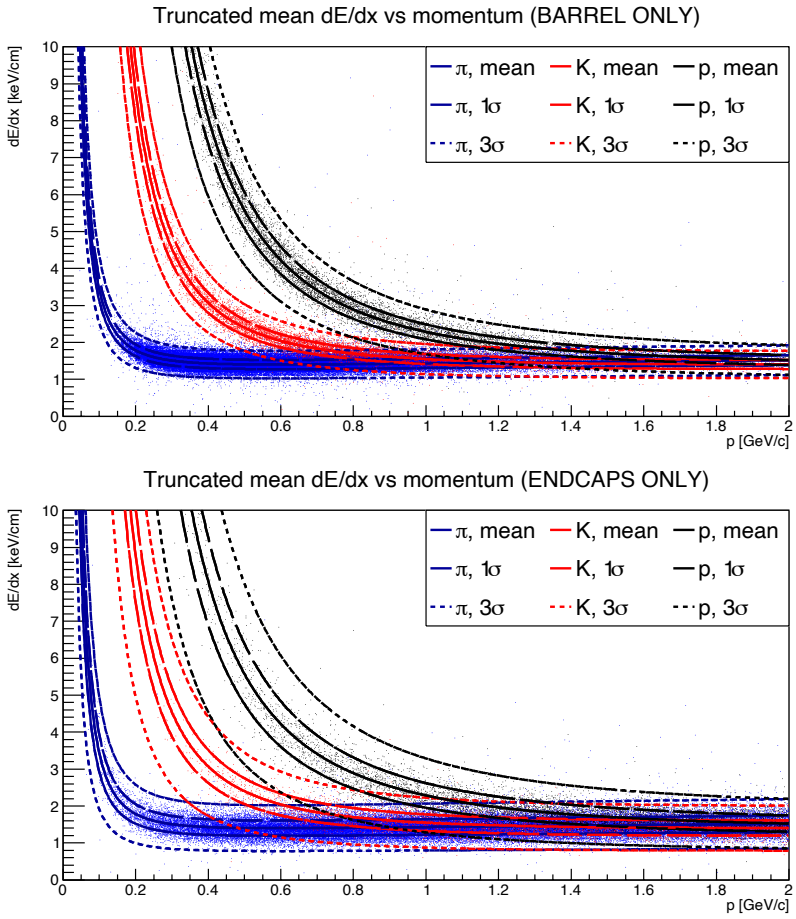

Figure 9.52: The performance for particle identification with dE/dx in the straw tracker. The dashed and dotted lines indicate 1σ and 3σ intervals, respectively. The upper plot shows tracks reconstructed in the ST barrel, the lower — in the ST end-caps.

Chapter 10

Beam-Beam Counter

1 Local polarimetry with beam-beam counters

The main goal of the local polarimetry at SPD is the permanent monitoring of the beam polarization during data taking to reduce the systematic error coming from the beam polarization variation. Another task for the local polarimetry at SPD is monitoring of the beam polarization, the independent from the major polarimeters (CNI and absolute), and possible usage of this tool to tune the beam polarization axis.

The energy range of SPD (below $\sqrt{s}$=27 GeV) is new, therefore, there is a lack of the polarization data to find an explicit solution for the local polarimetry. One of the methods to control the proton beam polarization is the measuring of the azimuthal asymmetry in the inclusive production of charged particles in collision of transverse polarized proton beams. Such a method is well adopted at the STAR detector. Two Beam-Beam Counters (BBCs) are used for this purpose. BBCs detect all the charged particles produced in the forward direction within their acceptance. The measurements by BBCs at STAR are sensitive to the transverse polarization of the colliding beams. The value of the effective analyzing power A_N for the inclusive production of charged particles at $\sqrt{s}$= 200 GeV is about $(6 \div 7) \times 10^{-3}$. At NICA energies, we could expect, in principle, the same or even larger value, due to a larger analyzing power for the p-p elastic scattering. Therefore, the BBC can be used for the local polarimetry at SPD.

2 Beam-beam counters

Two Beam-Beam Counters (BBCs) are planned to be located in front of the TOF system in the end-caps of the SPD setup [1]. Schematic view of the SPD Beam-Beam Counter, produced from the tiles of fast plastic scintillator, is presented in Fig.10.1. The BBC will cover the polar angles between 60 and 500 mrad, it will be divided into 6 concentric layers with 16 azimuthal sectors in each of them. The final granularity is the matter of further optimization for the entire energy range of collisions at SPD.

The main goals of the Beam-Beam Counters are: i) the local polarimetry at SPD, based on the measurements of the azimuthal asymmetries in the inclusive production of charged particles in the collisions of transversely polarized proton beams, ii) the monitoring of the beam collisions, and iii) participation in the precise determination of the collision time t_0 for events in which other detectors can not be used (for instance, in the case of elastic scattering).

Another important goal of BBCs is fast preselection of different types of events for monitoring purposes. The Monte Carlo simulation shows that in the p-p collisions at $\sqrt{s}$=27 GeV at least one BBC should have a signal in 79% of events (51% of events has a signal in the both BBCs). However, for the hard processes, in 97% of events the only one BBC will be hit, while hits for both counters could be expected

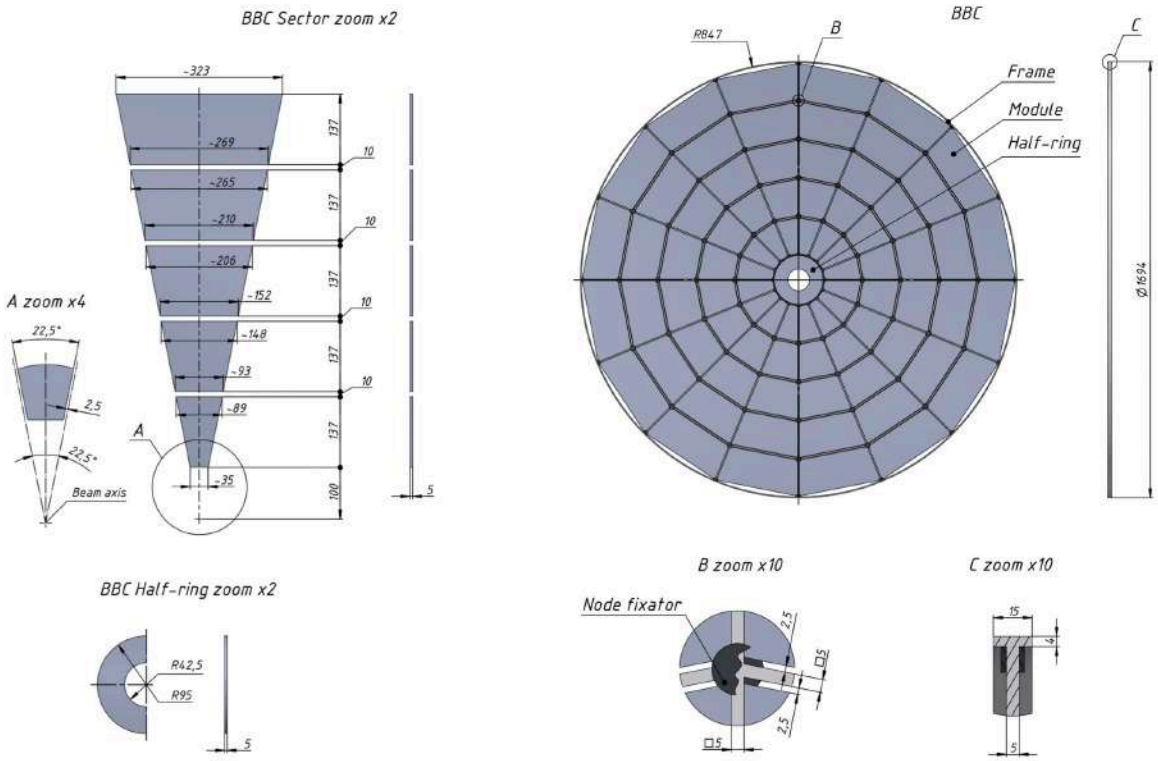

Figure 10.1: Schematic view of the SPD Beam-Beam Counter.

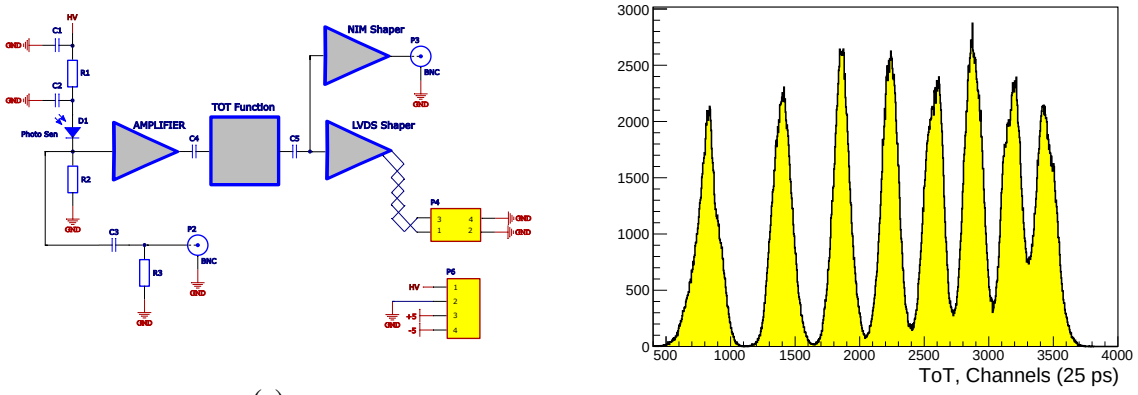

(a) (b)

Figure 10.2: (a) Schematic view of the front-end electronics with a ToT function, (b) Distribution of the ToT for different LED signal amplitudes.

in 68% of cases. Therefore, the requirement of the BBC signals allows one to preselect hard processes.

The BBC will consist of the tiles viewed by the SiPMs. The measurement of the signal amplitude is required for the time-walk correction to improve the time resolution.

2.0.1 First R&D results for FEE

With a single-channel prototype of the detector, we will be able to measure the amplitude using the developed FEE based on the Time-over-Threshold (ToT) technique. This technique is a well-known method that allows us to measure the energy deposited in the material by reconstructing the given property of

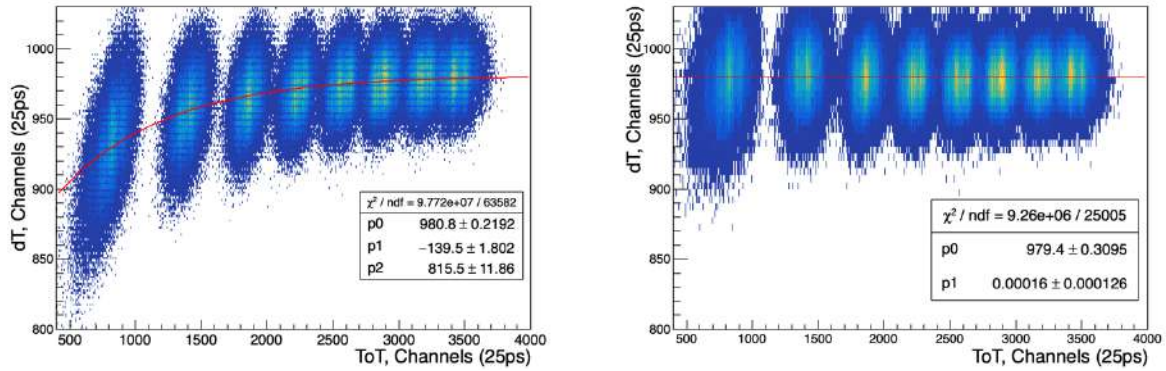

(a) (b)

Figure 10.3: (a) dT ($T_{SiPM1} - T_{SiPM2}$) correlation on the ToT. (b) Result after the time-walk correction for the dT ($T_{SiPM1} - T_{SiPM2}$) correlation on the ToT.

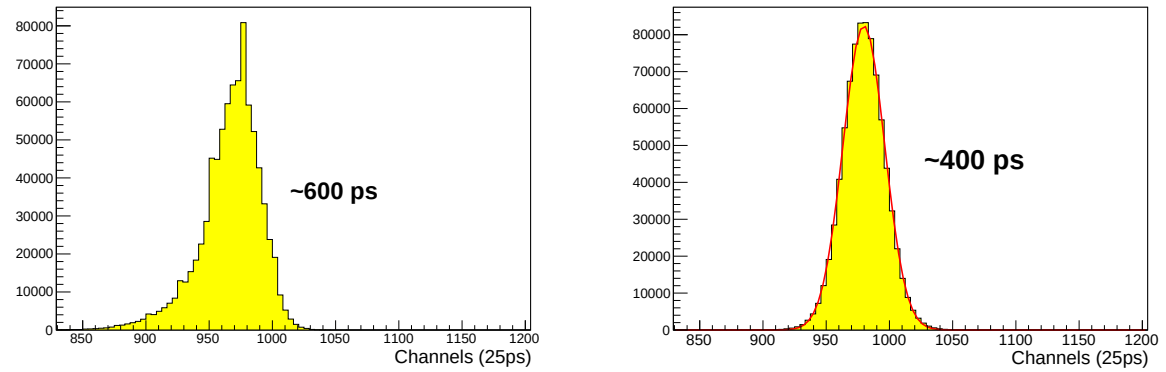

(a) (b)

Figure 10.4: (a) dT ($T_{SiPM1} - T_{SiPM2}$). (b) Result after the time-walk correction for the dT ($T_{SiPM1} - T_{SiPM2}$).

the output current pulse – the total charge collected, the pulse amplitude, etc. The ToT method converts the signal pulse height into a digital value in the early stage of the FEE, which greatly simplifies the system in comparison to analog detectors with serial readout through ADCs. The measurement of the ToT is composed of two measurements of time for the signal going above (leading) and returning below (trailing) the given threshold. The first version of the prototype includes a power supply and electronics (Fig. 10.2 (a)) made on a separate PCB used for a single SiPM. The power supply for the SiPM provides a voltage of up to 65 V with an individual channel adjustment within 0÷10 V, manual tuning, and a built-in voltmeter for the voltage monitoring. It is possible to connect eight PCBs simultaneously. The amplifiers used for that do not change the leading edge of the signal. This allows us to get a time stamp of the event. Afterwards, the signal is integrated and transmitted to the comparator.

The response of the Hamamatsu S12572-010P SiPM [66] with the FEE to the LED has been studied. A separate board with internal generator with controlled frequency and amplitude for LED has been used [67]. The NIM synchropulse from this board was used as a trigger. The illumination was performed by uniform light with different amplitudes in a light-isolated box. In addition to the ToT information (Fig. 10.2 (b)), the time stamp of the event for each SiPM was investigated. The distribution (Fig. 10.3 (a)) shows the correlation of these values and that the signal in the region of small amplitudes comes later in time. This is due to signal latency (the so-called time-walking effect). This delay occurs due to the

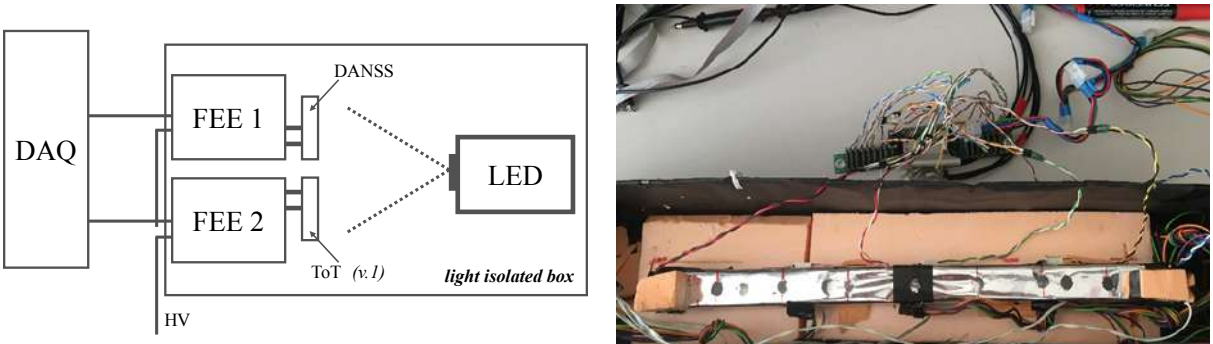

(a) (b)

Figure 10.5: (a) Schematic view of tests without a scintillator. (b) Picture of the tests with scintillator.

difference between the time when a photon or a charged particle passes through the detecting element and the time when the electronics register this signal. This leads to deterioration in the time resolution. After performing the correction (see Fig. 10.3 (b)), the time-walking effect has been removed [68].

The time resolution was defined as the RMS and was approximately 600 ps. Taking into account the non-Gaussian distribution (Fig. 10.4 (a)) and the fact that the time resolution is not the maximum allowed for this type of the detector, the time-walk correction has been applied. The most important result of the correction was a time resolution of approximately 400 ps (Fig. 10.4 (b)), which is 1.5 times better than the resolution before the correction.

Therefore, the first version of the front-end electronics based on the Time-over-Threshold method was tested with LED. After the time-walk correction, the time resolution improved up to 400 ps. Taking into account the SiPM suboptimal for precise time measurements, the result was promising. Further development of the FEE with a ToT function allows us to use standard TDCs for timing measurements.

2.0.2 Description of the detector prototype and test equipment

Since the concept of the BBC outer part is based on highly granular scintillation tiles with SiPM readout (SiPM), a prototype of a scintillation detector was developed (see Fig. 10.5) with two different types of FEE. Both types are based on the Hamamatsu SiPM readout (S12572-010P) [66].

The initial version of the scintillation detector for tests includes a 40-cm plastic scintillator and ten channels of electronics (Fig. 10.5 (b)). To increase the light collection, the scintillator is wrapped in a mylar film. Holes are made in the film on the upper face of the scintillator for studies related to the position of the source of calibrated light pulses (LED): in the center, in increments of 5 cm in both directions, and several additional holes on each side. Along the side face there is a similar version of electronics with SiPM in the holes: in the center and in increments of 10 cm in both directions. At the ends of the scintillator, one channel of each electronics option was located. In the case of electronics with the ToT function, the second version of the boards was used. This version is characterized by comparator stability and extended operating range.

Testing of the electronics and the prototype detector was carried out in a light-insulating box (Fig.10.5(b)), where the temperature during the measurements was $27.1 \pm 0.4\ ^{\circ}$C. As a light source, an LED was used. The synchropulse from the LED board [67] was used as a trigger for a VME-based data acquisition system [69]. The system included the FVME-V2.0 controller, digitizing modules TQDC16 and TDC32, and the trigger module TMWR [32]. The data collected was processed in the ROOT software package.

(a) (b)

Figure 10.6: (a) Single-channel FEE board with ToT method. (b) 15-channels FEE board from DANSS experiment [70] (b).

2.0.3 FEE used for detector prototype

First type of the electronics used for the detector prototype SiPM readout is the second release of the FEE, based on the ToT method described above. The single-channel electronics are made on a 4×2.5 cm^2 printed circuit board shown in Fig. 10.6 (a). As it was described above, the ToT method itself consists of two time measurements – the passage of a negative signal below (leading) and the return above (trailing) a given threshold, and allows to measure the charge along the width of the electric pulse. In addition, the amplifiers were used that keep the leading edge of the signal. After the amplifier the signal is integrated and transmitted to the comparator, from where it is outputted to the reading electronics via the LVDS interface. Thus, thanks to the developed electronics board, we have the opportunity to get a timestamp of the event and measure the charge. The power is supplied by a power supply (PS) with the possibility of simultaneous connection of up to eight channels of electronics. The PS contains a push-button interface, a display and a built-in voltmeter. The bias voltage consists of a constant (38/52/67 V) and an adjustable part for each channel (in the range from 0 V to +10 V).

Another FEE option for the prototype detector was the electronics produced by the ITEP group for the DANSS experiment [70]. It has a multi-channel platform created from several printed circuit boards. The first board provides power and communication with the PC via RS-232 and is connected via IDC-34 to a common board, on which 15 electronics boards are installed. Power is supplied in a wider range and consists of a constant (10-65 V) and a bias voltage adjustable for each channel ($\pm$10 V). Each 1.7×1.9 cm^2 board contains an offset voltage output for SiPM and an input for the signal. The signal passes through the amplifier and is then outputted via the IDC-34 connector to the reading electronics. The picture of the 15-channels FEE board [70] is shown in Fig.10.6 (b).

2.0.4 Test results

The SiPM response from a light source for two versions of the electronics was investigated in the presence and absence of a scintillator. Histograms of the time difference at different amplitudes of the LED were obtained and analyzed. Earlier, when testing the first version of the electronics with the ToT function [1], it was revealed that the signal in the region of small amplitudes arrives later in time.

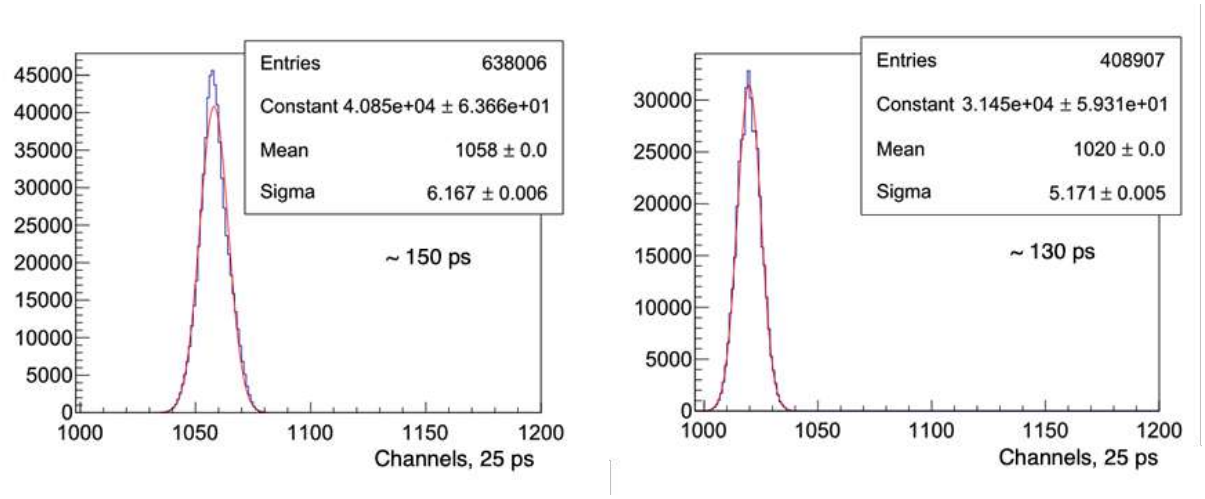

(a) (b)

Figure 10.7: T_{SiPM1} - T_{SiPM2} histogram after "time-walking" correction for tests of FEE with the ToT function [71] in the case of: absence of a scintillator (a); presence of a scintillator (b).

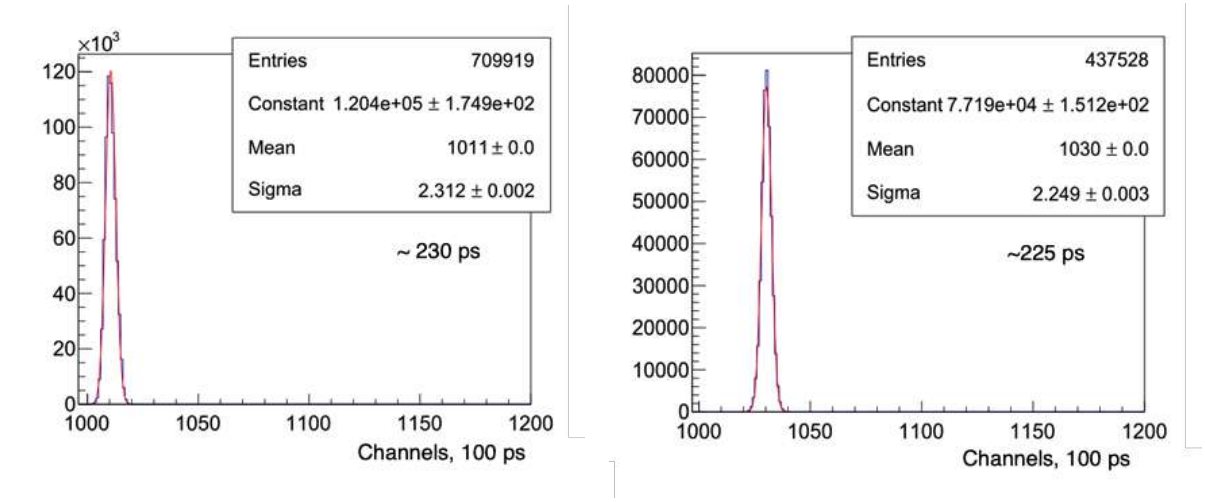

(a) (b)

Figure 10.8: T_{SiPM1} - T_{SiPM2} histogram after "time-walking" correction for tests of the DANSS exepriment FEE [70] in the case of: absence of a scintillator (a); presence of a scintillator (b).

The proposed correction is relevant when comparing time spectra in the presence and absence of a scintillator. Figures 10.7 and 10.8 show the difference in the arrival times of the $T_{SiPM1} - T_{SiPM2}$ signals for the SiPMs placed at the prototype end-caps after applying the correction. The distributions were approximated by the Gaussian function, and the time resolution was determined as a parameter of the sigma (σ) Gaussian function. It can be seen from the figures that in the presence or absence of plastic scintillator for two types of the electronics, the time resolution is almost invariable. When comparing the front-end electronics with the ToT function and the DANSS experiment, the time resolution was approximately 130 ps and 225 ps, respectively.

Therefore, the developed second version of the front-end electronics with the ToT function demonstrated good performance during LED tests. Two options of the FEE have been tested: with the ToT function and the electronics of the DANSS experiment with SiPM readout manufactured by Hamamatsu (S12572-010P). The difference in the time resolution for both FEE options was found to be approximately 40%. A

prototype of a scintillation detector was manufactured and tested. The proposed prototype is an important step in the development of the BBC subsystem. Given the suboptimality of the SiPM used for accurate time measurements, the result is promising.

2.0.5 Cost estimate

The cost estimate of the BBC outer part is presented in Table 10.1. The FEE and digitizers cost is estimated based on the options used for the tests.

Table 10.1: The cost estimation of the BBC outer part.

Item	number	cost, k$
Fast BC-404 scintillators	250	25
SiPMs	500	25
Composite frames	2	20
FEE	500	50
Digitizers	12	36
Cables, WLS etc.		12
LED boards	32	10
Assembling, tests		30
Total		208

Chapter 11

Silicon Vertex Detector

The SPD Silicon Vertex Detector (SVD) is a silicon-based part of the spectrometer, responsible for precise determination of the primary interaction point and measurement of the secondary vertices from the decays of short-lived particles (first of all, *D*-mesons). The Vertex Detector is divided into the barrel and two end-cap parts. A version of the vertex detector, based on Monolithic Active Pixel Sensors (MAPS), is discussed as the main one. Nevertheless, we keep in mind the possibility of using a vertex detector, based on the Double-Sided Silicon Detectors (DSSD).

1 MAPS-based vertex detector

To date, when creating tracking systems, the use of pixel sensors as a basic element of vertex detectors, is the most optimal experimental technique in high-energy physics. Besides demonstrating great registration efficiency for charged particles, produced in collisions of beams in modern collider experiments, the modern pixel detectors are resistant to hard radiation, allow to register short-lived particles with a good spatial resolution, and can detect rare processes and decays [72]. Current vertex detector systems use both hybrid pixel detectors and monolithic pixel detectors. Hybrid pixel detectors consist of a separately made sensor matrix and an electronic panel (chip). In the design of hybrid pixel detectors, the chip contact pads are made with the same dimensions as the implemented pixels, that is, an exact match is created between the size of the pixel and the size of the chip contact pad. Thus, a very important characteristic for hybrid detectors is pixel density. In addition, the electronic chip must be very close ($10 \div 20$ μm) to the touch panel.

In monolithic pixel detectors, the electronics and the touch panel are produced in the same process, on the same chip. This has the following advantages, compared to hybrid detectors: there is no need to connect the chip and the sensor array (in hybrid technology, to connect these two parts is quite time consuming, because of the high pixel density), and the capacity of each pixel is reduced, thus substantially reducing the noise level of the detector. Therefore, this technology of manufacturing pixel detectors is more reliable and less expensive [72]. Taking into account the main parameters of the beam collisions at NICA, we can use the existing solutions, implemented in the framework of the ALICE experiment Internal Track System upgrade [73]. The characteristics of the pixel sensors, developed by the ALICE Collaboration [73, 74] meet the requirements for the Silicon Vertex Detector in the SPD setup. It is assumed that this module will consist of 4 cylindrical layers of silicon detectors with a total square of 5.4 m^2, based on MAPS technology for high-precision reconstruction of the primary and secondary vertices.

1.1 MAPS technology

One of the key tasks of the SPD experiment is to study the production of particles, containing heavy quarks (D-mesons, Λ_c, etc.), with small transverse momenta. The main role in these studies will be played by the Silicon Vertex Detector, consisting of four cylindrical layers of pixel detectors, mounted on the ultralight supporting carbon fiber structures with a length of 1500 mm. The physics program of the future research imposes strict requirements on the characteristics and parameters of the detectors used. The key factors are to minimize the distance between the collision point and the first detector layer and reducing the amount of matter along particle tracks. At the same time, the increase in the frequency of beam collisons at the collider calls for fast detectors with high granularity. Based on the available experience of the ALICE Collaboration [73, 74], and after comprehensive experimental studies of the MAPS characteristics at SPbSU [75, 76], the following parameters of these detectors are proposed (see Table 11.1).

Table 11.1: Desired parameters of the MAPS-based SVD.

Parameter	Value
Silicon thickness, μm	50
Sensor size, mm^2	15×30
Detection efficiency, %	>99
Spatial resolution, μm	5
Average power consumption, mW/cm^2	40
Operating temperature, $^\circ$C	20÷30
Pixel noise rate, triggers / (pixel× event)	$< 10^{-6}$
TID radiation hardness (safety factor 10), krad	100
NIEL radiation hardness, 1-MeV n_{eq} / cm^2	10^{12}

To achieve these parameters, it is proposed to use 180 nm CMOS technology. The main advantages of this technology are good noise conditions, low power consumption, and radiation hardness of the pixel sensors used. The MAPS sensor consists of a high resistivity epitaxial layer (∼1 kΩ×cm) grown on a low resistivity substrate, a matrix of collecting diodes (pixels), and the front-end electronics. The scheme of charge collection by the pixel cell is shown in Fig. 11.1. The epitaxial layer is the active volume of the detector (can vary from 20 to 40 μm). The charge-collecting diode is implemented as a transition between the epitaxial layer and the n-type pocket (n-well). Due to the small thickness of the epitaxial layer, the collected charge (generated by the minimum ionizing particle) is relatively small for this type of detectors: $\sim 1000 \div 1600$ e$^-$. The size of the charge-depleted zone can be changed by applying a VRST bias voltage. To further increase the width of the depleted zone, a reverse bias voltage (V_{BB}) can be applied to the detector substrate (Fig. 11.1). Charges are collected by both drift (in the depleted zone) and diffusion (in the rest of the volume). Since diffusion plays a significant role in the charge collection process, the charge from a single particle (even for tracks perpendicular to the pixel matrix plane) is collected by several neighboring diodes (pixels), forming what is called a cluster. The ratio of the percentage of charge collection by drift and diffusion is determined by the size of the depleted zone, so that the V_{BB} can also influence the size of the cluster. The total detector bias voltage applied to the collecting diode is formed from voltage V_{RST}, which fixes the operating point of the input transistor, and the reverse bias voltage V_{BB} applied to the substrate. This greatly increases the depletion zone around the charge-collecting diode and lowers the input pixel capacitance, resulting in more efficient charge collection, reduced detector noise, and improved radiation resistance. To improve detector efficiency, a deep p-type pocket (p-well) is placed in the front-end electronics area (Fig. 11.1). Right above it, there

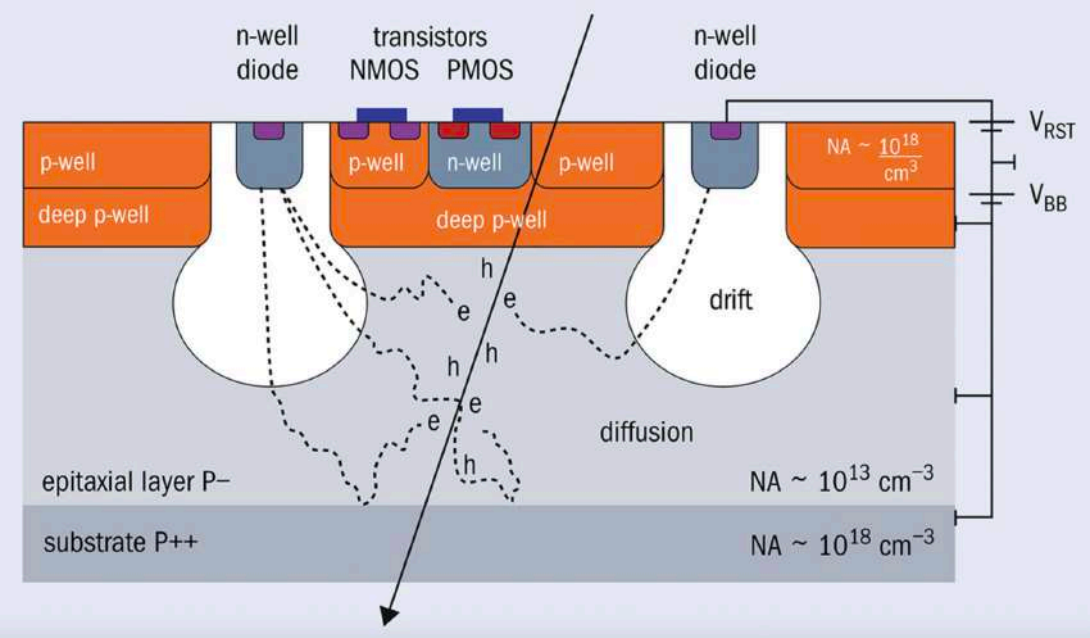

Figure 11.1: Scheme of a pixel sensor [77].

are elements of the detector's electronic circuits, implemented using PMOS structures with the pocket of n-well type. Thus, the p-type pocket shields the pixel electronics, preventing electrons from collecting on the n-well and, thereby, generating additional noise [73–75, 78].

As a result, each pixel already contains an amplifier and a signal shaper. The pixel size is 28×28 μm^2, and the pixel matrix size is 15.3×30 mm^2. The matrix consists of 512×1024 pixels, and is therefore divided into 512 rows and 1024 columns. Analog and digital electronics are formed on the periphery of the pixel matrix. The size of the peripheral circuit is 1.208×30 mm^2.

The signal arising from the passage of the particle is read by the Priority Encoder (PE) circuit, implemented according to the Address-Encoder Reset Decoder (AERD) principle [79]. In this case, the entire pixel matrix is divided into 512 double columns, each of which uses an AERD scheme is implemented to read the addresses of triggered pixels only. When the charge collected on the detecting diode exceeds a certain discriminator threshold, the single bit memory cell (if open) goes to state "1". The readout system gives priority to the encoding function for a column of pixels, in which all pixels have occupied the entire digital section. This allows the memory cells of all pixels to be read or zeroed.

This system enables the reading of signals from pixels in a binary form and storing them in the pixel cell. All analog signals, required to operate the front-end pixel electronics, are generated by fourteen digital-to-analog converters, built into the detector. The readers of each of the 32 regions contain SRAM memory cells for storing the event information. The accumulated data is transferred to a parallel 8-bit port. The high-level control unit provides full access to the control and status registers of the detector, as well as the memory cells of the readers.

We are also considering using MAPS-based detectors, developed as part of the ARCADIA project [80, 81]. The ARCADIA (Advanced Readout CMOS Architectures with Depleted Integrated sensor Arrays) project is developing FD-MAPS with an innovative sensor design, which uses backside bias to improve the charge-collection efficiency and timing over a wide range of operational and environmental conditions. The sensor design targets very low power consumption, in the order of 20 mW cm^{-2} at 100 MHz cm^{-2} particle flux, to enable air-cooled operation.

The FD-MAPS architecture, initially embodied in a 512×512 pixel matrix, should enable the scalability of the sensor up to the matrix size of 2048×2048 pixels. Maximizing the active area of a single sensor (10 cm^{-2} or bigger) simplifies and reduces the costs of the detector construction. The total thickness of such detectors could be from 50 to 300 μm.

1.2 Supporting structure for MAPS detectors

An important feature of silicon MAPS sensors, planned to be used in the creation of the vertex detector of the SPD experiment, is their high thermal power, which can reach up to 40 mW/cm^2. Therefore, with the use of CMOS technology for pixel sensors in the experiments at the NICA collider, the development of an effective cooling system is required. It should be capable to ensure optimal operation of electronics and detectors at temperatures not exceeding +30°C, with a minimal amount of matter in the particle collision region. The latter leads to minimization of multiple scattering, i.e. increase of radiation transparency of the whole detector complex. Thus, for the best reconstruction of vertex decays of unstable particles, the radiation thickness of all detector modules and their support structures should not exceed 1% of the radiation length. That is, the main elements of the vertex detectors (silicon sensors, cable systems, supporting and cooling systems) should have a minimum of material with a small charge number Z [82, 83]. At SPbSU, together with the ALICE Collaboration, ultralight carbon fiber structures were developed to support detectors based on MAPS for the new Internal Tracking System of this experiment [73, 82, 83]. Similar technologies can be used in the creation of the SPD SVD. The ultralight radiation-transparent carbon fiber support structures of MAPS with an integrated cooling system consist of trusses, on which thermal panels, made with carbon fiber, are attached. The cooling system consists of the polyamide tubes with a diameter of 1 mm. All ultralight support structures are spatial monolithic structures - trusses (see Fig. 11.2). The trusses are constructed using prepregs, consisting of high-modulus carbon fiber and impregnated with an appropriate binder. The combination of these components makes it possible to obtain MAPS sensor support structures with the best mechanical and strength properties with minimal substance content. The entire detector module (stave) will consist of three main components: (i) pixel detector, (ii) power bus, (iii) cold plate. The estimated contributions of one layer stave to the material budget is about 0.81% X_0 [73].

1.3 Cost estimate

A rough estimates of the cost of a MAPS-based vertex detector are given in Tab. 11.2. When estimating the cost of the chips, the possible manufacturing faults are taken into account. The total cost is 11.7 MEuro or 13.5 M$.

2 DSSD option

The DSSD SVD barrel consists of three layers, based on the Double-Sided Silicon Detectors (approximately 1.9 m^2). The end-cap regions consist of three disks each (approximately 0.22 m^2). The SVD barrel covers a radius from 32 mm to 250 mm. All three cylindrical layers are equipped with rectangular two-coordinate silicon strip detectors and give information on the coordinates of the tracks (r,ϕ,z), which makes it possible to measure a point in each layer). The end-cap regions detect particles in the radial region between 32 mm and 250 mm. Each of the three disks is set with a DSSD with concentric (r) strips and radial (ϕ) strips. The SVD has a length of about 1.2 m and covers the region of pseudo-rapidity up to $|\eta| < 2.0$. Each DSSD has a 300-μm thickness and a strip pitch in the range from 95 μm to 281.5 μm. The DSSDs are assembled into detector modules by two detectors per module, forming 18-cm long strips. General layout of the DSSD SVD is presented in Fig. 11.3.

The detectors and the front-end electronics boards (FEE-PCB) are connected via low-mass polyimide microcables and assembled on the extra-light carbon fiber mechanical supports with a cooling system

Table 11.2: Cost estimates for a MAPS-based vertex detector construction.

	Cost, kEuro
Pixel chips (per 1 m^2):	**2700** (500)
CMOS wafers + Thinning & dicing	1620 (300)
Series test	1080 (200)
Staves:	**1600**
FPC construction	350
FPC test	150
Module assembly & test	400
Carbon Space Frame & Cold Plate construction	200
Carbon Space Frame & Cold Plate tests	100
Stave assembly & test	400
Support and installation:	**1600**
Layers End-Wheels	100
Barrel Shell	250
Service Barrel	250
Installation mechanics & test	500
Read-out electronics:	**3000**
Development of Read-out Unit	2500
Test of Read-out Unit	500
Power Distribution System:	**1500**
Power supply	1000
Power regulation	500
Cooling System:	**1000**
Detector Control System:	**300**
TOTAL	**11700**

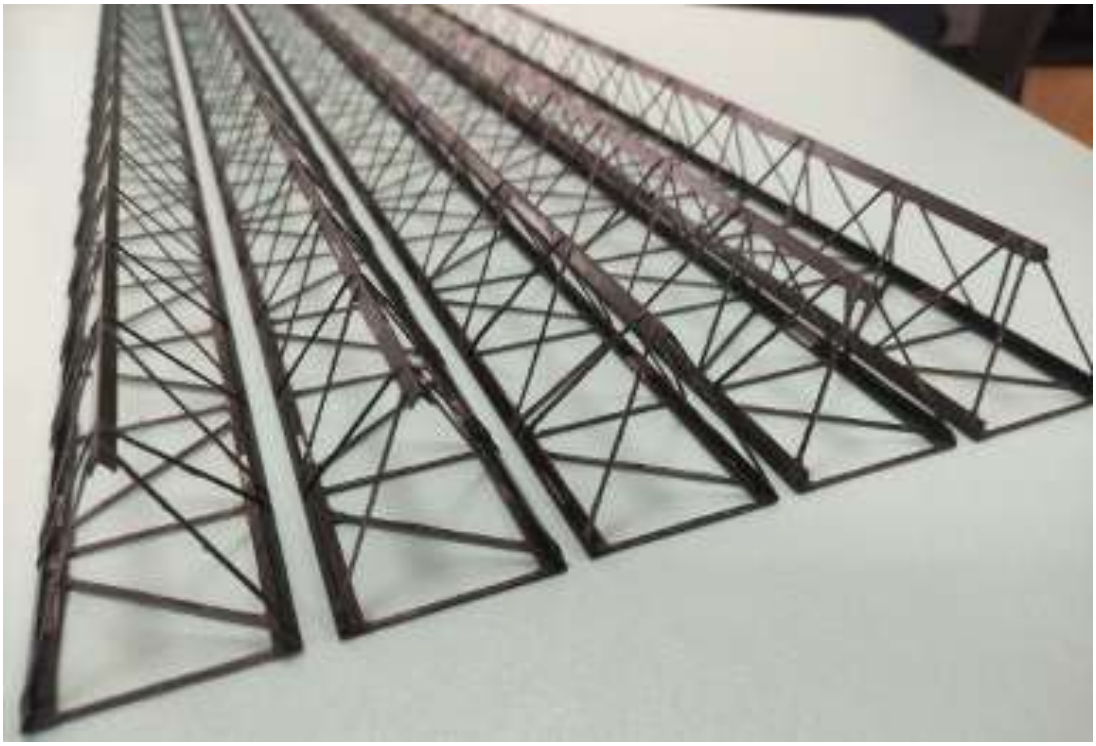

Figure 11.2: Examples of ultralight carbon-composite structures to support the cooling panels of the detector modules for SVD SPD.

in the similar way as it was done for the ALICE outer barrel. The relevant numbers for the barrel part and for the end-caps of the SVD for the DSSD configuration are presented in Tables 11.3 and 11.4, respectively.

From the general conditions of the SPD setup, the SVD performance requirements are i) geometry close to 4π; ii) track reconstruction efficiency for muons greater than 99% at $p \leq 13$ GeV/c (for $0 \leq |\eta| \leq 2.5$); iii) low material budget; iv) coordinates resolutions for vertexing: $\sigma_{r,\phi} < 50$ μm, $\sigma_z < 100$ μm. The lifetime of the Silicon Vertex Detector is required to be not less than 10 years of NICA operation.

Table 11.3: Number of the main components for the barrel consisting of 3 layers of DSSD.

Parameter	Layer 1	Layer 2	Layer 3	Total
N_{DSSD}/module	2	2	2	
$N_{modules}$/ladder	4	4	4	
$N_{ladders}$/layer	6	14	23	43
N_{DSSD}/layer	48	112	184	344
N_{chip}/module	10	10	10	
N_{chip}/layer	240	560	920	1720
$N_{channel}$/layer	30720	71680	117760	220160

The concept of a single DSSD module for the barrel part is shown in Fig. 11.4. The module consists of two silicon detectors, wire-bonded strip-to-strip for the $p+$ side (to reduce the number of readout channels), glued to the plastic frame and connected with two front-end electronics boards via a low-mass polyamide cable.

The Silicon Vertex Detector will be made using a planar double-sided technology based on the n-type

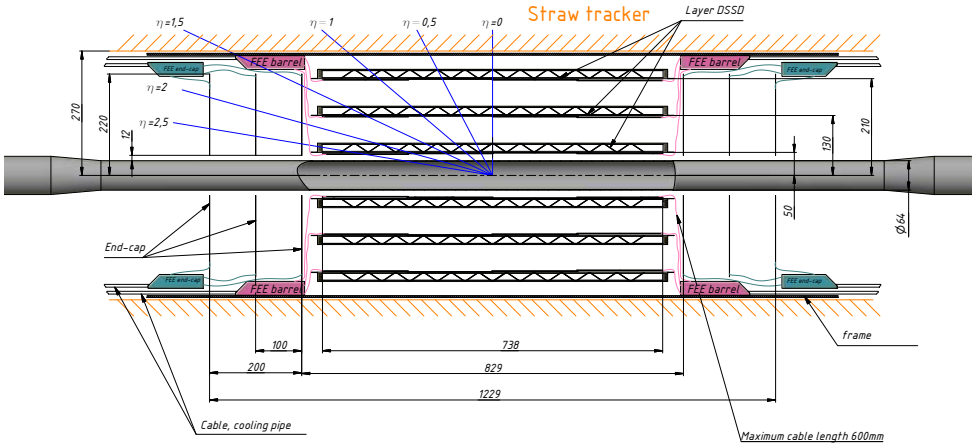

(a)

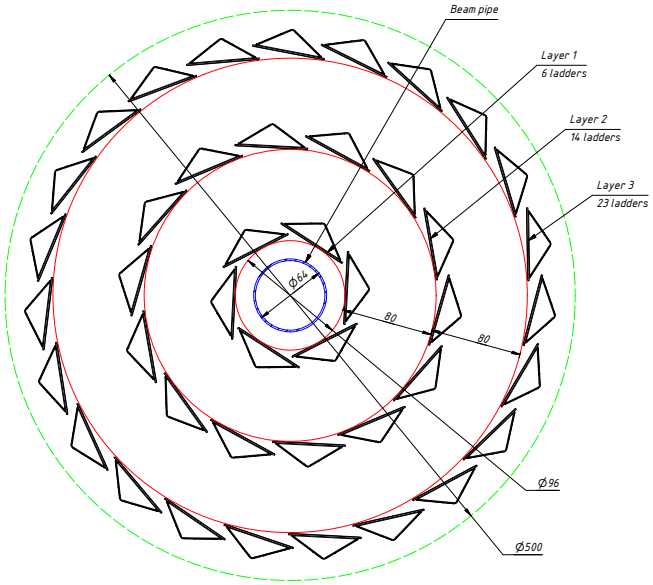

(b)

Figure 11.3: Longitudinal (a) and transversal (b) cross-sections of the DSSD Vertex Detector. All dimensions are given in millimeters.

conductivity 6-inch float-zone silicon wafers (produced by ZNTC, Zelenograd, Russia). Its size is 63×93 mm^2 and its thickness is 300 μm. The pitch for the $p+$ side is 95 μm and for the $n+$ side 281.5 μm. The number of strips is 640 and 320 for the $n+$ and $p+$ side, respectively. The stereo angle between the strips is 90 degrees. The expected spatial resolution for such a detector topology is $pitch_{p(n)+}/\sqrt{12} =$ 27.4 (81.26) μm for $r-\phi$ and $r-z$ projections, respectively. As mentioned before, the barrel DSSD

Table 11.4: Number of the main components for the end-cap consisting of 3 layers of DSSD-based on trapezoidal modules (640×640 strips).

Parameter	Layer 1	Layer 2	Layer 3	End-cap 1	End-cap 2	Total
N_{DSSD}/module	2	2	2			
$N_{ladders}$/layer	14	14	14	42	42	84
N_{DSSD}/layer	28	28	28	84	84	168
N_{chip}/module	10	10	10			
N_{chip}/layer	140	140	140	420	420	840
$N_{channel}$/layer	17920	17920	17920	53760	53760	107520

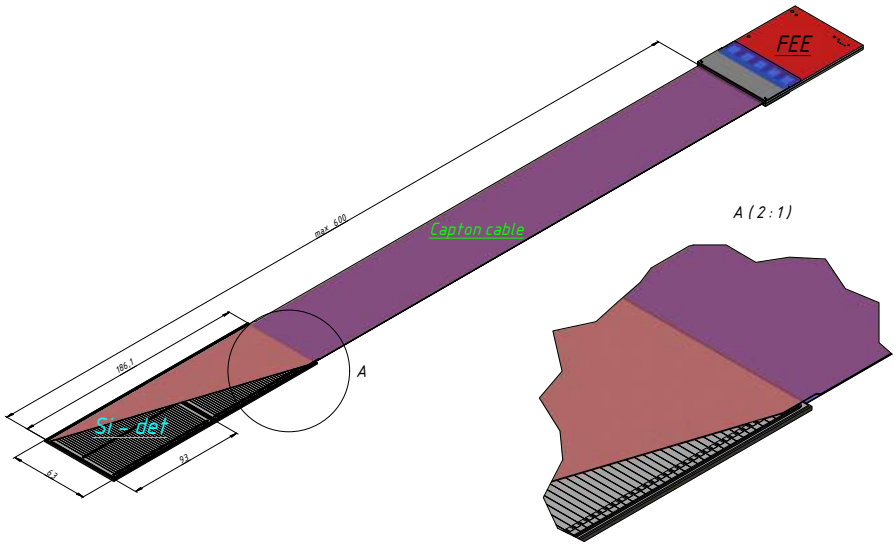

Figure 11.4: Concept of the barrel DSSD module. All dimensions are in millimeters.

module contains two DSSDs ($p+$ strips wire bonded strip to strip) and has 640 strips at each side.

To bring the front-end electronics out of the tracker volume, two thin polyimide cables with aluminum traces (for each side of the module) will be used. The cable consists of several layers: signal, perforated or solid dielectric (polyimide), and a shielding layer. Cable pins were designed for the tape-automated bonding with the detector and the pitch adapter sides. The maximum cable length is 60 cm, and the total thickness of all cable layers is less than 0.15% of X_0.

Since the DSSDs have a DC topology, it is necessary to supply bias voltage to the detector and electrically decouple the DC current from the ASICs electronics inputs. For this purpose, an integrated RC circuit (sapphire plates with Si-epitaxial layer Silicon On Insulator (SOI)) Pitch Adapter (PA) will be used for each side of the module (produced by ZNTC, Zelenograd), designed with different topologies for each side. After the pitch adapter, the detector signal goes to ASIC. Table 11.5 shows a possible ASIC readout solution. The optimal choice should be done after the ongoing R&D.

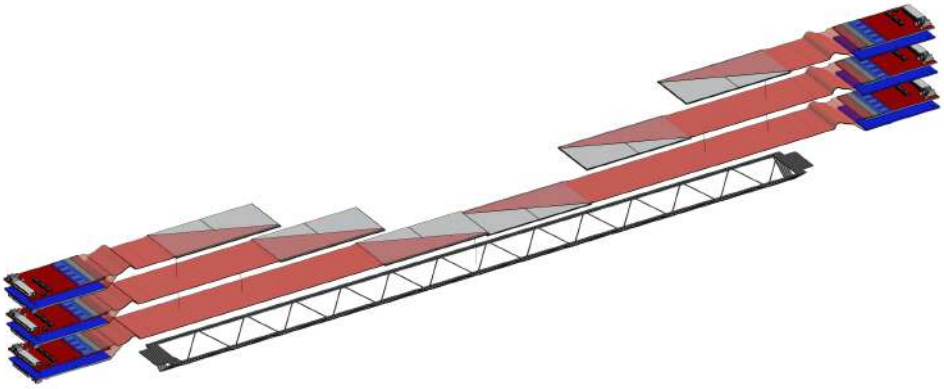

Figure 11.5: Sketch of the barrel ladder.

Table 11.5: Possible ASIC readout solution for the Vertex Detector.

ASIC	APV25	VATAGP7.3	n-XYTER	TIGER
Number of channels	128	128	128	64 (128)
Dynamic range	-40fC – 40fC	-30fC – 30fC	Input current 10 nA, polarity + and −	1–50fC
Gain	25mV/fC	20μA/fC		10.35mV/fc
Noise	246 e^-+36 e^-/pF	70e^-+12 e^-/pF	900 e^- at 30pF	2000 e^- at 100pF
Peaking time	50ns	50ns/500ns	30ns/280ns	60ns/170ns
Power consumption	1.15mW/ch.	2.18mW/ch.	10mW/ch.	12mW/ch.
ADC	No	No	16fC, 5 bit	10-bit Wilkinson ADC
TDC	No	No		10-bit Wilkinson ADC

2.1 Mechanical structure

The concept of the barrel DSSD ladder is shown in Fig. 11.5. The silicon modules are laying on a carbon fiber support, from the center out to the edges. The detectors are connected with the FFE via thin low-mass cables. The front-end electronics is located at the edges of the ladder and is placed in the conical caves to provide a connection to the voltage supply, DAQ, and the cooling ASIC chips subsystems. A sketch of an end-cap plane, consisting of trapezoidal modules, is presented in Fig. 11.6. Internal structure of the detector, the supporting frame, as well as its placement with respect to the beam pipe together with communications are shown in Figs. 11.7, 11.8, and 11.9, respectively.

2.2 Cooling system

A liquid cooling system is used to dissipate the thermal power ($\sim$2 kW) from the FEE, located on the two ends of the VD (1 kW each) to avoid thermal heating of the electronics and surrounding detectors. A water cooling system is chosen to dissipate the generated power. The readout electronics elements are placed on the ends of the detector barrel and on the ends of the end-caps. Using compact aluminum liquid-cooled heat exchangers the heat from the electronics boards will be dissipated. The complete SVD setup will run inside an insulated box. The box temperature should be kept below 20° C at all times of operation.

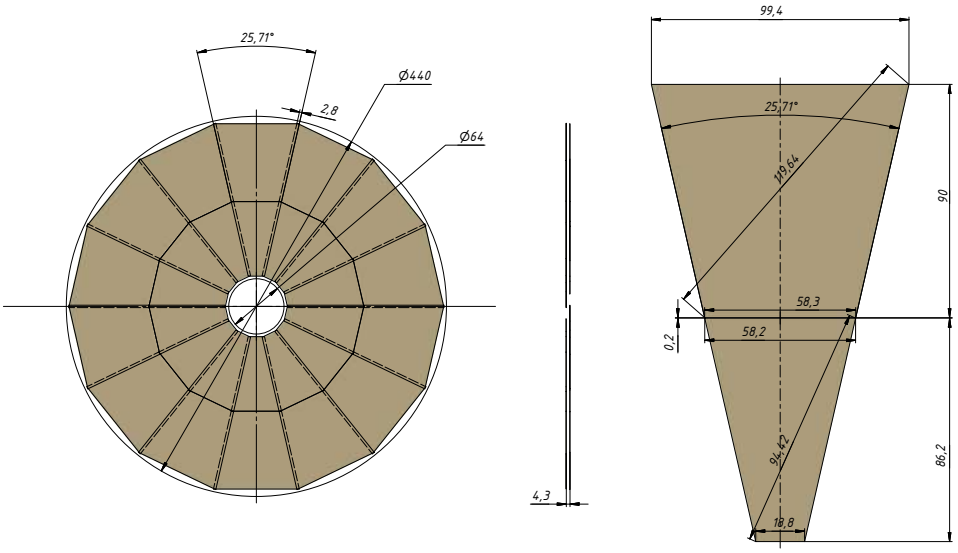

(a)

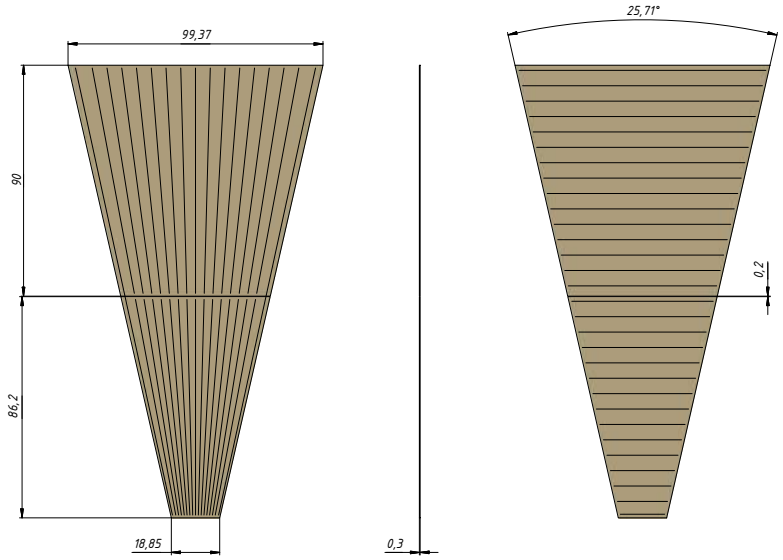

(b)

Figure 11.6: (a) Sketch of the SVD end-cap planes consisting of trapezoidal shape DSSD modules. (b) Sketch of a single trapezoidal module.

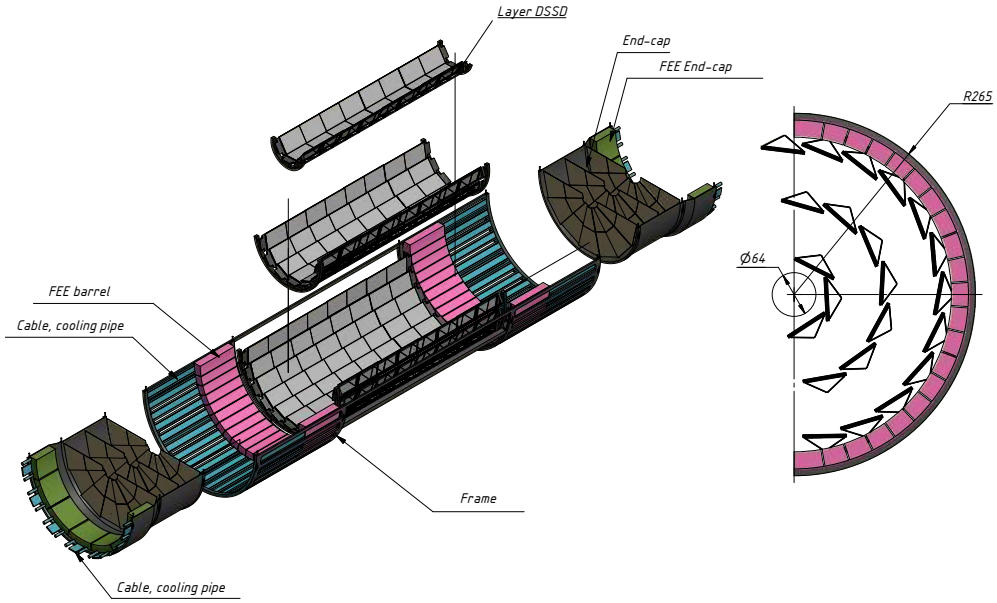

Figure 11.7: Sketch of the assembly of the end-cap and the barrel parts of VD.

The liquid cooling system is based on four Huber Minichillers 900w laboratory chillers with a total cooling capacity of 3.6 kW at 15° C coolant temperature. This chiller was chosen because of its high cooling capacity, compact size, and suction capacity of 18 l/min. The coolant used is deionized water. Two chillers are used to cool the barrel readout electronics (right, left side), two more chillers are used to cool the end-cap readout electronics. The chillers will be located 25 m away from the vertex detector of the SPD unit. The number of tube connectors and diameters are under development. Fig. 11.10 shows the principle and variant of heat removal from one of the end-caps, other parts of SVD will be cooled similarly, the only difference is the location of FEE.

2.3 Cost estimate

Preliminary cost estimate for the DSSD configuration of the Silicon Vertex Detector is presented in Table 11.6. It is based on the following assumptions:

- the cost of 1 m^2 of DSSD Si sensors is 0.6 MEuro;
- the cost of 1 channel (128 ch./chip) is 3 Euro.

The cost of the SVD, that includes also low anf high voltage supply, cables, cooling system and mechanics, is 1.9 MEuro per 1 m^2 or 2.2 M$. So, the total cost of the detector is 7.3 M$.

3 SVD performance

The Monte Carlo simulation for a VD configuration with 4 equidistant layers of MAPS and 3 layers of DSSD described above was performed. The primary vertex position resolution in X and Z coordinates

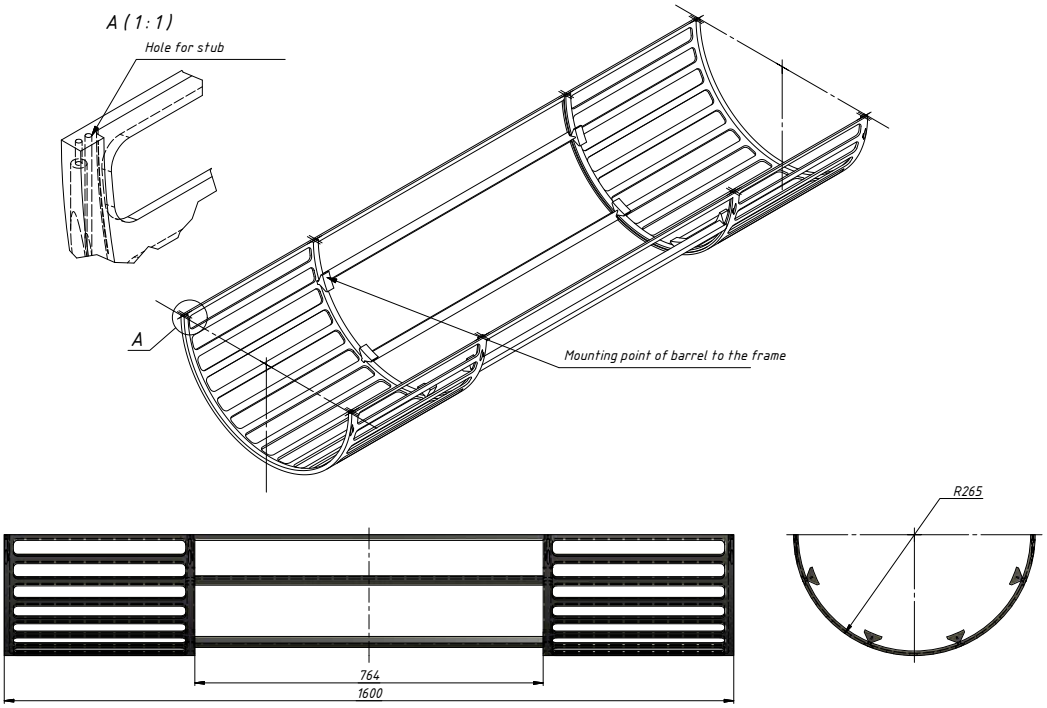

Figure 11.8: SVD supporting frame.

Table 11.6: Cost estimate for the SVD DSSD configuration.

Layer	Number of sensors	Number of ASICs	Barrel area, m^2	End-cap area, m^2	Cost barrel, MEuro	Cost (one) end-cap, MEuro
1	48	240	0.28	0.22 ($\times$2)	0.53	0.42
2	112	560	0.66	0.22 ($\times$2)	1.25	0.42
3	184	920	1.08	0.22 ($\times$2)	2.05	0.42
Total	344	1720	2.02	1.32	3.83	2.52 (two end-caps)

and the momentum resolution dp/p are presented in Fig. 11.11 (a) and (b), respectively. Because of the smaller amount of substance, the MAPS-based detector demonstrates better performance than the DSSD-based one. Such improvement in the momentum resolution should enlarge accordingly the significance of the J/ψ and D peaks. The choice of a Silicon Vertex Detector design, based on the DSSD technology, can only be motivated by the unavailability of MAPS technology for the SPD Collaboration.

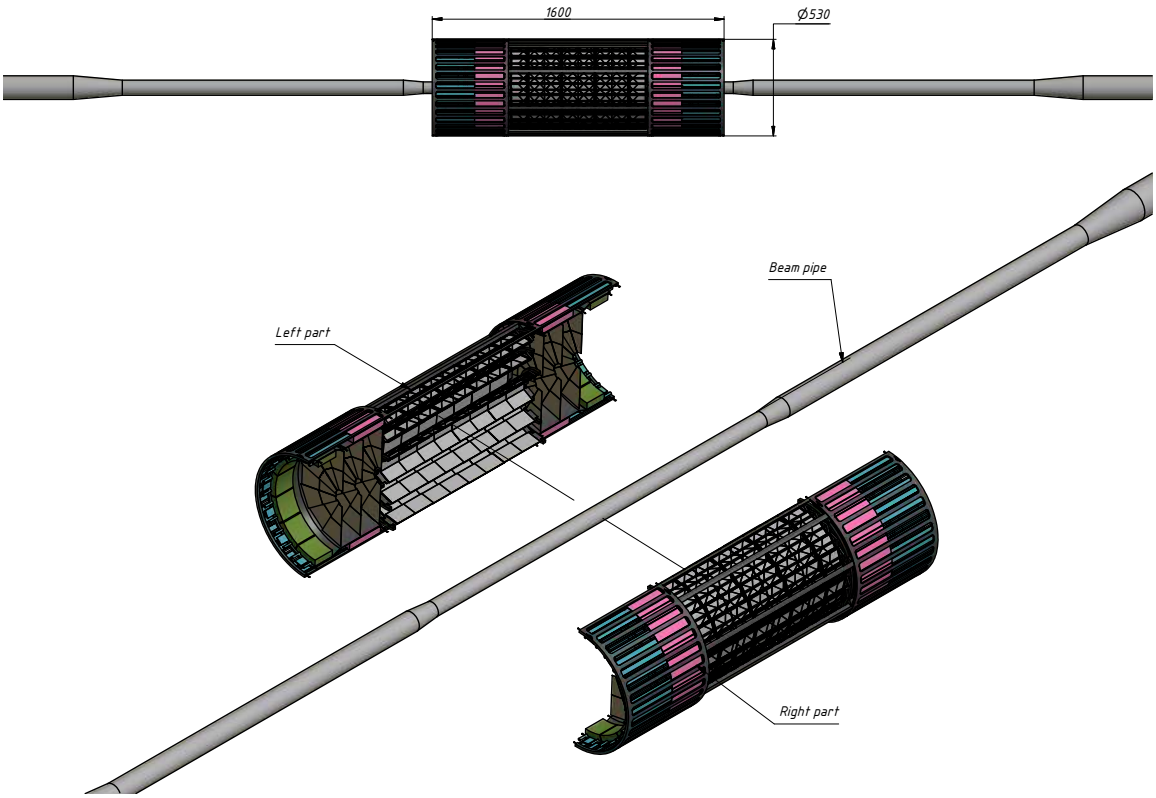

Figure 11.9: Sketch of the SVD mechanical support structure with the conical caves for the FEE.

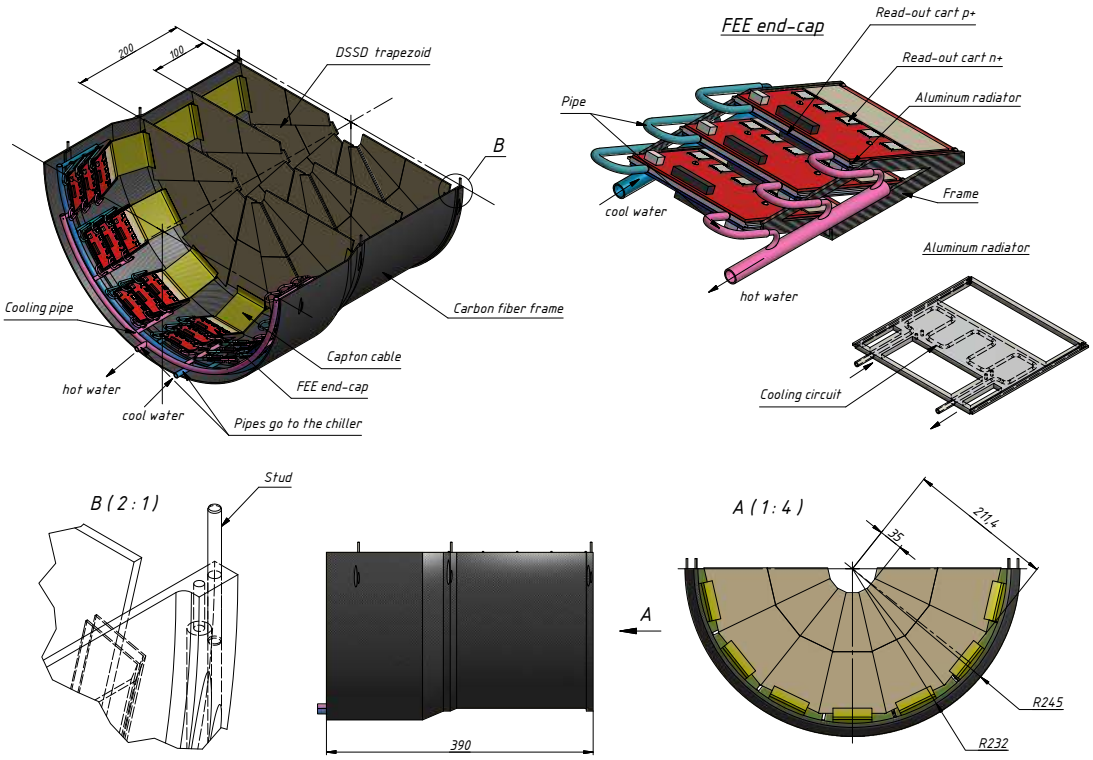

Figure 11.10: Sketch of the cooling system.

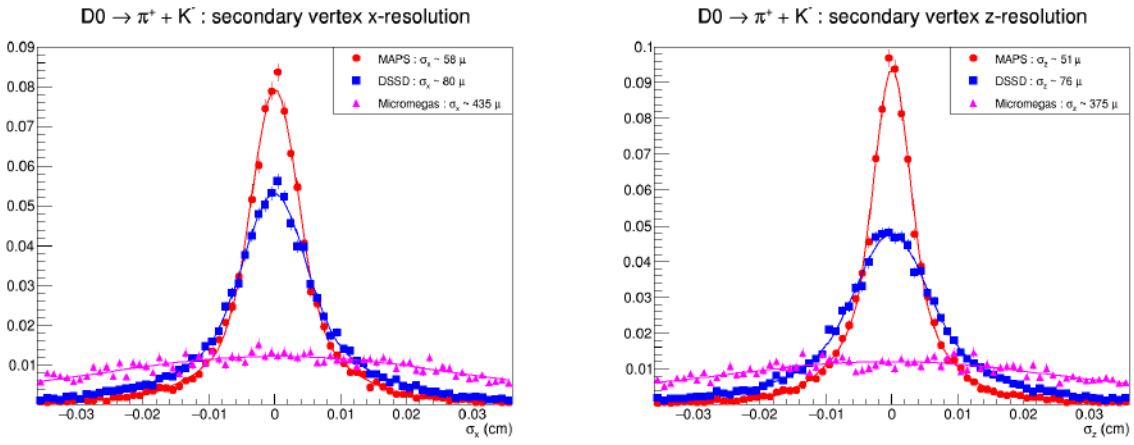

(a) (b)

Figure 11.11: Spatial resolution along X (a) and Z (b) axes for the secondary vertex of the $D^0 \to K^- \pi^+$ decay for MCT (magenta), 3-layer DSSD SVD (blue), and 4-layer MAPS SVD (red).

Chapter 12

Micromegas-based central tracker

1 Introduction

Registering charged particles and measuring their momenta is important to any task of the SPD physics program [3]. Tracking and determining of a particle momentum for SPD are performed with the vertex detector and the straw tracker [1]. The vertex detector based on MAPS technology (or DSSD as a backup option) will not be installed during the first stage of the SPD operation. The absence of the tracker close to the beam pipe leads to severe worsening of the detector momentum resolution, and also affects tracking efficiency and reconstruction of secondary vertices of the long-lived particles. To provide a performance adequate for the physics tasks, it is proposed to install a relatively simple and cheap central tracker, based on Micromegas technology. Such detector would be used during the first two or three years of the SPD operation.

In brief, the idea of the Micromegas(-based) Central Tracker (MCT) is to improve momentum resolution and tracking efficiency of the main tracking system during the first period of data taking. The main requirement is for the total cost to stay below 10% of one for Silicon Vertex Detector. MCT will not provide tracking in far forward region and precise secondary vertex reconstruction for D-tagging, but may be useful for reconstruction of hyperons and K_s^0 decays.

This proposal relies heavily on the Saclay group experience, who developed the Micromegas vertex tracker for the CLAS12 experiment [84].

2 Principle of operation

Micromesh gaseous structure (Micromegas, MM-detector), proposed by G. Charpak and I. Giomataris [85] , is a parallel plate counter with dedicated ionization and amplification gaps, separated by a fine mesh (Fig. 12.1). Typical thickness of the ionization gap is $3 \div 5$ mm with a drift field applied at about 600 V/cm, while the amplification gap is about 120 μm thick and the amplification field exceeds 30 kV/cm. High uniformity of the amplification gap and, hence, amplification field is ensured by the regularly spaced isolation pillars. High-energy particle crossing detector volume ionizes gas in the conversion gap. Electrons of primary ionization move toward the mesh and pass through it. Due to a very high field tension difference between the drift and the amplification gaps, the mesh transparency for primary electrons is above 95%. In the amplification gap an electron starts an avalanche, resulting in a final signal of about 10^4 electrons. Most of the electrons and ions in the avalanche are produced near the anode, so ions pass almost full amplification voltage before being collected on the mesh and produce dominant contribution to the signal. Ion collection time for single-cluster avalanche is about 150 ns. To get a good space resolution, the anode plane should be segmented. Usually, the readout electrodes are shaped as

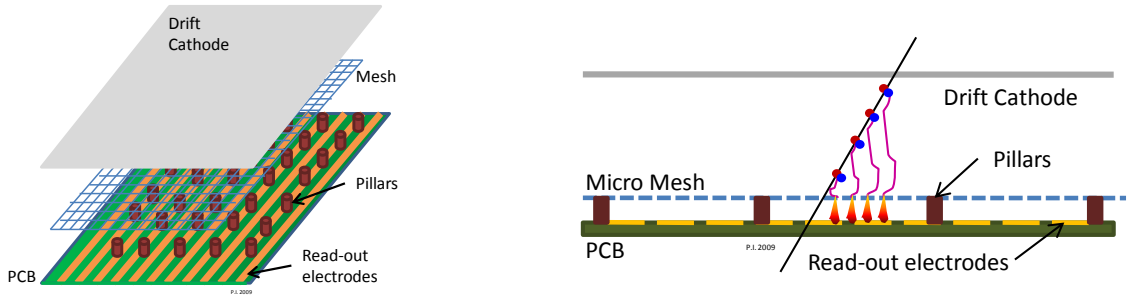

Figure 12.1: Sketch of the layout and operating principle of a Micromegas detector.

narrow strips with a typical pitch $0.35 \div 0.5$ mm.

3 Hit reconstruction and accuracy

Even a perpendicular track usually results in signals induced on several neighbor strips, a "signal cluster". For track angles close to 90°, a standard "charge centroid" method works perfectly. In this method a hit coordinate is calculated according to the following formula: $x = \sum A_i x_i / \sum A_i$, where A_i is a signal amplitude, x_i is a strip coordinate, and summation is done over all strips in a cluster. The experience of the COMPASS experiment [86] demonstrates that space resolution better than 100 μm may be routinely achieved for the perpendicular tracks. For the inclined tracks, accuracy is much worse. In this case the so-called "μ-TPC" algorithm is much more suitable. In this method a local track segment in the gas gap

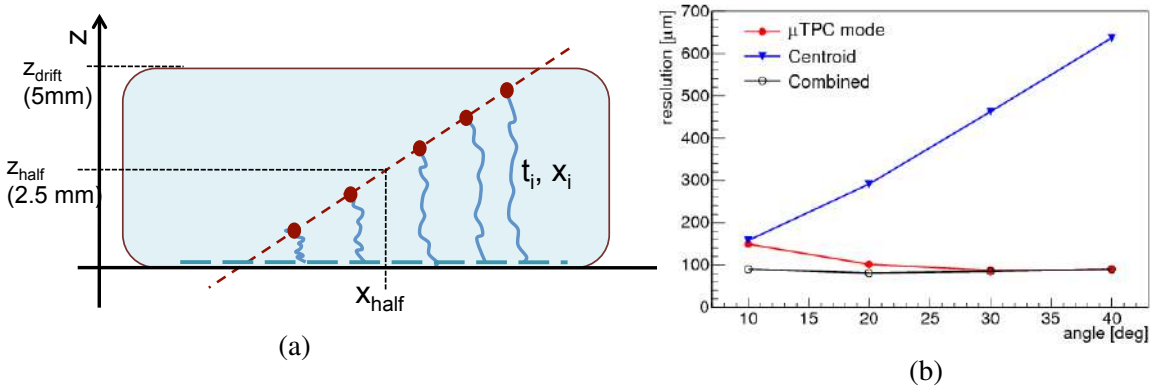

(a) (b)

Figure 12.2: (a) Principle of micromegas operation in μTPC mode. (b) Dependence of space resolution on incoming track angle for charge centroid and μTPC reconstruction methods, results of ATLAS Micromegas prototype test. Courtesy of the ATLAS Collaboration.

is reconstructed using precise timing information for each strip, similar to track building in a common Time Projection Chamber detector: x coordinate is a strip position, and the second coordinate is defined by the product of drift time and electron drift speed (Fig. 12.2 (a)). Accuracy vs incoming track angle dependence for the centroid and μ-TPC methods obtained at the beam test of the ATLAS MM prototype is shown on Fig. 12.2 (b). As it may be seen, a combination of the charge centroid and μ-TPC methods provides accuracy of $100 \div 150$ μm for incoming track angle from 0° to approximately 45°. The obvious disadvantages of the μ-TPC method are: necessity for the time measurement's accuracy better than 2 ns, and requirement for a better signal-to-noise ratio and, hence, a higher gas gain. For the SPD experiment, all tracks are almost perpendicular to the detector plane, but taking into account that the Micromegas Central Tracker operates in the magnetic field, a non-zero Lorentz angle results in drift line is inclined in respect to the electric field direction. For the hit reconstruction algorithms, the tracks looks like

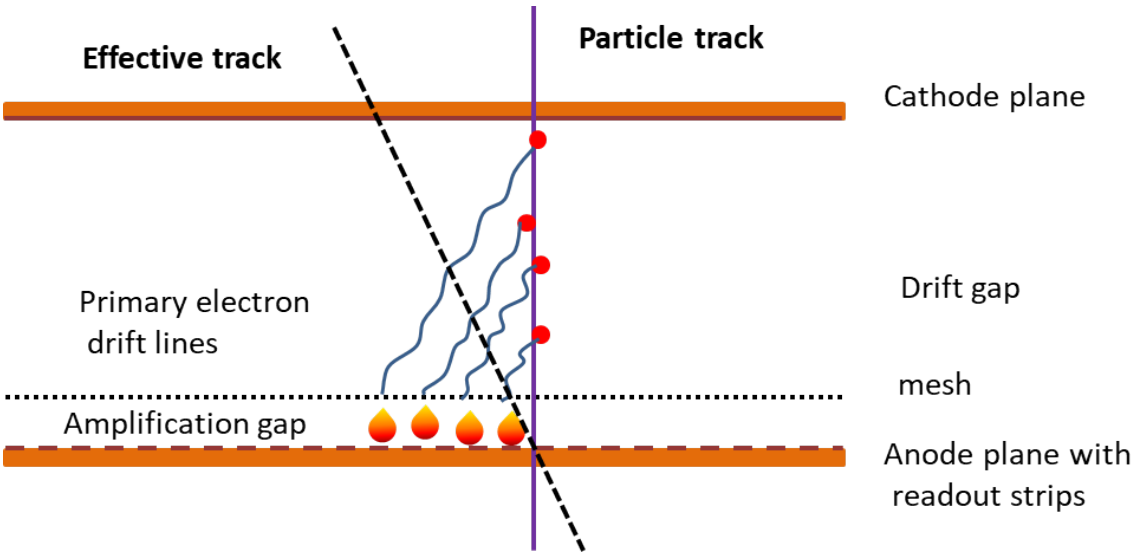

Figure 12.3: Micromegas operation in magnetic field.

"effectively inclined" as Fig. 12.3 demonstrates. There are several options to get a good space resolution for the MM operation in reasonable magnetic field:

1. use a μ-TPC algorithm for a hit reconstruction. This option requires a stable MM operation at a relatively high gas gain $G \approx 10^4$;

2. operate MM with increased drift field to reduce the Lorentz angle. The disadvantage of this solution is a reduced effective mesh transparency and detector efficiency. Reliability of this approach was demonstrated by the CLAS12 Collaboration [84]: the barrel Micromegas tracker operated effectively in 5 T magnetic field with drift field increased up to 8 kV/cm. Despite the mesh transparency being reduced to 60 %, final efficiency of well above 90% and accuracy of about 150 μm were obtained;

3. choose a gas mixture with a very low Lorentz angle. Possible candidates are mixtures like $CO_2 - Ar - iC_4H_{10}$(70-20-10) with expected Lorentz angle of about 5°-7°. Unfortunately, these mixtures are rather slow in weak drift fields and have never been used for the MM operation, so additional R&D is necessary.

Neither option needs any hardware modifications; a final decision will be taken only after additional tests.

4 Spark protection

As well as any parallel plate counter, the Micromegas detector is vulnerable to a spark discharge. If an avalanche charge exceeds the Raether limit ($10^6 \div 10^7$ electrons, depending on the gas mixture), an avalanche transforms to a streamer followed by a spark. Very high ionization may be easily produced by an interaction of a slow proton or neutron in the detector volume. In addition, even for a relativistic particle, fluctuations of primary ionization are very high: for 5 mm conversion gap and argon-based mixture, we can expect to find primary ionization cluster with charge above 500 e^- for more than 0.1% of the tracks, while the most probable value is 1 e^- per cluster. It means, that periodical sparks are unavoidable. Every discharge results in detector inefficiency for about 1 ms, effectively limiting the maximum flux capacity. To mitigate this effect, a special double-layer structure of readout electrodes

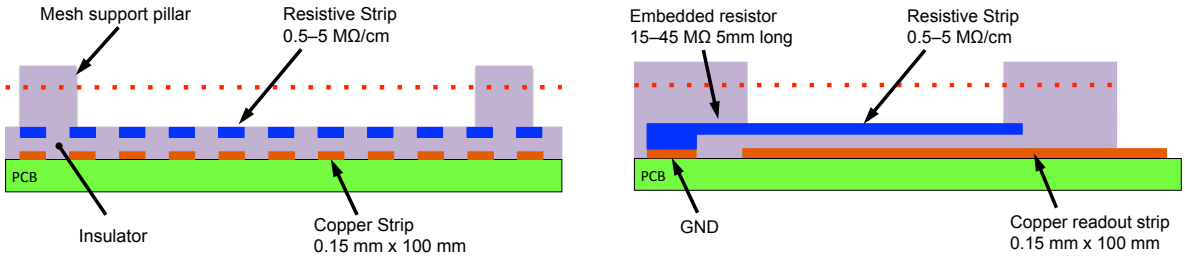

Figure 12.4: Scetch of spark-protected Micromegas detector. (front nd side views?)

will be used, as it is shown in Fig. 12.4. The ”top” or ”high voltage” strips are made of material with high resistivity and serve to create a high-tension electric field in the amplification gap. The second layer with copper ”pickup” strips collects the signal initially induced on the HV strip and transports it to the amplifier. Due to high resistivity, in case of a spark, only a small part of the HV strip (up to few mm) is discharged, while almost an entire detector area remains active. This principle is planned to be used in the SPD MCT.

5 Bulk micromegas technology

There are several methods of building a Micromegas detector. We propose to use bulk Micromegas technology [87] to build the SPD Micromegas Central Tracker. In this method, the readout PCB, the amplification gap and the mesh are produced as an entire module using photolithography. Production procedure includes the following steps:

1. A printed board with readout strips is laminated with a photoresist material. The thickness of the photoresist defines the amplification gap of the Micromegas detector.
2. Steel mesh pre-tensioned on a temporary frame is applied over PCB and the photoresist and is fixed by an additional photoresist layer.
3. the photoresist is exposed to UV light through a photo mask.
4. the unexposed photoresist is removed by chemical etching. the exposed photoresist forms an edge zone and pillars.

Production procedure is illustrated in Fig. 12.5. As a final step, a cathode plane should be fixed at a distance of a few mm from the mesh, to form the ionization gap. Bulk technology is simple, reliable and cheap; it allows to use commercially available materials and equipment and build rather large detectors. PCB with the mesh may be bent to build a cylindrical detector, multiple fixation points prevent appearing of the mesh waves or folds. The main disadvantage of this method is the inability to disassemble PCB+mesh module to fix possible problems. So here production is a ”single attempt” procedure.

6 Detector layer layout and production procedure

The SPD Micromegas Central Tracker will be produced using spark-protected bulk technology. Every single layer is an independent, one-coordinate cylindrically bent detector. As the MCT inner diameter is smaller than the vacuum tube flange diameter, it should be finally assembled around the fixed beam pipe. For this reason, every detector layer will consist of two independent half-cylindrical parts. the main steps of the half-cylindrical micromegas detector production are listed below:

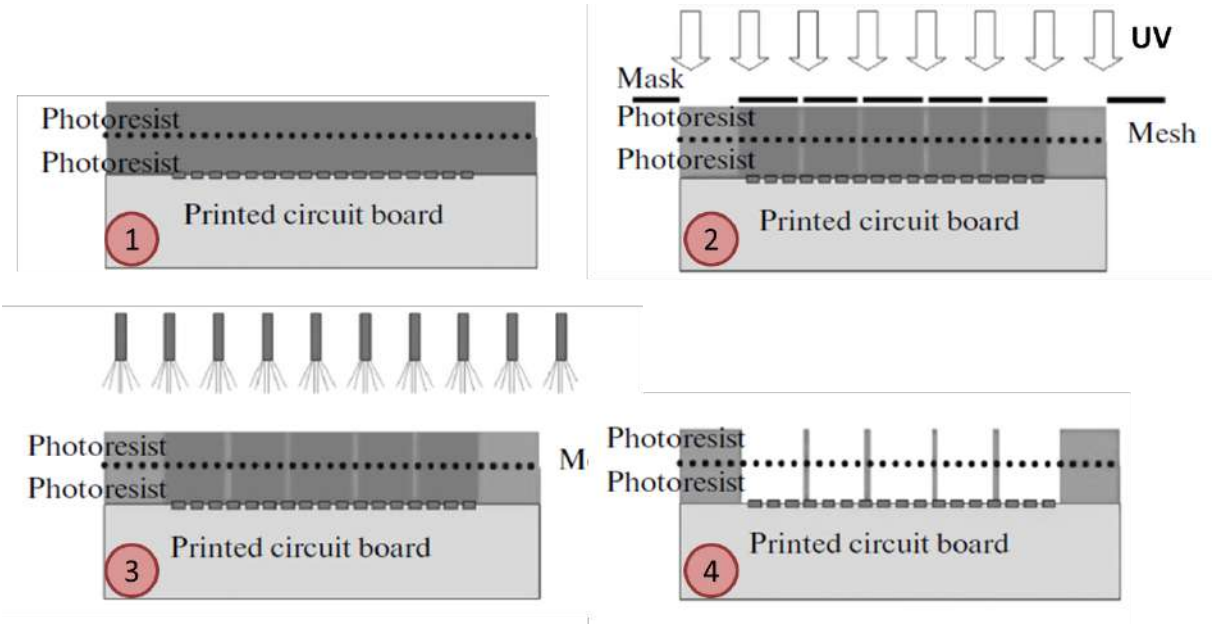

Figure 12.5: Main bulk micromegas production steps. 1 – readout PCB lamination with photoresist and fixation of pre-tensioned mesh; 2 – exposition of photoresist to UV light through mask corresponding to desired pillar pattern; 3 – etching of unexposed photoresist; 4 – finished bulk micromegas module (without anode plane).

1. The readout PCB+mesh module is produced using ”bulk micromegas” technology.

2. ”Bulk module” (readout PCB with fixed mesh) is bent on a cylindrical template. Carbon composite long-beames are glued on the long edge of PCB, and half-arcs are glued on the end-face edge of the active area.

3. Cathode PCB is glued on top of the long-beams and the arcs, forming a drift gap and closing the gas volume.

While the readout and cathode boards themselves are very thin and flexible, a detector layer after gluing is rigid enough to be self-supporting due to its shape. Long-beams are empty inside and will be used as gas distribution pipes. the total PCB length is approximately 50 mm bigger than the active area. This extra space will be used to put a signal and high voltage connector and for gas communication. To provide the required durability of ”communication” part of the layer, it will be reinforced by 3D printed plastic elements. Simplified sketch of a half-layer is shown in Fig. 12.6. Minimal layer radius is 50 mm; total material budget is about 0.4% of radiation length per layer. Micromegas design requires to have some dead area near the detector edges for mesh fixation. In our case, this area is also used for reinforcement elements (carbon fiber long-beams). We estimate a minimal width of the dead zone as 4÷5 mm, which will results in geometrical inefficiency of about 6% for the innermost detector level.

7 Front-end electronics

Micromegas operation in the μTPC mode requires precise amplitude and time measurement. Since one of the primary requirements for the Micromegas Central Tracker is moderate cost, FE boards will be based on existing and available for order VMM3 ASIC, and the board design itself will be very similar to one for the Straw Tracker, with minimal modifications to account for small size and high channel density of MCT.

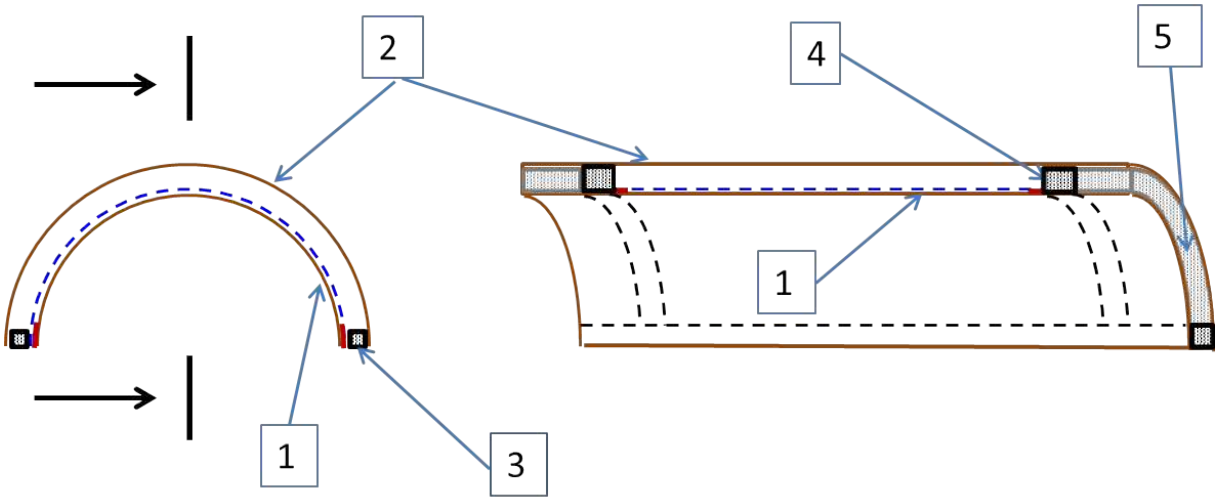

Figure 12.6: Simplified sketch of detector half-layer (not to scale). Left: perpendicular cross-section. Right: longitudinal cross-section. 1 - Readout board with mesh and amplification gap; 2 – cathode board; 3 – carbon fiber long-beams; 4 - carbon fiber arcs; 5 – 3D printed plastic reinforcement. Passivated areas are shown by red color.

VMM ASIC was developed to be used with sTGC and the MM detectors of the ATLAS New Small Wheel (NSW) and are very flexible to be configured to read out the most types of gaseous detectors. The ASIC provides the peak amplitude and time with respect to the bunch-crossing clock, or other external signal. A block diagram of one of the identical channels is shown in Fig. 12.7. Each channel

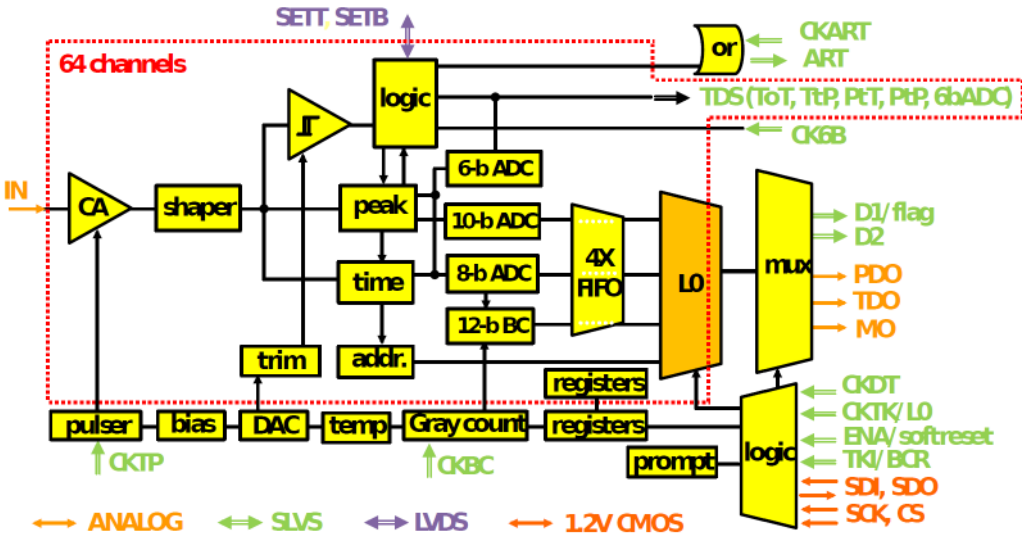

Figure 12.7: Block diagram of VMM3 ASIC.

is equipped with a fast comparator with an individually adjustable threshold. When a signal crosses a set threshold, a peak detection circuit is enabled. Neighbour-enable logic allows the threshold to be set relatively high and yet very small amplitudes to be recorded. At the peak, a time-to-amplitude converter is started and then stopped by the next bunch-crossing. The two amplitudes are digitized and stored in a de-randomizing buffer and read out serially with a smart token passing scheme that only reads out the amplitude, timing, and addresses of the active channels, thus dramatically reducing the data bandwidth required and resulting in a very simple readout architecture. So-called ”continuous” readout mode,

available for VMM3 allows simultaneous read/write of data, and provides dead-timeless operation that can handle rates up to the maximum of 4 MHz per channel. In addition to the main properties mentioned above, it includes a plethora of features that significantly increase its versatility. These include selectable polarity, gain (0.5, 1.0, 3.0, 9.0 mV/fC) and shaping time (from 25 to 200 ns). Integrated calibration circuit allows precise calibration of amplitude and time measurements on the channel-by-channel basis.

the RD51 Collaboration have developed a HYBRID128 front-end board, based on VMM3a ASIC, as a part of the Scalable Readout System project. This board is commercially available and fits most of MCT requirements very well. Its main limitation is insufficient radiation hardness, but it is not critical for SPD with quite moderate radiation conditions, see Chapter 16. We use the geometrical characteristics of HYBRID128 (50×80 mm^2, 7 mm thickness without cooling system) to estimate the space needed to locate the FE boards near the detector.

8 General detector layout

8.1 Preliminary simulation

To simplify the support structure and assembling procedure, the detector layers will be organized in few superlayers. a superlayer consists of 2 or 3 layers with a different strip orientation, rigidly connected together. The attractive option available for such a design is to use an outer readout PCB as a cathode PCB for the inner layer. It allows to save some material budget and to increase layer rigidity. A simplified MC simulation was performed to compare several detector geometries (with 1, 2 or 3 superlayers). the summary of the tested layouts is presented in Table 12.1. Space resolution of each layer was taken equal

Table 12.1: Summary of MCT detector layout variants used in the preliminary MC simulation.

	Superlayer 1			Superlayer 2			Superlayer 3		
	N layers	Strip angle	Min.R, mm	N layers	Strip angle	Min.R, mm	N layers	Strip angle	Min.R, mm
MCT-1	3	$0^\circ, \pm 5^\circ$	50						
MCT-2	3	$0^\circ, \pm 5^\circ$	50				3	$0^\circ, \pm 5$	190
MCT-3	3	$0^\circ, \pm 5^\circ$	50	2	$\pm 5^\circ$	120	2	$\pm 5^\circ$	190

to 150 μm. Momentum resolution was estimated for 90° and 45° 1 GeV track. Simulation results are summarized in Table 12.2. Resolution without the vertex detector is added for comparison. From the

Table 12.2: Results of preliminary simulation: momentum resolution for 1-GeV charged track without vertex detector and for 3 variants of the Micromegas CT

Tracks	Resolution $dP/P, \%$			
	No CT	MCT-1	MCT-2	MCT-3
1 GeV/c, 90°	2.50	1.30	1.39	1.34
1 GeV/c, 45°	2.56	1.45	1.54	1.53

point of raw resolution, a layout design with the single multilayer, located as close to the beam pipe as possible, looks preferable. But it will be the most vulnerable to the beam-induced background which is unknown now. For this reason we choose the design with 3 superlayers as a main solution. For this design, additional simulation with space resolution improved by factor 2 and 4 was done. Very descent improvement was observed: for 45° tracks momentum resolution improves from 1.53% to 1.47% and 1.35% accordingly. We can conclude, that it is inefficient to try to reach a space resolution better then 150 μm; momentum resolution is limited by multiple scattering.

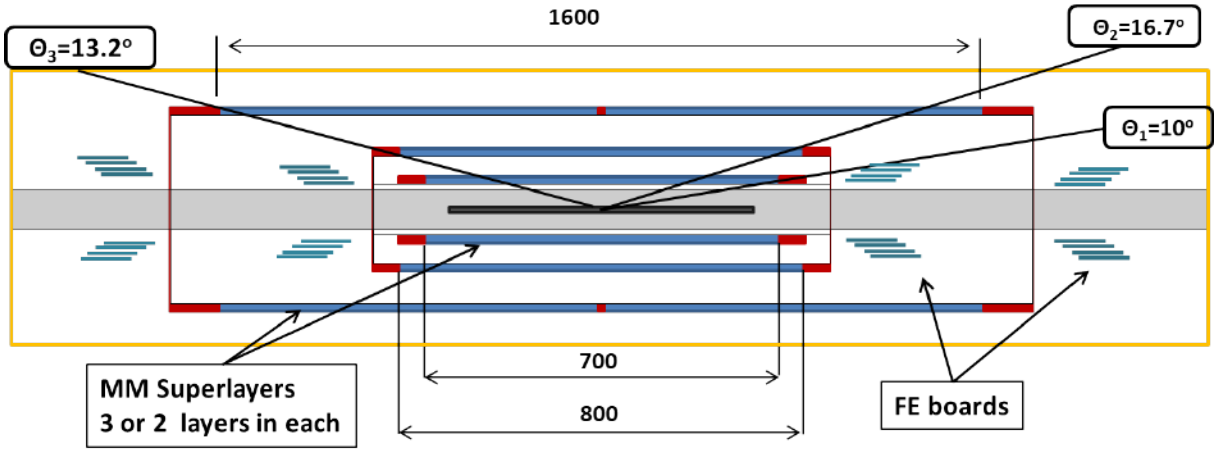

Figure 12.8: Layout of the MCT. Blue colors mark active area of superlayers. Dead areas are marked by red color. Inner border of the Straw Tracker is shown with yellow line. the beam pipe is shaded by gray color, black area in the middle of beam pipe – beam-crossing area.

8.2 General layout

The general detector layout of the MCT is shown in Fig. 12.8. Seven detector layers are organized in 3 superlayers. Each superlayer consists of two or three layers with a different strip orientation, rigidly connected together. an outer superlayer is divided into two parts along the beam direction, due to the limit on maximum detector size. Dead area between two parts is 10 mm. Detailed information on detector geometry is summarized in Table 12.3.

Table 12.3: Main characteristics of the suggested Micromegas Central Tracker.

Layer	Super-layer	Radius, mm	Strip angle	Active area length, mm	Pitch, mm	Number of chan-nels	Number of boards	Geometrical acceptance
1	1	50-54	0°	700	0.4	738	6	$10^\circ - 170^\circ$
2		54-58	$+5^\circ$	700	0.45	962	8	
3		58-62	-5°	700	0.45	1018	8	
4	2	112-116	$+5^\circ$	800	0.55	1484	12	$14^\circ - 164^\circ$
5		116-120	-5°	800	0.55	1530	12	
6	3	180-184	$+5^\circ$	2×800	0.55	2×2024	36	$13.2^\circ - 166.8^\circ$
7		184-188	-5°	2×800	0.55	2×2150	36	

the signal is transported from detectors to a FE board by a thin flat cable (not shown on the sketch). The board itself is placed in 4 disks about 15 cm from both ends of the detector, as close to the beam pipe as possible. Two inner disks are located at $|z| = 550$ mm and include boards to read out two inner superlayers. Due to the substantial power dissipation, the area near the boards needs active cooling. Presently, water cooling is considered as the main option. The cooling bar will be done as an integrated part of the support structure. With minimal cooling bar thickness of 6 mm, the inner FE board disks will have a maximum radius $R \approx 116$ mm. That limits the detector acceptance to $11.5^\circ \leq \theta \leq 168.5^\circ$.

9 Simulation of detector performance

Monte Carlo simulation of the SPD detector with and without Micromegas Central Tracker was conducted to estimate the detector perfomance. Center-of-mass energy $\sqrt{s} = 10$ GeV and minimal bias events were used. the results for momentum resolution, as a function of transverce momentum p_T (a), total momentum p (b), polar angle θ (c); and primary vertex reconstruction accuracy as a function of track multiplicity (d), are shown in Fig. 12.9. There is no discrepancy with a preliminary simulation presented in Table 12.2): both 90° and 45° tracks used for preliminary study hit the barrel Straw Tracker, while for the minimal bias events most of the tracks pass throught the end-cap Straw Tracker, which has very few active layers.

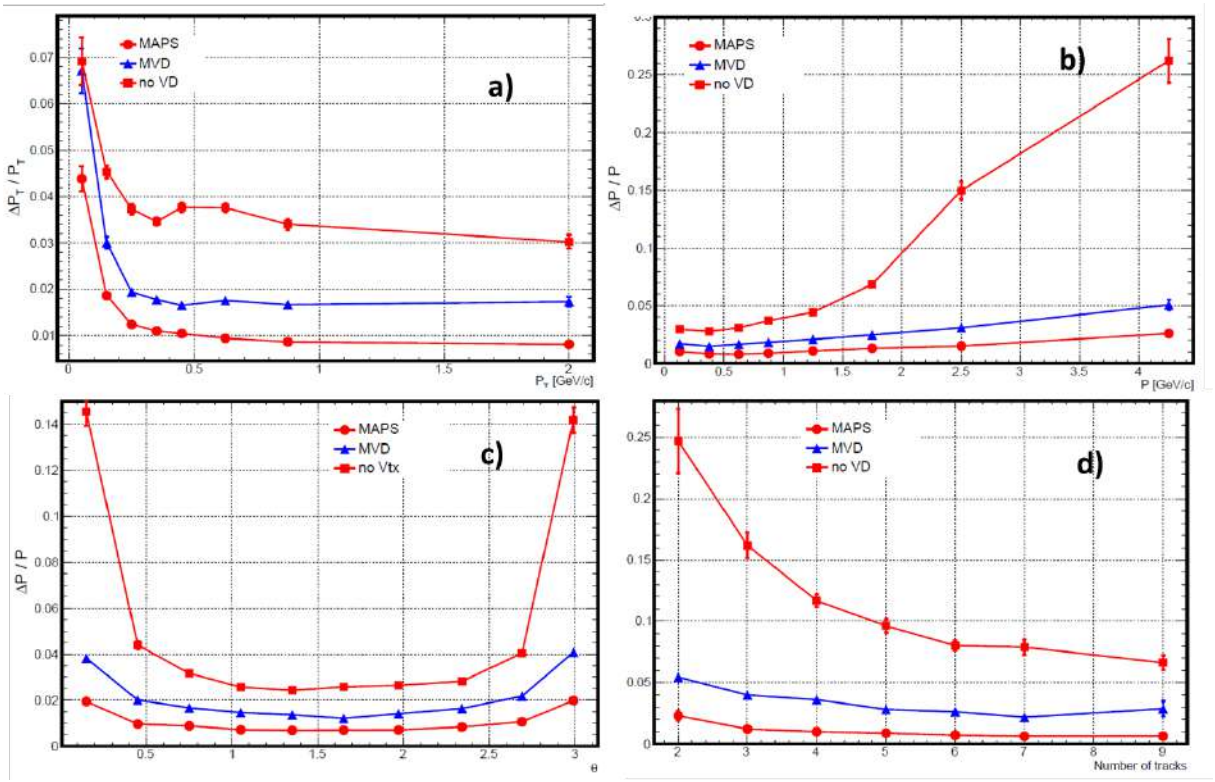

Figure 12.9: SPD detector tracking performance with and without MCT: red rectangular marks represent results without MCT, blue ones – with MCT, and red circles represent results with silicon MAPS vertex detector. (a) transverse momentum resolution; (b) momentum resolution (c); momentum resolution vs polar angle; (d) primary vertex reconstruction accuracy [UNITS???] vs number of tracks.

10 Detector occupancy and gas mixture choice

10.1 Requirements

Nominal CM energy for the SPD experiment is 27 GeV with luminosity about $10^{32} cm^{-2} s^{-1}$. These values result in about 3 MHz rate of inelastic events and an average event multiplicity ≈10 tracks per a minimal bias event. The Micromegas Central Tracker is planned to be used only at the first stage of the detector operation with beam collision energy below 10 GeV and luminosity at least an order of magnitude below nominal. Nevertheless, taking into account the unknown beam-induced background, we use the nominal luminosity and energy to estimate the detector working conditions.

A single strip count rate depends on the track multiplicity and an average number of hits per cluster N_{cl}.

For the perpendicular tracks without the magnetic field, the last value is defined mainly by diffusion, for the common gas mixtures $N_{cl} \approx 2$. In real experiment, the cluster size increased with the track angle, Lorentz angle, and the gas gap. For the inner layers, the average track angle in $r\phi$ plane is small ($< 2^{\circ}$) and may be neglected. For a rough estimate of the hit rate, we take $N_{cl} = s \times sin(\Theta_L)/d + 2$, where s is a drift gap depth, Θ_L is a Lorentz angle, and d is a signal strip pitch. For the common gas mixtures like $Ne - C_2H_6(10\%) - CF_4(10\%)$, used by the COMPASS experiment, or $Ar - CO_2(70\%)$, initially proposed for ATLAS, the Lorentz angle is rather large ($\Theta_L \geq 40^{\circ}$). That results in a single strip count rate of about 300 kHz and detector occupancy above 10%, assuming signal length 300 ns. Despite being manageable, these values are too high for a "temporary" detector. the obvious solution is to find a combination of gas mixtures and operation parameters with a much smaller Lorentz angle, ideally, below 10°.

Another two parameters, affected by the Lorentz angle are signal amplitude and space resolution. For the triggerless operation, noise will not be suppressed by time coincidence, so the threshold must be rather high. As the signal amplitude is inversely proportional to the cluster size, a small Lorentz angle gives a clear benefit. Small cluster size (1÷1.5 mm or 2÷4 strips) also allows to use a simple and reliable charge-weighting method for the coordinate measurement.

Summarising, a good gas mixture for the MCT must provide:

- stable long-term operation at gas gain $G \approx 10^4$;
- small Lorentz angle;
- short enough signal with full length $T_{full} \approx T_{drift} + T_{ion} \simeq 300$ ns. Here, T_{ion} is the full ion drift time in the amplification gap and T_{drift} is the maximum primary electron drift time.

10.2 Overview of gas mixtures

Expected dependence of a Lorentz angle and electron drift speed on the electric field tension for several gas mixtures was studied with the GARFIELD [60, 61] simulation. the magnetic field was set to $B = 1$ T. the result summary is presented in (Fig. 12.10), and a short overview is given below.

The $Ne - C_2H_6 - CF_4$ mixture was used by the COMPASS experiment for the Micromegas operation. The main advantages of the Ne-based mixtures are a low spark rate and a high achievable gas gain. Unfortunately, these mixtures have a too high Lorentz angle in the magnetic field 1 T and in the reasonable drift fields. Additional drawback is a low primary ionization and limited availability of neon on the market. We do not consider Ne-based mixtures as good candidates for the Micromegas Central Tracker operation.

The $Ar - CO_2$ and $Ar - CO_2 - iC_4H_{10}(2\%)$ mixtures with CO_2 fraction $7 - 30\%$ were studied by ATLAS as part of the New Small Wheel project. These mixtures also have a too high Lorentz angle and require the μ-TPC mode for a good spatial resolution.

The $Ar - iC_4H_{10}(10\%)$ mixture was used by the CLAS12 Collaboration for Micromegas operation in a strong magnetic field 5 T. Very high drift field of 8 kV/cm was used to reduce the Lorentz angle below 20° and reach ≈ 150 μm spatial resolution for the price of 40% loss of effective mesh transparency [88], [89] . Due to a much smaller magnetic field (1T) in the SPD spectrometer, the 2.5÷3 kV/cm drift field will be big enough to get $\Theta_L \approx 10^{\circ}$ and $T_{drift} \approx 100$ ns with an acceptable amplitude loss of $10 \div 15$ %. The only real drawback is the flammability of this mixture. We consider $Ar - iC_4H_{10}(10\%)$ as a very good reserve option, which was tested in a real experiment and guarantees to provide results, if a better variant is not found.

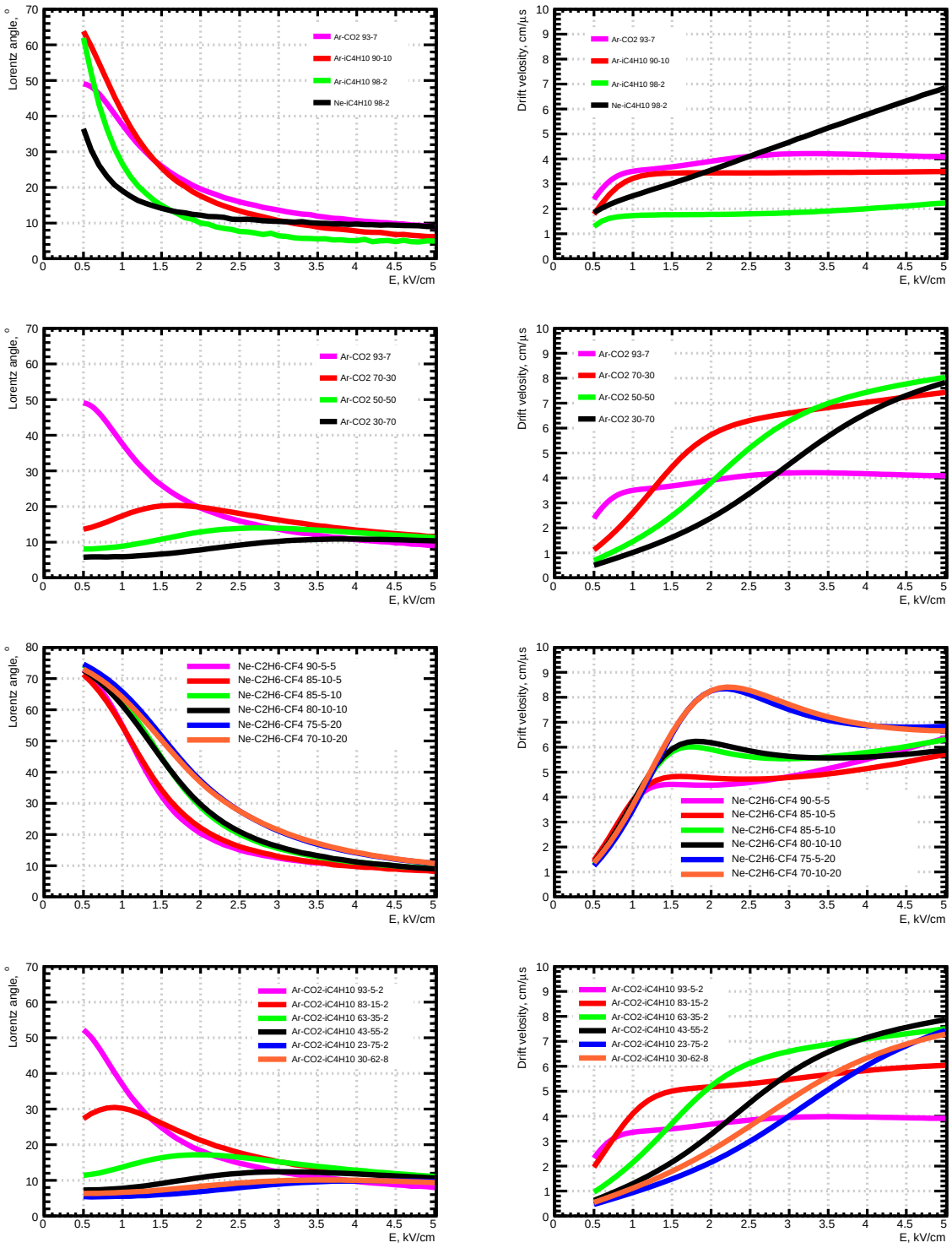

Figure 12.10: GARFIELD simulation results for the Lorentz angle (left) and electron drift speed (right) vs electric field tension (B=1 T).

The $Ar-CO_2$ mixtures with a high CO_2 fraction ($\approx 70\%$) have a very low Lorentz angle. These mixtures are too slow in a weak electric field, but the electron drift speed rises fast with the field tension, providing both Lorentz angle $\Theta_L = 8^\circ$ and $T_{drift} \approx 100$ ns with 3 kV/cm drift field. the $Ar-CO_2$ mixtures with CO_2 fraction 30%, 50% and 70% were studied with 10×10 cm^2 test detector with 128 μm amplification

gap, 500 μm strip pitch and resistive high voltage strip. All readout strips were connected in parallel to fast spectrometric amplifier with rise time $\tau_{rise} = 7$ ns and decay time $\tau_{decay} = 100$ μs. This setup allows to measure both the gas gain with ^{55}Fe source and the MM signal duration for a single-cluster signal (^{55}Fe) and cosmic muons. Maximum effective gas gain above 4×10^4 was reached with ^{55}Fe

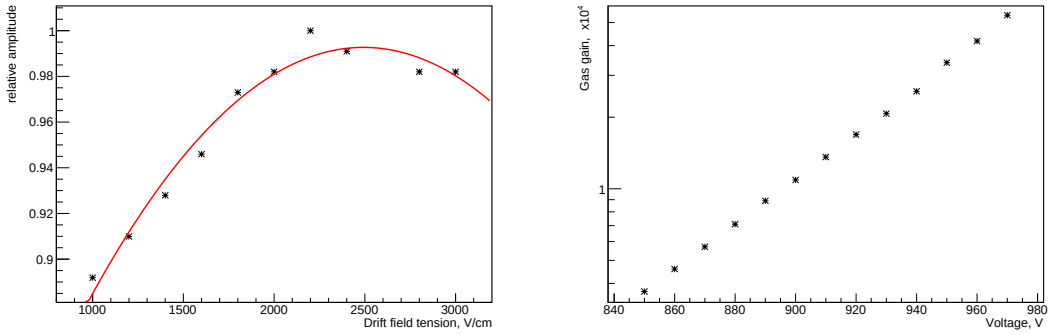

Figure 12.11: Relative signal amlitude vs drift voltage (a) and gain vs amplification voltage (b) for the test MM detector with $Ar(30\%) - CO_2(70\%)$ gas mixture.

source at amplification voltage $U = 960$ V, while $U = 900$ V was needed for $G = 10^4$. We consider 60 V to be a solid margin for a stable operation of the real detector. Measurements of the amplitude vs drift voltage dependence result in the optimum drift field about $2.2 \div 2.5$ kV/cm with a few percent drop at 3 kV/cm. Single-cluster signal duration was about 130 ns, and the full signal length for the MIP tracks was well within 300 ns, in accordance with expectation. We consider the $Ar(30\%) - CO_2(70\%)$ mixture as a very strong candidate for the Micromegas Central Tracker. Similar performance is expected for the $Ar - CO_2 - iC_4H_{10}$ mixtures with $60 - 80\%$ CO_2 fraction and a small addition of isobutane (2%). Such mixtures are also inflammable, as pure $Ar - CO_2$, and usually have better high-voltage stability. Further tests, including space resolution and maximum hit rate test at Linac electron beam are planned for the next year.

Summarizing, at this time we are considering the $Ar - CO_2$ and $Ar - CO_2 - iC_4H_{10}(2\%)$ mixtures with CO_2 fraction about 70% as very promising variants, which provide both a very low Lorentz angle and good speed, but require more tests, and the $Ar - CO_2(10\%)$ mixture as a reliable and well-tested backup solution.

11 Water cooling

To estimate the total power consumption of the reading electronics, we used real data of the typical consumption for MMFE-8 cards. These cards are used by the ATLAS Collaboration to read signals of Micromegas New Small Wheels cameras. Each card contains 8 64-channel VMM-3A chips, specialized ASICs for implementation of trigger logic and data exchange, and local voltage converters. Typical power consumption of such a card was 30 W. Assuming that the power consumption is proportional to the number of VMM chips and assuming a safety factor of 1.5, we expect that the maximum consumption of one 128-channel card will not exceed 12 W. The total heat dissipation of the MCT readout electronics in this case will be about 1.5 kW, and it depends on the hit rate of the cameras. The drift characteristics and gain of the gas detectors are strongly affected by temperature, so the cooling system must ensure a stable temperature of the FE cards. Water cooling is the easiest and most reliable way to meet these requirements.

It is proposed that the individual cooling plates be rigidly attached to a supporting carbon fiber structure. The FE boards will be attached to the plates with screws. In this way, the cooling plates will simul-

taneously act as mounting pads for the readout boards. Thermal contact between the heat-generating elements and the cooling plate will be provided by thermal pads. The proposed design of the radiator is shown in Fig. 12.12 (a). It consists of an aluminum plate with a U-shaped groove, in which a 4×2.5 mm metal tube is soldered in. Schematic illustration of one layer of the support structure with radiators is shown in Fig. 12.12 (b). Radiators in one layer are connected in series by copper or polyurethane tubes 4×2.5 mm. "Branches" of the radiators are connected to a larger opening manifold. Calculations show that at pressure in the cooling system 1 bar, total length of pipes less than 2 m, and heat dissipation 120 W, the temperature difference of water between input and output will not exceed 2.5 degrees.

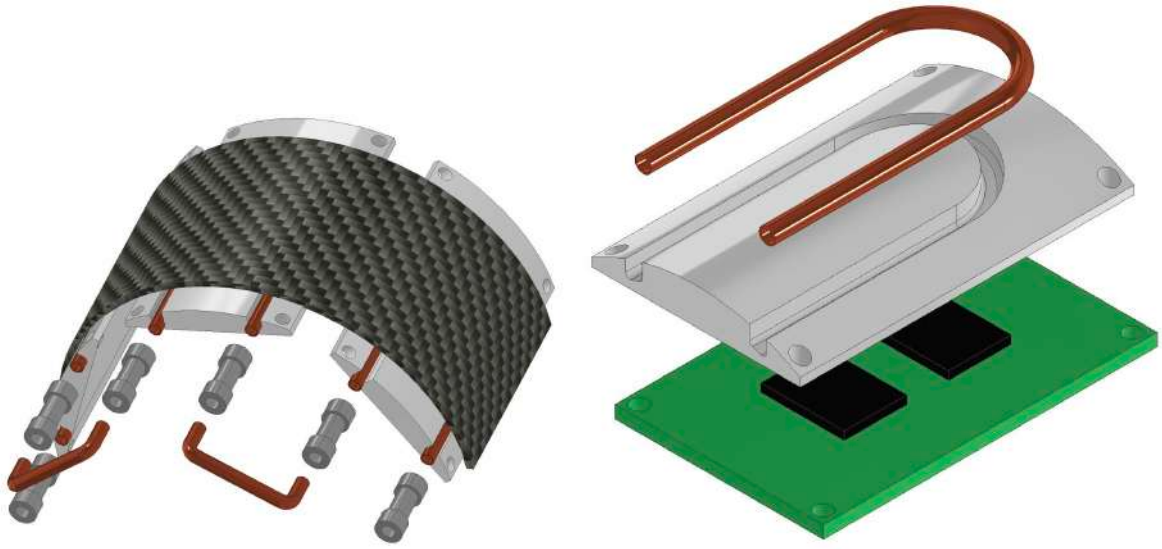

Figure 12.12: (a) Exploded-view diagram of a single cooling plate with the FE board. (b) Schematic view of the carbon fiber support structure with cooling plates fixed to it.

12 Cost estimate

The cost estimate is summarized in Table 12.4. The main contribution is coming from the readout board

Table 12.4: Estimate of the Micromegas Central Tracker cost.

	Cost per unit, k$	N units	Cost, k$
Detector materials	9	18	162
FE electronics	1.7	150÷200	340
HV PS, HV cables			23
Gas system			23
Assembly tools			230
Supporting structure			0
Water cooling system			100
TOTAL			878

production and the FE electronics. For the board production the cost estimate is based on the data available for the CLAS12 Micromegas tracker; the FE cost is estimated using price of commercially available HYBRID128 boards, developed by the RD51 Collaboration. Supporting structure is an integrated part of beam pipe container, so its cost is not taken into account here.

Chapter 13

Zero Degree Calorimeter

1 General layout

A Zero Degree Calorimeter (ZDC) is a standard device for the collider environment. It is placed in the space between the separation dipole magnet BV1E and the next dipole magnet BV2E1, about 13 m from the IP (Fig. 13.1). The strong magnetic field before ZDC efficiently removes all charged particles, allowing clean measurement of neutrals, so the device can work up to very high luminosities. Two ZDC devices are supposed to be placed symmetrically on both sides of the IP. A coincidence between them, as well as with other detectors, will be used.

ZDC's main tasks are:

- luminosity measurement;
- spectator neutron tagging;
- time tagging of the events for event selection;
- local polarimetry with forward neutrons.

To accomplish these tasks, the following performance parameters should be met:

- time resolution $150 \div 200$ ps;
- energy resolution for neutrons of about $20 \div 30\%$ at 10 GeV;
- neutron entry point spatial resolution 10 mm.

We plan to use a fine segmented calorimeter based on plastic scintillator active tiles with direct SiPM readout and tungsten absorber plates, similar to the calorimeter proposed for the CALICE [90]. A schematic view of the calorimeter is shown in Fig. 13.2.

2 Detailed description

The position of the ZDC is inside the cryostat of NICA magnets (see Fig. 13.3). This location provides several challenges:

- limited space between the two beam pipes;

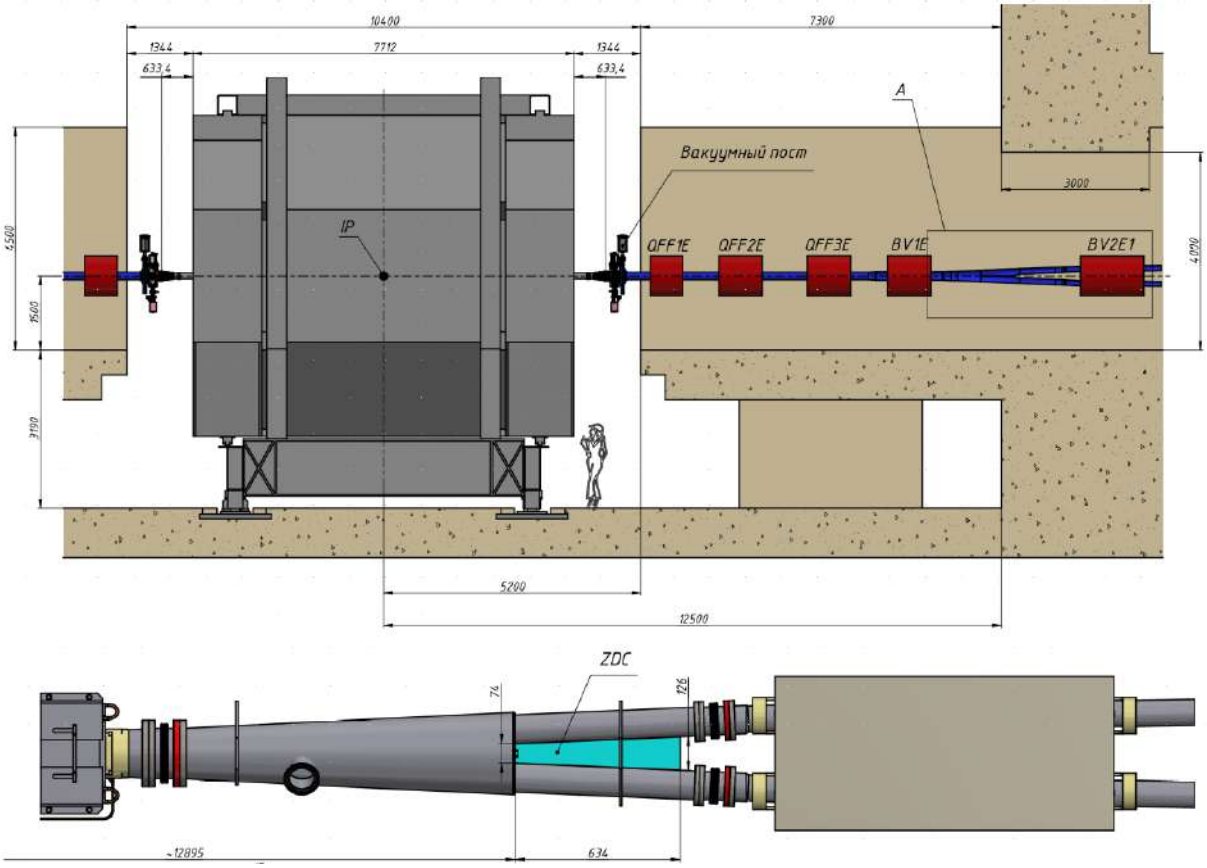

Figure 13.1: ZDC position on the one side from the IP. The top figure shows the general view while 5 times enlarged area ”A” is shown in the bottom. The cryostat is not shown.

- insulation vacuum $\sim 10^{-6}$ Torr;
- cryogenic temperature ~ 80 K;
- difficult accessibility.

The calorimeter is assembled from individual planes, as shown in Fig. 13.4. Each plane has a printed circuit board (PCB) with SiPMs 3×3 mm^2 S13360-3050PE by Hamamatsu, scintillator tiles, and tungsten absorber plate. The SiPMs and the tiles are organized into a matrix 7x5. Plane sizes are increasing from the front to the back side of the calorimeter, together with the increase of the gap between the beam pipes. Tile sizes are increasing accordingly. The scintillator tiles for better light collection are chemically whitened by UNIPLAST (Vladimir, Russia) [91]. Then a small polished burrow for the SiPM readout is made.

Each plane is attached to the top and the bottom rails (position 1 in Fig. 13.3). These rails are connected by thermal bridges to the thermal screen (position 5 in Fig. 13.3), cooled to the liquid nitrogen temperature. Signals from the SiPMs are lead out by flat cables to the vacuum tight connectors, placed on four 6-inch flanges (position 2 in Fig. 13.3) of the cryostat. We consider either circular or rectangular connectors 36÷40 pins each, 15 connectors per flange. Only SiPMs are going to be placed inside the cryostat with total dissipation power about 0.1 W. All the electronics, which includes front-end amplifiers, SiPM power supplies and signal digitization, will be placed outside the cryostat in the racks below and above the beam pipes. ZDC DAQ is based on the waveform digitization modules (WFD) designed for the experiment DANSS at Kalininskaya NPP [92]. It performs 125 MSPS 12-bit waveform recording.

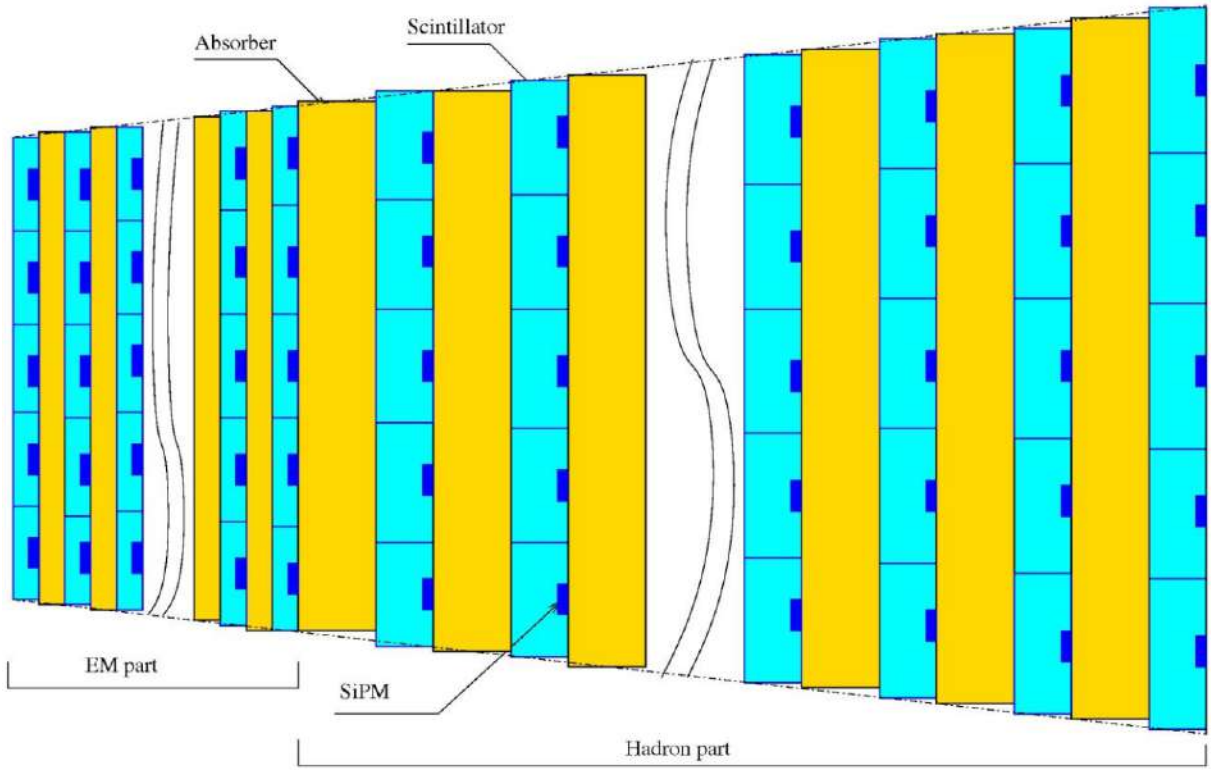

Figure 13.2: A schematic layout of the calorimeter

the modules have 64 inputs and are made as single units of VME64X standard. Both 64-bit addressing and data path are supported, as well as double edge data transfers. Each module is equipped with a 1 Gbit port for even faster readout. The modules use Xilinx Spartan-6 FPGA for signal processing and the readout interface, which provides nearly infinite flexibility of operation. A 4-Gbit SDRAM memory onboard allows deep data buffering for deadtimeless readout.

The calorimeter can be roughly divided into two parts - the front part and the rear part. The front part serves mostly as an electromagnetic calorimeter to measure gammas, and the rear part is responsible for measurement of neutrons. The preliminary parameters of the layers in each part are given in the Table 13.1.

The background conditions in the location of the ZDC could be found in the Chapter 16, devoted to NICA ring background estimates. The operational limit for Hamamatsu SiPM is $10^{11} - 10^{12}$ neutrons/cm^2. Beam halo calculations give an estimation of 10^{10} neutrons/(cm$^2\times$ year) at the ZDC position for the most intensive NICA beams.

3 Monte Carlo simulation

The MC model of the ZDC was created to determine the optimal ZDC configuration. The simulation is done within GEANT4 framework [93–95]. Neutrons and photons of different energies (1, 3, 6 and 12 GeV) are created by a box generator. The particle momentum is parallel to the longitudinal axis of the calorimeter. The interaction point distribution in the frontal transverse plane of the detector is uniform. Energy and space resolution, transverse and longitudinal leakage and neutron to photon separation have been studied. Different detector configurations are tested for neutron and photon identification. For the most longitudinally granulated configuration within available space energy resolution for neutrons is about $50\%/\sqrt{E}\oplus 30\%$ and for photons is about $20\%/\sqrt{E}\oplus 9\%$. Longitudinal energy distributions for 1

Table 13.1: Preliminary parameters of the calorimeter layers.

Parameter	Value
Electromagnetic part	
Number of layers	8
Scintillator thickness, mm	5
Absorber thickness, mm	5
PCB thickness, mm	1
Total absorber thickness, mm	35[1]
Total part thickness, mm	83
Part thickness, X_0	10
Part thickness, λ_i	0.4
Number of channels	280
Hadron part	
Number of layers	22
Scintillator thickness, mm	10
Absorber thickness, mm	13
PCB thickness, mm	1
Total absorber thickness, mm	286
Total part thickness, mm	528
The part thickness, λ_i	3.1
Number of channels	770
Total	
Thickness, mm	611
Thickness, λ_i	3.5
Number of channels	1050

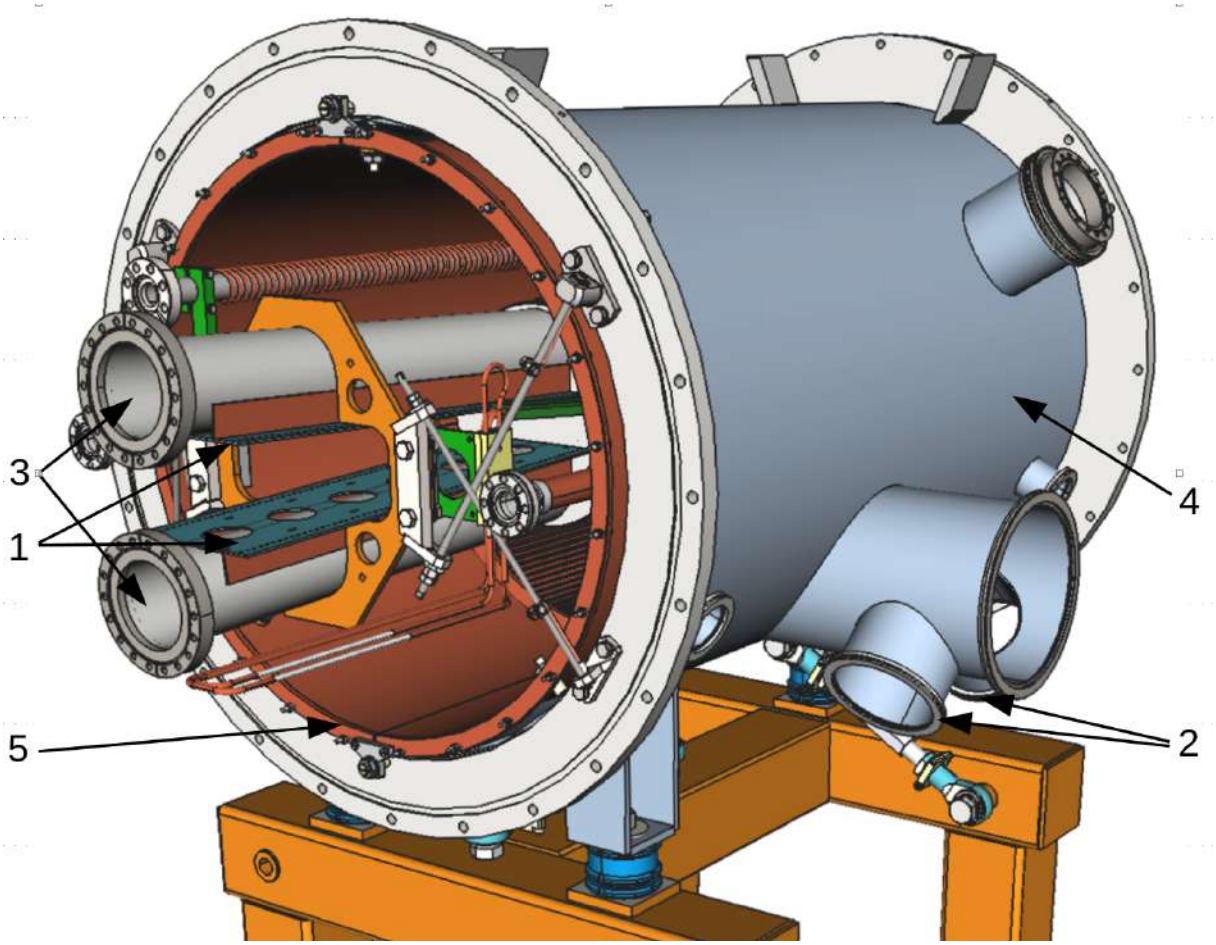

Figure 13.3: ZDC place inside the cryostat. 1 – ZDC supporting rails; 2 – flanges for the output connectors; 3 – beam pipes; 4 – the cryostat outer shell; 5 – copper screen cooled to liquid nitrogen temperature.

GeV and 12 GeV photons and neutrons are shown at Fig. 13.5. One can see from figure that longitudinal energy distributions for photons and neutrons are very different and can be used for neutron/photon separation. A jump at the 11th layer corresponds to its increased thickness.

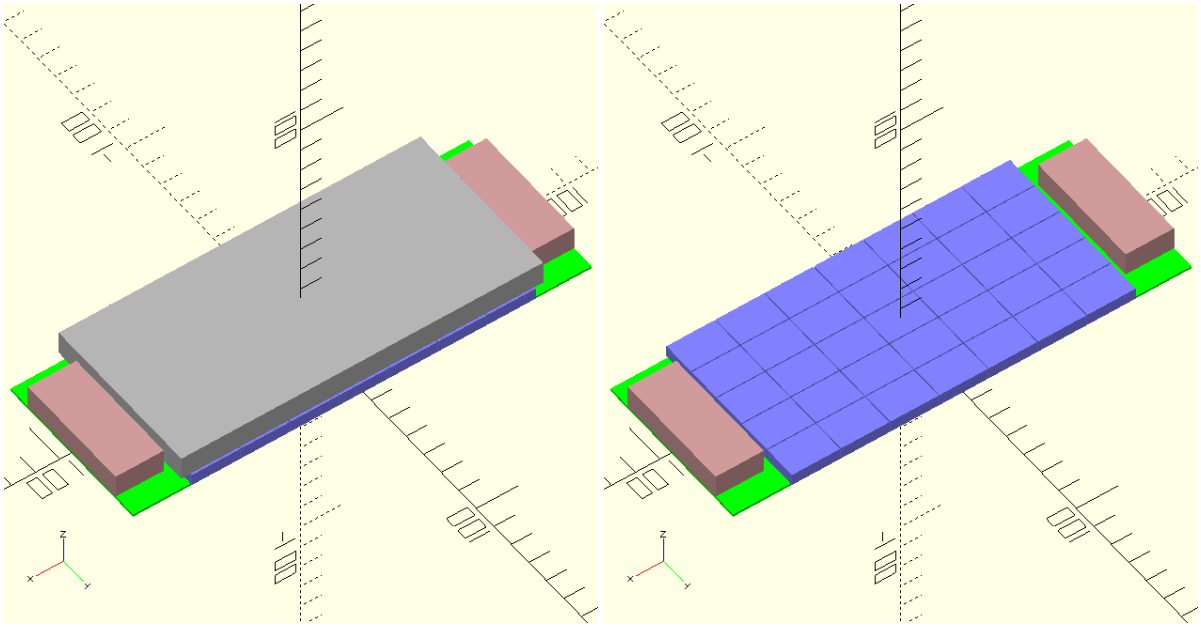

Figure 13.4: A single ZDC module with the absorber (left) and without (right). Parts are shown with colors: green - printed circuit board, blue – scintillator tiles, gray – absorber, magenta – connector area.

Table 13.2: The ZDC neutron rates for different beams and energies.

$L = 10^{26}\ cm^{-2}s^{-1}$	**d+d**	**He+He**	**Bi+Bi**
$T_{beam}(GeV)$	Neutrons per second	Neutrons per second	Neutrons per second
1	0.02	0.04	60
2	0.05	-	-
3	0.1	0.2	250

To estimate the ZDC occupancy during operation with various beams, the simulation was carried out using the GEANT FTF – Fritiof event generator [95]. At the initial stage of the NICA accelerator operation, it is planned to work with beams of light and heavy nuclei. Spectra of the total kinetic energy of the neutrons detected by ZDC for the single event in deuteron-deuteron, helium-helium, and bismuth-bismuth collisions at the kinetic energies 1, 2 and 3 GeV per nucleon are shown in Fig. 13.6.

In the spectrum of bismuth-bismuth interactions at energy 3 GeV, the contribution from the impact of two spectator neutrons is clearly visible. The Table 13.2 presents the results of the MC analysis for the number of neutrons registered per second in ZDC for different colliding beams and energies at the luminosity $L = 10^{26}\ cm^{-2}s^{-1}$. This value of luminosity is planned to have for NICA operation in the heavy-ions collision mode.

4 Time resolution measurements

For experimental estimates of the time resolution, an assemblage of 9 plastic cubes, laid on a printed circuit board with mounted SiPMs and fixed with a support board (see Fig. 13.7), was tested with cosmic muons. Each cube was of $30\times30\times30$ mm^3 in size and was chemically covered with a thin, light reflecting layer. A numerical simulation has shown the mean number of cells hit in an event is more than 20 for both photons and neutrons, and the energy deposit in the scintillator for each hit was in the range of

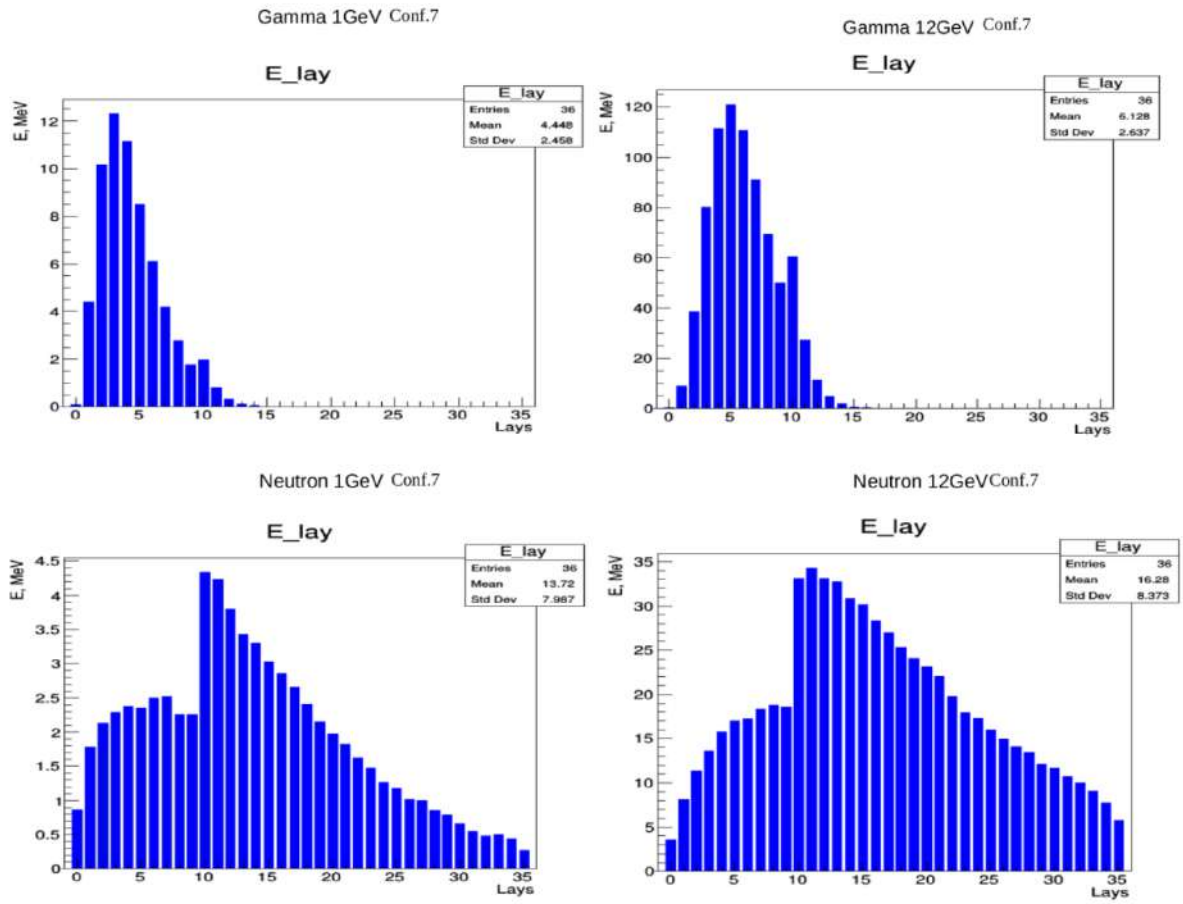

Figure 13.5: Photon (up) and neutron (down) longitudinal energy distributions for different particle energy (1 GeV – left and 12 GeV – right).

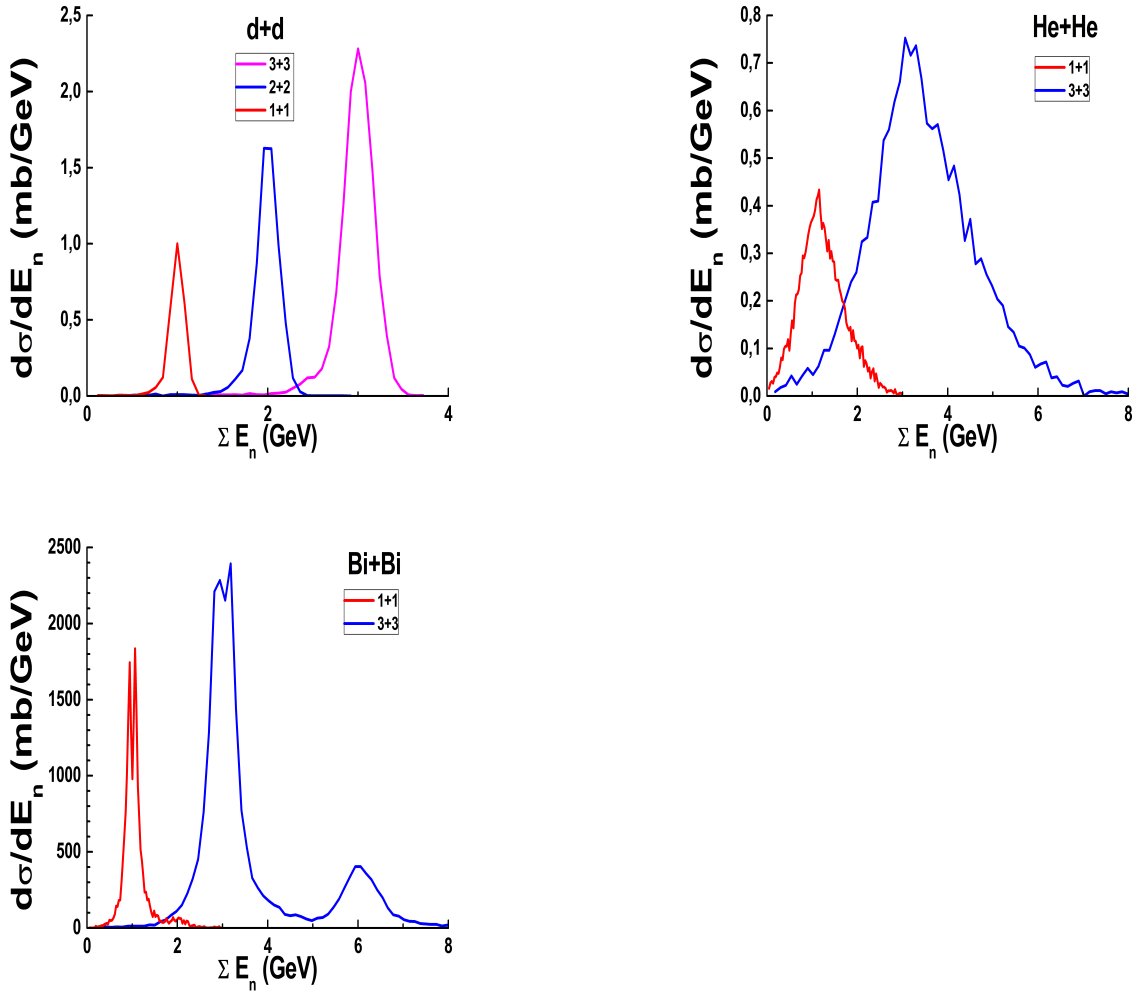

Figure 13.6: Spectra of the total kinetic energy of the neutrons detected by ZDC for the single event in deuteron-deuteron, helium-helium and bismuth-bismuth collisions at different beam energies.

3÷9 MeV. So the cubes of the test assemblage, with an average cosmic muon energy deposit of 6 MeV, provide a good approximation of the real tile response in the calorimeter.

The obtained result for the vertical muons is shown in Fig. 13.8. It gives a time resolution of a single cube 330 ps. Using different cube combinations, we found out that the resolution did follow the $1/\sqrt{E}$ law. So the aim of 150 ps will be reached at about 30 MeV energy deposit in the scintillator. For the approximately 1/12 energy deposit fraction of scintillator in ZDC, this means about 400 MeV energy of the incoming particle.

5 ZDC for the first NICA run

The development of ZDC will consist of two stages. During the initial NICA operation, when no other SPD devices will be installed, we want to test a partial ZDC with approximately 20% cost of the whole device. Its main tasks will be:

– test the device concept technology in the real position, with a special emphasis to the problems of high radiation, cryogenic operation temperature, and passing of the signals out of the vacuum;

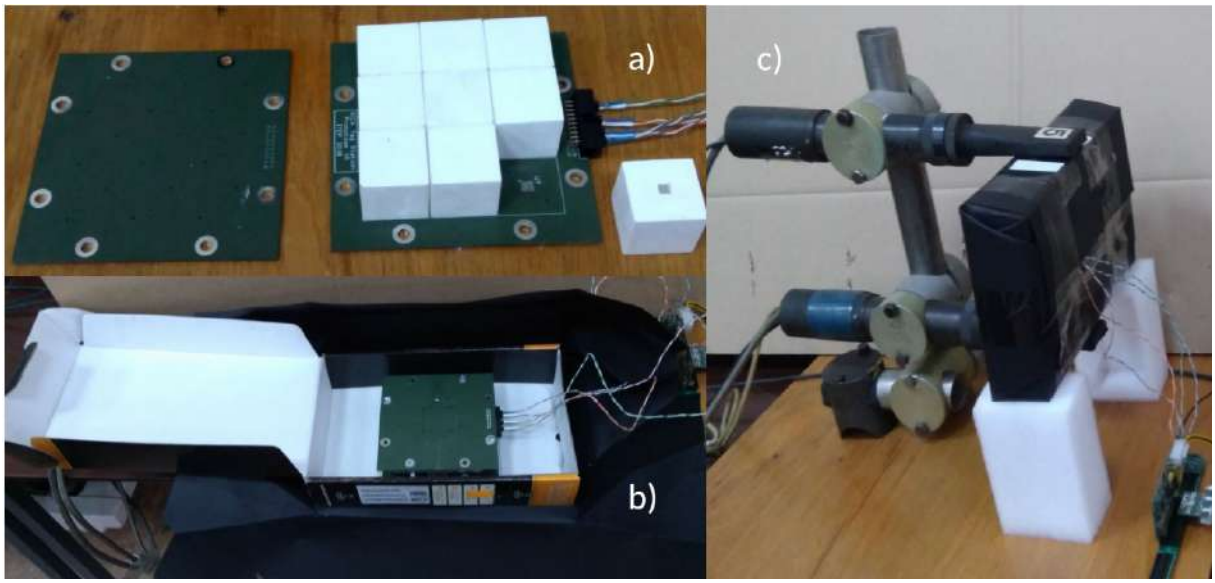

Figure 13.7: One layer prototype: a) 9 cubes of $30\times30\times30$ mm^3 plastic, SiPM board and support board; b) the prototype assembly in a box before wrapping in black paper; c) the box in place for cosmic muon tests.

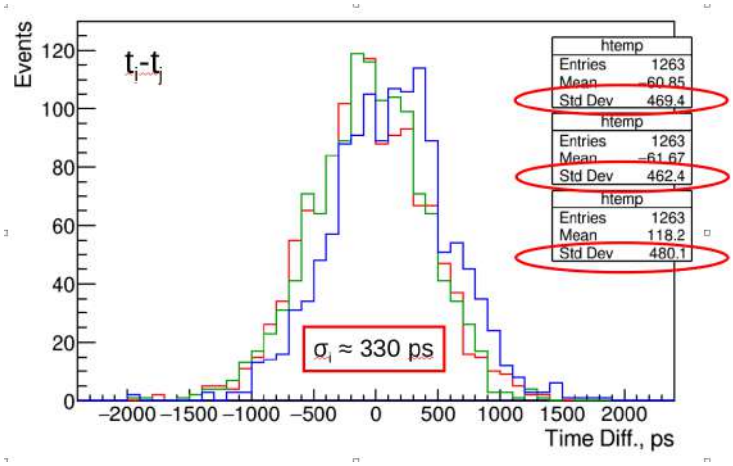

Figure 13.8: Time difference for the three cube pairs. The resolution of each cube is $1/\sqrt{2}$ of the resolution of difference.

- simple measurements with the beam, including beam luminosity and neutron to gamma discrimination efficiency;
- check background conditions in the location of ZDC;
- check MC simulations and compare the model results with real data;
- check if several configurations will be possible.

We assume that all the electronics of the partial ZDC will be later used as a part of the electronics for the whole ZDC, while scintillator tiles and absorber would be replaced.

The exact configuration of the partial ZDC will be a result of the optimization using MC simulations.

Table 13.3: Preliminary parameters of the partial calorimeter.

Layer	Parameter	Value
1	Absorber thickness, mm	0
	Layer thickness, mm	11
2	Absorber thickness, mm	30
	Layer thickness, mm	41
	Layer thickness, X_0	2.1
	Layer thickness, λ_i	0.2
3	Absorber thickness, mm	45
	Layer thickness, mm	56
	Layer thickness, X_0	3.2
	Layer thickness, λ_i	0.3
4	Absorber thickness, mm	45
	Layer thickness, mm	56
	Layer thickness, X_0	3.2
	Layer thickness, λ_i	0.3
5	Absorber thickness, mm	100
	Layer thickness, mm	111
	Layer thickness, λ_i	0.7
6	Absorber thickness, mm	100
	Layer thickness, mm	111
	Layer thickness, λ_i	0.7
Total		
	Number of layers	6
	Thickness, mm	386
	Thickness, λ_i	2.2
	Number of channels	210

The preliminary layout is given in Table 13.3. It will have only 6 sensitive layers of 10 mm thickness and 210 SiPM channels. We are going to use a copper absorber for this design.

6 Cost estimate

The cost estimate of a single ZDC device is given in Table 13.4.

Table 13.4: Cost estimate in USD.

			Partial design		Full design	
Item	Units	Unit price	Amount	Cost	Amount	Cost
SiPM S13360-3050PE	pc.	30	210	6030	1050	31500
Polystyrene scintillator	tile	5	210	1050	1050	5250
Tungsten absorber	kg	160			130	20800
Copper absorber	kg	15	30	450		
SiPM boards	pc.	50	6	300	30	1500
Cables in vacuum	m	15	24	360	120	1800
Preamp boards	pc.	100	24	2400	120	12000
SiPM power boards	pc.	100	24	2400	120	12000
WFD modules	pc.	7000	4	28000	20	140000
VME crate and CPU board	pc.	10000	1	10000	1	10000
SiPM bias power supply	pc.	500	1	500	1	500
Total				51490		235350

Chapter 14

Beam pipe and BBC MCP detector

1 SPD beam pipe

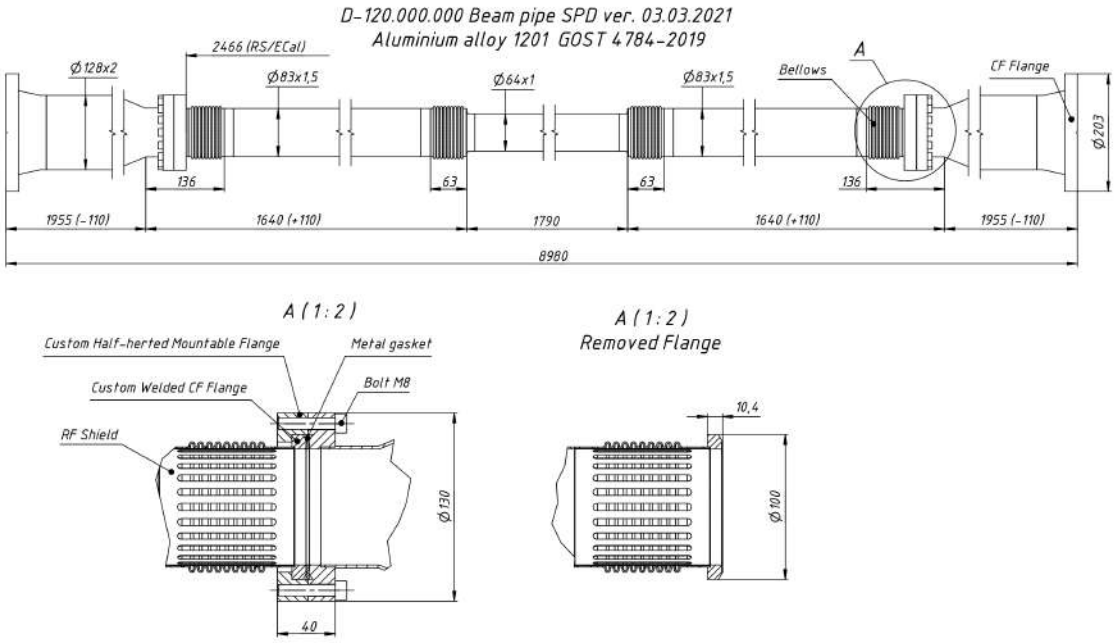

Figure 14.1: Part of the accelerator vacuum beam pipe that will pass through the SPD experimental setup. At the first stage of the experiment, the central segment of the pipe will be made of aluminum. Later it will be replaced with a beryllium segment. All dimensions are given in millimeters.

A beam pipe separates the detector and the high vacuum of the accelerator. It must be mechanically sturdy on the one hand and thin enough, in terms of the number of radiation lengths to minimize multiple scattering and radiation effects, on the other hand. The diameter of the beam pipe is a compromise between the radial size of the particle beams and the requirement to position detectors as close to the beam line as possible for better reconstruction of the tracks.

The beam pipe of SPD has similar geometrical parameters as the pipe of MPD and will be manufactured using the same technology. The schematic view of the pipe is shown in Fig. 14.1. The pipe is almost 9 m long. It is assembled from 5 segments, the diameter of which expands towards the ends. At the first stage of the experiment, we plan to start working with an aluminum pipe to gain installation experience. At a

later stage, the material of the central segment will be replaced by beryllium. The end parts of the pipe, providing connection with the accelerator pipe, will be made removable. They will be installed at a later stage of the assembly, after the ECal end-caps have been mounted, just before closing sections of the RS end-cap. In order to reduce the diameter of the joint between the end and inner segments, a conflat sharp edge vacuum connection with a removable bolt flange will be used. Several bellows will be inserted into the segments to provide the necessary working space in response to thermal expansion and contraction. They also provide the necessary tolerance for misalignment.

This assembly is part of the high vacuum system and must be cleaned and tested for leaks according to specification. To avoid electron clouds, a treatment of the inner surface of the beam pipe is required. Laser treatment or gettering is used for this purpose.

The cost of the pipe for the first phase of the experiment is estimated at 100 k$, while replacing the central part with beryllium would cost up to 400 k$.

2 BBC MCP detector

A pair of the MicroChannel Plate detectors will be installed at a distance of 4.5 m from the beam interaction point (just to the right and left of the pipe section, shown in Fig. 14.1), close to the beam pipe. These detectors are designed primarily to study a small-angle (mainly elastic) scattering of protons and deuterons at the polar angle of about 15 mrad and will operate together with the scintillator part of BBC. Due to azimuthal granulation, they can be used for determination and control of the beam polarization via the measurement of A_N asymmetries in the elastic pp and dd scattering. In combination with other detectors, the BBC MPC detector could contribute to t_0 reconstruction, which is of special value for the off-line analysis of the time-of-flight spectra and particle identification.

At maximum luminosity, the average beam current and the peak bunch current in the collider rings are about 0.5 and 10 A. That makes it challenging to obtain a stable circulation of the beams. A standard recipe to minimize problems is:

1. to make the vacuum chamber as smooth as possible, avoiding jumps in the vacuum chamber cross-section;
2. to cover all bellows between different elements of the vacuum chamber and vacuum ports by shields, to avoid getting cavities, where electromagnetic oscillations could be supported;
3. all plates, pickups, and other vacuum chamber elements, seen by the beam have to be installed into the same cross-section and properly loaded to minimize their excitation by the beam.

The quality of the vacuum chamber is characterized by its transverse and longitudinal impedances, which are functions of the frequency.

To minimize scattering and absorption by the vacuum chamber walls for particles produced in the collisions, the MCP detectors are suggested to be mounted, as shown in Fig. 14.3. Such a choice minimizes the amount of material, which a particle traverses on the way from the interaction point to the detector, and, thus, addresses problems of ions scattering and absorption by the vacuum chamber. However, it creates a cavity, which increases the ring impedances. To minimize the contribution of these cavities, their shape is chosen to have only the smooth transition in the chamber radius, and the maximum radius is chosen to be only slightly above the detector radius.

Figure 14.3 shows the cavity geometry, used in the simulations and Figure 14.4 presents the computed longitudinal impedance. As one can see, the impedance is significant only at frequencies above 1 GHz,

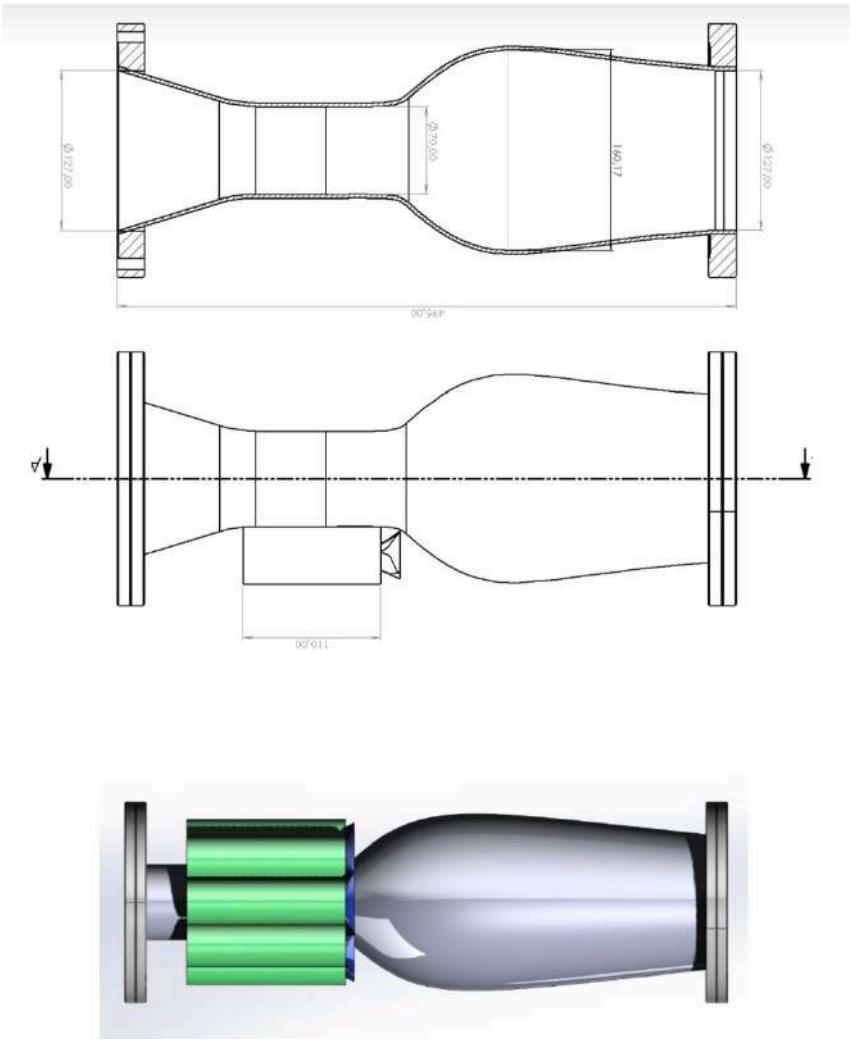

Figure 14.2: View of the BBC MCP detector around the beam line.

where two resonant peaks can be seen at frequencies of about 1.44 and 1.66 GHz, which are well above the frequency spectrum of NICA bunches. Note also, that the peak values of a single cavity are close to the peak values of a single BPM impedance (800 Ω, 0.87 GHz). The instability of a continuous beam is driven by Z_n/n, where Z_n is the impedance value at n-th harmonic of the revolution frequency. For the peaks presented in Figure 14.4, Z_n/n is about 0.3 Ω. This value is well below the space charge impedance

$$Z_n/n = i\frac{Z_0}{\beta\gamma^2} ln(\frac{a}{r}), \tag{14.1}$$

which sets up the scale of the problem. Here, β and γ are the relativistic parameters of the beam, $Z_0 = 377$ Ω, and a/r is the ratio of the vacuum chamber radius to the beam radius. Thus, we can conclude that an addition of two (or four) cavities, presented in Fig. 14.2, should not cause a significant effect on the beam stability in NICA. Calculated electric field distribution for the proposed smoothed beam pipe is shown in Fig. 14.5.

Thus, it was decided to place the BBC MCP detectors beyond the vacuum beam line of the accelerator, maximally close to the beam axis. The design of the BBC MCP detector, developed earlier (see SPD CDR [1]), is replaced by the one shown below. It was decided to use photomultipliers "TOPAZ", based on MCP, manufactured by the BASPIK company (Vladikavkaz) [96]. The prototypes of the "TOPAZ"-based detectors (see Fig. 14.6) were tested in the laboratory enviroment with radioactive sources and a

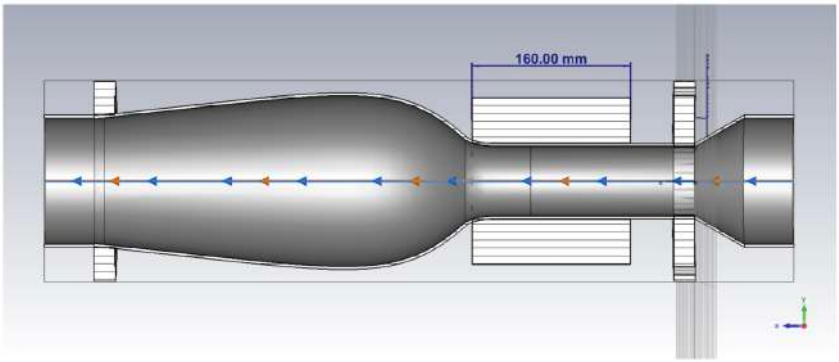

Figure 14.3: Geometry of the vacuum chamber used in simulations.

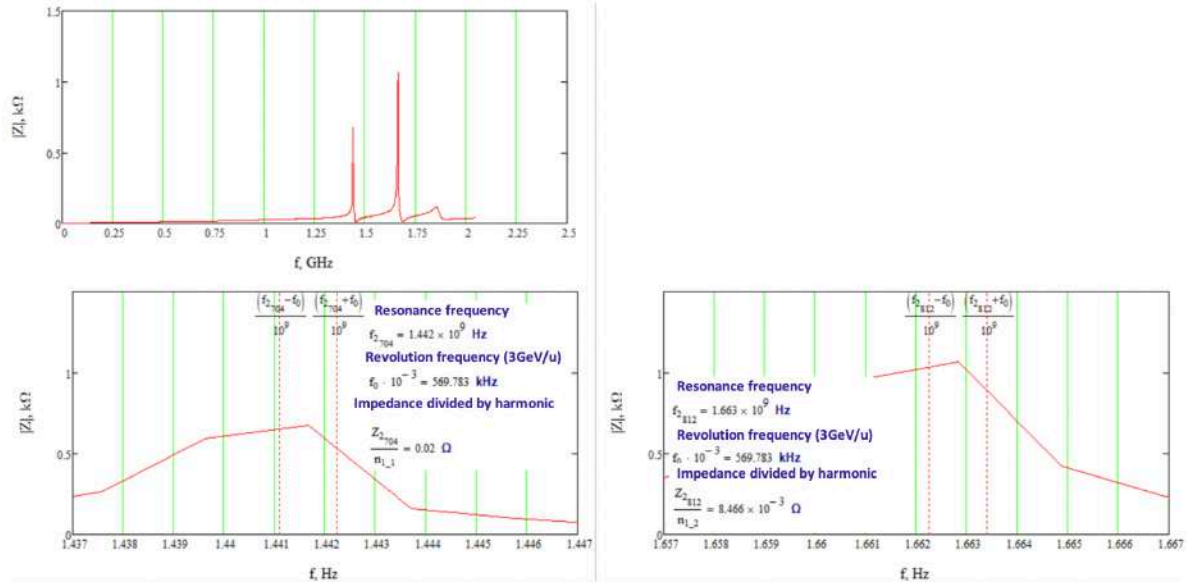

Figure 14.4: Results of simulations: (top) – longitudinal impedance, (bottom left) – impedance details near peak at 1.44 GHz, (bottom right) – impedance details near peak at 1.66 GHz.

picosecond laser, as well as at 200 MeV electron beam of LINAC-200 (DLNP, JINR). A time resolution of about 50 ps was achieved with these detectors. This time resolution allows one to find the position of the interaction point within 1.5 cm along the beam line.

It is obviously possible to upgrade these detectors for particle registration at angles larger than 2°, by increasing the assembly size and the number of detectors.

2.1 Cost estimate

The BBC MCP cost estimate is based on the cost of building the MCP-based profilers for the booster and NICA rings. For two rings with electronics, high voltage power suply, cables and connectors, it is about 260 k$.

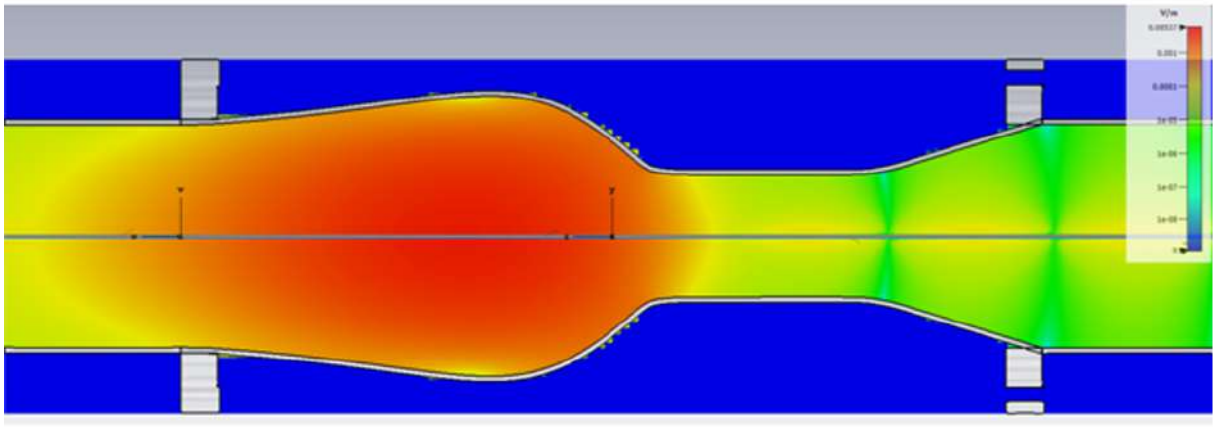

Figure 14.5: Calculated electric field (V/m) for the smoothed beam pipe without RF instabilities.

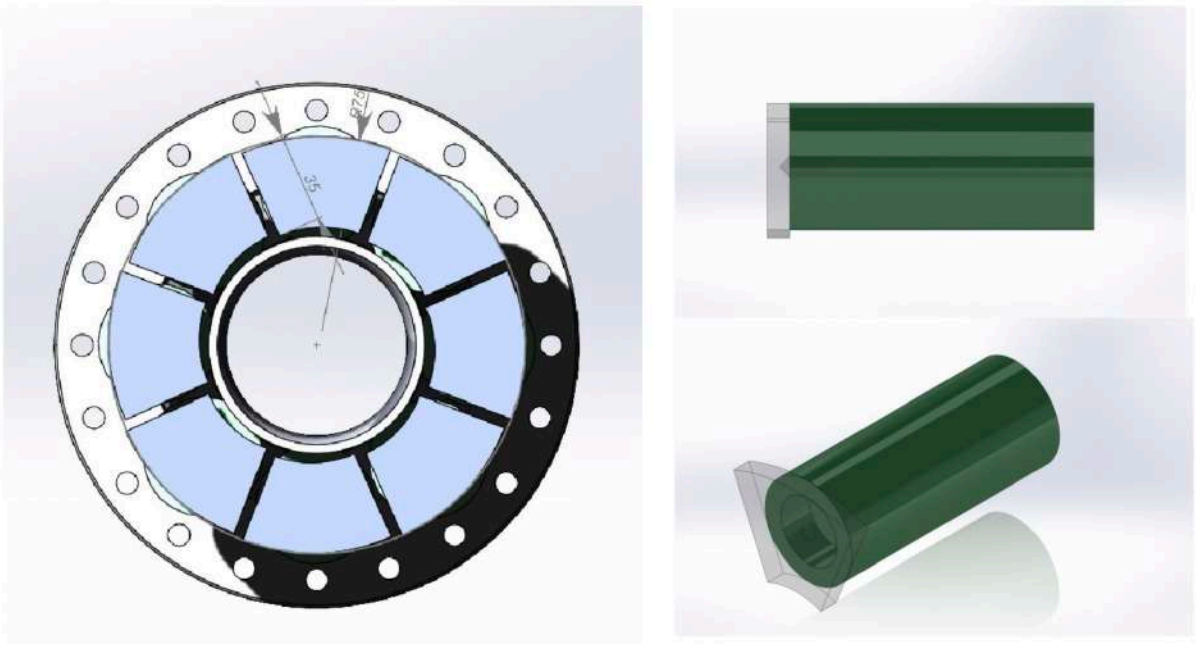

Figure 14.6: View of the photomultiplier casing and fast scintillator attached to its end.

Chapter 15

Integration and services

The NICA complex is shown in Fig. 15.1. It includes an injection complex, a booster, an upgraded Nuclotron and two storage rings with two interaction points aimed at the MPD and SPD detectors, respectively. The SPD area is located in the southern point of beam collisions.

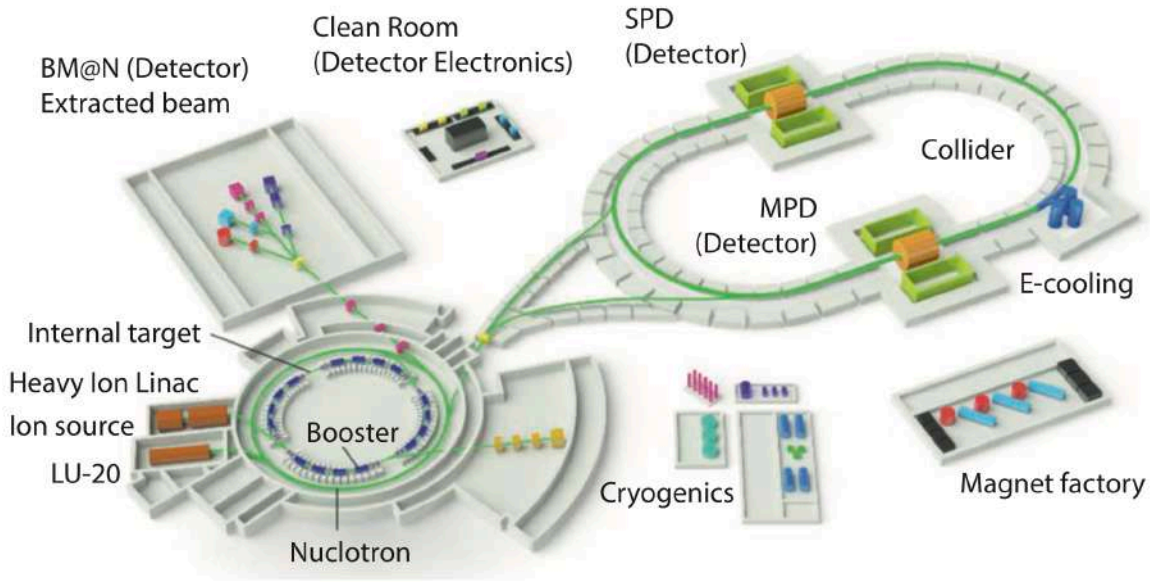

Figure 15.1: Schematic layout of the NICA facility with SPD (southern point) and MPD (northern point).

The layout of the SPD experimental hall is very similar to that of the MPD [97].

1 Experimental building of SPD

The SPD experimental facility is accommodated in a single-span steel hall with the overall dimensions of 32×72 m^2. The top and side views of the SPD building are shown in Figs. 15.2, 15.3, respectively. The building is divided into *production* and *experimental* sites with the total area of about 2000 m^2.

Since the *production site* has a gate, the site will be used for unloading materials. The size of the gate is $8\,\text{m} \times 8\,\text{m}$, which is large enough for trucks. The production site will also be used for preparation, testing and maintenance of the detector subsystems. Elements of the gas system can also be placed on the site,

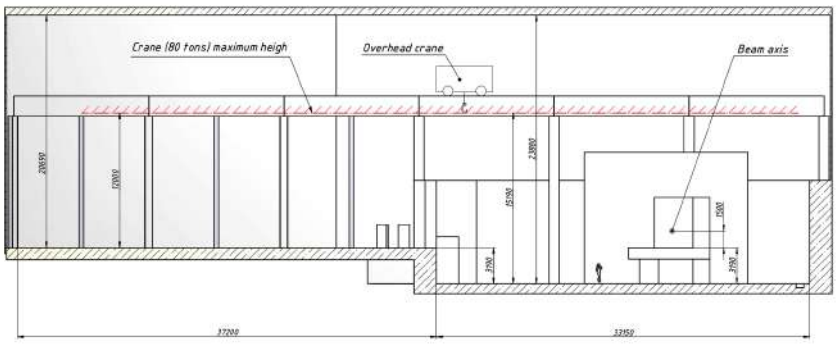

Figure 15.2: Side view of the SPD building. The production site is one on the left (ground level), and the experimental site is on the right (3.19 m below ground level). The maximum height accessible to the overhead crane is marked with a red line.

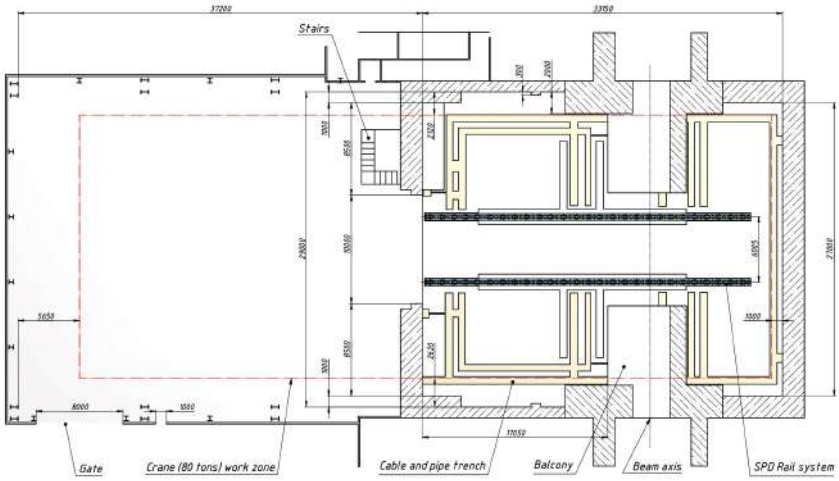

Figure 15.3: The view from the top of the SPD building. The production site is one on the left, and the experimental site is on the right. The area accessible to the overhead crane is marked with a red line. The gutters in the concrete floor used for laying communications are marked in yellow.

which will distribute, monitor, and supply the necessary gas mixtures to the gaseous detectors of SPD. The floor level of the production site coincides with the ground level.

The *experimental site* is shown on the right side of Fig. 15.2, 15.3. This part of the building is a reinforced array made of protective monolithic concrete with a wall thickness from 1 m to 3 m and height up to 11 m. The dimensions and configuration of the site were designed in accordance with the terms of reference, taking into account the provision of biological protection. The floor is lowered below the level of the production site by 3.19 m in order to match the levels of the beam-line and the symmetry axis of the SPD detector. There is a 10 m wide mounting opening in the 2 m thick wall separating the production and experimental sites. After installing the detector, this opening will be laid with concrete blocks. For the passage of personnel and transportation of small-sized equipment, a labyrinth is provided. It begins in the well at the production site and leads to the level of experimental site.

Two main rails are installed along the experimental site to provide transportation of the SPD detector from the assembly position to the operating (or beam) position. Schematic views of the SPD building with the detector in the assembly and operating positions are shown in Fig. 15.4. Potentially, two pairs of additional rails, located across the main ones, can be installed in the detector assembly area. They can be

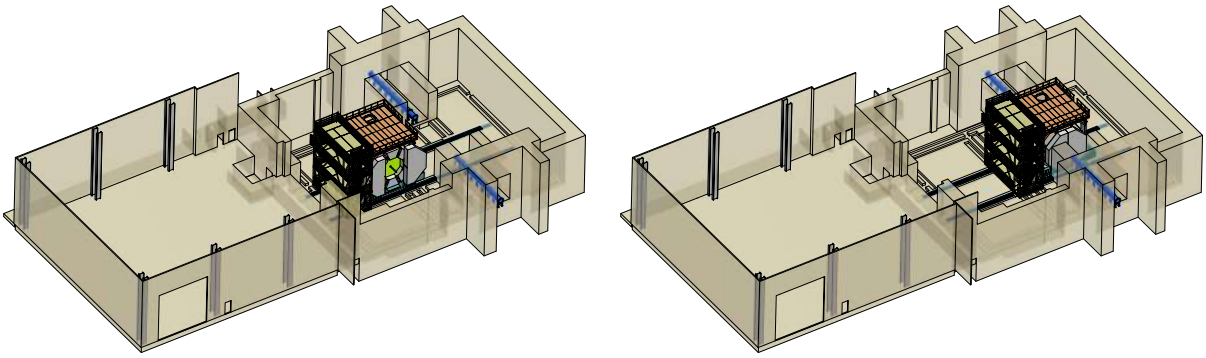

Figure 15.4: 3D rendering of the SPD building. The detector assembly position is shown in the left figure. The beam position of the detector is shown in the right figure. Beam line is shown in blue.

used for rail-guided support, in order to insert inner subdetectors. All rails are electrically connected to the metal reinforcement of the building, which, in turn, is connected to an array of rod-electrodes buried in the earth by 3 m below the building for grounding.

The concrete solid floor of the experimental site has sufficient load-bearing capacity to allow the assembly and operation of the SPD detector, including auxiliary structures. This capacity will be quite enough:

- to withstand the weight of the fully assembled detector with all necessary services;
- to preserve the integrity of the detector during its transportation between the assembly position and beam position;
- to provide a stable position of the detector with high accuracy during operating cycles.

The maximum permissible load on the floor of the experimental site was calculated based on the total mass of the experimental setup, and it was found that the load should not exceed 1200 tons. The weight of each detector subsystem contributing to the overall load is presented in Table 15.1. According to the project documentation, the shrinkage of the earth under the building will not be larger than 3 cm for the entire period of maintenance of the building.

An overhead traveling crane with a maximum lifting capacity of 80 tons is installed in the hall of the building. It will ensure the movement of the detector parts from the unloading to assembly area. The crane can be equipped with linear or H-shaped traverses with lifting capacity from few to 75 tons. The crane service area covers both the production and experimental sites. The area accessible to the crane is marked with a red line in the drawing of Fig. 15.3.

2 Gas supply systems

The SPD subsystems consuming special gases are listed in Table 15.1. With regard to gas supply systems, we will follow generally the same strategy as used by MPD. For safety reasons, as well as due to restricted access to the experimental area during the operation of the accelerator, pressurized gas tanks will not be placed on the experimental site. For those gases that will be used extensively and therefore require large storage tanks, the primary gas supply point will be located outside the SPD building. Vessels for other gases, which are used little and therefore do not require large storage tanks, can be placed on the production site. Those gases that are toxic and harmful to the environment (like freon) can be recycled. A top view of the NICA collider building with designations of the elements of the SPD gas systems is shown in Fig. 15.5.

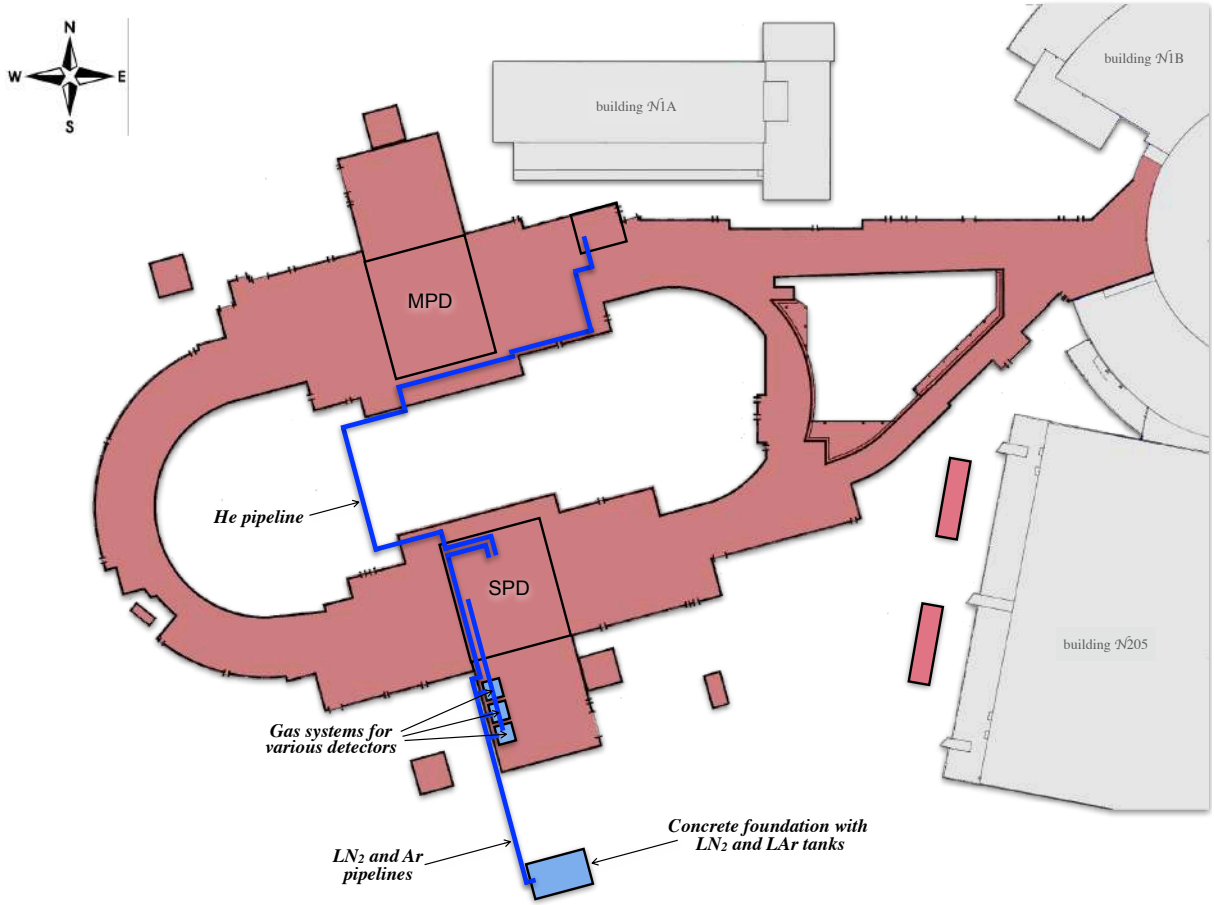

Figure 15.5: Top view of the NICA collider building with indications for elements of the SPD gas systems (shown in blue).

The *cryogenic helium plant* should be close to the detector to provide cryogenic fluids and gas to maintain low temperatures for the magnet operation. A refrigerator will be installed on a platform on top of the detector, as described in Section section 4.1. Helium will be delivered from the central cryogenic station, located on the MPD side of the NICA complex. A warm (non-cryogenic) pipeline with high and low pressure helium flows will connect the station with the refrigerator. The total length of the pipeline is about 220 meters.

A *nitrogen system* is required for operation of the cryogenic helium plant. The system will include two cryogenic storage tanks with liquid nitrogen and cryogenic pipeline connecting those tanks with the helium plant, as described in Section 4.2. The storage tanks will be located on a concrete foundation approximately 50 meters from the SPD building. The connecting pipeline will be raised to a height of 6 meters to pass over the road. Discharge of gaseous nitrogen into the atmosphere will be carried out according to the principle of the shortest path.

The gas system for the SPD *gas detectors* is planned to be implemented following a modular design, so it can be adapted to the requirements of each detector, but still be based on a common architecture. There are four detectors in SPD which need to be supplied with gas. Arranged in descending order of gas volume, they are RS, ST, TOF, and MM. As one can see from Table 15.1, the mixtures used by the detectors contain common components.

For instance, *argon* is used in the RS, ST, and MM detectors, due to a very low electron attachment coefficient, that ensures most of the free electrons to reach the multiplication region without interference.

Depending on the detector, the fraction of Ar in the gas mixture varies from 70% to 90% (see Table 15.1). In order to avoid using multiple Ar vessels for different detectors, a single tank with argon at cryogenic temperature will be employed. It will be installed on a concrete foundation that is also used for the nitrogen tanks. The argon will be warmed and fed into the SPD building via a pipeline, using the same trestle above the road that is used for the nitrogen pipeline.

A key requirement for the *TOF gas system* ($C_2H_2F_4$:C_4H_{10}:SF_6 = 90:5:5) is the possibility to recirculate and reuse the gas exiting from the detector. The gas mixture can, in fact, be collected after being used, and re-injected into the supply line after purification. Due to the relatively small volume of MRPC chambers that need to be filled with gas, all components of the system can be installed in a specially designated area of the production site of the SPD building. After mixing in the proper proportion, the gas mixture will be transferred to the detector via a pipeline running over the wall, separating the production and experimental sites. Another pipeline will return the used gas mixture back to pass through the purification module. Particular attention will be paid to the monitoring of gas leaks, as the mixture used by TOF contains toxic and flammable components. Moreover, they are quite expensive. If the leak is detected, the control system will block the gas circulation, and an audible alarm will alert people, giving them the opportunity to leave the area.

In order to optimize the space available in the SPD building, fenced zones, dedicated to the racks of the gas system of each detector, will be allocated on the west side of the building (the far side from the gate), as shown in Fig. 15.5.

3 Power supply system

The power supply system of SPD is schematically presented in Fig. 15.6. The sequence of power substations starting from the principal one to the SPD experimental setup is as follows:

$$\text{PSS1} \rightarrow \text{S15} \rightarrow \text{DS2} \rightarrow \text{TS3} \rightarrow \text{SPD setup},$$

where PSS1 is the Principal Step-down Substation 110/6 kV "Dubna" of the VBLHEP site; S15 is a recently rebuilt transmission Substation N15, which also supplies power to building N205 (test zone for extracted beams of Nuclotron); DS2 is a Distribution Substation N2; and TS3 is a Transformer Substation N3, which is adjacent to the SPD building. The collider building has a 6 kV radial power supply network with two distribution points DTS1 (MPD side) and DS2 (SPD side). This, in general, also makes it possible to receive the power for SPD from the transmission Substation N13.

A transformer substation TS3 is a termination of the distribution line intended to supply SPD with electric power. It contains two three-phase oil-immersed transformers of a sealed version, without oil conservators, each with a power of 2.5 MW. The substation also includes all the necessary devices for control and protection of itself and the lines. The transformers step down the voltage from the high transmission level of 6 kV to the low voltage output of 0.4 kV. This output from each transformer feeds a complete busbar trunking with a rated current of 4 kA, through which electricity is supplied to the power pannels, located along the walls of the SPD hall.

The power available to the SPD setup is determined by the 2-nd category of reliability of the entire system. According to the requirements of this category, consumers must be able to switch to an auxiliary power source within a few minutes in case of an emergency situation. In practice, this will mean that both 2.5 MW transformers will operate at half power, and that all power goes to one of them when the other fails. The summary of the power reduction factors:

- due to the 2-nd category of reliability on the 6 kV side, the power of two transformers is reduced down to 5 MW / 2 = 2.5 MW;

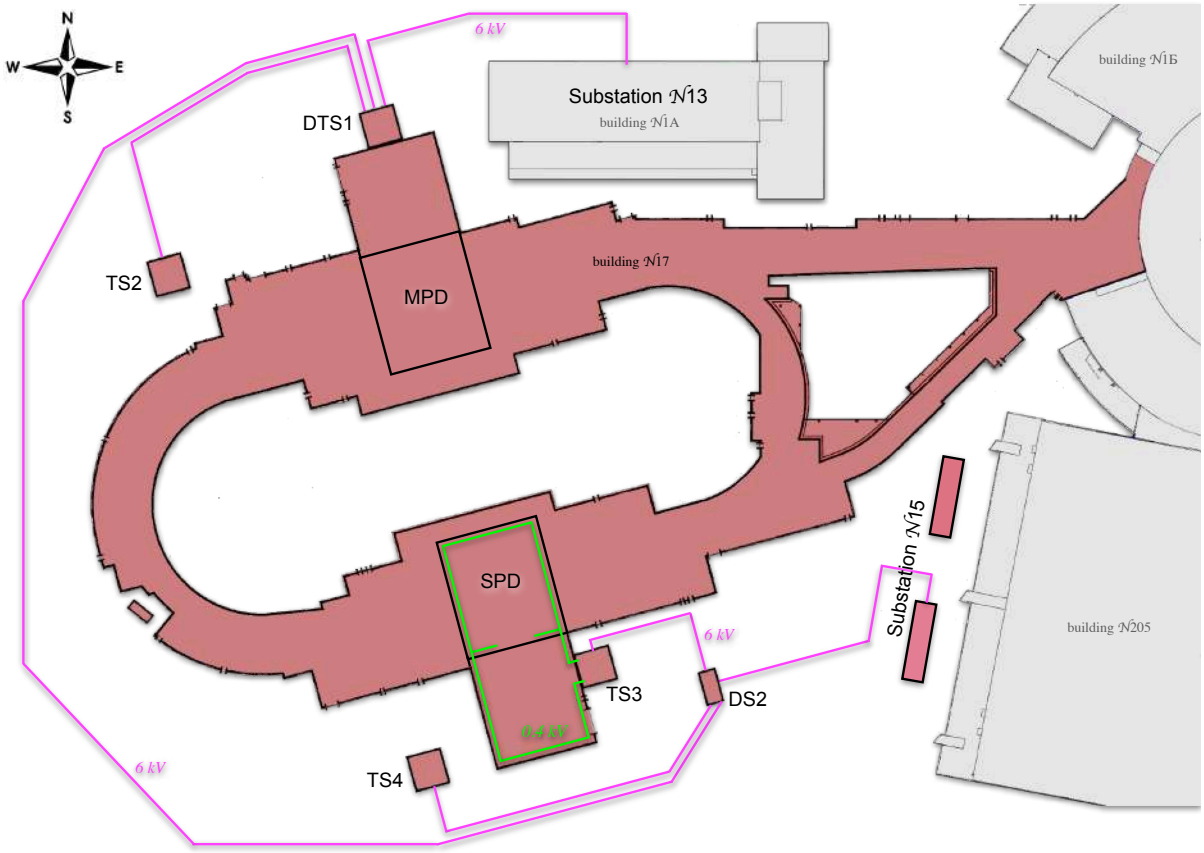

Figure 15.6: Top view of building N17 (the NICA collider) with indications for elements of the SPD power supply system. Power lines with an operating voltage of 6 kV are shown in pink. Power lines with an operating voltage of 0.4 kV are shown in green.

– due to the 2-nd category of reliability on the 0.4 kV side, the power is further reduced down to 2.5 MW / 2 = 1.25 MW (efficiency and own consumption are not taking into account).

Thus, as a result, the SPD can receive the power of about 1.2 MW which can be entirely consumed by the experimental setup. A tentative summary with the estimated consumption by each detector subsystem is give in Table 15.1. The current estimate of the consumption value is approximately 100 kW, which is an order of magnitude lower than the available capacity.

Despite the fact that most of the equipment in the hall belongs to the 2-nd category of power supply reliability, there is also equipment of the 1-st category. Equipment of this category must be able to switch to an auxiliary power source within a second in case of an emergency situation. It includes emergency ventilation systems, parts of fire fighting systems, and emergency lighting. Furthermore, there is a special group of the 1-st category of reliability, which includes technical means of automated control systems, radiation monitoring, and cryogenic system. All this equipment will be provided with uninterruptible power supplies with built-in rechargeable batteries for 1 hour of autonomous operation.

In order to avoid long cables, crates with electronics for the data acquisition systems and power supplies should be placed in the vicinity of the detector. They will be located either on a side platform attached to the detector or on the top platform together with the cryogenic equipment. Both platforms will be electrified and instrumented with an overhead cable carrier to ensure a continuous supply of electricity to the subsystems, even while the entire SPD setup is being moved from the assembly position to the

operating position on the beamline.

Table 15.1: Technical requirements for the SPD detector subsystems (to be completed).

Subsystem	Weight [ton]	Power [kW]	Gas compositions
VD (silicon MAPS)	< 0.1	22	-
VD (silicon DSSD)	< 0.1	2	-
VD (MM)	< 0.1	2	Ar:C_4H_{10} = 90:10
ST	0.2	2-4	Ar:CO_2 = 70:30
ECAL	44 + 2×12 = 68	12	-
RS	481 + 2×223 = 927	47	Ar:CO_2 = 70:30
TOF	4	4	$C_2H_2F_4$:C_4H_{10}:SF_6 = 90:5:5
BBC	0.1	0.5	-
Magnet	20		He
Cryogenics	5	23	He+N_2
Support & transporting system	80.3		
Top platform	40		
Side platform	100		
Total	1245	93 (113)	

Chapter 16

Radiation environment

1 Radiation background in the detector

It is well known that the intersection points of hadron collider beams are a powerful source of ionizing radiation because of the relatively large cross-section of hadron interactions and the significant multiplicity of secondary particles. Interaction with the material of the experimental setup leads both to attenuation of fluxes of some components and to generation of new particles. Beam halos, as well as induced radiation, also contribute to the radiation environment near the interaction point. However, we believe that their relative contribution is negligibly small. Correct estimation of fluxes and doses is necessary to calculate the loading of different detectors, as well as to take into account the effects of aging of the detector elements and electronics. The total ionizing dose determines the long-term damage effects on electronics and sensors, while the flux of high-energy hadrons determines the rate of stochastic failures, like Single Event Upsets.

The radiation environment in the SPD setup has been simulated using the Geant4-based SPDroot software with a recent description of the detector and the LHEP_HP physics list to take into account the flux of thermal neutrons. The primary interactions have a gaussian distribution along the beam axis with respect to the nominal center of the setup with $\sigma_Z = 30$ cm. The secondary interactions in the material of the setup, the multiple scattering, the decays of unstable particles, and the influence of the magnetic field modify the fluxes of particles in the SPD setup significantly. Figure 16.1 illustrates the fluxes of the charged particles, energetic and thermal neutrons, and photons at different points of the SPD setup for p-p collisions at $\sqrt{s} = 27$ GeV and $L = 10^{32}$ cm^{-2} s^{-1}: Z=1.2 m, in front of the EC ST (a), Z=1.87 m, in front of the EC ECal (b), R=1 m, in front of the barrel ECal (c), and R=3.5 cm, just after the beryllium beam pipe (d). Figure 16.2 shows a map of the absorbed dose distribution over the detector after one conditional year (10^7 s) of the data taking at maximum luminosity and energy of p-p collisions. As it follows from the calculations, even in the inner part of the SPD facility the annual dose does not exceed a few hundred Grays, while, for example, for the inner layer of the silicon detector of CMS at the LHC this value is up to 1 MGy [98]. So, the expected dose rate at the SPD seems to be quite comfortable for the electronics and the detectors.

In the case of the ion-ion collisions at SPD, despite the large multiplicity of tracks in an individual interaction, the dose rate is about two orders of magnitude lower than in the above-mentioned case of p-p collisions because of the low luminosity. However, such collisions will be accompanied by a much larger yield of energetic neutrons.

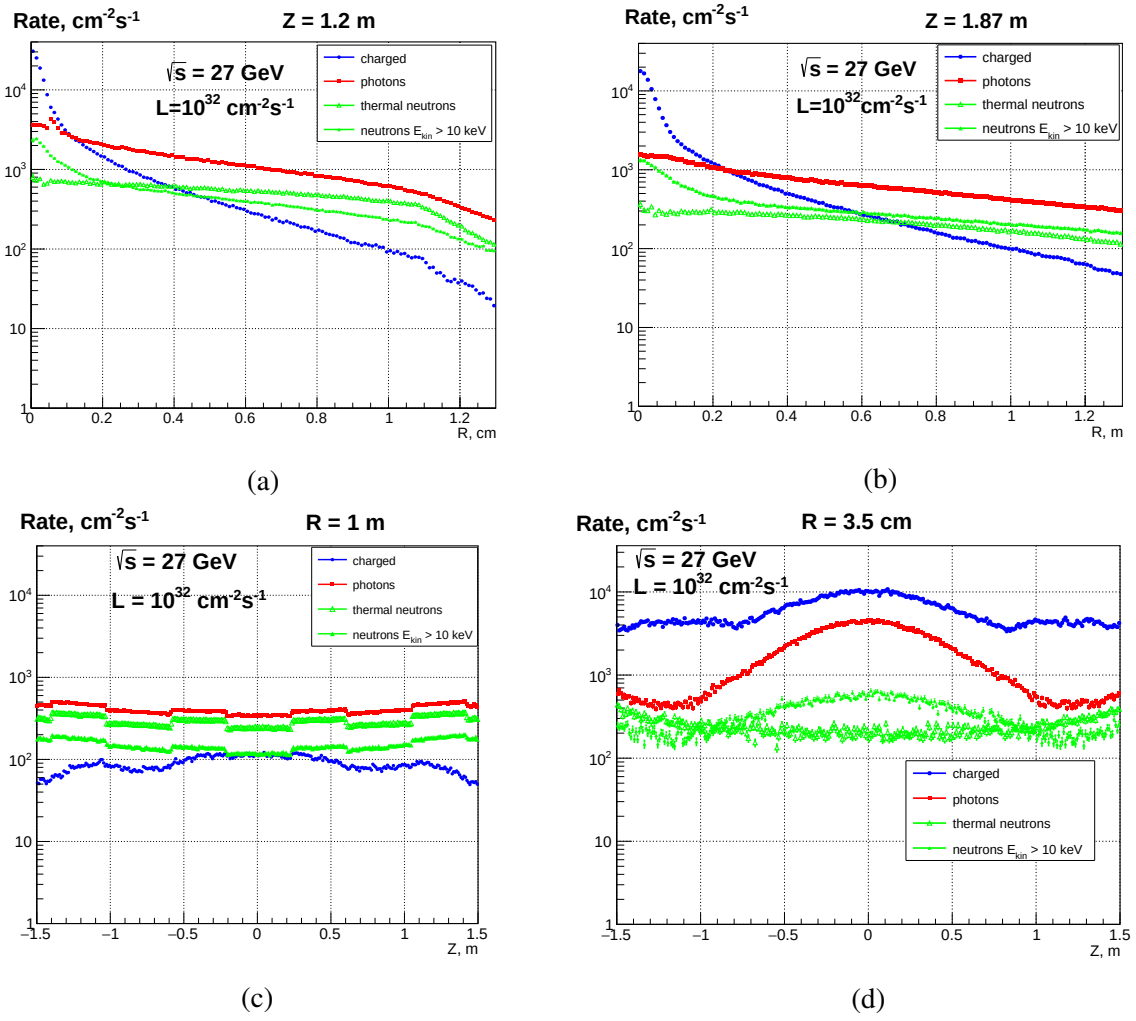

Figure 16.1: Flux of charged particles, energetic and thermal neutrons, and photons in the radial direction at (a) Z=1.2 m, (b) Z=1.87 m, and along the beam axis at (c) R=1 m and (d) R=3.5 cm.

2 Radiation background in the SPD experimental hall

The radiation environment in the pit of the SPD experimental hall is an issue of special importance. The radiation background during the initial period of the heavy-ion beam collider operation is important for the assembly and comissioning of the SPD detector. The background during operation with proton and deuteron beams is essential for the placement and maintenance of the equipment.

During NICA operation with heavy-ion beams, the main dose-forming component of radiation fields behind the biological shields of the collider and experimental facilities is neutrons of a wide range of energies [99]. The field of leakage neutrons from shields, repeatedly scattered in the air, ground, and surrounding objects (skyshine neutrons), also determines the radiation situation at large distances from the complex accelerators. The working Electron Cooling System (ECS) is also a source of gamma-quanta.

Three sources of ion losses responsible for the radiation environment in adjoining areas are considered in the collider rings: i) ion losses due to interaction with residual gas in the vacuum chamber uniformly distributed over the ring ($\sim$ 1% for $^{197}Au_{79^+}$ ions of 4.5 GeV/nucleon); ii) beam losses in the scrapers (24 in each ring placed mainly in the arcs of the collider), which serve to intercept ions dropped out of the acceleration or circulation process ($\sim$ 82%); and iii) recombination of ions with electrons in the

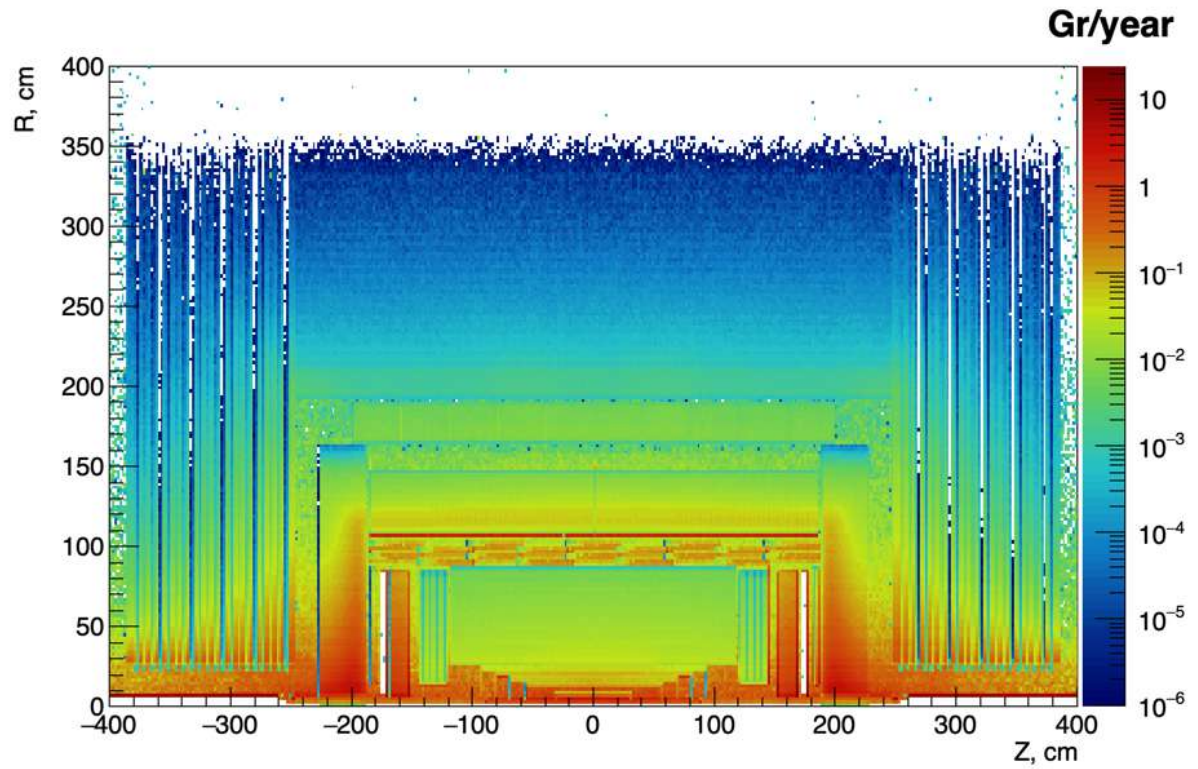

Figure 16.2: Dose in Gy after one year of data taking at $\sqrt{s} = 27$ GeV and L=10^{32} cm^{-2} s^{-1} (averaged over azimuthal angle ϕ).

ECS located in the vicinity of the MPD setup ($\sim$ 17%). Additional losses occur during injection in the injection section on the accelerator elements, such as the kicker and septum. The MPD experimental setup is not considered a significant secondary radiation source on the NICA complex [100].

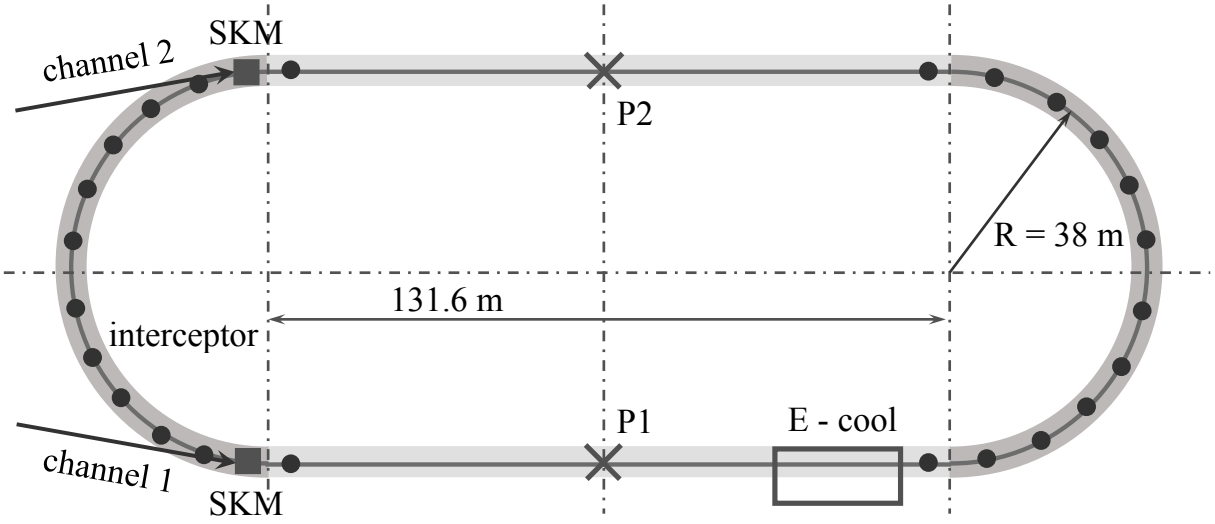

Figure 16.3: Location of the main sources of ion losses in the NICA collider [100].

Radiation zoning of the collider buildings and areas in four different modes of operation: i) collider doesn't work, ECS doesn't work; ii) collider doesn't work, ECS works; iii) collider and ECS are both in operation; iv) collider adjustment; are presented in Fig. 16.4. The collider spaces are divided into

two zones: the restricted access zone, where the level of human exposure may be at the level of 20÷200 mSv per year, and the exclusion zone, where the level of human exposure may exceed 200 mSv per year [101].

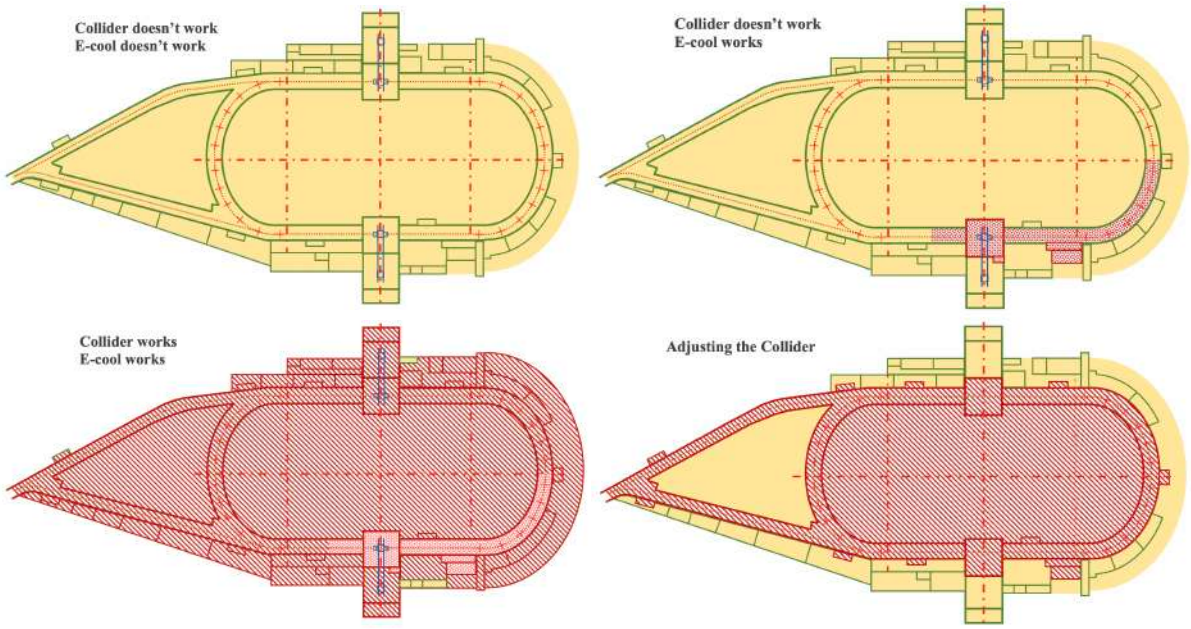

Figure 16.4: Radiation zoning of the collider buildings and areas in different modes of operation [100]. The restricted access zone is shown in yellow, while the exclusion zone is in red.

Despite the protection wall of concrete blocks, separating the main part of the SPD pit from the beam pipe when the collider operates with heavy-ion beams in the absence of collisions at the SPD interaction point, the SPD pit is considered to be the exclusion zone. The expected dose rate just behind the protective wall is expected up to 0.7 $\mu Sv/h$ [102]. This means that the assembly of the SPD setup can only be carried out when the collider is not running. This limits us to a guaranteed period of four months per year.

During SPD operation in the proton-proton collision mode, the dose rate in the pit will be in the range of XX-YY $\mu Sv/h$, which allows the computer equipment of the DAQ and the online filter to be placed there.

Chapter 17

Detector assembling procedure

The detector assembling procedure will be carried out at the experimental site of the SPD pavilion. At this time, the accelerator beam line will be separated from the pavilion space by the concrete blocks and slabs, which will provide a temporary biological protection. Nevertheless, due to the radiation background, the assembly can only take place during the shutdown of the accelerator. This limits the time that can be allocated for the assembly, and applies a clear requirement that parts of the detectors, which are delivered to the pavilion, should be maximally integrated modules.

The first step is to install the Range System. The RS is external to all other detector systems. It is also the largest and heaviest SPD system, weighting above 900 tons. Therefore, it will be mounted first. Due to the large weight and dimensions, it can only be assembled using the overhead crane and only on the experimental site of the SPD pavilion. The RS barrel is divided into eight sectors (octants). The octants are mounted by sequentially laying on the lodgement from the bottom up. During the installation procedure, a system of internal supports and struts will be required.

Once the barrel part of the detector is assembled, four sections of the end-caps are installed. Since the lifting capacity of the crane is limited to 80 tons, each of these sections has to be assembled in two parts. These parts are connected into a single one when transferred to the working position.

The RS barrel is the preferred structure for supporting or suspending other SPD systems, i.e. it can be used to install permanent or temporary mounting structures of other detectors. In addition, the RS as an external system is convenient to use as a reference coordinate system of SPD, tied to the coordinate system of the collider. For other detector systems, only tunnel assembly is available. The RS also serves a magnet yoke.

The installation of such structural components as the lower part of the movable lodgement, the barrel octants of RS with a supporting structure, the RS end-caps, and the upper and side platforms for cryogenics and electronics are shown in Fig. 17.1. Once the upper and side platforms are in place, one can also start installing cryogenic equipment, electronic racks, set cables and gas pipelines, as shown in Fig. 17.2.

The next step is to install the superconducting solenoid. The magnet has a cylindrical shape with terminals for cable and pipeline facilities. Structurally, the magnet is divided into an external cryostat and a ”cold mass” suspended inside the cryostat on stretchers. The total weight is approximately 16 tons. The magnet is delivered to the experimental site in an already assembled state. When switched on, the magnet creates a solenoid field with a magnetic induction of 1 T along the axis. This field has a retracting effect on the RS end-caps with a force of about 300 tons per every of two sections of end-cap. Two options for mounting the magnet are considered:

4308 – The magnet is lowered by a crane into a cradle, as shown in Fig. 17.3. The cradle contains lifting
4309 jacks for adjusting the height and aligning the magnet with the RS barrel. The magnet is then
4310 transported in the axial direction to the working position. The location of the guiding equipment
4311 (rails and rollers) is yet to be defined.

4312 – The magnet is lowered by a crane and held in the position to make it coaxial with RS. The guide
4313 beam with a rail is threaded through the magnet and fixed to the pillars on both sides, as shown in
4314 Fig. 17.4. It is necessary to check how feasible this procedure is, since the length of the beam is
4315 11 m. Finally, the magnet is moved on rollers along the rails to its working position.

4316 Once the magnet is in position, it will be bolted to the RS barrel and connected to the cryogenic equip-
4317 ment located on the top platform. The final configuration of the magnet in the RS barrel is shown in
4318 Fig. 17.5.

4319 The next step is to install the ECal barrel. It is lowered by a crane into the cradle, as shown in Fig. 17.6.
4320 The lifting platform of the cradle can be the same as for the magnet (see Fig. 17.3), but the vise mech-
4321 anism needs to be adjusted to the new size. The weight of the ECal barrel is close to 40 tons. The
4322 ECal power frame will have to support the detector itself, as well as all other interior parts of the central
4323 detectors. Two loading and fixation options are under consideration:

4324 – A fully or partially assembled ECal barrel is moved along the rails to the working position as
4325 shown in Fig. 17.7. Cam roller guides, attached to ECal, will have a mating rail structure that will
4326 be fixed to the magnet inner shell in the median plane. It may be necessary to thicken the walls
4327 of the inner shell of the magnet cryostat to reduce deflection. This mounting approach is used, for
4328 instance, to place the HCAL detector inside the magnet of CMS/LHC.

4329 – In this configuration, a power frame without active elements of ECal is installed first. The frame
4330 is supported at its ends, which, in turn, will be fixed to the RS barrel. The last step will be to load
4331 the active elements of ECal. This approach is used to mount the ECal detector inside the magnet
4332 of MPD/NICA.

4333 Nota bene. Due to the limited resources allocated to the first phase of the experiment, the production
4334 of ECal will most likely be delayed until a later time. However, in order to test the magnet cryostat for
4335 deflection, it will be necessary to make a mock ECal barrel at full weight. This mock-up can be a hollow
4336 steel cylinder filled with concrete. It can stay inside the magnet to maintain the load balance until ECal
4337 itself is installed.

4338 The next step is to install the TOF barrel. The TOF barrel consists of staggered MRPC chambers adjacent
4339 to the ECal barrel. Unfortunately, the ECal barrel cannot be used as a base for mounting MRPCs, due
4340 to uncertainties associated with the time of its appearance in the setup. Thus, it is proposed to use a
4341 self-supporting truss structure for mounting the chambers. This truss will lean on ECal (or its mock-
4342 up) only at its ends, which will simplify the installation. Individual MRPCs arranged in a row along
4343 the installation axis are combined into supermodules. The TOF barrel with inner and outer layers of
4344 MRPC-supermodules installed is shown in Fig. 17.8 (left). The estimated weight of the entire TOF
4345 barrel, including modules, is about $3 \div 4$ tons.

4346 Assembling of the TOF barrel is carried out outside the SPD pavilion. The barrel is delivered as a whole
4347 by a crane to the mounting position in front of RS. The barrel is rolled inside the ECal along the guides
4348 and fixed at the ends. Installation of the TOF barrel can also be done after installing the ST, VD, Aerogel,
4349 and BBC detectors inside the barrel.

The next step is to install the ST barrel. The ST barrel is divided into 8 sectors (octants). The position of each octant is determined in space using a frame. The central part of the frame is an octagonal prism that will house the vertex detector, while the ST octants are located outside this prism and fill the entire space up to the TOF barrel. The ST frame partially loaded with the ST octants is shown in Fig. 17.8 (right). Due to the low weight of the octants, they can be inserted into the frame manually. The frame will be fixed inside the TOF barrel and, in principle, can be a self-supporting structure. The total weight of the fully assembled ST barrel is approximately 120 kg.

The next step is to install the VD with the beam pipe. Since the beam pipe is a thin-walled tube of variable diameter expanding towards the ends, the installation procedure with passing the pipe through the VD is not feasible. Therefore, the detector is divided into halves, which are assembled separately and closed around the pipe during the mounting procedure. Thus, the VD and the beam pipe form a single module, which will be inserted into the center of the ST frame as a whole. The beam pipe and two halves of the VD detector in disassembled state are shown in Fig. 17.9. These two half-cages form a load-bearing power element that carries the weight of the VD and the beam pipe. To date, two options of the VD are being considered: MicroMegas and silicone detectors. The weight of VD in its MicroMegas option is close to 40 kg, while the silicone option of VD is lighter. The cage with VD and beam pipe, sliding into the central position inside the ST frame, are shown in Fig. 17.10.

The next step is to install end-caps of ST, Aerogel, BBC, and TOF. All these end-caps have a cylindrical shape with a hole in the middle for the beam pipe. The radial dimensions of the end-caps are similar. The end-caps are edge-mounted on the TOF frame. They will be inserted one-by-one by moving them along the beam pipe, as shown in Fig. 17.11. The last object in this sequence is a clamp that holds the pipe. The installation procedure is carried out manually. The assembling procedure can be carried out either directly in the experimental hall, or somewhere outside the experimental area. The latter case has an advantage in view of the fact that during the operation of the accelerator, access to the experimental area will be restricted. In this case, the whole assembly (TOF, ST, Aerogel, BBC, and VD) will be transferred by a crane to the cradle, as shown in Fig. 17.12. The lifting platform of the cradle can be the same as for the magnet (see Fig. 17.3), but the vise mechanism is to be adjusted to the size of the TOF frame. As the last step, the assembly is moved along the rails to its working position inside ECal.

The next step is to install the ECal end-caps. Assuming the same transversal dimension of the ECal end-cap as for the ECal barrel, the same configuration of the cradle as for the ECal barrel can be used. Therefore, the ECal end-cap will be lowered by a crane and placed into the the same cradle. The ECal end-cap is transferred along the rails to the working position and fixed to the RS barrel. The procedure is shown in Fig. 17.13. The beam pipe passes through the central hole of the ECal end-cap, and its flange comes out. This flange will be used to attach the outer segment of the pipe.

The last step is to mount the outer segments of the beam pipe and to close the two sections of the RS end-cap. The outer segments are the heaviest part of the beam pipe. Each of these segments will require two additional holding clamps. One clamp holds the beam pipe in the middle of the central hole of the ECal end-cap. At the outer end, the segment is held by four rods, which, in turn, are attached to the lower and upper parts of the support frame, as shown in Fig. 17.14 (left). Finally, two sections of the RS end-cap are closed, as shown in Fig. 17.14 (right), and the SPD detector is ready to be transported to the beam position.

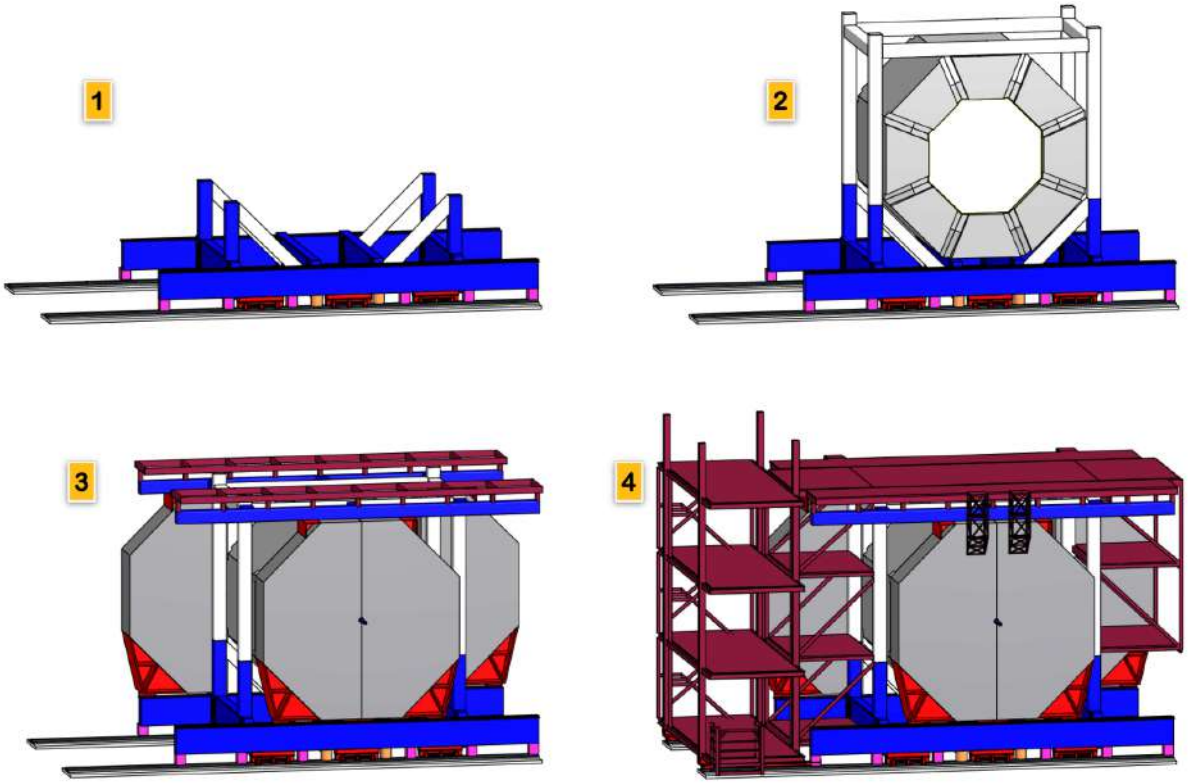

Figure 17.1: (1) Installation of the lower part of the movable lodgement. (2) Installation of the barrel octants of RS with a support structure. (3) Installation of the RS end-caps. (4) Installation of top and side platforms for cryogenics and electronics.

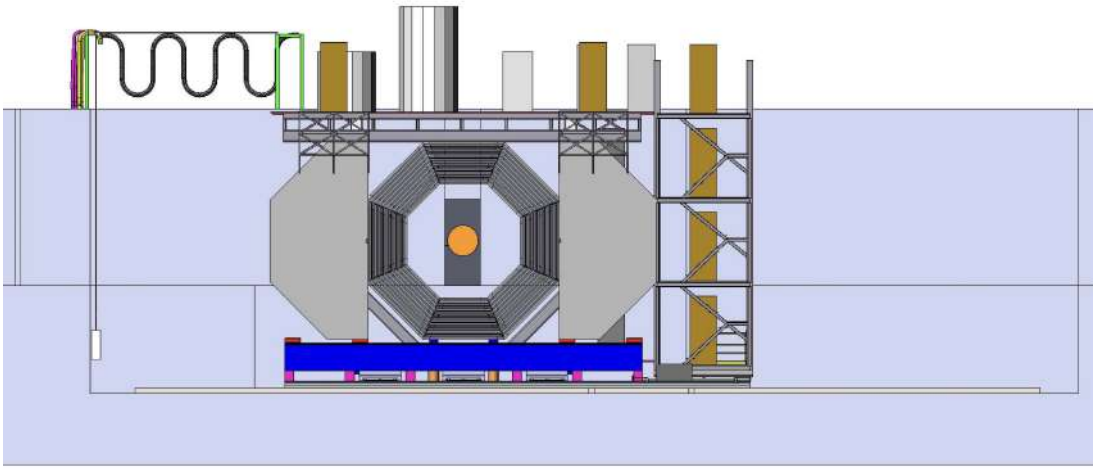

Figure 17.2: Side view of the detector. Once the upper and side platforms are ready, one can start installing cryogenic equipment, electronic racks, set cables and gas pipelines. This step, however, can be postponed to the moment after the magnet is installed (see Figs. 17.3 - 17.5).

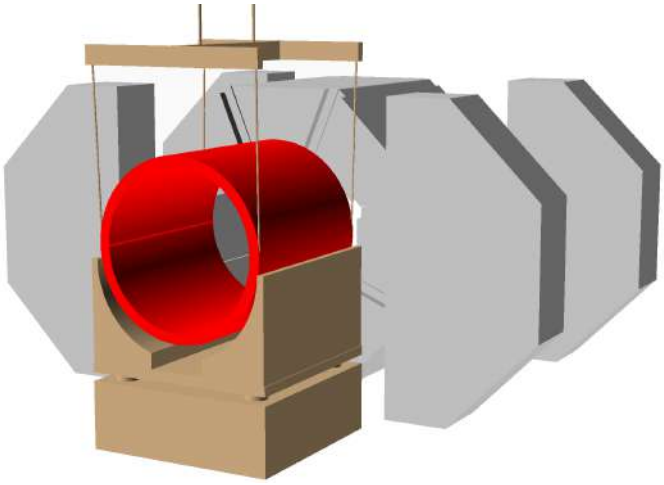

Figure 17.3: (Var-1) The magnet is lowered by a crane into the cradle. The cradle contains lifting jacks for adjusting the height and aligning the magnet with the RS barrel. The magnet is transported in the axial direction to the working position. The magnet weights 16 tons.

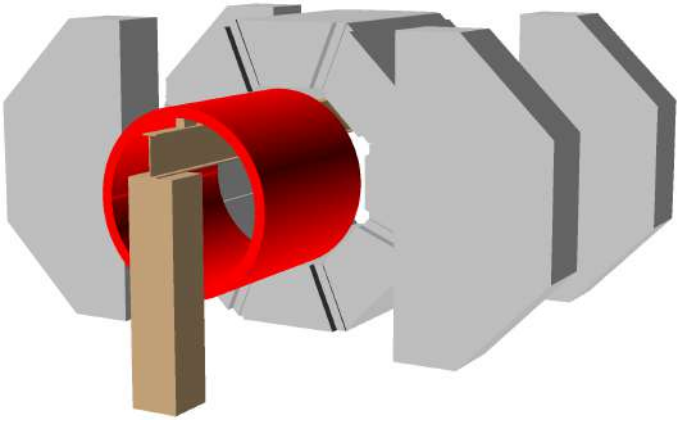

Figure 17.4: (Var-2) The guide beam with a rail is threaded through the magnet and fixed to the pillars on both sides.

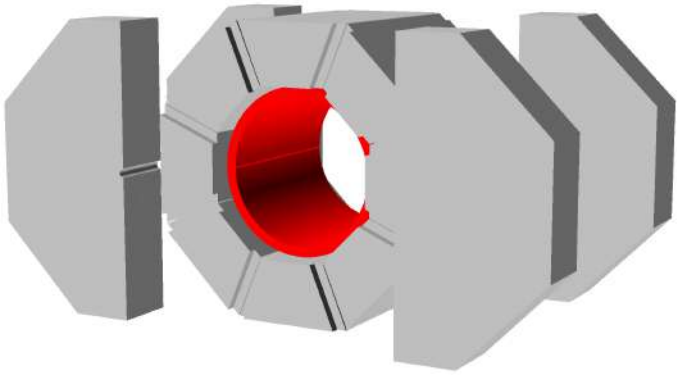

Figure 17.5: Final configuration with the magnet installed and bolted to RS.

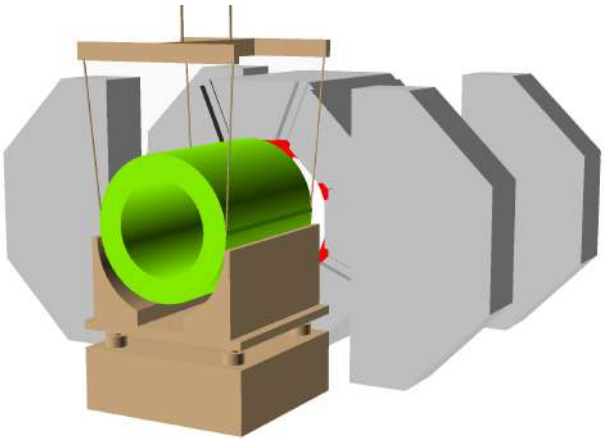

Figure 17.6: The ECal barrel is lowered by a crane into the cradle. The lifting platform of the cradle can be the same as for the magnet (see Fig. 17.3), but the vise mechanism needs to be adjusted to the new size. The weight of the ECal barrel is close to 40 tons.

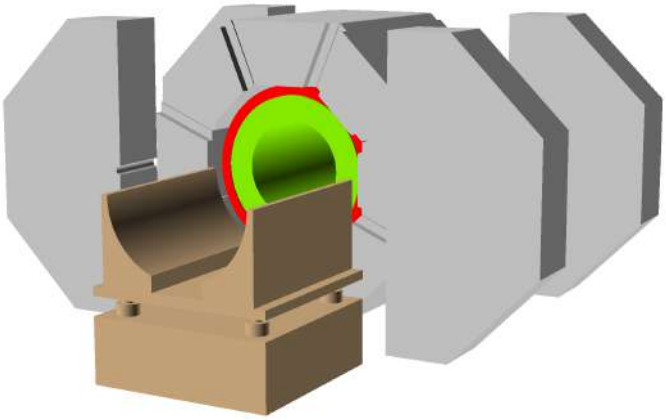

Figure 17.7: The ECal barrel is moved along the rails to the working position. Two fixation options are under consideration: (1) hanging ECal on the magnet, (2) ECal is supported at its ends (fixed to RS).

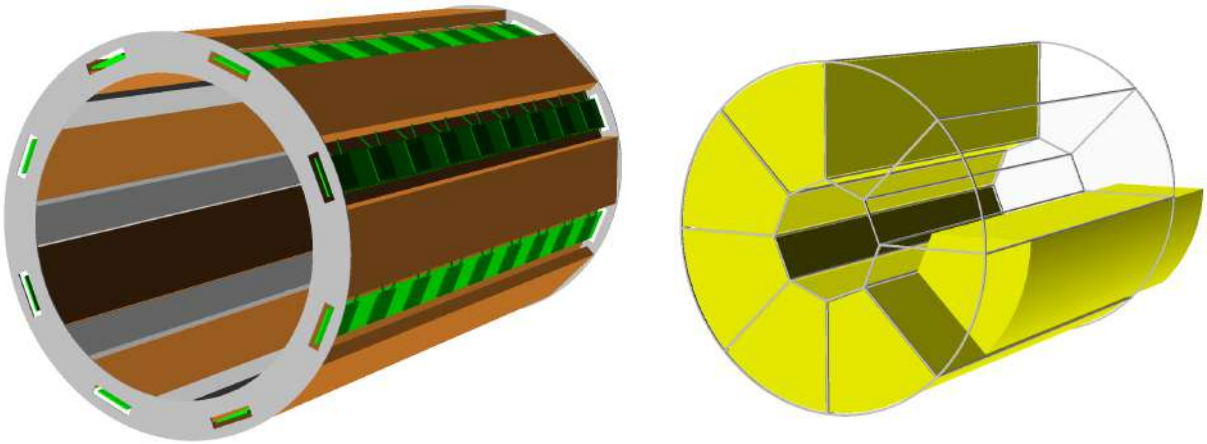

Figure 17.8: *Left*: The TOF barrel with inner and outer layers of MRPC-supermodules installed. The expected weight is close to 4 tons. *Right*: The ST frame partially loaded with the straw modules (octants). The weight of the ST barrel is about 120 kg. It will be inserted and fixed inside the TOF barrel.

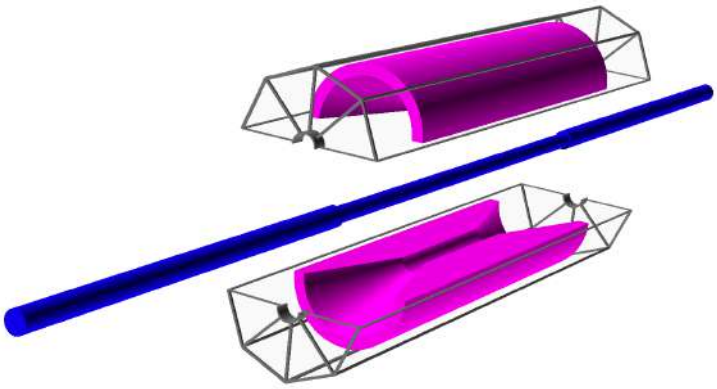

Figure 17.9: The beampipe and two halves of the VD detector, which are fixed on two half-cages. These two half-cages form a load-bearing power element that carries the weight of the VD and the beampipe. The weight of VD in its MM option is close to 40 kg. The silicone option of VD is much lighter.

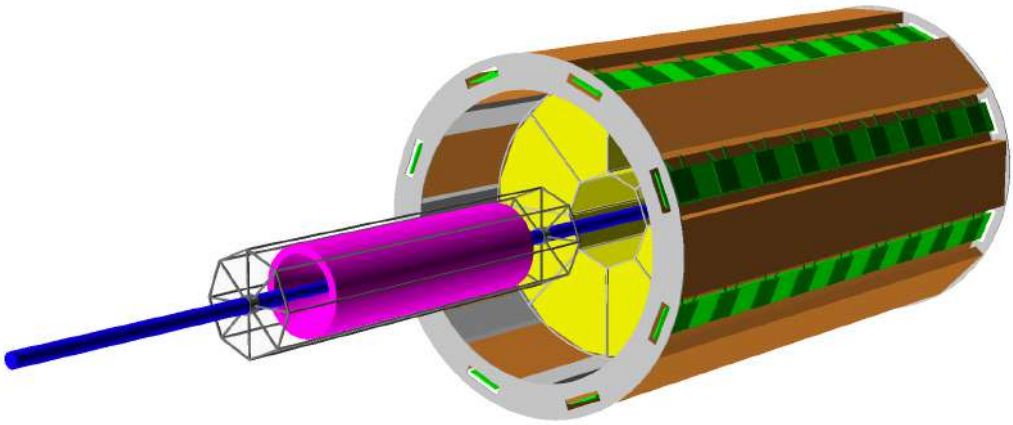

Figure 17.10: The cage with VD and beampipe slides into its central position inside the ST frame.

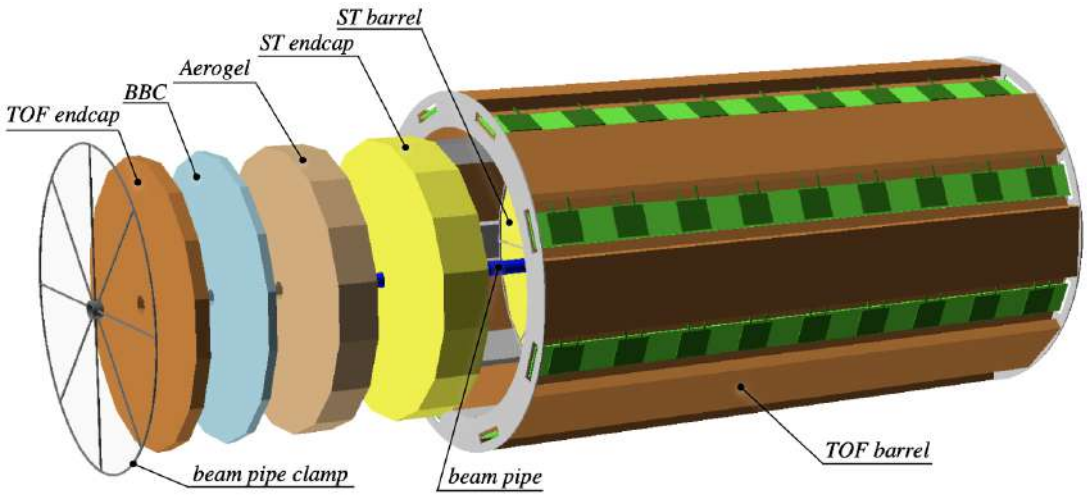

Figure 17.11: The End-caps of ST, Aerogel, BBC, and TOF are mounted one-by-one by moving them along the beampipe. The last object in this sequence is a clamp that holds the pipe. All end-caps and the clamp are braced to the TOF barrel frame.

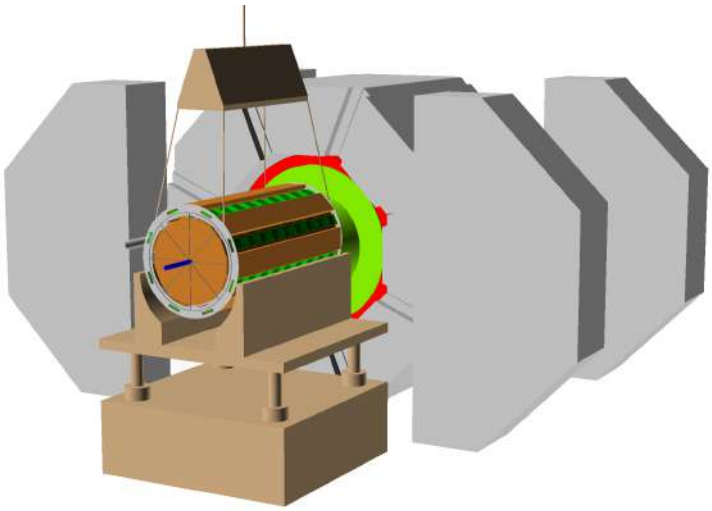

Figure 17.12: The TOF barrel with other inner detectors (ST, Aerogel, BBC, and VD) is lowered by a crane into the cradle. The lifting platform of the cradle can be the same as for the magnet (see Fig. 17.3) but the vise mechanism is to be adjusted to the new size.

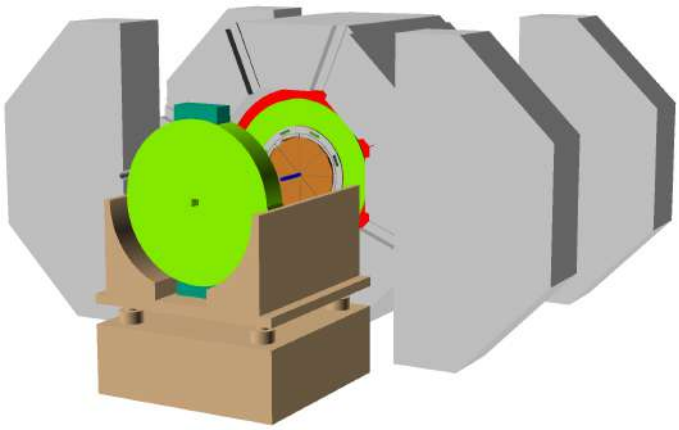

Figure 17.13: The ECal end-cap is lowered by a crane into the the same cradle. Assuming the same transversal dimention of the ECal end-cap as for the ECal barrel, the same configuration of the cradle can be used as for the ECal barrel.

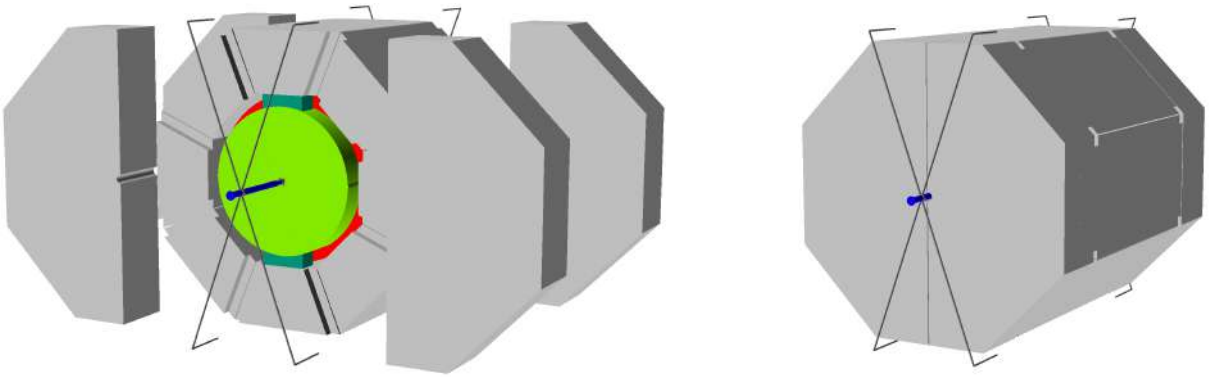

Figure 17.14: *Left*: The edge section is bolted to the beampipe at one end. At the outer end, the section is held by four rods, which, in turn, are attached to the lower and upper parts of the support frame. *Right*: Two sections of the RS end-cap are closed. The setup is ready to be transported to the beam position.

Chapter 18

Detector control system

The SPD detector control system (DCS) is designed to control the basic operating modes of the detector parts and the detector as a whole, and to continuously monitor slowly changing parameters of the detector, engineering means, which provide the detector operation, and the environment. The DCS is synchronized with the basic operating modes of the NICA accelerator complex by means of a synchronization subsystem shared between the DCS and the SPD DAQ. The DCS provides parameterization of the managed object (i.e. the SPD detector), implements algorithms for normalization, parameters measurement and control, based on these parameters, and generates the necessary sets of abstractions and options for presenting them to the operator in an intuitive manner. Critical values of the parameters going beyond the predefined limits in predetermined situations cause emergency events and initiate procedures for handling such events, including the procedure for an automatical detector shutdown in order to prevent its damage. Parameter values, archived in a database for long-term monitoring of the detector operation, identify possible failures in the operation of the equipment and emergency situations. The configurations of the detector parameters saved in the database make it possible to start the detector promptly with various preset parameters and in various operating modes, in accordance with the requirements of a particular physics experiment.

The DCS allows autonomous operation of each detector subsystem at the stage of the initial start-up, as well as its periodic maintenance, calibration sessions, and planned upgrades. The number of parameters in the system is expected to be significant, therefore, it is assumed that the system should be extendable and flexibly configurable. Architectural and software solutions, based on the event-driven model [103] and client-server and producer-consumer [104] interaction models, should be preferred for communications, when building the general DCS and the control systems of each part of the detector. Centralized systems operating in the master-slave polling mode should be avoided.

1 DCS concept

Most of the high-energy physics detectors include parts consisting of similar systems, built from devices, sensors, and actuators with similar or identical functionality. This determines parameterization of the entire detector as a managed object. Such systems include:

1. high voltage (HV) power supply system for powering gas detectors and light (photon) sensors (PMT and SiPM);
2. low voltage (LV) power supplies for powering magnets, digital and analog electronics;
3. cryogenic systems;

4. gas supply and mixing systems;
5. vacuum systems;
6. front-end electronics LV powering control and temperature monitoring;
7. different cooling and temperature control systems;
8. DAQ system;
9. accelerator interface and synchronization;
10. general external electricity and water cooling stations, etc.

The SPD detector is no exception and includes almost all of these systems spread among different parts of the detector, as shown in the layout diagram, Fig. 18.1. Each part of the detector refers to one or more subsystems. The architecture of the systems will be refined, as the individual parts of the detector are developed.

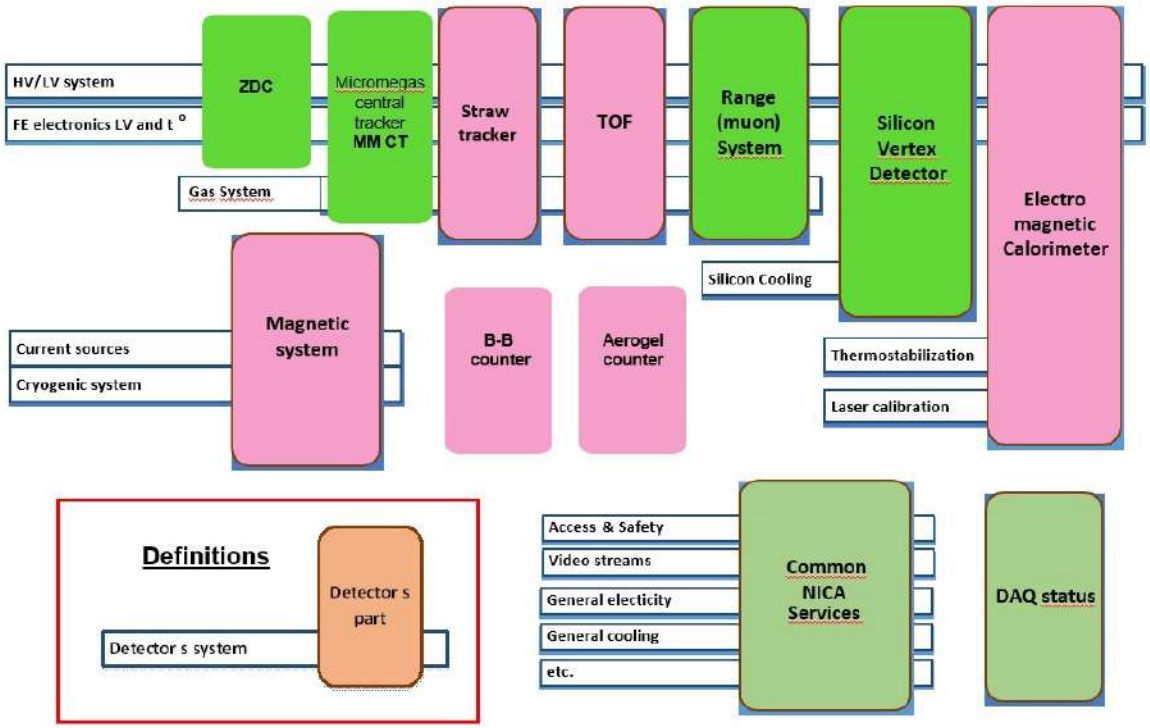

Figure 18.1: SPD detector control system layout.

All the systems can be similarly parameterized and shown to the operator in an intuitive presentation in order to simplify the operator's decision-making algorithm. However, the physical implementation of these elements at the hardware level may vary significantly in different parts of the SPD for the following reasons:

- the parts inherit the experience of their developers gained in previous experiments;
- hardware and software components are selected based on their cost and availability;

– parts of the detector are manufactured at different times.

Nevertheless, in order to optimize financial and human resources costs for the creation of the entire detector and the DCS, in particular, it is necessary to recommend to the developers of the detector parts to strive for standardization of the used hardware and embedded software. This will significantly reduce the efforts put into developing, deploying, and operating the detector, and will result in significant cost savings. To achieve these goals, at the stage of prototyping the detector systems it is advisable to work out not only the detector itself, the front-end electronics and the DAQ, but also the slow control systems. This work can be carried out in the beam test zone (BTZ), for which the BTZ slow control system must be made as similar to the final DCS version as possible.

2 DCS architecture

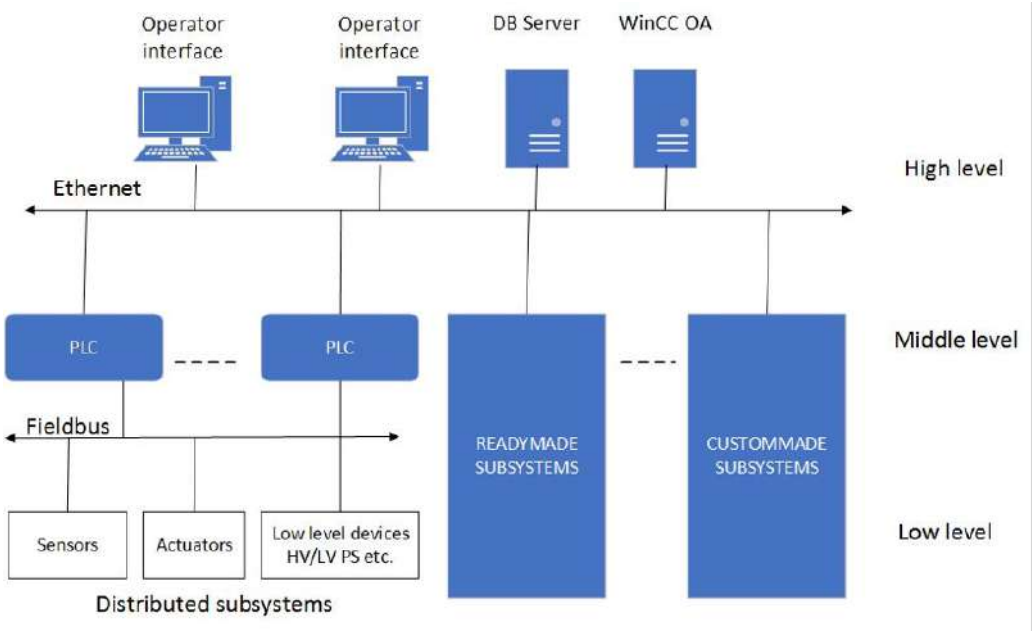

Figure 18.2: SPD detector control system architecture.

The detector control system is divided into three logical levels (Fig. 18.2). The lower level includes measurement channels built into the front-end electronics (FEE) and data acquisition system (DAQ) of the detector parts, various stand-alone sensors, I/O devices, and low and high voltage power supplies. The middle level is represented by programmable logic controllers and integrated ready-made and custom-made subsystems (vacuum posts, gas consoles, multichannel ready-made power subsystems, etc.). The interfaces to the FEE and DAQ that provide data for the detector control system are also on this level. The upper level is designed to provide a human-machine interface for operators, implement a database of detector parameters and configurations, communicate with the external world (accelerator, engineering support systems, access system, etc.), and implement macro-control algorithms, common for the entire detector. All these levels are connected in a hierarchical network using fieldbuses between the first and the second level, for example, a CAN-bus with a CANopen protocol. An Ethernet LAN is used between the middle and the upper levels. At the top level, special software, such as SCADA (Supervisory Control And Data Acquisition), is used, which provides control, collection, and storage of data in real time. It is proposed to use the WinCC OA system, common at CERN, as a SCADA system. We understand that for smooth and reliable communication with the control system of the Nuclotron, a gateway to the Tango Controls [105, 106] system should be developed and deployed.

3 SCADA for the DCS

WinCC OA (ex PVSS-II) [107, 108] is a commercial SCADA system. It is a software component constructor that allows one to use preinstalled prototypes and templates, as well as software modules and system components, developed in C. This system is actively used in many experiments at CERN and has support and safety certificates in the Russian Federation. The following properties make WinCC OA an attractive solution to be used in the DCS of the Spin Physics Detector:

- object-oriented approach, built into the system, ensures an efficient development process and the ability to flexibly expand the system;
- capability to create distributed systems - up to 2048 WinCC OA servers;
- scalability from a simple single-user system to a distributed redundant network system with > 10 million tags (physical and synthetic parameters);
- platform-independent system, available for Windows and Linux;
- event-driven system;
- hot standby and 2×2 redundancy (DRSystem), the required level of availability and reliability;
- wide range of drivers and options for communication OPC, OPC UA, S7, Modbus, IEC 60870-5-101/104, DNP3, XML, JSON, SOAP, etc.;
- support by major manufacturers of electronic devices for building automation systems in high energy physics.

Each functional unit of the system that is software implemented as a separate process is called manager. A set of managers forms a system. Data exchange and communications between managers are done via TCP. The data is exchanged by means of passing events. The system allows parallelizing processes (managers) by running them on different computers with different OS. The system is scalable and balances the load on the control computers. The required managers start only if necessary, and multiple instances may run simultaneously. Managers can be distributed across multiple computers/servers. The WinCC OA block diagram is shown in Figure 18.3.

The main process is the Event Manager. It contains and manages the process image (current values of all process variables), receives and qualifies data (central message manager), distributes data across other managers, acts as a data server for others, manages users authorization, as well as generation and status of the alarm messages.

The Database Manager receives data from the Event Manager and handles it according to its own algorithm. The historical database can use either a proprietary database (HDB) or an Oracle DBMS (the Oracle Real Application Clusters configuration is also supported). Parallel archiving in Oracle and HDB databases is possible. It is also possible to record user-defined data and log system events and messages in an external relational database (MS SQL, MySQL, Oracle, etc).

The WinCC OA Report Manager supports different ways of generating reports:

- in the Microsoft Excel format;
- in the *xml* format with the ability to display in any external tool for working with reports (Eclipse BIRT, Crystal Reports, SYMATIC Information Server etc.). SOAP (Simple Object Access Protocol) protocol is also supported.

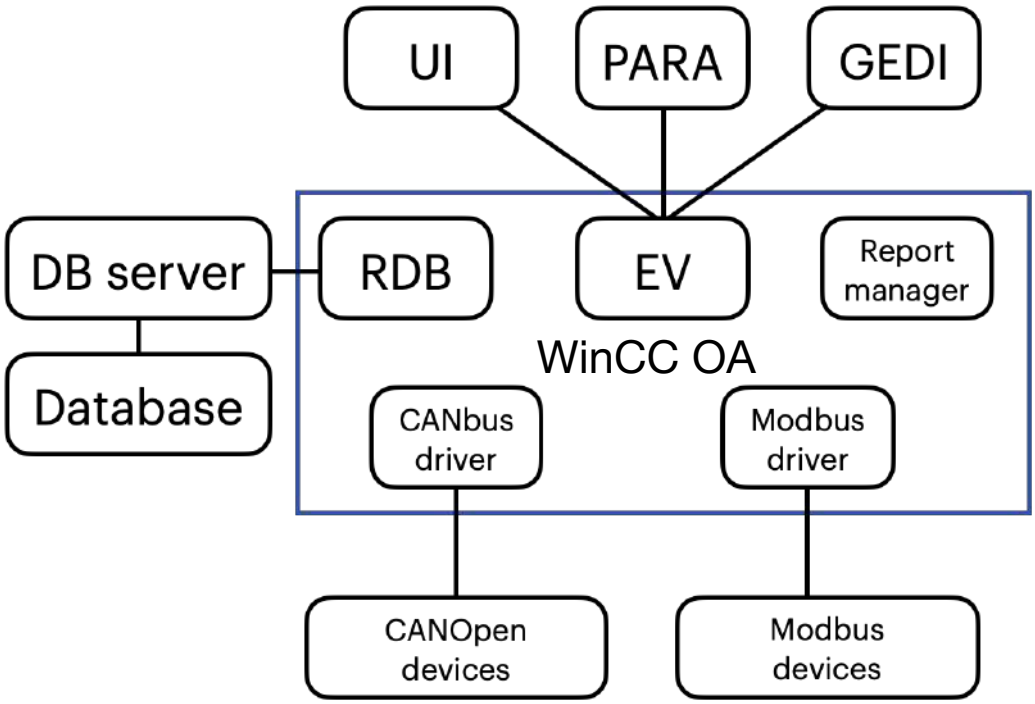

Figure 18.3: SCADA structural scheme of the WinCC OA software.

Project development for the WinCC OA system is based on an object-oriented approach. In the WinCC OA data model, objects are represented as data points (called tags) that characterize the image of a specific physical device or process. For each data point element, properties and actions, such as signal processing (smoothing, setting limits, etc.), communication with external systems, archiving, generation of alarm messages (alarms), etc. can be defined accordingly. Typing and inheritance are supported, therefore arbitrary hierarchical data structures can be created. Similarly, the principles of inheritance and reusability are implemented for graphical objects. The WinCC OA IDE includes the PARA configuration editor and the GEDI graphical editor of the User Interface Manager (UI) (includes a data model editor, mass configuration tools, administration tools, an interface to version control systems, a debugger, etc.).

Changes to data structures and graphics are applied without restarting the project. Writing custom scripts can be done using CONTROL++ (a programming language, the syntax of which is similar to C/C++). Such scripts can be both event handlers, associated with the elements of the graphical interface, and data processing procedures.

The system includes a standard graphical objects library; it can be extended by developing user objects or using the Qt Toolkit widgets. It is also possible to use the JavaScript libraries available on the market, or the included JavaScript scripts. Thanks to the open API (C++ / C# API), it is possible to create managers, drivers, widgets, and CONTROL++ extensions. A new set of tools is available for the concept of High Speed Programming implementation, which supports documentation build-up from the source code, unit testing, and autocompletion of program structures.

It is also planned to provide data exchange between the WinCC OA and Tango Controls, which is used as the upper level of the Nuclotron control system. This can be implemented using standard OPC technologies with a client-server architecture, or it can be implemented using SQL tools, as a common database for both SCADA systems used for the accelerator and the detector. The final choice of a suitable solution will be made at the stage of system implementation.

4 Cost estimate

The cost of the DCS development and implementation includes the cost of the off-the-shelf components, customized elements and the development of the application software including configuration of the selected SCADA. It seems to be optimal to carry out all the development of hardware and software during the phase one, while the additional purchase of the off-the-shelf components and additional production of custom components is reasonable to do during the phase two. In this regard, the cost of DCS implementing during the stage I is 1 M$, with a total cost estimate of 1.8 M$ for the stagges I+II.

Chapter 19

Data Acquisition System

1 Introduction

The data acquisition system (DAQ) of SPD should provide a readout and a transfer of data from all detector subsystems. These include:

- vertex detector (VD): a MAPS-based (or double-strip based) silicon tracking detector for precise determination of the primary interaction point and measurement of the secondary vertices from the decays of short-lived particles;
- micromegas-based central tracker (MCT): a tracking detector designed to improve the momentum resolution at the first stage of the experiment;
- straw tracker (Straw): the main tracking detector for measurement of the primary and secondary particle momenta based on curvature of tracks in a magnetic field, and also for the ionization loss measurement;
- particle identification detectors: i) time-of-flight resistive plate chambers (RPC), and ii) aerogel Cherenkov counters (Aerogel);
- electromagnetic calorimeter (ECal) for measurement of the energy of gammas and electrons (positrons);
- range system (RS) for detection and identification of muons;
- beam-beam counters (BBC) for local polarimetry and monitoring of the beam collisions;
- zero degree calorimeter (ZDC) for local polarimetry using forward neutrons and for luminosity measurement.

At the maximum center mass energy $\sqrt{s} = 27$ GeV and maximum luminosity 10^{32} cm^{2}s^{-1} the event rate was estimated as 3×10^6 s^{-1}. This high rate has brought us to the decision to build a triggerless DAQ. Such DAQ systems will be created in many new experiments under preparation, in particular, in GSI (PANDA, CBM, NUSTAR), PSI (Mu3e), in future HL-LHC experiments, also foreseen for ILC, CLIC etc.

With a free-running DAQ, there is no hardware trigger system, therefore the readout process is not controlled by a trigger anymore. All data that exceed the thresholds in the front-end electronics are read out together with their timing marks. Then in DAQ the data are grouped on the basis of timing and

Table 19.1: Summary of detector outputs to DAQ at the first stage. Information type: T means time, A – amplitude (or charge).

Sub-detector	Information type	Number of channels	Channels per FE card	Number of outputs
Micromegas central tracker*	T + A	25600	128	200
Straw tracker	T + A	34096	128	267
BBC (inner+outer)	T + (T + A)	256 + 500	32	8 + 12
Range system	T	130200	192	679
ZDC	T + A	1050	64	17
Total (max)		191702		1183

* – maximal estimation

detector affiliation, and finally are delivered to the input buffer of the online filter in the form suitable for analysis.

The front-end electronics of the detectors should meet the requirements of a free-running DAQ:

- self-triggered operation;
- digitizing on-board;
- timestamp included in the output format.

A reasonable estimation of the total data flux in the SPD DAQ was obtained, partly using the simulation, and partly – the results of the beam tests of the detectors of other experiments (MPD, PANDA, ALICE), or the parameters of the appropriate front-end electronics which already exist or are under development.

The data flux was estimated at the maximum energy 27 GeV, maximum luminosity 10^{32} cm^{2}s^{-1}, and at the correspondent event rate of 3×10^6 s^{-1}. According to CDR, multiplicity value was taken equal to 8 for charged particles and 6 for neutrals. With some approximations, the total flux was found to be 20 GByte/s. This number includes transfer of the measured quantities themselves (time, amplitude, coordinate), relevant headers, also takes into account clustering of hits and partly noise counts in some detectors. The largest contributions to the total flux are produced by VD, Straw and RS detectors, while the contributions of BBC and ZDC are almost negligible.

Note, that at the first stage of the experiment, with not all of the detectors implemented and at a reduced energy and luminosity, the data flux could be less by up to two orders of magnitude.

A total number of channels to be read out at the first stage is about 160 thousand. For the full scale experiment this number will not exceed 700 thousand. Some numbers for both stages are summarized in Tables 19.1 and 19.2.

2 DAQ structure

Data in the DAQ system is grouped by time into parts called slices. A slice length is 10÷100 μs. A sequence of slices forms a frame. The frame length is 0.1÷10 s. Each slice is stamped with two numbers: a frame number (the order of the frames inside the run) and a slice number (the order of the slice inside the frame). The frame and slice numbers start from 0.

Table 19.2: Summary of detector outputs to DAQ for the full scale experiment. Information type: T means time, A – amplitude (or charge).

Sub-detector	Information type	Number of channels	Channels per FE card	Number of outputs
Vertex detector 3 DSSD	A	107520	640	168
Vertex detector 4 MAPS	A			
Straw tracker	T + A	34096	128	267
Calorimeter	T + A	26112	64	408
PID-ToF	T	8832	16	552
PID-Aerogel	T + A	256	16	16
BBC (inner+outer)	T + (T + A)	256 + 500	32	8 + 12
Range system	T	130200	192	679
ZDC	T + A	1050	64	17
Total (max)		308822		2127

A clock called the global clock is used for synchronization in the DAQ system. A global clock frequency is 125 MHz (a period of 8 ns). The required jitter for the global clock is ≤ 50 ps.

The data of each hit must have a timestamp. Time in the SPD detector is measured from the beginning of the frame and makes sense only inside that frame. No correlation is assumed between the time in two frames. Thus, one frame is the maximum possible time interval in SPD between time-correlated events.

To control the operation of the DAQ system, the following commands are used:

- commands synchronous with the global clock signal;
- asynchronous commands.

The so-called Time Synchronization System (TSS) is responsible for the distribution of the global clock signal and synchronous commands throughout the whole setup.

Logically, the DAQ system can be divided into three subsystems: a Readout Chain, a Slice Building System, and a Time Synchronization System.

Now the interaction of the DAQ system with the front-end electronics is well developed for the already existing electronics of the Range System. The current requirements for the front-end electronics are developed assuming an easy implementation to supposed readout systems of other detectors.

All information about the DAQ settings (slice and frame length, enabled subdetectors, etc.), configuration of the front-end electronics (calibration, the mapping of electronics channels, etc.) and experimental conditions (beam energy, polarization, etc.) will be stored in a database.

3 Readout chain

The general view of the readout chain is shown in Fig. 19.1. The readout chain consists of the front-end electronic FEE cards (the example of the RS FEE cards is used at the presented scheme), a data concentrator of the 1st level (L1 concentrator) and a data concentrator of the 2nd level (L2 concentrator).

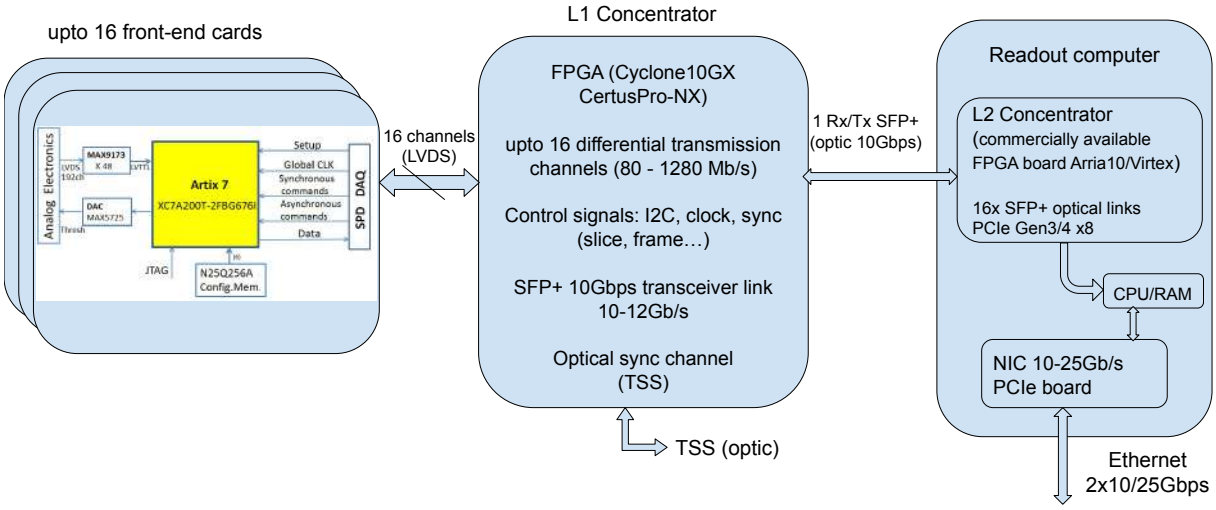

Figure 19.1: SPD readout chain.

The FEE cards are connected to the L1 concentrator using a copper cable or a flexible cable, depending on the technical design of the detectors. The length of the cables can be up to $5 \div 7$ meters, depending on the data transfer rate.

The following LVDS signals are used: data transmission channel, global clock and signals for the implementation of synchronous commands. In addition to the LVDS signals, other signals are used: signals for implementing the I^2C bus (SDA, SCL) and a reset signal.

The I^2C bus is used to transmit asynchronous commands. These commands are used to control and monitor FEE cards and are specific for various electronics.

It is expected that a Displayport cable will be used to connect to the Range System (RS). Fig. 19.2 shows the pinout of the Displayport connector on the FEE card side.

The L1 concentrator board allows to connect up to 16 FEE cards, with a data transfer rate of up to 1.2 Gbps per channel, and to manage them. The L1 concentrator is based on FPGA chips such as Intel Cyclone10GX or Lattice CertusPro-NX. Data for setting up and managing the FEE cards are received from the L2 concentrator via an optical link. Up-level connection of the board is supposed to be high speed optical bidirectional channel GBTx with the rate up to $10 \div 12$ Gbps. The main limitation for the L1 concentrator is the requirement that the input data flow rate does not exceed the transfer rate at the output of the concentrator. If this requirement is violated (for example, all 16 links of the FEE cards have the rate 1 Gb/s), then the number of the input links is to be reduced to the bandwidth of the output optical link. Thus, the data stream from the FEE cards can always be transferred to the L2 concentrator without data loss.

The global clock signal and synchronous commands are generated and distributed through the L1 concentrators using a Time Synchronization System (TSS). An optical fiber is used to connect TSS to the L1 concentrators. The readout chain operates under the control of TSS: frames and slices begin and end in accordance with the commands coming from TSS. On the other hand, data transmission is initiated by the front-end electronics as a reaction to the commands from TSS, but there is no strict time correlation between TSS commands and data transmission.

A commercially available PCIe card installed in the readout computer is used as the L2 concentrator (see Fig. 19.3). Up to 16 L1 concentrators can be connected to one L2 concentrator (or upto 256 FEE cards). Data is written directly to the computer memory (RAM) at a speed of 4–8 GBps through the PCIe bus.

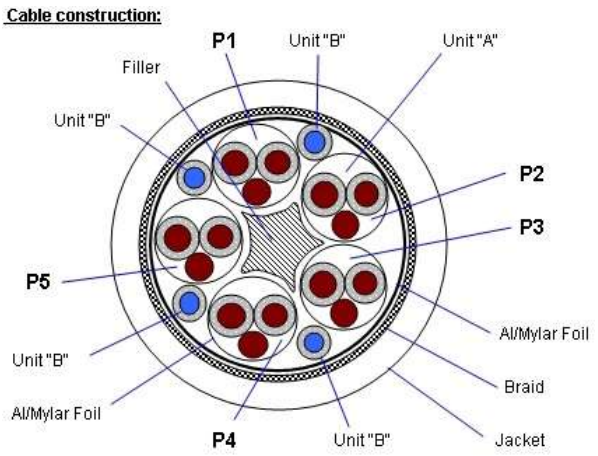

FrontEnd DisplayPort Connector		
Signal Type	Pin Name	Pin
GND	GND	2
Out	ML_Lane 0 (p)	1
Out	ML_Lane 0 (n)	3
GND	GND	5
In	ML_Lane 1 (p)	4
In	ML_Lane 1 (n)	6
GND	GND	8
In	ML_Lane 2 (p)	7
In	ML_Lane 2 (n)	9
GND	GND	19
In	Hot Plug Detect	18
IO	CONFIG1	13
In	CONFIG2	14
GND	GND	11
In	ML_Lane 3 (p)	10
In	ML_Lane 3 (n)	12
GND	GND	16
In	AUX_CH (p)	15
In	AUX_CH (n)	17
	DP_PWR	20

Data e-link

Start of slice

Start of frame

Reset

I2C SDA SCL

Set Next Frame

Global clock

spare signal

Figure 19.2: Displayport cable and pinout for the Range System.

4 Slice-building

The main task of the slice building subsystem is to receive data from the L2 concentrators, combine them into fragments of sufficient duration in terms of astronomical time and acceptable size, and write this data to an intermediate data storage.

The natural choice of the length of these data fragments is the frame length (0.1÷10 s). In some cases the volume of data in a frame may happen to be too large for convenient processing in the building subsystem. Therefore, the frame is divided into parts called chunks. With an expected total data flow up to 20 GB/s, a reasonable chunk length is 0.1÷1 s, depending on the actual data flow. Splitting of a frame into chunks is performed at the slice boundary if the frame length exceeds the established chunk length. Thus, the chunk is a data processing unit in the slice-building subsystem.

The general view of the slice building is shown in Fig. 19.4. The slice building subsystem consists of readout computers, a supervisor computer, a network switch, and builder computers.

From the software point of view, slice building includes readout processes, a supervisor process, and builder processes. Slice building is controlled by the readiness messages from the builder processes, in response to which the supervisor process assigns chunks for processing to certain builder processes. Each builder process works with one chunk at a time.

A separate readout computer is used for each L2 concentrator. (For collecting all data from a big detector, an option of installing 2÷3 L2 concentrators into one readout computer should be investigated.) The expected data flow through one readout computer is about 1 GB/s, which gives a number of readout computers of about 20. The readout computer has 2×10 Gbit/s or 25 Gbit/s network interface(s) used to transmit data further to the builder computers.

The readout processes are performed on the readout computers, one process for each L2 concentrator.

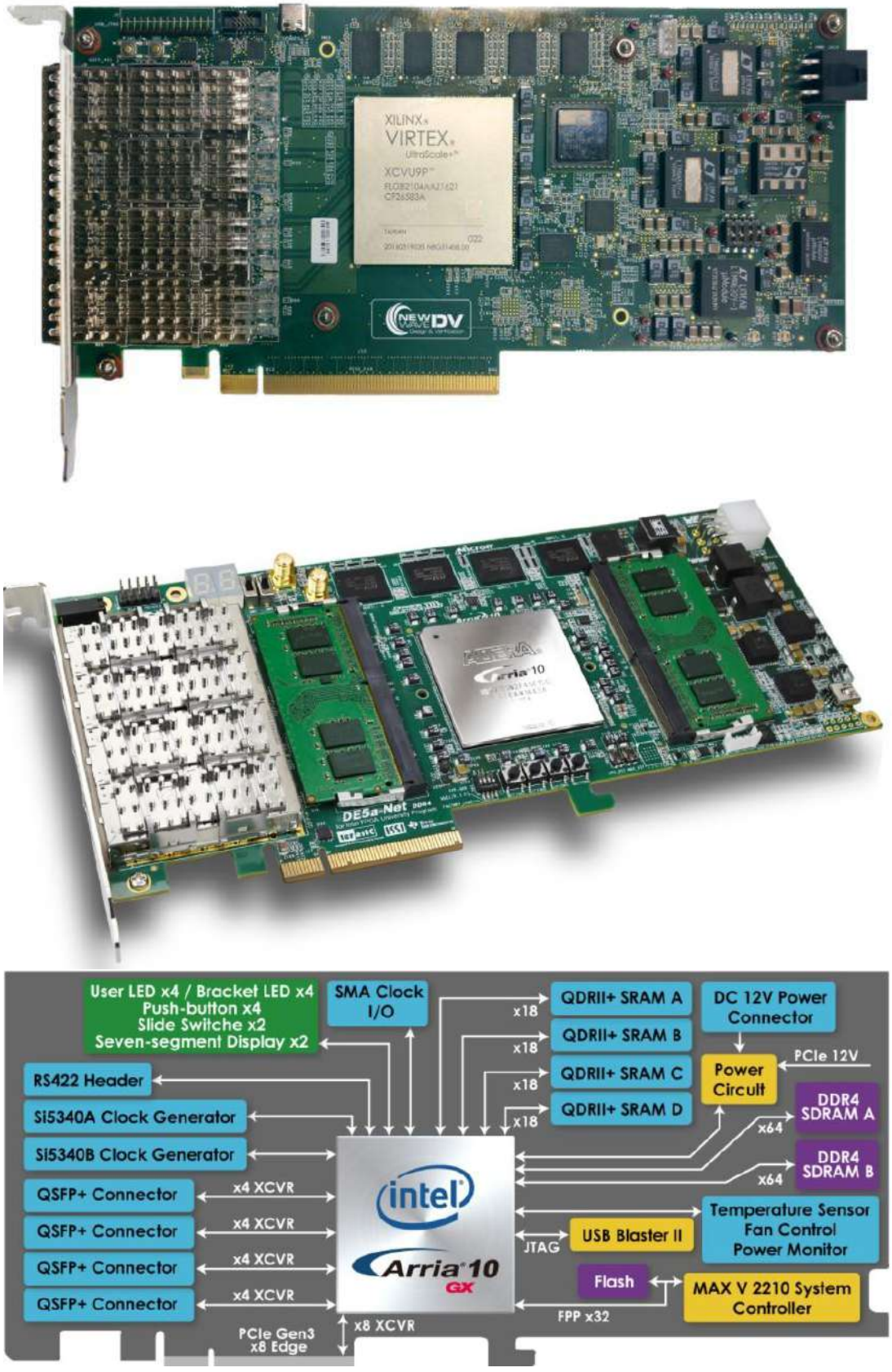

Figure 19.3: Possible hardware for L2 concentrator.

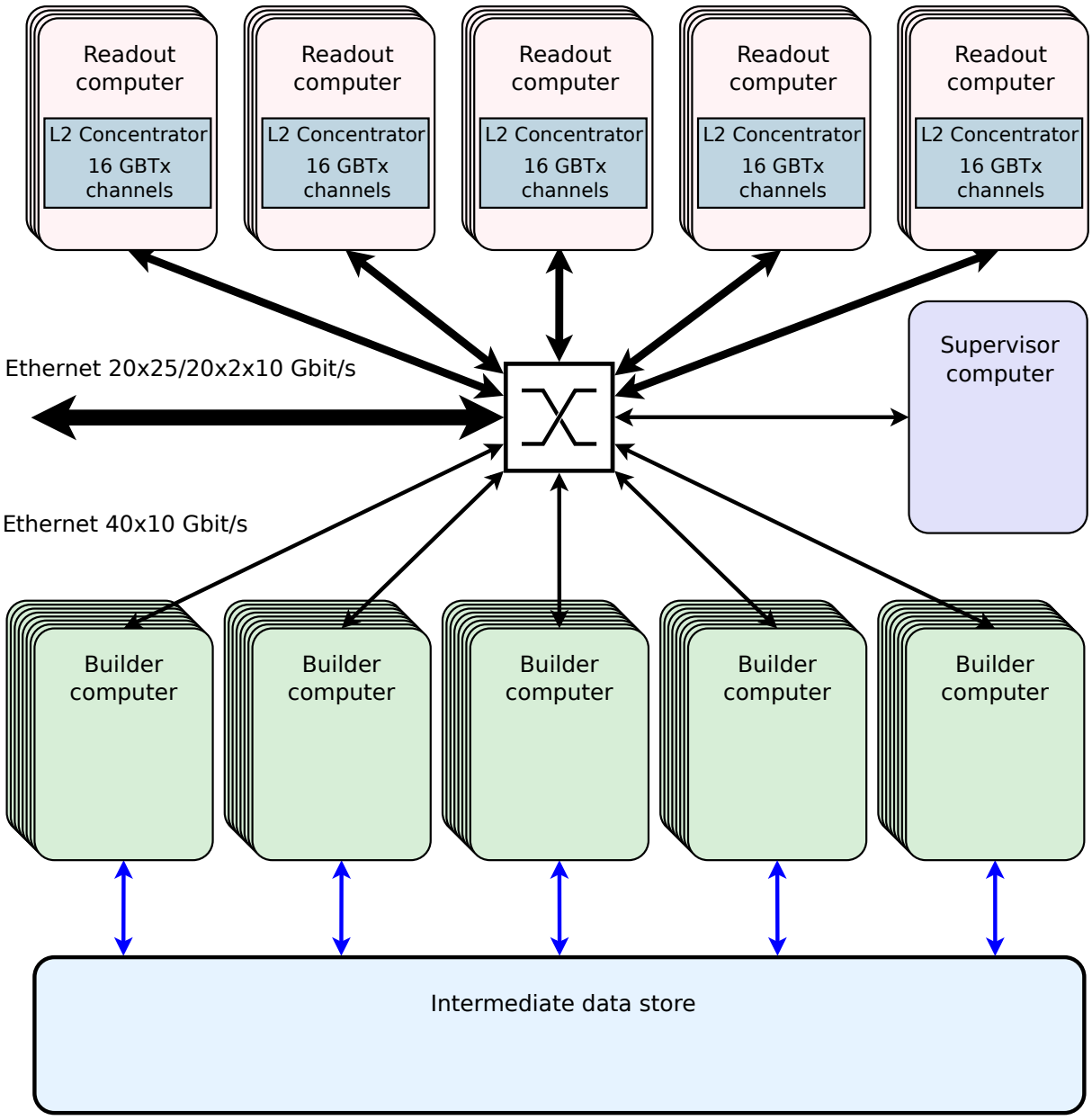

Figure 19.4: SPD slice-building.

Depending on the actual implementation of the L2 concentrator, the data coming from the L2 concentrator may already be formed as sub-slices or may be independent streams from each front-end card. In the latter case, the readout process must first reorganize data in the form of sub-slices. The data organized into sub-slices is buffered in RAM of the readout computer.

The buffering depth should be sufficient, taking into account the architecture of the slice building subsystem and possible emergencies, such as delays in data transmission and recording. A reasonable buffering time is 30–60 s, which requires 64–128 GB of RAM.

The builder process is responsible for building the complete data block chunk. The builder process extracts all sub-slices of a single chunk from all readout processes, composes a complete chunk and stores it in an intermediate data store.

The builder processes run on the dedicated computers that are part of the builder pool. The computer running the builder process can be attached to or detached from the builder pool at any time, including runtime. The number of computers in the builder pool must be sufficient to operate without data loss. At the same time, the absence of a free builder process should not disorganize the DAQ system. If there are no builder processes available, the data of one chunk is dropped by a command from the supervisor process.

The builder computers have a 10 Gbit/s network interface for communication with the readout computers and a separate connection to the intermediate data store. Assuming that there are 20 readout computers, around 40 builder computers must run simultaneously to ensure operations with data flows from each readout computer at 1 GB/s. This approximate calculation assumes that the speed of reading data from the readout computers is approximately equal to the speed of writing data to an intermediate storage. The time of building a chunk is insignificant compared to the time of reading and writing data, and the operations of reading data, building a chunk, and writing data are performed sequentially.

The supervisor process collects information about the received chunks from the readout processes and data processing requests from the builder processes, and basing on this decides which builder process will handle a particular chunk. The supervisor process informs the selected builder process, it connects to all readout processes, and starts receiving the chunk data. When chunk data transfer is complete, the builder process closes the connections to the readout processes. The builder process informs the supervisor process when data transfer from the readout computers has finished and when it is ready to process the next chunk.

The supervisor process and readout processes form the critical core of the DAQ system. A problem with this part of the DAQ system will abort the current run. At the same time, any problem with one of the builder processes can lead to data loss for one chunk, but should not stop data taking.

5 Synchronization and time measurement

Synchronization and time measurement are based on a single clock signal, which is distributed throughout the setup. This clock is called the global clock.

Two types of commands are used to control the readout chain: synchronous with a global clock and asynchronous.

The following synchronous commands are used:

- *Set Next Frame* (SNF),
- *Start of Frame* (SOF),
- *Start of Slice* (SOS).

Synchronous commands together with the global clock are sent to the L1 concentrator from a special system called Time Synchronization System (TSS). All synchronous commands are broadcast commands.

The *Set Next Frame* command loads the number for the next frame into the front-end electronics.

The *Start of Frame* command completes the current frame (if there was one) and simultaneously starts a new frame if the new number for the frame has been loaded. The command *Start of Frame* marks the loaded number of the next frame as used. Before the next *Start of Frame* command, a new value for the number of the next frame must be loaded. The command starts the first slice of the frame simultaneously with the start of the frame, and simultaneously with the stop of the frame, the command stops the last slice in the frame.

The *Start Slice* command completes the current slice and starts a new one inside the frame. The front-end electronics automatically numbers the slices, the slice number is reset to 0 by the *Start of Frame* command.

The *Set Next Frame* command transmits the next frame number and therefore may require more than one clock cycle to implement. The technical implementation of synchronous commands has not yet been defined, but this implementation must ensure that the commands are atomic, i.e. if the transmission of a command takes several clock cycles, then the front-end electronics must be able to completely accept the entire command or skip it, regardless of which cycle of the transmission of the command electronics detected this transfer.

The following asynchronous commands are used:

- *Disarm*;
- *Arm*;
- other commands specific for various front-end electronics.

Asynchronous commands are sent to the L1 concentrator from the L2 concentrator.

Two standard asynchronous commands *Disarm* and *Arm* are used to control the reset signal line that comes from the L1 concentrator to the front-end module. These commands are executed by the L1 concentrator and are not directly visible to the front-end modules. The *Disarm* command sets the active level of the reset signal, in response to which the front-end module enters the reset process. The *Arm* command removes the active level of the reset signal. All the time when the reset signal is active, the front-end module must ignore any synchronous commands. Thus, the *Arm* command enables and *Disarm* disables synchronous commands for the front-end electronics. The *Disarm* and *Arm* commands can be addressed to a single front-end module or to all modules connected to a single L1 concentrator.

In addition to the standard asynchronous commands, various front-end electronics may have different sets of specific asynchronous commands for their initialization and monitoring. Monitoring commands that do not change the state of the front-end electronics can be used at any time, even in parallel with the synchronous commands. These asynchronous commands are transmitted to the front-end module in the form of I^2C commands, and are address commands.

Synchronous commands are generated by the TSS, which in turn is controlled by the corresponding commands. A detailed description of TSS is given in section 19.6. Here we list only two main commands:

- *Start of Sequence* — upon receiving this command, TSS starts generating a sequence of synchronous commands according to the specified parameters;
- *Stop of Sequence* — upon receipt of this command, TSS stops the generation of synchronous commands.

The start of the run procedure is shown in Fig. 19.5 and is as follows:

- The generation of all synchronous commands is disabled by issuing the *Stop of Sequence* command to TSS.
- The *Disarm* command is issued for all front-end modules, in response to which the modules enter the reset process.

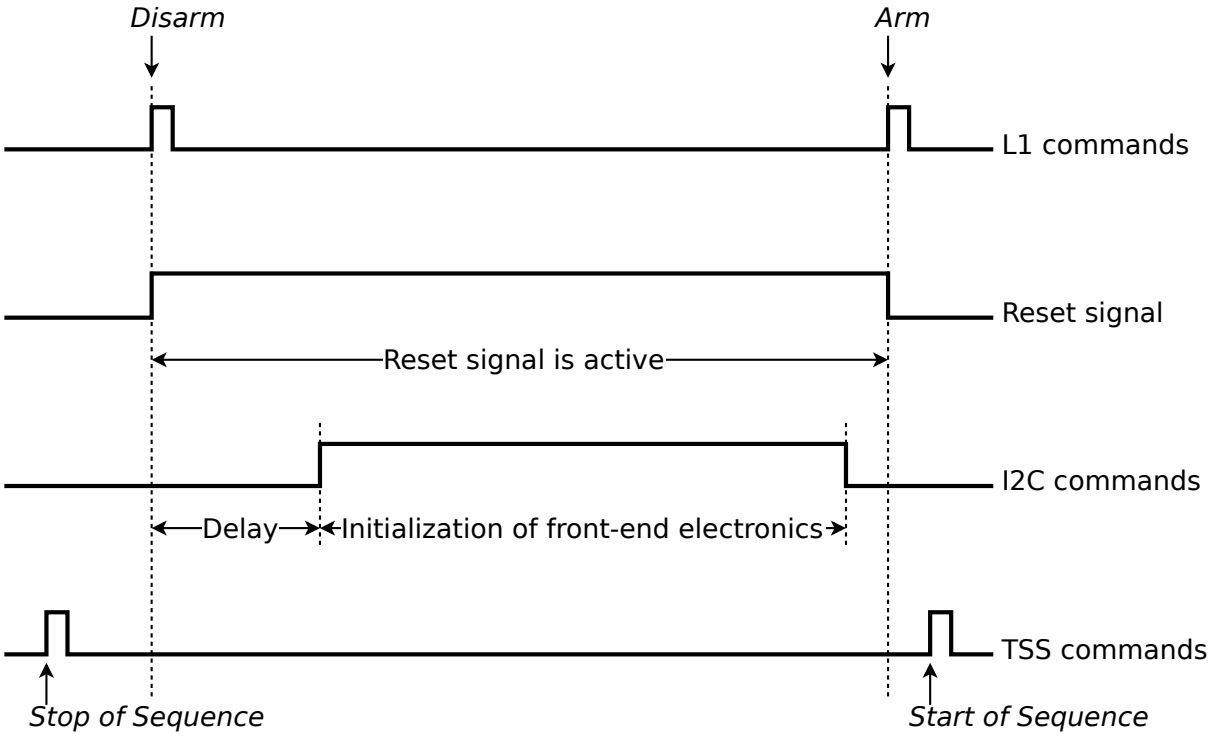

Figure 19.5: The procedure for starting the run.

- After some delay necessary to bring the electronics into a state of readiness to receive incoming commands, the DAQ system begins initializing the front-end electronics using specific I^2C commands.

- The *Arm* command is issued for all front-end modules. Now the front-end electronics are ready to receive synchronous commands. It should be noted that the *Arm* command, as well as the *Disarm* command, is not atomic for the entire installation: it is a sequence of *Arm* (*Disarm*) commands addressed to various front-end modules.

- The generation of a synchronous command is started by issuing the *Start of Sequence* command to TSS.

The structural unit of the run is a package of frames, called a frame batch. A frame batch contains a continuous sequence of frames following each other, without time intervals between frames. On the other hand, there are time intervals between frame batches that can be used by the front-end electronics to perform the necessary periodic actions, such as resetting. In the absence of such a need, one frame batch can be stretched for the entire run. In addition, the frame batch is interrupted when the run is put into a suspended state. Frames in the run have continuous numbering, independent of the grouping of frames into batches. There is no direct limit on the number of frame batches per run or on the number of frames per batch. There is only a general limit on the number of frames per run, resulting from the size of the corresponding field in the data format.

The frame batch is shown in Fig. 19.6. Before the first frame in the batch, the *Set Next Frame* command is executed, which loads the number for the first frame in the batch into the front-end electronics. All frames in the batch, excluding the last frame, contain the *Set Next Frame* command closer to their end. There is no *Set Next Frame* command in the last frame of the batch, and therefore the last *Start of Frame* command ends the frame without starting a new one.

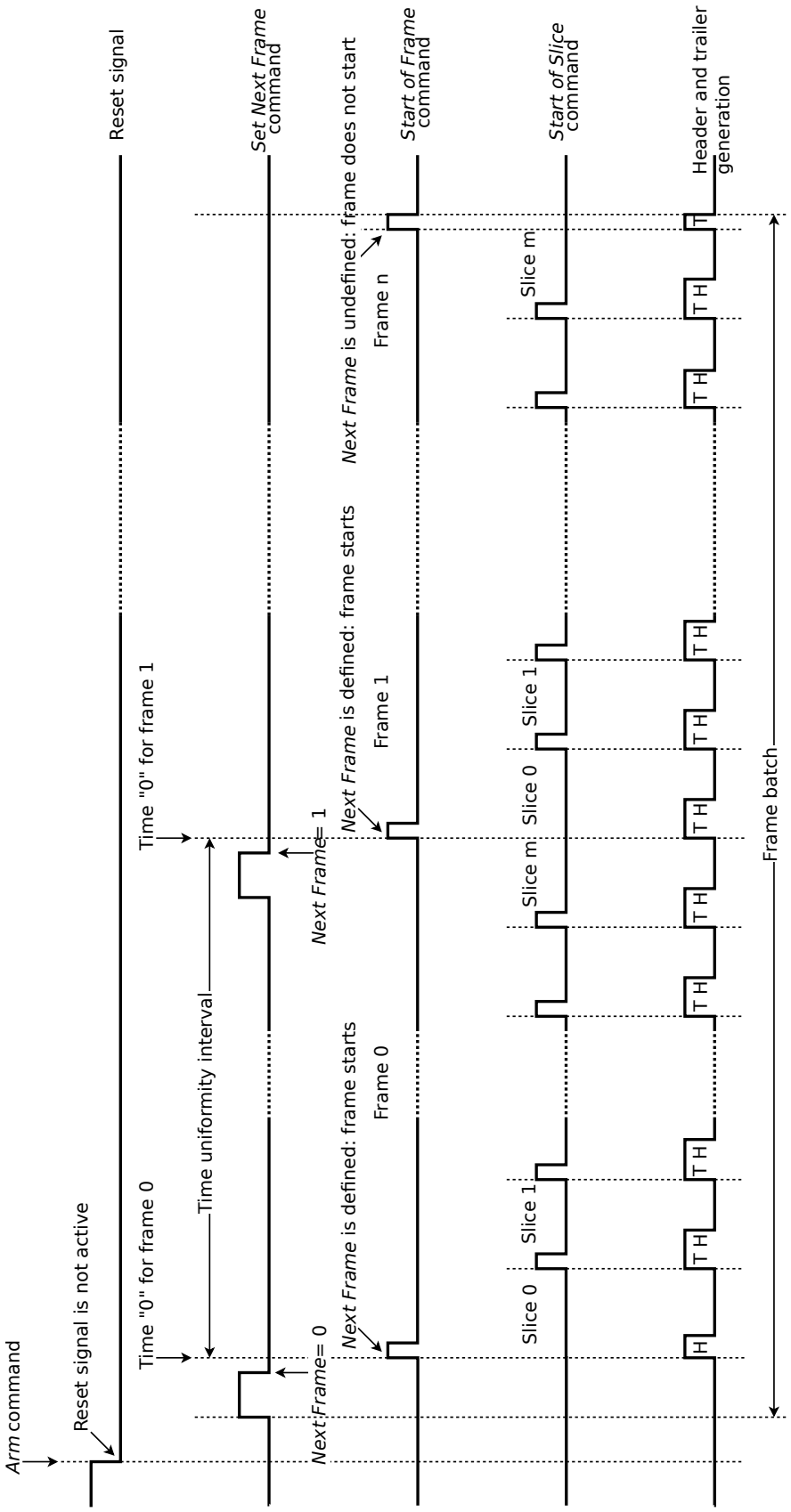

Figure 19.6: Time structure of a frame batch.

The frame, in turn, consists of slices. The *Start of Frame* command simultaneously with the start of a new frame starts the first slice of this frame and simultaneously with the completion of the frame completes the last slice of this frame. Inside the frame, the *Start of Slice* command has completed one slice and is starting a new one.

If necessary, the front-end electronics can be reset during the run by commands from the DAQ system in one of two ways:

- All front-end electronics can be reset simultaneously using a procedure similar to the run start procedure, but with the preservation of frame numbering. This involves stopping and then restarting of the frame batch.
- Individual modules of the front-end electronics can be reset during the run without stopping the frame batch. To do this, the active level must be set on the reset signal lines of the required modules by the corresponding *Disarm* command(s). After that, the required modules can be initialized. The modules will return to operation when the active level on the reset signal lines is removed by the corresponding *Arm* command(s) (see Fig. 19.7).

The time in the DAQ system is measured inside the frame and from the beginning of the frame. No correlation is assumed between the time in two different frames. The time measurement must provide a continuous and uniform time inside one frame, in particular, there must be no breaks in the calculation of time within the frame. Each hit processed by the front-end electronics must have a time stamp that allows the time of the hit from the start of the frame to be calculated.

To measure the time, the front-end electronics can use various clocks, called internal clocks. From an abstract point of view, time is measured by counting the pulses of the internal clock. It is assumed that the internal pulse counter operates in the so-called rollover mode: when the counter reaches its maximum value, it is reset to 0. The actual implementation of time measurements may be different.

Two different methods of measuring the hit time are used:

Reset at Start of Frame (RSOF): It is based on a synchronous reset performed at the start of the frame, which sets the time to zero. In this case, the number of internal clock pulses (taking into account the possible rollover of the counter) corresponds to the hit time from the beginning of the frame. Since this type of reset is usually time-bound to the internal clock signal, in order to ensure that the reset is time-bound to the global clock signal, the internal clock must be synchronized with the global clock, and its frequency must be a multiple of the frequency of the global clock.

Measuring of Start of Slice (MSOS): This method does not require a common zero time for the entire installation: each module of the front-end electronics can have its own zero time. It is based on the measurement of the moment of the beginning of the slice. In this case, the difference between the numbers of internal clock pulses for a hit and the start of slice (taking into account the possible rollover of the counter) corresponds to the hit time from the beginning of the slice. This method does not require a correlation between the global clock and the internal clock, provided that both clock signals are "sufficiently" stable.

A front-end electronics developer can choose one of these methods that is better suited for their electronics.

The reaction of the front-end electronics to the commands depends on which method of measuring time is used.

To describe a hypothetical front-end electronics, assume that this electronics has the following registers:

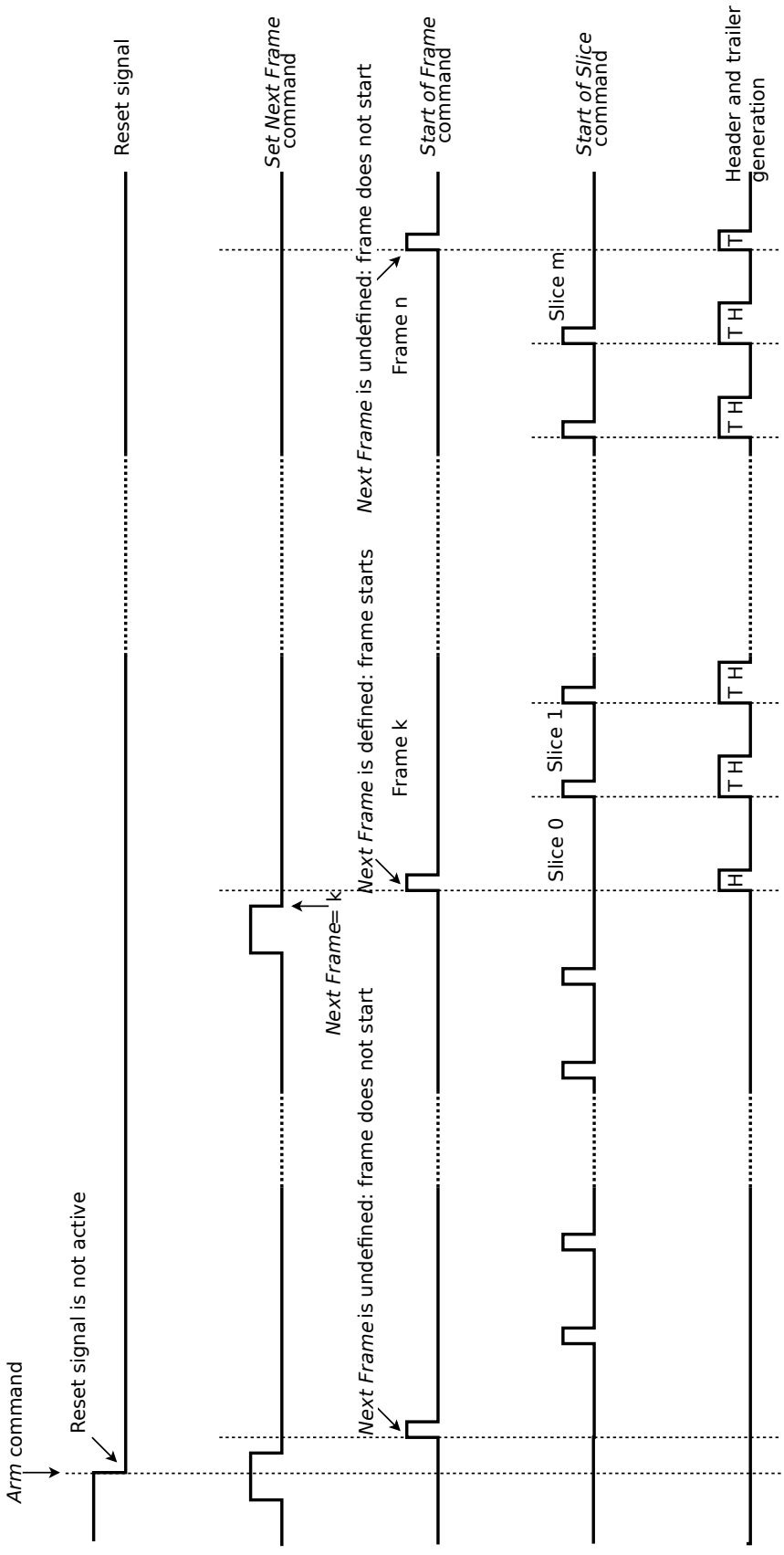

Figure 19.7: Returning the front-end module to operation after reset.

4817 – *Frame Number* - contains the number of the current frame inside the run.

4818 – *Next Frame* - contains the number of the next frame, this register is loaded by the *Set Next Frame*
4819 command. In addition to the register value itself, this register has an initialization state: the initial
4820 state of this register is 'uninitialized', the *Set Next Frame* command changes the state to 'initial-
4821 ized', and the *Start of Frame* command resets the state back to 'uninitialized'.

4822 – *Slice Number* - contains the number of the current slice inside the frame.

4823 The contents of the *Frame Number* and *Slice Number* registers are used to assign hit data to a specific
4824 frame and slice. In addition, the front-end electronics stores the frame status: the frame status is 'active'
4825 inside the frame and 'inactive' otherwise.

4826 The actions of the front-end electronics in response to receiving commands are described in detail below.

4827 • The *Disarm* command sets the active level on the reset signal line. This command is executed by
4828 the L1 concentrator and is not directly visible to the front-end electronics. The reset signal must
4829 have the highest priority for the front-end electronics. With this signal, the electronics must be
4830 reset to some initial state. What exactly is reset in electronics is determined by the electronics
4831 developer. But the following conditions must be met:

4832 1. Digitization of new hits must be stopped.
4833 2. Data transmission in the direction of the L1 concentrator must be stopped.
4834 3. The untransmitted data from the internal buffers must be deleted.
4835 4. The frame status must be reset to 'inactive'.
4836 5. The state of the *Next Frame* register must be reset to 'uninitialized'.
4837 6. All synchronous commands must be ignored and remain ignored for as long as the reset
4838 signal is active.
4839 7. The electronics must be ready, perhaps with some delay, to receive I^2C commands for ini-
4840 tialization.

4841 • The *Arm* command removes the active level on the reset signal line. This command is executed
4842 by the L1 concentrator and is not directly visible to the front-end electronics. After removing the
4843 reset signal, the front-end electronics must start executing synchronous commands.

4844 • In response to the *Set Next Frame* command, the electronics must load the number received with
4845 this command into the *Next Frame* register and change the state of this register to 'initialized'.

4846 • The response to the *Start of Frame* command depends on two conditions: status of the frame and
4847 state of the *Next Frame* register. There are four possible options which may happen:

4848 – the command starts the first frame in the frame batch or the front-end module goes into
4849 operation mode after reset;
4850 – the command completes one frame and starts another inside the frame batch;
4851 – the command completes the last frame in the frame batch;
4852 – the interface module received this command during the transition to operation mode after
4853 reset, but did not receive the previous *Set Next Frame* command, since the reset signal was
4854 shot in between these commands.

4855 In response to the *Start of Frame* command, the following actions must be performed:

Frame status — any, *Next Frame* register — 'initialized': This situation occurs when a new frame is started, regardless of the position of the new frame in the frame batch.

1. **RSOF method:** All time-related counters are reset to their initial state. This is called synchronous reset and sets the start of time in the frame. The number of the global clock pulses required for synchronous reset must be fixed for a specific front-end electronics, but may vary from one electronics to another, which leads to a time zero offset in different front-end electronics.

   MSOS method: The time of the global clock pulse corresponding to the SOF signal is measured, the data obtained must be attributed to a new slice.
2. The *Frame Number* register is reloaded from the *Next Frame* register.
3. The status of the *Next Frame* register is changed to 'uninitialized'.
4. The *Slice Number* register is reset to 0.

Frame status — 'inactive', *Next Frame* register — 'initialized': This situation occurs when starting a new batch of frames or when switching the front-end module to operating mode after reset. The actions performed at the start of any new frame and described above must be supplemented with the following:

1. The frame status is changed to 'active'.
2. The front-end electronics starts digitizing new hits.
3. As soon as the data is ready, the front-end electronics starts transmitting data to the L1 concentrator.

Frame status — 'active', *Next Frame* register — 'uninitialized': The following actions must be performed for stopping the current frame and frame batch:

1. The frame status is changed to 'inactive'.
2. The front-end electronics stops digitizing new hits.
3. The front-end electronics continues transmitting the already collected data to the L1 concentrator.

Frame status — 'inactive', *Next Frame* register — 'uninitialized': This situation occurs in the process of switching to the operating mode after the reset. The command must be ignored.

- The front-end electronics responds to the *Start of Slice* command only when the frame status is 'active', otherwise the command must be ignored. In response of *Start of Slice* command, the following actions must be performed:

  1. **RSOF method:** Nothing.

     MSOS method: The time of the global clock pulse corresponding to the SOS signal is measured, the data obtained must be attributed to a new slice.
  2. The *Slice Number* register is incremented by 1.

The result of digitizing the hit time is 3 numbers: the value of the internal clock counter, the frame and slice numbers. All 3 numbers should (ideally) correspond to a single point in time. The value of the internal clock counter is transmitted in a front-end electronics specific format in the body of the front-end data block. The frame and slice numbers are used in order to group data by slices and are recorded in the header of the front-end data block.

The calculation of the hit time from the beginning of the frame depends on which time measurement method is used. In the case of the MSOS method, the calculation of the hit time is obvious, and requires

the fulfillment of the condition that the rollover period of the internal clock counter in astronomical units is longer than the slice duration.

Consider the case of the RSOF method.

Taking into account the rollover of internal clock counter, the hit time can be calculated as:

$$t = (n + NR)\Delta_{\text{int}}, \tag{19.1}$$

where t is time from the start of the frame (in physical units), n is recorded value of the internal clock counter, N is a number of internal clock rollovers since the start of the frame, R is the internal clock counter rollover period (in internal clocks), and Δ_{int} is the internal clock period. The unknown value N can be found knowing the slice number m calculated as an integer part from dividing the time t by duration of a slice:

$$m = \lfloor t/(S\Delta_{\text{clk}}) \rfloor, \tag{19.2}$$

here S is the slice length (in the global clocks) and Δ_{clk} is the global clock period.

Equations 19.1 and 19.2 have a unique solution only when

$$R\Delta_{\text{int}} >= S\Delta_{\text{clk}}, \tag{19.3}$$

that is, when the rollover period is equal to or greater than the length of the slice. This limits the possible length of the slice depending on the bit depth of the internal clock counter.

All of the above is the ideal case when the electronics outputs 2 matched numbers n and m. In the case where n is calculated by some ASIC, and m is calculeted using an FPGA that provides a front-end card interface, it can be difficult to compute these two values in a consistent way. The FPGA, if it calculates the value of m after reading hit data from the ASIC, will do it with some delay, when a new slice can already begin and the value of m will differ from the correct one upwards.

In order to simplify the front-end electronics development, it is possible to require a softer condition: m may differ from the correct value by no more than +1. In this case, one of the following equations must be true:

$$\begin{aligned} m - 1 &= \lfloor t/(S\Delta_{\text{clk}}) \rfloor, \\ m &= \lfloor t/(S\Delta_{\text{clk}}) \rfloor \end{aligned} \tag{19.4}$$

and for a unique solution it is necessary

$$R\Delta_{\text{int}} >= 2S\Delta_{\text{clk}}. \tag{19.5}$$

The algorithm for calculation of the hit time is reduced to finding such a value of N, in which the time t calculated by formula 19.1, substituted into formula 19.2, leads to the fact that equation 19.2 becomes true. The following value can be used as an initial approximation for the number N:

$$N = \lfloor (mS\Delta_{\text{clk}})/(R\Delta_{\text{int}}) \rfloor. \tag{19.6}$$

If equation 19.2 is not true, then the number N should be increased by 1, if the value of m calculated by formula 19.2 is less than the required value, and reduced by 1 otherwise. Repeat this step until equation 19.2 becomes true.

In the case discussed above, when the value of m recorded in the data may differ from the true by 1, it is necessary to check expressions 19.4 accordingly: the algorithm stops as soon as one of the equations 19.4 becomes true.

6 Time Synchronization System

The main purposes of the Time Synchronization System (TSS) are:

- distribution of the global clock signal throughout the installation;
- generation and distribution of synchronous commands throughout the installation.

At the same time, the design of this system should also provide the possibility of obtaining information about the bunch crossing and beam polarization, as well as the possibility of recording this information in the general data stream. The interaction interface with NICA and the method of obtaining such information are currently not defined.

The main part of the TSS is the so-called TSS controller. The TSS controller generates synchronous commands, which are then distributed throughout the installation. The TSS controller is managed by setting the values of its registers and issuing commands to it. In response to these commands, the TSS controller generates a sequence of frame batches separated by a certain time interval. The structural unit of the sequence is the frame batch described in the section 19.5 and shown in Fig. 19.6.

The TSS controller has the following read/write registers:

- *Slice Length* — the length of the slice, measured in the clock cycles of the global clock signal.
- *Frame Length* — the length of the frame, measured in the number of slices.
- *Batch Length* — the length of the frame batch, measured in the number of frames. The value 0 means unlimited batch length.
- *Sequence Length* — the length of the sequence of batches in the number of batches. The value 0 means unlimited length of sequence.
- *Batch Interval* — time interval between batches in the sequence, measured in the clock cycles of the global clock signal.
- *Next Frame* — the number used as the next frame number when generating the *Set Next Frame* command. With each generated command, the contents of the register increases by 1.
- *Last Frame* — the number of the last frame. The generation of a sequence of frame batches must be stopped after the completion of the frame with the number specified in this register.

The TSS controller implements the following commands:

- *Start of Sequence* — upon receiving this command, the TSS controller must start the generation of a sequence of frame batches using parameter values loaded into its registers.
- *Stop of Sequence* — upon receiving this command, the TSS controller must complete the generation of a sequence of frame batches.

At the start of the run, the registers of the TSS controller are initialized. Then, at the *Start of Sequence* command, the TSS controller starts generation of a sequence of frame batches. The TSS controller completes the generation of a sequence of frame batches when one of the following conditions is met:

- The specified number of batches in the sequence *Sequence Length* have been reached.

4964 – The value of the *Next Frame* register has reached the value of the *Last Frame* register.

4965 – The command to stop the sequence *Stop of Sequence* was received.

4966 In the first two cases, the generation of a sequence of frame batches stops at the frame boundary, while
4967 the TSS controller knows about this event in advance. Stopping the generation of a sequence of frame
4968 batches with the *Stop of Sequence* command is performed on the slice boundary as soon as possible.
4969 Depending on the implementation of the command delivery to the L1 concentrators (see below), this may
4970 take some time, because in the case of WR-based delivery, commands will be sent to the L1 concentrators
4971 in some portions in advance and the implementation of canceling of commands already sent to the L1
4972 concentrators leads to unjustified complication of the L1 concentrators. To stop the sequence, the TSS
4973 controller must issue the *Start of Frame* command, provided that no *Set Next Frame* command has been
4974 issued since the previous *Start of Frame* command. If this is no longer possible, then the TSS controller
4975 starts a new frame in the usual way and stops at the end of the first slice of this frame.

4976 Two approaches for obtaining information about bunch-crossings and beam polarizations can take place.

4977 The first involves the transmission of information from NICA in the form of electrical signals and the
4978 measurement of the moment of signal reception to obtain the time of bunch-crossing by the global clock.
4979 In this case, embedding the bunch-crossing data into the general SPD data stream seems to be a fairly
4980 standard task, similar to the situation with any other subsystem. The difference may lie in the fact that
4981 the spatial location of the measurement of the bunches crossing can be significantly remote from the rest
4982 of the installation and signal propagation delays can be significant. Using a White Rabbit can solve this
4983 problem.

4984 The second approach assumes that the information from NICA comes in digital form and, accordingly,
4985 such information must have an absolute timestamp with an accuracy of 1 ns or better in the NICA clock,
4986 the global clock must be synchronized with the NICA clock, and each frame must have an absolute
4987 timestamp according to the NICA clock. With embedding this data into the overall SPD data stream
4988 there is a lot more uncertainty, because at present the interface for transmitting information from NICA
4989 is not defined. We assume that, in any case, White Rabbit will be used, even if not to control NICA, but
4990 to distribute a common clock to NICA and to SPD, and this signal will be used as the signal of our global
4991 clock.

4992 To implement both approaches, it is proposed to use White Rabbit as the basis for the TSS system. This
4993 leads to the fact that the TSS controller will combine the functionality of the White Rabbit node and the
4994 L1 concentrator. The TSS controller will receive a global clock signal as a WR network node from the
4995 NICA master clock or from the SPD master clock, depending on which scheme for obtaining information
4996 about the bunches crossing will be implemented. In addition to generating synchronous commands, the
4997 TSS controller will timestamp each frame using the master clock and send this data to the L2 concentrator
4998 in the same way as any other L1 concentrator.

4999 The TSS controller will be managed via the WR interface.

5000 Currently, two approaches are being considered to implement the delivery of the global clock signal and
5001 the synchronous commands to the L1 concentrators: using the TCS system or White Rabbit.

5002 ### 6.1 TCS-based delivery

5003 The first approach (Fig. 19.8) uses TCS (Trigger/Timing and Control System) to distribute the global
5004 clock signal and the synchronous commands to the L1 concentrators. The TCS system is based on passive
5005 optical splitters. Initially, TCS was developed for the COMPASS experiment, and the modernization of
5006 this system is necessary, in particular, the frequency of the system clock should be changed to 125 MHz,

which is determined by compatibility with White Rabbit.

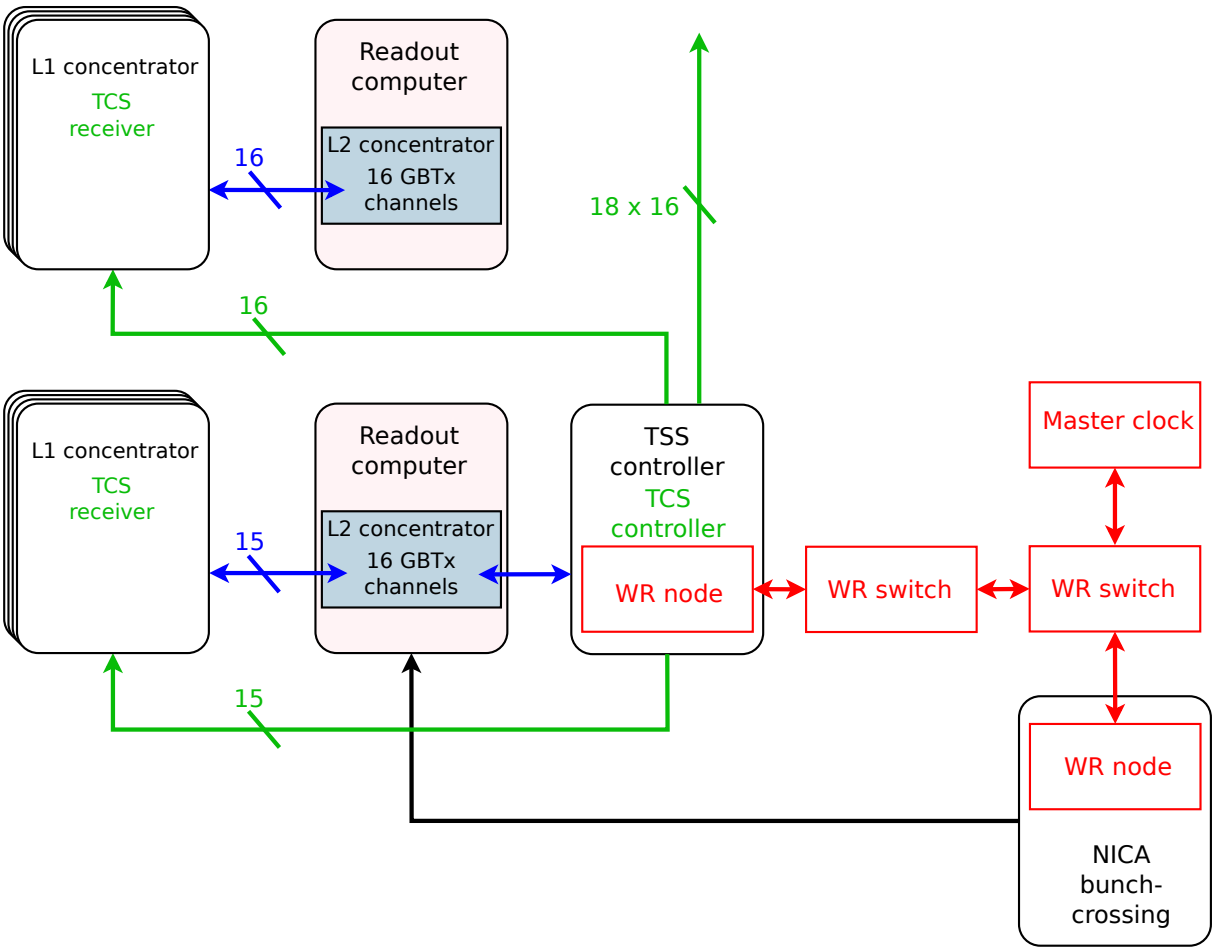

Figure 19.8: Time Synchronization System with TCS-based delivery.

In this case, the TSS controller, in addition to the functions described above, must have the functionality of a TCS controller. The TCS controller will generate a signal including a global clock signal and synchronous commands, which will then be delivered via optical lines to the L1 concentrators.

The main disadvantage of this approach is that in this case it is difficult to ensure the same delay of signal propagation from the TSS controller to different L1 concentrators. To do this, it will be necessary to align the lengths of the optical cables between the TSS controller and all L1 concentrators. This, in turn, may require calibration to be performed directly on the installation. Opportunities for this should be provided at the electronics design stage, for example, the possibility of applying an external signal and measuring the time of its arrival at the L1 concentrator or at the front-end electronics. At the same time, there remains the problem of phase shift with temperature.

6.2 WR-based delivery

The second approach (Fig. 19.9) involves the integration of a White Rabbit node in each L1 concentrator. In this case, the L1 concentrators will receive the global clock signal directly from the master clock as any node of the WR network. The L1 concentrators will receive synchronous commands from the TSS controller in the form of WR control data.

This approach has some advantages compared to TCS-based delivery:

- The global clock signal is automatically aligned to astronomical time in different parts of the installation with an accuracy better than 1 ns, and, as a result, adding a new L1 concentrator is much easier. This improvement is very important, especially if the SPD detector will be created in several stages.
- Ethernet link of a WR node can be used to control the L1 concentrator.
- There is no need for a dedicated powerful optical splitter.
- WR switch is a commercially available product.

The main disadvantages of this approach are:

- An L1 concentrator with a WR node will be more complex, especially for a radiation-resistant implementation.
- The development and testing time will be longer.
- Higher cost. The cost of the L1 concentrator will increase slightly due to the addition of the WR node. The main increase will occur due to the need to purchase a significant number of the WR switches ($>$ 100 k$).

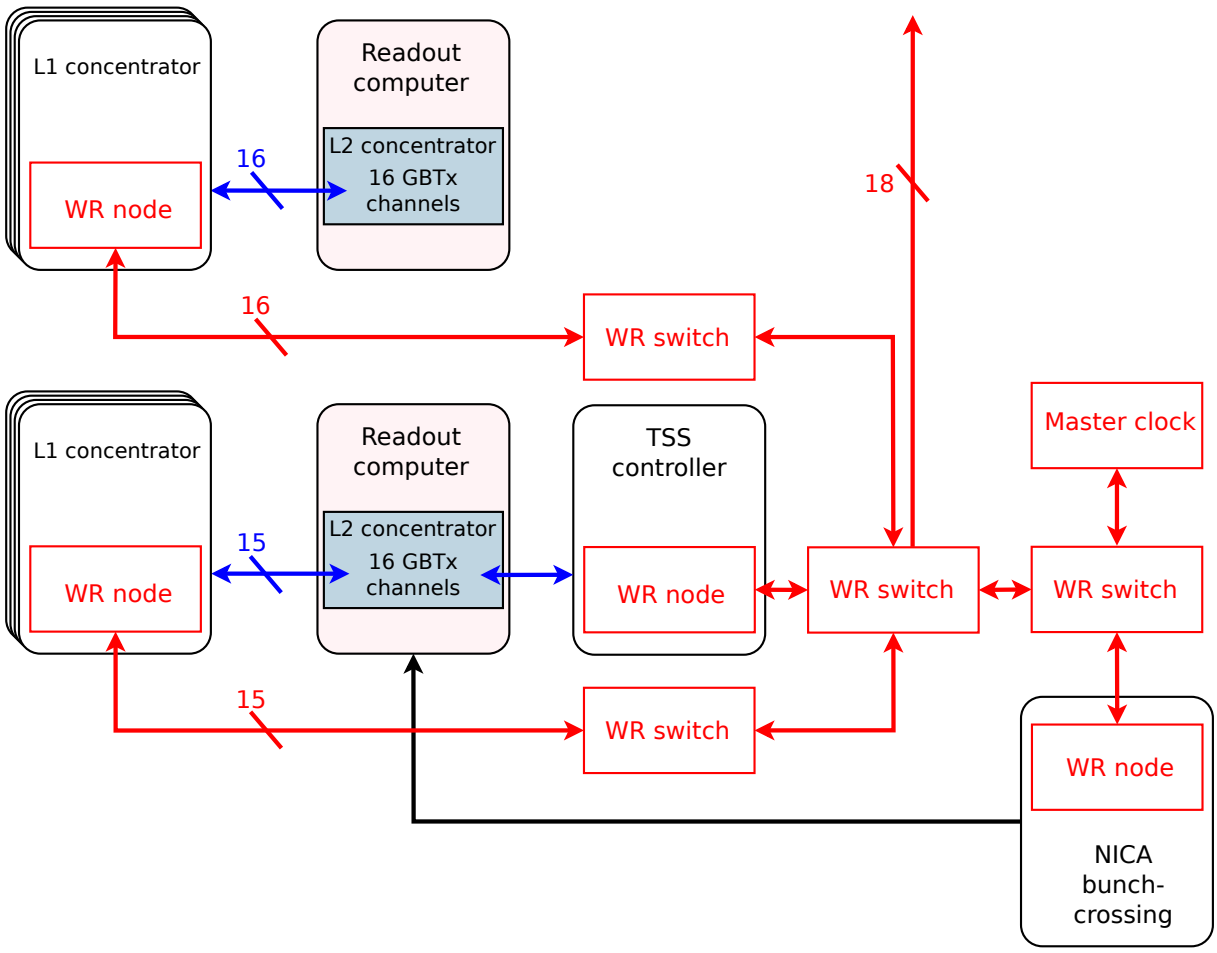

Figure 19.9: Time Synchronization System with WR-based delivery.

7 Data Format

The choice of data format is an important point in the development of a data acquisition system. On the one hand, the data should contain as much information as possible:

- the location of the hits;
- the hit registration time;
- the value of the measured signal (for a certain type of detectors);
- information about measurement and/or data acquisition errors;
- some other information, which we may not even assume now.

On the other hand, even one extra byte per slice in data of a front-end card can increase an overall data flux approximately by 0.5 GB/s (for 10 μs slice).

Nevertheless, for the convenience of data processing and transmission, the total size of the data and all its logical units must be aligned to the size of a 32-bits word. Thus, if the front-end electronics data format assumes 24-bits, 16-bits, or some other data representation, then the data acquisition system at some level will have to automatically align them to the 32-bits word boundary.

An important property of any data acquisition system is its flexibility for different working conditions. Obviously, the data received during detector commissioning should contain more information about the operation of these detectors and electronics. Thus, we must provide the possibility of working of our data acquisition system with different data formats and have the ability to filter debugging information.

The unit of information in our data acquisition system is a slice. It must contain all the necessary information for an unambiguous reconstruction of all events received during the time of one slice. (The cases when an event occurres on the border of two neighboring slices and is therefore divided into two parts will require an additional discussion and we do not consider them now.) The data structure of a slice is quite simple, and since the cost of one additional byte of data in a slice structure is relatively small (no more than 100 kB/s for 10 μs slice), we may not limit ourselves here.

The slice structure is presented in Fig. 19.10 and consists of:

- 4 words of the slice header:
  - size of the slice in 32-bits words including sizes of the header and trailer;
  - run number;
  - frame number;
  - 8-bits reserved field, 24-bits slice number;
- a slice body containing blocks of data received by each readout computer and written sequentially;
- 2 words of the slice trailer:
  - error code;
  - size of the slice in 32-bits words including sizes of the header and trailer.

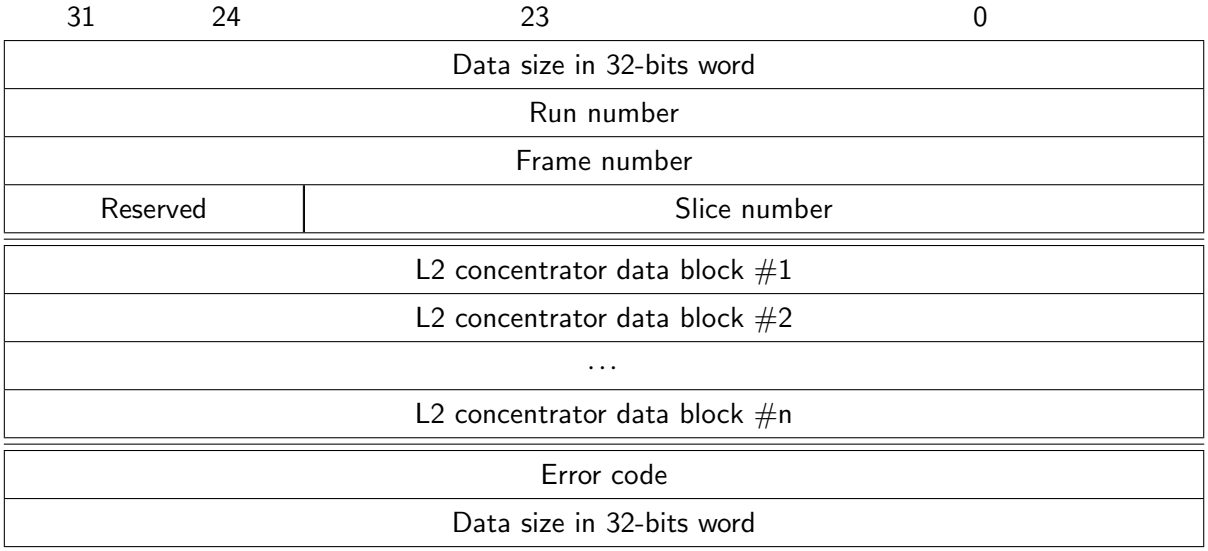

Figure 19.10: Slice data block.

Obviously, the data sizes in the header and the trailer of the data block must match, and that will be used to assess quickly the integrity of the data during processing. The error code will be determined by the L1 and L2 concentrators and will be used by the data filter.

The total size of the service information per slice will be 24 bytes (4 header words + 2 trailer words), which increases total data flux of about 2.4 MB/s for 10 μs slice.

The data blocks from the L2 concentrators are collected by the readout computers. Their structure is presented in Fig. 19.11 and consists of:

- 4 words of block header:
  - size of the data block in 32-bits words including sizes of the header and trailer;
  - run number;
  - frame number;
  - 8-bits L2 concentrator ID, 24-bits slice number;
- data block body, which contains a sequential record of data from all front-end cards connected to the concentrator;
- size of the data block in 32-bits words including sizes of the header and trailer.

Thus, with a slice length of 10 μs, the overhead of each readout computer (4 words of the header plus 1 trailer word) will add approximately 2 MB/s to the total data flux.

The body of the L2 concentrator data block contains sequentially recorded information from each of the 256 front-end cards connected to the L2 concentrator. The format of the front-end data block is shown in Fig. 19.12. The data coming from the front-end card will be converted to this format on the readout computer as described below.

The format of data transmission from the front-end card to the L2 concentrator depends on the electronics, an example of such format for RS is presented in Fig. 19.13.

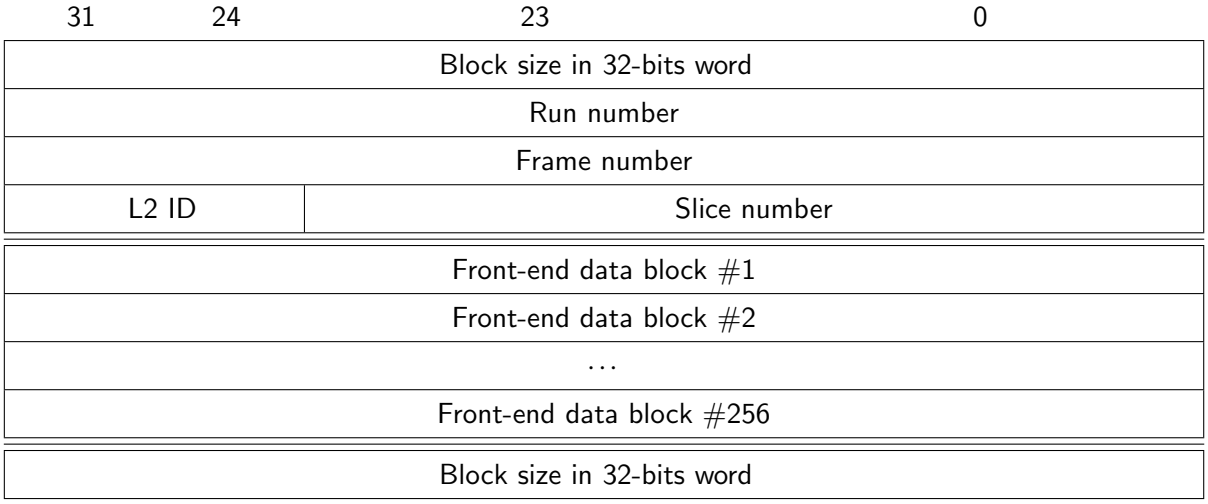

Figure 19.11: L2 concentrator data block.

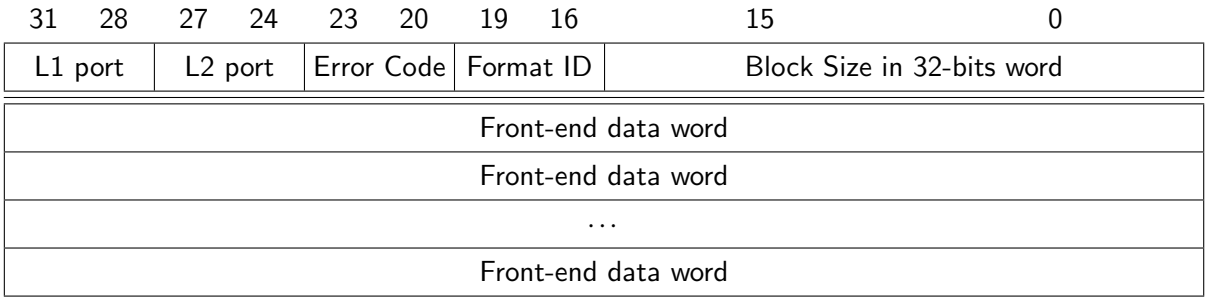

Figure 19.12: Front-end data block.

Front-end data will be sent to the L2 concentrator sequentially, as soon as information arrives from the detector, and it is assumed that each slice will begin with a header containing the number of the current slice and frame (or just their LSB) and data format ID. And at the end of the slice, the front-end card should send a trailer containing the size of the data transferred for the slice and the error code.

To split the data stream into slices, it is necessary to be able to quickly find the header and the trailer of the slice in the data stream. For this purpose, it is assumed that at least two of the most significant bits of the front-end data words must contain a flag that uniquely distinguishes the header and the trailer from the data itself. This flag can later be removed from the data stream on the readout computer to reduce the overall data flow.

As mentioned above, each additional overhead byte in the front-end data block makes a significant contribution to the overall data flow. So, we have to delete all the information that is repeated in the header of the data block of the L2 concentrator, leaving only the geographical address, error code, and front-end data format identifier in the header of the front-end data block (see Fig. 19.12).

31	28	27	24	23	20	19	16	15	0
1	0	X	X	Format ID		LSB of Frame Number		LSB of Slice Number	
0	0	X	X	Channel Number		Hit Time			
0	0	X	X	Channel Number		Hit Time			
0	0	X	X	Channel Number		Hit Time			
...									
0	0	X	X	Channel Number		Hit Time			
1	1	X	X	Error Code		Total Number of Hits (Data words)			

Figure 19.13: Proposal of the data structure of RS.

8 Cost estimate

Based on the number of the front-end electronics to be read out at different stages of the experiment (see Tables 19.1 and 19.2), the corresponding cost estimate of the SPD DAQ system is shown in the Table 19.3.

Table 19.3: DAQ cost estimate.

Item	Quantity stage 1	Quantity stage 2	Price per piece, k$	Price, k$ stage 1	Price, k$ stage 2
L1 concentrator	90	180	1	90	180
L2 concentrator	12	20	10	120	200
TSS	1	1	–	50	50
Supervisor computer + spare	2	2	4	8	8
File server (master, slave)	2	2	10	20	20
Database server (master, slave, proxy)	3	3	7	21	21
Readout computer	15	20	4	60	80
Builder network switch	1	1	50	50	50
Builder computer	24	40	4 + 1	120	200
Network infrastructure	–	–	7	7	7
General infrastructure	–	–	25	25	25
UPS 50 kVA	1	1	30	30	30
Cooling system 50kW	–	–	20	20	20
Spare parts	–	–	15	15	15
R&D	–	–	–	200	200
Total cost				824	1106

Chapter 20

Computing and Offline Software

1 Introduction

The expected event rate of the SPD experiment is about 3 MHz (pp collisions at $\sqrt{s} = 27$ GeV and 10^{32} $\mathrm{cm}^{-2}\mathrm{s}^{-1}$ design luminosity). This is equivalent to a raw data rate of 20 GB/s or 200 PB/year, assuming a detector duty cycle is 0.3, while the signal-to-background ratio is expected to be on the order of 10^{-5}. Taking into account the bunch-crossing rate of 12.5 MHz, one may conclude that pile-up probability cannot be neglected.

The key challenge of the SPD computing is the fact, that no simple selection of physics events is possible at the hardware level, because the trigger decision would depend on measurement of momentum and vertex position, which requires tracking. Moreover, the free-running DAQ provides a continuous data stream, which requires a sophisticated unscrambling prior to building individual events. That is the reason why any reliable hardware-based trigger system turns out to be over-complicated, and the computing system will have to cope with the full amount of data supplied by the DAQ system. This makes a medium-scale setup of SPD a large-scale data factory (Fig. 20.1).

Continuous data reduction is the key point in the SPD computing. While simple operations like noise removal can be still done by DAQ, it is an online filter that is aimed at fast partial reconstruction of events and data selection, thus being a kind of software trigger. The goal of the online filter is at least to decrease the data rate by a factor of 20, so that the annual growth of data, including the simulated samples, stays within 10 PB. Then, data are transferred to the Tier-1 facility, where a full reconstruction takes place and the data is stored permanently. The data analysis and Monte-Carlo simulation will likely run at the remote computing centers (Tier-2s). Given the large data volume, a thorough optimization of the event model and performance of the reconstruction and simulation algorithms are necessary.

2 SPD computing model

2.1 Input parameters

The assumptions in Table 20.1 are used to calculate the storage and computing resources. At present, all processing times are higher than assumed here.

2.2 Data flow and event data model

Data processing is supposed to be done in several stages. At the first stage, the data undergoes the fast reconstruction and events are built from a continuous byte stream. This task will be performed online

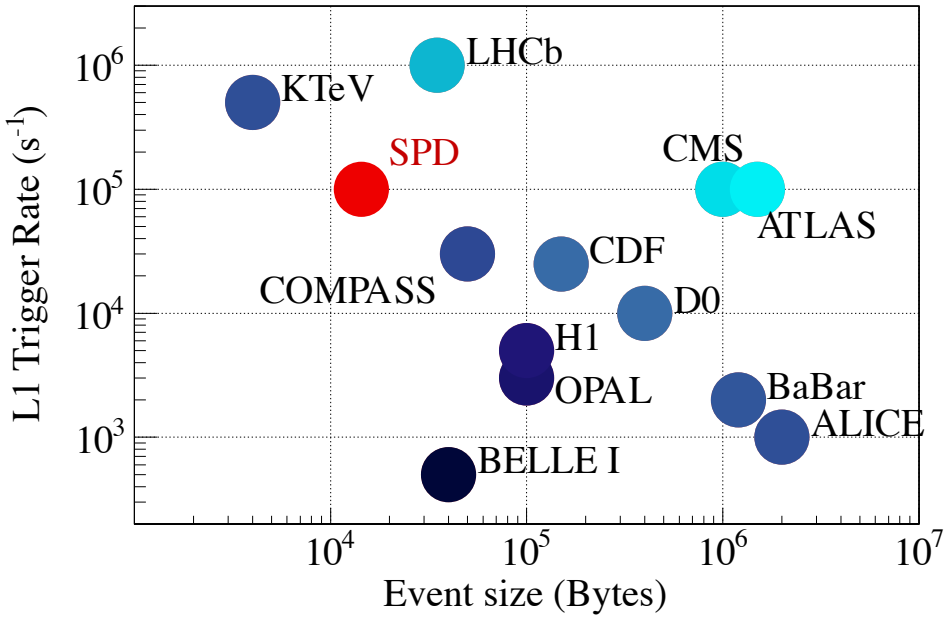

Figure 20.1: Expected event size and event rate of the SPD setup after the online filter, compared with other experiments [109].

Table 20.1: The assumed event data sizes for various formats, the corresponding processing times and related operational parameters.

Item	Unit	Value
RAW event	kB	7
RECO event	kB	15
Time for Reconstruction (1 ev)	HepSPEC	100
Time for Simulation (1 ev)	HepSPEC	500
Event rate at maximum luminosity	kHz	3000
Event rate after online data filter	kHz	150
Operation time	seconds/day	50000
Operation time	days/year	200

using a dedicated high-performance computing cluster (online data filter). After fast reconstruction, the events are selected according to a set of physical criteria to suppress the contribution from background processes. Then, the selected data are saved for long-term storage and subsequent full reconstruction. Full reconstruction differs from fast reconstruction by more accurate and complex algorithms that use information about the slow control system, calibration constants, and combined analysis of information from various subsystems to identify particle types.

Two reconstruction cycles are foreseen. The first cycle includes reconstruction of some fraction of each run, which is necessary to study the detector performance and derive calibration constants, followed by the second cycle of reconstruction of the full data sample for physics analysis. Detector simulation will run in parallel. The amount of simulated data is expected to be comparable to the amount of selected experimental data. A large amount of data, the computing resources required for their processing, and analysis within the framework of an international collaboration naturally require the construction and use of a distributed data storage and processing system.

2.3 Event building and filtering

The main goal of the SPD online filter is to reconstruct events from the continuous byte stream and to suppress the background by a factor of 20 or so. The input for the online filter is the raw data files. The format of these files is determined by the front-end electronics and the DAQ system. The result of the data processing at the online filter is a set of reconstructed events, containing also raw information for the more detailed offline reconstruction. HDF5 will be used as the output format for the online filter, to simplify data treatment by the offline computing system. Because of data reduction, it is likely that merging of several small output files to a bigger one will be necessary.

2.4 Offline data processing

Offline data processing includes offline reconstruction and MC simulation. Offline reconstruction starts with the output of the online filter. Detailed calibration and more precise algorithms will be used to refine the data sample and to improve the efficiency and precision of reconstruction of physics objects. Particle identification will be made at this stage as well. The output of the offline reconstruction will be stored in ROOT trees in RECO format, to allow direct use in a further physics analysis.

Simulation is necessary both for the data analysis and for the training of neural networks at the online filter. Tha latter should reproduce not only the event topology and kinematics, but also a time structure similar to the one in real data. The output of the simulation will be stored in the same format as for the reconstruction of the real data, with addition of the MC truth information.

2.5 User analysis

User analysis will be done using pre-selected RECO data or derived ROOT trees.

3 Online data filter

3.1 Introduction and requirements

The SPD online filter facility will be a high-throughput system, which will include heterogeneous computing platforms, similar to many high performance computing clusters. The computing nodes will be equipped with hardware acceleration. The software framework will provide the necessary abstraction, so that the common code can deliver selected functionality on different platforms.

The main goal of the online filter is a fast reconstruction of the SPD events and suppression of the background events by at least a factor of 20. This requires fast tracking and fast clustering in the elec-

tromagnetic calorimeter, followed by a reconstruction of an event from a sequence of time slices and an event selection (software trigger). Several consecutive time slices shall be considered, tracker data unpacked and given for a fast tracking. The result of the fast track reconstruction is the number of tracks, an estimate of their momentum, and an estimate of primary vertex (to distinguish between tracks belonging to different collisions). Using this outcome, the online filter should combine information from the time slices into events and add a trigger mark. The events will be separated in several data streams using the trigger tag, and an individual prescale factor for each stream will be applied.

Besides the high-level event filtering and the corresponding data reduction, the online filter will provide input for the run monitoring by the shift team and the data quality assessment, as well as local polarimetry.

3.2 Computing system

Fast reconstruction and filtering of data from an SPD detector cannot be performed on a single node. A specialized high-performance cluster is neccesary, which includes several data storage systems (for receiving detector data, for temporarily storing filtered data before transferring it to a long-term storage, and for storing software and auxiliary data), a large number of identical working nodes for data processing, and few servers managing this system and the movement of data in it (Fig. 20.2). To control the operation of the system, it is proposed to use auxiliary programs (pilots) that are constantly executed at each working node and exchange messages with the dispatcher server. Fast messaging system (ZeroMQ or nanomsg) will be used for communication. Depending on received messages, the pilot programs will initiate copying of new data from the storage system to the working node, call the program for fast reconstruction and filtering of data, and copy the processing result to the output buffer. In addition, pilots will be able to perform other, auxiliary operations, such as data merging, monitoring, etc. The data flow from the detector, which will reach values on the order of 20 GB / s, determines high requirements for the performance of data storage systems and for the speed of data processing algorithms.

3.3 Fast event reconstruction

3.3.1 Fast tracking and vertex reconstruction

The most important and complicated task in the data reconstruction chain is tracking. Traditional tracking algorithms, such as the combinatorial Kalman filter, are inherently sequential, which makes them rather slow and hard to parallelize on modern high-performance architectures (graphics processors, or GPUs). As a result, they do not scale well with the expected increase in the detector occupancy during the SPD data taking. This is especially important for the online event filter, which should be able to cope with the extremely high data rates and to fulfill a significant data reduction based on partial event reconstruction ‘on the fly’. Parallel resources like the multicore CPU and GPU farms, will likely be used as a computing platform, which requires algorithms, capable of effective parallelization, to be developed, as well as the overall cluster simulation and optimization.

Machine learning algorithms are well suited for multi-track recognition problems because of their ability to reveal effective representations of multidimensional data through learning and to model complex dynamics through computationally regular transformations, that scale linearly with the size of input data and are easily distributed across CPU or GPU cores. Moreover, these algorithms are based on the linear algebra operations and can be parallelized well, using standard ML packages. Two algorithms of track recognition in strip and pixel detectors are considered. The first algorithm, TrackNetv3, relies on the use of a recurrent neural network (RNN), which allows to combine track extrapolation with testing the hypothesis that a set of points belongs to a true track and is compatible with a smooth curve. Essentially, it reproduces the idea of a Kalman filter with the difference that the physical parameters describing the track are approximated by a neural network, using synaptic weights, determined during its training.

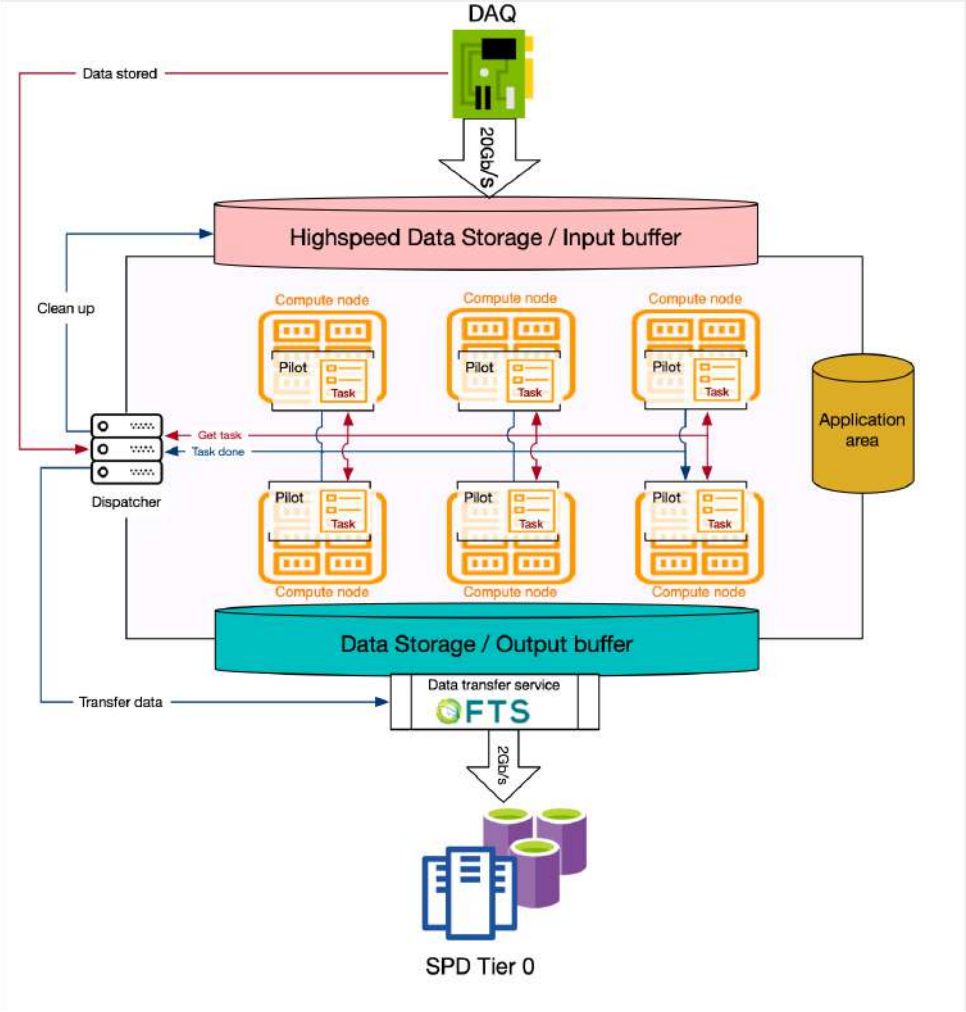

Figure 20.2: Design of the online data filtering system.

The second approach, RDGraphNet, uses a graph network and allows to implement a global search for tracks in an event, which is especially attractive when analyzing events with a large multiplicity. These approaches have already been successfully used for track recognition in the BM@N experiment at JINR and in the BESIII experiment at IHEP CAS in China [110–114]. These algorithms will be adapted to find and reconstruct particle tracks in SPD data from the vertex detector and the main straw tracker. The main difficulty is the adaptation of neural networks to recover tracks in drift detectors, which requires solving the "left-right" ambiguity. To prototype neural networks and to study the quality of their work, the Ariadne software package [115] will be used.

3.3.2 ECAL clustering

Algorithms based on convolutional networks will be developed to search for clusters in the SPD electromagnetic calorimeter and to reconstruct π^0s.

3.3.3 RS clustering

To identify muons in a muon system, the convolutional neural network will be used. Another option is to apply a simpler gradient boosting algorithm on trees.

3.3.4 Event unscrambling

Data stream from the DAQ will be stored in files of about 4 GB. Each file will be processed independently from other ones. Data blocks corresponding to a certian duration of data taking (from 5 to 15 μs) will be used as a reconstruction unit. Data from different subdetectors in each data block will be fed to a series of consecutive neural networks. First, vertices and track seeds will be determined, using vertex detector data. Tracks will be associated with vertices, and bunch crossing time will be determined for each vertex. Then, tracks will be reconstructed, using track seeds from the vertex detector. Hits in the straw tracker, which are not associated with any track, will be collected in a selected time window according to the bunch crossing time and attached to the events for possible use in the offline reconstruction. ECAL and RS hits will be reconstructed by other neural networks and associated with vertices according to the bunch crossing time. Raw data from other subdetectors will be attached to the events according to bunch crossing time. The block of information, associated with each vertex following the procedure described above, will be called an event.

3.4 Implementation of machine learning algorithms

3.4.1 Training and validation

Training of the neural networks will be based on a dedicated large sample of simulated data.

The caution is necessary, though, to avoid possible bias due to an inadequacy of the training data to the real ones, including possible machine background and the detector noise. A dedicated workflow that includes continuous learning and re-learning of neuron network, deployment of new versions of network, and the continuous monitoring of the performance of the neural networks, used in the online filter, will be applied.

3.4.2 Integration to the online data filter

For the effective use of deep learning algorithms, besides the design of the neural networks and their training, it is necessary to solve a number of technical problems. First, open-source machine learning tools (TensorFlow, sklearn, PyTorch, etc.) tend to have python interfaces, making them difficult to use in real-time systems. To solve this problem, it is planned to choose a package that has an advanced C++ API, and also to separate the network training (which can be implemented in any way) and its application.

Secondly, there is a risk that the neural network will malfunction, if the initial data is very different from the data that was used for training. In a physical experiment, these differences can be caused, for example, by a fluctuation of the background from the accelerator or by a change in the detector performance or noise. Therefore, it is required to foresee a procedure for monitoring the correct operation of the neural networks. For this, it is proposed to process a certain fraction of data independently, using classical algorithms, and to compare the output with the output of deep learning algorithms. In case of large differences, one should either mark the data as questionable or retrain the neural network to work in new conditions. Third, the application itself for fast reconstruction and filtering of data is proposed to be implemented in the form of a framework in order to flexibly customize the sequence and content of the data processing procedure.

3.5 Online data processing framework

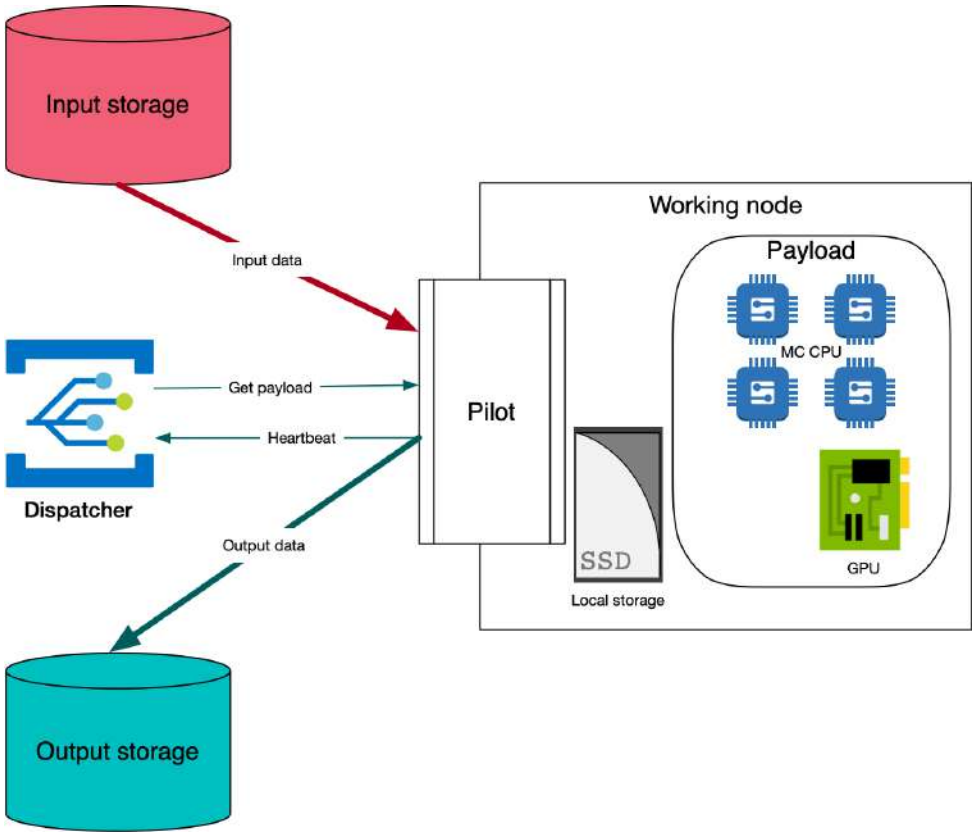

Figure 20.3: Operation of the online data processing framework at a selected working node.

3.6 Online monitoring and data quality assurance

4 Offline software

4.1 Introduction and requirements

Offline software is a toolkit for event reconstruction, Monte-Carlo simulation, and data analysis. Linux is chosen as the base operating system.

Recent developments in computing hardware resulted in the rapid increase of potential processing capacity from increases in the core count of CPUs and wide CPU registers. Alternative processing architectures

have become more commonplace. These range from the many-core architecture based on x86_64 compatible cores to numerous alternatives such as other CPU architectures (ARM, PowerPC) and special co-processors/accelerators: (GPUs, FPGA, etc). For GPUs, for instance, the processing model is very different, allowing a much greater fraction of the die to be dedicated to arithmetic calculations, but at a price in programming difficulty and memory handling for the developer that tends to be specific to each processor generation. Further developments may even see the use of FPGAs for more general-purpose tasks.

The effective use of these computing resources may provide a significant improvement in offline data processing. The development of the concurrent-capable software framework is needed to provide the offline software for Day-1 of the SPD detector operation, as well as a dedicated R&D effort to find proper solutions for the development of efficient cross-platform code.

4.2 Choice of the framework

4.2.1 SpdRoot

Currently, the offline software of the SPD experiment – SpdRoot – is derived from the FairRoot software [116]. It is capable of Monte Carlo simulation, event reconstruction, and data analysis and visualization. The SPD detector description is flexible and based on the ROOT geometry package. This is the main tool to study the physics performance and to do the detector optimization during the preparation phase of the experiment.

4.2.2 A Gaudi-based framework

To take advantage of modern computing hardware, the offline software for the processing of experimental data should be capable of taking advantage of concurrent programming techniques, such as vectorization and thread-based programming. This is the reason why another framework based on Gaudi [117] will be developed by the beginning of the SPD data taking.

4.3 Detector description, calibration, and alignment

The GeoModel class library [118], which is presently in use in both the ATLAS and FASER experiments, will be used for the SPD detector description. The GeoModel tool suite includes a set of tools to allow much of the detector modeling to be carried out in a lightweight development environment, outside of the offline software framework. These tools include the mechanisms for creating persistent representation of the geometry, an interactive 3D visualization tool, various command-line tools, a plugin system, and XML and JSON parsers.

Calibration and alignment constants, and run conditions will be stored in the offline database. The use of these data in the offline algorithms will be facilitated by a dedicated service in the Gaudi framework.

4.4 Simulation

Proton-proton collisions are simulated using a multipurpose generator Pythia8 [119]. Deuteron-deuteron collisions are simulated using a modern implementation of the FRITIOF model [120, 121], while UrQMD [122, 123] generator is used to simulate nucleus-nucleus interactions. Transportation of secondary particles through the material and magnetic field of the SPD setup and the simulation of detector response is provided by Geant4 toolkit [93–95].

4.5 Reconstruction

Track reconstruction uses GenFit toolkit [124], and KFparticle package [125] is used to reconstruct primary and secondary vertices.

4.6 Physics analysis tools

ROOT and Python-based tools (NumPy, SciPy, Pandas) are expected to be widely used.

A DIRAC [126] framework will be used to run user simulation at distributed computing resources.

4.7 Software infrastructure

A git-based infrastructure for the SPD software development is already established at JINR [127].

5 Computing system

Current timeline of evolution of the NICA complex is split into two phases according to maximum achievable luminosity. The the number events to be processed (real data and MC), between the first and second phases will increase by an order of magnitude: from $2*10^{11}$ to $2*10^{12}$ per year. The expected number of events and the concomitant amounts of data, measured in petabytes, are comparable to the LHC experiments. Distributed computing systems, based on resources provided by collaborators, are proven and already well instrumented solutions, for processing such amounts of HEP data. Event level granularity of HEP data allows independent simultaneous processing by splitting the workload among a set of jobs. Like in the MapReduce paradigm, each of these jobs will perform the same algorithm for processing a small amount of data from the same dataset. All these jobs should be performed in a controlled way to avoid duplication of data processing, and processing the whole scope of dataset. Efficient usage of compute resources requires high-speed access to processed data. This is achieved not only by usage of high-speed wide area networks, but also by the possibility of controlled distribution and replication of data between both intermediate and long-term storage systems, associated with data processing centers.

Already existing methods and solutions for building such distributed systems allows achieving a sufficient level of scaling and automation of experimental data processing, along with the possibility of implementing various data processing models. Development of required systems started more than twenty years ago, and continued development allows to meet new operational conditions and evolving computing systems. The opportunity of usage of ready-made solutions makes it possible to significantly reduce and accelerate their commissioning, while directing the main efforts to adapt the middleware components to the specific needs of the experiment.

Processing of a large volume of experimental data is organized in stages (Fig. 20.4). Each of the major stages will produce derived data in appropriate formats that ensure optimal data handling, and storage. Derived data should be able to be reproduced, if needed. The organization of the processing will be determined in accordance with the current policy agreed upon the physical program of the experiment.

In order to avoid large-scale modernization of the entire computing system in preparation for the second phase, when building a model for collecting, storing and processing data from the SPD experiment, it is initially necessary to focus on the data amount indicators when the accelerator is operating at high luminosity. The components of the data processing infrastructure should be selected based on the maximum expected load values.

5.1 Data processing workflows

The rough estimation of number of physical events, which should be processed per year to fulfill the physical program of the SPD experiment, after reaching the planned performance indicators of the NICA complex during the second stage, are: $2 * 10^{12}$. It is assumed that it will take in average 1 second to process one event on one CPU core, regardless of the type of processing. Thus, in order to cope with such a volume of calculations, the computing infrastructure of the experiment must consist of at least

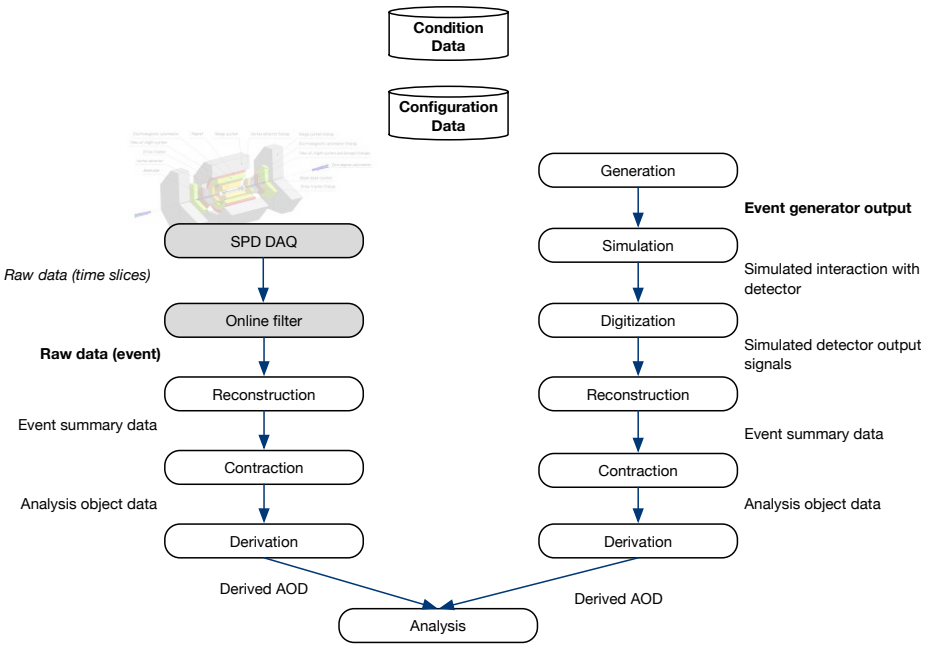

Figure 20.4: Processing stages and data types.

60,000 processor cores. For optimal load distribution, the initial data stream should be divided into tasks that will be performed for about 8 hours, for example, 28,800 events each. If the size of one event is 15 kilobytes, the file will be 450 megabytes. To achieve optimal loading of computing nodes, as well as the optimal file size for storage (on tape and disk storage systems) and for transmission over the network, it is proposed to combine such files in 16 pieces. Thus, the size of the merged file will reach 7 gigabytes, and the number of events in it will be 460,800. About 4.5 million raw data files will be created each year.

The main requirement for the application software, that it supports multithreaded data processing. This will significantly reduce the load on the IT infrastructure by reducing the number of tasks running in the system: in the case of a single-threaded data processing at least 60,000 jobs should be managed simultaneously. The scheme of data flow in the process of performing real data reconstruction tasks is shown in Fig. 20.5.

The process of the Monte Carlo simulation task consists of the following steps: generation, simulation, reconstruction. It can be expected that the number of files generated during the Monte Carlo simulation will be comparable to the processing of data collected from the detector. Jobs of this type can be easily parallelized, so it can be assumed that there will be about 4,000 tasks of the Monte Carlo simulation in the system at the same time. The scheme of data flow of the Monte Carlo simulation is shown in Fig. 20.6.

5.2 Data volumes

Based on the large expected volumes of data flow, it is possible to formulate the requirements for the computing infrastructure for each of the stages:

- Zero stage: preparation for the experiment. Monte Carlo simulation from 2023 to 2028 will provide 2 PB per year. Total per stage: 10 PB.

- First stage: running at low luminosity of the NICA collider. Monte Carlo simulation and real data taking from 2028 to 2030 will provide 4 PB per year. Reprocessing: 2 PB per year. Total per stage:

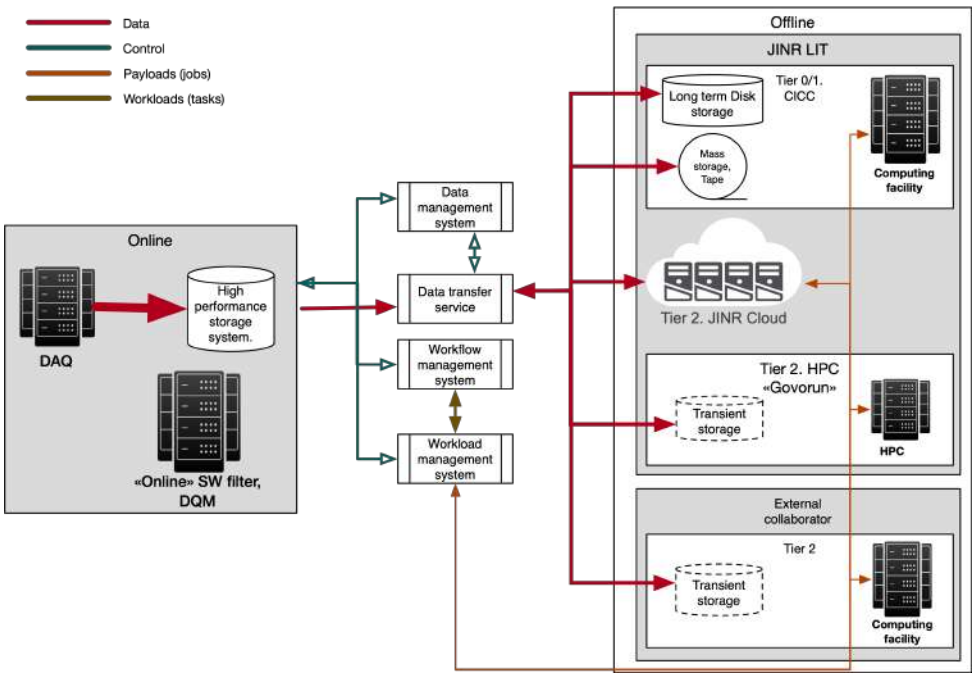

Figure 20.5: Real data reconstruction and involved services.

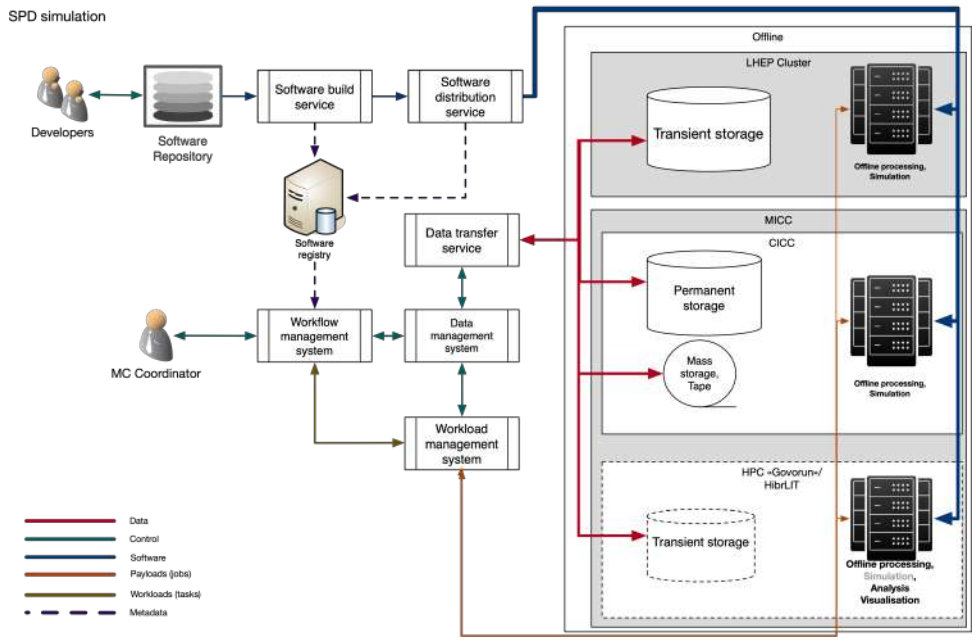

Figure 20.6: Monte Carlo simulation and involved services.

18 PB.

– Upgrade of the setup for operation at high luminosity Monte Carlo simulation from 2031 to 2032 will provide 2 PB per year. Reprocessing: 2 PB per year. Total per stage: 8 PB.

– Second stage: running at design luminosity of the NICA collider. Monte Carlo simulation and real data taking from 2033 to 2036 will provide 20 PB per year. Reprocessing: 10 PB per year. Total per stage: 120 PB.

Total for all stages: 156 PB.

5.3 Data processing infrastructure

The experimental facility and the SPD online filter computing farm will be located on the VBLHEP JINR site, and the computing resources of the primary data processing center will be located on the DLNP site. The campuses are connected by a high-speed communication channel with a bandwidth of 400 gigabits per second. It is planned to use a wide range of storage systems for data storage and processing: disk storage systems for short-term and medium-term storage of initial and intermediate data during their processing, and tape storage systems for long-term storage of the most important data. The JINR computing infrastructure provides a number of different computing systems: CICC which will include the SPD primary data processing center, the Govorun high-performance computing complex which is designed for artificial intelligence tasks and resource-intensive computing, a cloud computing infrastructure that can be used for user analysis. The distributed system has to provide the capability of using each of the listed computing systems, as well as geographically distributed resources provided by the collaboration participants. The organization of a sufficiently reliable and scalable distributed computing infrastructure for experimental data processing is carried out by a set of systems and services of an intermediate level providing: safe use of resources, efficient distribution of tasks between computing resources, distribution and management of data, and a high level of automation of data processing. An additional requirement for the computing system is the ability to connect opportunistic resources that do not work within the framework of the agreements established in the collaboration. These can be: supercomputing centers, commercial cloud infrastructures, resources provided on a volunteer basis.

The main processes that require mass data processing can be divided into two groups: those that involve transferring large amounts of data over the network and those that do not (Fig. 20.7). The process involving the transfer of a large amount of data is the process of real data reconstruction. The Monte Carlo simulation process can be attributed to a process that is not accompanied by a mass transfer of a large amount of data. To perform the data reconstruction process on distributed resources, they must be connected by communication channels with a sufficiently high throughput, taking into account the expected volumes, at a level of at least 100 gigabits per second. To work as a computing center of a distributed computing infrastructure and to participate in the processing of Monte Carlo simulation, the communication channel between the center and other participants must be at least 10 gigabits per second.

Currently, the most obvious centers for participation in the processing of data from the SPD experiment are the centers involved in the processing of data from the Large Hadron Collider, which have access to fast communication channels, and have a sufficient level of expertise and technical equipment: NRC “Kurchatov Institute”, PNPI, IHEP, SPbSU, MEPhI (Fig. 20.8). In addition, voluntary or temporary resources, such as external academic and commercial clouds and supercomputers, can participate in the Monte Carlo simulation process.

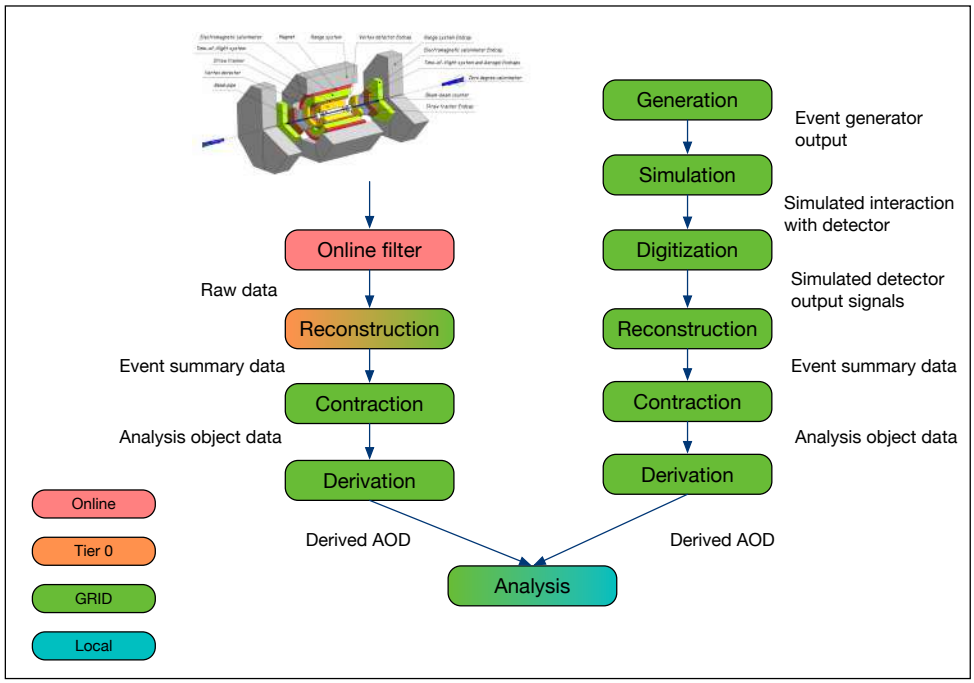

Figure 20.7: Data processing stages and their distribution over various types of computing resources.

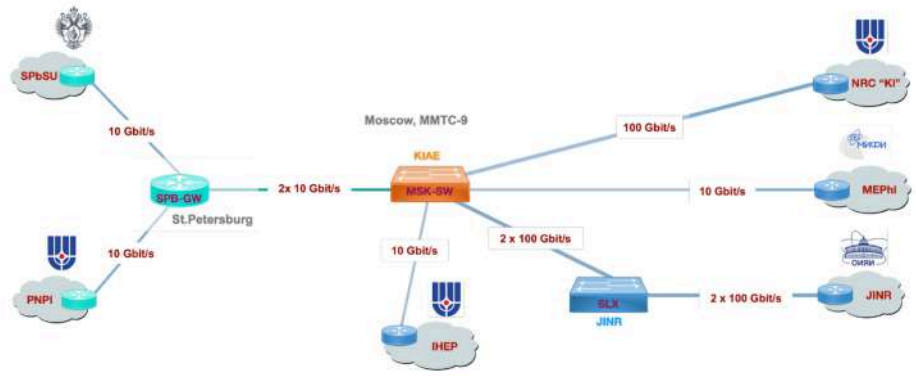

Figure 20.8: Existing Russian research centers, connected by high-speed network channels.

5.4 SPD production system

To ensure a high level of automation of data processing, it is necessary to use a production system. Such a system allows one to describe in the form of a task graph the process of certain processing of a given amount of data. Each task, which is a node of such a graph, is a set of jobs of the same type that process part of the initial data. Moving along the execution graph is possible only after the successful completion of the entire task.

The production system interacts with the distributed data management system and the workload management system, implementing a high-level control and abstracting from the architectures of computing and storage systems.

The task of the production system is to manage mass production of data sets, combined into tasks on the computing resources available to the experiment. The Monte Carlo simulation and the reconstruction of real data should be implementated within the production system. Each operation is usually splitted into separate processing steps, such as preparing data, processing individual jobs, merge results, deleting temporary files, checking intermediate and final results, and so on.

Since every physics experiment is unique, the SPD production system should be developed taking into account the specifics of the experiment. At the same time, keeping in mind the expected volumes of data, the production system must be based on the components that will ensure data processing on geographically distributed resources of various types. This implies both the delivery of jobs to remote computing nodes, and the relevant data management.

Such software components have already been developed by experiments at the LHC and are used both by them and by other scientific projects dealing with high-throughput data processing on geographically distributed computing resources of various types. These components include the PanDA workload management system and the Rucio distributed data management system. Each of these software products is used by various scientific experiments. Considering that these products are being developed by the ATLAS and CMS experiments at the LHC for processing data volumes comparable to SPD on the resources of the WLCG (Worldwide LHC Computing Grid) distributed infrastructure, we can count on their development in the future, sufficient for the implementation of the SPD project.

5.5 PanDA workload management system

Responsibilities of the PanDA (Production and Distributed Analysis system) workload management system include the delivery of jobs to the computing nodes of remote computing centers and control over their execution [128]. The system has a multicomponent architecture and allows organizing high-throughput computing, using heterogeneous computing resources, such as grid sites, cloud infrastructures, and high-performance systems. The PanDA system is widely used in scientific computing, usually in projects where it is required to manage the processing of a large number of simultaneously executing jobs by distributing them across a large number of data centers. PanDA allows one to distribute jobs across computing centers, finding the most suitable computing nodes based on a large set of metrics, such as resource requirements, current load on each of the computing centers, the presence or absence of the necessary data on it, the state of network connections, and so on. Within the PanDA system, it is possible to work not only with jobs, but also with tasks, which makes it possible to achieve better system scalability and ensure optimal loading of the experimental computing infrastructure. Deep integration of PanDA with the Rucio distributed data management system allows implementing of various work strategies: both delivery of tasks to data, located on remote storages, and delivery of data by the time processing starts at one of the data centers.

5.6 Rucio distributed data management system

Rucio distributed data management system [129] is a software platform that provides all the necessary functionality for organizing, managing and accessing data, hosted on heterogeneous, geographically distributed storage resources. Rucio is designed to manage billions of files and exabytes of data. For many scientific projects, data management is becoming an increasingly complex and complicated challenge. The number of data-intensive instruments generating unprecedented volumes of data is growing, and their surrounding workflows are becoming more complex. Their storage and computing resources are heterogeneous and can be distributed at numerous geographical locations, belonging to different administrative domains and organizations. These locations do not necessarily coincide with the places where data are produced, nor where data are stored, analyzed by researchers, or archived for safe long-term storage. Rucio has been built as a comprehensive solution for data organization, management, and access for scientific experiments, which incorporates the existing tools and makes it easy to interact with them. One of the guiding principles of Rucio is dataflow autonomy and automation, and its design is geared towards that goal.

5.7 Software distribution and deployment

CVMFS and docker-based containers will be used for the software distribution.

5.8 Databases

The central database is going to be established to keep and distribute the detector hardware configuration, run information, slow control data, and calibration constants. ClickHouse [130] is going to be used as a database engine.

5.9 Resource requirements

For the online filter we assume the CPU consumption of 1000 SPD events/core/second. This requires 3000 cores simultaneously for the fast tracking. Taking into account additional expenditures to the data unpacking and event unscrambling, and including a real efficiency of CPU, which will be lower than 100%, one derives the CPU resources for the online filter as 6000 CPU cores. This number sets the upper limit, and the required computing power may decrease substantially, if an efficient way to use GPU cores is implemented for the event filtration. As for the data storage, a high performance disk buffer of 2 PB is needed, capable of storing about one day's worth of data taking.

For the offline computing, the data storage is determined by the data rate after the online filter, or 4 PB/year of raw data. Besides that, we may expect the comparable amount of simulated data and estimate the long-term storage as 10 PB/year, assuming two cycles of data processing and possible optimization of the data format and data objects to be stored permanently. We assume that half of the annual data sample ($\sim$5 PB) is kept on the disk storage, and the rest is stored on tape. The CPU power, necessary to process the amount of data like this and to run Monte-Carlo simulation is estimated as many as 60000 CPU cores. The summary of the computing resources is given in Table. 20.2. The cost estimate is conservative and will be defined more exactly in the TDR, when detailed hardware solutions and their actual prices in the market will be considered.

The estimate above is made for the design luminosity of the NICA collider. For the low luminosity stage, all numbers will be one order of magnitude smaller.

The burden of the SPD computing system operation is a subject to sharing between the computing centers of the participating institutes.

Table 20.2: Required SPD computing resources

	CPU [cores]	Disk [PB]	Tape [PB]
Online filter	6000	2	none
Offline computing	60000	5	9 per year
Cost estimate [kUSD]	7000	8000	4500 per year

Chapter 21

Overall cost estimate

The estimated cost of the Spin Physics Detector at current prices for two stages of the project implementation is presented in Table 21.1. Estimates are rounded to one significant digit after the decimal point. The cost of the first stage is 43 M$, while the full setup in the most preferrable configuration is priced at 82.3 M$. This amount does not include possible R&D for the second stage of the project. Any expenses related to the development and construction of an infrastructure for polarized beams at NICA are also out of the scope of this estimation.

Table 21.1: Cost estimate of the SPD setup.

Subsystem	Option	Phase	Cost, M$
SPD setup	Vertex detector:		
	– DSSD	II	7.3
	– MAPS	II	13.5
	Micromegas Central Tracker	I	0.9
	Straw tracker	I+II	3.0
	PID system:		
	– TOF	II	2.0
	– Aerogel PID system	II	2.4
	ECAL		
	– Phantom	I	0.4
		I+II	9.4
	Range system	I+II	16.1
	ZDC	I+II	0.6
	BBC	I+II	0.5
	Magnetic system		
	Novosibirsk option	I+II	9.2
	JINR option	I+II	8.6
	& cryogenic infrastructure		
	Novosibirsk option	I+II	6.4
	JINR option	I+II	6.1
	Beam pipe		
	– Al	I	0.1
	– Be	II	0.4
General infrastructure		I	1.2
		I+II	1.7
Slow control system		I	1.0
		I+II	1.8
Data acquisition system		I	0.8
		I+II	1.9
Computing		I	5
		I+II	15*
	* + 4.5 M$ per year for tapes		
TOTAL COST	stage I		45.2
	stage I+II		84.8

Chapter 22

Summary

We have presented the technical design of the Spin Physics Detector at NICA, a sophisticated experimental apparatus for the study of the spin structure of the proton and deuteron, as well as fundamental properties of the strong interaction. The building of this detector and conducting research on it are included in the JINR long-term development plan. We realize that the construction of a detector on such a scale is a very challenging task, even considering the extensive experience of the SPD Collaboration's members. Nevertheless, we express our hope that we will be able to implement all our plans within the framework of international cooperation in a full-scale manner.

Bibliography

[1] V. M. Abazov et al. Conceptual design of the Spin Physics Detector. 1 2021, 2102.00442.

[2] A. Arbuzov et al. On the physics potential to study the gluon content of proton and deuteron at NICA SPD. *Prog. Part. Nucl. Phys.*, 119:103858, 2021, 2011.15005.

[3] V. V. Abramov et al. Possible Studies at the First Stage of the NICA Collider Operation with Polarized and Unpolarized Proton and Deuteron Beams. *Phys. Part. Nucl.*, 52(6):1044–1119, 2021, 2102.08477.

[4] Z. Igamkulov, M. Cruceru, A. B. Kurepin, A. G. Litvinenko, E. I. Litvinenko, and V. F. Peresedov. Luminosity Measurement and Control at NICA. *Phys. Part. Nucl. Lett.*, 16(6):744–753, 2019.

[5] V. M. Abazov, G. D. Alexeev, Yu. I. Davydov, V. L. Malyshev, V. V. Tokmenin, and A. A. Piskun. Comparative analysis of the performance characteristics of mini-drift tubes with different design. *Instruments and Experimental Techniques*, 53(3):356–361, May 2010.

[6] V. M. Abazov, G. D. Alexeev, Yu. I. Davydov, V. L. Malyshev, A. A. Piskun, and V. V. Tokmenin. Coordinate accuracy of mini-drift tubes in detection of an induced signal. *Instruments and Experimental Techniques*, 53(5):648–652, Sep 2010.

[7] PANDA Collaboration. Technical Design Report for the: PANDA Muon System (AntiProton Annihilations at Darmstadt). Strong Interaction Studies with Antiprotons `https://panda.gsi.de/publication/re-tdr-2012-003`. September 2012.

[8] V. M. Abazov et al. The Muon system of the run II D0 detector. *Nucl. Instrum. Meth.*, A552:372–398, 2005, physics/0503151.

[9] P. Abbon et al. The COMPASS experiment at CERN. *Nucl. Instrum. Meth.*, A577:455–518, 2007, hep-ex/0703049.

[10] G. D. Alekseev, M. A. Baturitsky, O. V. Dvornikov, A. I. Khokhlov, V. A. Mikhailov, I. A. Odnokloubov, and V. V. Tokmenin. The eight-channel ASIC bipolar transresistance amplifier D0M AMPL-8.3. *Nucl. Instrum. Meth.*, A462:494–505, 2001.

[11] G.D Alexeev, M.A Baturitsky, O.V Dvornikov, V.A Mikhailov, I.A Odnokloubov, and V.V Tokmenin. The eight-channel fast comparator IC. *Nucl. Instrum. Meth.*, A423(1):157 – 162, 1999.

[12] G. D. Alekseev, M. A. Baturitsky, O. V. Dvornikov, A. I. Khokhlov, V. A. Mikhailov, I. A. Odnokloubov, A. A. Shishkin, V. V. Tokmenin, and S. F. Zhirikov. The D0 forward angle muon system front-end electronics design. *Nucl. Instrum. Meth.*, A473:269–282, 2001.

[13] G.D. Alekseev, A. Maggiora, and N.I. Zhuravlev. Digital Front-end Electronics for COMPASS Muon-Wall 1 Detector. *JINR Preprint*, E13-2005-37, 2005.

[14] P. Bredy, F. P. Juster, B. Baudouy, L. Benkheira, and M. Cazanou. Experimental and theoretical study of a two phase helium high circulation loop. *AIP Conf. Proc.*, 823(1):496–503, 2006.

[15] N Dhanaraj, G Tatkowski, Y Huang, T M Page, M J Lamm, R L Schmitt, and T J Peterson. An analytical approach to designing a thermosiphon cooling system for large scale superconducting magnets. *IOP Conference Series: Materials Science and Engineering*, 101(1):012142, nov 2015.

[16] A.M. Baldin, N.N. Agapov, A. Averichev, A.M. Donyagin, E.I. D'yachkov, H.G. Khodzhibagiyan, A.D. Kovalenko, L.G. Makarov, E.A. Matyushevsky, and A.A. Smirnov. Superconducting fast cycling magnets of the nuclotron. *IEEE Transactions on Applied Superconductivity*, 5(2):875–877, 1995.

[17] Martin N. Wilson. *Superconducting Magnets*. Oxford Science Publications, 1983.

[18] H. G. Khodzhibagiyan et al. Superconducting Magnets for the NICA Accelerator Collider Complex. *IEEE Trans. Appl. Supercond.*, 24(3):4001304, 2014.

[19] The SPD proto collaboration. Conceptual design of the Spin Physics Detector.

[20] O.P. Gavrishchuk, V.E. Kovtun, and T.V. Malykhina. Simulation studies of the moliere radius for em calorimeter materials. *Problems of Atomic Science and Technology*, page 171–174, Dec 2021.

[21] O. P. Gavrischuk A. I. Maltsev V. V. Tereshenko V. N. Azorskyi, N. O. Graphov. Electromagnetic calorimeter for the spd experiment. *Physics of Particles and Nuclei*, 52:975, 2021.

[22] T.V. Malykhina O.P. Gavrishchuk, V.E. Kovtun. Simulation study of energy resolution of the electromagnetic shashlyk calorimeter for different of layers and absorber combinations. *East European Journal of Physics*, 3:73–80, 2020.

[23] p-Terphenil `http://omlc.ogi.edu/spectra/PhotochemCAD/html/003.html`.

[24] POPOP `http://omlc.ogi.edu/spectra/PhotochemCAD/html/077.html`.

[25] Kuraray page `http://kuraraypsf.jp/psf/ws.html`.

[26] IHEP page `http://exwww.ihep.su/scint/mold/product.htm`.

[27] IHEP page `http://www.newchemistry.ru/material.php?id=12`.

[28] Hamamatsu web page `https://www.hamamatsu.com/eu/en/product/optical-sensors/mppc/index.html`.

[29] AFI Electronics web page `https://afi.jinr.ru/ADC64`.

[30] HVSys web page `http://hvsys.ru/images/data/news/3_small_1368802865.pdf`.

[31] HVSys web page `http://hvsys.ru`.

[32] AFI Electronics `https://afi.jinr.ru`.

[33] Botan Wang, Xiaolong Chen, Yi Wang, Dong Han, Baohong Guo, and Yancheng Yu. The High-Rate Sealed MRPC to Promote Pollutant Exchange in Gas Gaps: Status on the Development and Observations. *Appl. Sciences*, 11(11):4722, 2021.

[34] A.N. Akindinov et al. Latest results on the performance of the multigap resistive plate chamber used for the ALICE TOF. *Nucl. Instrum. Meth. A*, 533:74–78, 2004.

[35] V. Ammosov et al. The HARP resistive plate chambers: Characteristics and physics performance. *Nucl. Instrum. Meth. A*, 602:639–643, 2009.

[36] The STAR TOF Collaboration, Proposal for a Large Area Time of Flight System for STAR, 2004.

[37] J. Velkovska et. al., Multi-gap Resistive Plate Chambers: Time-of-Flight system of the PHENIX high-pT Detector. Conceptual Design Report.

[38] A.Golovin et. al., Technical Design Report of the Time of Flight System (TOF-700) BM@N, 2017.

[39] Yi Wang and Yancheng Yu. Multigap Resistive Plate Chambers for Time of Flight Applications. *Appl. Sciences*, 11(1):111, 2020.

[40] Talk by E. Ladygin, S. Nagorniy, A. Semak `https://indico.jinr.ru/event/2616/contributions/15165/attachments/11660/19232/Semak_SPD_14.12.21.pdf`.

[41] B. Wang, D. Han, Y. Wang, X. L. Chen, and Y. Li. The CEE-eTOF wall constructed with new sealed MRPC. *JINST*, 15(08):C08022, 2020.

[42] Jinxin Liu, Lei Zhao, Liujiang Yan, Zhenyan Li, Shubin Liu, and Qi An. Design of a prototype readout electronics with a few picosecond time resolution for mrpc detectors. *Nuclear Instruments and Methods in Physics Research Section A: Accelerators, Spectrometers, Detectors and Associated Equipment*, 925:53–59, 2019.

[43] Jinhong Wang, Shubin Liu, Lei Zhao, Xueye Hu, and Qi An. The 10-ps multitime measurements averaging tdc implemented in an fpga. *IEEE Transactions on Nuclear Science*, 58(4):2011–2018, 2011.

[44] M. Cantin, M. Casse, L. Koch, R. Jouan, P. Mestreau, D. Roussel, C. Saclay, F. Bonnin, J. Moutel, and S. J. Teichner. Silica aerogels used as Cherenkov radiators. *Nucl. Instrum. Meth.*, 118:177–182, 1974.

[45] T. Sumiyoshi et al. Silica aerogel Cherenkov counter for the KEK B factory experiment. *Nucl. Instrum. Meth. A*, 433:385–391, 1999.

[46] V.V. Anashin et al. PEPAN v.44, (2013) 1263 (in Russian).

[47] I.V.Ovtin et al. "Aerogel Cherenkov Counters of the KEDR Detector", CERN-BINP Workshop for Young Scientists in e^+e^- Colliders 2016, Geneva; CERN-Proceedings-2017-001 (CERN, Geneva, 2017).

[48] T. Iijima et al. Aerogel Cherenkov counter for the BELLE detector. *Nucl. Instrum. Meth. A*, 453:321–325, 2000.

[49] A. Abashian et al. The Belle Detector. *Nucl. Instrum. Meth. A*, 479:117–232, 2002.

[50] Y. Allkofer, Claude Amsler, S. Horikawa, Christian Regenfus, and J. Rochet. A new aerogel Cherenkov detector for DIRAC-II. *Nucl. Instrum. Meth. A*, 595:84–87, 2008.

[51] A. Sergi. NA62 Spectrometer: A Low Mass Straw Tracker. *Phys. Procedia*, 37:530–534, 2012.

[52] H. Nishiguchi et al. Development of an extremely thin-wall straw tracker operational in vacuum – The COMET straw tracker system. *Nucl. Instrum. Meth. A*, 845:269–272, 2017.

[53] M. Anelli et al. A facility to Search for Hidden Particles (SHiP) at the CERN SPS. 4 2015, 1504.04956.

[54] MyeongJae Lee. The Straw-tube Tracker for the Mu2e Experiment. *Nucl. Part. Phys. Proc.*, 273-275:2530–2532, 2016.

[55] V.N. Bychkov et al. Construction and manufacture of large size straw-chambers of the COMPASS spectrometer tracking system. *Part. Nucl. Lett.*, 111:64–73, 2002.

[56] K. Platzer, W. Dunnweber, N. Dedek, M. Faessler, R. Geyer, C. Ilgner, V. Peshekhonov, and H. Wellenstein. Mapping the large area straw detectors of the COMPASS experiment with X-rays. *IEEE Trans. Nucl. Sci.*, 52:793–798, 2005.

[57] V.Yu. Volkov, P.V. Volkov, T.L. Enik, G.D. Kekelidze, V.A. Kramarenko, V.M. Lysan, D.V. Peshekhonov, A.A. Solin, and A.V. Solin. Straw Chambers for the NA64 Experiment. *Phys. Part. Nucl. Lett.*, 16(6):847–858, 2019.

[58] Eduardo Cortina Gil et al. The Beam and detector of the NA62 experiment at CERN. *JINST*, 12(05):P05025, 2017, 1703.08501.

[59] D. Moraes, W. Bonivento, Nicolas Pelloux, and W. Riegler. The CARIOCA Front End Chip for the LHCb muon chambers. 1 2003.

[60] R. Veenhof. Garfield, a drift chamber simulation program. *Conf. Proc. C*, 9306149:66–71, 1993.

[61] R. Veenhof. GARFIELD, recent developments. *Nucl. Instrum. Meth. A*, 419:726–730, 1998.

[62] F Hahn, F Ambrosino, A Ceccucci, H Danielsson, N Doble, F Fantechi, A Kluge, C Lazzeroni, M Lenti, G Ruggiero, M Sozzi, P Valente, and R Wanke. NA62: Technical Design Document. Technical report, CERN, Geneva, Dec 2010.

[63] `https://garfieldpp.web.cern.ch/garfieldpp/`.

[64] LTspice Simulator `https://www.analog.com/ru/design-center/design-tools-and-calculators/ltspice-simulator.html`.

[65] D. Pfeiffer et al. Rate-capability of the VMM3a Front End in the RD51 Scalable Readout System. 9 2021, 2109.10287.

[66] Hamamatsu S12572-010P Datasheet.

[67] `http://hvsys.ru/images/data/news/2_small_1368802824.pdf`.

[68] A.V.Tishevsky et al., talk at ICAPP2020, submitted to J.Phys.:Conf.Ser.

[69] Alexander Isupov. VME–based DAQ system for the Deuteron Spin Structure setup at the Nuclotron internal target station. *EPJ Web Conf.*, 204:10003, 2019.

[70] I. Alekseev et al. DANSS: Detector of the reactor AntiNeutrino based on Solid Scintillator. *JINST*, 11(11):P11011, 2016, 1606.02896.

[71] A.V. Tishevskiy et al. Scintillation detector prototype for Beam-Beam Counter at NICA SPD, Proceedings of the LXXI-st International conference "NUCLEUS-2021. 2021.

[72] L. Rossi, P. Fischer, T. Rohe, and N. Wermes. *Pixel Detectors: From Fundamentals to Applications*. Particle Acceleration and Detection. Springer-Verlag, Berlin, 2006.

[73] B Abelev et al. Technical Design Report for the Upgrade of the ALICE Inner Tracking System. *J. Phys. G*, 41:087002, 2014.

[74] M. Mager. ALPIDE, the Monolithic Active Pixel Sensor for the ALICE ITS upgrade. *Nucl. Instrum. Meth. A*, 824:434–438, 2016.

[75] V. I. Zherebchevsky, V. P. Kondratiev, E. B. Krymov, T. V. Lazareva, N. A. Maltsev, A. O. Merzlaya, D. G. Nesterov, N. A. Prokofyev, and G. A. Feofilov. Investigations of the new generation pixel detectors for ALICE experiment at LHC. *Bull. Russ. Acad. Sci. Phys.*, 80(8):953–958, 2016.

[76] V. I. Zherebchevsky, V. P. Kondratiev, V. V. Vechernin, and S. N. Igolkin. The concept of the MPD vertex detector for the detection of rare events in Au+Au collisions at the NICA collider. *Nucl. Instrum. Meth. A*, 985:164668, 2021.

[77] L. Musa and S. Beole. ALICE tracks new territory. *CERN Courier*, June, 2021.

[78] Felix Reidt. *Studies for the ALICE Inner Tracking System Upgrade*. PhD thesis, Heidelberg U., 2 2016.

[79] P. Yang et al. Low-power priority Address-Encoder and Reset-Decoder data-driven readout for Monolithic Active Pixel Sensors for tracker system. *Nucl. Instrum. Meth. A*, 785:61–69, 2015.

[80] ARCADIA project (INFN) `https://www.pg.infn.it/en/technological-research/arcadia-eng/`.

[81] Coralie Neubüser, T. Corradino, G-F. Dalla Betta, L. De Cilladi, and Lucio Pancheri. Sensor Design Optimization of Innovative Low-Power, Large Area FD-MAPS for HEP and Applied Science. *Front. in Phys.*, 9:625401, 2021, 2011.09723.

[82] V. I. Zherebchevsky et al. Experimental investigation of new ultra-lightweight support and cooling structures for the new Inner Tracking System of the ALICE Detector. *JINST*, 13(08):T08003, 2018.

[83] V. I. Zherebchevsky, S. N. Igolkin, E. B. Krymov, N. A. Maltsev, N. A. Makarov, and G. A. Feofilov. Extra lightweight mechanical support structures with the integrated cooling system for a new generation of vertex detectors. *Instrum. Exp. Tech.*, 57(3):356–360, 2014.

[84] A. Acker et al. The CLAS12 Micromegas Vertex Tracker. *Nucl. Instrum. Meth. A*, 957:163423, 2020.

[85] Y. Giomataris, Ph. Rebourgeard, J.P. Robert, and G. Charpak. Micromegas: a high-granularity position-sensitive gaseous detector for high particle-flux environments. *Nuclear Instruments and Methods in Physics Research Section A: Accelerators, Spectrometers, Detectors and Associated Equipment*, 376(1):29–35, 1996.

[86] P. Abbon et al. The COMPASS experiment at CERN. *Nucl. Instrum. Meth. A*, 577:455–518, 2007, hep-ex/0703049.

[87] I. Giomataris, R. De Oliveira, S. Andriamonje, S. Aune, G. Charpak, P. Colas, A. Giganon, Ph. Rebourgeard, and P. Salin. Micromegas in a bulk. *Nucl. Instrum. Meth. A*, 560:405–408, 2006, physics/0501003.

[88] P. Konczykowski et al. Measurements of the Lorentz angle with a Micromegas detector in high transverse magnetic fields. *Nucl. Instrum. Meth. A*, 612:274–277, 2010.

[89] Gabriel Charles. *Mise au point de détecteurs micromegas pour le spectromètre CLAS12 au laboratoire Jefferson*. PhD thesis, U. Paris-Sud 11, Dept. Phys., Orsay, 2013.

[90] C. Adloff et al. Construction and Commissioning of the CALICE Analog Hadron Calorimeter Prototype. *JINST*, 5:P05004, 2010, 1003.2662.

[91] Scintillation materials: manufacturing and treatment, by UNIPLAST, Ltd., Vladimir, Russia, `http://www.uniplast-vladimir.com/scintillation`.

[92] I.G. Alekseev et al. Digitization of Waveforms from Photosensors of the DANSS Detector. *Instruments and Experimental Techniques*, 61:349–354, 2018.

[93] S. Agostinelli et al. GEANT4–a simulation toolkit. *Nucl. Instrum. Meth. A*, 506:250–303, 2003.

[94] John Allison et al. Geant4 developments and applications. *IEEE Trans. Nucl. Sci.*, 53:270, 2006.

[95] J. Allison et al. Recent developments in Geant4. *Nucl. Instrum. Meth. A*, 835:186–225, 2016.

[96] Vladikavkaz Technological Center BASPIK web page `https://baspik.com`.

[97] A. N. Sissakian, A. S. Sorin, V. D. Kekelidze, et al. The MultiPurpose Detector – MPD to study Heavy Ion Collisions at NICA (Conceptual Design Report), Dubna, (2014). 2014.

[98] M. E. Dinardo. The pixel detector for the CMS phase-II upgrade. *JINST*, 10(04):C04019, 2015.

[99] G. Timoshenko and M. Paraipan. Formation of secondary radiation fields at NICA. *Nucl. Instrum. Meth.*, B267:2866–2869, 2009.

[100] I.S. Gordeev, A.R. Krylov, M. Paraipan, G.N. Timoshenko, Justification of radiation safety in the operation of the NICA complex, 2019 (in Russian).

[101] V.N. Buchnev, S.V. Kulikov, V.Yu. Schegolev, Regulation no. IP on the procedure of work in the fields of ionizing radiation at JINR, 2001 (in Russian).

[102] NICA project documentation, ZAO "Kometa", Vol 5.7.2, 2019 (in Russian).

[103] B.M. Michelson. Event-Driven Architecture Overview. Patricia Seybold Group / Business-Driven ArchitectureSM, February 2, pp. 1–8 (2006).

[104] Etschberger, K. IXXAT Automation GmbH. Controller Area Network (CAN) Basics, Protocols, Chips and Applications. IXXAT Press, 2001. ISBN3-00-007376-0.

[105] J. Chaize, A. Götz,W. Klotz, J. Meyer,M. Perez, E. Taurel, and P. Verdier,. TANGO, 8th International Conference on Accelerator & Large Experimental Physics Control Systems, 2001, San Jose, California (JACoW, 2001).

[106] E.V. Gorbachev, V.A. Andreev, A.E. Kirichenko, D.V. Monakhov, S.V. Romanov, T.V. Rukoyatkina, G.S. Sedykh, and V.I. Volkov. The Nuclotron and Nica control system development status. *Phys. Part. Nucl. Lett.*, 13(5):573–578, 2016.

[107] WinCC-OA: Introduction for Newcomers `https://lhcb-online.web.cern.ch/ecs/PVSSIntro.htm`.

[108] H Boterenbrood, H J Burckhart, J Cook, V Filimonov, Björn I Hallgren, and F Varela. Vertical Slice of the ATLAS Detector Control System. 2001.

[109] Ph. Abbon et al. The COMPASS Setup for Physics with Hadron Beams. *Nucl. Instrum. Meth. A*, 779:69–115, 2015, 1410.1797.

[110] Dmitriy Baranov, Sergey Mitsyn, Pavel Goncharov, and Gennady Ososkov. The Particle Track Reconstruction based on deep Neural networks. *EPJ Web Conf.*, 214:06018, 2019, 1812.03859.

[111] G. Ososkov et al. Tracking on the BESIII CGEM inner detector using deep learning. *Computer Research and Modeling*, 10:1–24, 20.

[112] P. Goncharov et al. BM@N Tracking with Novel Deep Learning Methods. *EPJ Web of Conferences*, 226:03009, 2020.

[113] E. Shchavelev et al. Global strategy of tracking on the basis of graph neural network for BES-III CGEM inner detector. *AIP Conference Proceedings*, 2377:060001, 2021.

[114] A. Nikolskaia et al. Local strategy of particle tracking with TrackNETv2 on the BES-III CGEM inner detector. *AIP Conference Proceedings*, 2377:060004, 2021.

[115] P. Goncharov et al. Ariadne: PyTorch library for particle track reconstruction using deep learning. *AIP Conference Proceedings*, 2377:040004, 2021.

[116] M. Al-Turany, D. Bertini, R. Karabowicz, D. Kresan, P. Malzacher, T. Stockmanns, and F. Uhlig. The FairRoot framework. *J. Phys. Conf. Ser.*, 396:022001, 2012.

[117] G. Barrand et al. GAUDI - A software architecture and framework for building HEP data processing applications. *Comput. Phys. Commun.*, 140:45–55, 2001.

[118] Merkt, Sebastian Andreas, Bianchi, Riccardo Maria, Boudreau, Joseph, Gessinger-Befurt, Paul, Moyse, Edward, Salzburger, Andreas, and Tsulaia, Vakhtang. Going standalone and platform-independent, an example from recent work on the atlas detector description and interactive data visualization. *EPJ Web Conf.*, 214:02035, 2019.

[119] Torbjörn Sjostrand, Stefan Ask, Jesper R. Christiansen, Richard Corke, Nishita Desai, Philip Ilten, Stephen Mrenna, Stefan Prestel, Christine O. Rasmussen, and Peter Z. Skands. An Introduction to PYTHIA 8.2. *Comput. Phys. Commun.*, 191:159–177, 2015, 1410.3012.

[120] Bo Andersson, G. Gustafson, and B. Nilsson-Almqvist. A Model for Low p(t) Hadronic Reactions, with Generalizations to Hadron - Nucleus and Nucleus-Nucleus Collisions. *Nucl. Phys. B*, 281:289–309, 1987.

[121] Bo Nilsson-Almqvist and Evert Stenlund. Interactions Between Hadrons and Nuclei: The Lund Monte Carlo, Fritiof Version 1.6. *Comput. Phys. Commun.*, 43:387, 1987.

[122] S.A. Bass et al. Microscopic models for ultrarelativistic heavy ion collisions. *Prog. Part. Nucl. Phys.*, 41:255–369, 1998, nucl-th/9803035.

[123] M. Bleicher et al. Relativistic hadron hadron collisions in the ultrarelativistic quantum molecular dynamics model. *J. Phys. G*, 25:1859–1896, 1999, hep-ph/9909407.

[124] Johannes Rauch and Tobias Schlüter. GENFIT — a Generic Track-Fitting Toolkit. *J. Phys. Conf. Ser.*, 608(1):012042, 2015, 1410.3698.

[125] S. Gorbunov and I. Kisel. Reconstruction of decayed particles based on the kalman filter. Technical Report CBM-SOFT-note-2007-003, CBM Collaboration, 2007.

[126] F. Stagni, A. Tsaregorodtsev, L. Arrabito, A. Sailer, T. Hara, and X. Zhang. DIRAC in Large Particle Physics Experiments. *J. Phys. Conf. Ser.*, 898(9):092020, 2017.

[127] Offline Framework for the SPD experiment `https://git.jinr.ru/nica/spdroot`.

[128] Fernando Barreiro Megino et al. PanDA: Evolution and Recent Trends in LHC Computing. *Procedia Comput. Sci.*, 66:439–447, 2015.

[129] M. Barisits, T. Beermann, F. Berghaus, et al. Rucio: Scientific data management. *Comput. Softw. Big Sci.*, 3:11, 2019.

[130] Clickhouse inc.